SOLUTION-PHASE AND BIOPHYSICAL CHARACTERIZATION OF SEQEUENCE-DEFINED OLIGOTHIOETHERAMIDES

A Dissertation

Presented to the Faculty of the Graduate School

of Cornell University

In Partial Fulfillment of the Requirements for the Degree of

Doctor of Philosophy

by

Joseph Scott Brown

May 2019

Solution-phase and biophysical characterization of sequence-defined oligothioetheramides

Joseph Scott Brown, Ph. D.
Cornell University, 2019

ABSTRACT

Nature ubiquitously utilizes precise chemical arrangement to create and tune advanced structures and interactions. Within synthetic and natural scaffolds, this arrangement can often be read as a "sequence," which creates particular functions and/or phenotypes. Much research has sought to understand chemical sequences to guide the design of molecules and materials for therapeutic benefit. Examples and additional background are discussed in Chapter 1. In this work, I have explored a new class of sequence-defined polymers called oligothioetheramides (oligoTEAs) described in Chapter 2 in search of sequence-structure-function relationships by employing solution-phase and biophysical characterization. In Chapter 3, we demonstrate the challenging solution-phase structural characterization of a flexible sulfonated oligoTEA, utilizing a range of techniques including variable temperature pulse field gradient (PFG) NMR, double electron−electron resonance (DEER), molecular dynamics (MD) simulations, as well as the combination of PFG NMR and DEER within Stokes−Einstein−Sutherland diffusion theory.

I apply these techniques along with biophysical characterization toward a specific class of antibacterial oligoTEAs to evaluate their potential as antibiotics. Motivated by the need to new antibiotic development, these oligoTEAs are designed as

membrane-targeting AMP mimetics, featuring cationic and hydrophobic groups to potently and selectively disrupt bacterial membranes. However, this physical design has struggled to guide broad success for AMPs *in vivo*. Thus, we have investigated additional properties for optimization of these antimicrobials. We completed solution-phase characterization including small- and wide-angle x-ray scattering (SAXS/WAXS), as well as fluorescence microscopy and surface plasmon resonance (SPR), both with Staphylococcus aureus mimetic membranes.

In Chapter 4, I have examined the characterization a pair of constitutional oligoTEA isomers that show a unique ~ 10-fold difference in antibacterial potency. In Chapter 5, I present the characterization of oligoTEAs with different cationic groups and with hydrophobic backbone sequences. Across all studies, oligoTEAs direct the formation of multimeric lipid aggregates that correlates with biological activity and helps establish a framework for the kinetic mechanism of action. Thus, revealing new parameters for antimicrobial optimization. Overall, this work highlights the importance of sequence definition and biophysical characterization for the design of new membrane-targeting antibiotics.

BIOGRAPHICAL SKETCH

Joseph Scott Brown was born in Pilot Mountain, North Carolina in July of 1991. He attended the North Carolina School of Science and Mathematics and graduated in 2009. Joseph had broad interests in focusing his capabilities in organic chemistry for the improvement of medical care, the process of drug discovery, the relationship between science and society, and not least of all, music. He then attended North Carolina State University in Chemical Engineering to maintain a focus on the application of chemistry and earned his Bachelor of Science as a Valedictorian. Afterward, he attended graduate school to obtain his Doctorate of Philosophy at Cornell University in Chemical Engineering under the supervision of Professor Christopher A. Alabi.

ACKNOWLEDGEMENTS

This work would not be complete without thanking the support and help I have generously received throughout my time at Cornell. I consider myself very fortunate and lucky to have such people support me along my journey in graduate school.

First and foremost, I would like to thank my advisor Professor Chris Alabi for his guidance, support, enthusiasm, dedication, and constructive criticism through the years, which has shaped both me and my work for the better. I wish him and the lab nothing but the best in their future directions. I would also like to thank my special committee: Professor Susan Daniel for her unwavering support, enthusiasm, candor, and time she has shared so willingly over the years; Professor Uli Wiesner for his insight, constructive criticism, and support that has improved my work greatly; and Professor Claude Cohen, for kindly sharing his time, support, broad perspective to the project. Thank you all.

I must also thank my outstanding labmates in the Alabi group, both former and present for listening patiently and giving support to my work as I have struggled. I thank all of my undergraduate mentees through the years, especially Andrew Cosachov and Grace He for working with me during difficult times before my project was established. I thank Professor Mintu Porel for your unbridled happiness you brought to lab; Dr. Sudipta Biswas for your time and kind support; Michelle Sorkin for your patience and focus on safety and outreach; Meghan O'Leary for the energy, spirit, and enthusiasm you have brought to lab; Dr. Emily Hoff for your friendship, kind support, and time; Christine

Artim for your hard-work with numerous bacterial assays and distinct candor over the years; Ngoc Phan for your support and camaraderie in lab and the office over the years; Dana Thornlow for the times we have shared in and more importantly out of lab and kind support; and Josh Walker for your candor and camaraderie as one of the founding members of the Alabi lab along with Dana and Mintu.

I must also thank my colleagues in the department for your friendship and time outside of work, enjoying and experiencing Ithaca, which greatly added to my time at Cornell: Winston Black, Arna Pálsdóttir, Morgan Ludwicki, Jon Ludwicki, Dr. Andrew Shah, Dr. Yaset Acevedo, Carolyn Shurer, Dr. Lillian Johnson, Colleen Lawlor, Andrew Ruttinger, Alex Warren, Paxton Thedford, Andy Sanchez, Monet Roberts, and Stephanie Palcich for her outstanding administrative role. Outside of the department: Dr. Alise Muok.

I also thank my friends from the Big Red Barn for providing perspective, friendship, camaraderie, with drinks between. Kris Corda, Irene del Real, Chris Furman, Andrew Harding, Franscisco Klaassen, Sander Oosterom, Erin Routon, Yagna Chowdhuri, Dr. Ruth Mullett, Kyle Murray, and many others.

I am very thankful to have had the opportunity to serve as Co-Founder and Executive Producer of Science Blender, a podcast that blends a person with their science. I grateful for Kevin Weyant for his dedication to the soul of the podcast, outstanding co-hosting skills, time, dedication, focus on story-telling, and support through the whole process. I

thank Aravind Natarajan for making it all possible and his enthusiasm. Charlie Hienke for his excellent co-hosting skills, enthusiasm, and dedication to detail. I also thank Professor Susan Daniel again for her outspoken support, along with Professor Matt DeLisa. Professor Abraham Stroock for his time, candor, leadership, and kind support as the podcast has grown.

I would also like to thank those that are closest to me in life. I am very thankful for my partner Laura Sinclair for her love and support through my challenges and disappointments in graduate school, but also for the times we have relaxed and celebrated our successes. I am incredibly thankful of my parents, Charlie and Bonnie, and my family April, Brandon, David, Tabetha, Michael, and Nicole, as well as all six of my nephews and nieces for their unwavering love, inspiration, and constant support throughout my struggles and successes in graduate school and in life.

Table of Contents

List of Figures

List of Equations

List of Tables

Chapter 1 : Introduction to Sequence-defined Materials

Acknowledgements

Part of this this chapter has been adapted with permission from M. Porel, J. S. Brown, and C. A. Alabi, *Synlett* **2015**, 26 (5), 565-571. Copyright © 2015 Georg Thieme Verlag Stuttgart (License #4518230433130). Part of this chapter has been adapted with permission from J. S. Brown; Y. M. Acevedo; G. D. He; J. H. Freed; P. Clancy; C. A. Alabi, *Macromolecules* **2017**, 50 (21), 8731–8738. Copyright © 2017 American Chemical Society.

Motivation from Nature

Nature utilizes precise chemical arrangement to create and tune advanced structures and interactions. Molecular forces of hydrogen bonding, hydrophobicity, electrostatic charge, and many others come together to create all necessary pieces for life: sensitive and complex stimuli-response, information management, growth, homeostasis, and reproduction. Thus, much work has been devoted to understand the chemical "sequence" or molecular basis for the structures that create particular functions and/or phenotypes, often including the processes of macromolecular binding and target recognition. With these understandings, research continues toward the design of molecules or materials to interact with biological systems to provide therapeutic benefit and repair diseased states of health.

The use of sequence to build structure

Examples of molecular engineering in Nature are inspiring, motivating the development of synthetic scaffolds and training observant scientists to understand and speak a natural chemical "language." Take for example the peptide scaffold. Peptides and many other evolutionarily optimized structures frequently utilize hydrogen bonding to develop structure and subsequently functional states.[1] Hydrogen bonding is a shorter-range molecular force, limited to specific participating atoms. Peptides make use of the hydrogen bonding of their secondary amides in a truly elegant way, where the amino acid backbone is the main mode of structural development.

For peptides, the sequence of amino acids affects the resulting structure (α-helix, β-sheet, etc), but the formed structures are robust and somewhat independent of sequence to enable tuning of the final functionality of the structure.[2] First hypothesized by William Astbury in the 1930s and fully described by Linus Pauling, Robert Corey, and Herman Branson in 1951,[3,4] the α-helix structure was slowly understood to be a universal part of protein structure, still allowing a significant range in function. These α-helices and similar helical structures (3_{10}-helix) are one of the most common transmembrane motifs,[5,6] enabling signal transduction (e.g., A_{2A} Adenosine receptor,[7] see Figure 1). With a similar sequence to impart basicity and hydrophobicity, the α-helix also participates as a membrane penetrant (e.g., melittin,[8] see Figure 1). However, other α-helices are capable of interacting and regulating very hydrophilic structures including DNA (e.g., Max transcription factor,[9] see Figure 1). All of this demonstrates the versatility of peptides as a model sequence-defined material, able to prepare diverse structures that predicate function.

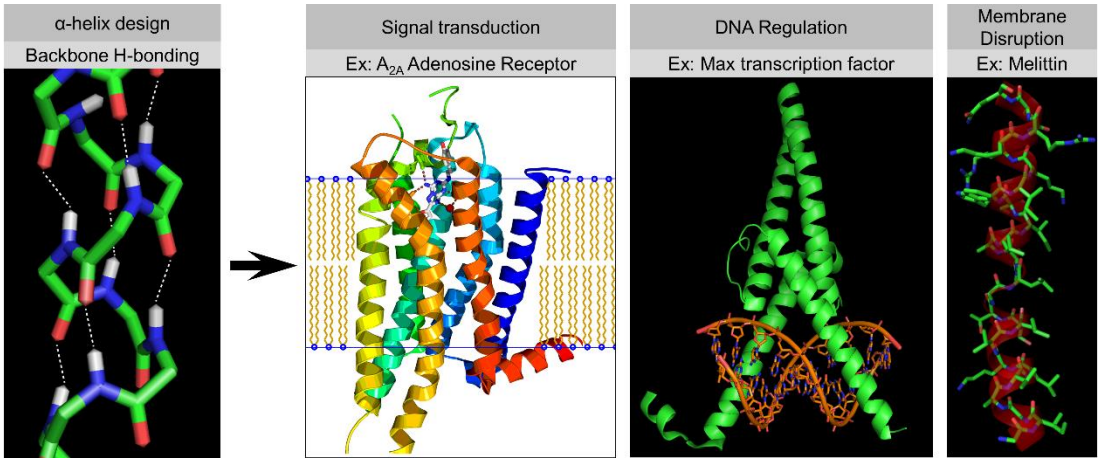

Figure 1-1: *Peptides as model scaffold of sequence-defined material*
The amino acid backbone of peptides naturally forms structures including the α-helix to enable a wide variety of functions, which are ultimately defined by the exact sequence. ***(Left)*** *White dotted lines highlight the hydrogen bonding in the peptide backbone of the α-helix. Originally sourced from the RCSB Protein Data Bank (ID: 2NRL), with attribution to E.R. Schreiter et al., Journal of Biological Chemistry 2007, 282 (27) 19773-19780*[10] ***(Middle left)*** *The alpha helix enables cellular signal transduction in the A_{2A} adenosine receptor,*[7] *adapted with permission from V. Jaakola et al., Science 2008, 322 (5905) 1211-1217. Copyright © 2008 American Association for the Advancement of Science (License #4513170763724).* ***(Middle right)*** *The alpha-helix also enables transcription regulation in the Max transcription factor,*[9] *adapted with permission from P Brownlie et al., Structure 1997, 5 (4) 509-520 Copyright © 1997 Elsevier (License #4511421202898).* ***(Right)*** *The alpha-helix also enables stochastic membrane disruption,*[8] *Originally sourced from the RCSB Protein Data Bank (ID: 2MLT), with attribution to M. Gribskov, L. Wesson, and D. Eisenberg (unpublished work, deposition version 1.3, 2011).*

Structure: ordered or disordered?

While structured materials are commonly understood and recognizable, ordered molecular conformation is not a prerequisite for function. Indeed, recent understanding of intrinsically disordered domains in proteins and peptides has challenged the importance of a typical fixed three-dimensional structure (e.g lock-and-key mechanism).[11] Just under half (~44%) of the human proteome contains intrinsically

disordered domains of 30 amino acids or longer, many with no currently understood function.[12] Of those that are understood, many disordered domains play critical roles in protein-protein interactions, substrate-ligand binding, the arrangement of protein functional states, and binding to various nucleic acids (DNAs and RNAs). For chemists and others focusing on sequence-defined materials, this demonstrates i) the daunting challenge to locate and evolve toward functional sequence space, ii) our underestimation of dynamic allostery, iii) the functional advantage of transient and induced binding fits,[13] and iv) Nature's evolutionary harmony with entropy.[12,14,15] Fortunately, the tools and lessons in structural biology are available for researchers working and developing sequence-defined materials. The techniques and findings can be co-opted to characterize disordered materials to enable optimization, track progress toward structured materials, and understand the function of disordered materials. Several common methods include nuclear magnetic resonance (NMR), small- and/or wide-angle x-ray scattering (SAXS/WAXS), pulsed electron paramagnetic resonance (EPR), and molecular simulation.[16] A brief review of methods is included in Chapter 3 (see Solution-phase characterization of flexible macromolecules). Overall, structural biology highlights that it should be no surprise that dynamic disorder materials can have distinct functions, but with dynamic structures, the development of sequence-structure-function relationships can also be challenging.[14,17]

The quest to harness sequence-definition for therapeutic use

Sequence-definition as a convergence of effort and properties

With such a precedent set by Nature, scientists have long sought to utilize precise chemical arrangement to specifically direct interactions within natural systems. Generally speaking, sequence-defined materials can be described from the viewpoint of three major fields of chemistries: i) small-molecule chemistry, ii) synthesis of naturally existing scaffolds, and iii) polymer synthesis.

First, small-molecule drug discovery has sought to apply chemistry for the development of therapeutics, gathering several lessons along the way for nearly a century. Most modern medicines are small-molecules, meaning substantial improvements in quality and length of life are owed to their development. While some lessons for small-molecules are not as applicable (e.g. Lipinski's rules),[18,19] sequence-defined materials seek to have similar levels of synthetic diversity and information density as small molecules. Moreover, sequence-defined materials can be utilized for the delivery or controlled release of small-molecule therapeutics in either a conjugates or other biomaterials.[20–22]

Second, the reproduction and engineering of naturally-existing scaffolds, often called "biologics," has seen ever-growing attention primarily due to its high degree of specificity within biological systems.[23] Protein and peptides comprise one of the largest classes of biologics, frequently demonstrating a near consistent level of synthetic diversity based on the number of available amino acid functionalities. However, even for only of α-amino acids, non-natural monomers has expanded synthetic capability well beyond the 20 common amino acids to include abiotic, engineered, and/or biosynthetic

amino acids.[24–26] While the capability of peptide synthesizers continues to grow,[27] protein engineering and expression of bacterial or mammalian cells is usually required for the production of very large proteins including monoclonal antibodies or full proteins (e.g. insulin).[28,29] Overall, these naturally-existing scaffolds provide a significant density of chemical and structural information, across a variety of sizes. But ultimately, they still are limited in terms of absolute synthetic diversity that small-molecules or synthetic sequence-defined systems could provide.

Third, sequence-defined polymers evolved from polymer chemistry make up one of the most diverse sets of sequence-defined materials. Precise sequence-definition is a natural result of advancements in polymer chemistry, which has always sought to combine multiple units or monomers in a polymer.[22] Advancements in polymer chemistry over the years have focused on precision, especially with regard to their dispersity (*Đ*). Most of all, sequence-defined polymers are not restricted to specific chemistries or scaffolds. Thus, polymer chemistry has broadened from step-growth methods that provided bulk plastic materials to precise chain-growth polymerizations, multi-step polymerizations, and iterative assembly of monomer units. Similar to polypeptides, sequence-defined polymers can span a large range of sizes. While ever-increasing, the traditional chemical and/or structural information density of polymers is lower than small-molecules and polypeptides.

Together, these three fields paint differing perspectives on the developing field of sequence-defined materials for therapeutic use. Generally speaking, they each come from differing levels of three core properties of chemical information density, size, and

synthetic diversity (Figure 1-2). Thus, one can conclude that an ideal sequence-defined scaffold should combine and improve on the standard set by these model materials.

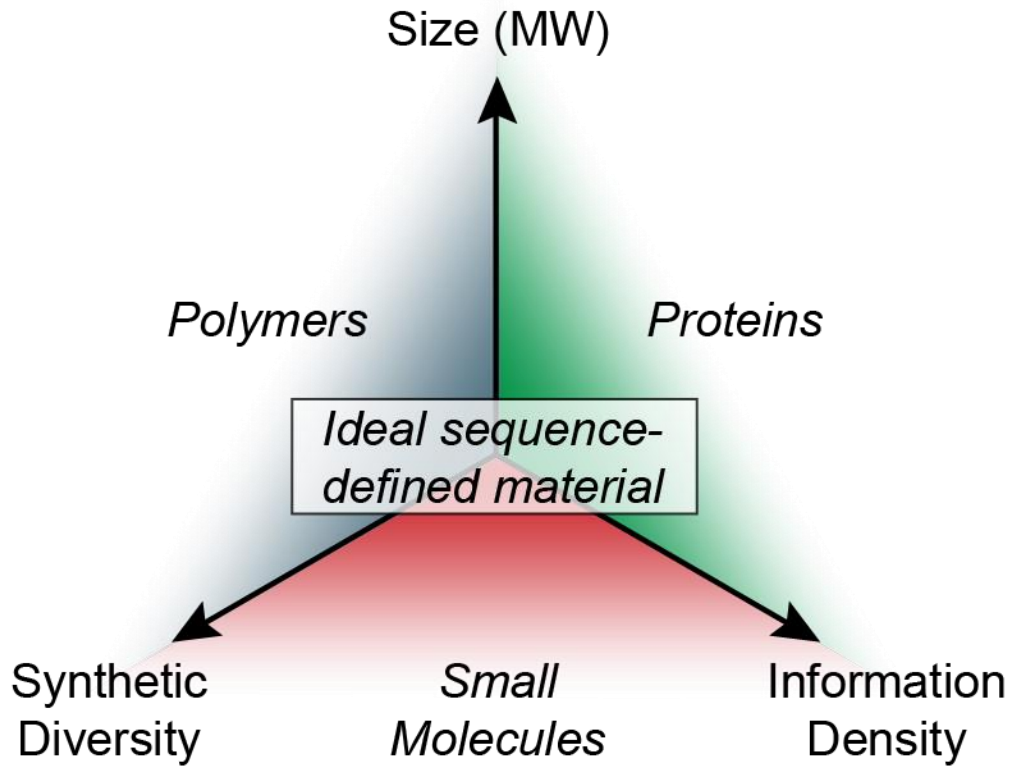

Figure 1-2: *Precedent set by three major fields for sequence-defined materials Individual efforts in these fields all seek to provide an ideal sequence-defined material with varied levels of size (molecular weight), synthetic diversity, and chemical information density.*

Small-molecule chemistry: The veteran in the background

Over the past century, small-molecules chemistries have provided the majority of therapeutic drug development, realizing unique modes of chemical communication within biological systems. The dominance of small-molecule drugs could possibly be attributed to their size, ease of characterization and purification, and the evolution of synthetic capabilities.[30] For example, well before modern-day analytical techniques of NMR became common, chemists were still able to unambiguously elucidate the

structure of morphine in 1923 and achieve its total synthesis in 1955.[31,32] In current day, improvements to small-molecule drug discovery continues with high-throughput screening and characterization, fragment-based discovery,[33] and the advancement of structured molecules (e.g. macrocycles).[34–37] Even with development of biologics and biomaterials, small-molecule drug discovery continues to have a strong outlook and role in therapeutic development, especially with the rising aid of automated synthesizers and applications of computational design algorithms (e.g., machine learning, artificial intelligence).[38–40] While important to therapeutic development, small molecules are not immediately considered "sequence-defined" materials, due to the fact that their structures cannot typically be encoded into a "sequence" of monomer units. However, more recent developments in small-molecule drug discovery frequently focus on specific targets and interactions similar to the targets of biologics and sequence-defined polymers (e.g. RNA,[40–42] and protein-protein interactions[43]). In some ways, small-molecules represent the spirit behind some of the advancements of sequence-defined materials as therapeutics. Thus, researchers should take note of the lessons and techniques that can apply toward sequence-defined materials of smaller sizes (e.g. oligomers).

Scope of discussion of sequence-defined materials

The continued understanding of Nature has inspired researchers to produce sequence-defined materials at all levels of biomimicry ranging across i) the synthetic preparation of natural scaffolds, ii) the non-natural modification of natural scaffolds, iii) new biologically inspired scaffolds, iv) the fully synthetic scaffolds designed for the

purpose of precise sequence definition, and v) the evolution of polymerization techniques toward sequence-control. All of these fields and techniques have co-evolved over the years and conscientious researchers would be remiss to take note from each significant advance within each field toward the production of large-scale, precisely-defined, functional materials.

Herein, this discussion will be primarily focused on sequence-defined polymers that can be chemically produced, specifically excluding methods based on biosynthetic cell or even cell-free production. Many of these methodologies are promising and seek to both expand the chemical diversity of naturally-occurring scaffolds and provide scalability. While not discussed here, these methods have been well-reviewed and include portions of protein engineering,[28,44,45] polyketide synthesis,[46] engineered ribosomes that can encode aforementioned non-canonical amino acids,[47,48] and non-ribosomal synthases.[49] Protein engineering methods are especially notable, providing significant therapies over the past few decades. From its beginnings with large peptides and recombinant proteins, such as humanized insulin in 1982, protein engineering has led the field of biologics. [29,44] Current day advancements in biotechnology of protein expression, recombination, and purification truly marked a new era for drug development, delivering complex proteins including antibodies, soluble receptors, and fusion proteins.[28,50] Thus, the discussion will begin with the synthetic production of naturally occurring scaffolds; then, move on to the development of other sequence-defined scaffolds that draw significant biological inspiration; lastly, the discussion will conclude with scaffolds that are predominantly focused on pushing the boundary of synthetic diversity often derived from polymer chemists. As the production of synthetic

sequence-controlled polymers has utilized both one-pot and iterative approaches, a brief discussion on supported methods will be presented.

Synthetic production of natural scaffolds

Nucleic acids

Arguably, the field of synthetically produced sequence-defined materials started with preparation of oligonucleotides. Deoxyribonucleic acid (DNA) is a biopolymer assembled with repeating base pair monomers in a sequence (e.g. adenine "A,") linked together in a phosphodiester backbone. Shortly after the structural elucidation of the double helix of DNA by Watson and Crick (with data from R Franklin and R Gosling),[51] Michelson and Todd reported in 1955 the (3'->5')-internucleotidic linkage, which is identical to natural DNA.[52] Within twenty years, oligonucleotide methods were becoming advanced with the phosphoamidite synthesis approach automated in the 1970s,[53] efficient sequencing methods by F. Sanger et al,[54] and polymerase chain reaction (PCR) demonstrated by R. K. Saiki et al.[55] These and many efforts have lead to incredible feats including the sequencing of the human genome.[56] And in current day, the production of oligonucleotides can be accomplished at staggeringly impressive lengths and rates, typically ≥100 monomers per day up to thousands of monomers.[57] Such synthetic achievement is likely due to the fact that the monomer units are very similar and hydrophobic collapse is not as much of a factor as it is in other syntheses (e.g. peptides).[58,59]

Aptamers

One result of both biosynthetic engineering and the ability to chemically synthesize nucleic acids is the sequence-defined scaffold of aptamers. Nucleic acid aptamers can achieve affinities on the order of antibodies, made possible by the process of their enrichment and also their structural properties.[60] Production of nucleic acids chemically and biosynthetically is rapid and robust, even allowing for any desired chemical modification. Moreover, nucleic acids scaffolds often have high physical stability and low immunogenicity.

The enrichment of apatmers was one of the first methods of molecular evolution and is generally referred to as Systematic evolution of ligands by exponential enrichment (SELEX)[61,62]. Briefly, the process begins with a very large library of approximate size 4^n, where n is the length of the randomized sequence, with constant regions on the 5' or 3' ends for primers. Then, the library is exposed to the target to allow binding interactions. Afterward, the target is isolated by affinity chromatography, immunoprecipitation, or paramagnetic beads and the bound nucleic acid is eluted and amplified by polymerase chain reaction (PCR) (error-prone) to regenerate the library. The selection process can be repeated multiple times with increasing stringency by changing the target and/or buffer concentration. One main drawback is that the selection method does not have regiospecificity on the target itself. For example, researchers may desire to block a specific site on a protein such as an allosteric or enzymatic site, but it is very possible for the aptamer to bind in any location on the protein. Thus, additional means of selection would need to be coupled to the SELEX process.

While quite successful *in vitro*,[63,64] aptamers have struggled to gain similar success *in vivo*, likely due to their physicochemical properties. Aptamers are generally physically small and have extensive opportunity for hydrogen bonding. Intramolecular hydrogen bonding also causes conformational restriction and further enables tight binding to the target. Moreover, aptamers are highly charged due to the use of the phosphodiester backbone, which can decrease bioavailability.[60]

Peptides

The reproduction of naturally occurring peptides came next with seminal work by Merrifield to accomplish amide coupling in the production of a tetrapeptide in 1963[65] and Bradykinin in 1964.[66] For peptides, the N-terminal amine must be orthogonally protected from the C-terminal connection to the solid support to prevent unintentional detachment during peptide assembly. Throughout the history of peptide synthesis, a few prominent orthogonal chemistries have been used, evolving through several chemistries over the years with carbobenzoxy (Cbzo), tert-butyloxycarboxyl (t-Boc), eventually fluorenylmethyloxycarbonyl (Fmoc) protecting groups for blocking and deblocking.

Merrifield originally used the carbobenzoxy (Cbzo) group, susceptible to 10% HBr, to protect the N-terminal while the C-terminal was protected by the benzyl ester, susceptible to 30% HBr[65] or Pd reduction.[67] Developed before Merrifield's seminal paper, another popular method was N-terminal protection with the tert-butyloxycarbonyl (t-Boc) group that can undergo orthogonal deprotection with trifluoroacetic acid (TFA). Together, these developments allowed orthogonal use of t-Boc and the benzyl ester for the synthesis of many peptides.[67] Despite its success with

some active enzymes, growth factors, and small proteins, the t-Boc/benzyl ester protection strategy required repetitive acidolysis, meaning acid-sensitive amino acids could not be used.[68] Subsequent development of the fluorenylmethyloxycarbonyl (Fmoc) protection strategy for the N-terminal amine allowed complete orthogonal deprotection under mildly basic conditions, meaning the acid-labile t-Boc could be used for side-chain protection and C-terminal support coupling.[68,69] Ultimately, this high degree of orthogonality between the Fmoc and t-Boc groups led to important synthetic improvements in the field of peptide synthesis and is commonly used today.[58,59,68] In current day, peptides have been widely-adopted by scientists as an excellent sequence-defined scaffold to pursue therapeutic development. As a natural material, peptides have expanded rapidly with over 60 FDA approved peptide therapies and 155 in clinical trial as of 2018.[70–72]

Shortcomings of peptides

Though wide-adopted, peptides delivered systemically *in vivo* often suffer from several naturally occurring processes including natural posttranslational modifications and immune recognition. There are several potential post-translational modifications peptides can experience including asparagine deamidation, isomerization (Asp), oxidation (Met, Trp, and Cys), and notably degradation (chemical or proteolytic), all of which can impact the stability and development of a potentially therapeutic peptide.[73] Proteolytic degradation is a natural post-translational modification of endogenous proteins, causing structural and also functional changes to target sequences. While a natural pathway of protein turnover, proteolytic degradation can serve as a regulator

and/or activator of biological processes.[74] Immunological recognition can occur via either an innate (commonly Toll-like receptors[75]) and/or adaptive response (MHC receptors). Both of these biological responses have been well-studied and been utilized toward therapeutic uses. Proteolytic degradation has been utilized for several pro-drug strategies, drug delivery,[76] self-assembly,[77] and conjugate linker degradation,[78] and many more applications.[74] Immunological recognition has been reengineered to activated the immune system for vaccine development,[79,80] One relevant finding for the development of antimicrobial / host-defense peptides is a requirement of peptide length to activate the adaptive immune response via binding to MHC class II receptors (11-14 amino acids in length).[81]

Methods to improve peptide stability

As a proven class of materials for therapeutic development, researchers have sought out to improve upon the weaknesses of peptides, commonly improving stability. One simple way to avoid immune recognition is to utilized short peptides, which are not large enough to be recognized.[81] However, there do not appear to be more broad recommendations from literature. To prevent against proteolytic degradation, there are a variety of robust methods that can be employed including the use of amino acid analogues, non-natrual amino acids,[82] C- and/or N-terminal modification, macrocyclization,[34] stapling,[83–85] lipidization, and/or PEGylation.[86–88] Use of different amino acid analogues is common often swapping natural L- and D-amino acids and frequently done, with D-amino acid scanning as a complementary technique to alanine scanning.[89,90] In addition to stabilizing the peptide and improving half-life, some

techniques can stabilize the binding of the peptide into its binding pocket and/or increase cellular internalization, as is the case with macrocyclization and peptide stapling.[91,92]

Sequence-defined polymer scaffolds

With peptides employed with such success, researchers have sought to improve upon the synthetic diversity, chemical information density, and the shortcomings of peptides (proteolytic degradation and immune recognition). Thus, a massive amount of research has created sequence-defined scaffolds. There are several broad types of scaffolds that have been developed that will be briefly reviewed herein. In this section, all scaffolds presented are completely sequence-defined, meaning when oligomers or polymers are prepared within that scaffold, they consist of the same single molecule and not distributions of molecules (e.g. monodisperse). All of these materials are generally considered sequence-defined polymers. Generally speaking, sequence-defined materials presented herein are in order of their similarity to α-peptides.

Terminology: Classes of sequence-defined polymers

There are several fields that are not precisely defined within this section including peptidomimetics, foldamers, and sequence-defined polymers itself. The field of sequence-defined polymers includes sequence-defined oligomers, which can be difficult at times to differentiate between small molecules with periodic structure. In a historical perspective, the field of sequence-defined polymers has developed through improvements to polymer chemistry methods and new completely synthetic strategies to achieve absolute macromolecular or molecular definition. This field co-evolved with

peptidomimetics, which predominantly has focused on mimicry of peptides, already a sequence-defined biopolymer. Peptidomimetics are defined as peptide-like, and thus could be chemically or structurally similar to peptides (e.g., helix- or sheet-formation).[93] Also, an explicit requirement of similarity does not appear to be in literature. Lastly, foldamers are defined by their quest toward discrete conformational structures, and is also broadly defined.[94] Foldamers can be produced utilizing peptidomimetics or sequence-defined materials that are significantly more synthetic in appearance. Frequently, success has been found with backbones that appear completely different than the polyamide backbone of peptides, including additional sterically blocking and/or hydrogen bonding groups.[95,96] At times, both the fields of peptidomimetics and foldamers encompass each other. Here, all are considered sequence-defined polymers because of their ability to be defined with a chemical "sequence."

Brief history of polymer chemistry

While there has been much work surrounding sequence-defined materials through biomimicry, sequence-definition has been a long-standing goal of polymer chemistry. Moreover, there are sequence-defined scaffolds of note that are not particularly suited in the sections above, meaning they were not designed as peptide mimetics or with explicit molecular structural designs in mind (e.g., foldamers). In contrast, several of these sequence-defined polymers systems were developed to push the boundary of synthetic diversity further. However, by the definition set throughout this discussion, many would consider all scaffolds presented in this chapter to be sequence-defined polymers.

At the onset, man-made homopolymers and statistical copolymers were incredible materials, establishing a full new commodity of plastics used in nearly every industry today. Synthetically produced polymers have historically had less chemical density with simpler structures. But, even simple homopolymers or copolymers have found incredible utility throughout all aspects of society as materials. This is likely owed to the tunable material properties of plastics and for their preparations at scale, far beyond those of biological scaffolds even in modern-day.

Nonetheless, polymer chemists continued to broaden methodologies from step-growth methods to more advanced methods of precise chain-growth polymerizations, multi-step polymerizations, and iterative assembly of multiblock structures.[97] This progression of methods has been well-reviewed in great detail, including discussions around specific types of polymerization methods (e.g., ionic living, radical living, etc.).[97–99] Today, polymer chemists have pushed the boundary of synthetic diversity, across a large range of sizes and chemical densities approaching those seen in biology. Even from its beginning, traditional polymers have significant similarities to proteins. For example, nylon and peptides are both polyamides, just with different functional groups and chemical density.

Overall, these efforts continue to bridge the gap between proteins and synthetic polymers. While ever-increasing, some researchers regard the chemical and/or structural information density of these polymers is lower than small-molecules and proteins.[100] Often, these increases in synthetic diversity and chemical density are focused on the development of structured and functional materials. Thus, some contrast can be seen in the directions of polymer chemistry with biological understanding. As

polymer chemists focus on increasing chemical density and diversity, structured macromolecules often result and are valued. Meanwhile structural biologists are now more focused on intrinsically disordered protein structures, which are more similar to traditional polymers with high degrees of disorder and entropy. Some researchers have called explicitly for this era of polymer chemistry to be described as the development of fully synthetic protein-mimetics, with sequence-definition, structure, and function in tune.[101] Indeed, many applications of advanced sequence-defined materials are molecular recognition,[102] catalysis, or information storage,[103] all which have distinct biological solutions utilizing natural sequence-defined biopolymers.[99]

Bringing sequence to polymers

In contrast to many of other scaffolds (peptides, peptidomimetics, etc.), polymer chemists started the quest for sequence-definition with a significant consideration for scalability, rather than biomimicry. After all, polymer chemistry derives its history from providing scalable methods as material commodity. Thus, polymer chemists have been driven to create scaffolds that provide both sequence-definition and scalability. With two core values, a wealth of approaches and method evolved with varying degrees of importance placed on each value. These methods differ not only by their chemistry, but by their purification, assembly, and supports, beyond the solid-phase supports utilized by the majority of the previous scaffolds mentioned.

Sequence-controlled vs sequence-defined

At the onset toward sequence-definition, several researchers have sought and still seek polymer preparations with improved sequence control. Current-day research achieves varying degrees of exact sequence-definition, often working with "sequence-controlled" polymer preparations. To be clear, "sequence-controlled" methods do not, by definition, have to create monodisperse exact sequence-defined materials, but they do demonstrate improved in dispersity and arrangement of the chemical sequence.[97,99] Moreover, sequence-controlled materials demonstrate that in some applications, exact sequence-definition may be unnecessary. Successes in this area demonstrates the necessity of research at this interface to determine applications where sequence-control is sufficient and where exact sequence-definition is necessary. This topic is further discussed in the last two sections of this Chapter.

Sequence-controlled methods frequently utilize one-pot approaches, though not exclusively. Some sequence-controlled methods are better classified as iterative as they complete the addition of one monomer unit at a time, by either tuning monomer reactivity or addition, or by the use of protecting groups. Moreover, some one-pot methods do produce exact sequence-defined polymers including those prepared utilizing reactive templates. Thus, one-pot approaches are generally employed due to their potential for larger-scale preparations, with the primary alternative being iterative addition of monomers. Due to their popularity, both methods (one-pot or iterative approach) are discussed next, and their degree of sequence-control mentioned for each.

One-pot approach

In the one-pot approach, desired monomer units are precisely added or designed to react in a defined order. Several sequence-controlled methods are performed to maintain scalability, while enhancing the degree of sequence control in comparison to "traditional" polymer preparations aforementioned (e.g. homopolymer, block copolymer, etc.). Sequence-controlled one-pot methods make use of several techniques including the advancement of radical polymerization by tailoring monomer reactivity,[104,105] design,[106–108] or addition time.[109] Tuning of radical polymerization methods have been demonstrated to the near-point of exact sequence-definition, with a prime example given by near single-monomer addition achieved by tuning atom-transfer radical polymerization (ATRP)[110] Another popular approach polymerizes sequence-defined units, producing polymers colloquially termed "segmers." With sequence-defined units, the monomer design focuses on tuning monomer reactivity in low-dispersity multiblock schemes.[111,112] Other segmer methods perform controlled polymerization with sequence-defined monomers,[113] such as ring opening metathesis (ROMP).[107,114]

Though many one-pot approaches produce sequence-controlled polymers, they demonstrate exact sequence-definition through the use of templated reactions. The design the template encodes the location and order of the monomer reactions.[115,116] In some cases, this template can be evolved when coupled with a selection method (discussed next). One of the most incredible demonstrations utilizing a pre-defined template was performed by the molecular machine.[117]

Scaffolds designed specifically for molecular evolution

Some templated methods are able to perform molecular evolution beyond just the directed the assembly of monomers in sequence-defined materials.[99,118] Typically, in this case, nucleic acids are utilized as the template in combination with a biosynthetic approach to generate a slight degree of randomization.[119] Thus, coupled with a selection technique and a target (e.g. enzyme, receptor, etc.), a library of sequence-defined polymers can be screened and evolved. There are similarities to these methods and the SELEX method described earlier. These approaches have been well-reviewed,[120] and represent an incredible harmony between chemistry and biological processes for the development of sequence-defined polymers.

Iterative assembly enabled by supports synthesis

While successful, complex one-pot approaches utilize advanced templates, multifunctional monomers, precisely timed methodology, which can limit scalability.[121] And some argue that exact sequence-definition is not possible to achieve with one-pot approaches, specifically calling for iterative assembly.[100] Iterative approaches frequently utilize a support, seen prominently in the production of nucleic acids, peptides, and other peptidomimetics. Supported synthesis methods execute iterative addition of monomer units to grow a sequence-defined polymer unit by unit. This approach is largely attributed to Merrifield for the synthesis of peptides on an immobilized solid support.[65]

Synthesis with solid-phase supports

Since Merrifield's demonstration in 1963, solid-phase supported synthesis methods have become wide-spread. Typically, the solid-phase method is completed utilizing an insoluble resin or nanoparticle that can be coupled to an initial monomer unit to begin iterative extension of the oligomer or polymer. Reactions add each monomer unit, often using excess reagent to achieve quick reaction rates. Then, the solid support can be isolated via filtration and washed, before moving on to the next monomer unit reaction. Since its development, solid-phase synthesis has had a huge impact, leading to the development of modern day- techniques of oligonucleotide synthesis,[53,122] peptide synthesis,[58] and peptidomimetics[123–126] including peptoids[127] and oligomers produced from thiolactone aminolysis.[128]

However, a solid-phase approach does have drawbacks. Reactions at solid interfaces often demonstrate slow kinetics, hence the use of excess reagent. Moreover, a solid-phase support localizes all polymers close together, which can enhance the possibility of polymer-polymer association or polymer-support association that prevents addition of subsequent monomer units. Generally speaking as an example, many medium-sized 30–50 amino acid peptides can be synthesized using solid-support methods, but some sequences with as short as 10 amino acids experience aggregation or collapse, and cannot be prepared using common techniques.[58,59] Thus, these shortcomings have motivated the use of other supports including liquid-phase, polymer-supported, and fluorous-phase supports.[129]

Synthesis with liquid-phase supports

Reactions performed with a liquid-phase support inherently benefit from quick solution-phase kinetics without the need for large reagent excesses. Overall, the "liquid-phase" definition of these supports refers to the elongation of the sequence-defined polymer during a liquid-phase reaction. In other words, the purification does not have to be performed in the liquid-phase as well, and in fact, selective precipitation of the support can also be used as a means for purification. Generally, liquid-phase supports have been accomplished utilizing polymers of various types and sizes,[130–133] but has also more recently been accomplished utilizing fluorous supports.[134] Both are discussed below.

First, polymer supports utilizing iterative approaches were developed less than ten years after Merrifield's demonstration, seeking to improve on the drawbacks of solid-supports.[130] Polymer supported scaffolds could take advantage of liquid-phase reaction kinetics, and then be precipitated and filtered for isolation and has been well-reviewed.[135] Other benefits are that polymer-supported scaffolds often have fewer issues with solubility since the polymer overwhelms the extended oligomer or polymer. Also, liquid-phase reactions also enable a variety of analytical chemistry techniques to monitor the reaction.[130] Thus, polymer-supports have been successfully used to synthesize peptides (1972),[131] oligonucleotides,[132] oligosaccharides[133] and other unique polymers including oligomers prepared by the Passerini three-component reaction[136] utilizing precipitation-based purifications. Moreover, "polymer-supported" methods are excellent at the elongation of the polymer-support itself, enabling the production of monodisperse polyethylene glycol (PEG).[137]

However, as aforementioned, polymer supported methodologies generally purify after each reaction by precipitation and filtration. Therefore, the main drawback is co-precipitation of either reagents or monomers, which is difficult to predict and sequence-dependent.[135] In comparison, solid-phase scaffolds are able to perform multiple washes with a variety of polar or nonpolar solvents, whereas the solvent choice for polymer-supported scaffolds is more limited.[129] Aside from precipitation, column chromatography has also been utilized, where the polymer support is simply purified from free monomer and reagents.[130,137] However, the separation of truncated sequences would be challenging.[129]

Second, fluorous-phase supports take advantage of both liquid-phase reaction kinetics and solid-phase characteristics, similar to polymer- and liquid-phase supports. Fluorous supports are short perfluorinated alkyl chains ($C_{3\text{-}10}F_x$), often called "fluorous tags," which take advantage of fluorous self-association for purification.[134] Historically, fluorous-tagged purifications were utilized to isolate small molecules during difficult synthetic procedures.[134] Originally, fluorous purifications were demonstrated utilizing fluorous solvents, which would sequester the fluorous-tagged material from organic and/or aqueous (i.e. triphasic extraction).[138] Later on, fluorinated solid-phases of silica beads were developed allowing smaller scale reactions (<100 mg) to be purified efficiently. Termed fluorous solid-phase extraction, FSPE isolates fluorous-tagged materials onto the solid-phase in the presence of a fluorophobic solvent that washes away other impurities, examples include 70–80% MeOH–H_2O, 50–60% CH_3CN–H_2O, or 100% DMSO.[134,139] The purified fluorous-tagged material can then be eluted with a variety of fluorophilic solvents, often 100% organic. While somewhat apparent, the

solvent systems chosen do somewhat correlate with solvent polarity,[140] and have even been applied to aid regular silica column chromatography.[141] Overall, FSPE has been widely adopted,[134,142] extended to combinatorial methods including 96-well plate[143] and most recently by A. J. Vegas et al. to microarrays for the discovery of histone deacetylase inhibitors.[144]

However, as with any purification method, fluorous supports do have some drawbacks. Fluorous tags and supports themselves are challenging to synthesize, sometimes requiring the use of hydrofluoric acid, but are commercially available.[140] Extraction with fluorous solvents is best applied at medium to large scales (+100 mg), with FSPE working well down to small amounts (~10 mg). Specific to FSPE, fluorophobic solvent choice is important to prevent breakthrough or pre-mature elution. However, strongly fluorophobic solvents can cause clogging of columns. Other issues are similar to silica and other solid-phases including finite lifetime of the fluorous solid-phase and insufficient contact with the solid-phase (i.e. channeling)[139]

Nevertheless, fluorous-based supports have been successfully applied to the synthesis of sequence-defined polymers and perhaps has been overlooked as a useful support until recently. One of the first demonstrations was by Jain and Tour in their synthesis of oligo(phenylene-vinylene)s, though very short in length.[145] One seminal demonstration for fluorous-based supports was made by our lab by M. Porel and C. A. Alabi in 2014 for the preparation of oligothioetheramides (oligoTEAs), for oligomer lengths as long as 10 monomers prepared in approximately one day.[146,147] OligoTEAs will be discussed much more in Chapter 2. Afterward, several sequence-defined

macromolecules were prepared including oligo(hydroxyproline)s by R. Langer D. G. Anderson and colleagues,[148] and monodispersed PEGs by Li et al[149]

Support free iterative assembly

While supports can be utilized to provide purification handles for iterative approaches to sequence-defined polymer synthesis, researchers have also developed support-free methods. Frequently, these methods function by monomers with designed reactive orthogonality. To be clear, these methods that do not utilize a polymer support, but are only required to be in solution. Some have called for a more rigorous re-definition of the liquid-phase support as the approaches below only need to be solubilized into solution (i.e. "supported" by the solvent), whereas the above liquid-phase supports could be defined explicitly as polymer or fluorous supports.[129]

One main method that highlights the potential of support-free methods is the strategy of iterative exponential growth (IEG).[121] In IEG, a monomer with two orthogonally protected groups is split into two batches. The batches are separately deprotected or activated under two different conditions, providing each batch a different deprotected group. Then, the batches can be mixed together to react together to form dimers of the monomer. From there, the process repeats to prepare tetramers, octamers, etc. For purification, the IEG approach generally requires simple liquid extraction workups during assembly and provides access to gram-scale quantities. However, this strategy does rely on the completion of both deprotection and coupling reactions and complicates the incorporation of sequence diversity. First reported by M.C. Whiting,[150] and demonstrated at scale by C. J. Hawker,[151] significant advances for IEG were made

was when it was automated[152] and side-chain diversity was introduced by Johnson and Jamison.[121]

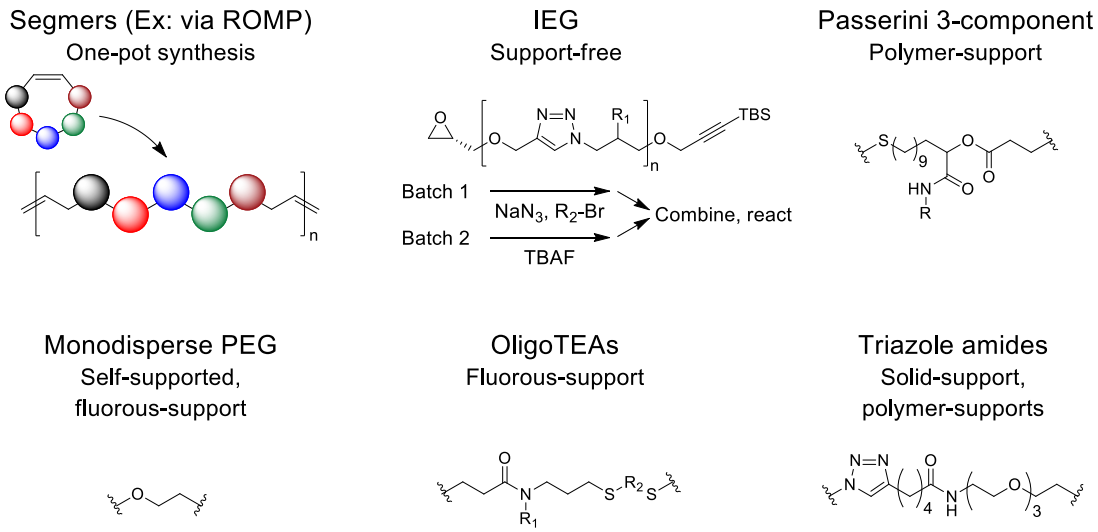

Figure 1-3: *Selected methods and scaffolds from polymer chemistry*

Peptidomimetics

Peptidomimetics are defined as sequence-defined polymers that are peptide-like.[93] Multiple properties of α-peptides can be mimicked including chemical similarities (e.g. amide backbone, chiral centers) and also structural similarities (e.g. helix- or sheet-formation). There have been multiple attempts to classify peptidomimetics both based on their chemical similarity (Type I, II, and III)[93] and degree of structural similarity (Type A, B, C, and D).[153] It is not immediately clear when a scaffold or material would be classified as only a sequence-defined polymer and not a peptidomimetic. It could depend on the chemist's intention or inspiration, or as aforementioned, be defined chemically or structurally. In addition, there are a number of scaffolds that have been developed, not always classified by the originators.

However, the field of peptidomimetics is very large and consists of some of the most well-known sequence-defined polymers that exist today.

For this section, peptidomimetics will be presented based on their chemical similarity to nature's own α-peptides, specifically the polyamide backbone. This choice is predominantly due to the fact that that not all α-peptides are structured as aforementioned with intrinsically disordered proteins and peptides.[12] Thus, mimicking the structural characteristics of α-peptides, which are occasionally disordered, is an uncertain goal. Therefore, researchers seeking to mimic structural elements of peptides as peptidomimetics should be explicit in the structure they are mimicking. Indeed, researchers have embraced specific structural definitions including α-helix mimetics.[154]

The smallest difference one can make to the α-peptide scaffold to generate a peptidomimetic is by changing the chirality of the central carbon, as a D-amino acid. As a frequent tool for researchers preparing α-peptides,[89,90] the inclusion of d-amino acids has be considered a peptidomimetic and has been used successfully to generate protease resistant ligands.[155] And, in one case, researchers were able to generate a fully functional enzyme specific to only the substrate enantiomer, demonstrating full protein mirror image protein folding.[156]

Scaffolds with additional methylenes in peptide backbone

Another set of popular peptidomimetics including β-peptides,[157,158] γ-peptides,[157,159] and even δ-peptides,[160] change the backbone structure by adding in a methylene or methylenes in the repeat unit. From β to δ, the Greek letter refers to the chemical position of the functional group with reference to its unit carbonyl group. Of these, the most popular is β-peptides, which is commonly prepared as the β^3 version,

where the β^2 version moves the functional group back α to the carbonyl. β-peptides introduce only one methylene and thus one element of disorder into the peptide. However, the β-peptide does allow the introduction of a cyclic ring into the peptide backbone between the β and α carbons. The addition of a cyclic ring is sterically blocking and has been successful in preparing an alpha-helix mimetic from aminocyclohexane carboxylic acid (ACHC), and has notably been used by S.H. Gellman and N.L. Abbott to begin to understand water ordering at hydrophobic interfaces.[161,162] Other researchers have taken this further in the case of I.S. Radzishevsky et al., who demonstrated robust antibacterial activity with oligo(acyl-lysines).[163]

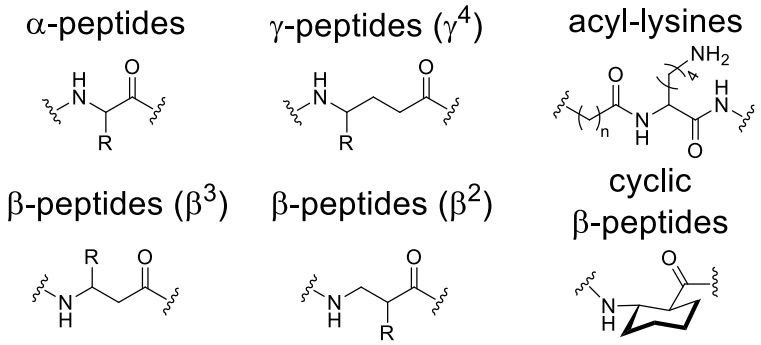

Figure 1-4: *Selected scaffolds with methylene additions to the α-peptide backbone*

Scaffolds with additions or changes to the amide backbone

Several scaffolds have made changes to the poly-amide backbone, which is one of the main chemical identifiers of α-peptides. First, depsipeptides are α-peptides that include ester linkages rather than amide linkages between amino acid units; the exclusion of amides is not required.[164] Aminoxy acids have been utilized to create aminoxy peptides that are prone to forming intramolecular N-O turns within the peptide backbone.[165,166] Some scaffolds have sought to include larger number of hydrogen

bonding groups than α-peptides. Oligosulfonamides are structurally similar to β-peptides, except the amide of the β-peptide unit is replaced with sulfonamide, which can accept a larger number of hydrogen bonds.[167] Other scaffolds have included substituted urea groups including azapeptides,[95,168] which replace one or more of the α-carbon(s) with nitrogen. With this urea within the peptide backbone, a variety of chemistries have been applied to perform cyclizations and other functionalizations.[168] Taking this inclusion of ureas further, the scaffolds of oligoureas[169,170] and azatides[167,171] do not include any type of amide.

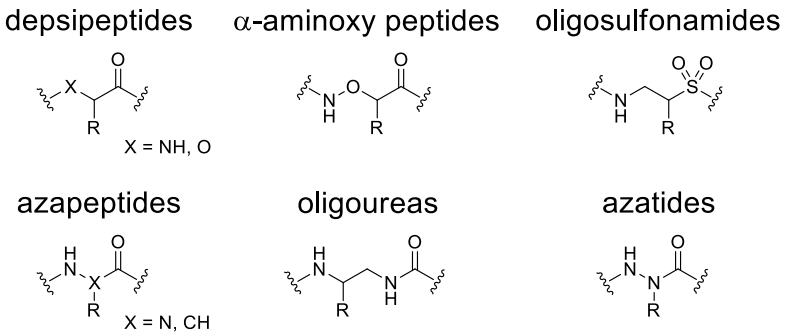

Figure 1-5: *Selected scaffolds with nonamide backbones*

Peptide nucleic acids (PNAs)

Peptide nucleic acids (PNAs) could also be considered derivatives of β-peptides, with a repeating (2-aminoethyl) glycine backbone, but are significant on their own right as combinations of the DNA and peptide scaffolds. The nucleobase is attached to the internal amide of the repeating unit, with similar spacing and distance to the DNA backbone itself.[172] Thus, this elegant sequence-defined system has demonstrated several similar functions to DNA itself including hybridization to other complementary DNA, RNA, or PNA strands.[94,173]

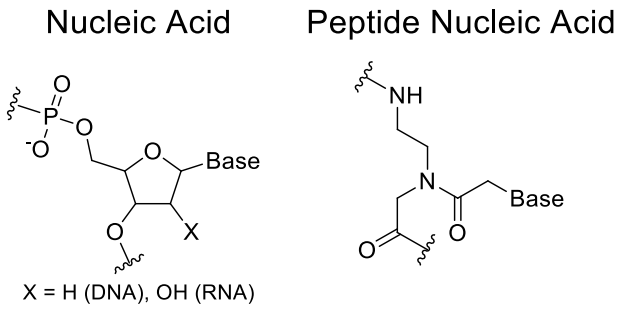

Figure 1-6: *Diagram comparing nucleic acids to PNAs*

Peptoids

Peptoids, or N-substituted glycines, are a broadly popular sequence-defined peptidomimetic. In comparison to α-peptides, peptoids feature the functional side chain on the amide rather than the central carbon.[174,175] The first synthetic attempt to produce peptoids was designed to mimic peptide synthesis with Fmoc-protected monomers coupled onto a solid-phase support.[174] However, this approach required a difficult monomer synthesis that could not keep pace with demand.[127] The second attempt led to the development of the submonomer method,[176] which employed two orthogonal reactions per monomer addition cycle; acylation followed by SN2 displacement. The displacement was achieved with primary amines, allowing the submonomer method to benefit from their extensive commercial availability.

The assembly of peptoids by the submonomer method facilitated the expedient and efficient synthesis of peptoids for use in a wide variety of applications including the search for structured macromolecules.[100,101,127] However, exchanging the hydrogen bonding of the secondary amide for a methylene meant that the backbone is no longer independent of the functional groups. The functional groups of peptoids are solely responsible for any specific molecular structure that develops.[100]

In their design, peptoids have drawn strong inspiration from α-peptides, meaning from the onset the search for structural mimetics was on. In particular a helical mimetic was investigated first, with computational simulations completed on prospective functional groups that could constrain the backbone.[100] Within a few years of peptoids inception, P Armand et al[177] as well as K Kirshenbaum[178] et al found computationally and experimentally that both phenylethyl groups and napthylene groups were sufficient to develop helical structures in solution as observed by circular dichroism and NMR. Thus, peptoids were able to have sequences that provided a alpha-helix mimetic.

Since then, there have been several excellent peptoid structures developed through combinatorial and computation research. With an alpha-helix mimetic, a functional nanostructure was developed to be able to clamp and chelate zinc with high affinity (~1 nM).[102] Sequences were also discovered to provide nanotube (~9.3nm in diameter) formation from co-block peptoid sequence of decyl and polyethylene oxide groups.[179] Another important case was the preparation of free-standing peptoid nanosheets from also from a combination of two peptoids with alternating sequence of benzyl and either amine or carboxylic acid groups.[180] The nanosheets were prepared in organic solvent with both peptoids present. The charge groups assemble together with with hydrophobic benzyl groups facing "outward" from the sheet core. Overall, these demonstrations are impressive and the amount of work performed with peptoids is convincing. However, the length of time and work put in to generate the alpha-helix mimetics (~5 years) and the beta-sheet mimetic (~16 years), highlights the challenge peptoids face only use of the functional groups to control their structure. In some

reported cases, substitution of these functional groups destabilize the desired structure.[181]

peptoids

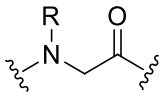

Figure 1-7: *Molecular structure of peptoids scaffold*

Foldamers

As aforementioned, foldamers are a broad class of sequence-defined polymer that focus on structure forming molecules or macromolecules.[95,96] With specific structures in mind (e.g., helicies), foldamers could be classified as peptidomimetics or vice-a-versa. Some researchers claim all of the scaffolds presented above are foldamers because of their abilities to form specific molecular conformations and thus would should be considered a broader class.[94–96] To this point, there are several foldamer scaffolds that do not appear at all similar to peptides; and with little to no similarity to peptides, they would not be defined as peptidomimetics. This is commonly due to the inclusion of aromatic groups, conjugated bonds, and hydrogen bonding groups.[95,96]

Thus, in this section, a remaining set of scaffolds will be presented that have less similarity to peptides than those in the section above. Generally, molecular conformation can be secured with hydrogen bonding groups, similar to α-peptides. Some foldamers have been considered both foldamers and peptidomimetics include oligopyrrolinones and arylamides. Oligopyrrolinones are quite unique in their design that derives from the rearrangement of the moieties of β-peptides.[167] Their conjugated system with an enaminone NH that can stabilize a β-sheet-like intermolecular

structure.[182] Arylamides have been considered both peptidomimetics and foldamers, and accomplish an additional degree of steric hinderance over the cyclic β-peptides utilizing an unsaturated benzyl ring rather than a cyclohexane.[183,184] From such an example, several scaffolds build upon the level of hydrogen bonding available in the backbone including oligohydrazides,[185] oligoisophthalamides,[186] and oligotriazines.[187]

Another strategy employed in the pursuit of defined conformational structure is the use of steric blocking groups or conjugated bonds to restrict conformational freedom. Thus, several scaffolds have been developed including oligo(phenylene-ethynylenes) (also called oligo(phenylene-acetylenes))[188–191] and oligothiophenes.[192] Oligo(phenylene-acetylenes) are incredibly conjugated, but typically difficult to synthesize. Due to their degree of conjugation, these systems have found use in other fields. Specifically, oligothiophenes have favorable electronic and optical properties for semiconductor design.[193]

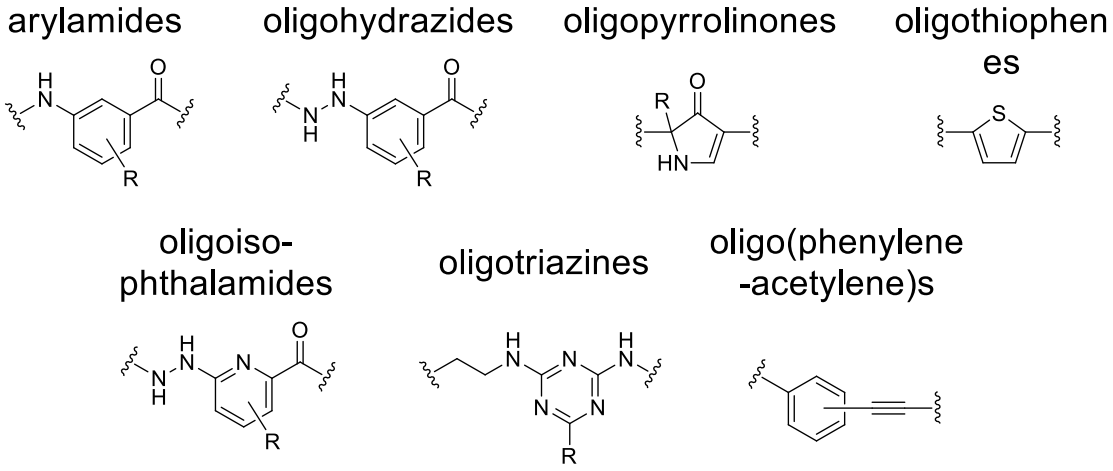

Figure 1-8: *Selected structures of foldamer scaffolds*

Sequence-defined polymers for information storage

Sequence-defined polymers find variety of uses, generally at the interface of biology, hence the biomimicry, or in materials (next section). However, with the concomitant emergence of computer systems as polymer chemistry improved toward sequence-definition, information storage has also been an application of interest for sequence-defined polymers. For this application, exact sequence-definition is required for high fidelity information writing and reading. As presented previously, nucleic acids and in particular DNA have been excellent information storage, with significantly higher information density of 5.5 petabits/mm^3 than any other man-made silicon nanostructure (e.g., hard-drive disk).[194] Under the right conditions, DNA can be stored and re-accessed via sequencing thousands of years later and storage fidelity has been measured to be between 99.99% and 100% accurate to original record.[195,196]

However, other sequence-defined polymers have also been prepared toward this application, with the goal to improve data storage density, stability, as well as synthetic assembly and reading by MS/MS. Generally, these systems can be designed with MS-liable bonds to increase MS/MS efficient fragmentation to enable sensitive access to the stored information. The design can also incorporate either binary or higher order modes of information storage. One advantage within these systems is that the data system (e.g., binary) defines the number of monomer units utilized, providing opportunity for optimized syntheses with relatively simple functional units that can be decoded by mass spectrometry (e.g., methyl group).[103,197]

Sequence for bulk polymer materials

While paramount in biology and a goal of polymer chemistry, the extent of the importance of sequence-definition in bulk materials is currently being debated. There is an overwhelming amount of evidence within biology concerning the importance of sequence-definition. But, as aforementioned, common-day polymeric materials are typically prepared with little to no sequence-definition, questioning its importance and utility in designer bulk materials. Thus, polymer chemists have recently set out toward to determine both the extent of the impact of sequence on physical and chemical properties of bulk materials. Currently, there are a few demonstrations. In 2017, T. Y. Meyer et al. have demonstrated that the sequence of poly(lactic-*co*-glycolic acid)s (PLGA) was the primary factor in their swelling behavior and hydrolytic degradation rate.[198] And in 2018, J. A. Johnson et al. demonstrated that block copolymer sequence affected the phase behavior and assembly of polymers prepared by iterative exponential growth (IEG).[199]

Conclusions

There are an overwhelming variety of ways to prepare sequence-defined macromolecules across many scales, molecular weights, degrees of sequence-definition, synthetic diversity, and chemical density. In this chapter, a broad review of chemical methods was discussed including the synthetic production of natural scaffolds, scaffolds predominantly inspired by nature, and scaffolds sought out through advancements in polymer chemistry. It is clear from Nature that sequence-definition is incredibly

important within dynamic biological processes. However, to develop specific functions within biological systems, the length of the sequence-defined polymer serves as a gateway, with longer sequences producing more advanced structure and function. In some cases, biologically active sequences can be quite short, placing biological function well-within synthetic chemists' abilities. For example, consensus sequences as short as three amino acids have been utilized to target o attached into integrin proteins ("RGD")[200] or develop hydrogel materials ("KYF").[201] Increasing in length can then start to elicit immunological response, with amino acids as short as 13 residues activating major histocompatibility complex (MHC) class II response.[79] Further increases to near 20 residues can allow α-helices to begin forming.[202]

Thus, researchers have sought out sequence-control from several avenues and will continue to advance and understand sequence-structure-function relationships across a variety of scaffolds. Similar to the challenges face in structural biology, sequence-structure-function relationships will be difficult to establish given that defined molecular conformations are not required for biological function. Researchers will continue to evolve our ability to perform molecular engineering, taming entropy and creating designer structures for specific purposes both in biological contexts and materials.

Chapter 2 : Sequence-defined Oligothioetheramides

Acknowledgements

Part of this this chapter has been adapted with permission from M. Porel, J. S. Brown, and C. A. Alabi, *Synlett* **2015**, 26 (5), 565-571. Copyright © 2015 Georg Thieme Verlag Stuttgart (License #4518230433130). Other parts of this chapter are taken from a manuscript in preparation by J.S. Brown, A.W. Ruttinger, A.J. Vaidya, P Clancy, and C.A. Alabi, "Mechanistic Insight into the Thiol-Michael Addition Utilized in Oligothioetheramide Assembly," where J.S. Brown and A.W. Ruttinger contributed equally the work.

Individual contributions

For the article by M. Porel, J. S. Brown, and C. A. Alabi: M.P. and C.A.A. conceptualized oligothioetheramides. M.P. demonstrated proof-of-concept synthesis, purification, and chemical characterization, also published in M. Porel, and C. A. Alabi, *Journal of American Chemical Society*, **2014**, 136 (38), 13162-13165. J. S. B. and M. P. wrote the manuscript. All authors discussed, edited, and approved of the manuscript. For the manuscript in preparation by J.S. Brown and A.W. Ruttinger et al.: J.B. and A.J.V. conceptualized the experimental work and A.W.R. conceptualized the computational work. J.B. and A.J.V performed synthesis, purification, and kinetic experiment, and analyzed the results. A.W.R. designed and performed molecular simulation and analyzed the results. A.J.W. and J.B wrote the manuscript. All authors discussed the results and edited the manuscript.

Article acknowledgements

For the article by M. Porel, J. S. Brown, and C. A. Alabi: The work described in this review was supported by funds from Cornell University and the Nancy and Peter Meinig Investigator Fellowship. For the manuscript in preparation by J.S. Brown and A.W. Ruttinger et al.: This project was supported in part by Cornell University Start-Up funds (C.A.A.), the National Science Foundation CAREER Award (CHE-1554046), the Army Research Office (W911NF-15-10179), and the Nancy and Peter Meinig Investigator Fellowship (C.A.A.). The authors thank the Cornell Institute for Computational Science and Engineering (ICSE) (P.C.) and the Maryland Advanced Research Computing Center (MARCC) for the provision of computational resources. A.W.R. gratefully acknowledges the financial support of the NSERC Postgraduate Scholarships-Doctoral (PGS-D) award and the Cornell University Graduate School. J.S.B. acknowledges financial support from the National Science Foundation Graduate Research Fellowship Program (DBE-1144153). This work made use of the Cornell University NMR Facility, which is supported, in part, by NSF-MRI (CHE-1531632).

Abstract

The importance of sequence-defined polymers is evident in highly developed biological systems. As such, their synthetic *de novo* production with similar macromolecular diversity, efficiency, and speed has been the focus of considerable research. In this chapter, the rationale behind the new synthesis of sequence-defined oligothioetheramides (oligoTEAs) will be placed in context with the accepted methods

of peptide and peptoid synthesis, where all methods notably utilize chemical orthogonality in their design. Along with the conceptual design, we will discuss the assembly of oligoTEAs by highlighting the solution-phase kinetics of each orthogonal reaction and the liquid-phase fluorous purification methodology. OligoTEAs are assembled through iterative thiol-ene "click" and thiol-Michael reactions, which will both be discussed in detail. The thiol-Michael reaction in particular is mechanistically discussed and examined thoroughly across multiple *N*-allyl-*N*-acrylamides, both experimentally and also computationally. Calculations in to the mechanism of each transition state have begun to explain and rationalize substituent effects. The success of oligoTEAs stems from the rapid orthogonal chemical reaction of the thiol-ene and thiol-Michael and thus should be discussed. OligoTEAs seek to contribute and advance the field of sequence-defined polymers by providing additional structural diversity to fundamentally study sequence-structure-function relationships for both material science and biological applications.

Introduction

Introduced and discussed in Chapter 1, sequence-defined polymers are macromolecules with precisely controlled monomer organization. Biological systems, including nucleic acids and peptides, have long demonstrated the importance of sequence control and have used this as a tool to create and tune their structural, physical, and chemical properties.[99,203,204] In an effort to mimic these well-behaved systems, researchers have sought out precise primary sequence by biomimicry of natural

scaffolds, deviations thereof, and control over synthetic polymerizations with the goal of creating new materials with engineered properties such as solubility, conductivity, molecular recognition, biocompatibility, and reactivity.[95,99,101,129,205] Moreover, combinatorial production of sequence-defined polymers has powerful opportunities for high-throughput screening of reactivity, binding, and biological function.[167,174,206] As such, efficient synthetic methods to control monomer sequence within a polymer scaffold have been the focus of intense research through a variety of methodologies and approaches detailed in Chapter 1.

Inspired by some of these methods, the *de novo* assembly of sequence-defined oligothioetheramides (oligoTEAs) has been developed in our lab by M. Porel and C.A. Alabi.[146] In this chapter, the rationale behind the synthesis of oligoTEAs will be discussed, along with a discussion around the reactions that are used to assemble oligoTEAs: the photo-initiated thiol-ene and thiol-Michael addition. The kinetic mechanism of the thiol-Michael will be discussed in depth from experiments and computational calculations, which were completed by Andrew W. Ruttinger in Professor Paulette Clancy's research group.

Reactive orthogonality to create sequence-definition

Use of protecting groups

Several of the sequence-defined scaffolds presented in Chapter 1 demonstrate reactive orthogonality in the design of their monomer units to achieve iterative assembly of exact sequences. To some degree, all of the scaffolds presented demonstrate some

orthogonality. The assembly of most peptides and nucleic acids is accomplished by the use of protecting groups that are deblocked during specific conditions orthogonal to coupling reactions. Without the use of protecting groups, the peptide assembly in a sequence-defined manner is not possible. Each amino acid must be carefully modified to enable its use in typical peptide assembly.[58,207] For example, with peptides utilizing the common Fmoc strategy, each amino acid must be modified prior to assembly with an Fmoc group and purified. Thankfully, peptides are a high demand sequence-defined scaffold, and Fmoc-protected amino acids are readily commercially available. Once prepared, the Fmoc-protected amino acid is ready for assembly and can be coupled to the support. Coupling proceeds utilizing a variety of reagents that do not lead to the unintended deprotection of the Fmoc group, which would result in polymerization. Afterward, the Fmoc group is removed by a nucleophilic base (e.g., piperidine) and the cycle can continue. As another part of its design, the entire peptide assembly proceeds orthogonally to the acidic conditions required to remove the peptide from the support and any protecting groups on functional side-chains.[58,207]

Protecting groups can enable diverse schemes of sequence-defined polymers and there are multiple examples. Aforementioned, The iterative exponential growth (IEG) scheme aforementioned demonstrates reactive orthogonality utilizing a protecting group well.[151,152] In the most recent example of IEG by Johnson and colleagues, each monomer is prepared with an epoxy and protected alkyne, which can be orthogonally reacted to either add in each subsequent azide and side-chain or activate the alkyne.[121] Then, coupling between the activated monomers can occur using the copper(I)-catalyzed azide-alkyne cycloaddition (CuAAC) reaction (Figure 2-1).

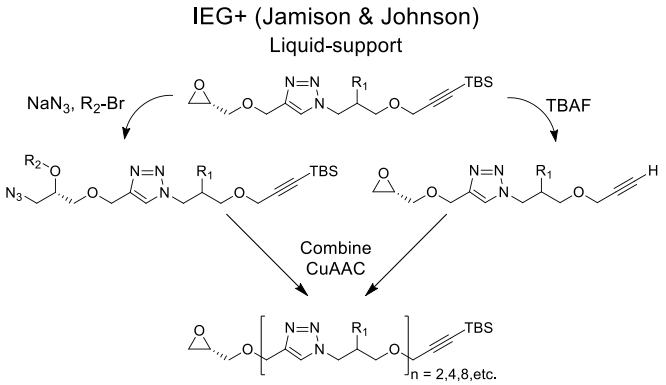

Figure 2-1: *Example of approach that utilizes producting groups (IEG+)*[121]

Design of orthogonal reactions without protecting groups

Without the use of protecting groups in the design of a sequence-defined scaffold, complete reactive orthogonality is required. However, there are then fewer reactions required to prepare the oligomer or polymer, potentially speeding along the assembly process and avoiding any potential truncation due to an incomplete reaction. One can argue that the monomer units should be simpler to prepare without the use of protecting groups; however, the development of completely orthogonal monomers can be complex.

To accomplish reactive orthogonality without protecting groups, sub-monomer or co-monomer approaches are often employed. This is most commonly seen with revised preparation of peptoids, where bromoacetic acid is coupled to a supported amine, then a subsequent amine can be reacted (Figure 2-2).[176] Also in the family of these sub- or co-monomer schemes, “click” chemistry is frequently utilized. “Click” reactions are a relatively new class of reactions designed to be bioorthogonal and proceed with quick kinetics at high yields.[208] Thus, these “click” chemistry groups are

stable to a variety of reactions conditions and functional groups including amines, thiols, carboxylic acids, heat, etc found in biology.[208] Moreover, the reactivity of some of these groups are orthogonal to each other and can be used in combination. In one example, the assembly of triazole amides was accomplished by J.-F. Lutz and colleagues by alternating between the CuAAC reaction and amide coupling.[209] In another, Solleder and Meier assemble amide-substituted oligo(ester-thioether)s by alternating between the thiol-ene and Passerini three-component reactions (Figure 2-2).[136]

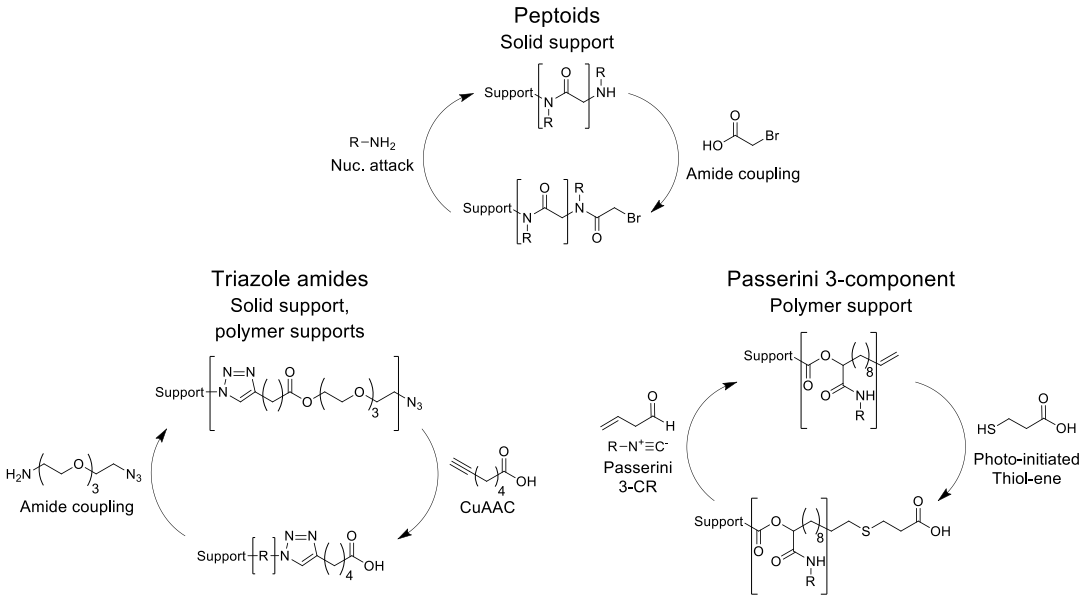

Figure 2-2: *Examples of sequence-defined scaffolds that use submonomer approaches*

Oligothioetheramides

Inspired by the aforementioned orthogonal methods used for the synthesis of peptides and peptoids, our lab reported a new and efficient synthetic strategy for the assembly of oligothioetheramides (oligoTEAs).[146] Our goal was to increase the scaffold

diversity and accessibility of sequence-defined polymers for drug discovery and delivery applications by designing a protease-resistant scaffold with tunable backbone and pendant functionalities. To our knowledge, there were not any known sequence-defined scaffolds that provide extensive access to the backbone of the resulting polymer.

To do this, we designed a unique monomer with two orthogonal reactive sites that can react with the same nucleophile under different reaction conditions. The two reactive sites in the monomer framework are an acrylamide and allyl functional group. The acrylamide can undergo a phosphine-catalyzed Michael addition with thiols while the allyl group is a great candidate for the photoinitiated thiol-ene 'click' reaction. These two reactions were selected because of their quantitative conversion as well as their fast solution kinetics.[210,211] Each of these reactions will be discussed in detail in the next section.

Example of model monomer

Once selected, M. Porel and C. A. Alabi prepared a trial monomer to understand the combination of these functional groups, with the simplest combination being an *N*-allyl-*N*-acrylamide (Figure 2-3). The *N*-allyl-*N*-acrylamide could be prepared from two simple steps: (a) synthesis of *N*-allyl-*N*-alkyl/arylamines intermediates from a primary amine or halide, and (b) acylation of this intermediate with acryloyl chloride to give the final *N*-allyl-*N*-acrylamide functional monomer. There were some examples in literature with similar combinations of these chemical groups. Chan, Hoyle, and Lowe utilized sequential thiol-Michael and thiol-yne/ene reactions for the preparation of dendrimer-like structures.[210] Additionally, C. A. Alabi et al. utilized the aza-Michael addition and

thiol-yne reactions for the combinatorial preparation of lipids to study their gene transfection potential as lipid nanoparticles.[212] Nevertheless, to our knowledge the combination of two orthogonal "click" reactions within a single monomer for the production of sequence-defined polymers had not been designed before.

With a simple *N*-allyl-*N*-methylacrylamide, M. Porel and C. A. Alabi went on to verify the speed of the thiol-ene and thiol-Michael reactions.[146,147] As shown in Figure 2-3b, the Michael addition of *N*-allyl-*N*-methylacrylamide (0.16 M) and 1,3-propanedithiol in the presence of a catalytic amount of dimethylphenylphosphine (DMPP) was almost complete in 300 seconds with a bimolecular rate constant of 0.07 $M^{-1}s^{-1}$. During this reaction, there was no cross-reaction with the allyl functional group, demonstrating clearly the reactivity orthogonality of these groups. As arranged, the thiol-Michael addition would occur before the thiol-ene and thus the thiol-ene kinetics were explored on an octyl-modified *N*-allyl-*N*-acrylamide monomer. Moreover, the thiol-Michael addition is orthogonal to the thiol-ene, but not vice-a-versa. The thiol-Michael reacts preferentially with electron-deficient olefins, whereas the thiol-ene can react with nearly any olefin. The resulting *N*-allyl-*N*-methyl-3-(octylthio)acrylamide was synthesized and used along with 1,3-propanedithiol and 2,2-dimethoxy-2-phenylacetophenone (DMPA) as a photoinitiator to measure the kinetics of the thiol-ene reaction. This reaction was extremely fast and was complete in 90 seconds with a unimolecular rate constant of 0.03 s^{-1} (Figure 2-3b).

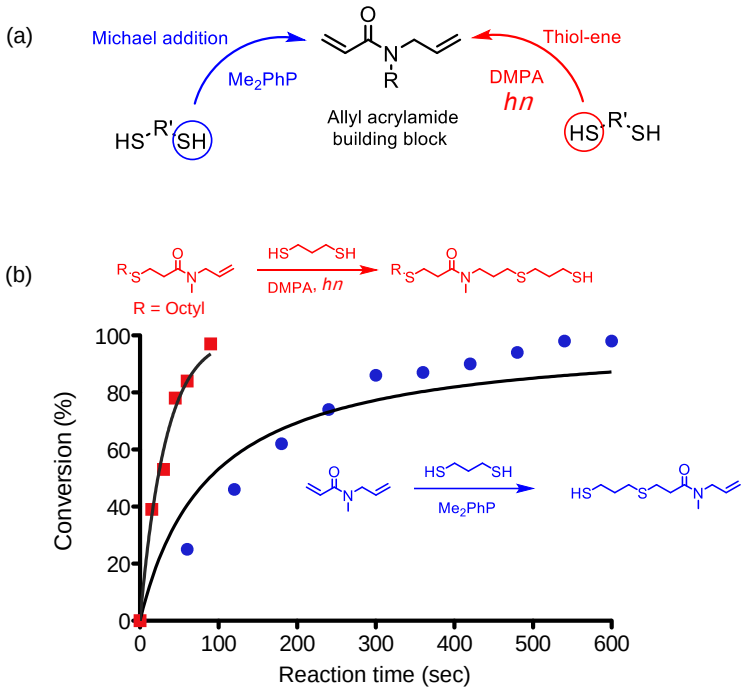

Figure 2-3: *Thiol-ene and thiol-Michael addition with methyl N-allyl-N-acrylamide Used with permission from M. Porel, J. S. Brown, and C. A. Alabi, Synlett* ***2015****, 26 (5), 565-571. Copyright © 2015 Georg Thieme Verlag Stuttgart (License #4518230433130)*

Assembly on the fluorous support

While the thiol-ene and thiol-Michael has been performed on solid-phase surfaces before in literature,[213–215] several attempts to perform the Michael and thiol-ene reactions on resins yielded much slower reaction kinetics and poor reaction efficiencies. Nevertheless, there have been some reports of the challenges the thiol-ene faces if diffusion-limited.[216] Thus, aforementioned in Chapter 1, a fluorous support was chosen to maintain these rapid solution-phase kinetics, enabling fluorous solid-phase extraction (FSPE). Specifically, an acid cleavable Boc-functionalized fluorous tag (F19-Boc-On) was used, which could be prepared into a fluorous-tag allyl amine. Using the fluorous support, the kinetics were verified again to investigate any effect of the support

on the reactions. The photo-initiated thiol-ene reaction between 1,3-propanedithiol and fluorous-tagged allylamine was complete in 90 seconds to give the monosubstituted derivative as the only product, which was surprising. In solution, an unsupported dithiol would likely have shown some di-addition of the allyl groups. We further examined the effect of different amounts of dithiol (0.5 equiv to 5 equiv) relative to the fluorous-tagged allylamine on product distribution (mono-addition vs. di-addition) and observed the mono-addition adduct to be the sole product in all cases.[146] Our results also indicated that for fluorous-tagged substrates, a two- to five-fold excess of dithiol was necessary to push the reaction to completion in 90 seconds. The phosphine-catalyzed Michael addition of an *N*-allyl-*N*-acrylamide monomer to a fluorous-tagged thiol was complete in a similar timeframe to the monomer alone.

For the FSPE conditions, methanol was the preferred solvent for reaction and purification due to its compatibility with the monomers and fluorous-tagged substrates. Thus, a fluorophobic wash (20% aqueous methanol) was used to elute all non-fluorous molecules. While FSPE is quick, its limitations in the preparations of oligoTEAs have also been observed. The purification of hydrophilic or charged oligomers can be challenging and low-yielding, as it appears to disrupt the fluorous self-association to the solid-phase. An example of this challenging appears in the preparation of an oligomer with a high degree of ethylene oxide content.[21] For acidic groups (e.g. carboxylic acids), purification can be improved from yields of 20% to the standard 80%[217] by adding dilute acid to the wash solution (e.g., 0.1M HCl). Moreover, recent work by J.S. Brown et al. has demonstrated that increasing the aqueous content of the fluorophobic wash can increase yield and prevent breakthrough of the oligomer during washes, as understood

in literature.[140,217] With increased aqueous content, excess monomer and catalyst occasionally precipitate as well, but usually purify; nevertheless, verification by NMR will determine the purity. A fluorophilic wash (100% methanol) was used to elute the desired oligomer from the fluorous stationary phase to be dried for the next cycle.

Once elongated to desired length, the oligomer can be cleaved from the fluorous support using a strong acid (trifluoroacetic acid). This final mixture can again be purified by FSPE; however, the product will elute with the fluorophobic aqueous methanol wash and the fluorous tag will be removed. The resulting oligoTEA will yield an amine functional group at one end (F-terminal) and an allyl group at the other (A-terminal), both of which are useful for post-synthetic modifications. High-performance liquid chromatography (HPLC), ^{1}H nuclear magnetic resonance (NMR), and liquid-chromatography mass spectrometry (LCMS) can then chemically confirm and verify the oligoTEA.

Under this scheme, M. Porel and C. A. Alabi prepared several proof-of-concept oligoTEAs varying in length and functionalities by cycling between the two reactions with FSPE purification after each reaction (Figure 2-4).[146] In comparison to the sub-monomer methods aforementioned by peptoids and others (Figure 2-2),[136,176,209] the assembly of oligoTEAs could be characterized as a sub-monomer method. However, the dithiol monomer is not predetermined and can be varied easily across a diverse number of commercially available dithiols to precisely control and craft the backbone of the oligomer. Therefore, oligoTEA assembly is best thought of as a co-monomer method, because every monomer can be varied or modulated with extreme ease.

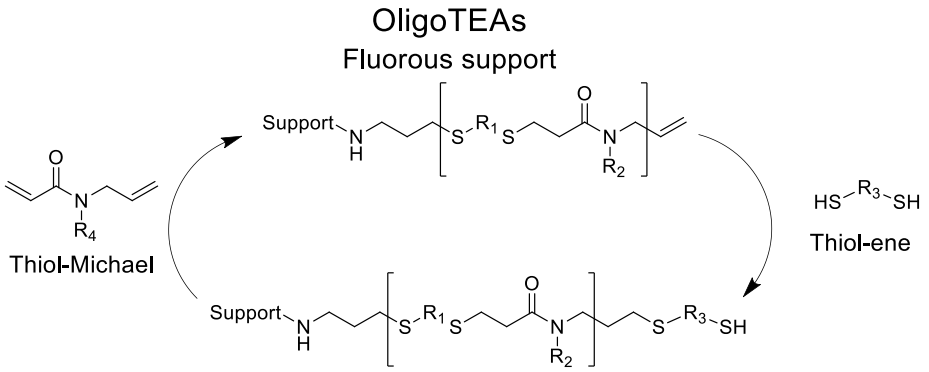

Figure 2-4: *Scheme of oligoTEA assembly via alternating co-monomer reactions*

Thiol-ene reaction

As a core reaction of oligoTEA assembly, the thiol-ene reaction has a longer history and utility, covalently linking a thiol and an alkene to form an alkyl sulfide, often a thioether. It has been well-studied and reviewed in literature.[218–221] The first applications of the thiol-ene was the vulcanization of rubber, largely attributed to the work of Charles Goodyear in the mid-19th century, featuring the radical addition of sulfur and thiols to alkenes in rubber.[219] Another significant utility of the thiol-ene reaction came later in the mid-20th century to crosslink materials and improve polymerizations.[222] Generally speaking, polymerizations methods improved and the chemical utility of thiol-ene crosslinking fell out of favor. The thiol-ene was use historically in these applications due to its robust nature, demonstrating tolerance to a variety of solvent and reaction conditions; thus, it was not long until it began to reappear within more specialized context.[219,220]

The thiol-ene is now understood to be thermally, radically, base-, or nucleophile-initiated with a variety of alkene groups including acrylates, acrylamides,

vinyl sulfones, norbornenes, and maleimides.[219–221] The thiol-ene can proceed by two routes: i) the radical addition through the use of a thermal or radical initiator and by ii) the Michael addition through the use a base or nucleophile.[223] Generally, the thiol follows the anti-Markovnikov addition to the alkene, though the Markovnikov addition has been seen in literature and its percentage of formation depends on the reaction conditions (e.g., solvent polarity)[224,225] For oligoTEAs, the Markovnikov addition has been observed, but in small amount isolated amount of approximately 5% per thiol-ene (see Appendix A, Figure A-1 and A-2).

Technically speaking, the thiol-Michael addition is usually considered a thiol-ene reaction;[221] however, they will be discussed separately in this chapter. For the remainder of this section, we will discuss the kinetics and applications of the photoinitiated thio-ene, because of its common usage and extent of control demonstrated, more so than with thermal initiation.

Kinetic understanding of the photoinitiated thiol-ene

Once in the hands of researchers, the thiol-ene became extensively studied and understood. Efficient kinetics and high yields allow the thiol-ene to be considered a "click" reaction.[218–221] However, there are several factors that can limit the kinetic rate of the photoinitiated thiol-ene and rapid kinetics are not always guaranteed. The thol-ene has been kinetically studied in several way including considerations for the alkene reactivity and stability of radical intermediates since the step of addition have been understood.[220] One seminal publication on this topic was presented by N. B. Cramer, S. K. Reddy, A. K. O'Brien, and C. N. Bowman in 2013.[226] Cramer et al. presented

kinetic data from a variety of alkenes as they were photopolymerized with a tetrafunctional thiol and were able to successfully model the data across multiple stoichiometries. The model they presented was based on the ratio of the reaction rates between the propagation and chain transfer steps within the mechanism of the thiol-ene (Figure 2-5). Across the available alkenes used, Cramer et al. concluded their findings suggesting that the electron density of the alkene likely affected this balance of reactivities.[226] Indeed, computation calculations by B. H. Northrop and R. N. Coffey (2012) were able to verify the direct impact the electron density at the alkene center, specifically indicating electron rich ene have quick propagation rates (k_P).[227] Additionally, recent calculations by V. Fındık et al. (2019) demonstrated decreases in electron density around the thiol favor the rate of propagation over chain transfer, likely through the decreased carbon radical stability.[226,228]

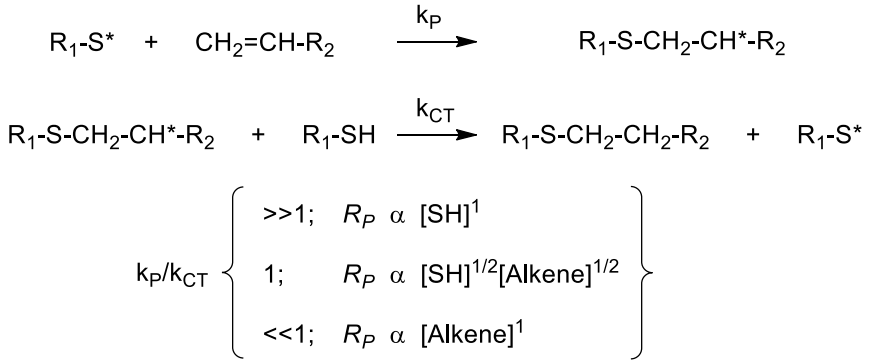

Figure 2-5: *Summary of kinetic understanding about the thiol-ene reaction Radical is represented as an asterisk (*),* k_P *refers to the rate of propagation of the radical during thiol addition to the alkene,* k_{CT} *refers to the rate of chain transfer from the radical alkene to a new thiol, and* R_P *refers to the rate of polymerization. Several other combinations of radical transfer can occur (notably termination), but these are the ones N. B. Cramer et al. proposed as critical to the rate limiting step of the photoinitated thiol-ene.*[226] *Moreover, several empirical results suggest that the rate of reaction depends on the initial concentration of the initiator, which is not shown, but would directly increase the reaction rate. Example data studied by J S Brown of this finding shown in Table 2-1.*

Applications of the thiol-ene

Similar to other "click" chemistries,[208] there are a broad range of potential applications for the thiol-ene and much of the work has been well-reviewed in literature.[221] Aforementioned, thiol-ene has been performed on solid-phase surfaces and thus it has been used in variety of diffusion-limited applications including surface functionalization, nanoparticle synthesis, post-functionalization of polymers.[221,229,230] Though, there have been reports where diffusion limitation hinders the thiol-ene.[216] In biological contexts, the thiol-ene has been utilized in a variety of bioconjugations[231] with examples including the glycosylation of glutathione[232] and label alkyne-bearing proteins expressed within E. coli.[233] Aforementioned, the thiol-ene is utilized in the scheme to prepare sequence-defined oligo(ester-thioether)s via the Passerini three-component reaction.[136] One of the most remarkable examples of thiol-ene utility was demonstrated by D. W. Yee et al. (2017), where two-photon lithography was utilized to build nanoscale 3-dimensional structures, made possible by 7-diethylamino-3-thenoylcoumarin (DETC), an efficient two-photon photoinitiator.[234] Because of these and other studies, there are is a wealth of understanding around the effect of molecular substituients on the rate of reaction.[235]

The use of the thiol-ene for oligoTEA assembly

Thus, the thiol-ene was an excellent candidate reaction for the assembly of sequence-defined polymers as designed with oligoTEAs. As demonstrated before by our lab, the thiol-ene provided quick kinetics and high conversion, generally in less

than five minutes. Further control experiments with *N*-allyl-*N*-acrylamides have demonstrated that the reaction is insensitive to air and solvent conditions (DCM, THF, MeOH, etc). However, under stringent conditions (2 equivalents thiol), one can see the thiol-ene reaction with *N*-allyl-*N*-acrylamides is sensitive to concentration and highly sensitive to the amount of photoinitiator used (DMPA) (Table 2-1).

Table 2-1: *Conversion of the thiol-ene versus catalyst and solvent concentration*

Concentration, mM	0.1 mol%	0.5 mol%	1 mol%	DMPA, 5 mol%
400	9%	33%	69%	98%
250	-	15%	29%	93%
100	-	-	-	78%

Note: These conversions were quantified by NMR. The exact reaction conditions were 2 equivalents of 1,3-propanedithiol, 1 equivalent of protected sulfonate N-allyl-N-acrylamide (Chapter 3) after thiol-Michael addition of octanethiol, in dichloromethane at varying concentration and amount of DMPA photoinitiator. The percentage of photoinitiator is in reference to the amount of thiol used.

Thiol-Michael addition

Introduction

In addition to the radical mechanism, the thiol-ene can proceed through the base- or nucleophile-initiated mechanism, typically called the thiol-Michael addition.[223] Similarly rich in history, the thiol-Michael addition derives its name from the more general Michael addition, which was first understood in 1887 by Authur Michael.[236,237] In the Michael addition, a carbanion or nucleophile is reacts onto an electron-deficient alkene in the presence of a catalyst.[213,236] Thus, the Michael addition has been demonstrated in a variety of ways with amines,[238] hydroxyl groups,[239,240] and thiols,

which was demonstrated in 1964.[213,213,241] In its own right, the thiol-Michael addition is considered a "click" reaction, providing efficient and quick reactions.[213,235] This reaction has been demonstrated to be simple, robust, compatible with aqueous solutions, and without side reaction, except the formation of the catalyst complex if utilizing a nucleophile.[213,223,242–244]

The mechanism of the thiol-Michael reaction follows similar elementary steps and to the photoinitiated thiol-ene, except an anion is propagated and transferred rather than a radical.[213] Aforementioned, the thiol-Michael addition can be initiated with either a base or nucleophile, affecting the mechanism and kinetics that follow. In the base-catalyzed mechanism, the base abstracts a proton from the thiol to form a negatively charged thiolate nucleophile, which can then attack the Michael acceptor.[213] Thus, the properties of the base affect reaction rate and yield, including concentration, pKa, sterics, as well as solvent polarity and pH.[213] A common base utilized to study the base-catalyzed mechanism is triethylamine, which does not participate in the nucleophile-initiated mechanism.[245,246] In the nucleophile-initiated mechanism, the nucleophile reacts with the Michael acceptor directly to form a strong base (e.g. carbanion), which then deprotonates the thiol to generate a thiolate.[213] In this way, the nucleophile-initiated mechanism is not a proper catalyst, since it is not regenerated at the end of the reaction cycle. Generally, the rates for nucleophile-initiated reactions are faster than with base-catalysis, and the reaction is well-reported with common nucleophiles including unhindered amines and phosphines.[210,211,213,242,247–251]

Applications of the thiol-Michael addition

As a "click" reaction, the thiol-Michael addition reaction has found broad utility from materials chemistry to bioconjugation, which has been well-reviewed in literature.[213,218,235,245,252] There are several material and polymeric applications of the thiol-Michael addition including the synthesis and post-functionalization of polymers,[213] the surface grafting of designer polymers to surfaces[253] and nanoparticle surfaces,[254] as well as the creation of hydrogel networks for tissue engineering.[22] Because of its tolerance to aqueous conditions, the thiol-Michael has also found broad utility in bioconjugation including the creation of antibody-drug-conjugates (ADCs)[255] and thiol-activated fluorogenic probes,[256] predominatly through the use of the maleimide.[257] In one other elegant example, both spatial and temporal control of the thiol-Michael addition was achieved to form two-stage polymer lithography networks made possible from a "photocaged" base catalyst.[258] Since functionalization continues to be critical to the development of complex, highly specific macromolecules, the thiol-Michael addition will continue to be the target of research. Moreover, precise kinetic control of the thiol-Michael addition is required to make these and other potential applications possible.

The thiol-Michael utilized by oligoTEAs

The quick, clean kinetics of the thiol-Michael addition demonstrated in literature made it an ideal candidate to be utilized for the assembly of sequence-defined polymers. In the scheme of oligoTEAs, the thiol-Michael addition is the first reaction that attaches the *N*-allyl-*N*-acrylamide monomer to the scaffold, with no cross-reactivity of the allyl

group via the thiol-ene. This reactive orthogonality clearly highlights the differences in their mechanisms.

In practice, the thiol-Michael has been tolerant to aqueous content during oligoTEA assembly, which occasionally remains after fluorous purification from the fluorophobic wash. However, if there is sufficient water content, the fluorous tag will precipitate and the thiol-Michael will not go to completion. Thus, thiol concentration of the reaction can be monitored by a dithiodipyridine (DTDP) assay to determine if the reaction was complete. Over a variety of monomers, the kinetic rate of the thiol-Michael addition could vary from 5 minutes reported originally[146] to other slower monomers like the *N*-allyl-*N*-acrylamide azide monomer, which required 30 minutes to react.[21] In extreme cases, some monomers would take days to react, including the phthalimide-protected amine *N*-allyl-*N*-acrylamide monomer (see Appendix A, Figure A-3). However, based on comparison to literature,[251] *N*-allyl-*N*-acrylamide monomers generally react faster than their acrylamide counterparts.

To better understand the variability of this reaction, we have studied the mechanism and kinetics of the reactions across a variety of functional groups to better understand the thiol-Michael generally and in the context of oligoTEA assembly. With broader understanding of the thiol-Michael addition, the reaction could be completed reliably, enabling automated synthesis. Moreover, with an understanding about the molecular substituent effects similar to others in literature,[259] *N*-allyl-*N*-acrylamide monomers with enhanced kinetics could be prepared to potentially enable bioconjugation or biosensing, which is not typically possible with acrylamides.[255,256]

Literature background of kinetic mechanism

In literature, both the base-catalyzed and nucleophile-initiated mechanisms have been studied and compared. As aforementioned, multiple studies have experimentally and computationally confirmed that the nucleophile-initiated mechanism is faster.[218] This is further supported by research suggesting the degree to which a base can act through the nucleophile-catalyzed mechanism increases the reaction rate.[246,250] Of the potential nucleophiles, Nair *et al.* provide a comprehensive review discussing the use of unhindered amines and phosphines, with the strength of the nucleophile increasing the reaction rate.[213] Overall, multiple reports support the use of the phosphine nucleophiles as potent initiators of the thiol-Michael addition.[211,223,247,260]

Based on these results, we will focus on the nucleophile-initiated mechanism utilizing a phosphine catalyst. In this mechanism the following steps proceed: i) the nucleophile attacks the electron-deficient alkene, resulting in a carbanion, ii) the carbanion extracts a proton from a thiol to generate a thiolate (initiation), which enters the common mechanism, iii) the thiolate attacks another electron-deficient alkene, forming another carbanion (propagation), iv) the new carbanion is stabilized through a second proton transfer from an additional thiol, generating a new thiolate and the desired product (chain transfer) (Figure 2-6). Overall, the thiol-Michael addition appears proceeds at a constant concentration of anionic species within the common mechanism, similar to other living polymerizations. With experts in the field generally agreeing on this scheme, research has focused on determining substituent effects that direct the rate limiting step.[213,246,247,251]

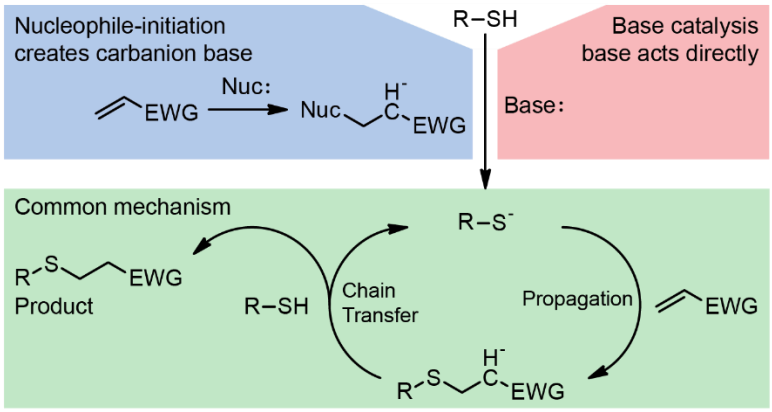

Figure 2-6: *The mechanism of the thiol-Michael addition*

Identifying the rate-limiting step (RLS) is critical for improving any reaction kinetics. Generally speaking, steric hinderance or lack of electron-deficiency in the alkene will slow the overall reaction rate.[252] However, there is much debate over the exact RLS for the thiol-Michael addition, likely indicating substituent effects. Most researchers have claimed the thiolate attack (propagation) to be rate-limiting,[213,252] while others argue the proton transfer to the carbanion (chain transfer),[246] or the nucleophile attack on the alkene is slower.[247] Furthermore, there is also lack of agreement on the reversibility of the reaction. While most agree that the thiolate attack is reversible,[213,252] some researchers suggest that the entire Michael addition is reversible.[260,261]

Herein, our work aims to clarify these discrepancies in the thiol-Michael addition kinetics by providing a systematic case study for the thiol-Michael addition within oligoTEA assembly. We performed this study by experimentally and computationally examining a variety of *N*-allyl-*N*-acrylamides. Dithiodipyridine (DTDP) experiments measured the thiol and thiolate concentration of the reaction, to quantitatively determine the kinetic rate of reaction. Across temperatures, we then

calculated the activation energy using the Arrhenius relation.[262] Density functional theory (DFT) was coupled with a transition state determining method to determine the energy barriers between each of the mechanistic steps. A comparison of experimental and computational results demonstrated the importance of hydrogen bonding between the thiol and the *N*-allyl-*N*-acrylamide Michael acceptor, suggesting that the decomplexation of the product in the chain transfer step could be rate-limiting.

Results

Experimental kinetics

Experiments were completed to measure the thiol-Michael reaction rate at room temperature (25°C) and elevated temperature (40°C) using the methyl, ethyl, butyl, hexyl, benzyl, and ethylenephenyl *N*-allyl-*N*-acrylamides. Monomers were chosen based on their ability to show an increasing alkyl substituent effect[263,264] and aromaticity,[265,266] which was qualitatively known to affect the reaction time. While mass or infrared spectrometry is typically used, high-throughput kinetic assay was desired; therefore, we chose to adapt the dithiodipyridine (DTDP) assay[267,268] to a 96-well plate format. The DTDP assay measures the combined thiol and thiolate concentration of the reaction to track the reaction conversion. DTDP was chosen over an Ellman's assay because these reactions are completed in organic solvent. Modifications to the DTDP assay as presented in literature were required to make the 96-well plate format quantitative (see Materials and Methods).

The kinetic rates of the reaction were revealed from the data by fitting a simple bimolecular rate equation to the data, as has been done before (Figure 2-7, see Materials

and Methods).[213] To prepare for each reaction, dimethylphenylphosphine (DMPP) was incubated with *N*-allyl-*N*-acrylamide monomer for fifteen minutes to create the phosphine initiator, which acts as carbanion base (Figure 2-6 in blue). In addition to the carbanion, there is a positive charge on the phosphorous center after the reaction, making the phosphine initiator a zwitterion. Then, to start the reaction, the fluorous thiol (F-DTT) was added. This initial fifteen minute incubation was performed because a delay in conversion would otherwise occur while the carbanion catalyst is generated, as seen in literature.[251] For additional confirmation, the kinetics of the reaction between the phosphine nucleophile and a model monomer was analyzed to confirm this reaction completion prior to thiol introduction (see Appendix A, Figure A-4). Starting the reaction at a consistent concentration of carbanion will allow us to specifically examine the balance between the rates of propagation, chain transfer, or any other rate-limitations.

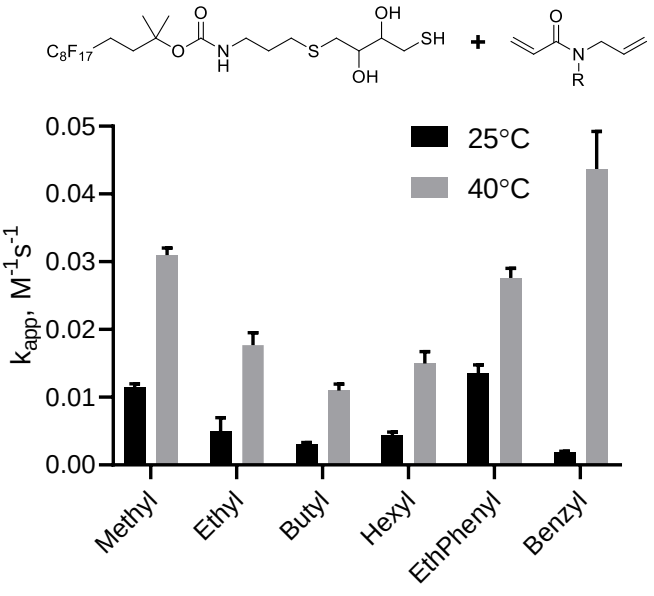

Figure 2-7: *Apparent kinetic rate of N-allyl-N-acrylamide reaction with fluorous thiol*

The kinetic rate of the *N*-allyl-*N*-acrylamides varied significantly (Figure 2-7). The methyl monomer was significantly faster than the other alkyl monomers, with a decreasing reaction rate observed with longer alkyl chains. The increase in alkyl chain length could indicate an increase in steric hinderance, a potential effect of electron donation, or another substitutive effect. But, the effect did not persist significantly past the ethyl functional group, as the butyl and hexyl functional groups demonstrated statistically similar reaction speeds as the ethyl at both temperatures (see Appendix A Table A-1 for statistical summary). Interestingly, the methyl and ethylene phenyl monomers had statistically similar reaction rates at both temperatures ($p = 0.0994$ and $p = 0.0631$ for T = 25 and 40°C, respectively, see Appendix A Table A-1 for statistical summary). However, there were large significant differences between the ethylenephenyl and the benzyl, which rapidly increased in reaction rate with the addition of heat.

Overall, these data proved interesting and indicated that simple explanations about contributions of electron density could not alone explain these results. Usually, studies that investigate the kinetics of the thiol-Michael report on the differences across alkene classes (e.g., vinyl sulfone vs acrylates)[211,251,269] or different catalysts (e.g., amines vs phosphines)[247,257,260,270] but this is the first time to our knowledge that such large kinetic rate differences have been observed within the same alkene class. This is especially true when comparing the kinetic data of the aromatic groups, which differ significantly in activation energy. Indeed, converting these kinetic rates to activation energies (E_A) utilizing the Arrhenius relation reveals that the benzyl and ethylenephenyl are dramatically different (Figure 2-8).

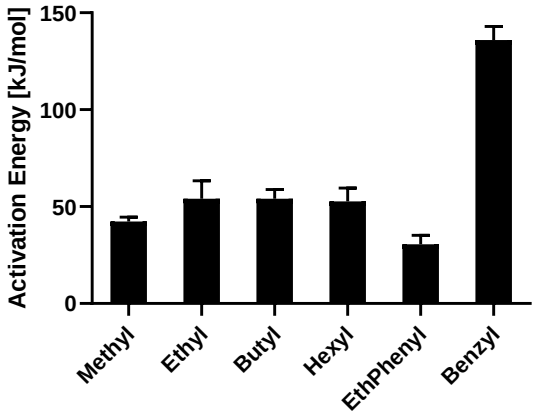

Figure 2-8: *Activation energies for thiol-Michael addition with fluorous thiol*

Computational background to mechanistic study

Thus, to understand these effects and the thiol-Michael addition more broadly, we investigated these reactions utilizing computational techniques. A number of studies have used computational work for the study of Michael addition kinetics.[246,247,263,271] In each case, the researchers employ Density Functional Theory (DFT) to determine reaction energies and kinetic rates. DFT uses a quantum mechanical approach to determine the ground-state energy of a group of atoms. Coupled with a transition state determining method, this provides a basis to calculate temperature independent enthalpies fundamental to the quantification of reaction kinetics. For our purposes, we divided each step in the thiol-Michael addition into an energy barrier separating two minima on a Potential Energy Surface (PES), corresponding to a chemical, or even structural transition of atoms. Then, using the Nudged Elastic Band (NEB) method,[272–274] we determined the transition state, corresponding to the highest energy atomic configuration along the Minimum Energy Pathway (MEP) between minima (see

Materials and Methods). With this we calculated activation energies, allowing comparison between each reaction step to determine which is rate-limiting. Our previous computational work provides an example of this partitioning of a reaction mechanism to determine reaction energies.[275] A final comparison between our computationally derived rate-limiting step and our experimentally observed activation energy will provide validation for our mechanistic study.

Mechanism of the thiol-Michael with methyl N-allyl-N-acrylamide

Prior to studying the effect of all functional groups, we look at a model case using a methyl *N*-allyl-*N*-acrylamide monomer to confirm agreement between experimental and theory. A full mechanistic study is performed for this particular reaction, with the results shown in Figure 2-9. The activation energy of each reaction step was extracted from Figure 2-9a and is presented more clearly in Figure 2-9b. Interestingly, the reaction energies of the traditional rate-limiting steps of initiation propagation, and chain transfer demonstrated poor agreement with the experimental data. Of these traditional steps, our results show do show that the chain transfer step is rate-limiting, matching what Desmet *et al.* reported.[246] However, this chain transfer step (15.5 kJ/mol) is still significantly below our experimental value (42.3 ± 2.3 kJ/mol).

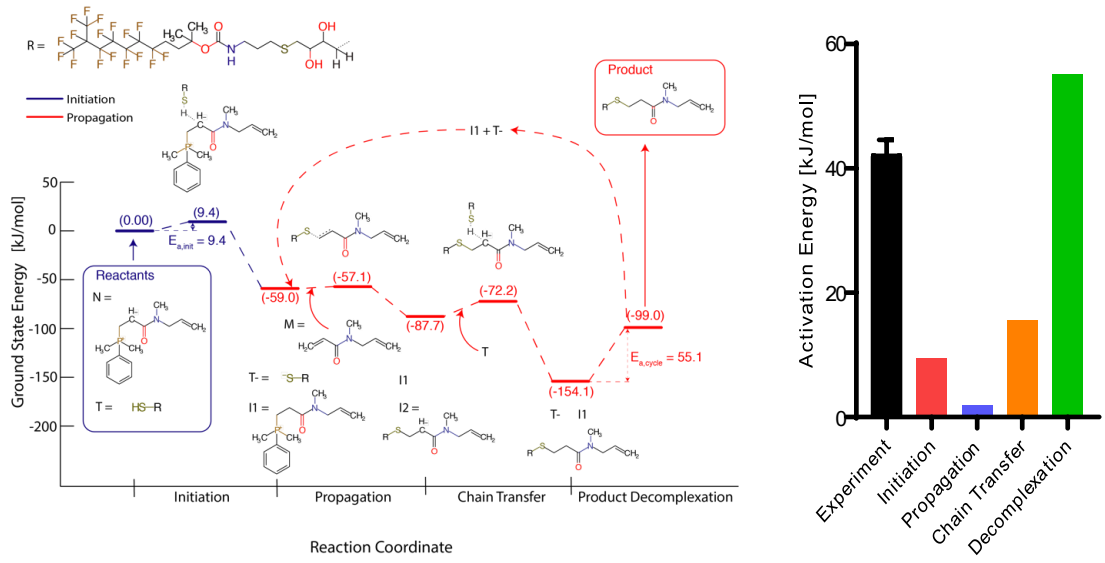

Figure 2-9: *Computational energies of thiol-Michael mechanism versus experiment (left) The energy profile of the reaction mechanism of the methyl N-allyl-N-acrylamide monomer undergoing a thiol-Michael addition with a fluorous thiol. All reaction energies were calculated using DFT. The step in which the thiolate is initially formed is shown in blue (initiation). The remaining steps (propagation, chain transfer, and decomplexation) are shown in red because they cycle multiple times throughout the course of the reaction. Atomic configurations are provided, with transition state complexes indicated by a dashed line. Reaction intermediates are shown below the energy pathway. The fluorous R-group is explicitly shown in the upper left corner. (right) The reaction energies for each step, along with the experimental value.*

Thus, we analyzed the reaction behavior at the molecular-scale, following the anionic charge transfer, noting several molecular complexations along the pathway. Before the start of this pathway, the zwitterionic phosphine initiator (I±) was prepared. In experiments, the zwitterionic phosphine initiator (I±) was formed during the incubation the phosphine with the *N*-allyl-*N*-acrylamide to the point of completion (5 mol%), as a source of carbanion base (Figure 2-6 in blue). Thus, the first step is the initiation (Figure 2-9 in blue) can start with the phosphine initiator (I±). In this step, the carbanion of the zwitterionic phosphine initiator acts as a Brønsted-Lowry base,

extracting a proton off of the thiol (T), making thiolate and used initiator. The anionic charge is now located on the thiolate (T-), electrostatically stabilizing its complexation with the now positive phosphine initiator (I+).

Next, the propagation and chain transfer occur. In the propagation, the thiolate (T-) attacks the alkene of an unreacted methyl *N*-allyl-*N*-acrylamide (M). The energy required to separate the negatively-charged thiolate (T-) and used initiator (I+) is much higher than for the neutral methyl *N*-allyl-*N*-acrylamide (M) to join the complex. Thus, the unreacted methyl *N*-allyl-*N*-acrylamide likely approaches and thiolate attack proceeds, propagating the anion charge onto the carbanionic product (TM-), which will become product (TM) after chain transfer. Similar to the unreacted methyl *N*-allyl-*N*-acrylamide, it is easier for another thiol (T) to approach than dissociate the complex for the chain transfer to occur. With the addition of new thiol (T), the carbanionic product (TM-) extracts the proton from the thiol (T), making product (TM) and a new thiolate.Then, in order to continue the thiol-Michael addition cycle, the product (TM) must be removed from its electrostatically stabilized complex, also containing the used initiator (I+) and new thiolate (T-), to allow a new alkene monomer to react. We refer to this step as "product decomplexation" and calculate the energy barrier associated with this molecular dissociation.

When the product decomplexation step is considered, the results show better agreement with the experimental data, indicating the rate limiting step is likely this decomplexation. For the methyl *N*-allyl-*N*-acrylamide, the product decomplexation step (55.1 kJ/mol) now overpredicts the experimental value (42.3 ± 2.3 kJ/mol). However, it is not uncommon for theoretically calculated energies to overpredict experimental

values, since the NEB method follows an energy gradient from high values to low. This is further reconciled when the mean absolute error of an energy barrier, calculated with a range-separated functional, is considered (~ 3 kcal/mol [12.5 kJ/mol]).[276] Moreover, the energy barrier of product decomplexation is much larger than the chain transfer energy barrier, allowing us to confidently label product decomplexation as rate-limiting.

Discussion about the thiol-Michael addition in oligoTEA assembly

At the time of this writing, the data collected from these computational calculations is preliminary and will be finalized before potential preparation as a manuscript for publication. Additional calculations will be performed for other functional groups presented, with special focus placed on the aromatic substituents. While not discussed in depth here, there are two explanations that additional preliminary data has started to clarify and allow rationalization of the experimental results. First, there are multiple hydrogen bonds between the thiol and thiolate to the molecular complexes (initiator, *N*-allyl-*N*-acrylamide monomers). This hydrogen bonding stabilizes the transition states during the initiation, propagation, and chain transfer steps, but must be broken for the decomplexation. The exact hydrogen bonding network is shown in Figure 2-10, showing the hydrogen bonding network that forms between the product, initiator, and next thiol that reacts. The breaking of these hydrogen bonds is the product decomplexation process.

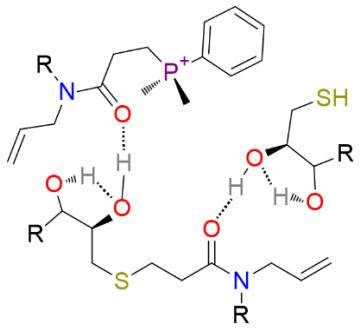

Figure 2-10: *Hydrogen bonding network between product, initiator, and thiol.*

A control experiment and calculation should reveal that without these stabilizing forces, decomplexation will be easy and the other steps will not be stabilized. Second, the alignment and sterics of the aromatic groups can rationalize differences between the activation energies observed between the benzyl and ethylenephenyl functional groups. The added carbon in ethylene phenyl adds distance between the aromatic groups, anionic thiolate, and other substituents. Thus, the attractive forces are less strong and it is easier for the ethylenephenyl to dissociate. However, in the case of benzyl, to dissociate the product, an aromatic-aromatic interaction, anion-aromatic interaction, and additional short-range interactions must be broken, leading to a higher energy barrier.

Conclusions

Using both the photoinitiated thiol-ene "click" and thiol-Michael addition reactions, the assembly of oligothioetheramides (oligoTEAs) is possible through their reactive orthogonality in a co-monomer approach. Our approach was inspired by the robust orthogonal strategies discussed and demonstrated, including peptoids and other submonomer approaches that accomplish sequence-definition without the use of

protecting groups. Moreover, we have detailed a brief understanding of the thiol-ene and its reaction requirements for effective oligoTEA assembly. We have also focused on the kinetic and mechanistic understanding of the thiol-Michael addition to a much greater extent given its broad utility and variability, even within the same alkene class of *N*-allyl-*N*-acrylamides. Comparing experimental activation energies to computational calculation of transition state energies has begun to reveal the importance of molecular complexation as a potential rate limiting step in the thiol-Michael addition. More specifically, mechanistic examination of the thiol-Michael addition has started to rationalize complex results seen in experiment through the visualization of hydrogen bonding, aromatic stacking, and other short-range interactions that affect transition state energies.

Through oligoTEAs, we have significant sequence and backbone diversity, which will help elucidate sequence-structure-function relationships and provide new avenues for advanced materials from the molecular scale. Since establishing oligoTEAs,[146,147] we have prepared several studies ranging from their solution-phase characterization,[217] ability to produce advanced structures including macrocycles,[37] utility as multifunctional bioconjugates,[21] intracellular delivery,[277] antibacterial activity,[278–280] and biophysical characterization.[281,282] We hope that our work will help advance the field, featuring peptides and peptoids, toward the goal of achieving rapid and efficient production of highly diverse and functional sequence-defined polymers.

Materials and Methods

Reaction conditions

The thiol-Michael addition was performed across a variety of monomers at 30 mM fluorous (4-10mg, 6.8-17 µmol). 2 equivalents of *N*-allyl-*N*-acrylamide monomer (13.6-34 µmol) from a 200mM methanol stock was activated for 15 minutes with 0.1 equivalents of dimethylphenyl phosphine (0.68-1.7 µmol DMPP) from a 2.5 v/v% stock in methanol. Fifteen (15) minutes was chosen as a catalyst incubation time from literature precedent demonstrating monomer incubation delayed reaction initiation.[251]

Experimental quantification of the thiol-Michael addition

Monitoring the thiol-Michael addition is typically observed by FTIR, but was not possible in this case due to anticipated crowding in the spectra. Two assays were completed to determine thiol-Michael addition kinetics with *N*-allyl-*N*-acrylamide monomers using i) dithiodipyridine (DTDP) to quantify the fluorous thiol concentration and ii) high-performance liquid chromatography mass spectrometry (LCMS) to quantify the product concentration using single ion mode (SIM). All data was plotted and analyzed in GraphPad Prism 7.05 using nonlinear regression fitting to an integrated solution of the bimolecular kinetic rate equation as described below.

Bimolecular rate equation

The following mass action kinetics were assumed and subsequently solved to determine an analytical solution for nonlinear regression fitting to experimental data.

$$F + M \xrightarrow{k_{obs}} FM$$

Where *F* is the concentration of the fluorous thiol, *M* is the concentration of the *N*-allyl-*N*-acrylamide monomer, and *FM* is the concentration of the product. This results in the following rate equations, leading to a integrated analytical solution of the bimolecular rate equation.

$$\frac{dFM}{dt} = k_{obs}(F)(M)$$

$$F_{total} = F(t=0)\ or\ F_o = F + FM \quad \therefore \quad F = F_o - FM$$

$$M_{total} = M(t=0)\ or\ M_o = M + FM \quad \therefore \quad M = M_o - FM$$

$$\frac{dFM}{dt} = k_{obs}(F_{total} - FM)(M_{total} - FM)$$

$$\int \frac{dFM}{(F_{total} - FM)(M_{total} - FM)} = \int kdt$$

$$\frac{FM - F_o}{FM - M_o} = C \cdot exp\big(kt(F_o - M_o)\big), \qquad where\ C\ is\ a\ constant\ from\ integration$$

$$FM(t=0) = 0 \quad \therefore \quad C = \frac{F_o}{M_o}$$

$$\frac{FM - F_o}{FM - M_o} = \frac{F_o}{M_o} exp\big(kt(F_o - M_o)\big)$$

$$FM = \frac{F_o M_o\,[\exp(kt(F_o - M_o)) - 1]}{F_o \exp\big(kt(F_o - M_o)\big) - M_o}$$

All kinetic data gathered was normalized between 0 and 1, where 0 represents the start of the reaction (no conversion), and 1 represents the complete conversion to the product of the resulting fluorous tagged olefin. Thus, this equation was normalized to the reaction by F_o.

$$\frac{FM}{F_o} = \frac{M_o\,[\exp(kt(F_o - M_o)) - 1]}{F_o \exp\big(kt(F_o - M_o)\big) - M_o}$$

Quantification of thiol concentration by 2,2' dithiodipyridine (DTDP)

Thiol concentration was quantitatively assessed during the thiol-Michael addition by modification from previous reported literature.[267,268] Assay concentration was designed to be 100uM final, with a final volume of 210uL. Microcentrifuge tubes held the bulk of the assay volume of 1.4 mL, constituted from 45 µL 12mM 2,2' dithiodipyridine (386 µM final) and 1350.1 µL 0.1 v/v% triethylamine (TEA) in DMSO. Time point aliquots (4.9 µL) were taken from the reaction containing the prospective fluorous thiol at a reaction concentration of 30mM. The initial (t=0) time point was taken before the reaction was started (43.9 mM) and diluted appropriately. Preliminary studies showed thiolate concentration was detected by DTDP consistently after being aliquoted into the microcentrifuge tube termed the "thiol incubation." However, there was a modest decrease in detected thiolate concentration after being placed into the 96-well plate with the subsequent acetic acid addition termed the "acid incubation" (Figure S1).

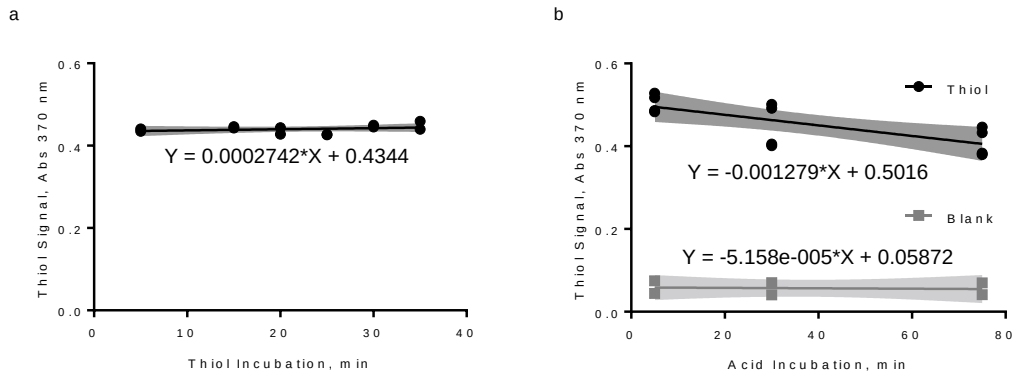

Figure 2-11: *Thiol and acid incubations that affect the DTDP signal*
(a.) *Thiol signal from DTDP absorbance versus thiol incubation time revealing that the fluorous thiol can remain in the DTDP assay for long periods of time without affecting the resulting signal (F test for significantly non-zero slope, p = 0.3652, n = 2, df = 1).* ***(b.)*** *Thiol signal from DTDP absorbance versus acid incubation time revealing the*

fluorous thiol signal decreases modestly over time in the presence of acid (F test for significantly non-zero slope, p = 0.0076, n = 2, df = 1) while the blank remains constant (F test for significantly non-zero slope, p = 0.8492, n = 2, df = 1). The shaded area is the 95% CI around the linear regression line.

Thus, from the 1.4mL bulk assay volume, 200 µL was transferred to a Grenier or Corning 96-well UV-transparent flat plate or a ThermoFisher Scientific flat 96-well plate and 10 µL of acetic acid was added immediately before reading sample absorbance (370±5 nm) using a multi-channel pippette. Samples were normalized to 450 nm to account for well-to-well variation in the 96-well plate, where no absorbance of the reaction substituents was observed, and blank subtracted. Nonlinear regression fitting analysis was performed within GraphPad 7.05 using the F_o-normalized integrated equation described in the methods above to find an apparent rate k_{obs}, reported with standard error.

Detailed theoretical background

Density Functional Theory (DFT), the method used by many theoretical researchers in determine reaction energies, uses a quantum mechanical approach to determine the ground-state energy of a group of atoms. When Schrodinger developed his famous equation in 1926,[283] he provided the means to determine the electronic and nuclear energy of atoms. Unfortunately, his equation could only be solved exactly for one atom. Thomas and Fermi were able to simplify this issue with their ground-breaking discovery in 1927 that the ground state of a system of electrons can be described fully using the electron density distribution.[284,285] This greatly reduces the degrees of freedom needed to mathematically solve for the energy of the system. With the growth of

computational resources, researchers turned to a numerical way to solve for this ground-state energy. However, it was not until the 1960s that a solution was found.

In 1964, Hohenberg and Kohn presented an important principle providing a basis for DFT: the ground-state properties of a system of atoms can be uniquely determined with a functional of the electron density of the group of atoms in 3 dimensions.[286] This is important because rather than having to know the positions of every particle in the system, one only needs to know the density of the electrons throughout the system. Kohn and Sham built upon this principle stating that the energy determined by this functional will always be greater than or equal to the true ground-state energy. For the case when the energy of the electron density functional equals the ground-state energy, the exact electron density has been determined.[287] The deviation of the energy from the ground-state energy is caused by the exchange and correlation in the functional. Throughout the years, many electron density functionals have been developed to better predict the ground-state energy, allowing for better understanding of molecules at an atomic level.[288,289] Based off of these fundamental principles, we perform similar calculations using DFT.

When using DFT for a fixed system of atoms, we can describe the energy level of each configuration of atoms as a point on a Potential Energy Surface (PES). Then, the motion of these atoms in space creates a continuous energy surface from which we can understand chemical and structural transitions. In fact, the classical energy barrier that scientists are familiar with is a transition of atoms from one energy minimum on this PES to another, across some barrier. This trajectory is known as the Minimum Energy Pathway (MEP), with the maximum energy on this MEP corresponding to the

ubiquitous activation energy definition. Arrhenius was the first to recognize activation energy, formulating his well-known Arrhenius equation.[262] Trautz further elucidated this activation energy by proposing collision theory.[290] In the context of this study, we describe this activation energy in the quantum mechanical sense outlined earlier. Therefore, we quantify this apex on the MEP as a first-order saddle point between two minima.

If the mechanism between two energy minima is known, the transition state can be found through simple search methods.[291] However, this concept is frustrated when studying a complex system of atoms. Analyses of a PES have shown that even small displacements in the position of an electron can lead to an energy difference.[292] Therefore, it is more reasonable to think of the PES as a "rough" surface that is the superposition of multiple electronic movements, rather than smooth, Gaussian-like curves depicted in most representations. By isolating these movements, we can uncover the lowest energy mechanism between minima, connected by multiple, smaller energy barriers bounded by intermediate complexes. To perform this, researchers need a combination of intuition and a transition state searching method.

The Nudged Elastic Band (NEB) method (described further in the succeeding section) is the leading method for locating transition states on a MEP.[272] First defined in 1998, several modifications have been implemented to improve the algorithm, leading to the one in use today.[273,274] Simply put, the NEB method provides an accurate estimate of a transition state. Mathematically, this is achieved by optimizing an initial guess of the MEP of a transition. Oftentimes, the initial guess is a linear interpolation between the two minimum energy structures characterizing the start and end of the

transition.[293] From a methodical perspective, one would have sets of Cartesian coordinates that span an energy barrier. We refer to these as "frames". The NEB method optimizes this initial guess of frames by connecting the frames with a fictitious harmonic spring force and minimizing the total force on each frame. The harmonic spring force constrains each frame from falling into an energy minimum, while the potential energy gradient allows the structure of the frame to be optimized downward on the PES. Once converged to the MEP, the approximation of the transition state corresponds to the frame with the highest energy. Then, we can use transition state optimization, which locates the saddle point, to converge to the true transition state. With this atomic configuration, the activation energy can easily be calculated, along with other kinetic properties using Transition State Theory (TST).[294]

Although powerful, the NEB method has a significant drawback: it assumes the existence of a single energy barrier as a geometric change between minima (*i.e.* proton transfer, substitution). If this assumption is ignored, the MEP can easily be over-predicted. Henkelman echoes this concern in a recent review, stating: "a precise rate calculated for an assumed reaction mechanism is misleading if there is a lower-energy pathway that was not discovered."[295] This concern presents a need for a meticulous approach to pinpoint the MEP for subsequent engineering. The solution is to isolate each geometric change in a mechanism, both chemical and structural. A recent paper by the Clancy group gives an example of partitioning a reaction mechanism to determine the true MEP.[275] This approach is important for the thiol-Michael addition, which has several steps in the overall mechanism.

Nudged elastic band simulation

All NEB simulations for our study were performed using a custom NEB algorithm for compatibility with the Orca DFT software package.[296] These calculations were performed at the B97-D3 level of theory[297] with Ahlrichs' def2-TZVP basis set.[298–300] Several parameters also needed to be specified within the NEB algorithm. We chose the LBFGS optimizer[301] based on the recommendation from Herbol *et al.*[302] A spring constant, required for the harmonic spring force that help the band together, was given as 0.1 eV/Å. We used the Climbing-Image NEB algorithm,[273] which came into effect after 5 iterations of the NEB optimizer, to provide a more accurate guess of the transition state atomic geometry. Additional parameters included a dimensionless step size, dimensionless step size adjustment, and maximum step size of 1.0, 0.5, and 0.04 Å, with an accelerated linesearch method for faster convergence. The step size was reset every 20 steps. For all energy barriers related to chemical transitions (initiation, propagation, chain transfer), the convergence criteria were either a root mean squared force of 0.0272 Ha/Å or maximum force of 0.0272 Ha/Å. For all energy barrier related to structural transitions (product decomplexation), the convergence criteria were either a root mean squared force of 0.005 eV/Å or maximum force of 0.005 eV/Å. The tighter convergence criteria provide a better prediction of the transition state in the absence of a transition state optimization that requires a stable first-order saddle point not present in a structural transition such as decomplexation. An example of the NEB method for the chain transfer step in the *N*-butyl-*N*-allylacrylamide monomer reaction is shown in Figure 2-11. The transition state corresponds with the x-value of 2 along the reaction coordinate.

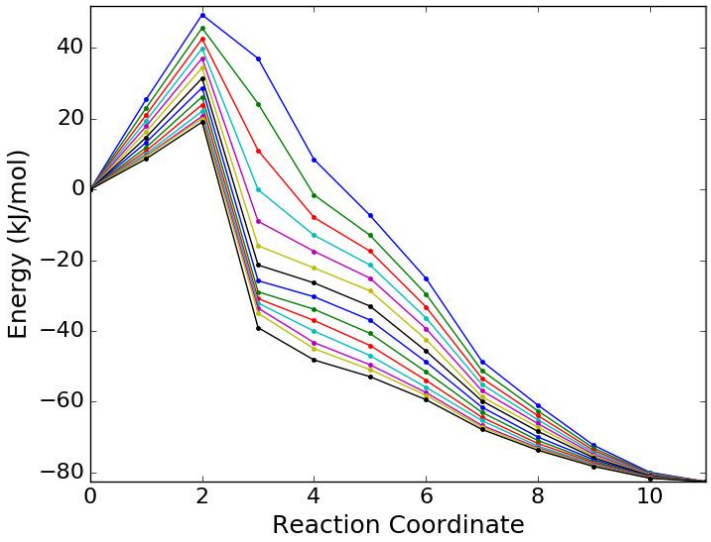

Figure 2-12: *Iterative reduction of energy from our custom NEB method*
The iterative reduction of energy from our custom NEB method. Shown in this figure is the chain transfer step of the N-butyl-N-allylacrylamide, calculated using the B97-D3 functional with the def2-TZVP basis set in an implicit methanol solvent. The colors shown the energy barrier at each iteration, moving downward to the final energy barrier of 20 kJ/mol.

Comparison of energies between levels of DFT theory

Common to all computational studies, our study faced the trade-off between cost and accuracy for the calculation of our stationary points and reaction energies. As reported by Smith *et al.*, range-separated functional are necessary for modeling the thiol-Michael addition, as it properly predicts an energy minimum for the carbocation intermediate.[271] Moreover, another article suggests the ωB97X-D3 range-separated functional due to its ability to accurately predict proton transfers, a transition present in the thiol-Michael addition.[303] However, the computational cost for the ωB97X-D3 range-separated functional is high, making it infeasible to perform all calculations at this level of accuracy. Instead, we employ a two-step approach. We calculate all stationary points at the Generalized Gradient Approximation (GGA) level of theory using the B97-D3 functional, recommended by Grimme *et al.* as fast and accurate,[288,289]

then perform final single point energy calculations using the more accurate ωB97X-D3 range-separated functional. Beyond these reasons, these two functionals were also chosen because of their compatibility. Both functionals calculate the short-range interactions using the same algorithm, with the ωB97X-D3 functional having additional capabilities to calculate long-range interactions. Therefore, an energy barrier of discrete atomic positions will have coincident minima and maxima for both levels of theory. The ωB97X-D3 functional predicts larger energy barriers than B97-D3, due primarily to the inclusion of important long-range interactions present in a system with ions, such as ours.

Chapter 3 : Synthesis and Solution-Phase Characterization of Flexible Sulfonated Oligothioetheramides

Acknowledgements

This chapter has been adapted with permission from J. S. Brown; Y. M. Acevedo; G. D. He; J. H. Freed; P. Clancy; C. A. Alabi, *Macromolecules* **2017**, 50 (21), 8731–8738. Content has been added to this chapter outside of the publication including additional discussion of sulfated materials and the biological testing of sulfonated oligoTEAs as heparin mimetic for antithrombin binding.

Individual contributions

J.S.B and C.A.A conceptualized the project. J.S.B. and G.D.H synthesized the oligoTEAs and performed biological experiments. J.S.B. wrote the manuscript, performed solution-phase characterization (PFG NMR, DEER EPR) and analyzed the data, and combined the results within the Stokes-Einstein-Sutherland equation. A.Y.M. performed and analyzed molecular dynamics simulations. All authors discussed the results and edited the manuscript.

Article acknowledgements

From the article by Brown J.S. et al: The authors sincerely thank personnel at the National Biomedical Center for Advanced Electron Spin Resonance Technology (ACERT) for training in using the EPR spectrometer, as well as invaluable guidance and support with the acquisition and processing of EPR data. Computational resources were provided by the Cornell Institute for Computational Science and Engineering

(ICSE). Acknowledgment is made to the donors of the Petroleum Research Fund, administered by the American Chemical Society, for partial support of this research. This project received funding from the Army Research Office (W911NF-15- 1-0179), Cornell University Startup funds and the Nancy and Peter Meinig Investigator Fellowship. J.S.B. acknowledges financial support from the National Science Foundation Graduate Research Fellowship Program (DGE-1144153). Equipment used to perform this research was funded in part by the Cornell Center for Materials Research (DMR-1120296), ACERT Grant NIH/NIGMS P41GM103521, and NSF-MRI (CHE-1531632).

Abstract

Nature has long demonstrated the importance of chemical sequence to induce structure and tune physical interactions. Investigating macromolecular structure and dynamics is paramount to understand macromolecular binding and target recognition. To that end, we have synthesized and characterized flexible sulfonated oligothioetheramides (oligo-TEAs) by variable temperature pulse field gradient (PFG) NMR, double electron−electron resonance (DEER), and molecular dynamics (MD) simulations to capture their room temperature structure and dynamics in water. We have examined the contributions of synthetic length (2−12mer), pendant group charge, and backbone hydrophobicity. We observe significant entropic collapse, driven in part by backbone hydrophobicity. Analysis of individual monomer contributions revealed larger changes due to the backbone compared to pendant groups. We also observe screening of intramolecular electrostatic repulsions. Finally, we comment on the combination of DEER and PFG NMR measurements via Stokes−Einstein−Sutherland diffusion theory.

Overall, this sensitive characterization holds promise to enable de novo development of macromolecular structure and sequence−structure−function relationships with flexible, but biologically functional macromolecules.

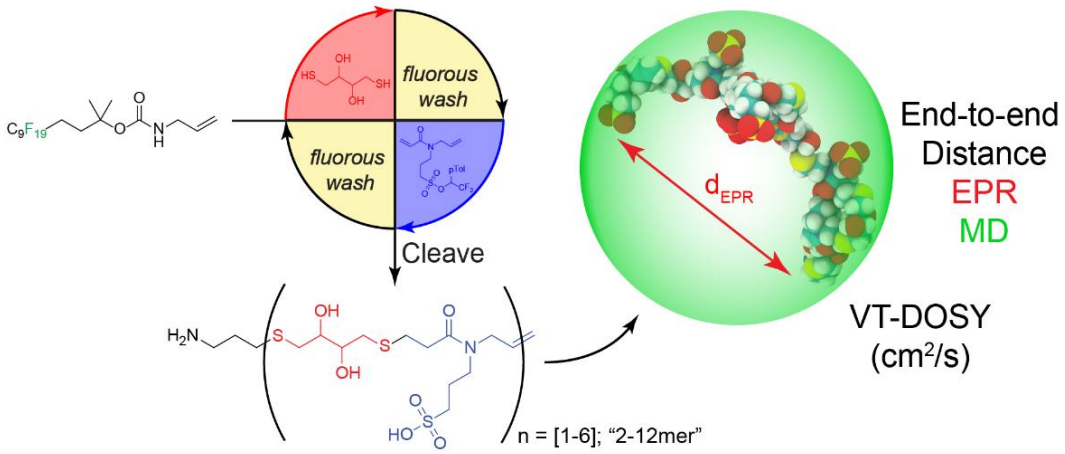

Figure 3-1: *Graphical abstract describing synthesis and solution-phase characterization of flexible sulfonated oligothioetheramides*

Introduction

Motivation

Biological macromolecules perform advanced functions by controlling the relationship between their chemical functionalities and structure. Higher-order structures including α-helices, β-sheets, stem-loops, and many others represent the potential of optimized sequence-structure-function relationships to generate sensitive stimuli-response, allostery, information management, and expression.[304–308] Precise sequence control, as seen in biological scaffolds, can be used to control local enthalpic and global entropic contributions, important factors that dictate folding, self-assembly, and biological interactions.[309] The ability to control structure and function by

composition and sequence has prompted significant research in the development of sequence-defined polymers.[97,99] Motivated by this call, we recently described sequence-defined oligothioetheramides (oligoTEAs) featuring a rapid and efficient synthesis, access to the backbone, and the use of diverse pendant groups.[146,147] The synthetic strategy utilizes the reactive orthogonality of *N*-allyl acrylamide monomers, rather than protection/deprotection groups for iterative assembly.[147] The accessibility of the oligoTEA backbone and pendant groups render them ideal for exploring macromolecular conformation and dynamics.

Development of sequence-defined sulfated materials

Sulfates and sulfonates have long been sought after for materials development for their ability to impart water-solubility, surfactant action, non-fouling, and self-assembly.[310,311] In biology, sulfated carbohydrates comprise significant portions of the extracellular membrane surface and proteins often experience glycosylation, which can be sulfated. The sulfation and sulfonation of these carbohydrates adds a layer of complexity on top of the saccharide (glucose, galactose, fructose, mannose, etc.), let alone the remaining modifications of alkylation, phosphorylation, and N-acetylation. This structural diversity provides limitless potential to encode complex biological information. Thus, researchers have shown that sulfated carbohydrates play diverse and important biological roles in the regulation of blood clot formation, viral infection, neural cell growth, angiogenesis and tumor growth, cartilage structure, and metastasis.[312–317] However, sulfates and sulfonates are highly polar and can dominate their physical properties and solubility, often requiring the use of protecting groups.[318]

To study sulfated or sulfonated materials, several methods have been employed ranging from isolation from natural sources, to post-sulfation or sulfonation of designer polymers, to the bottom-up synthesis of glycomemetics. Low-molecular weight heparin sulfate from natural (porcine) sources containing the active heparin pentascchairde sequence is often isolated by enzymatic and/or chemical depolymerization of tissue. This isolation suffers from batch to batch variability, posing a safety risk because of the sensitive nature of anticoagulation. In one recent case in 2007, contaminated heparin sulfate was associated with over 200 deaths in the US.[319] Post-sulfation has commonly been employed with sulfur trioxide complexes across a variety of designed polymers, but results in heterogeneous sulfation patterns.[320–324] Other researchers have been working with polymerization of defined, sulfated glycan monomers can produce libraries of mimetics with relative monodispersity.[325–327]

While bulk sulfation is likely sufficient for some materials and applications, precise sequence control of sulfation is biologically prescribed, though poorly understood. However, synthesis of sequence-defined sulfated or sulfonated materials is challenging, especially within the use of the saccharide backbone. A primary example of this challenge is seen in the slow throughput in the decades long development of the heparin pentasaccharide, the isolated five sugar sequence sequence responsible for high affinity anticoagulant binding.[328–331] Total synthesis provides strict replication of the saccharide backbone with sequence-defined sulfation, but can often be a difficult, low-yield, multi-step process, even with advances in chemoenzymatic methods.[332,333]

Peptides and peptoids (N-substituted glycines) have long struggled to incorporate sulfates or sulfonates due to the frequent use of TFA and nucleophilic bases

for deblocking, both of which compromise sulfate esters, making their exploration difficult, even in replication of natural sulfotyrosine form[334,335]. This is largely due to the innate sensitivity of sulfate esters to acid and nucleophiles[336]. Several protecting group strategies have been tried over the years including phenyl, 2,2,2-trichloroethyl, 2,2,2-trifluoroethyl, neopentyl, isobutyl, and most recently 2,2,2-trichloroethyl sulfuryl imidazolium salts all with increasing degrees of chemical protection and utility[337]. However, protecting groups that are stable to acidic conditions or nucleophiles (e.g., neopentyl) often require harsh conditions for deprotection that limits their use.

In comparison to sulfate esters, sulfonates provide better chemical stability while maintaining important hydrogen bonding, negative charge, and hydrophilic characteristics of the sulfate ester. The development of protecting group chemistries for sulfonates has also struggled, since sulfonate esters are also potent electrophiles.[318] Nevertheless, sulfonate protecting groups progressed and initial success was found with the neopentyl group, which was stable but slow to deprotect decreasing potential yields. Modification of the neopentyl group to a first-generation TFA-liable "neoN-B" (N-Boc-4-amino-2,2- dimethylbutyl-1-sulfonate ester), which allowed better cleavage via intramolecular nucleophilic attack. Advancements were made in the pursuit of esterase cleavable sulfonates from self-immolative trifluoromethylbenzyl substrates, which were more economical than the neoN-B and similarly stable.[338] This effort culminated in work by S Pauff and S Miller to produce an α-trifluoromethyltolyl (TFMT) sulfonate protecting group that provided ideal stability to *N*-allyl-*N*-acrylamide monomer synthesis, oligoTEAs assembly, and a clean TFA-cleavage without nonvolatile side-

products.[339] The TFMT sulfonate protecting group was well-suited for the following work.

Solution-phase characterization of flexible macromolecules

The solution-phase structure and dynamics of macromolecules are challenging to characterize because they are a complex product of intramolecular interactions, entropy, and solvent interactions derived from the chemical composition and sequence. For characterization of small macromolecules or molecules, structure and dynamics can be challenging due to the small length- and time-scales, which can limit common experimental structural elucidation techniques. Current techniques characterize structure at various resolution and throughput, depending on the size and flexibility of the macromolecule. These limitations are of concern because OligoTEAs contain a significant number of unconstrained methylenes within their repeat unit, meaning they should be quite flexible in solution, limiting potential methods of characterization.

As a cornerstone in high resolution structure determination, X-ray crystallography is limited by the production of quality crystals, difficulty with flexible domains, and the stochastic nature of crystallization to visualize only low-energy conformers without solution phase dynamics.[340–343] NMR can serve as a high-resolution method for protein structure elucidation[344,345] and primary ligand screening,[346] but robust methods to study synthetic non-peptide structure are lacking. Small-angle x-ray scattering (SAXS) has proven to be a robust low-resolution tool providing solution-phase ensembles, but can be limited by structure flexibility because of time- and space-averaged scattering.[347–349] Comprehensive techniques have improved upon individual weaknesses including combinations of SAXS and crystallography,[350] NMR and

crystallography,[351] SAXS and molecular dynamics (MD),[352] and even SAXS, crystallography, and MD.[353] Each type of methodology combines information to generally refine the solution-phase structure observed. Inspired by these methodologies, we sought to explore additional means of solution-phase characterization that was not limited by macromolecular flexibility.

Objectives

Highly sulfated macromolecules have potential to show a diverse array of biological interactions and will continue to be explored.[354] In this work, we have sought to simultaneously i) demonstrate the ease of assembling sequence-defined sulfonated oligoTEAs, ii) develop methodology to characterize the extent of single-chain collapse of these oligomers, iii) thus allowing us to determine the structural effects of intramolecular electrostatic repulsion. Herein, we present the synthesis and solution-phase characterization of sulfonated oligoTEAs as a function of length (2-12mer). We also explored the effect of pendant group charge and backbone composition on dynamics of the oligoTEA chain. Structural investigation was performed by variable temperature pulsed field gradient (PFG) NMR, pulsed electron paramagnetic resonance (EPR), and molecular dynamics (MD) simulations. Variable temperature PFG NMR most directly measures the macromolecular hydrodynamic radius.[355] EPR and MD can both observe solution-phase dynamics. Double electron-electron resonance (DEER) EPR can quantify the distance distribution between paramagnetic spin-labels[356,357] and has been done for a few oligomer case studies[358–361]. MD simulation visualizes oligoTEA time evolution and molecular configuration space. All characterization was carried out to capture room temperature structure and dynamics in water. We also

comment on the combination of these data within the Stokes-Einstein-Sutherland equation with size and shape factors to quantify size and aspect ratio within simple geometries.[362]

Results and Discussion

OligoTEA assembly as shown in Figure 3-2 begins with a fluorous-tagged soluble support functionalized with an allyl group. The first monomer is attached by a UV-initiated thiolene utilizing dithiol in the presence of a photoinitator. Fluorous solid-phase extraction isolates the resulting fluorous thiol. The next monomer is attached via a thiol-Michael addition of an *N*-allyl acrylamide monomer in the presence of phosphine catalyst. The orthogonal reactivity ensures that the acrylamide reacts with the fluorous thiol with minimal cross-reactivity of the allyl group. To incorporate sulfonated pendant groups, a protected sulfonate *N*-allyl acrylamide monomer (PSM) was prepared utilizing an α-trifluoromethyltolyl (TFMT) group (Figure 3-11).[339] With the attachment of an *N*-allyl acrylamide by the thiol-Michael addition, the allyl group is reestablished to begin the cycle again.

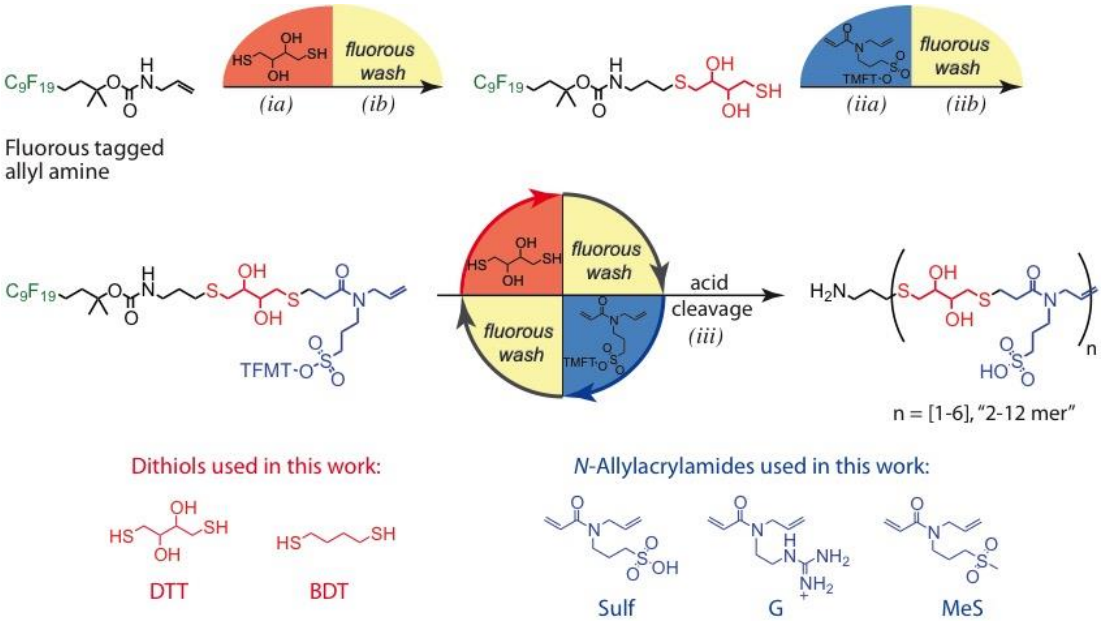

Figure 3-2: *Sulfonated oligothioetheramide assembly where (ia) A fluorous olefin is reacted with a dithiol in a UV-initiated thiolene and the product is purified in (ib) by fluorous solid-phase extraction (FSPE). (iia) A fluorous thiol is reacted with an N-allyl acrylamide monomer in a phosphine initiated thiol-Michael addition and purified by FSPE (iib). These two reactions are cycled until the desired oligomer length is reached. (iii) The fluorous support is cleaved with trifluoroacetic acid and HPLC purified to give the final desired oligomer. TMFT: α-trifluoromethyltolyl protecting group.*

The first set of oligomers was synthesized by iterating dithiothreitol (DTT) dithiol and the protected sulfonate *N*-allyl acrylamide monomer and tracked by ^{1}H NMR, ^{19}F NMR, and a dithiodipyridine (DTDP) assay (Figure 3-3). As detailed in earlier reports, the synthetic progression of oligoTEAs can be tracked by ^{1}H NMR by focusing on the disappearance of the allyl protons to confirm thiolene conversion.[146] To track the completion of the thiol-Michael addition, ^{1}H NMR has previously focused on the consumption of the thiol peak and appearance of allyl peaks. However, the monomer thiol peak of dithiolthreitol appears within the t-Boc of the fluorous support (Figure 3-3, methyl protons designated as 'E'). Additional evidence of the Michael addition

conversion can be observed with the growth of protons ‘C’ and ‘D’ located on the aromatic tolyl group of the protected sulfonate N-allyl acrylamide. Also, a DTDP assay can determine the thiol concentration and subsequent consumption.[267,268] Finally, sensitive ^{19}F NMR can also be used to verify the completion of the Michael addition by observing the trifluoro group of the protected sulfonate *N*-allyl acrylamide (Figure 3-3, trifluoro group designated B). All monomer peak intensities increase and broaden with respect to the fluorous support as the oligomer is elongated as expected. Oligomers after each cycle were sequestered, cleaved, purified by HPLC, and confirmed by ^{1}H NMR and LCMS (Appendix B see Supplementary Spectra) providing synthetic lengths of 2-12 “mers.” To explore the effect of each chemical group, additional oligomers were synthesized at the 10mer length with 1) a positively charged guanidine (G) group 2) a non-charged methyl sulfone (MeS) pendant group and 3) a methylene backbone using butanedithiol (BDT) (Figure 3-2, Appendix B see Supplementary Spectra).

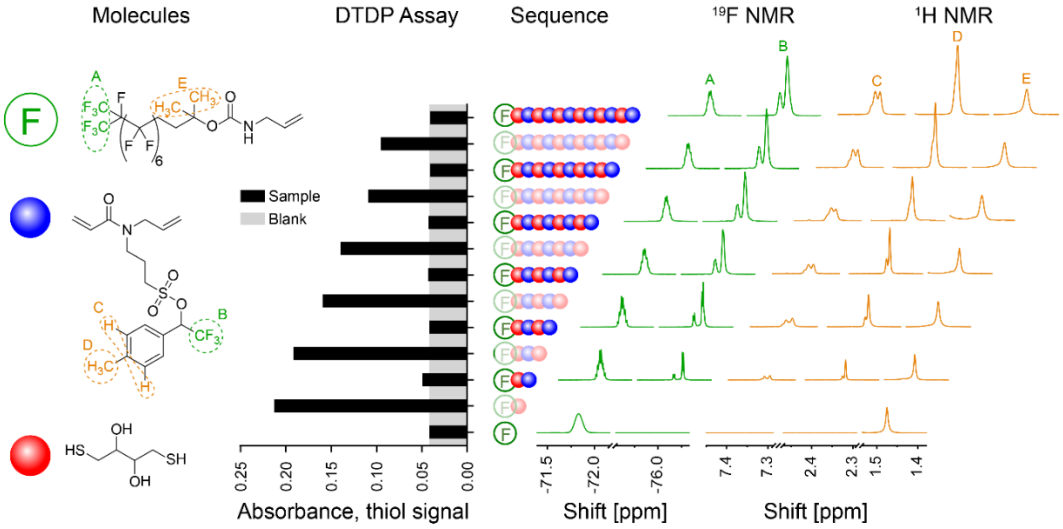

Figure 3-3: *Assembly of hydroxylated sulfonate oligoTEAs*
Full molecular structures are shown with green trifluoro and orange proton groups on the fluorous support (A and E, respectively) and the PSM (B and C,D respectively). DTDP assay determination of thiol concentration, indicating thiol-Michael addition

completion and qualitative yield. ^{19}F NMR spectra are shown with fluorous trifluoro group A normalized. PSM trifluoro group 'B' intensity increases and becomes broader as a function of oligomer length. Similarly, ^{1}H NMR spectra normalized by Boc protons 'E' shows intensity increases and broadening of PSM tolyl protons 'C' and 'D.'

Characterization of oligoTEAs by variable temperature PFG NMR visualizes macromolecular diffusion as a linear function of viscosity normalized temperature (Figure 3-4). This linearity rules out any intramolecular transitions as a function of temperature and constrains the prospective size within Stokes-Einstein-Sutherland equation (Equations 3-2 to 3-4, Materials and Methods, Diffusion Theory). It additionally suggests minimal intermolecular interactions (e.g., aggregation, repulsion). Accurate measurements were obtained using 3 mm tubes, high gas flow rate, an optimized eddy current delay, convection compensation, and gradient pulse control experiments (Figures 3-12 to 3-14).[355] The translational diffusion of the backbone was compared to the diffusion of the oligomer end to discern any heterogeneity, revealing the uniform diffusion of each oligomer (Figure 3-15).

Diffusion is affected by the hydrodynamic size, shape, and hydration state of a given macromolecule. The data in Figure 3-4 follow expected trends in that these macromolecules diffuse quicker at higher temperatures or shorter synthetic length. The oligomers with hydroxylated (DTT) backbone diffused slightly faster than the aliphatic backbone (BDT). This result can be rationalized by a number of factors including differences in shape, hydration effect caused by the more hydrophobic BDT backbone, or stronger hydrogen bonding in the DTT hydroxylated backbone resulting in a more compact faster diffusing oligomer. Additionally, the slope of the diffusion versus

normalized temperature establishes a relationship between the hydrodynamic radius and aspect ratio depending on the assumed geometric model (Equations 3-5 to 3-12).

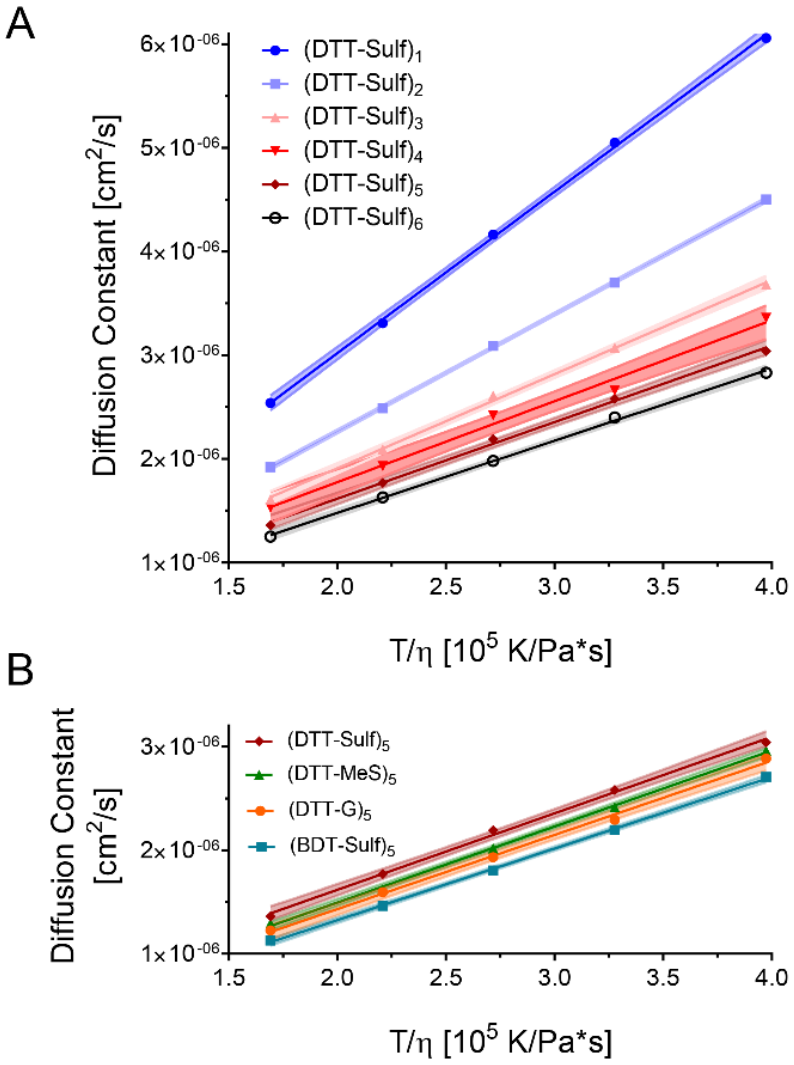

Figure 3-4: *Diffusion coefficient versus viscosity normalized temperature Translational diffusion coefficient as measured by PFG-NMR of oligoTEAs over a range of 10-40 °C of 1-3 mM (DTT-Sulf)$_{1-6}$ in D_2O.* ***B.*** *Diffusion coefficients of 1-3 mM oligomers in D_2O with different pendant and backbone groups as a function of temperature, shown with the same scaling. Solid-line linear fits are shown with shaded regions representing the 90% CI.*

To observe the dynamics of these oligoTEAs in an aqueous environment double electron electron resonance (DEER) EPR distance measurements and molecular

dynamics (MD) simulations were completed. DEER measurements were performed on dispin-labeled oligomers prepared by reaction of an oligoTEA diamine with a Proxyl NHS ester. The oligoTEA diamines were prepared by via an additional thiolene reaction of 2-(Boc-amino)ethanethiol on the terminal allyl group. TFA cleavage then liberates an amine at each end. Dispin-labeled oligomers were purified by HPLC, verified by LCMS (Figure 3-16, see Appendix B Supplementary Spectra), measured by 4-pulse double electron-electron resonance (DEER), and reconstructed by Tikhonov regularization using the L-curve method. Molecular dynamics simulations of single oligomer chains were performed for 50ns in a water-filled box with periodic boundary conditions in an NVT ensemble to represent a dilute oligomer solution. Specifically, the (DTT-Sulf), (DTT-MeS), and (BDT-Sulf) oligoTEAs were simulated at all lengths (2-12mer) to aid in the visualization of trends as a function of synthetic length. To validate the simulations, the translational diffusion constant was calculated and compared to PFG NMR measurements, revealing good agreement (Figure 3-17). With respect to the $(DTT\text{-}Sulf)_{1\text{-}6}$ series (Figure 3-5A), the probability distribution from EPR data shows an increase in end-to-end distance with increasing oligomer length, as well as a concomitant increase in conformational freedom as measured by the full width of half max (FWHM). The mean end-to-end distance of the oligomers calculated by MD is also in reasonable agreement with the EPR data, showing a modest increase with oligomer size. MD simulations observe a slightly greater end-to-end distance with the $(DTT\text{-}Sulf)_{5,6}$, which falls within the experimentally observed conformational ensemble (Figure 3-5B). Overall, this data highlights oligomer flexibility, especially when

considering they show an average ~50% collapse from their fully extended theoretical length (Figure 3-5B and Appendix Figure B-3).

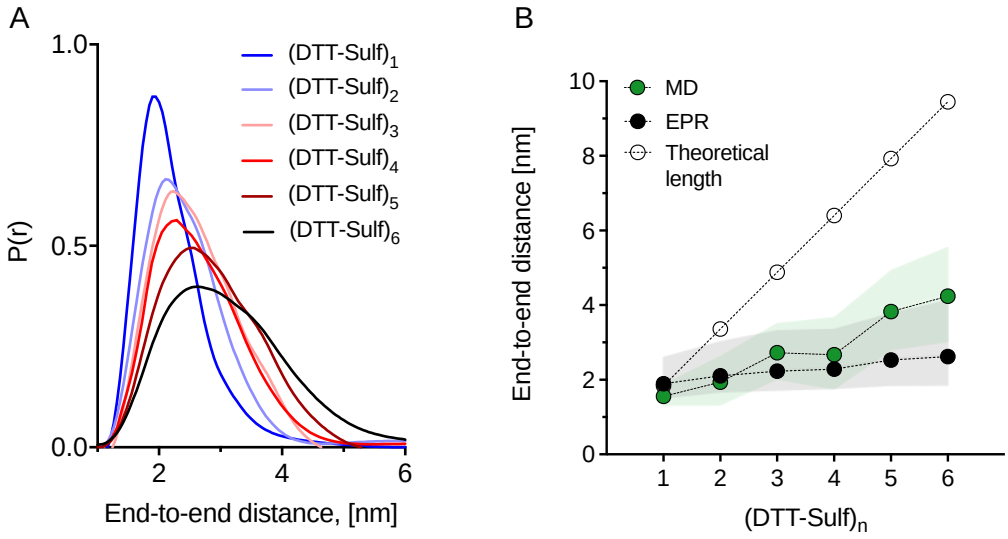

Figure 3-5: *$(DTT\text{-}Sulf)_x$ sulfonated oligomer end-to-end distances*
A. *Distance reconstructions of the end-to-end distance distribution function generated from DEER EPR of 100 uM $(DTT\text{-}Sulf)_{1\text{-}6}$ in 20% ethylene glycol in water vitrified (70K) from room temperature.* ***B.*** *Mean end-to-end distance versus synthetic length from DEER distance reconstruction and single-chain MD simulation (300K, explicit water solvent). Data points represent the mean end-to-end distance. Transparent bands represent the full-width at half maximum (FWHM) from EPR or standard deviation from the MD simulation time after equilibration. Supplementary methods detail sample spin-labeling (Figure 3-16), DEER measurement, and MD simulation detail.*

End-to-end distance measurements from DEER and MD were used to visualize the individual contributions of backbone hydroxylation and pendant groups, revealing a larger effect from the backbone. 10mers with a methylene backbone, i.e., $(BDT\text{-}Sulf)_5$, positive charge $(DTT\text{-}G)_5$, and neutral charge $(DTT\text{-}MeS)_5$ were characterized (Figure 3-6). The EPR results show that the pendant groups have minimal influence on the average end-to-end distance and the conformational flexibility of the 10mer oligoTEAs.

The length scale of these results are sensible given literature.[363] The MD data on the other hand shows that the cationic $(DTT\text{-}G)_5$ results in a relatively smaller end-to-end distance than predicted for the $(DTT\text{-}Sulf)_5$ and $(DTT\text{-}MeS)_5$. The methylene backbone of $(BDT\text{-}Sulf)_5$ results in a smaller end-to-end distance in both DEER and MD experiments. This effect could be rationalized by greater hydrophobic collapse without backbone hydroxylation. However, PFG NMR suggests that the $(BDT\text{-}Sulf)_5$ diffuses slower than all other 10-mers with pendant group modifications (Figure 3-4B). Together these results can be rationalized by two possible explanations. The Proxyl spin-probes could be participating in hydrophobic collapse and thus locate closer to one another in BDT-Sulf. Though possible, the MD simulations predict similar collapse and were performed without spin probes on the molecular structure (Figure 3-6B), casting doubt on the ability of the spin probes to direct the collapse of the BDT-Sulf oligomer. Thus, the hydroxylated backbone likely participates in intramolecular interactions, aiding collapse by attractive forces (i.e., hydrogen bonding) to result in a smaller hydrodynamic size than the BDT-Sulf.

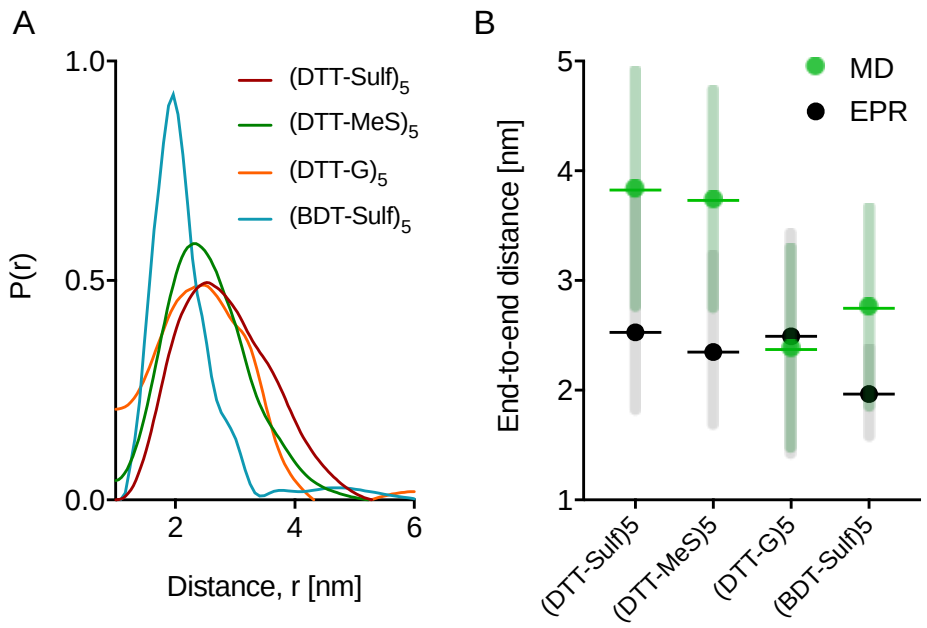

Figure 3-6: *End-to-end distance of alternative 10mer oligomers*

A. *Distance reconstructions of the end-to-end distance distribution function generated from DEER EPR of all 10mers at 100 uM in 20% ethylene glycol in water vitrified (70K) from room temperature.* ***B.*** *Mean end-to-end distance from DEER distance reconstruction and single-chain molecular dynamics simulation (300K, explicit water solvent). Data points represent the mean end-to-end distance. Error bars represent the full-width at half maximum (EPR) or standard deviation (MD). Supplementary methods detail sample spin-labeling (Figure S12), DEER measurement, and MD simulation detail.*

The effect of intramolecular electrostatic repulsion on chain dynamics can be visualized with DEER and MD by screening these interactions with ammonium cations (Figure 3-7). Aqueous ammonia was added to the oligoTEA sample preparation to give an estimated [NH_4^+] concentration of 8.5 mM (K_b of 1.8 x 10^{-5}), with oligoTEA concentration at 100 μM. The neutral oligoTEA $(DTT\text{-}MeS)_5$ does not experience a change conformational flexibility or end-to-end distance with the addition of ammonium ions as would be expected (Figure 3-7E). However, the addition of ammonium ions in the $(DTT\text{-}Sulf)_5$ oligoTEA results a slightly shorter end-to-end

distance presumably due to screening of intramolecular electrostatic interactions (Figure 3-7A). Conversely, without salt present, intramolecular electrostatic repulsion is stronger, marginally broadening the conformational ensemble. This effect can is seen more prominently in the $(DTT\text{-}Sulf)_6$ oligoTEA (Figure 3-7B). Addition of ammonium ions to the positively charged $(DTT\text{-}G)_5$ oligoTEA leads to a slight narrowing of the distribution and little to no change in the average end-to-end distance (Figure 3-7C). The distribution and average end-to-end distance of the backbone modified $(BDT\text{-}Sulf)_5$ oligoTEA showed similar results with slight narrowing of the distribution and little to no change in the average end-to-end distance (Figure 3-7D).

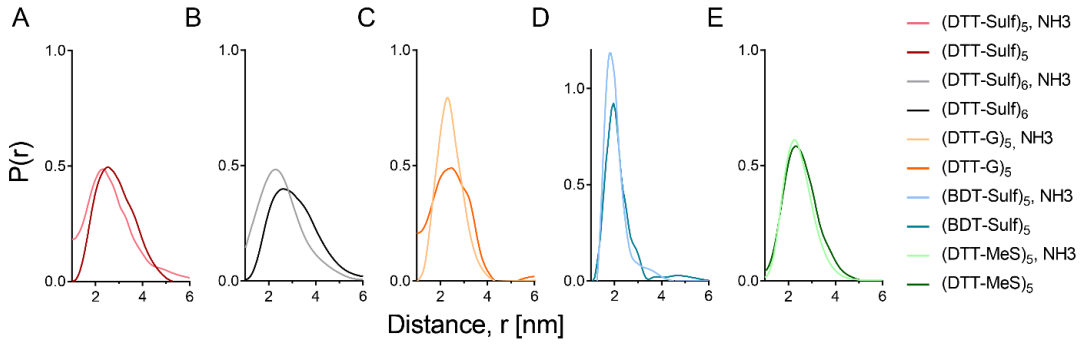

Figure 3-7: *Effect of ammonium salt on oligoTEA end-to-end distance*
End-to-end distance distributions from DEER measurement of 100 uM oligoTEAs in 20% ethylene glycol in water vitrified (70K) from room temperature revealing that all charged oligoTEAs experience electrostatic screening by the addition of ammonia during sample preparation. Lighter color lines indicate distributions measured with ammonia sample preparation.

DEER and PFG NMR measurements both provide an indication of macromolecular size; DEER gives the end-to-end distance while PFG NMR measures the translational diffusion coefficient. The Stokes-Einstein-Sutherland (SES) relation can be used to relate diffusivity to the macromolecular size and shape, given simple

geometries (Equations 3-1 to 3-5).[362,364] Shape models have been developed by F. Perrin (oblate, prolate ellipsoids) and more recently by A. Ortega and J. García de la Torre (rod) (Equations 3-6 to 3-8).[365–368] While an ellipsoid is geometrically preferred, the rod model is mathematically continuous over its range of aspect ratio, making it more robust. To solve for size and shape simultaneously, a constraint is needed outside of the data gathered from the PFG NMR (Equation 3-4). DEER and MD end-to-end distances can be assumed to describe the length of the rod, allowing discrete solutions to be obtained for the hydrodynamic radius and aspect ratio (Equations 3-9, 3-10).

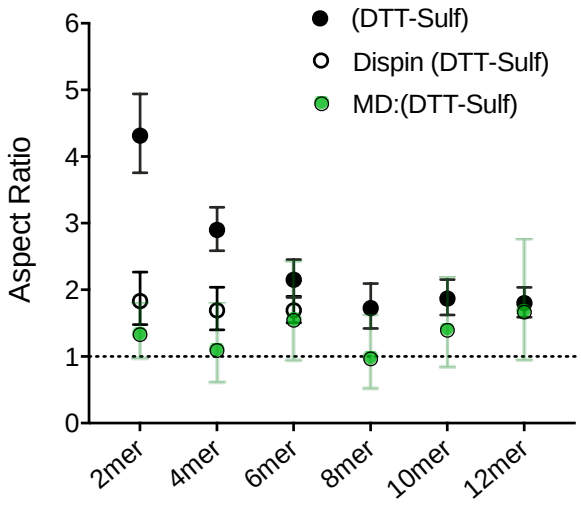

Figure 3-8: *$(DTT\text{-}Sulf)_x$ aspect ratio versus synthetic length*
The aspect ratio of the $(DTT\text{-}Sulf)_{1\text{-}6}$ series calculated from the solution to the SES rod model assuming the end-to-end distance data describes the long dimension (length) of the rod. Data in the black filled circles were computed using end-to-end distance measurements from EPR and the diffusion coefficient of oligomers without the spin probes present. The filled green circles represent solutions to the SES rod model using the end-to-end distance data obtained from MD simulations. The open circles represent the aspect ratio of the $(DTT\text{-}Sulf)_{1\text{-}6}$ oligomers computed using the diffusion coefficient of the oligomers bearing the two spin probes. The error bars on the experimental $(DTT\text{-}Sulf)_{1\text{-}6}$ data series represent errors from the PFG NMR data and a 95% confidence level in the DEER data, all propagated through the SES model.

Similar to the end-to-end distance data (Figures 3-5 through 3-7), this additional analysis confirms increases in size, as indicated by the hydrodynamic radii from the SES rod model, at longer oligomer lengths (Figure S12). However, the aspect ratio data derived from the MD end-to-end distances appear lower than what is observed experimentally (Figure 3-8). One possible explanation of this observation is that the addition of spin-labels for DEER measurement adds significant size or length to the smaller oligomers. This concern is compounded because the aspect ratio is exponentially sensitive to the difference between the end-to-end constraint and twice the hydrodynamics radius (Appendix B Figure B-6). To investigate this theory, the first three di-spin labeled oligomers ((DTT-Sulf)$_{1\text{-}3}$) were oxidized, measured by PFG NMR (Appendix B Figure B-7) and re-analyzed with the SES rod model. The new aspect ratio which takes into account the spin labels on (DTT-Sulf)$_{1\text{-}3}$ confirms that the original aspect ratio of the smaller oligomers was inflated by the length added by the spin labels (Figure 3-8). Although the paramagnetic nitroxides can affect the NMR quality (i.e., oxidation is necessary), the shape and size analyses are best performed on the same macromolecule when shorter oligomer lengths are involved. Beyond a synthetic length of six monomers (three dithiol and three *N*-allylacrylamide monomers), the spin-probes have minimal (< 10%) impact on diffusion (Appendix B Figure B-8). The overall SES shape analysis with the rod model utilizing PFG NMR and DEER data, and the MD data, indicate that all oligoTEAs prepared in this work have a low aspect ratio (1-2) as expected for relatively short and flexible macromolecules.

Biological testing of sulfonated oligoTEAs

Note: this work was not included in Brown, J. S.; Acevedo, Y. M.; He, G. D.; Freed, J. H.; Clancy, P.; and Alabi, C. A. *Macromolecules* **2017**, *50* (21), 8731–8738.

Additional background

With sulfonated oligoTEAs of varying length produced, biological testing could reveal their potential as sulfated glycomimetics. As briefly aforementioned, heparin sulfate is one of the most-well known sulfated glycosaminoglycans and has clinically been utilized toward a variety of anticoagulant and antithrombotic indications since the 1940s.[369] Thrombosis of cerebrovascular, cardiovascular, and peripheral vasculature, is the leading cause of mortality in the western world and developing countries.[370] Short term treatment with heparin sulfate includes any extracorporeal procedure (hemofiltration, catheter, etc) as well as acute coronary syndrome (i.e. reduced blood flow to the heart) with or without percutaneous coronary intervention ("stent"). Longer term treatment requires an excellent safety profile with reliable phenotypical response. General indications includes i) atrial fibrillation, a leading risk factor for stroke, affecting 2.3 million people in the US as of 2008, ii) treatment or prophylaxis of venous thromboembolism following surgery, iii) or prophylaxis for myocardial infarction ("heart attack") or reinfarction, a leading cause of death worldwide.[371–373]

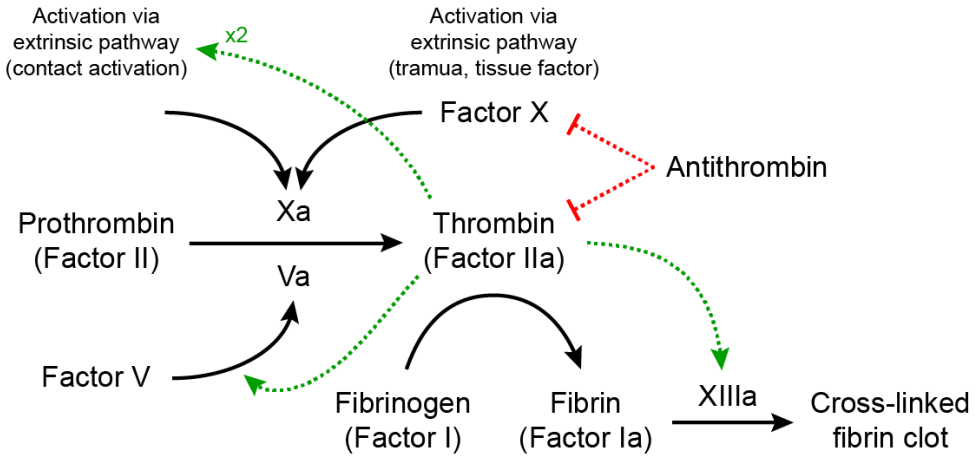

Figure 3-9: *Common pathway of the coagulation cascade. Modified from reference*[304,374] *demonstrating the location of antithrombin as the main inhibitor of thrombin, which amplifies several other parts of the coagulation cascade.*

Hemostatic regulation of coagulation cascade is a complex and the pathway centers around the activation of thrombin (Factor II). Thrombin itself is highly responsive to the progression of thrombosis and its activity is highly tuned, modified, and ultimately attenuated by cofactors that bind to its exosites[304,375] (Figure 3-9). Therapy to attenuate the sensitivity and activity of these reactions has been a focus of much research ranging from inhibition of thrombin, Factor Xa, and antithrombin. Antithrombin serves to be a straightforward method to inhibit thrombin action. Thus, a strategy to manage this process and prevent possible clot formation is to activate antithrombin, which can then inhibit thrombin.

Little to no binding to antithrombin

While it facilitates several parts of the coagulation cascade, heparin sulfate binds and activates antithrombin to then inhibit thrombin to maintain a controlled level of coagulation. With this known mechanism, we attempted to observe binding of sulfonated oligoTEAs to antithrombin. Work in literature has connected changes in the

tryptophan fluorescence of antithrombin to binding of heparin sulfate into its binding pocket. This method was chosen over the use of exogenous molecular probes including 6-(p-Toluidino)-2-naphthalenesulfonate (TNS), which can encode information about changes in protein conformation.[376–378] According to the binding assay, the prepared sulfonated oligothioetheramides show little to no binding to antithrombin up to 0.6 mM at low salt concentrations.

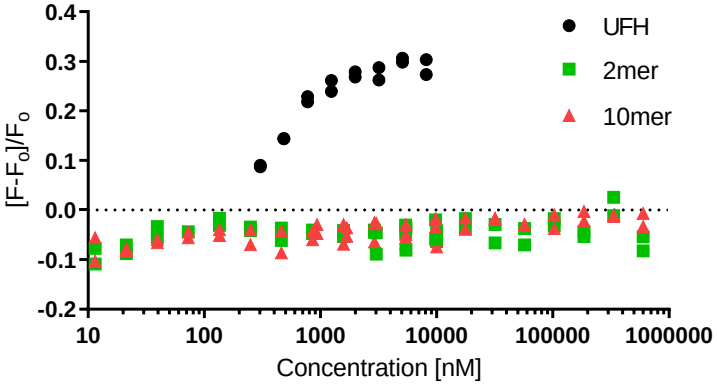

Figure 3-10: *Antithrombin binding assay*
Unfractionated heparin sulfate (UFH) is shown, analyzed to have a binding affinity (K_d) of approximately 100 nM, close to literature value of 45 nM, given the assumption of molecular weight (see Materials and Methods, Antithrombin binding assay). No binding of either the short (DTT-Sulf)1 "2mer" or the (DTT-Sulf)5 "10mer" was observed. The 2 and 10mer were used in this assay as representatives of short and long oligomers sequences. While the 10mer has a larger total charge, it has the same repeat unit and a greater degree of conformational freedom, which increases the entropic cost of binding. Total ionic strength was 20 mM.

While disappointing, lessons from literature of the development of heparin derived therapeutics explain the lack of binding of our sulfonated oligoTEAs. Overall, successful antagonism of the heparin-binding site on antithrombin has been primarily completed by mimetics that still utilize the saccharide backbone.[379] The structure of the antithrombin ligand is a key determinate of its functionality. Potential ligands with the

same charge density and slightly different structure vary significantly in their binding affinity.[329,380] The isolated ligand to antithrombin, heparin pentasaccharide, proceeds to bind by allosteric activation of antithrombin, suggesting a highly specific and cooperative mechanism[377]. Evidence for this particular binding mechanism strongly suggests that mimetics that merely associate or interact with the binding site will be insufficient to produce the necessary conformational activation.

Conclusions

In this venture, we successfully synthesized sulfonated oligoTEAs and characterized their size, chain dynamics, and conformational ensemble by PFG NMR, DEER EPR, and MD simulations as a function of synthetic length (2-12mer) and individual monomer functional groups. We confirm the strength of entropy and hydrophobicity to create oligomer "collapse" of flexible structures. Our results suggest that this collapse can overwhelm intramolecular electrostatic repulsion. Analysis of individual monomer contributions revealed larger changes due to modulation of the backbone as opposed to pendant groups. Charged oligoTEAs were observed be affected by the addition of ammonium salt, resulting in fewer conformations of similar end-to-end distances, likely by ionic screening.

In biological testing, we were unable to bind our sulfonated oligoTEAs onto antithrombin even at concentrations up to 0.6 mM in low ionic strength (20mM) buffer. This lack of interaction is likely due to the flexible nature observed of these oligoTEAs, unlike the natural saccharide backbone within heparin sulfate itself. Additionally, the heparin pentasaccharide itself experiences a unique induced fit transitioning from a low affinity to a higher affinity binding conformation.[377]

While low resolution, these characterization techniques have provided insight into the ensemble of highly flexible oligoTEAs. The characterization of other short flexible oligomers will enable understanding of sequence-structure relationships for sequence-defined oligomers toward to design of single-chain folding behavior. Meanwhile, this methodology can be applied to the structural characterization and development of flexible, but biologically functional materials.

Materials and Methods

Supplementary methods

General chemicals were purchased from Sigma Aldrich, Alfa Aesar, or Acros Organics. Fluorous tag and fluorous silica were purchased from Boron Specialties. Routine NMR spectra were recorded on INOVA 400, 500, or 600 MHz spectrometers and analyzed by MestReNova (version 10.0.0). 1H NMR chemical shifts are reported in units of ppm relative to the deuterated solvent. LCMS experiments were carried out on an Agilent 1100 LCMS system with a Poreshell 120 EC-C18 (3.0x100mm, 2.7um) column monitoring at 210nm with positive or negative mode for detection. Solvents for LCMS were water with 0.1% acetic acid (solvent A) and acetonitrile with 0.1% acetic acid (solvent B). A flow rate of 0.6 mL/min was used with a gradient starting at 5% solvent B, followed by a linear gradient of 5% to 95% solvent B over 10 min, 95% solvent B for 2 min, before returning to 0% solvent B over 2 min. Most all tabulated data was processed with GraphPad Prism 7.01.

Synthesis of the protected sulfonate allyl acrylamide monomer (PSM):

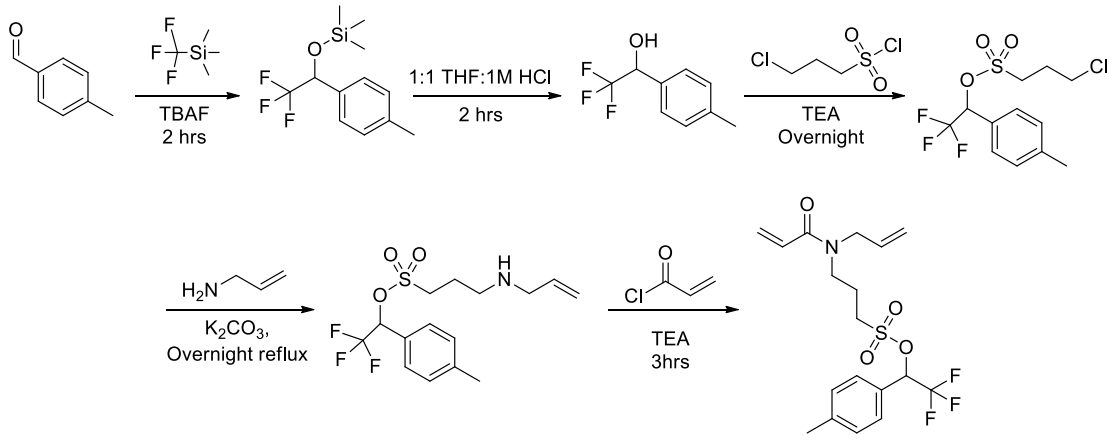

Figure 3-11: *Synthetic scheme summarizing the assembly of the protected sulfonate allyl acrylamide monomer (PSM)*

The protecting group was prepared as described in S Pauff and S Miller[339] Briefly, 1.4 equivalents of trimethyl(trifluoromethyl)silane was added to a solution of benzaldehyde in THF at 500 mM at 0 °C. Approximately 1 drop per mmol of 1M TBAF solution in THF catalyzed the Ruppert-Prakash reaction and was brought to RT to stir for 1hr. The solution was concentrated and purified by flash chromatography (0-1% ethyl acetate in hexanes) to give the trimethyl(2,2,2-trifluoro-1-(p-tolyl)ethoxy)silane at 85% yield after purification as a light yellow oil. The age of the silane reagent was seen to be a significant factor for the reaction conversion.

The TMS-protected alcohol was dissolved in 1:1 1M HCl:THF at 250 mM and stirred vigorously at RT for 2hrs. The reaction was extracted using ethyl acetate and the combined organic layer was washed with 0.1M HCl, water, and brine. The 2,2,2-trifluoro-1-(p-tolyl)ethanol (TFMT) was obtained as a light yellow liquid in 90% yield.

The TFMT was dissolved in dry DCM at 110 mM with 2.0 equivalents of triethylamine and stirred on ice. 1.3 equivalents of chloropropylsulfonyl chloride was prepared in a 1.3 M solution of DCM and added dropwise. The 100 mM mixture stirred on ice for 1hr and then at RT overnight. The reaction was quenched with water, extracted using DCM washed with 0.1M HCl, water, and brine. Concentration and purification with flash chromatography (0-15% ethyl acetate in hexanes) yielded the 2,2,2-trifluoro-1-(p-tolyl)ethyl 3-chloropropane-1-sulfonate as a white amorphous solid at 90% yield. The melting point was observed to be just above room temperature, but not quantified.

The alkyl halide protected sulfonate was then put through *N*-allyl acrylamide monomer synthesis[146] with modifications. The chloropropane protected sulfonate (2.6 g, 8 mmol) was dissolved into 100 equivalents (800 mmol, 60 mL) of allyl amine and 5 equivalents (40 mmol, 5.6 g) of potassium chloride. The solution was stirred at a 50C reflux overnight. The solution was then filtered over Celite and concentrated to yield an amber oil. The conversion of the chloropropane to the *N*-allyl propane protected sulfonate was checked by NMR and TLC and assumed to be pure. Thus, the *N*-allyl propane protected sulfonate (2.8 g, 8.0 mmol) was dissolved in dry DCM at 150 mM and stirred with 1.2 equivalents of triethylamine. Acryloyl chloride (1.4 equivalents, 11.1 mmol, 880 uL) was diluted in DCM (3mL) and added dropwise. The reaction stirred over 1 hour and then allowed to come to RT for two hours. The reaction was then extracted using DCM and washed with 0.1M HCl, water, and brine. The concentrated amber oil was then purified by flash chromatography using 0-60% ethyl acetate in hexanes to give a clear light yellow liquid in 65% yield.

Sulfonated oligothioetheramide assembly

General method for fluorous allyl amine synthesis:

2-[2-(1H,1H,2H,2H-Perfluoro-9-methyldecyl)isopropoxycarbonyloxyimino]-2phenylacetonitrile (fluorous tag) was dissolved in THF (10mg/mL). Two equivalents of allyl amine and two equivalents of triethylamine were added to the reaction mixture and stirred at room temperature for at least 3 hours. Afterward, the THF was completely removed by vacuum centrifuge and the reaction mixture was dissolved in fluorophobic 20% Water in MeOH wash solution, directly loaded onto fluorous silica, and purified by FSPE. Methanol was evaporated under reduced pressure to yield fluorous allyl amine as an off-white solid.

General method for thiolene reaction:

Two equivalents of dithiothreitol and 2,2-dimethoxy-2-phenylacetophenone (DMPA, 10 mol % of dithiol) were added to a solution of corresponding fluorous-olefin in methanol (>80 mM). The reaction mixture was UV irradiated for 270 s at 20 mW/cm2. The product (fluorous-thiol) was purified by FSPE. Methanol was removed by vacuum centrifuge or dry nitrogen at 40 °C. The product was confirmed by NMR for reaction completion and purity or DTDP assay for approximate yield.

General method for Michael addition:

Two equivalents of the protected sulfonate allyl acrylamide monomer activated by dimethylphenylphosphine (DMPP, 5 mol% of monomer) were added to the fluorous-

thiol (variable mM) in methanol. Thirty minutes of reaction time was sufficient to reach completion verified by NMR and DTDP assay at 100 mM concentration. The reaction mixture was then purified by FSPE.

Purification by fluorous solid-phase extraction (FSPE):

The fluorous column was preconditioned with water (1 mL / g of fluorous silica). The fluorous organic mixture was precipitated by adding one-fourth of the reaction volume of water and loaded onto the fluorous silica column (500 mg or 2 g per scale of reaction). Any remaining fluorous material in the reaction vessel was resolubilized in methanol, again precipitated by water addition, and transferred to the fluorous column. A fluorophobic wash (20 vol% Water in MeOH) was used to elute all non-fluorous molecules while the fluorous-tagged material was retained on the fluorous silica gel (Thiolene wash: 0.33 mL/mg of fluorous material; Michael addition wash: 0.5 mL/mg of fluorous material). A fluorophilic wash of methanol was then used to elute the fluorous material (0.2 mL/mg fluorous material). For the FSPE purification of the MeS containing oligomers, the wash solution was made more fluorophobic by the addition of water up to 60 vol%.

Generalized method for oligoTEAs synthesis:

Fluorous allyl amine was synthesized and cycled through the thiolene and Michael additions until desired oligomer length was reached as described. Upon completion, oligoTEAs were treated with 5 mM TFA with 5 v/v% deionized water for 2hrs if the PSM was used in its preparation; otherwise, the oligoTEA was treated with 1:1

TFA:DCM at 5 mM. Then, the mixture was dried at room temperature under argon and HPLC purified.

HPLC purification of oligoTEAs

HPLC purification was performed on an 1100 Series Agilent HPLC system using a reverse phase Agilent Eclipse Plus C18 column (4.6x150 mm, 5µm) or an Agilent Eclipse XDB-C18 (9.4x250 mm, 5µm) column and collected using an automated fraction collector. The column compartment was kept at 40 °C. Solvents for HPLC were water with 0.1% trifluoroacetic acid (solvent A) and acetonitrile with 0.1% trifluoroacetic acid (solvent B). Compounds were eluted at a flow rate of 1 mL/min or 4 mL/min over specified gradients.

Assay of organic thiol concentration by 2,2' dithiodipyridine (DTDP)

Thiol concentration was qualitatively assessed after purification at the end of each thiolene and during the Michael addition to track the oligoTEAs synthesis. Following previously published procedure[267,268] 5 µL of 12 mM DTDP and 300µL of 0.1 v/v% TEA in DMSO were prepared for each assay sample. Aliquots of fluorous material were added to the assay such that the concentration would be 100 µM, mixed, and allowed to sit for 3-5 minutes. The reaction was quenched with 10uL of acetic acid and 150uL were analyzed by an absorbance scan from 325-450 nm (step size 2 nm). Spectra were normalized to 450 nm and analyzed.

Pulse-field gradient nuclear magnetic spectroscopy (PFG NMR)

Measurements were performed with a Varian Unity INOVA 600 MHz spectrometer equipped with a Varian 600 triple resonance XYZ PFG (HCN) inverted probe. 1H spectra were first acquired with optimized 90° pulse angle from -2 to 14 ppm using 4 scans, a relaxation delay of 2 seconds, and an acquisition time of 1.7 seconds. Diffusion measurements were accomplished using the double-stimulated echo convection compensated sequence[381] using 3 mm tubes and 20 LPM of VT gas flow to diminish convection. Measurements were completed with an array of 20 linearly developed pulse field gradient strengths, an acquisition time of 1.7 seconds, 8 steady state pulses, diffusion gradient length of 2.0 milliseconds (ms), 0.0 ms of off-center delay (del2), 0.00 unbalancing factor, and alternating gradient pulse sign. The diffusion delay was set to 120 ms as it attenuated the $(DTT\text{-}Sulf)_5$ to approximately 10% of its original intensity at the maximum gradient pulse. Scout diffusion measurements of small scan numbers were completed to estimate and determine the best gradient stabilization delay (1.0-2.5 ms) to minimize the phase errors caused by eddy currents[355]. A standard of 99.9% D_2O was run to calibrate the probe (gcal) by the observed diffusion coefficient of HDO for each temperature as described by a Speedy-Angell power law fit[382] of Longsworth's data[383] (Figure 3-12, Equation 3-1). Example processing is shown in Figure S4 and S5.

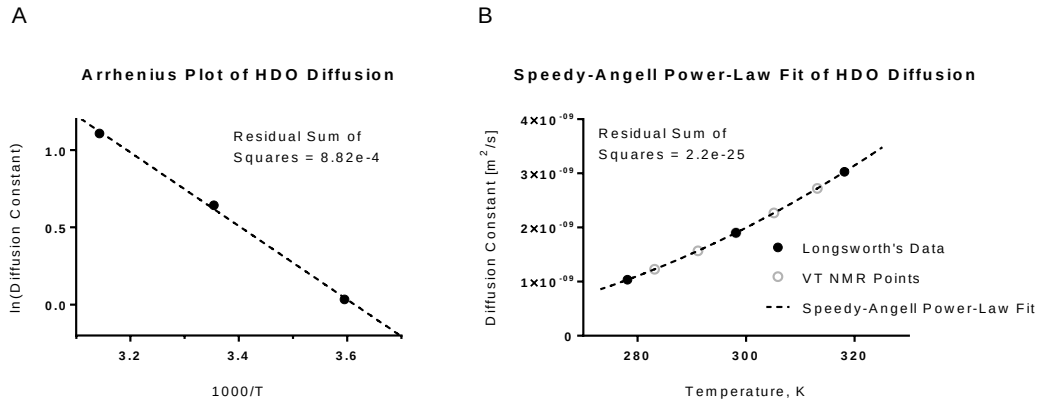

Figure 3-12: *HDO Self-diffusion versus temperature for PFG-NMR calibration* ***A.*** *Arrhenius plot of HDO diffusion in 99.9% D_2O as measured by Longsworth*[383]*. The Arrhenius plot can fit diffusion data in a linear fashion with some small error.* ***B.*** *As seen in literature,*[382] *a better fit can be achieved using the Speedy-Angell power-law using parameters listed in the equation below to eliminate nearly all error. This data allowed a control experiment to measure the HDO diffusion in 99% D_2O at each temperature provided as described in literature*[355]*.*

$$D = D_0\left[\frac{T}{T_s} - 1\right]^{\gamma} \quad ; \quad D_0 = 1.62421 \times 10^{-4},\ T_s = 223.36,\ \gamma = 1.96$$

Equation 3-1: *The Speedy-Angell power-law as applied to translational diffusion. While an Arrhenius plot does show appreciable linearity of HDO diffusion measured by Longsworth*[383]*, systemic error can be reduced by the use of the Speedy-Angell power-law as previously seen*[382]*. Fitted parameters to Longsworth data are listed and used in Figure 3-4.*

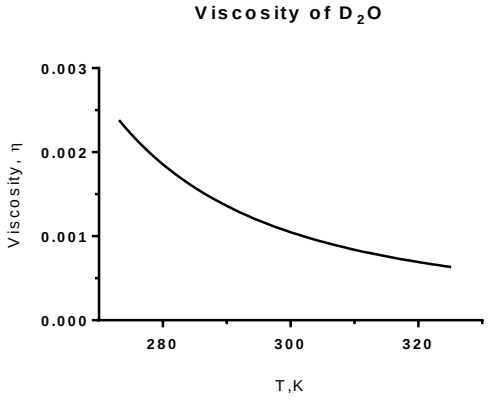

Figure 3-13: *Viscosity vs temperature used in PFG-NMR analysis.*

Plot of D_2O viscosity that was utilized in DOSY analysis from J Lapham et al[384]. This data was used in the analysis of PFG NMR data.

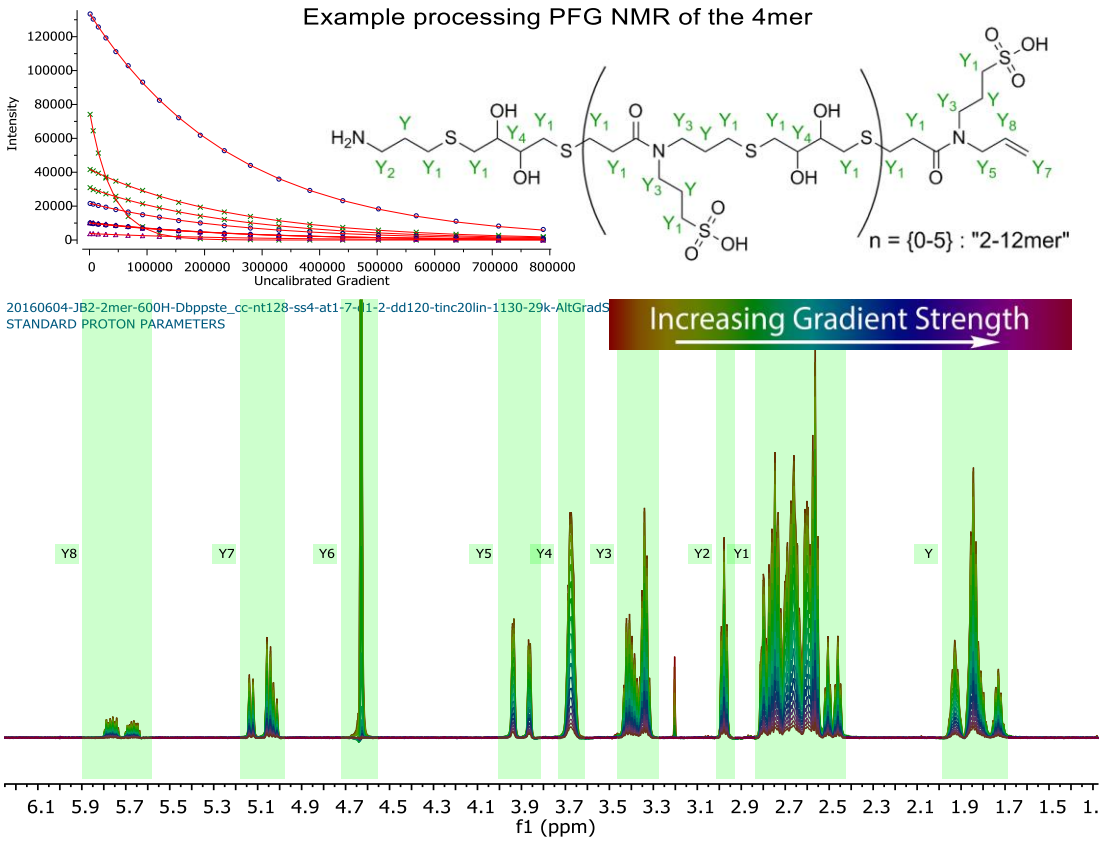

Figure 3-14: *Example of PFG-NMR data processing.*
Example of PFG NMR processing of the 2 mer at 25 °C. Acquisition parameters are in Supplemental Methods. ^1H spectra was examined for quality signal-to-noise and phase errors associated with eddy currents, phased manually, and baseline corrected. Sets of peaks were integrated as a function of the pulse field gradient strengths that was applied to reveal a single exponential decay of each molecule. This serves as an example for all collected PFG NMR spectra.

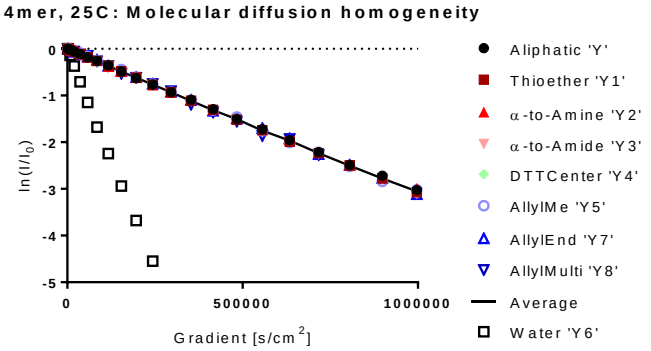

Figure 3-15: *Example result of PFG-NMR data analysis.*
The natural logarithm of the normalized intensity versus the calibrated gradient strength to observe the molecular diffusion homogeneity of the 4mer at 25C. Individual sets of peaks from different regions of the oligomers demonstrate that the end of the oligomer (e.g. allyl protons Y5, Y7-8) diffuses the same as the backbone of the oligomer (e.g. aliphatic Y or thioether Y1). This observation demonstrates there were no major differences between the end and backbone groups. This serves as an example for all spectra.

Conjugation of proxyl spin label to sulfonated oligoTEAs

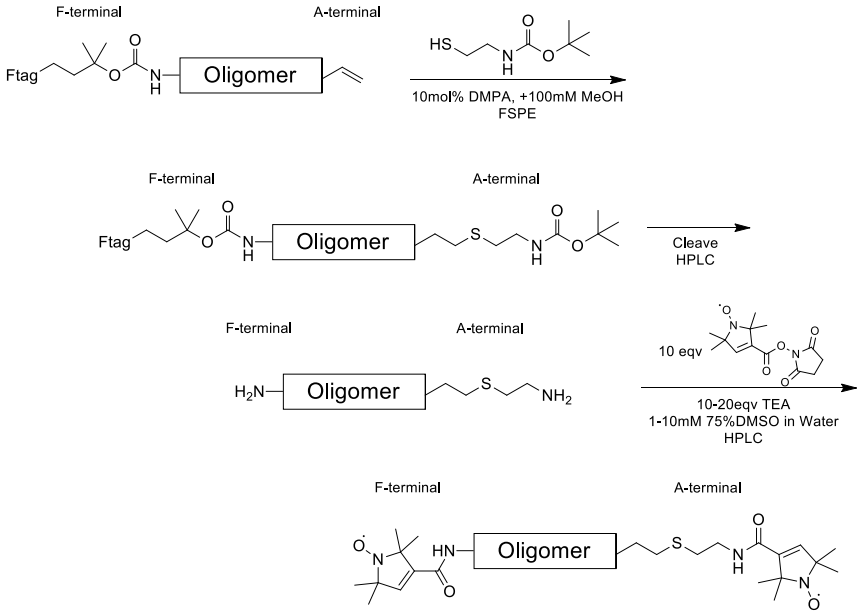

Figure 3-16: *Scheme to produce di-spin labeled sulfonated oligoTEAs.*

Before TFA cleavage of the fluorous support, 3 equivalents of 2-(Boc-amino)ethanethiol and DMPA (10 mol%) were reacted with the elongated oligoTEA allyl (A) terminal. Cleavage and HPLC purification was completed as described generally. During confirmation of the cleaved product by ^{1}H NMR, ^{19}F NMR was completed with a trifluoroethanol standard to quantify residual trifluoroacetic acid (TFA) from the HPLC to inform the equivalency of base to be used in subsequent conjugation. The confirmed oligoTEA was reacted with 5 equivalents of 2,2,5,5-Tetramethyl-3-pyrrolin-1-oxyl-3-carboxylic acid N-hydroxysuccinimide ester (Proxyl NHS ester) and with 5-20 equivalents triethylamine at 1-10mM in 30% water in DMSO at room temperature for 4 hours. Upon reaction completion, the di-spin labeled oligoTEAs was HPLC purified and confirmed by LCMS.

Electron spin resonance distance measurements

ESR measurements were completed at the Advanced Electron Spin Resonance Technology (ACERT) Center. Di-spin labeled oligoTEAs were reduced using aqueous ammonia for 1-2 hours at 50-500 µM at room temperature. Some samples as labeled were dialyzed against ultrapure water using a 100-500 MWCO Micro-Float-A-Lyzer (Spectrum Labs) and monitored by a calibrated Accumet Four Cell Conductivity/ATC probe (Cat 13-620-165) with an Accumet Excel XL20 conductivity meter. All samples were prepared at 100 µM and vitrified to 70K rapidly from room temperature. A working frequency of 17.3 GHz with a 30G magnetic component in a rotating reference frame was sufficient for distances of 10 Å or longer. Most samples were measured by 4-pulse sequence double electron-electron resonance (DEER) and some were measured

by double quantum coherence (DQC). Time domain data was processed in MATLAB; an example is shown in Figure S16. Then, distance distributions were calculated by Tikhonov regularization based on the L-curve method ($\alpha \sim 2\text{-}7$) using modified MATLAB scripts from the ACERT website (acert.cornell.edu).

Molecular Dynamics (MD) simulations

The oligomer simulations were run in the Large-scale Atomic/Molecular Massively Parallel Simulator (LAMMPS), Sandia's molecular dynamics software package[385]. A single oligomer chain was simulated for 50 ns with 1 fs timesteps in a water-filled box with periodic boundary conditions to simulate the motion of disperse oligomers in aqueous solution. An isothermal, NVT, ensemble was implemented in the MD simulation using a Nosé−Hoover thermostat set to 300 K. The OPLS (Optimized Potential for Liquid Simulations) force field developed by Jorgensen[386] was used for the oligomers and is expected to well represent the system since OPLS parameters are optimized to fit experimental properties of liquids, such as density and heat of vaporization, in addition to fitting gas-phase torsional profiles. To supplement the core OPLS parameters, the sulfonate parameters were taken from research by J N C Lopes, A A H Padua, and K Shimizu which studied ionic liquids.[387,388] Since ionic liquid properties are heavily derived from charge interactions, we expect this force field to appropriately handle charge contributions to the system's dynamics. Finally, the force field selected for the water solvent was the TIP4P model, which offers a good compromise between computational efficiency and charge accuracy.[389]

Accurately simulating an isolated oligomer required careful design of physical constraints and charge constraints. The periodic simulation box was made large enough to minimize self-interaction errors. This was done by running a relatively long 10 ns simulation for each oligomer size to determine the approximate end-to-end distance distribution. Less than 1% of the collected data is affected by self-interaction. The box sizes selected were from 3.7 nm for the shortest oligomers to 7 nm for the longest oligomers. The amount of water molecules required to fill those respective simulation boxes, ranged from 1700 molecules to 7200 molecules. The total amount of atoms simulated, including the oligomer, ranged from 5100 atoms to 22000 atoms.

The charge calculation was done using a long-range particle-particle particle-mesh solver in LAMMPS. In solution, the $(DTT\text{-}Sulf)_{1\text{-}6}$ have a permanent negative charge on each sulfonate group. Charge neutrality was achieved in the simulations by using sodium ions.

Circular dichroism measurements

Circular dichroism data is shown in Appendix B. Spectra were collected from 185-400 nm (2 nm step size) on an AVIV Biomedical Circular Dichroism Spectrometer Model 400 (Lakewood, NJ) using a 0.2 cm cuvette filled with 700 µL of oligoTEA at variable concentration {45-300 µM}. The automatically calculated CD signal, Dynode (PMT voltage), CD current (Abs), CD Delta – Absorbance (Raw data) were collected. Sample concentration was found to be optimal at approximately 200 µM based on a maximized Dynode (PMT voltage) with regards to the resulting signal to noise.

Diffusion theory

Compiled and made explicit from Stokes-Einstein-Sutherland, Chen and Chen[390], and G. de la Torre[368], and F. Perrin[365–367] with a review by A. Macchioni[362].

$$D_t = \frac{k_B T}{f} = \frac{k_B T}{c(r_H) f_S(p) \pi \eta r_H} \xrightarrow{for\ "large"\ spheres} \frac{k_B T}{6\pi\eta r_H}$$

Equation 3-2: *Stokes-Einstein-Sutherland (SES) equation*

The SES equation relates the Boltzmann temperature and the translational molecular diffusion where k_B is the Boltzmann constant, T is the temperature in Kelvin, r_H is the prospective hydrodynamic radius, η is the dynamic viscosity, c is a size-dependent modification to transition between the slip/no-slip boundary conditions, p is the geometrically defined aspect ratio, and f_s is the shape-modified friction factor.[362]

$$D_t = \left(\frac{k_B}{c(r_H) f_S(p) \pi r_H}\right) \frac{T}{\eta}$$

Equation 3-3: *Algebraic rearrangement of the SES equation*

This rearrangement clearly shows there is a linear relationship between the translational diffusion and the normalized temperature (T/η), then the quantity in the parentheses is equal to the slope, if linear and constant.

$$\alpha \equiv \left(\frac{k_B}{c(r_H) f_S(p) \pi r_H}\right) \rightarrow \beta \equiv \frac{k_B}{\alpha \pi} = c(r_H) f_S(p) r_H$$

Equation 3-4: *Definition of experimental slope from SES equation.*

This yields an experimentally derived parameter (β) as it constrains the prospective size and aspect ratio, two unknown parameters.

$$c(r_H) = \frac{6}{1 + 0.695 \left(\frac{r_{solv}}{r_H}\right)^{2.234}} \qquad 4 < c(r_H) < 6$$

Equation 3-5: *Microfrictional correction to the SES by H Chen and S Chen*

This relates the van der Waals radius of the solvent to the prospective molecule hydrodynamic radius. The expression was derived to correct the translational diffusion of crown ethers, which are notably smaller than the prospective sulfonated oligoTEAs[390].

$$f_{Prolate} = \frac{\sqrt{1-p^2}}{p^{2/3}\ln\left(\frac{1+\sqrt{1-p^2}}{p}\right)} \;;\; p \equiv \frac{b}{a} < 1$$

Equation 3-6: *The prolate ellipsoid friction factor*

This friction factor for a prolate ellipsoid was defined by F Perrin 1934,1936 and corrected by S Koenig 1975 with the limits of the aspect ratio[365–367]*.*

$$f_{Oblate} = \frac{\sqrt{p^2-1}}{p^{2/3}\arctan\left(\sqrt{p^2-1}\right)} \;;\; p \equiv \frac{b}{a} > 1$$

Equation 3-7: *The oblate ellipsoid friction factor*

This friction factor for an obalte ellipsoid was defined by F Perrin 1934 and1936 with the limits of the aspect ratio[365,366]*.*

$$f_{Rod} = 1.009 + 1.395\times10^{-2}(\ln p) + 7.88\times10^{-2}(\ln p)^2 + 6.040\times10^{-3}(\ln p)^3 \quad ;\; 0.1 < p \equiv \frac{L}{d} < 20$$

Equation 3-8: *The friction factor for a rod (cylinder)*

This semi-empirical friction factor for a rod was defined by A Ortega and J García de la Torre with the limits of the aspect ratio[368]*.*

$$V_{equivalent\ sphere} = V_{shaped} = \frac{4}{3}\pi {r_H}^3$$

$$V_{Rod} = \pi r^2 L \rightarrow r_H = \sqrt[3]{\frac{3r^2L}{4}}$$

Equation 3-9: *Constant volume constraint for non-spherical shapes*

The volumetric constraint that assumes the prospective oligomer shape fills a volume that to be equivalent in volume to a sphere described by the hydrodynamic radius, r_H. The parameters in these equations are described in Appendix Figure B-6 where r is the geometric rod radius, and L is the rod length.

$$d_{ESR} = long\ dimension\ of\ rod = L \rightarrow r = \frac{d_{ESR}}{2}$$

$$p \equiv 0.1 < \frac{L}{2r} < 20 = \frac{d_{ESR}}{2r} \rightarrow r = \frac{d_{ESR}}{2p}$$

$$r_H = \sqrt[3]{\frac{3r^2L}{4}} = \sqrt[3]{\frac{3{d_{ESR}}^3}{16p^2}}$$

$$\beta = c(r_H)f_S(p)r_H =$$

$$= \frac{6}{1 + 0.695\left(\frac{r_{solv}}{\sqrt[3]{\frac{3{d_{ESR}}^3}{16p^2}}}\right)^{2.234}} \times \sqrt[3]{\frac{3{d_{ESR}}^3}{16p^2}} \times \begin{bmatrix} 1.009 + 1.395 \times 10^{-2}(\ln p) \\ +7.88 \times 10^{-2}(\ln p)^2 \\ +6.040 \times 10^{-3}(\ln p)^3 \end{bmatrix}$$

Equation 3-10: *Final algebraic expression relating experiment to aspect ratio with a known end-to-end distance. This algebraic relates the diffusion constant within β to the constrained SES with the rod model, assuming the ESR distance applies in the long dimension as described by Appendix Figure B-6. This equation was solved using fsolve in MATLAB R2013a with MaxIter = 800, MaxFunEvals = 200, a tolerance of 10^{-25}, and a multiplier on the residual of 10^{15}.*

Antithrombin binding assay

Human α-antithrombin III was purchased from Haematologic Technologies (Essex Junction, VT, 58 kDa) and stored as received in 50% glycerol at -20C prior to use. Unfractionated heparin (UFH) (CAS 9041-08-1, Grade 1-A, ≥180 USP units/mg, assumed to be 13kDa within the range of manufacturer specification and literature use[391,392]) and PEG8000 was purchased from Sigma-Aldrich. Protocols for the binding of unfractionated heparin (UFH) and heparin mimetics has been previously established in literature.[376–378] Briefly, binding assays were completed in 20 mM $NaPO_4$, 0.1 mM EDTA, 1 mg/mL PEG8000, and optional 25 mM NaCl for higher salt conditions. Concentrations of an intermediate stock of antithrombin were calculated using the

extinction coefficient of 36000 1/(M*cm) and the TECAN NanoQuant plate (2 µL) before delivering a final concentration of 1uM into a Greiner UV-Star® flat bottom 96 well plate for the assay. UFH and any sulfonated oligoTEAs were distributed by serial dilution (ranging from a factor of 1.6-1.85) with a final well volume of 100uL. Fluorescence measurements were taken using a TECAN Infinite® M1000 PRO Microplate Reader (Männdorf, Switzerland). Fluorescence excitation and emission scans were performed to reveal peak excitation of 280nm (tryptophan fluorescence) and emission at 324nm. The fluorescence was normalized $(F_i-F_0) / F_0$, where F_i is each well and F_0 is the baseline fluorescence. Affinity was calculated using nonlinear regression in GraphPad Prism 7.01 using the normalized equation in literature.[376–378]

Chapter 4 : Antibacterial isoamphipathic oligomers highlight the importance of multimeric lipid aggregation for antibacterial potency

Acknowledgements

This chapter has been adapted with permission from J. S. Brown; Z. J. Mohamed; C. M. Artim; D. N. Thornlow; J. F. Hassler; V. P. Rigoglioso; S. Daniel; C. A. Alabi. *Communications Biology* **2018**, 1 (220) under a Creative Commons Attribution 4.0 International License (http://creativecommons.org/licenses/by/4.0/). Content has been added to this chapter that is not included in the publication about additional background of other antibacterial oligothioetheramides leading up to this work. As well as an additional library of oligomers that were designed based on the isoamphipathic oligomers examined at the beginning of the chapter.

Individual Contributions

J.S.B. and C.A.A. conceptualized the project. J.S.B., C.A.A., and S.D. wrote and edited the manuscript. J.S.B. performed solution-phase characterization, designed and performed SPR, and analyzed the data. J.F.H. and V.P.R. performed synthesis. C.M.A. and D.N.T. performed and analyzed biological experiments. J.S.B. and Z.M. designed, performed, and analyzed microscopy, FRAP, and lipid extraction experiments. J.S.B. and C.A.A. discussed and modeled the SPR data. All authors discussed the results and edited the manuscript. For the additional oligomer library discussed in the Chapter, J.S. Brown conceived the project and oligomer library advised by C.A. Alabi, Joseph F Hassler performed monomer and oligoTEA synthesis, Nana Antwi performed monomer

synthesis, and J.S. Brown and Manisha Kunala synthesized the oligomers. J.S. Brown chemically purified and verified the oligomers as well as performed all biological experiments.

Article Acknowledgments

From the article by Brown J.S. et al: This project received funding from the NSF CAREER (CHE-1554046), Cornell University Startup funds and the Nancy and Peter Meinig Investigator Fellowship. J.S.B., Z.M., and D.N.T. acknowledge financial support from the National Science Foundation Graduate Research Fellowship Program (DGE-1650441). D.N.T. acknowledges the Fleming Fellowship. CHESS is supported by the NSF & NIH/NIGMS via NSF award DMR-1332208, and the MacCHESS resource is supported by NIH/NIGMS award GM-103485. Equipment used to perform this research was funded in part by the Cornell Center for Materials Research (DMR-1120296). The authors thank ACERT personnel for EPR spectrometer and support with data acquisition and processing; ACERT Grant NIH/NIGMS P41GM103521 and NSF-MRI (CHE-1531632).

Abstract

Cationic charge and hydrophobicity have long been understood to drive the potency and selectivity of antimicrobial peptides (AMPs). However, these properties alone struggle to guide broad success in vivo, where AMPs must differentiate bacterial and mammalian cells, while avoiding complex barriers. New parameters describing the biophysical processes of membrane disruption could provide new opportunities for antimicrobial

optimization. In this work, we utilize oligothioetheramides (oligoTEAs) to explore the membrane-targeting mechanism of oligomers, which have the same cationic charge and hydrophobicity, yet show a unique ~10-fold difference in antibacterial potency. Solution-phase characterization reveals little difference in structure and dynamics. However, fluorescence microscopy of oligomer-treated *Staphylococcus aureus* mimetic membranes shows multimeric lipid aggregation that correlates with biological activity and helps establish a framework for the kinetic mechanism of action. Surface plasmon resonance supports the kinetic framework and supports lipid aggregation as a driver of antimicrobial function.

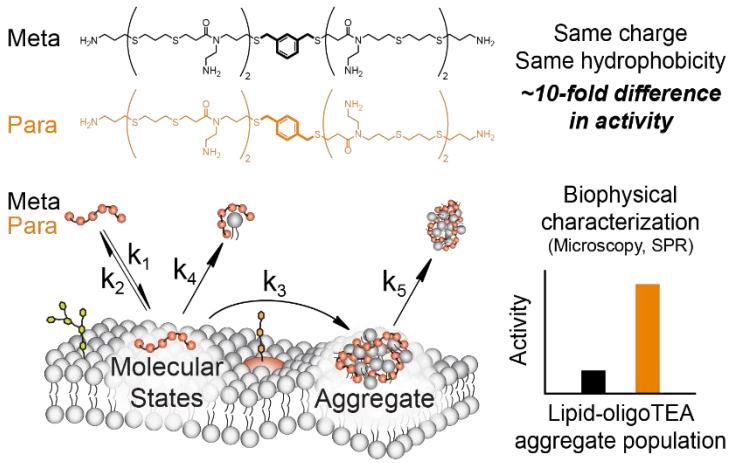

Figure 4-1: *Graphical abstract for Chapter 4*

Introduction

Motivation

Antibiotics are a cornerstone of modern-day medical care. Before penicillin was discovered by Alexander Fleming in 1928, a cut could be deadly if infected, surgery was impossible, childbirth often complicated, and illnesses like pneumonia and

tuberculosis were untreatable. Now, antibiotics are widely used, with over 269 million antibiotic prescriptions in the United States alone in 2015, many of them for children.[393] Antibiotics have been so effective, we can hardly imagine a world without them. However, as Fleming predicted in his Nobel lecture in 1945, bacteria can evolve to survive antibiotic treatment, commonly termed antibiotic resistance. Antibiotic resistance continues to grow as a world health crisis due to the natural evolution of bacteria, an increase in antibiotic use and accessibility, as well as a substantial decline in development.[394,395] With the rise of "superbugs" resistant to all antibiotics, the age of antibiotic therapy could be ending. Unaddressed, antibiotic resistant bacteria are predicted to kill more people annually than cancer by 2050.[396]

As resistance accumulates, researchers have turned to the development of new antibiotic strategies including cationic antimicrobial peptides (AMPs).[397] As a structurally broad class, AMPs encompass short, amphipathic peptide units that share common cationic and hydrophobic features. They naturally serve as a part of the innate immune system and are an evolutionarily conserved response to foreign pathogens.[398,399] Several modes of action have been proposed, with some AMPs acting by disrupting and permeabilizing the bacterial membrane.[400,401] Additional steps can contribute to bacterial death including membrane polarization, disruption of cytoplasmic components, immunomodulatory response, or adjuvant function.[402–404] Since the bacterial membrane is essential and AMP disruption is diverse and stochastic, bacteria can have difficulty circumventing this mechanism.[400,405] Understanding the fundamental mechanism of antibiotic action is critical, considering that almost every

new antibiotic produced in the past sixty years has succumbed to bacterial resistance within a few years of release.[406]

AMPs have encountered barriers to their systemic use, predominantly due to their toxicity, proteolytic degradation, and low bioavailability.[398,402,407] Several AMPs and lipophilic AMPs including polymixin B, nisin, gramicidin S, and colistin have been developed, but relegated to topical application, food packaging, or as drugs of last resort, with the exception of daptomycin.[398,408–411] Toxicity is primarily due to insufficient selectivity, where AMPs generally interact more strongly with bacterial membranes based on their lipid composition and properties. Anionic lipids within bacterial membrane are broadly targeted by AMPs over the more neutral and rigid cholesterol-containing mammalian membrane.[399,412] Low bioavailability is primarily due to rapid proteolytic degradation of peptides by serum proteases. Using this knowledge, researchers have worked toward enhancing serum stability with the development of sequence-defined peptidomimetics including peptoids,[413] β-peptides,[183,414,415] oligothioetheramides (oligoTEAs),[278,416] and many others. To control activity and selectivity, AMPs and AMP mimetics have focused on tuning the nature, quantity, and spatial positioning of cationic charge and hydrophobicity.[398,400,404,407] This optimization generally holds, even within structured macromolecules containing α-helices, where these fundamental properties lead to interfacial amphipathicity.[417–419] Thus, with these design parameters, some AMPs and AMP mimetics with promising prospects have been developed (e.g. brilacidin in Phase II clinical trial).[163,420]

Researchers have also established limitations within the optimization of potency and selectivity using cationic charge, hydrophobicity, and amphipathicity.[400,404] For

example, hydrophobicity improves membrane insertion and potency, but can increase both *in vitro* and *in vivo* toxicity.[278,413,421–423] Similar trends have been seen for the level of amphipathicity.[417] Thus, researchers have called for the advancement of design principles to include targeting strategies or biophysical parameters.[400,424,425] Beyond these common molecular-scale physicochemical properties, biophysical characterization potentially holds the next level of parameters to direct the design of therapeutically-relevant membrane-disrupting antimicrobials.[400,401] Several biophysical techniques probe the interaction of these membrane disruptors with supported bacterial mimetic bilayers including surface plasmon resonance (SPR),[426,427] quartz crystal microbalance,[428,429] and more recently dual polarization interferometry.[401,430] Thus far, these studies have revealed a complex sequence of events that are often indistinguishable including binding, insertion, and structural changes made to bacterial membranes by disruptive AMPs and their mimetics.[426,427] Moreover, these studies have developed the concept of a critical threshold concentration of membrane disruption, argued to direct the minimum inhibitory concentration (MIC),[400] or another concentration in which irreversible structural changes are made to the membrane.[401]

Prior work in the Alabi lab

Prior to this work, our lab has performed a couple of studies with other antibacterial scaffolds as AMP mimetics. The first work was completed by M Porel, D.N. Thornlow, N.P. Phan, and C.A. Alabi (2016),[416] explored a diverse set of pendant groups and structures including macrocycles. Macrocyclic structures were created with oligoTEAs by an acid-catalyzed reaction between a TFA-liable aldehyde pendant group (acetal) and an alkoxyamine to forming an oxime. Biologically, several structures were

tested including macrocycles of varying size and tail lengths, as well as simple linear oligomers. Structured materials like macrocycles often have been better potential to bind to challenging drug targets including protein-protein interactions.[34] However, the linear structures showed more selectivity than the macrocyclic oligoTEAs in this original study. In addition, other successes in literature came to light. Specifically, I. S. Radzishevsky et al (2007) presented research on synthetic acyl-lysines with excellent promise as potent and selective antibacterial agents with successful in vivo challenges (intraperitoneal, mouse model). Combined, these findings lead to the antibacterial scaffold explored by M. Porel, D.N. Thornlow, C.M. Artim, and C.A. Alabi (2017), which expanded the search for antibacterial candidates using a polyamine scaffold with a variety of pendant and backbone groups. This work showcased the ability of oligoTEAs to decouple molecular properties including hydrophobicity and charge to understand their contributions to antimicrobial action. Within the library of oligoTEAs synthesized were the oligomers discussed in this Chapter.

Objectives

Toward understanding new parameters for AMP optimization and development, we have explored a unique pair of sequence-defined oligothioetheramide (oligoTEA) constitutional isomers of the same length, cationic charge, hydrophobicity and thus amphipathicity.[278] These antibacterial oligoTEAs (AOTs) have the same physical and chemical properties that typically guide optimization of membrane-disrupting antimicrobials, but have displayed a unique differential in potency and toxicity of nearly 10-fold. Thus, they were ideal for exploring new parameters for sequence-structure-function optimization of membrane-disrupting antimicrobials. We confirmed similar

solution-phase structures using small- and wide-angle x-ray scattering (SAXS/WAXS) as well as pulsed field gradient (PFG) NMR and pulsed electron paramagnetic resonance (EPR) processed within the molecular Stokes-Einstein-Sutherland relation.[217] However, directed by differences in biophysical observations, we explored the interaction of these oligomers with supported bacterial mimetic bilayers using fluorescence microscopy, fluorescence recovery after photobleaching (FRAP), and oligomer-lipid extraction. All biophysical experiments created a *de novo* kinetic framework that was then tested and supported by modeling oligomer-membrane interactions observed by surface plasmon resonance (SPR). Thus, we are able to present new parameters that can enable further development of membrane-disrupting antibacterial agents beyond typical physicochemical parameters of cationic charge and hydrophobicity.

Results

Different potency yet similar solution-phase structures

Membrane disrupting antimicrobials make use of cationic charge and hydrophobic moieties to bind and insert into bacterial membranes, respectively.[398,400,407] In previous work, we examined structural features such as oligomer length (total charge), hydrophobicity, sequence, and composition.[278,416,423] Relationships observed between chemical and physical properties with activity corroborate conclusions made across multiple molecular classes: a threshold of cationic charge is required for activity and hydrophobicity increases potency while increasing toxicity. However, exceptions were found based on the conformation of a benzyl group at the center of the first-generation AOT scaffold (Figure 4-2a). The oligomer with a para-substituted benzyl

group (“Para”) showed nearly an order of magnitude higher potency than the meta-substituted version (“Meta”) against several clinically relevant pathogens as measured by a minimum inhibitory concentration (MIC) assay (Figure 4-2b, see Materials and Methods, Figure 4-7 for MIC definition). The MIC of the Meta and the Para were recorded as the minimum concentrations that prevented 90% of visible bacterial growth, also called a MIC_{90}. A similar trend was observed with toxicity as measured by the hemolysis assay (Appendix C Figure C-1). However, these oligomers showed the exact same hydrophobicity as demonstrated by their retention on reverse phase HPLC (Figure 4-2c) and are thus isoamphipathic.

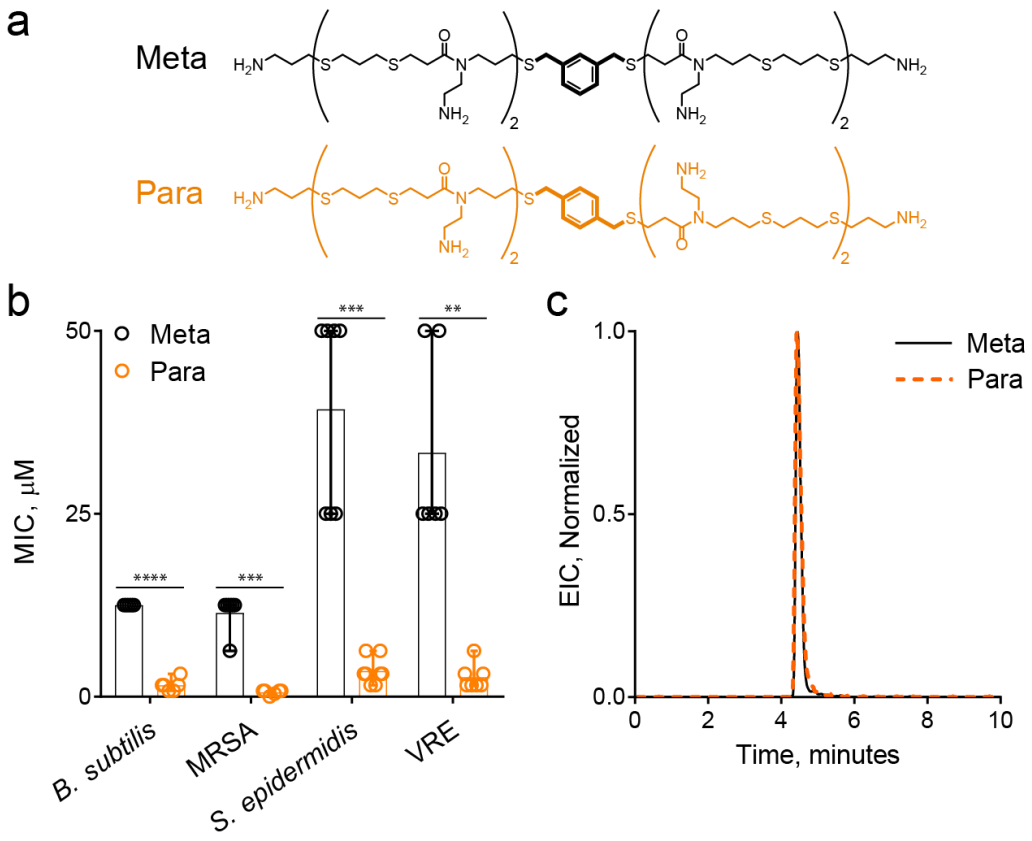

Figure 4-2: *Antibacterial and hydrophobicity characterization*

(a) *Structures of the Meta and Para* ***(b)*** *Minimum inhibitory concentration (MIC) results showed nearly a 10-fold difference in potency across several clinically relevant bacterial strains. Error bars represent the range of the MIC observed. (n=3 biological replicates each with n=2 technical replicates shown. See Materials and Methods for MIC definition (Figure 4-7). MRSA is methicillin-resistant Staphylococcus aureus and VRE is vancomycin-resistant Enterococcus. Significant difference in potency: $p < 0.0001$, 0.0002, 0.0005, and 0.0021 paired t-test, two-tailed, df = 5 for all, B. subtilis, MRSA, S. epidermidis, and VRE, respectively.* ***(c)*** *Reverse phase HPLC-MS chromatogram of the extracted product mass (EIC) of the Meta and Para demonstrated the same retention and hydrophobicity.*

Since these isomeric oligoTEAs have different connectivity, their solution-phase structure was initially suspected to be responsible for the differences seen in their antimicrobial potency. Solution-phase size, shape, and conformation were examined by pulsed field gradient (PFG) NMR, double electron-electron resonance EPR, and small-angle x-ray scattering (Figure 4-3). PFG NMR is a label free technique to measure the self-diffusion of molecules observed by NMR within the solution-phase, encoding information about the hydrodynamic size and shape. Variable temperature (VT) PFG NMR revealed similar diffusion coefficients across a range of viscosity normalized temperatures (identical slopes, p = 0.862, two-tailed t-test) for both isomers. This linearity indicated minimal intermolecular interactions or intramolecular transitions during measurement, which would appear as functions of temperature (e.g. aggregation, repulsion). To gauge the solution-phase structure at the lipid membrane, VT PFG NMR was also performed in a lipid mimetic solvent of 1:4:4 water:methanol:chloroform, previously used for structure determination of transmembrane proteins.[431,432] In this lipid mimetic solvent, both the Meta and Para present similar diffusion characteristics (identical slopes, p = 0.485, two-tailed t-test). The oligomers show slower diffusion,

likely due to expanded hydrodynamic radii, a sign of improved solvation. This expansion and solvation could indicate an entropic gain if the oligomer were to bind and then insert into the hydrophobic space in the lipid bilayer.

To investigate the dynamics of these oligoTEAs, double electron-electron resonance (DEER) EPR was performed. End-to-end distance measurements by DEER measures the dipolar coupling between two unpaired electrons from "spin" probes on the molecule using pulsed EPR. Reconstruction of the observed data extracts a distance distribution between the spin probes. The di-spin labeling of the oligomers was made possible by use of a phthalimide protected *N*-allyl-*N*-acrylamide monomer during oligomer assembly. Thus, only the terminal amines were di-spin labeled with a proxyl nitroxide (Materials and Methods, Figure 4-9). Deprotection of the di-spin labeled oligoTEA *N*-phthalimides was optimized using a sodium borohydride reduction and acid hydrolysis to provide the final di-spin labeled Meta and Para (Appendix C Supplementary Spectra).[433] DEER measurement was completed on 50 µM oligomer after rapid vitrification from room temperature (RT) in PBS with 10 v/v% ethylene glycol. Reconstructed distance distributions revealed similarities in both end-to-end distance distributions (Figure 4-3b).

Together, the end-to-end distance from DEER and diffusion measurements enable calculation of the hydrodynamic radius and aspect ratio with the Stokes-Einstein-Sutherland (SES) equation (Figure 4-3c and d; Materials and Methods). This calculation uses the slope of the plot of diffusion versus viscosity-normalized temperature (Figure 4-3a), and allows structural elucidation of highly flexible, small structures[217]. The calculated hydrodynamic radii were under 1 nm and the aspect ratios reveal similar

spherical oligoTEA shapes (Figure 4-3c and d). Spherical appearance of the oligomer indicated clear space-averaging during observation from single-chain collapse. These dynamics were also visualized in a similar broad DEER distribution (Full-width at half maximum of ~2nm). These data from DEER demonstrate that the oligomers have similar dynamics due to the same size and distribution, likely indicating similar flexibilities.

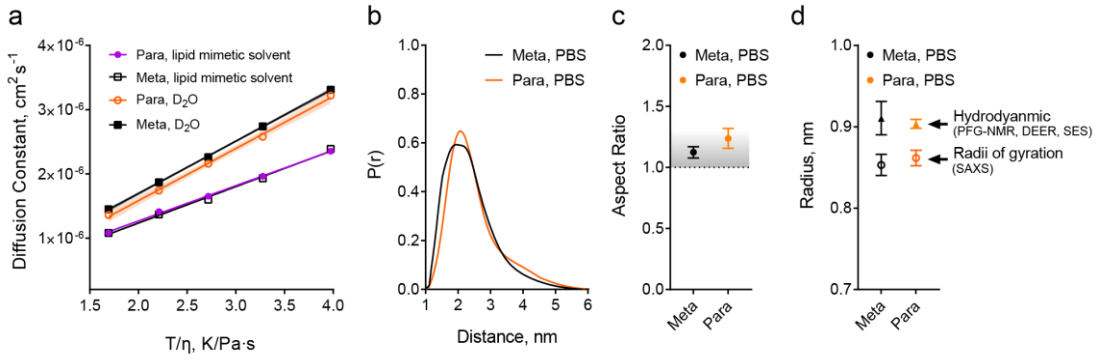

Figure 4-3: *Meta and Para have highly similar solution-phase structures* ***(a)*** *Variable temperature PFG-NMR (1mM) completed from 0-40°C in D_2O and a lipid mimetic solvent (1:4:4 D_2O:dMeOD:$CDCl_3$) shown and shaded regions indicating standard deviation. The diffusion constant is plotted versus the viscosity (η) normalized temperature. Statistical significance for D_2O: identical slopes, p = 0.862, two-tailed t-test and for lipid mimetic solvent: identical slopes, p = 0.485, two-tailed t-test.* ***(b)*** *Reconstructed end-to-end distance profiles from DEER EPR of samples rapidly vitrified to 70K from room temperature (RT, 22°C) 50 μM in PBS.* ***(c)*** *Aspect ratio calculated from diffusion and end-to-end distance measurements and a molecular Stokes-Einstein-Sutherland (SES) equation at RT. The shaded region reflects the aspect ratio of an ideal, well-solvated polymer (AR ~1.1).* ***(d)*** *The calculated hydrodynamic radii from the SES equation and the radii of gyration for the Meta and Para from Guinier fits of SAXS data (see Appendix C Figure C-2 and Table C-1). In (c) and (d) error bars represent standard deviation, propagated from the PFG NMR measurement and the DEER end-to-end distance.*

To complement the SES analysis, X-ray scattering was completed to confirm similarities in the Meta and Para oligomers and verify the SES-calculated hydrodynamic

radii (Appendix C Figure C-2). When done in the solution-phase, small- and wide-angle x-ray scattering (SAXS / WAXS) is a label-free technique that encodes information about macromolecular size, shape, and dynamics by measuring the scattering of x-rays from a sample. Scattering was examined at both small- and wide-angle due to the small size of these oligomers to measure their radii of gyration.[434,435] Broad scattering was observed decaying toward the baseline around q ~ 0.4-0.5 (Appendix C Figure C-3). Guinier fits provided the radii of gyration in good agreement with the SES analysis at ~0.5 Å below the hydrodynamic radii, expected from oligomer hydration (Appendix C Figure C-2 and Table C-1). Moreover, exceptional overlap in calculated SAXS pair-wise distributions was observed between the Meta and Para (Appendix C Figure C-3). Overall, these results demonstrate remarkable similarities between the highly dynamic and spherical solution-phase structures of the Para and Meta oligoTEAs, strongly suggesting they are indistinguishable in solution. Thus, these flexible and dynamic oligomers likely initiate their interaction with the bacterial membrane in highly similar fashions. Traditionally, membrane-disrupting AMPs and mimetics initiate this binding via electrostatic interactions, but their composition and structure influences the thermodynamics and kinetics of the interaction. Structure in solution is not a prerequisite for activity, however, and structure can develop within subsequent binding states[408,426,436].

Meta and Para are distinguishable at the bacterial membrane surface

Since the mechanism of AMPs and AMP mimetics includes membrane disruption,[278,401] additional biological testing was pursued on the mechanism of the

Meta and Para. A propidium iodide (PI) assay was completed on methicillin-resistant *Staphylococcus aureus* MRSA. PI is a membrane impermeable agent that fluoresces upon binding and intercalation with nucleic acid. Thus, PI displays fluorescence if the bacterial membrane is permeabilized to allow either diffusion of PI into the bacteria or diffusion of nucleic acid out of the bacteria. The PI assay demonstrate that the Para rapidly compromised the bacterial membrane (Figure 4-4a), with significantly higher permeabilization shown by the Para than the Meta as expected. The differential between the Meta and Para is similar when tested with *B. subtilis* (Appendix C Figure C-4). Membrane depolarization was measured with fluorescent 3,3'-dipropylthiadiacarbocyanine ($diSC_35$), which binds and quenches at the membrane surface from the natural bacterial polarization. Membrane disruption leads to depolarization, releasing and dequenching $diSC_35$.[437] Using this assay, the Para shows a greater extent of depolarization than Meta (Figure 4-4b), with less of a difference than the PI assay. Both the PI and $diSC_35$ assays demonstrated results expected for membrane-disrupting agents such as melittin. These results also corroborated the differences between the Meta and Para, despite their extensive similarities in solution-phase structure, size, charge, and hydrophobicity.

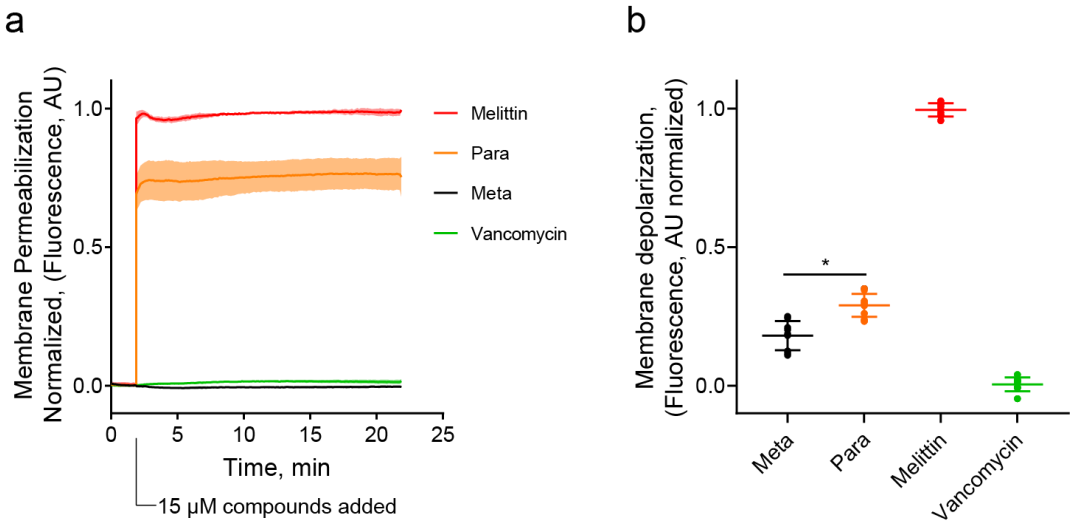

Figure 4-4: *Meta and Para were distinguishable and active on the bacterial membrane* ***(a)*** *Propidium iodide (PI) assay demonstrated the ability of the Para to disrupt and permeabilize the bacterial membrane of MRSA (ATCC 33591) at significantly greater activity than the Meta ($p = 0.0015$, $df=2.018$, unpaired t-test, two-tailed). The shaded region indicates the standard deviation around a solid line (mean) of n = 3 biological replicates with n=2 technical replicates each.* ***(b)*** *$diSC_35$ membrane depolarization assay performed against MRSA (n = 3 biological replicates). The Para shows stronger membrane depolarization, (* $p < 0.028$, $df = 3.995$, unapaired t-test, two-tailed). In both assays, oligomers and controls were added at 15 μM to compare their activity. Vancomycin inhibits cell wall synthesis, and serves as a negative control.*

Meta and Para triggered lipid surface aggregates formation

Since the Meta and Para presented distinguishable membrane interactions, we sought to investigate their interaction and disruption on a *S. aureus* mimetic supported lipid bilayer (SLB) via fluorescence microscopy. Bacteria innately have different lipid compositions within their membranes, which can influence the interaction and effectiveness of AMPs. Since MRSA results in a significant percentage of deaths from antibiotic-resistant bacteria,[438] we focused on simulating its lipid membrane composition. A head group composition of 4:5:11 neutral lipids, cardiolipin, and

phosphatidylglycerol was compiled from literature on the *S. aureus* membrane (see Supporting Information). Lipids tail groups were chosen to maintain fluidity at room temperature, specifically neutral 18:1 diacylglycerol (DG), tetrapalmitoyl cardiolipin (TPCL), and 1-palmitoyl-2-oleoyl-sn-glycero-phosphoglycerol (POPG). Small unilamellar vesicles (SUVs) were prepared with this composition and labeled with Octadecyl Rhodamine (R18). SLB preparation was enabled by pre-coating glass slides with poly-L-lysine (PLL)[439] (See Materials and Methods, Appendix C Figure C-5). The resulting lipid bilayers were visualized and fluorescence recovery after photobleaching (FRAP) was completed to verify their quality and fluidity (Appendix C Figure C-6, C-7). FRAP can determine the lateral diffusion of two-dimensional lipid bilayers, even on living cellular membranes, by observing the recovery of a photobleached spot.

Treatment of the *S. aureus* mimetic membranes for 10 minutes with 5 μM Meta and Para revealed the formation of micron-sized lipid aggregates and lipid particle evolution from the surface into the bulk solution (Figure 4-5a, see online version for Supplementary Movie 1 and 2 (doi: 10.1038/s42003-018-0230-4), Appendix Figure C-7). Treatment at 5 μM was chosen as it is in between the MIC of the oligomers to discern any difference. Control experiments demonstrated the phenomena was not specific to the R18 label. SUVs prepared with Texas Red™ DHPE in place of R18 revealed similar lipid aggregation and particle evolution phenomena (See online version for Supplementary Movie 3 (doi: 10.1038/s42003-018-0230-4)).

To further understand their participation in membrane disruption, the Meta and Para were fluorescently labeled to visualize oligomer co-localization with the aggregates. Fluorescein acrylamide was conjugated to the oligoTEAs via the terminal

thiol at the end of oligomer assembly. Following acid cleavage, the final product was purified by HPLC and verified via 1H NMR and LCMS (see Materials and Methods, Figure 4-10, Appendix C Supplementary Spectra). The fluorescein-labeled Meta and Para were mixed with unlabeled oligomer and placed onto *S. aureus* mimetic membrane using the same conditions (5μM, 10 minutes, RT, 50% labeled). Due to the fluorescence of the solution, imaging was completed after buffer exchange with PBS to remove solution-phase and loosely-bound fluorescein-labeled oligomers. The fluorescent microscopy images showed that the fluorescein-labeled Meta and Para were co-localized with the lipid aggregate, likely directing its formation (Figure 4-5b). Additionally, the biological activity was also checked, revealing decreased potency and differential between the Meta and Para after fluorescein labeling (Appendix C Figure C-8). Thus, the fluorescein oligomers did not fully represent the mechanism of action of the unlabeled oligomers, but all shared the physical phenomena of aggregate formation. Fewer aggregates were observed relative to the unlabeled oligomers with size differences, likely because of the attenuated biological activity.

Lipid removal from the SLB membrane was confirmed by measuring the fluorescence of bulk solution in the microscopy well via R18. The *S. aureus* mimetic SLBs labeled with R18 were incubated with the oligomers for 5 minutes, as time-lapse imaging showed the lipid particles could settle after 7-10 minutes. The bulk solution was removed and treated with Triton-X detergent at 5 mM final concentration to solubilize any lipid particles.[440] The remaining SLB membrane in the microscopy well was also extracted fully by treatment with Triton-X detergent (verified in Appendix C Figure C-9). Comparison of the fluorescence revealed 1-2.5% of the membrane is

extracted into the bulk solution during oligomer exposure over a concentration range of 0.25-40 μM (Figure 4-5c). The Para showed more extraction at lower concentrations. Moreover, lipid extraction was observed below concentrations where lipid particles were observed in the fluorescence microscopy, indicating lipid extraction can occur in smaller, non-aggregate forms (e.g. micelles).

Analysis of the aggregates at equilibrium revealed the Para forms smaller and more numerous micron-sized aggregates at lower concentrations (Figure 4-5d and 4-5e). A higher number of aggregates formed per oligomer concentration defines efficient aggregate formation. ImageJ particle analysis revealed the Para and Meta form aggregates at similar rates and efficiency at higher concentrations of ≥7.5 μM (Figure 4-5e and 4-5f), closer to where both oligomers are antimicrobial (Appendix C Figure C-10, C-11). However, at lower concentrations of ≤5 μM, the Para remains active against MRSA and retains efficient aggregate formation, whereas the Meta is inactive and shows attenuated aggregate production (Figure 4-5e). Efficient aggregate formation appears to have a concentration threshold in similar style to the MIC and could be important for oligomer antimicrobial function. However, the MIC_{Meta} is much higher than this concentration, undermining any immediate quantitative correlation, likely because of differences in experimental set up. With regards to size, a smaller size aggregate increases surface density, possibly increasing any antimicrobial action of the aggregate per oligomer mass. The smaller size or the efficiency of aggregate formation could be a potential explanation as to why the Para is much more potent than the Meta. Overall, the particle count and size data obtained from fluorescence microscopy show

differences between the Para and Meta that could correlate with their differences in antimicrobial activity.

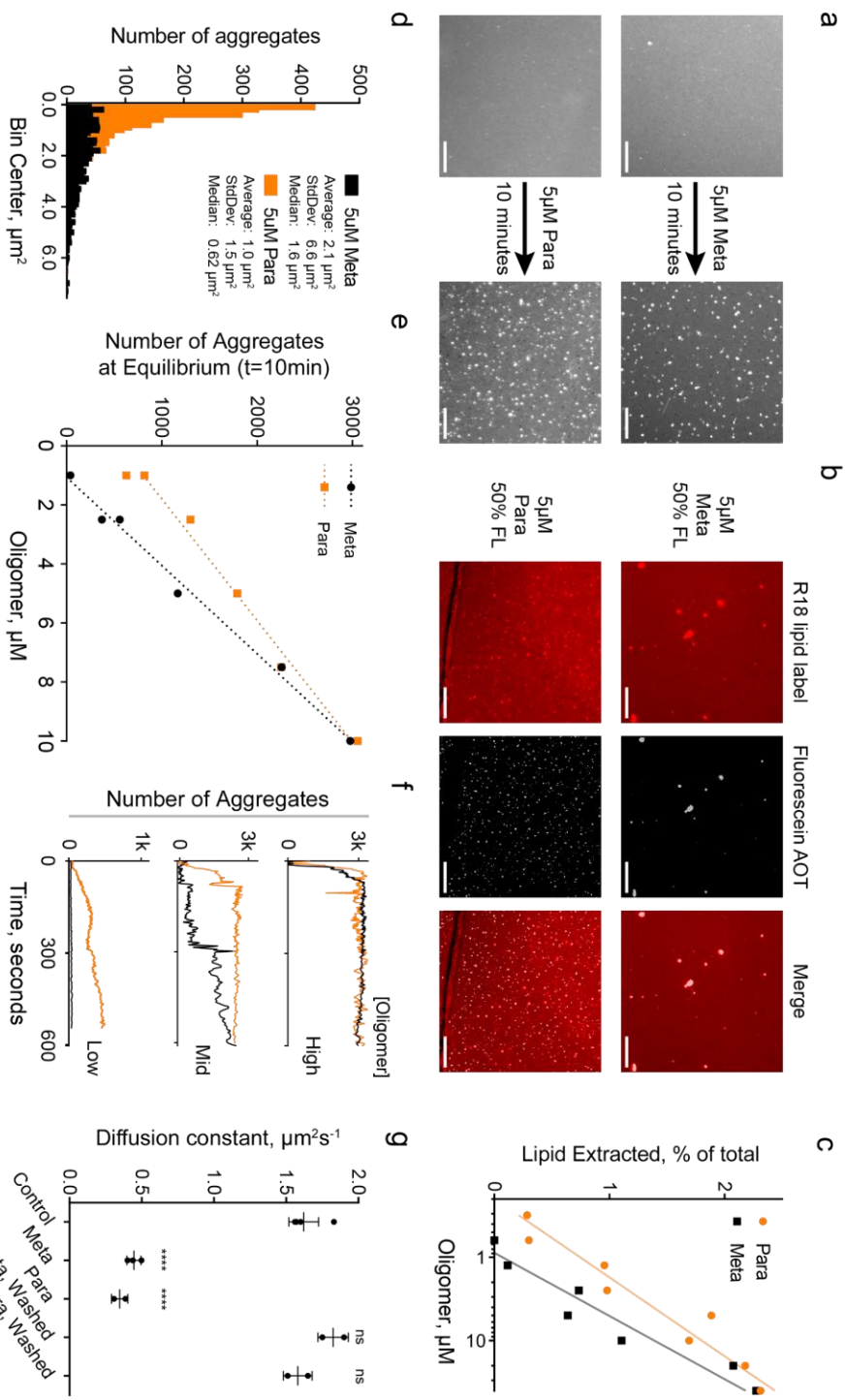

Figure 4-5: *Visualization of aggregate count, size, and kinetic formation, as well as evidence of membrane loss and binding*

(a) *Fluorescent micrographs of before and after 10 minutes of oligomer exposure, R18 visualizes the lipids.* ***(b)*** *Use of fluorescein Meta and Para demonstrated oligomer*

participation via co-localization in the aggregate (10 minutes, 5 μM total, 50 %FL, washed with PBS). All scale bars are 25 μm. ***(c)*** *Capture of lipid particles evolved from surface quantified by plate reader fluorescence as a percentage of total within the microscopy well. Semi-log lines are an aid to the eye (n=1).* ***(d)*** *Histogram of aggregate sizes on microscopy images determined by ImageJ particle analysis* ***(e)*** *Total number of aggregates in microscopy image after 10 minutes versus oligomer concentration showed a threshold of efficiency. A linear regression is shown to aid the eye. At high (active) oligomer concentration the oligomers were indistinguishable; at low concentration the Para developed more aggregates, as it is more potent. Individual SLBs were observed (n=1) for all concentrations except 1 μM Meta and 2.5 μM Para, where n=2.* ***(f)*** *Kinetics of aggregate formation showing the oligomers are indistinguishable at high concentration, but distinguishable at intermediate and low concentrations. 10 μM, 7.5 μM, and 1 μM are the high, mid, and low concentrations, respectively. Note for 1 μM the y-axis is 1k, whereas for 10 μM and 7.5 μM the scale is 3k aggregates.* ***(g)*** *FRAP experiment revealing reversible decrease in membrane diffusivity when equilibrated with 10 μM oligomer from a molecular, non-aggregate state (****p < 0.0001; ns p > 0.05, unpaired t-test, two-tailed). FRAP replicates represent membrane heterogeneity, n = 4,3,2,2 for the Control, Meta, Para, Meta Washed, and Para Washed, respectively. (See Appendix C Figure C-14 for mobile fraction).*

Kinetic mechanism proposed from microscopy observations

Time-lapse fluorescence microscopy of oligomer disruption of the *S. aureus* mimetic SLB clearly showed irreversible aggregate formation, where few to no aggregates re-adsorbed into the mobile lipid bilayer after their formation or washing. Analysis of aggregate count in all frames over time revealed kinetic behaviors that are dependent on oligomer concentration, supplementing evidence of a threshold in similar style to the MIC (Figure 4-5f). At high concentration, both oligomers exhibited quick aggregate formation kinetics to a level of ~3k particles, or ~20k particles per mm^2. At intermediate concentration, aggregate formation from the Para quickly reached an equilibrium aggregate density, while the Meta is slow. At low concentrations, the Para

shows slower aggregate formation, while the Meta shows little to no aggregate formation. Overall, these data indicated concentration dependence on kinetic formation of the aggregate, also in a similar style to the biological activity (MIC).

FRAP of the *S. aureus* mimetic SLB membrane revealed evidence of sub-micron, reversible oligomer binding, in contrast to the irreversibly-formed aggregate. Treatment of the membrane with the Meta and Para showed a decrease in diffusivity by FRAP (Figure 4-5g). The aggregates only contributed ≤4% of the FRAP laser spot size (Materials and Methods, Particle Analysis, Appendix C Figure C-12). Therefore, the decreased diffusion measured by FRAP represented changes in the membrane not due to the immobile aggregates. At 10 μM, there is not a large difference between the Meta and Para, also in contrast to the aggregate, indicating the sub-micron binding events progress to a similar equilibrium. The SLB was thoroughly washed with PBS to remove solution-phase and loosely-bound oligomer. Afterward, FRAP shows the membrane diffusivity returned to its native state, indicating this binding was reversible (Figure 4-5g). Additional oligomer concentrations of 2.5 and 5 μM were also tested (Appendix C Figure C-13). At these lower concentrations, the decrease in diffusion lessened in a concentration dependent manner, and binding remained reversible. Molecular binding states that reversibly changed the membrane diffusivity could be the oligomer cross-linking the phospholipid head-groups or inserting into the membrane to cause viscoelastic changes. As described in literature, there are several hypothesized molecular- and macromolecular-scale binding states seen with AMPs including “bind and insert” mechanisms, which would not be visible by microscopy.[401,404,407,426]

All data from the fluorescence microscopy and FRAP guided the development of a kinetic framework around the mechanism of the Meta and Para membrane disruption. The FRAP showed molecular-scale states that bind reversibly. These reversible states reached equilibrium faster than the FRAP time-scale (minutes), but binding could be quick if initiated by electrostatic interactions. Aggregate formation is irreversible and entraps oligomer onto the membrane surface, occurring after molecular binding. Lipid losses from particle or micelle formation likely includes oligomer as well, as some aggregates are observed dissociating from the membrane surface via a meta-stable "worm" (See Supplementary Movies in online version (doi: 10.1038/s42003-018-0230-4)). Altogether, these observations begin to describe both the kinetics and mechanism of the oligomers' membrane disrupting action (Figure 4-6a).

Kinetic hypothesis supported by surface plasmon resonance

With a hypothesized kinetic framework (Figure 4-6a), surface plasmon resonance (SPR) tested the kinetic model against observed data of *S. aureus* mimetic membrane disruption by the oligomers (Figure 4-6b). SPR is a label-free technique that uses an optical biosensor to observe effective refractive index changes near the gold sensor surface. It encodes both mass and structural changes, making it ideal to observe biomolecular interactions, such as membrane disruption, in real-time. Using a Biacore L1 chip,[427,441,442] *S. aureus* mimetic membranes were formed on the sensor and the Meta and Para were injected to observe the kinetics of binding and membrane disruption (Appendix C Figure C-15). Upon injection of oligomer, all response curves ascended quickly and then slowed toward an equilibrium, consistent with two-phase binding

kinetics (Figure 4-6c). Specifically, it appears oligomer was quickly bound to the lipid membrane (OL) and then shifted into another second, subsequent bound state (OL*). After the membrane was washed with PBS, a quick drop to an elevated baseline was observed to indicating the presence of both reversible and irreversible states (Figure 4-6c, Appendix C Figure C-16).

The proposed model based on fluorescence microscopy, lipid extraction, and FRAP fit well to the experimental SPR data, unlike literature models (Figure 4-6b, Materials and Methods, Equation 4-1). Several models have been developed for AMPs binding to SPR mimetic membranes, commonly utilizing two reversible steps including loss or lipid expansion on the second step.[426,441,442] However, attempts to fit the SPR sensorgrams with literature-based two state models with or without loss on the second step were unsuccessful (Appendix C Figures C-17 and C-18). The model could fit parts of the sensorgram (e.g. association, dissociation phase), but not the complete curve. Addition of loss on the first step (OL) to the model successfully described the SPR data (Figure 4-6c). This loss was rationalized by the sub-micron losses observed in the lipid extraction experiments, as well as the remainder of the data once a singular aggregate state is assumed (Appendix C Figure C-19). Physically, the observations by SPR within the model are consistent with all previous observations. The aggregate formation likely accounts for the irreversible baseline shift due to the permanent addition of oligomer to the membrane surface and dramatic structural changes. The intermediate step corresponds to molecular- or macromolecular-binding states that are revealed to be rapid and reversible by the SPR.

Across concentrations, the SPR model fitted and suggested the irreversible aggregate (OL*) to have a concentration threshold similar to the MIC. Model fits were obtained for all oligomer concentrations (Appendix C Figure C-20, Table C-2). Within the model, any parameter responsible for directing antimicrobial activity should demonstrate favor for the Para at concentrations below the MIC_{Meta} while showing similarity near the MIC_{Meta}. Within the fitted parameters, three matched this criteria i) K1, the equilibrium constant for molecular binding states, ii) OL*, the population of irreversible surface aggregates, and to some extent iii) Loss(OL*), which was lipid particle loss from the aggregate. K1 showed a favorable differential for the Para and occurred at a fast time-scale (seconds), typical of electrostatic associations (Appendix C Figure C-22 and C-23). However, the time-scale of the oligomer antimicrobial action was much longer (hours) as previously reported.[278] Thus, K1 was likely not the parameter responsible for biological activity. The population of aggregates (OL*) showed a good correlation with the differential in biological activity, and has a slower time-scale to match biological experiment. Lipid particle evolution from the aggregate Loss(OL*) showed some concentration dependence as well (Appendix C Figure C-24). Thus, the SPR modeling corroborated the importance of the aggregate formation as it relates to the biological activity of these isoamphipathic oligomers.

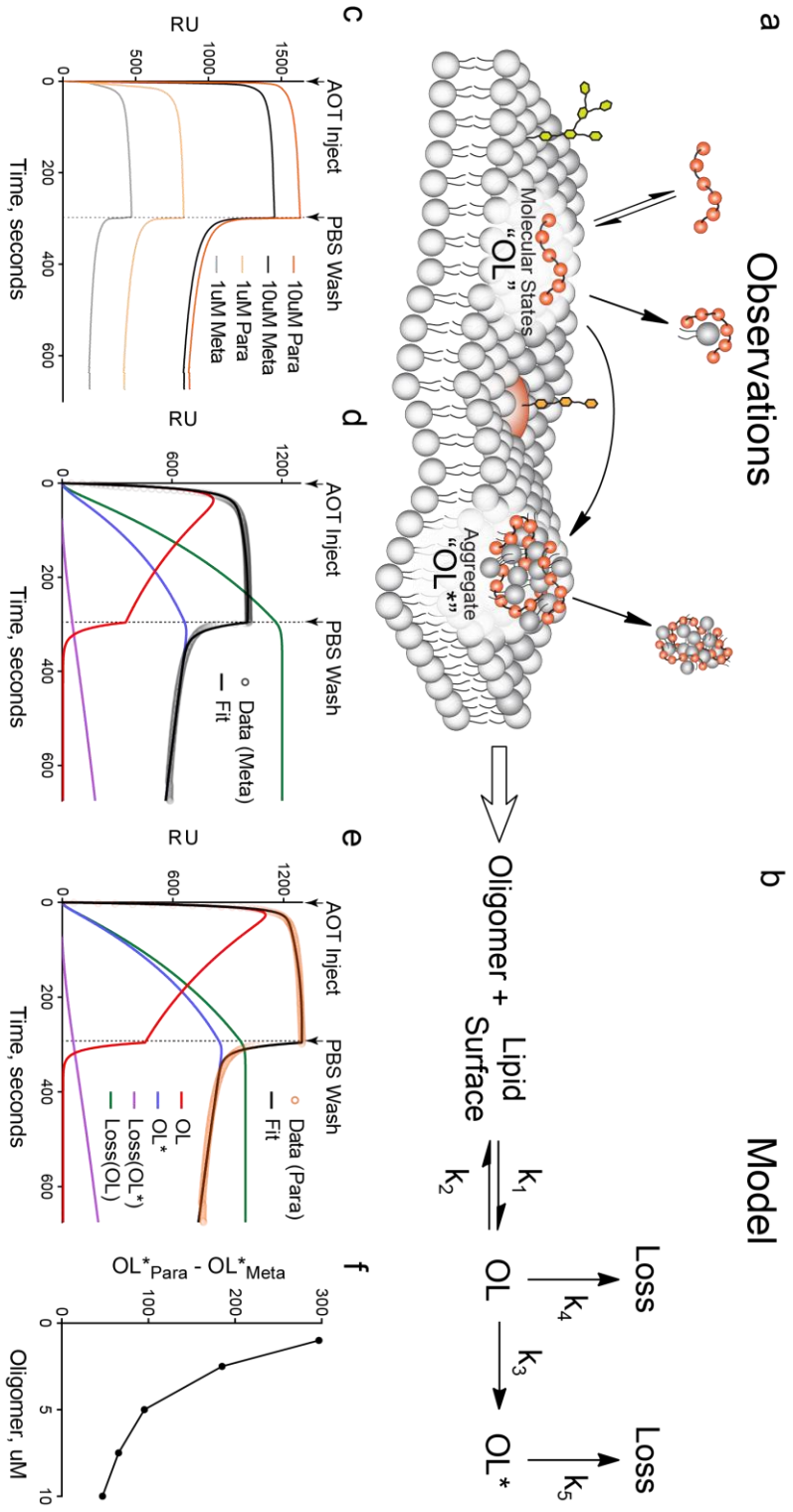

Figure 4-6: *Kinetic model based on observations tested and supported by SPR*
(a) *Kinetic framework was developed from all observations from time-lapse fluorescence microscopy (aggregates, lipid particle evolution), lipid extraction*

experiments (nanoscale losses), and FRAP (molecular-scale binding) and translated into ***(b)*** *a testable hypothesis of oligomer membrane disruption.* ***(c)*** *SPR sensorgram of a high (10 μM) and low (1 μM) concentration. The Meta and Para showed similarities at high concentration, especially within the dissociation phase (PBS wash). At low concentrations, the oligomers were significantly different in both the association and dissociation phases. All runs did not return to the original baseline, with some irreversible changes.* ***(d)*** *Model fit of 5 μM Meta.* ***(e)*** *Model fit of 5 μM Para.* ***(f)*** *Concentration dependence of differential aggregate formation (OL*), where the Para showed higher activity at lower concentration, below the MIC of the Meta.*

Discussion

This work has focused on the development of new experimental parameters for membrane-targeting antimicrobials, outside of the known properties of cationic charge and hydrophobicity. OligoTEAs have enabled the synthesis of isoamphipathic oligomers to specifically probe additional parameters in membrane-disruption. With extensively similar physicochemical properties, the Meta and Para also displayed similar solution-phase structure and dynamics, indicating they approached the bacterial membrane in similar fashions. However, at the membrane surface, the action of the Meta and Para was distinguishable and clear, as shown by the PI and di$SC_3$5 assays.

Fluorescence microscopy visualized the formation of a multimeric lipid aggregate, a differential of the two isoamphipathic oligomers. The kinetics, size, and efficiency of aggregate formation favor the Para, potentially connecting it to the biological differential in MIC. FRAP allowed the general visualization of molecular-scale diffusivity, indicating reversible molecular-scale binding. The oligomer-membrane disruption was observed across multiple length-scales by time-lapse fluorescence microscopy, quantification of lipid extraction, and FRAP, all culminating

into a kinetic framework that was tested and supported by SPR. The aggregate population (OL*) correlated with the observed behavior in the microscopy and the biological activity across concentrations.

Much research has focused on nano- and/or molecular-scale including models including the barrel-stave pore model, toroidal pore model, carpet model, and others by use of transmission electron microscopy (TEM), atomic force microscopy (AFM), and x-ray scattering. More recent work has highlighted the dynamic nature of some these states, possibly allowing for reversibility as seen in the FRAP data herein.[399,401,443–445] Other investigations into the mode of action of AMPs and their mimetics have also visualized dramatic, micron-scale membrane changes by electron microscopy and confocal microscopy.[417,446–448] These techniques frequently show morphological changes indicative of pore formation, but lack quantitative description this work has demonstrated. With SPR, AMPs and AMP mimetics have demonstrated elevated baselines after injection, meaning aggregate formation or a similar process could be shared between the Meta and Para with others scaffolds.[401,426,441,449] Outside the scope of this work, the robust appearance of this multimeric lipid aggregate on supported bacterial-derived membranes[429] will be explored in future work with other AMP and AMP mimetic scaffolds to see if similar behaviors are observed.

Thus, in conclusions to this work on these isoamphipathic oligomers, lipid aggregate formation is implicated in the mechanism of action of membrane-disrupting materials. However, it is not immediately clear how aggregate formation induces antimicrobial action. The Para produces both a greater number and smaller size of aggregates and either parameter (size or quantity) could be responsible. A smaller

aggregate indicates efficient aggregate formation, requiring a lower oligomer-to-lipid ratio, analogous to the peptide-to-lipid ratio.[400] However, it is also possible that the oligomers have similar ratios, but the Para provides more favorable kinetics for irreversible aggregate formation. Either way, the states of future interest lay somewhere between oligomer binding (OL) and aggregate formation (OL*). In this work, SPR could not distinguish additional states without introducing redundancy in the model. Investigating deeper into these quick transitions at the molecular and nanoscale states remains challenging. With respect to these oligomers, the challenge also included connecting the molecular conformation to the nano- and micron-scale. With requirements of high time- and length-scale resolution, we expect that further investigation with molecular simulation will provide answers when focused on the complexation of the oligomer with lipids and subsequent multiplex formation.

Tri-guanidine oligoTEA library designed from the Meta/Para

The nearly 10-fold difference in activity between the Meta and Para oligomers can be described as an exception to the general rule of physicochemical optimization of membrane-targeting AMPs and AMP mimetics. Thus, we sought to expand upon this exception to determine the extent to which the Meta and Para groups can differ in antimicrobial potency, as additional parameters for optimization would be hugely beneficial to understand further. A short 6-mer library of oligoTEAs were designed to contain the Meta and Para groups containing guanidine cationic groups rather than amines. During the time the oligomers were conceived, shorter oligoTEA sequences were demonstrated to have modest activity when utilizing guanidines. For example, the

MIC of PDT-3G is just above 10 µM against MRSA USA 300, whereas PDT-3Am has very little activity.[278] The experiment is then designed to review any cooperative action of the Meta and/or Para groups, where the oligomer would become more active and visualized by the MIC assay. Thus, for all of these compounds, the *N*-(*bis*-Boc-ethylguanidine)-*N*-allyl-*N*-acrylamide was used during assembly for the pendant group, rather than the *N*-(Boc-aminoethylene)-*N*-allyl-*N*-acrylamide used in the preparation of the Meta and Para. To discuss and name these compounds, dithiol codes were used, similar to prior work, specifically: 3 encodes 1,3-propandithiol, M encodes 1,3-benzenedimethanethiol, and P encodes 1,4-benzenedimethanethiol. A small cohort of oligomers were prepared to initialize the study and determine if the differences observed between the Meta and Para aforementioned translated to the 6-mer guanidine scaffold, specifically 333-3G, 3M3-3G, and 3P3-3G were synthesized and tested against MRSA and *P. aeruginosa* (Figure 4-7). Testing was completed against these bacteria to capture the potency against both Gram-negative and Gram-positive pathogens.

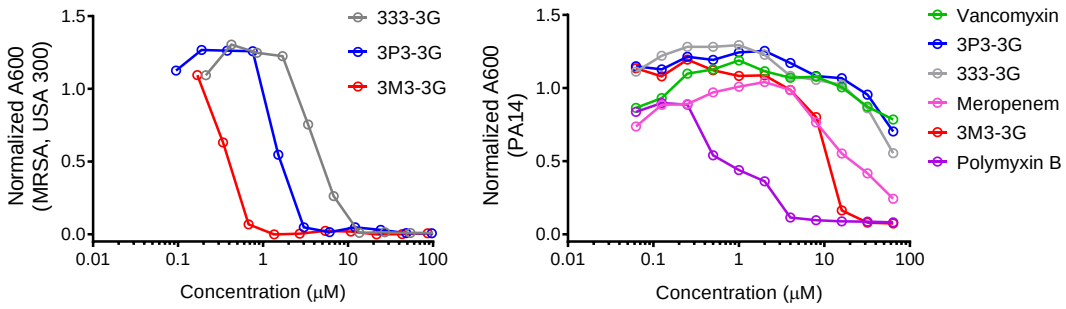

Figure 4-7: *MIC characterization of guanidine containing Meta / Para compound set. Minimum inhibitory concentration (MIC) was characterized as described in Materials and Methods. The three oligoTEAs 333-3G, 3M3-3G, and 3P3-3G were tested against MRSA USA 300* ***(left)*** *and against P. aeruginosa* ***(right)*** *with controls, as available. In both experiments, the oligomers were evaluated n = 3 biological replicates and no error bars are shown for clarity to see the MIC. Credit to Meghan O'Leary for this biological testing.*

In an interesting turn of events, the Meta containing compound (3M3-3G) was found to be modestly more active than the Para (3P3-3G) against both MRSA and *P. aeruginosa*; thus, motivating further library development. While single Meta and Para containing compounds were of interest and could have been synthesized (e.g., 33M-3G), there was significant interest to determine if the Meta and Para could be act cooperatively, meaning compounds containing two or more of these groups were of interest. Another consideration in the design of the oligomer library was to increase the speed of synthesis to capture as many possible compounds without limitation from single-shot syntheses that are typically done. Thus, potential compounds were organized around the order of dithiols proposed for the tri-guanidine (3G) scaffold in a twelve-member library (Figure 4-8). To synthesize these twelve oligoTEAs, three separate batches of fluorous allyl amine were reacted with the specific dithiol of choice and then split into six batches after complete reaction of the thiol-Michael addition with the guanidine monomer. These six batches were then carried through another cycle adding each specific dithiol for the desired sequence and similarly split into twelve batches after completion of the thiol-Michael addition (Figure 4-8).

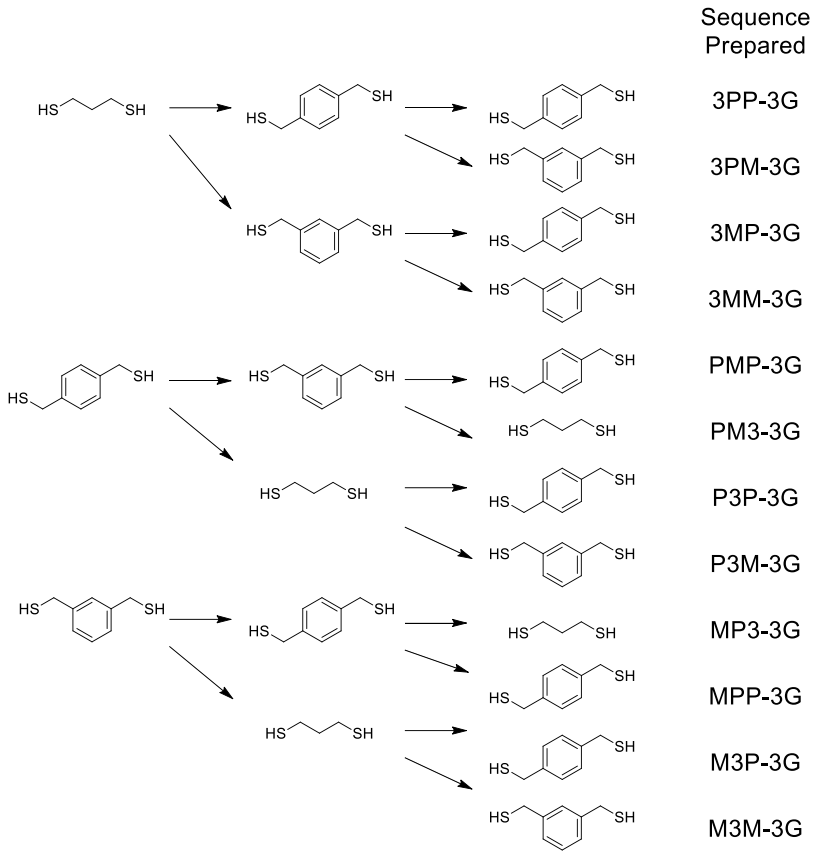

Figure 4-8: *Meta and Para containing oligoTEA library prepared by split syntheses. All syntheses were performed by J. S. Brown and Manisha Kunala, with guanidine monomer prepared by Nana Antwi.*

These oligoTEAs were then HPLC purified, confirmed by LCMS, and quantified by ^{1}H NMR against a known standard. To facilitate discussion, the oligoTEAs were divided and names by their first dithiol that began their synthetic sequence as either the 3-, M-, or P-series 3G oligoTEAs. In the spirit of the original Meta and Para, this 3G library was prepared to be isoamphipathic and ideally, they would have similar hydrophobicities by HPLC. However, there were some differences as visualized by analysis on the HPLC column retention time of the LCMS (Figure 4-

9). The original three oligomers (333-3G, 3M3-3G, and 3P3-3G) are also included in the data in Figure 4-9 for comparison.

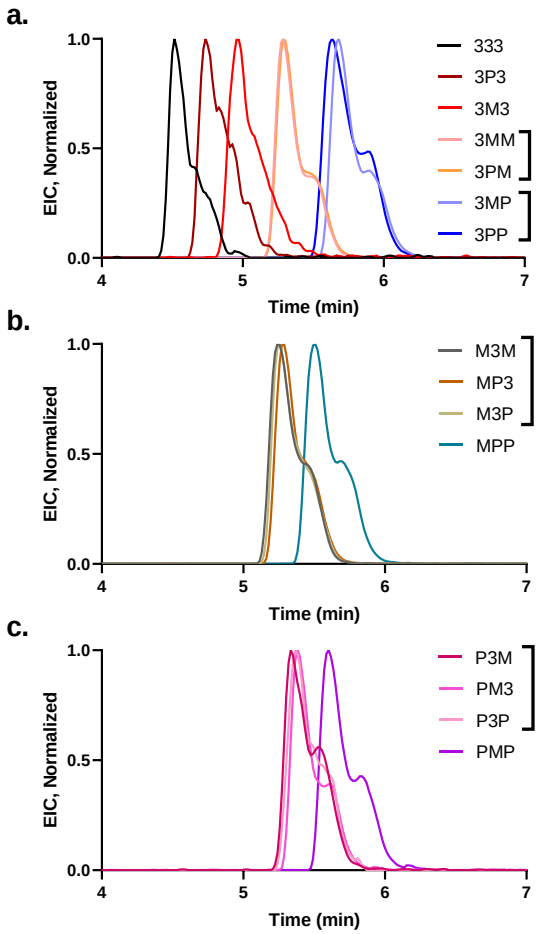

Figure 4-9: *Extracted ion count for hydrophobicity comparison of 3G oligoTEAs.* ***a.*** *3-series oligomers that begin with 1,3-propanedithiol,* ***b.*** *M-series oligomers that begin with the meta-benzendimethanethiol, and* ***c.*** *P-series oligoTEAs that begin with para-benzenedimethanethiol in the triguanidine (3G) scaffolds.*

Generally speaking, the inclusion of more the aromatic dithiols over the 1,3-propanedithiol increased the hydrophobicity of the oligomer, as would be expected. The 333-3G was the most hydrophilic; with a small difference between the 3M3 and 3P3, where the 3P3 is more hydrophilic. As in other studies, this trends well with the biological activity of these oligomers as the more hydrophobic 3M3 was modestly more

active. Interestingly, there is some sequence dependence in the observed hydrophobicity of the 3-series, where both the 3MM and 3PM are more hydrophilic than the 3MP and 3PP oligoTEAs. These data indicate that in the terminal position, the Para creates a more hydrophobic oligomer than the Meta; though, this trend is not observed in the M- or P-series oligoTEAs, which sequences start with one of the aromatic substituents. One of the last differences observed in these data is that the 3G oligoTEAs that contained three of the Meta/Para substituents (PMP and MPP) carried the most hydrophobicity. However, true to the design of the library, there are some isoamphipathic oligomers with similar retention times and hydrophobicity, specifically: the 3MM, 3PM, M3M, MP3, M3P, P3M, PM3, and P3P. The 3G oligoTEA library was then tested against MRSA and *P. aeruginosa* to reveal that there was little difference between all members of the library (Figure 4-10) and all MICs were within a single dilution of each other. Even with some increased hydrophobicity measured by LCMS, the MIC of the MPP and PMP landed in the middle of the oligoTEA library, showing no differences.

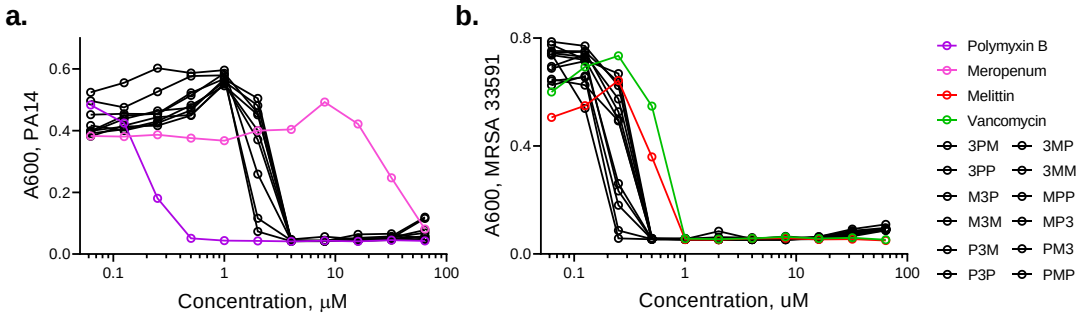

Figure 4-10: *3G oligoTEA library bacterial testing (MIC).*
The 3G oligomer library was tested against: ***a.*** *PA 14 in cationic adjusted tryptic soy broth (n=2 biological replicates). P3M, P3M, and PMP were not available for testing.* ***b.*** *MRSA 33591 in non-cationic adjusted tryptic soy broth (n=4 biological replicates, except P3M, P3M, and PMP where n=2).*

Discussion

Overall, the polyamine Meta/Para and the 3M3/3P3 did show measurable differences in antibacterial activity, while all other oligomers with additional (+2) meta- and para-substitutions did not. Moreover, the increased incorporation of these conformational substituents did not demonstrate any cooperativity, as originally hypothesized. However, there are many possible explanations for how the 3M3 and Para from the previous section can out-perform their constitutional counterparts while the highly substituted (+2 aromatic dithiols) 3G library did not. First, we observed that the Meta and Para have nearly a 10-fold difference in activity, whereas the tri-guanidine 3M3 and 3P3 had a less dramatic 3-5-fold difference. Overall, this initially indicates that the tri-guanidine system is less sensitive to the conformational difference between the meta- and para-substitutions. The guanidines present more sites for hydrogen bonding during membrane disruption, which could be altering the mechanism of membrane disruption, such that the process is no longer sensitive to the conformation of the oligoTEAs. This is discussed further in Chapter 6, where future effort toward understanding the molecular mechanism of membrane disruption (e.g. barrel-stave, toroidal, and carpet models) is recommended. In another perspective, these data could be indicating that the increase in hydrophobicity that is incurred by the addition of more meta- and para-substitution in the backbone could reduce the nuanced differences in conformation. It is also worthwhile to consider that the both the Meta/Para and the 3M3/3P3 are mostly symmetric, while the (+2) meta- and para-substituted oligomers are not. This could indicate that symmetry is a prerequisite for observing these

specialized effects of conformation on antibacterial activity. Specifically, oligomers that present the arrangement of a flexible "lipid-like" backbone surrounding a more "structured" benzene center could be explored further.

Conclusions

In the quest to develop new antibiotics in the face of antimicrobial resistance, we hope this work underlines multimeric lipid aggregation as a new biophysical parameter for further design and optimization of membrane-targeting antimicrobials. Advances in chemistry continue to enable the development of sequence-defined polymers and oligomers designed to ask specific fundamental questions about the impact of sequence, structure, conformation, and composition. While not directly observed in this work, a specific mode of antimicrobial action, pore formation, has been seen to be sensitive to differences as small as chirality in AMP mimetic structure, necessitating precise chemical control.[444] Here, oligothioetheramides (OligoTEAs) provided isoamphipathic oligomers (Meta/Para), demonstrating the same physicochemical properties as well as the same solution phase structure and dynamics, but a unique differential allowing the demonstration of this new biophysical property of lipid membrane surface aggregation. While this work did not fully conclude the molecular contributions that direct differences in the antibacterial activity of the Meta and Para, more work was done with an advanced tri-guanidine scaffold. The effects of conformation on antibacterial activity are complex, but specific parameters such as symmetry and specific mechanistic pathway (e.g., carpet model) should be considered

further. Overall, attention that can be directed to understanding the mechanism by which the lipid aggregates form, as well as the molecular properties that drive that process.

Materials and Methods

Chemicals and Reagents

Chemicals were purchased from Sigma Aldrich, Alfa Aesar, or Acros Organics, Ark Pharm, or Avanti Polar Lipids. Fluorous tag and fluorous silica were purchased from Boron Specialties. Strains of *Bacillus subtilis* were kindly donated by the Helman Research Group (Microbiology, Cornell University). Methicillin-resistant *Staphylococcus auerus* (MRSA; ATCC 33591), Vancomycin-resistant E. faecium (VRE; ATCC 700221), and *Staphylococcus epidermidis* (ATCC 14990) were obtained from ATCC. Human red blood cells were purchased from Innovative Research (Novi, MI).

Supplementary Methods

NMR spectra were recorded on an INOVA 600 MHz spectrometer and analyzed by MestReNova (version 10.0.0). ^{1}H NMR chemical shifts are reported in units of ppm relative to the deuterated solvent. LCMS experiments were carried out on an Agilent 1100 LCMS system with a Poreshell 120 EC-C18 (3.0x100 mm, 2.7 µm) column monitoring at 210 nm in positive mode for detection. Solvents for LCMS were water with 0.1% acetic acid (solvent A) and acetonitrile with 0.1% acetic acid (solvent B). A flow rate of 0.6 mL/min was used with a gradient starting at 5% solvent B, followed by

a linear gradient of 5% to 100% solvent B over 10 min, 100% solvent B for 2 min, before returning to 5% solvent B until equilibrated (3 min). HPLC purification was performed on an 1100 Series Agilent HPLC system using a reverse phase Agilent Eclipse XDB-C18 column (9.4x250 mm, 5 μm) at 40 °C and collected using an automated fraction collector. Solvents for HPLC were water with 0.1% trifluoroacetic acid (solvent A) and acetonitrile with 0.1% trifluoroacetic acid (solvent B). Compounds were eluted with either a 3.17 %B/min gradient or a 1.25 %B/min gradient at 4mL/min. Pure and chemically confirmed oligoTEAs were quantified by being lyophilized into a tared microcentrifuge tube. Single stock solutions were prepared at either 1 or 5 mM in ultrapure water and used for all experiments. (1x) PBS was pH 6.8 unless otherwise stated. Most all tabulated data was processed with GraphPad Prism 7.01. Statistical analysis was performed on specific data sets as described in the main text. Means are defined as $\bar{x} = \frac{1}{n}\sum_i x_i$; standard deviation defined as $\sigma = \sqrt{\frac{\sum_i (x_i - \bar{x})^2}{n}}$; and pooled variance was defined as $s^2 = \frac{\sum_i (n_i - 1)\sigma_i^2}{\sum_i (n_i - 1)}$. Where used, confidence intervals are provided as a measure of uncertainty.

General method for oligothioetheramide assembly

Oligomers were prepared as described starting with a C_8F_{17} fluorous tag.[146,147,217] The oligomer was iteratively assembled by reacting fluorous-bound allyl groups with dithiol monomers via thiolene to produce a mono-substituted thiol to be reacted in a thiol-Michael addition with an allyl acrylamide monomer. After thiol-Michael addition, the fluorous olefin was regenerated with each cycle. Fluorous solid-phase extraction (FSPE)

after each reaction purified and removed excess reagent. The fluorous product was retained selectively and purified on fluorous silica (~40 mg/mg fluorous tag) during a fluorophobic wash of 20-30% Water in MeOH (0.4 mL/mg fluorous tag) and eluted with MeOH (0.2 mL/mg fluorous tag). Oligomers were dried by nitrogen or by vacuum centrifuge (both RT). OligoTEAs were cleaved with 100% TFA, HPLC purified, verified by LCMS and/or ^{1}H NMR where appropriate.

General method for fluorous allyl amine synthesis:

2-[2-(1H,1H,2H,2H-Perfluoro-9-methyldecyl)isopropoxycarbonyloxyimino]-2phenylacetonitrile (fluorous tag) was dissolved in THF (15 mg/mL). Two equivalents of allyl amine and two equivalents of triethylamine were added and stirred at RT for at least 3 hours. The THF was completely removed and the reaction mixture was fluorous purified to yield fluorous allyl amine as a light yellow solid.

General method for thiolene reaction:

Two equivalents of 1,3-propanedithiol or meta- or para-benzyl dimethanethiol and 2,2-dimethyoxy-2-phenylacetophenone (DMPA 10 mol% of dithiol) were added to a solution of fluorous olefin in methanol or 1:1 acetone:methanol and irradiated at 20 mW/cm^2 for 270 s. The fluorous thiol product was purified by FSPE.

General method for thiol-Michael addition:

Two equivalents of the Boc-amine ethylene N-allyl-N-acrylamide was activated by dimethylphenyl phosphine (DMPP, 5 mol% of monomer) and added to the fluorous

thiol (50-300 mM in methanol or 1:1 methanol:acetone). The reaction completion was tracked by thiol detection via an assay with 2,2' dithiodipyridine (DTDP) as described.[217]

Minimum Inhibitory Concentration (MIC) Assay

Approximately five colonies were selected and grown overnight in broth media (*B. subtilis*, LB; *S. epidermidis*, MRSA, VRE, Tryptic Soy Broth). A subculture was then grown to mid-exponential phase (37°C) and OD 600 was measured and diluted to 0.001 with designated media (approximately 5 x 10^5 CFU/mL). OligoTEA or antibiotic and bacterial suspension were combined (5:95 v/v%) in a 96-well plate and incubated (37°C) with agitation to the final concentration reported by serial dilution. After 14 hr, the OD 600 was measured. Data were normalized to the media blank (0) and solvent control (1). The MIC was recorded as the lowest (minimum) concentration required to kill all visible bacteria cells (See Figure 4-7).

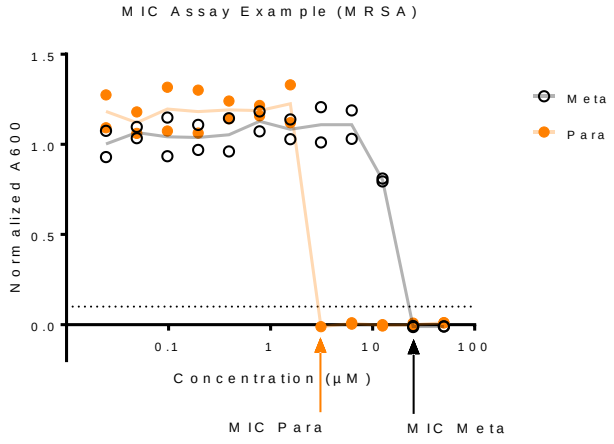

Figure 4-11: *Example of MIC Assay to demonstrate MIC definition*

The minimum inhibitory concentration is defined as the concentration at which all bacteria cells (>90%) are killed; as indicated by the arrows for the Meta and Para. This has also been termed a MIC_{90}.

Pulse-field gradient nuclear magnetic spectroscopy (PFG NMR)

Measurements were performed with a Varian Unity INOVA 600MHz spectrometer with a Varian 600 triple resonance XYZ PFG (HCN) inverted probe. The 90° pulse angle was optimized. Diffusion measurements were accomplished using the double-stimulated echo convection compensated sequence[381] using 3 mm tubes and 20 LPM of gas flow to diminish convection.[355] Measurements were completed with an acquisition time of 1.7 seconds, 8 steady state pulses, diffusion gradient length of 2.0 milliseconds (ms), 0.0 ms of off-center delay (del2), 0.00 unbalancing factor, alternating gradient pulse sign, and diffusion delay of 120 ms. Scout measurements helped determine the gradient stabilization delay (1.0-2.5 ms) to minimize eddy currents. A standard (99.9% D_2O) was run to calibrate the probe (gcal) by the observed diffusion coefficient of HDO for each temperature as described by a Speedy-Angell power law fits[382] of Longsworth's data.[383]

Use of VT-PFG NMR, DEER EPR, and Stokes-Einstein-Sutherland Equation.

This method to measure the size and aspect ratios of flexible macromolecules has previously been discussed extensively[217] and makes use of work from Stokes-Einstein-Sutherland (SES), Chen and Chen,[390] and G. de la Torre,[368] and F. Perrin[365–367] with a review by A. Macchioni.[362]

$$D_t = \left(\frac{k_B}{c(r_H)f_S(p)\pi r_H}\right)\frac{T}{\eta}$$

$$slope \equiv \left(\frac{k_B}{c(r_H)f_S(p)\pi r_H}\right) \rightarrow \frac{k_B}{(slope)(\pi)} = c(r_H)f_S(p)r_H$$

The SES equation above relates the Boltzmann temperature and the translational molecular diffusion where k_B is the Boltzmann constant, T is the temperature in Kelvin, r_H is the prospective hydrodynamic radius, η is the dynamic viscosity, c is a size-dependent modification to transition between the slip/no-slip boundary conditions,[390] p is the geometrically defined aspect ratio, and f_s is the shape-modified friction factor.[365–367] By measuring the diffusion by variable temperature PFG-NMR, the two remaining unknowns in this equation of hydrodynamic radius and shape are constrained. This is especially sensitive with the slope of the normalized temperature (T/η) is used. Then, the end-to-end distance can serve as a prospective diameter and allow the equation to be solvable, revealing the hydrodynamic radius and aspect ratio given a geometric shape, either an ellipsoid[365–367] or rod.[368] For this analysis, a prolate ellipsoid was assumed and the end-to-end distance was assumed to describe the longer dimension of the ellipsoid. The final equation was solved using fsolve in MATLAB R2017a with MaxIter = 800, MaxFunEvals = 200, a tolerance of 10^{-25}, and a multiplier on the residual of 10^{15} as it solved for meters.

Spin labelling of polyamine AOT scaffold

With the use of several primary amine groups in this scaffold, an amine protecting strategy orthogonal to base (synthesis of monomer), nucleophile (phosphine of thiol-

Michael), UV of thiolene, and acid (TFA, fluorous tag deprotection) had to be utilized to enable spin labeling. The phthalimide-protected amine N-allyl-N-acrylamide was thus developed (Figure 4-8). Generally, monomers are produced by alkylation (allyl group) and then acylation (acrylamide) or vice versa starting with either functional amine or alkyl halide. However, insufficient yield was obtained from the alkylation and then acylation of a phthalimide protected ethylene diamine. Also, the phthalimide was unstable in the presence of NaH, needed to for the acylation-then-alkylation route. Deprotection of the N-Boc ethylene N-allyl-N-acrylamide with TFA and re-protection with phthalic anhydride was not feasible due to immediate polymerization.

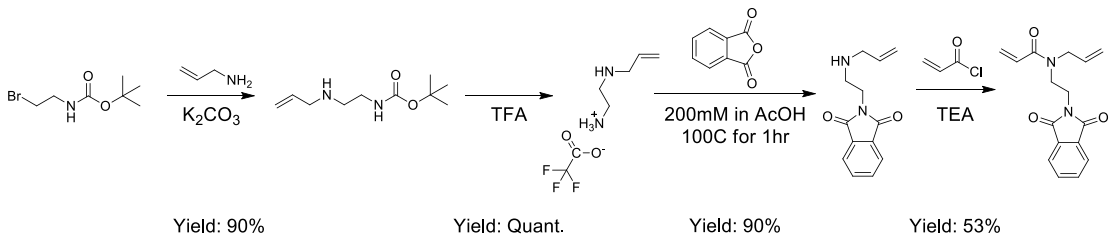

Figure 4-12: *Scheme for N-phthalimide protected ethylene N-allyl-N-acrylamide*

Thus, the following scheme was developed (Figure 4-8): 1) alkylation of N-Boc ethylene bromide with 50 eqv of allyl amine 5eqv of K_2CO_3 purified by filtration, 2) deprotection with 200 mM 1:1 TFA:DCM stirred at RT for 1 hour, 3) treatment with 1eqv phthalic anhydride 200 mM in acetic acid at 100C for 1 hour, dried, precipitated in water and dried, and 4) acylation as previously described[146] and flash purified, eluting at 60% ethyl acetate in hexanes. In Step 3, the selectivity of the phthalic anhydride to protect primary amines over secondary amines was critical, but was reported in literature before.[450,451]

With the N-phthalimide ethylene N-allyl-N-acrylamide, assembly of the antibacterial oligoTEA was completed as previously described.[278] The standard TFA deprotection then yields two primary amines for conjugation with a Proxyl-NHS (Toronto Research Chemicals, North York, Canada) with conditions previously reported.[217] Full deprotection of the oligomer (4 phthalimide groups) was modest with hydrazine, even with heat. Thus, a previously reported route of reduction with sodium borohydride and hydrolysis with acid[433] was optimized to utilize a stronger acid and less heat (Figure S4, shown again below). The oligomer was purified by HPLC and verified by LCMS (See Appendix C, Supplementary Spectra). The paramagnetic label prevents against full ^{1}H NMR of the compound.

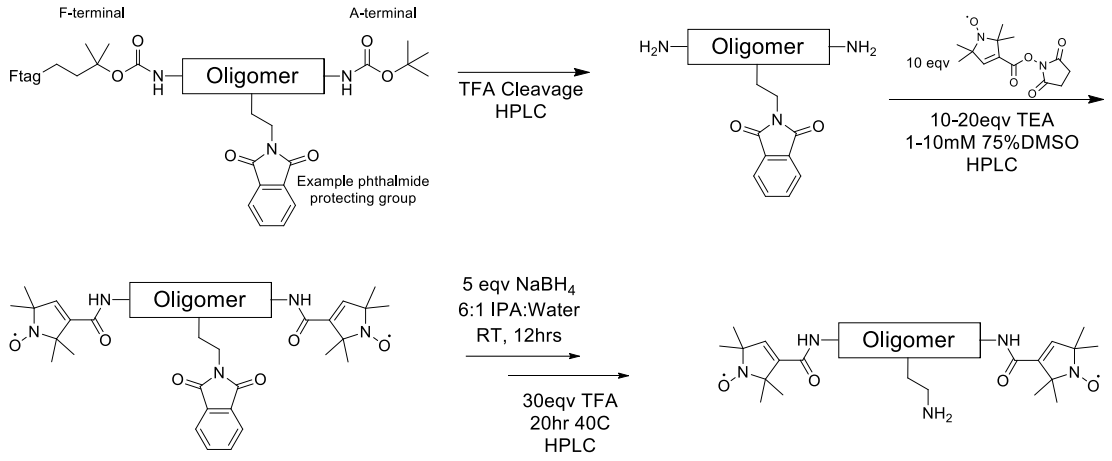

Figure 4-13: *Proxyl spin-labeling scheme orthogonal to N-phthalimide protection*

Double electron-electron resonance (DEER) EPR

DEER ESR measurements were completed at the National Biomedical Center for Advanced ESR Technology (ACERT) Center at Cornell University. Di-spin labeled oligoTEAs were reduced using 1N aqueous ammonia for 1-2 hours at 50-500 µM at room temperature and dialyzed against ultrapure water using a 100-500 MWCO Micro-

Float-A-Lyzer (Spectrum Labs) and monitored by a calibrated Accumet (Cat 13-620-165) conductivity meter. All samples were prepared at 50 μM and vitrified to 70K rapidly from room temperature. A working frequency of 17.3 GHz with a 30G magnetic component in a rotating reference frame was sufficient for distances of 10 Å or longer. Samples were measured by 4-pulse sequence double electron-electron resonance (DEER) for 1μs. Time domain data was processed in MATLAB to determine sensitivity to baseline fitting. Then, distance distributions were calculated by Tikhonov regularization based on the L-curve method ($\alpha \sim 2\text{-}7$) using MATLAB scripts from the ACERT website (acert.cornell.edu).

General method for X-ray scattering

All samples were centrifuged at 14,000 RPM for 10 minutes. SAXS data were collected at Cornell High Energy Synchrotron Source (CHESS) beamline G1 at ~12.68 keV (0.98 Å) at 5.5×10^9 photons per second. The X-ray beam was collimated to 100 μm^2 diameter and centered on a sample cell with 1.5 mm path length and 5 μm thick glass walls (Nippon Electric Glass America, Schaumburg, IL). The sample cell and full 1.5m X-ray flight path, including beamstop, were kept *in vacuo* (1×10^{-3} torr) to eliminate air scatter. Sample plugs of 30 μl were delivered to the capillary. To reduce radiation damage, sample plugs were oscillated in the X-ray beam using a peristaltic pump (Ismatec, Cole-Parmer GmbH, Germany). Images were collected on a dual Pilatus 100K-S detector system (Dectris, Baden, Switzerland) for small- and wide-angle scattering observation with 20-80 sequential 1 s exposures being used to assess possible radiation damage. Sample and buffer solutions were normalized to equivalent exposure before subtraction

using beamstop photodiode counts. Sample-to-detector distance was calibrated using silver behenate powder (The Gem Dugout, State College, PA). Images were averaged to profiles and buffer subtracted using the BioXTAS RAW software (1.4.0), which includes a statistical check for radiation damage during reduction. Slight buffer mismatch was observed, evident most in the WAXS region. The offset sample signals were seen to decay fully in the WAXS region at approximately q=0.6-0.7 and data were thus scaled appropriately at q=0.7 (scale factors were ~3% from original). The useful q-space range ($4\pi Sin\theta/\lambda$ with 2θ being the scattering angle) was generally from qmin= 0.01 $Å^{-1}$ to qmax= 0.7 $Å^{-1}$.

Propidium iodide (PI) membrane permeabilization assay

A single colony was cultured overnight and then subcultured and incubated 3 h until the OD600 measured between 0.5 and 0.6. Bacteria were harvested, washed, and resuspended in a solution of 5 mM HEPES buffer, 5 mM glucose, and 10 μM propidium iodide at pH 7.2. A total of 150 μL of bacteria solution was added to each well of a black 96 well plate. Fluorescence measurements were taken at 535 nm excitation/617 nm emission on a TECAN Infinite M1000 PRO Microplate reader (Männdorf, Switzerland) for 2 min. Oligomer stock solutions in water were added to give a final concentration of 15 μM, and fluorescence measurements were taken for an additional 20 min.

$DiSC_3$5 membrane depolarization assay

A single colony was cultured overnight and then subcultured. The bacteria were harvested and washed twice with HEPES buffer. 0.5 M EDTA solution (pH 7.4) was

added for a final concentration of 0.2 mM EDTA, and 3,3'-dipropylthiadiacarbocyanine ($diSC_35$) was added for a concentration of 0.4 µM. The solution was incubated 30 minutes, before adding 100 mM KCl and incubating 1 minute. This bacterial solution was added to oligomer stocks in a black 96 well plate and the fluorescence intensity (610 nm excitation, 660 nm emission) was recorded for 60 minutes. The data were analyzed by subtracting the baseline (water) from the sample intensity at 60 minutes.

Small unilamellar vesicles (SUVs) preparation.

1-2-dioleoyl-sn-glycerol (18:1 DG), 1-palmitoyl-2-oleoyl-sn-glycero-3-phosphocholine (16:0-18:1 PC, POPC), 1-palmitoyl-2-oleoyl-sn-glycero-3-phosphoglycerol (16:0-18:1 PG, POPG), 1',3'-bis[1,2-dipalmitoyl-sn-glycero-3-phospho]-sn-glycerol (16:0 cardiolipin, TPCL), 1',3'-bis[1,2-dioleoyl-sn-glycero-3-phospho]-sn-glycerol (18:1 cardiolipin, TOCL) were purchased from Avanti Polar Lipids, Inc. Cholesterol (≥99%) was purchased from Sigma Aldrich. SUVs were prepared similar to the Avanti Polar Lipids protocol. Lipids were combined from chloroform stock solutions and dried using dry nitrogen at room temperature and dried for at least 6 hours at ≤10 mtorr. The dried lipids were suspended in 1x phosphate buffered saline (PBS) by vigorous vortexing for 5 minutes. Light sonication was needed for any lipid mixture with TPCL. The suspension was gently mixed overnight to age. The suspension was then sonicated for 10-30 minutes in a water bath (RT) using a QSonica Q125 probe-tip sonicator (20kHz) at 50% power, pulsing for 7 seconds with a 2 second rest. The resulting translucent suspension was then centrifuged at 17k RCF for 7 minutes to remove any metal particles. The solution was then filtered through a 0.2

μm PES filter. Dynamic light scattering (DLS) was then completed on a Malvern Zetasizer XS determining the hydrodynamic size to be 20-80 nm (Figure S8a). Particle concentrations such that the attenuator was automatically set at 7 or 8, preset parameters of a liposome (RI 1.34) dispersed in PBS (0.9103 cP at 25C) were used. Zeta potential measurement was completed at the same particle concentration (Figure S7b). With the exception of TPCL lipid mixes (1 week), SUVs were stored at 4C and seen to be stable for approximately 3-4 weeks.

Literature compilation of data on lipid composition of Staphylococcus aureus.

Several articles were gathered on *Staphylococcus aureus* to understand the lipid composition in growth conditions similar to MIC assay (exponential growth). This includes understanding the amount of neutral lipids present in the membrane, effects of growth phase, and antibiotic resistance mechanism based on the lipid composition. Ultimately, the main goal is to determine a lipid composition to use in membrane mimetic studies. While bacterial membranes are anionic, a simple, fully-charged lipid bilayer would likely be mechanically frustrated from electrostatic repulsion and does not serve as a good mimetic.

Three reports quantified the neutral lipid (NL) component of *S. aureus* to be 19±7% of the membrane. Five other reports mentioned/showed qualitative support of the neutral lipid fraction but did not quantify it. Phosphatidylglycerol (PG) is a major headgroup component in the *S. aureus* membrane with eleven reports quantifying it at an average of 57±5% Cardiolipin (CL) was also quantified in similar reporting to be 16±4% of the

membrane. Lastly, lysylphosphatidylglycerol (lysyl-PG or PG) was reported at 16±3% of the *S. aureus* membrane. LPG has an attached lysine via the carboxylic acid, meaning there are two free amines on the structure. The predicted pKa (Marvin Sketch 16.5.23) of these amines is 7.4 (amino group) and 10.21 (functional group), meaning at physiological pH, it has a net +0.5 charge. On a surface, there are additional effects on these pKa numbers and molecular association. LPG has been shown to impart resistance to cationic antimicrobials, including nisin and human defensins in *S. aureus*.[452] However, LPG is expensive (~$200/mg) and its use was prohibitive for study in the scope of this work, which seeks only to understand the interaction of antibacterial oligoTEAs and an *S. aureus* mimetic membrane. LPG within the native *S. aureus* membrane should attenuate the activity of any cationic membrane disrupting agent, but likely does not broadly change the mechanics of interaction.

Two lipid compositions were thus utilized:

1) 70% PG and 30% CL or 7:3 PG:CL
   Reflects the often larger amount of PG to CL in the *S. aureus* while still being significantly different than 100% PG
2) 20% neutral lipid (e.g., diacylglycerol), 55% PG, and 25% CL or 4:5:11 NL:CL:PG

List of publications that detail the lipid composition in S. aureus:

Publication:	Lipid compositions known in MRSA:

P Beining et al (1975)[453]

	Value	Percent
MonoGlu	0.003	0.3%
DiGlu	0.026	2.6%
PhosGlu	0.004	0.4%
PG	0.306	30.1%
Cardiolipin	0.224	22.1%
Carotenoid	0.132	13.0%
Vitamin K	0.320	31.5%
Sum	1.015	100%

J Cheng et al (2011)[454]	1:1 (TO)CL:POPG and 1:1 POPC:POPG are acceptable models (Gram postitive) 1:1 POPE:POPG is not though
N Mishra and A Bayer (2013)[455]	Carotenoid (neutral) present, unquantified LPG: 13.9%; PG: 79.6% CL: 6.5% Measured across 9 strains.
C Haest et al (1972)[456]	Neutral lipids mentioned, not quantified Carotenoids/VitK not mentioned LPG: 38% PG: 57% CL: 5%
Y Kanemasa et al (1972)[457]	CL increases and PG decreases as the *S. aureus* transitions from exponential to stationary phase. Neutral lipids (TLC ~50%) -- Mid-log, CL: 11% PG 72% LPG 11% Other 6%
E Garcia-Fernandez et al (2017)[458]	Emphasizes importance of carotenoids in beta-lactam (methicillin) resistance in *S. aureus* No quantification of lipid compositions.
M Tsai et al (2011)[459]	Phospholipids only: PG: 43% CL: 46% LPG: 11%
N Mishra et al (2011)[460]	Carotenoids are in higher proportion in MRSA compared to regular *S. aureus*.

	Decreases membrane fluidity (more stiff, like CL), thought to be mechanism for resistance for AMPs
M Hayami et al (1979)[461]	Neutral lipids mentioned 5-10% of total Phospholipids reported: CL: 20% PG: 43% LPG: 32% Other 5%
D White and F Frerman (1967)[462]	Neutral lipids (VitK, Glycolipid) shown
D White and F Frerman (1968)[463]	Neutral lipids are 5-10% of lipids Experimentally observed 12.5% LPG: 9% PG: 60% CL: 19% The amount of neutral lipids depends on the growth media (especially if serum is present)
S Short and D White (1970)[464]	During exp phase PE: 2% and stationary phase PE: 14%

Fluorescein labeling of the Meta and Para

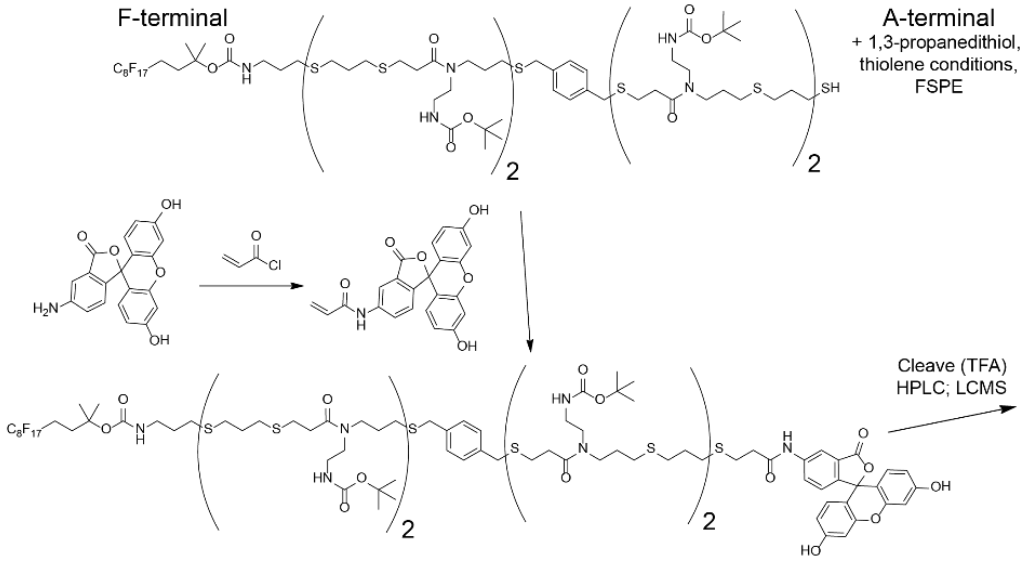

Figure 4-14: *Scheme to fluorescein label the Meta and Para*

Before the termination of oligomer assembly, fluorescein acrylamide was conjugated to the terminal thiol of 1,3-propanedithiol by thiol-Michael addition conditions catalyzed by 1,8-Diazabicyclo[5.4.0]undec-7-ene (DBU) instead of DMPP, as DMPP did not lead to efficient reaction conversion conditions detailed below.

Fluorescein acrylamide was prepared from the treatment of fluorescein amine (227 mg, 0.606mmol, Acros Organics) with 2eqv of N-methylmorpholine (pKa 7.4, to minimize di-addition product) in 100mM THF, with 1.1eqv of acryloyl chloride added dropwise while stirring at 0C for 6 hours. The crude mixture was extracted into ethyl acetate and washed with 1M HCl twice and brine. Flash chromatography 0-20% MeOH in DCM eluted the product at 5% MeOH (Yield: 40 mol%). Once the fluorescein acrylamide was conjugated to the fluorous terminal, FSPE was performed, followed by 100% TFA cleavage, HPLC, and verification by LCMS.

Fluorescence microscopy and FRAP

To form planar supported lipid bilayers, polydimethylsiloxane (PDMS) wells of ~1cm diameter were attached to piranha-washed glass slides (70% sulfuric acid, 30% hydrogen peroxide). PDMS consisted of 10:1 elastomer:cross-linker mixture of Sylgard 184 (Robert McKeown Company). Wells were coated with 100 µL of poly-L-lysine (0.1%wt/vol in water, Sigma P8920) for 30 minutes (RT), then washed with PBS pH 6.8. SUVs were labeled with 0.05-0.1 mol% Octadecyl Rhodamine B or Texas Red™ DHPE (Molecular Probes). The labelling amount was kept low to prevent surface quenching. G25 spin column (GE Healthcare) removed excess fluorophore. Labeled vesicles were added to well and incubated for 10 minutes to rupture and form a bilayer. The well was gently rinsed with PBS to wash away excess vesicles. Scratches were made on the bilayer to aid in determining the focus. Imaging was performed with a Zeiss Axio Observer.Z1 microscope with α Plan-Apochromat 20× objective. Fluorescence recovery after photobleaching (FRAP) measured lipid diffusion after photobleaching[465] after oligomer exposure (1hr) and after washing (5-10 mL PBS). A ~20 µm diameter spot in bilayer was photobleached by 150 mW 561 nm optically pumped semiconductor laser (Coherent, Inc.) for 100 ms. The recovery of was recorded and fit in comparison to the background following the method reported by Soumpasis.[466] The diffusion coefficient was calculated using the equation, $D = w^2/4t_{1/2}$, where the full width half-maximum w of the Gaussian profile is used for calculation.

Particle analysis

Thresholding was performed to select the brightest pixel populations using the "Triangle" method.[467] While ImageJ was set to analyze particles from 0.0-10 μm, the smallest aggregates of ~0.1 μm were at the resolution and threshold limit, limiting the accuracy of their quantification in number and size by generally undercounting. Aggregates 0.2 μm and greater were reliably counted. The upper limit of particle analysis was 10 μm, with most oligomer induced aggregates ranging from 0.2-7.5 μm for the Meta and 0.2- 5 μm for the Para. For equilibrium and kinetic counts, the total count of particles was subtracted from the number initial defects (e.g. spots) present on the membrane to determine the number of aggregates that formed during oligomer exposure.

Calculation to estimate the aggregate area percentage of the FRAP laser spot.

At maximum concentration, approximately 1500 aggregates were counted in the full viewing area of 450 x 335 μm, meaning the aggregate density is on average 1e-2 aggregates per μm^2. Thus, in the ~315μm^2 FRAP spot (Appendix C Figure C-12), ~3 aggregates will be present with variation. In this case, five aggregates were photo-bleached. Assuming each aggregate averages approximately 2 μm^2 in area, the average area of aggregates in the FRAP laser spot would be a total of 6 μm^2, which is approximately 2% of the FRAP spot area. For the maximal aggregate count observed in this study of ~3000 aggregates (at 10 μM), that would double this estimation such that the aggregates would be approximately 4% of the FRAP laser spot size.

Surface plasmon resonance (SPR)

SPR was completed using a Biacore 3000 with an L1 Chip at 25C modified slightly from manufacturer protocol. Before use, desorb, sanitize, and an overnight wash with ultrapure water were completed. 1x pH 6.8 PBS was used throughout all runs and solutions. The chip was conditioned with 7 µL 40 mM octyl-β-glucopyranoside (Alfa Aesar) at 10 µL/min at the start and end of each run. Additional manufacturer recommended washes were used. SUV capture was done for 10 minutes (5 µL/min) to ensure surface coverage. The following control runs were performed: i) 1 minute pulses of 10 mM NaOH showed little response to indicate minimal formation of multilayers, ii) injections of the oligomer alone showed no response, and iii) injections of 0.1 mg/mL BSA showed little to no response. At an equilibrated flow of 30 µL/min, samples were injected (kinject) for 5 minutes and dissociated for 6 minutes with PBS.

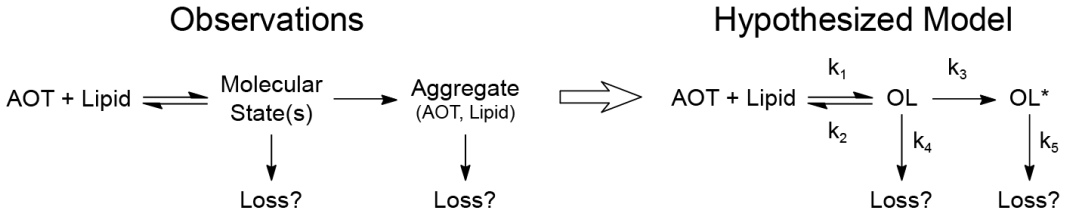

$$\frac{dOL}{dt} = k_1[AOT][C_{Lipid,Total} - OL - OL^* - Loss(OL) - Loss(OL^*)] - k_2OL - k_3OL - k_4OL \quad (1)$$

$$\frac{dOL^*}{dt} = k_3OL - k_5OL^* \quad (2)$$

$$\frac{dLoss(OL)}{dt} = k_4OL \quad (3)$$

$$\frac{dLoss(OL^*)}{dt} = k_5OL^* \quad (4)$$

$$\frac{dSignal_{SPR}}{dt} = \frac{dOL}{dt} + \frac{dOL^*}{dt} \quad (5)$$

Equation 4-1: *Ordinary differential equations from kinetic framework*
Excerpt of two-state model with loss on each step translated to mass action kinetics rates (Equations 4-1). SPR observes effective refractive index changes near the gold sensor surface, encoding both mass and structural changes. Thus, the SPR cannot observe material lost from the surface seen in Equation 3 and 4 and Equation 5 sums up the combined observations.

Use of MATLAB to model and fit SPR data

Fitting of the kinetic rates to the SPR sensorgram data was completed in MATLAB R2017a (9.2.0.538062) using lsqcurvefit. The function was two separate nested ODEs, one each for the association and dissociation phases where $C_{oligoTEA}$ was the designated concentration and 0uM, respectively. The ODEs were numerically solved by ode15s with RelTol and AbsTol as 1e-8. Convergence of lsqcurvefit was seen typically in less than 1k function iterations to a resnorm less than 1e6 to capture the behavior of the curve. Kinetic rate parameters k_1,k_2,k_3,k_4, and k_5 were not bounded, while $C_{Lipid,total}$ was kept constant (3000 ± <0.01%). $C_{Lipid,total}$ should be dependent on the physical number of binding spots of the lipid surface, only changing based on SUV lipid composition, not the oligomer concentration (only the *S. aureus* lipid composition was fit). $C_{Lipid,total}$ must be greater than the highest RU value in the experimental data. For example, $C_{Lipid,total}$ must be at least ~1650 RU worth of lipid in order to fit the 10μM Para from Appendix C Figure C-20. $C_{Lipid,total}$ scales the curve response, with little change to the curve shape. Since the kinetic rates significantly affect curve shape, $C_{Lipid,total}$ was held constant to allow comparison of kinetic rates.

Supplementary MATLAB Code

The code is broken into a script that calls a custom function. Within the function are the ODEs for association and dissociation ([Oligomer] = 0) are called by the script to be numerically integrated in a sequential manner.

Script:

```
close all
clear all

global M1 M2 M3 M4 MSPR xswitch

% point where buffer flows in
xswitch = 296;

filename = 'Para_2p5uM_SAureus.txt';
fileopen=fopen(filename,'r');
filein = fscanf(fileopen,'%f',[2 Inf]);
data = filein';
fclose('all');
t = data(:,1);
y = data(:,2);

%initial values of k
%k0=[2e3; 0.01; 0.01; 0.01; 0.005; 1.5e+4]; Working with Melittin
%   k1    k2     k3     k4      k5     k6      LipTot
k0=[2.3e4; 0.078; 0.0041;  0.0;  0.0045;  0.00042;  3e3];

% %bounds for parameters
%       k1     k2   k3    k4     k5    k6      LipTot
lb = [1e2;  1e-4;  1e-8;  0;     0;    0;      2.95e3]; %lower boundary
for parameters
ub = [1e5;    1;   1;     1e-12;  0.1;   0.01;  3.05e3]; %upper boundary
for parameters

%Plot curve with initial values
timestmp = datestr(now);
timestmpfix = regexprep(timestmp,'[:]','');
figure(1), clf
set(gcf,'units','points','position',[100,100,800,600])
f1                                                                    =
plot(t,y,'o',t,Funct2StateWithLossOn1And2(k0,t),t,M1,t,M2,t,M3,t,M4);
xlabel('Time, s')
ylabel('RU')
hold off
set([f1(2)],'LineWidth',2)
set([f1(3)],'LineWidth',2)
set([f1(4)],'LineWidth',2)
set([f1(5)],'LineWidth',2)
```

```
set([f1(6)],'LineWidth',2)
legend('Exp     Data','Fit','Component     1,     M1','Component     2,
M2','Loss1','Loss2','location','best')
str = {['k(1) ', num2str(k0(1))];...
          [' k(2) ',num2str(k0(2))];...
          [' k(3) ',num2str(k0(3))];...
          [' k(4) ',num2str(k0(4))];...
          [' k(5) ',num2str(k0(5))];...
          [' k(6) ',num2str(k0(6))];...
          [' k(7) ',num2str(k0(7))];...
         mfilename};
dim = [0.2 0.06 0.3 0.45];
annotation('textbox',dim,'String',str,'FitBoxToText','on')
%ylim([0 2000])
saveas(figure(1),[filename(1:end-4),' ',timestmpfix],'png')

%options for running algorithms
options     =     optimoptions('lsqcurvefit','Algorithm','trust-region-
reflective');
options.OptimalityTolerance = 1.0000e-09;
options.FiniteDifferenceStepSize = 1; % default is eps
options.FiniteDifferenceType = 'central';
options.Diagnostics = 'on';
options.Display = 'iter';
options.FunctionTolerance = 1.0000e-016;
options.FunValCheck = 'on';
options.MaxFunEvals = 5000;
options.MaxIter = 1000;
options.StepTolerance = 1.0000e-012;

% % fit the data
[k,resnorm,output,exitflag]                                                =
lsqcurvefit(@Funct2StateWithLossOn1And2,k0,t,y,lb,ub,options);
figure(2), clf
set(gcf,'units','points','position',[100,100,800,600])
f2                                                                         =
plot(t,y,'o',t,Funct2StateWithLossOn1And2(k,t),t,M1,t,M2,t,M3,t,M4);
xlabel('Time, s')
ylabel('RU')
hold off
set([f2(2)],'LineWidth',2)
set([f2(3)],'LineWidth',2)
set([f2(4)],'LineWidth',2)
set([f2(5)],'LineWidth',2)
set([f2(6)],'LineWidth',2)
legend('Exp     Data','Fit','Component     1,     M1','Component     2,
M2','Loss1','Loss2','location','best')
loc = [.65 .1 .9 .4];
str = {['k(1) ', num2str(k(1))];...
          [' k(2) ',num2str(k(2))];...
          [' k(3) ',num2str(k(3))];...
          [' k(4) ',num2str(k(4))];...
          [' k(5) ',num2str(k(5))];...
          [' k(6) ',num2str(k(6))];...
          [' k(7) ',num2str(k(7))];...
          [' Residual ',num2str(resnorm)];...
         mfilename};
```

```
annotation('textbox',loc,'String',str,'FitBoxToText','on')
saveas(figure(2),[filename(1:end-4),'_Output',timestmpfix],'png')

newdata(:,1) = t;
newdata(:,2) = Funct2StateWithLossOn1And2(k,t);
newdata(:,3) = M1;
newdata(:,4) = M2;
newdata(:,5) = M3;
newdata(:,6) = M4;
endfilename = [filename(1:end-4),timestmpfix,'Output.txt'];
endfile = fopen(endfilename,'w');
dlmwrite(endfilename,newdata,'delimiter','\t')
fclose('all');
```

Function:

```
function R = Funct2StateWithLossOn1And2(k,t)

global M1 M2 M3 M4 MSPR xswitch

Cp=2.5*10^-6;    %effective molar concentration of peptide in solution
ode_options    =    odeset('RelTol',    1e-8,    'AbsTol',    1e-08);    %,
'Stats','on');
y0 = [0;0;0;0;0]; %initial conditions; set by number of ODEs used
(including dSPR/dt)
[~,Fit1]=ode15s(@DiffEq1,t(1:xswitch),y0,ode_options);

yswitch                                                                    =
[Fit1(end,1),Fit1(end,2),Fit1(end,3),Fit1(end,4),Fit1(end,5)];     %Cp
should now be zero
[~,Fit2]=ode15s(@DiffEq2,t(xswitch+1:end),yswitch,ode_options);

Fit = cat(1,Fit1,Fit2);

R = Fit(:,5); % pulling just observable signal

M1 = Fit(:,1);
M2 = Fit(:,2);
M3 = Fit(:,3);
M4 = Fit(:,4);
MSPR = Fit(:,5);

function dy = DiffEq1(t,y)
%answer matrix
dydt=zeros(4,1);
%Unknown Constants
%k(1)    forward rate constant of step1 (1/Ms) State 1, Reversible
%k(2)    reverse rate constant of step2 (1/s)
%k(3)    forward rate constant of step1 (1/Ms) State 2, Irreversible
%k(4)    reverse rate constant of step2 (1/s)
%k(5)    lipid extraction term, coming from Reversible binding
%k(6)    lipid extraction term, coming from Irreversible binding
%k(7)    maximum amount of peptide that can be bound (M)
%Model equations
```

```
dydt(1) = k(1)*Cp*(k(7)-y(1)-y(2)-y(3)-y(4)) - k(2)*y(1) + k(4)*y(2) -
k(3)*y(1) - k(5)*y(1); % dR1/dt
dydt(2) = k(3)*y(1) - k(4)*y(2) - k(6)*y(2); % dR2/dt
dydt(3) = k(5)*y(1); % dR3/dt
dydt(4) = k(6)*y(2);
dydt(5) = dydt(1) + dydt(2); %total observed R, dR/dt
dy=dydt;
end

function dy = DiffEq2(t,y)
%answer matrix
dydt=zeros(4,1);
dydt(1) = k(1)*0*(k(7)-y(1)-y(2)-y(3)-y(4)) - k(2)*y(1) + k(4)*y(2) -
k(3)*y(1) - k(5)*y(1); % dR1/dt
dydt(2) = k(3)*y(1) - k(4)*y(2) - k(6)*y(2); % dR2/dt
dydt(3) = k(5)*y(1); % dR3/dt
dydt(4) = k(6)*y(2);
dydt(5) = dydt(1) + dydt(2); %total observed R, dR/dt
dy=dydt;
end
end
```

Chapter 5 : Biophysical Characterization of Antibacterial Oligothioetheramides

Acknowledgements

This chapter contains two bodies of work discussed based on their biophysical characterization by surface plasmon resonance to visualize oligomer-lipid membrane interactions, with similar methods as at the end of Chapter 4. The first piece of work adapted into this chapter was done with permission from C. M. Artim, J. S. Brown, and C. A. Alabi, Analytical Chemistry **2019**, 91, 3118-3124 Copyright © 2018 American Chemical Society. The second piece of work was done with permission from E. A. Hoff, C. M. Artim, J. S. Brown, C. A. Alabi, *Macromolecular Bioscience* **2018**, 1800241 Copyright © 2018 John Wiley and Sons (License #4507220586910). Outside of those two works, additional analysis has been performed and added to enrich the biophysical understanding of the first article from E.A. Hoff et al (2018), specifically with modeling of the biophysical characterization.

Individual contributions

For C.M. Artim, J.S.Brown, and C.A. Alabi (2019): C.M.A. and J.S.B. contributed equally to this work. C.MA. and C.A.A conceived the project. C.M.A. synthesized and confirmed the oligomers in the study, performed biological experiments, and data analysis. J.S.B. performed surface plasmon resonance, analyzed and modeled the data. The manuscript was written through contributions of all authors. All authors have given approval to the final version of the manuscript. For E.A. Hoff et al. (2018): E.A.H. and C.A.A. conceived the project. E.A.H. synthesized and chemically confirmed the

oligoTEAs used in the study. C.M.A. performed all biological testing and analysis. J.S.B. performed surface plasmon resonance and analyzed the data. The manuscript was written through contributions of all authors. All authors have given approval to the final version of the manuscript.

Article Acknowledgements

For the second piece of work included in this chapter (For C.M. Artim, J.S.Brown, and C.A. Alabi (2019): This work was supported in part by startup research funds from Cornell University and the National Science Foundation CAREER Award (CHE-1554046). J.S.B. acknowledges financial support from the National Science Foundation Graduate Research Fellowship Program (DGE-1650441). Equipment used to perform this research was funded in part by the NSF-MRI (CHE-1531632). The authors thank Professor Susan Daniel and Zeinab Mohamed for help with fluorescence microscopy and discussion. For the first piece of work included in this chapter (E.A. Hoff et al. (2018): This project was supported in part by Cornell start-up funds (C.A.A.), the National Science Foundation CAREER Award (CHE-1554046), and the Army Research Office (W911NF-15-10179). J.S.B. acknowledges financial support from the National Science Foundation Graduate Research Fellowship Program (DBE-1144153). This work made use of the Cornell University NMR Facility, which is supported, in part, by the NSF through MRI award CHE-1531632.

Abstract

Biophysical analysis into the mechanism of action of membrane-disrupting antibiotics such as antimicrobial peptides (AMPs) and AMP mimetics is necessary to improve our understanding of this promising but relatively-untapped class of antibiotics. In this chapter, we utilized oligoTEAs to explored two libraries designed 1) the nature of the cationic charge chosen (guanidine versus amine) and 2) to examine the effect of local backbone hydrophobicity via sequence control. The first oligoTEA library evaluated the impact of cationic nature. Specifically, oligoTEAs were synthesized at a consistent number of total cationic charge and length, varying between guanidines and amines groups. Relative to amines, guanidine groups demonstrated improved antibacterial activity. With regard to the first library, we examined constitutional isomers of the polyamine antibacterial scaffold previously discussed. All oligoTEAs in the first library had the same molecular mass and amine-based pendant groups, but the backbone sequence was varied to create different local hydrophobicity within each molecule. Despite local differences, the total (global) hydrophobicity of each molecule remained the same, highlighting oligoTEA design to decouple molecular properties from each other. Biological and biophysical data showed that local hydrophobicity differences in the backbone affected antibacterial activity and lipid bilayer interaction. Both libraries are biophysically studied with surface plasmon resonance in complement to other techniques. Both studies continued to highlight the importance of the oligoTEA-lipid aggregate at the lipid surface, described first in Chapter 4. This is directly observed with the guanidine containing compounds, which increase the extend of lipid aggregation and its morphology to a stable tubular structure.

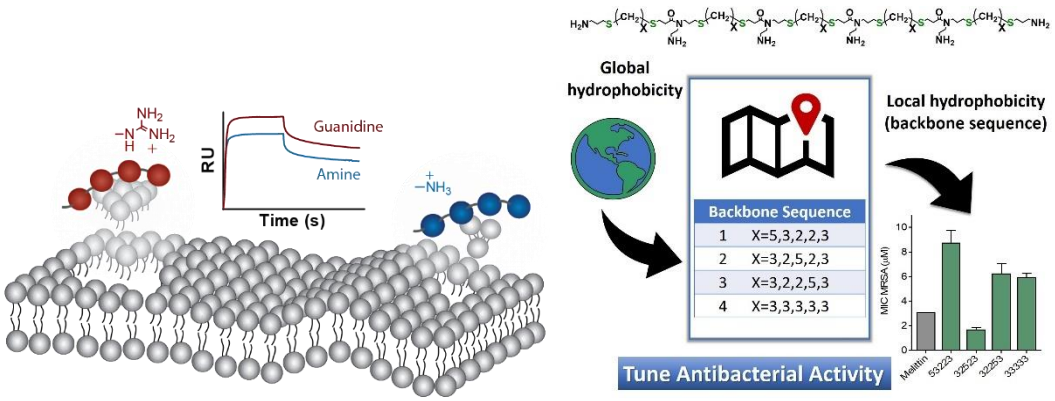

Figure 5-1: *Graphical abstracts for the two bodies of work discussed and analyzed.* ***(left)*** *The first work discussed the biophysical investigation of and testing of an antibacterial guanidine and amine containing oligoTEA library.* ***(right)*** *The second work discussed the sensitivity of antibacterial activity to constitutional isomers of oligoTEAs.*

Introduction

The motivation of this work extends from Chapter 4. Briefly, there is a continued unmet need to develop new antibiotic strategies in the face of antibiotic resistance. We have specifically worked with oligothioetheramides (oligoTEAs) as synthetic mimetics to antimicrobial peptides (AMPs), which are a promising but underdeveloped class of antibacterials. Although AMPs display broad sequence diversity, they are generally amphipathic and composed of hydrophobic and cationic residues.[398] Abiotic molecular design provides proteolytic stability and enables incorporation cationic charge and hydrophobic groups, known influencers of antibacterial action. Beyond the synthetic design, we have also engaged in biophysical testing of these materials at the interface of bacterial mimetic membranes, since their antibacterial mechanism involves membrane disruption. We continued to investigate these materials as started in Chapter

4 with surface plasmon resonance (SPR) fluorescence microscopy, and modeling with two specific libraries of oligoTEAs, adding breadth and testing the ability of our biophysical methods to describe and rationalize observed biological trends.

Library 1: Antibacterial action affected by cationic group

In this work, we investigated the effect of cationic group (guanidine versus amine) on the antibacterial action of several oligoTEAs. Recent studies involving antibacterial oligoTEAs have evaluated the impact of backbone composition, length, sequence and conformation on potency.[37,278,280] However, direct studies on the nature of the cationic pendant group on the oligoTEA scaffold have not been done. Overall, our aggregated studies indicate that oligoTEAs with guanidine pendant groups are more active than those with amine pendant groups. Herein, we confirm these relative differences in activity and specifically explore differences in the mechanism of action by membrane permeabilization, fluorescence microscopy, and SPR. We have focused our efforts on interactions of oligoTEAs with the membrane of methicillin-resistant *Staphylococcus aureus* (MRSA). Our results are consistent with some literature studies that highlight improved activity of guanidine groups over amines.[468–470] Moreover, results from microscopy and SPR additionally suggest that guanidine-containing compounds form larger, meta-stable, tubular lipid aggregates on the bacterial membrane surface that correlate with activity.

Results

Synthesis and characterization of cationic oligoTEAs

A library of 3-mer and 4-mer oligoTEAs was synthesized according to our previously reported method for fluorous-supported assembly of sequence-defined oligoTEAs.[37,278,280] The oligoTEA sequences prepared in this work along with their notation are described in Figure 5-2. The first five compounds listed were prepared to examine the effect of cationic group type on antibacterial activity. While several reports in literature confirm the enhanced antibacterial activity of compounds containing guanidines over amines,[468–470] a few studies conclude the opposite.[183] To explore this effect in-depth, we systematically increased the guanidine content in our oligoTEA scaffold by decreasing the ratio of amine to guanidine pendant groups from 4:0 to 1:3 (Figure 5-2). The terminal amine group on the oligomer scaffold after cleavage of the fluorous tag guarantees that there will always be an amine group present on the scaffold. The last four compounds in Figure 5-2 (PDT-4Am, PDT-4G, BDT-4Am and BDT-4G) were created to examine cationic 4-mer oligoTEAs with differing backbones, i.e. propane versus butane, in addition to pendant group type. This set of oligoTEAs include PDT-4G, a promising compound that has previously been shown to be viable *in vivo*. Oligomers in this set contain amine to guanidine ratios of 5:0 versus 1:4. Following HPLC purification, all nine oligoTEAs in Figure 5-2 were characterized and confirmed via ^{1}H NMR and LCMS (Appendix D Supplementary Spectra).

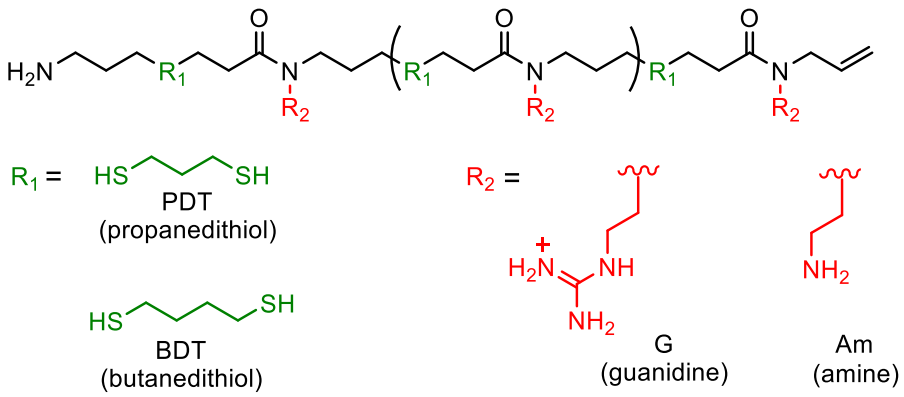

	OligoTEA	Full Sequence
1	PDT-3Am	NH_2-PDT-Am-PDT-Am-PDT-Am
2	PDT-G2Am	NH_2-PDT-G-PDT-Am-PDT-Am
3	PDT-2GAm	NH_2-PDT-G-PDT-G-PDT-Am
4	PDT-Am2G	NH_2-PDT-Am-PDT-G-PDT-G
5	PDT-3G	NH_2-PDT-G-PDT-G-PDT-G
6	PDT-4Am	NH_2-PDT-Am-PDT-Am-PDT-Am-PDT-Am
7	PDT-4G	NH_2-PDT-G-PDT-G-PDT-G-PDT-G
8	BDT-4Am	NH_2-BDT-Am-BDT-Am-BDT-Am-BDT-Am
9	BDT-4G	NH_2-BDT-G-BDT-G-BDT-G-BDT-G

Figure 5-2: *OligoTEA library to investigate antibacterial activity of cationic group* ***(Top)*** *Scheme breaking down each moiety of the oligoTEA* ***(Bottom)*** *Table of the oligoTEAs synthesized in this work.*

The guanidine-containing oligoTEAs in this library are more hydrophobic than their amine variants as determined by LCMS retention time, similar to previous observations.[280] Systematically increasing the guanidine content (4:0, 3:1, 2:2, 1:3) led to a concomitant increase in retention time (Figure 5-3A). A similar effect is seen with the 4-mer amine versus guanidine oligoTEAs irrespective of their backbone (Figure 5-3B). We attribute this effect to the enhanced bidentate hydrogen bonding between the guanidinium group and residual silanols or hydrogen bonded water network on the C18 column.[471,472] This causes the guanidinium groups to have stronger interactions with the

stationary phase and appear more hydrophobic relative to the amine-containing compounds.

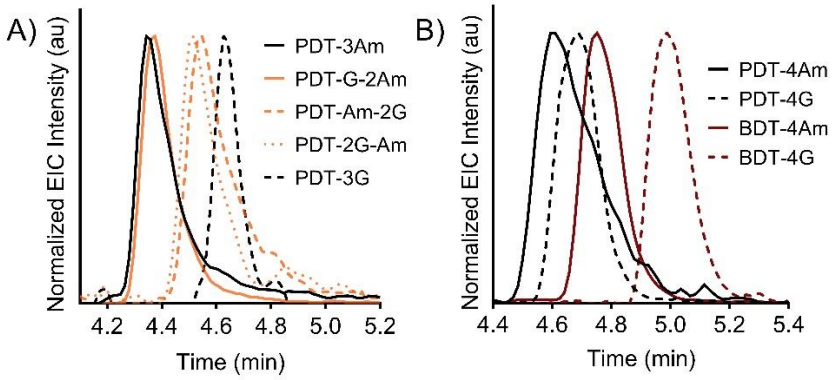

Figure 5-3: *Retention time of cationic oligoTEAs*
Results were obtained by the extracted ion chromatogram of the product mass. ***(A)*** *3-mer oligoTEAs.* ***(B)*** *4-mer oligoTEAs.*

Effect of increasing guanidine to amine ratio

In a recent publication, we observed that a guanidine-containing oligoTEA, BDT-4G was more active against bacteria than its amine counterpart, BDT-4Am.[280] To further elucidate this effect, we first assessed the antibacterial activity of 3-mer oligoTEAs containing varied ratios of amine to guanidine pendant groups (Figure 5-9), compounds 1-5) via the MIC assay. The results in Figure 5-4A confirm that antibacterial activity increases with increasing guanidine content relative to amines. PDT-3G is 64-fold more active than PDT-3Am against MRSA (Figure 5-4A). Compounds containing both amine and guanidine headgroups, PDT-2GAm, PDT-Am2G, and PDT-G2Am, had comparable activities falling between that of PDT-3Am and PDT-3G. The 4-mer compounds (Figure 5-4, Compounds 6-9) with different backbones showed a similar trend; the guanidine-functionalized compounds (PDT-4G and BDT-4G) outperformed

the amine-functionalized compounds (PDT-4Am and BDT-4Am) by greater than 20-fold (Figure 5-4B).

Cationic antimicrobial agents are known to bind and compromise the bacterial membrane, leading to rapid fluid exchange and cell death.[183,398,473–475] This membrane permeabilization can be measured indirectly by assessing the uptake of a membrane-impermeable agent, such as propidium iodide (PI).[476] In addition to reducing MIC, the use of guanidine groups increased the membrane permeabilization (Figures 5-11C and 5-4D). Additionally, backbone hydrophobicity improved both the membrane permeabilization (Figure 5-4D) and activity (Figure 5-4B). One caveat to the PI data is that its inverse correlation with the MIC data is only maintained within groups of oligomers with the same number of repeat units and backbone type. For example, PDT-4Am is less active than PDT-3G (higher MIC) but displays higher membrane permeabilization. These results highlight the use of the PI membrane permeabilization assay to rationalize the interactions with the bacterial membrane, but not necessarily predict antibacterial potency.

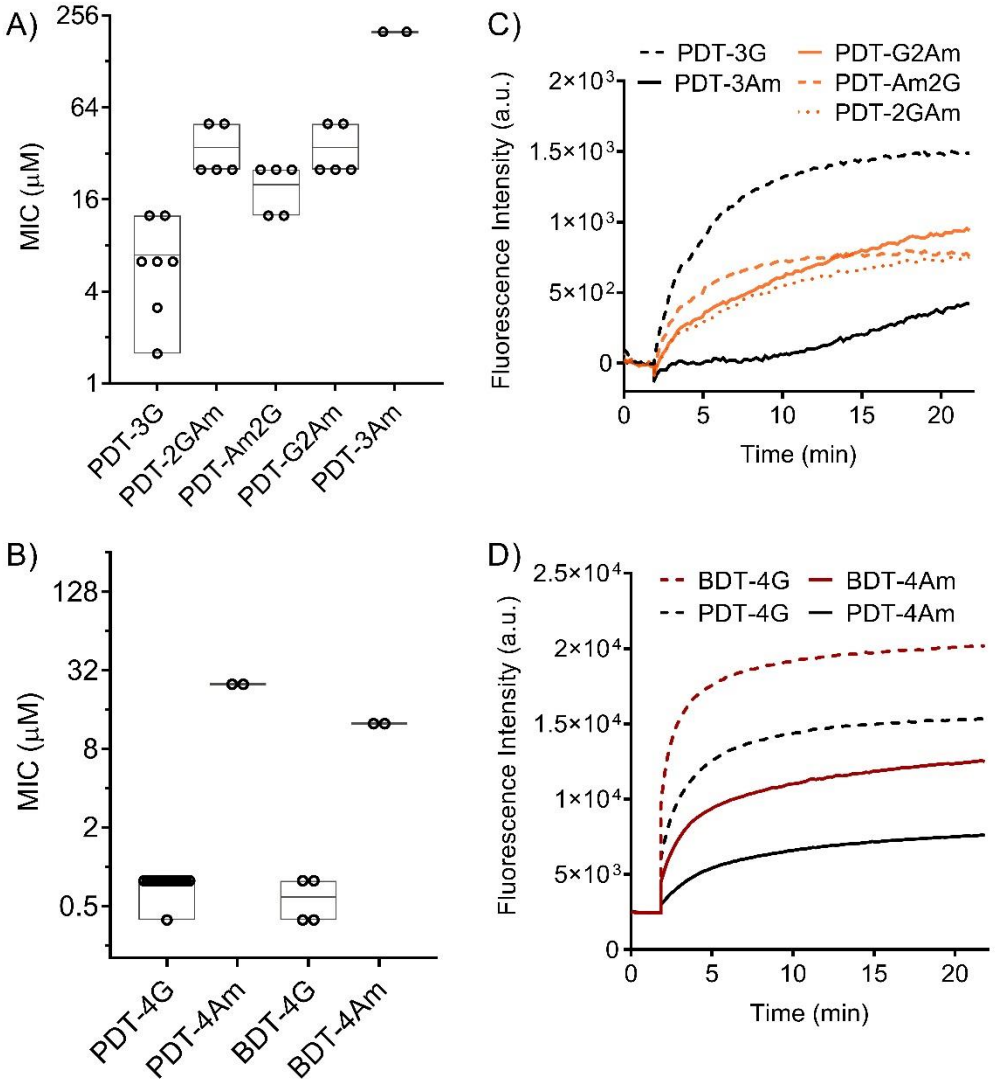

Figure 5-4: *Biological characterization of cationic oligoTEAs*
(A) *Minimum inhibitory concentration assay of 3-mer compounds.* ***(B)*** *Minimum inhibitory concentration assay of 4-mer compounds.* ***(C)*** *and* ***(D)*** *Propidium iodide (PI) assay as a measure of extent of membrane permeabilization with 25 μM oligoTEA.*

Biophysical characterization via fluorescence microscopy

To further elucidate the mechanisms of action of these antibacterial oligomers, we employed fluorescence microscopy and SPR. These methods utilize bacterial

mimetic membranes assembled from synthetic lipids to model binding and disruption of the bacterial membrane. The lipid head group composition of the bacterial membrane is known to vary with growth phase. Mid-exponential phase represents the most aggressive growth phase during bacterial infection and was thus considered in the selection of the membrane mimetic lipids. Previously, we have reported literature consensus across twelve sources on the membrane lipid headgroup composition of MRSA to be 4:5:11 neutral lipid: cardiolipin: phosphatidylglycerol (PG) (Chapter 4, Materials and Methods).[281] Lipid tails were chosen to ensure lipid bilayer fluidity at room temperature, specifically neutral DG, TPCL, and POPG. SUVs were prepared with this lipid composition and used to create supported lipid bilayers (SLBs) for biophysical characterization. Fluorescence microscopy was made possible by incorporation of an octadecyl rhodamine (R18) fluorophore and slides pre-coated in poly-L-lysine (PLL).

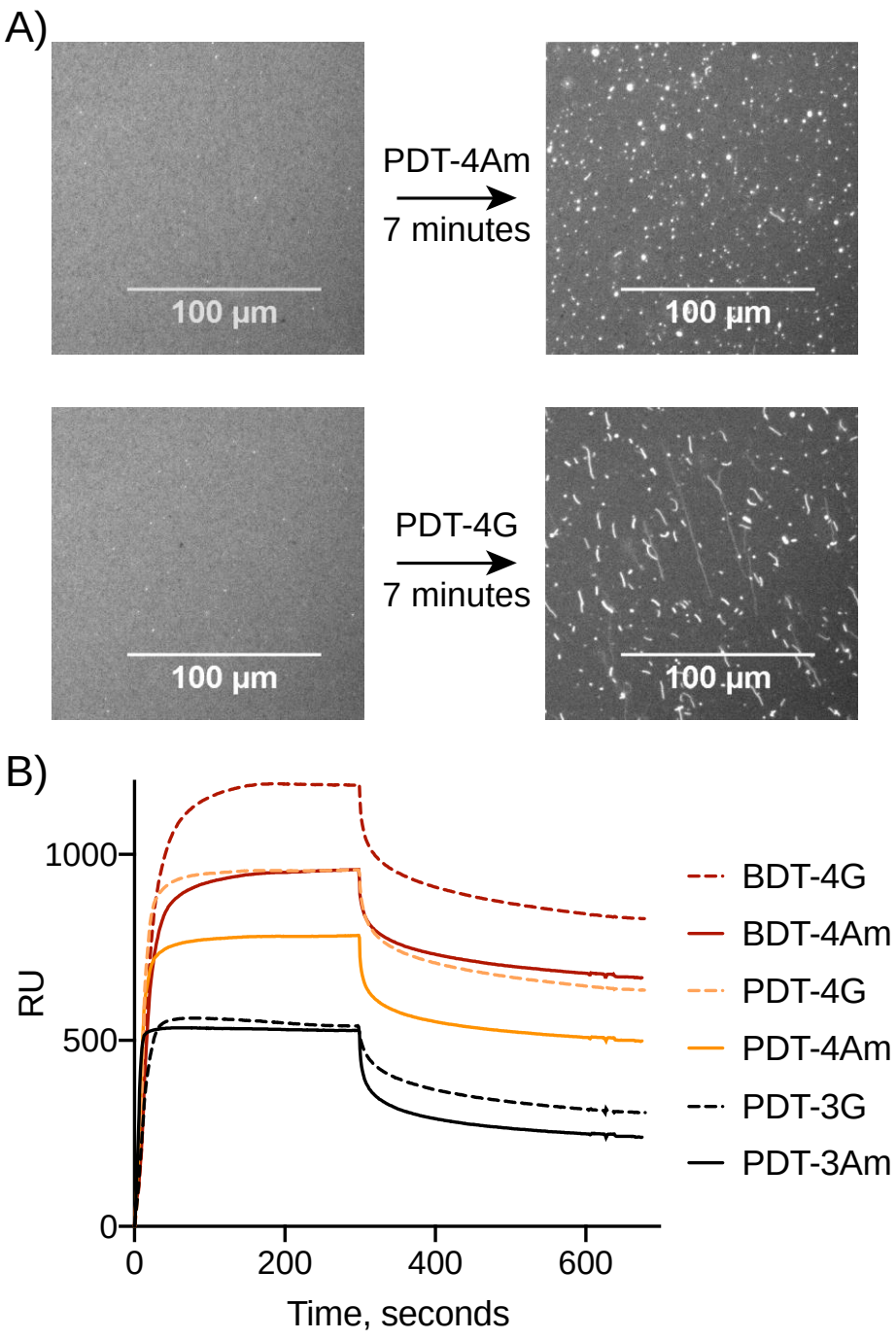

Figure 5-5: *Fluorescence microscopy and SPR of cationic oligoTEAs*
(A) *Fluorescence microscopy images showing the supported lipid bilayer before and after exposure to 5 µM PDT-4Am or PDT-4G. Lipid bilayer is visualized via incorporation of R18 into the SUV before bilayer formation. Microscopy slides were precoated with poly-L-lysine (PLL) to enable bilayer formation.* ***(B)*** *SPR sensorgrams of selected oligomers demonstrating the benefit of guanidine groups over amines on any*

scaffold. OligoTEAs (5 μM) were injected onto the bacterial mimetic membrane at t = 0 and washed with 1X PBS (pH 6.8) at t = 300 seconds.

Time-lapse imaging with fluorescence microscopy was completed with PDT-4G and PDT-4Am on the SLBs to observe differences in their mode of membrane disruption (see Supplementary Videos online, doi: 10.1021/acs.analchem.8b05721). Both oligoTEAs showed quick formation of single-micron aggregates at the membrane surface. Additionally, they both formed tubular, meta-stable aggregates that can either retract into a surface aggregate or detach completely from the membrane surface. Notably, the stability of the tubular aggregate was enhanced for PDT-4G relative to PDT-4Am (Figure 5-5A). This enhanced stability could be attributed to the additional, bidentate hydrogen bonding in guanidine groups compared to amines. The tubular aggregates formed during exposure to PDT-4Am rapidly retract or break away from the membrane surface, although it is unclear if this leads to significantly more lipid removal from membrane surface, since there can also be pore formation.

Biophysical characterization via surface plasmon resonance

SPR was completed to further discern the oligomer binding evolution and disruption of a MRSA mimetic membrane. SPR is a label-free technique that detects changes in refractive index near a biosensor surface due to changes in mass or structure. SUVs composed of the MRSA bacterial mimetic lipids were deposited onto the surface of a Biacore L1 Chip and allowed to equilibrate. The sensorgrams of each of the 6 oligoTEAs show a quick rise in response level that plateaus after 200 seconds (Appendix D). Upon washing with PBS after 300 seconds, the signal drops quickly and

fades toward an asymptote above the baseline. Within the same scaffold (i.e. same length and same backbone), guanidine-based oligoTEAs generally show higher signal responses relative to their amine variants, especially in the dissociation (PBS wash) phase.

To further understand the phenomena observed by SPR, we then sought to fit the data using a kinetic model, which can deconvolute the binding curve. Generally, multiple binding states between the oligomer and lipid evolve throughout time and can be represented by differential equations. In this way, several models have been proposed in literature for the binding evolution of AMPs at lipid membrane surfaces, as observed by SPR. While not fully unanimous with each other, these models often propose reversible binding of oligomer and lipid together (state #1), which can then reversibly evolve onward to a tighter binding complex (state #2), where loss or lipid expansion can occur.[426,441,442] However, in previous work performed in Chapter 4, we determined two distinct differences between the generalized form of literature models and the model that fits our data. Our model is also in a two-state form (Figure 5-6A). However, the aggregates observed by fluorescence microscopy were irreversibly formed (OL*, state #2), which is different than proposed in literature. Second, we have allowed loss from the first state (OL), which has been observed previously using similar compounds (Chapter 4)[281] and by other groups in the form of pore formation or lipid bilayer expansion.[426,427] Otherwise, the model is consistent with literature observations. The reversible binding state (OL) is observed by the rapid initial increase at the beginning of oligomer injection and decrease at the beginning of the PBS wash, respectively. Also,

the irreversible binding state (OL*) is observed by the SPR signal that remains above baseline in the dissociation phase after PBS washing.

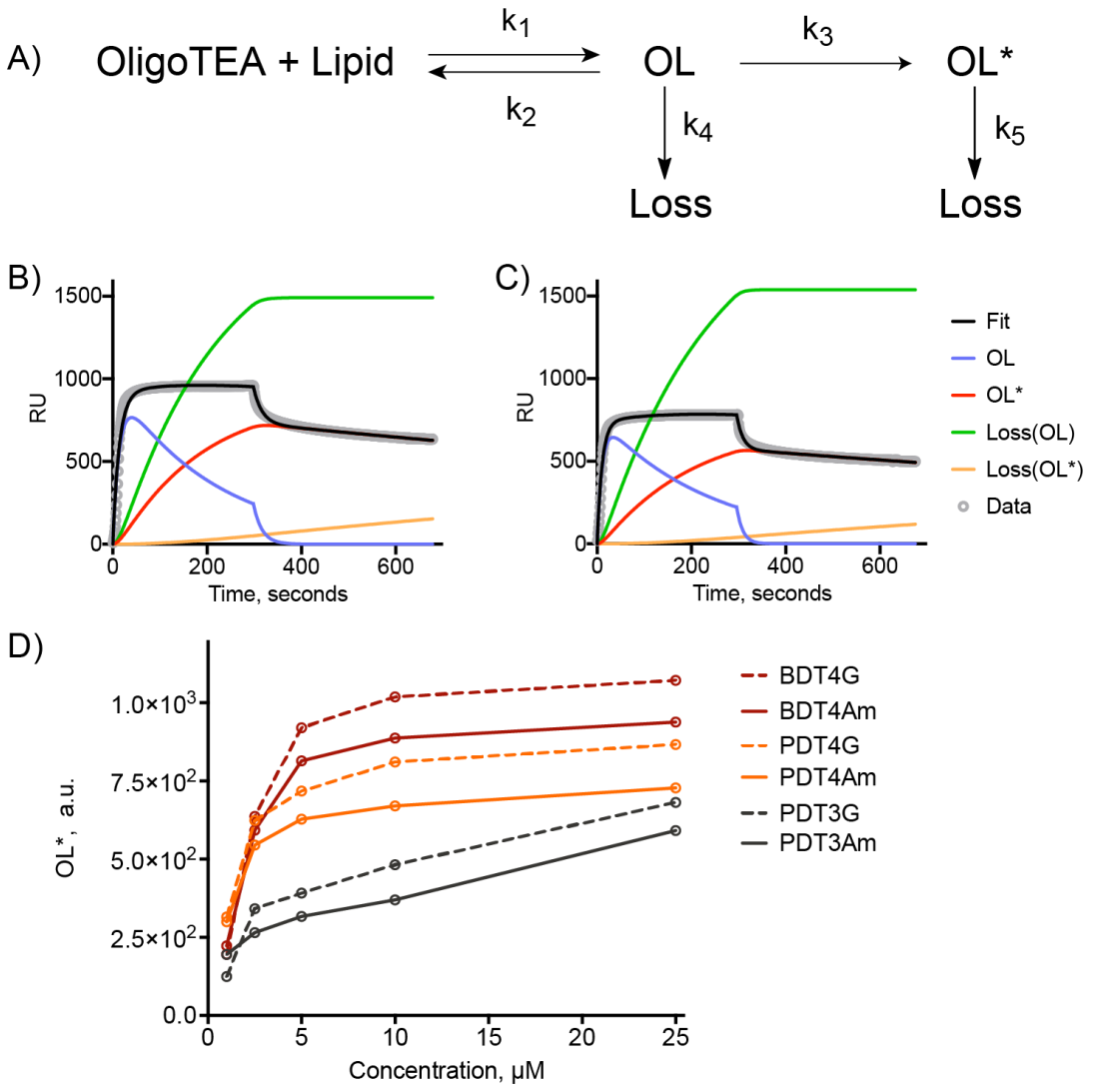

Figure 5-6: *SPR characterization of cationic oligoTEAs*
(A) Two-state model with loss on both steps developed previously (Chapter 4).[281] *OL* represents the oligoTEA-lipid aggregate and OL represents any binding state including all types of potentially loose or tight binding not observed by fluorescence microscopy. Loss can occur from OL or OL*. (B) Model fit to PDT-4G and (C) PDT-4Am 5 μM SPR data along with the predicted kinetic evolution of states. (D) Population of oligoTEA-induced aggregates (OL*) formed during the kinetic run.*

The two-state model was fit over a concentration range of 1-2 5μM for each oligoTEA in good agreement with the data. Figures 5-6B and 5-6C show the fits for PDT-4G and PDT-4Am, and others are shown in Appendix D. Analysis of the population of states ((OL), (OL*), Loss(OL), Loss(OL*)) data across concentrations revealed strong correlations between the extent of aggregate formation (OL*) and nature of the cationic group. Searching for a parameter that correlates with the biological activity is done over the range of concentrations and examining which parameter correlates best with the MIC. Across concentrations, the kinetic rate of Loss(OL*), demonstrates differences between the 3mer and 4mer length oligomers, but only a low concentration. Physically, this finding could mean the 4mer-length oligoTEAs are much slower at allowing surface aggregates to detach from the surface because of their added length and binding interaction (Appendix D). However, this finding can only serve as preliminary and the base for a hypothesis as it was not the focus of the study. More data would be needed to support this finding.

Considering the populations from the fit (OL, OL*, Loss(OL), and Loss(OL*)), we see that within the same scaffold type, guanidine groups generally result in a higher population of bound aggregates (OL*), consistent with the PI data (Figure 5-13D). This strongly implicates this aggregate state as a critical determinant for membrane permeabilization and antimicrobial activity. The population of the (OL) state is higher for the guanidine 4-mers over the amine 4-mers (Appendix D). In contrast, this correlation does not hold for the pre-aggregate binding (OL) for the 3-mer compounds as the 3-mer amine has a higher population of bound (OL) states than the 3-mer

guanidine. Losses from the (OL) and (OL*) states are nearly identical between guanidine and amine containing compounds across all concentrations (Appendix D) indicating that these states are not the critical drivers or directors of oligoTEA antimicrobial activity, different than the findings from the first library. Thus, from all populations and parameters determined, the lipid-oligomer aggregate population (OL*) appears most directly related with activity as it shows a consistent benefit for the use of guanidine groups over amines.

Discussion

In this work, we have evaluated the benefit of guanidine groups over amines on oligoTEA scaffolds for antimicrobial activity. Biological characterization *in vitro* as well as biophysical characterization with fluorescence microscopy and SPR demonstrate key differences between oligoTEAs made with guanidines versus amines. We conclude that these oligomers operate by binding bacterial membranes, where they facilitate the development of lipid aggregates and disrupt membrane integrity. We were further able to investigate the difference between guanidine and amine-containing oligoTEAs through SPR data fit to a recently-developed two-state model with an irreversible aggregation step. Within each set of oligoTEAs made with identical backbone and length, guanidine-containing compounds demonstrated increased ability to cause lipid aggregate formation (OL*) over their amine variants. This is consistent with biological activity against MRSA. The populations of Loss(OL) and Loss(OL*) did not correlate across all concentrations with the biological activity, although (OL) showed partial correlation with biological activity within 4-mers containing the same

backbone. Our kinetic data and conclusions were directly supported and corroborated by fluorescence microscopy observations of stabilized tubular aggregates that appear during membrane disruption by PDT-4G over PDT-4Am. Overall, this body of work highlights the potential importance of oligoTEA-induced lipid aggregation during membrane disruption and warrants further investigation with other membrane-disrupting compounds.

Library 2: Antibacterial action affected by local backbone hydrophobicity

In this work, we investigated the effect of backbone hydrophobic sequence, i.e. the local hydrophobic contribution, on antibacterial activity while holding the overall hydrophobicity constant. OligoTEA assembly is the only approach to date that offers a simple synthetic method to vary the backbone hydrophobic sequence while keeping other aspects of the macromolecule fixed. We exploit this design for the assembly of four constitutional isomers all with the same global hydrophobicity. An antibacterial oligoTEA with amine pendant groups that was previously determined to have desirable antibacterial activity and low cytotoxicity[278] served as the basis for three new synthetic isomeric variants. Evaluation of the antibacterial activity of these macromolecules showed backbone sequence-dependence. Biophysical studies on supported lipid bilayers (SLBs) and membrane penetration studies were performed and used to rationalize the observed differences in biological activity. Since the publication of this work, modeling of the biophysical characterization of surface plasmon resonance (SPR) has been completed using the model discussed in Chapter 4.

Results

Our overall synthetic design is used the incorporation of backbone dithiol groups to vary the local hydrophobicity while keeping the overall carbon count constant. To do this, three constitutional isomers of "AOT-33333" were synthesized by lead author Dr. E.A. Hoff (Figure 5-2) according to the previously reported method for the assembly of sequence-defined oligoTEAs.[146,147] The oligomers created here are named with a five-digit code, where each number refers to the number of carbons in each backbone monomer (Figure 5-2). Thus, the AOT-33333 bears five propane dithiol groups (3) in its backbone. The isomers all bearing the same pendant primary amine group and linear architecture differ only in the relative location of the ethane dithiol (2), propane dithiol (3) and pentane dithiol (5) backbone groups.

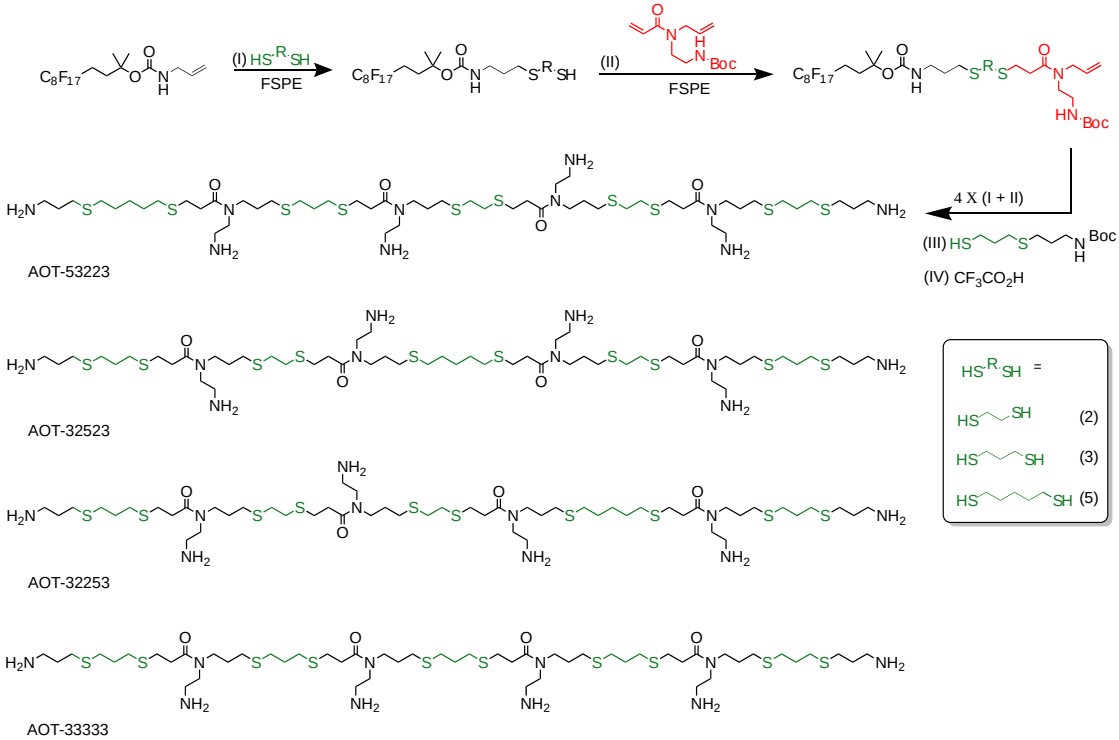

Figure 5-7: *Scheme to produce antibacterial oligoTEA constitutional isomers*

Following synthesis and purification, all four oligoTEAs were characterized and confirmed via ^{1}H NMR and liquid chromatography mass spectrometry (LCMS) (See online version at doi:10.1002/mabi.201800241). The mass spectrometry data by Dr. E.A. Hoff confirmed that all four compounds have the same mass and are thus isomers. The liquid chromatograms of all four oligoTEA sequences were also identical as shown in Figure 5-3A, indicating their global (overall) hydrophobicity, as represented by their retention time, is similar and thus differences in their functional behavior can be attributed to local sequence differences. The four oligoTEAs synthesized by Dr. E.A. Hoff were tested for antibacterial activity by co-author C.M. Artim on methicillin-resistant *Staphylococcus aureus* (MRSA, ATCC33591) as aforementioned with the minimum inhibitory concentration (MIC) shown in Figure 5-8.[477,478,479] The main takeaway was that the symmetric AOT-32523 showed ~ 4-5-fold higher antibacterial activity than its other isomers at a MIC of 1.7 µM against MRSA (n=5).

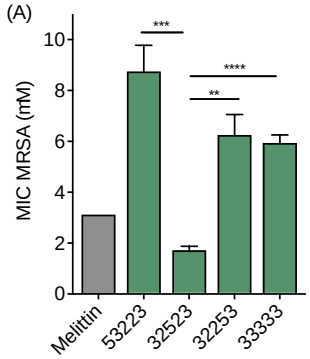

Figure 5-8: *Biological characterization (MIC and toxicity) of oligoTEA isomers Minimum inhibitory concentration (MIC) of AOT isomers against* ***(A)*** *MRSA (ATCC33591)*

Cationic antibacterial oligoTEA compounds, including AOT-33333 from previous studies,[278] have been shown to lyse bacteria via membrane binding and destabilization. To determine if the members of the new isomer library also worked via the same mechanism, C.M. Artim performed a propidium iodide (PI) assay on MRSA to analyze the structural integrity of the membrane upon exposure to the four oligoTEA isomers, as previously described in Chapter 4. The data from the PI assay on MRSA in Figure 5-9 shows different permeabilities among oligoTEA isomers again indicating that local backbone sequence does matter and can influence biophysical interactions between the oligoTEAs and a biological membrane. AOT-53223 and AOT-32523 enable rapid and greater PI uptake into MRSA cells relative to AOT-32252 and AOT-33333. This result is interesting and contrasts the MIC data that shows AOT-53223 having the least antibacterial potency relative to other members of the isomeric library.

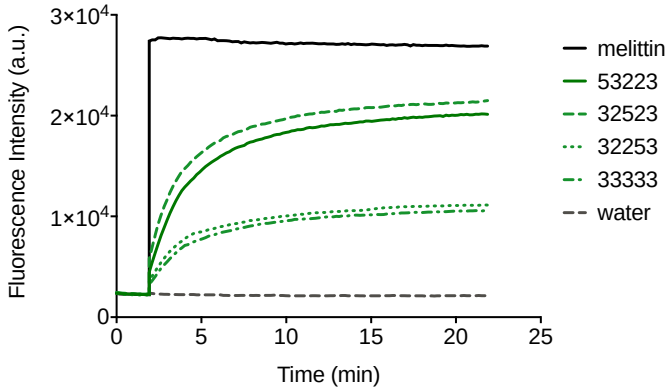

Figure 5-9: *Propidium iodide assay with isomeric oligoTEA on MRSA*

To further rationalize these conflicting observations, we turned to SPR performed by J.S. Brown for analysis of membrane-oligoTEA interactions utilizing bacterial mimetic membranes, as described before (See Materials and Methods).[281] Following bilayer formation on the SPR sensor surface, oligoTEAs at various concentrations were flowed over the sensor chip for 300 seconds (binding phase),

followed by washing with buffer alone for another 400 seconds (dissociation phase) (Figure 5-10A-D). SPR sensorgrams report back the extent of oligoTEA association with the SLB on the SPR chip. The sensorgrams in Figures 5-10A-D indicate that the isomeric oligoTEAs have similar extents of association with the SLB at high concentrations. However, at low concentrations (< 3 μM), AOT-53223, AOT-32523, and AOT-32252 show slightly faster and a greater extent of association with the SLB relative to AOT-33333. To better visualize these subtle differences, we selected the 3 μM sensorgrams (Figure 5-11A) for comparison and ascribed a value to the binding response at saturation (i.e. response unit (RU) at 300 s). The 3 μM data was selected because it represents a concentration above the MIC of AOT-32523 (i.e. antibacterial activity is observed at this concentration) and below the MIC of AOT-53223, AOT-32252, and AOT-33333 (i.e. no antibacterial activity is observed at this concentration, see Figure 5-8).

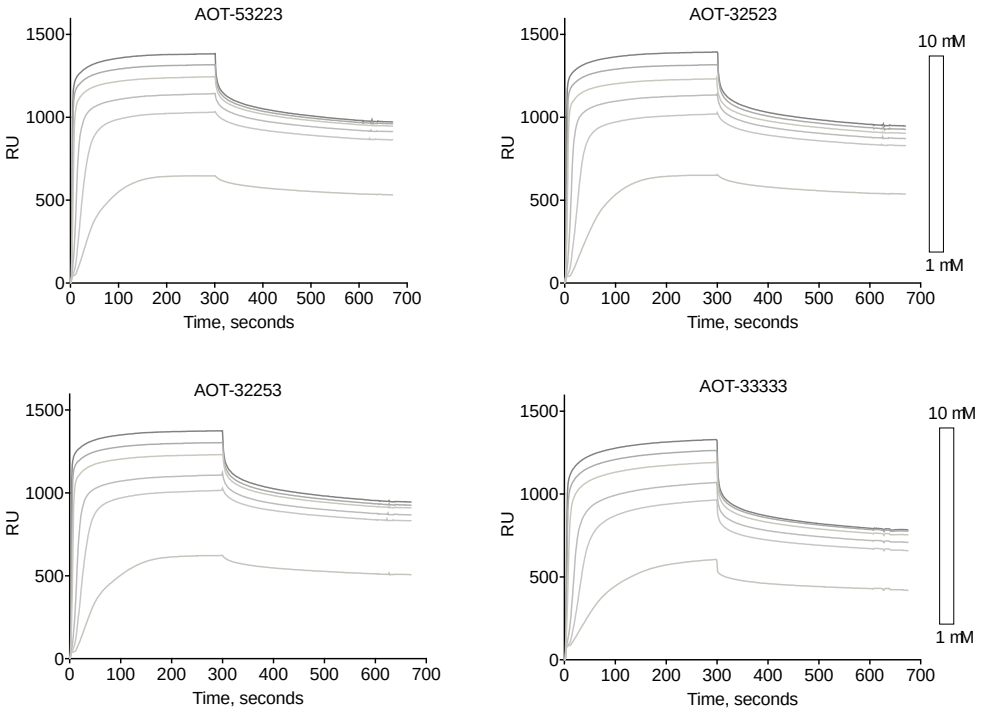

Figure 5-10: *SPR of isomeric oligoTEAs of lipid bilayer interaction (L1 Chip) Association of oligoTEAs at 1, 2, 3, 5, 7.5 and 10 μM (bottom to top) with a MRSA mimetic SLB: (A) AOT-53223 (B) AOT-32523, (C) AOT-32253 and (D) AOT-33333.*

The RU value at 300 seconds represents a wide range of interactions taking place at saturated surface coverage, including binding, surface induced oligomer association, surface aggregation and membrane insertion. In Figure 5-7B the SPR response (i.e. RU at 300s) for all isomeric oligoTEAs is plotted alongside their equilibrium PI permeability data. The latter is obtained from the fluorescence value at equilibrium (@ ~22 mins in Figure 5-10). The SPR data is in general agreement with the PI data. The association of AOT-53223 and AOT-32523 are similar and slightly higher than AOT-32253. AOT-33333 shows the least association with the SLB (Figure 5-11b). These results indicate that these two AOTs (AOT-53223 and AOT-32523) have a stronger preference for the *S. aureus* mimetic membrane. This data alone correctly predicts that AOT-32523 should outperform AOT-33333. However, it also indicates that AOT-

53223 and AOT-32523 should have similar affinities for the membrane and perhaps similar anti-MRSA activity. Contrary to this reasoning, AOT-32523 is 3-fold more active than AOT-53223 against MRSA. Both SPR and PI parameters individually and together correctly confirm that AOT-32523 should outperform AOT-33333, yet they both fall short at describing the overall trend seen in the MIC data.

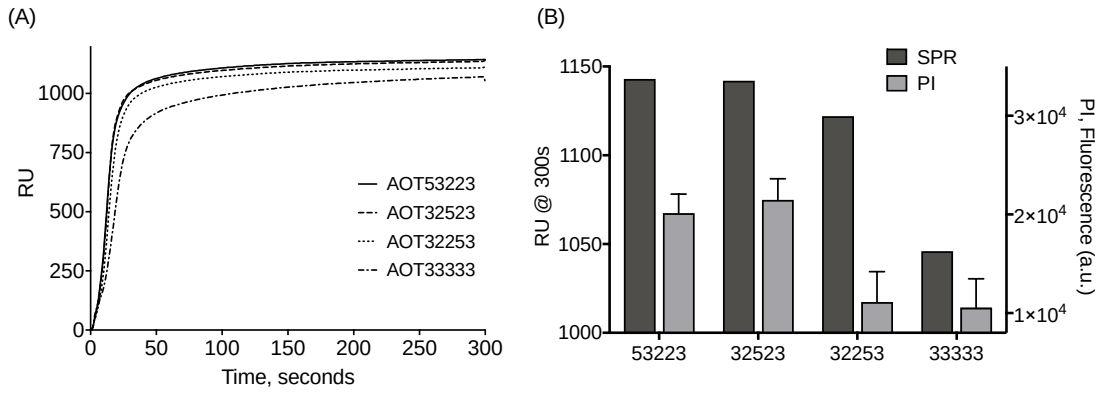

Figure 5-11: *Comparison of SPR sensorgrams at 3μM*
(A) *SPR association sensorgrams of AOT-53223, AOT-32523, AOT-32253, and AOT-33333.* ***(B)*** *A comparison of the saturation response values from SPR data (RU @ 300s) with extent of membrane permeability (measured via PI fluorescence assay).*

Additional modeling of published results

At the time of publication, we hypothesized that more factors and parameters could understood from the data at hand. However, the model detailed in Chapter 4 was not solidified and the fluorescence microscopy that helped develop and propose the model was just being done. Now, the two-state model with loss on each state can be fit to the SPR data and allow to investigate if any of the mechanistic steps (molecular scale binding, aggregate formation, etc.) can potentially describe the biologically observed differences between the isomers (see Appendix D Figures D-{2-5}). Similarly

suggested in Chapter 4, parameters of kinetic rates (e.g., k3, k4, etc) and/or populations (e.g., OL, OL*, etc) that correlate with biological activity should demonstrate a benefit for AOT-32523 over the other oligomers (Figure 5-12A). Moreover, the biological (MIC) data demonstrated that AOT-32523 is an effective antibacterial at lower concentrations (~2 µM), whereas the other oligomers have higher MICs (≥6 µM).

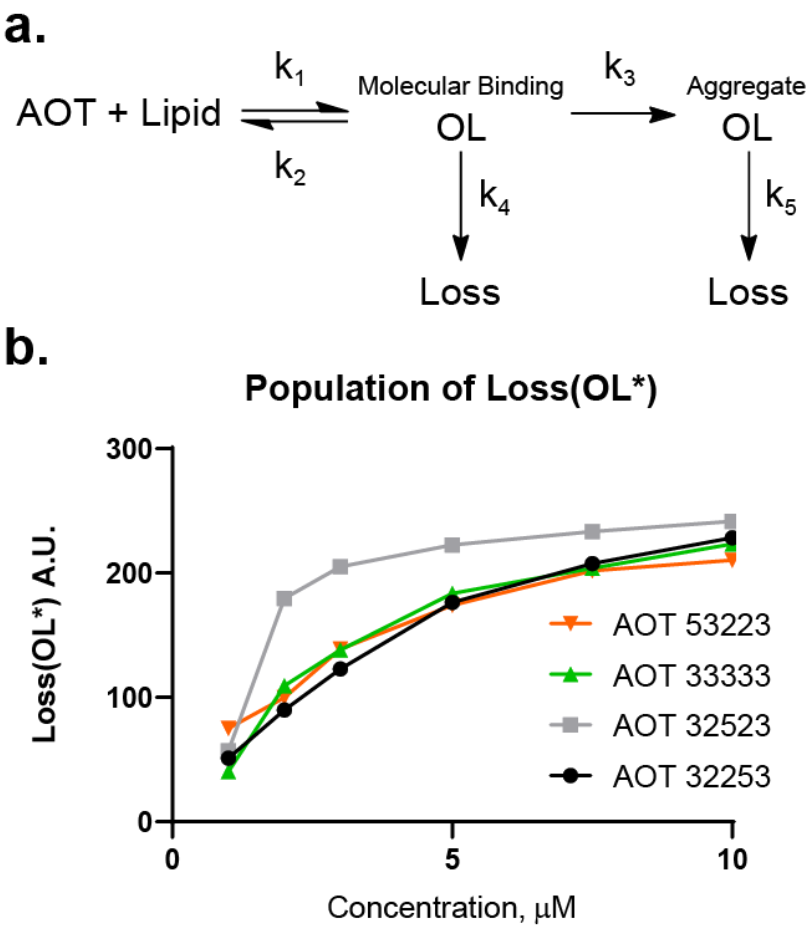

Figure 5-12: (A) *Two-state with two loss SPR model* ***(B)*** *Loss(OL*) model results demonstrating a benefit for AOT-32523 at low concentrations (2-3 µM) that disappears at higher concentrations. See Chapter 4 "Kinetic mechanism proposed from microscopy observations" and onward for more details*

After model fitting was completed across all concentrations and oligomers, the populations and parameters were analyzed to match these criteria to show benefit for AOT-32523 either outright or in a concentration dependent matter (Appendix D Figures D-{5-6}). Overall, the parameters and populations showed a clear distinction of the AOT-33333 from the other oligomers in the data set, which is also clear in the original data (Appendix D Figure D-7). Aside from that difference, the antibacterial oligoTEA isomers are very similar and all kinetic rate parameters appear to overlap. However, the population of loss from the aggregate Loss(OL*) demonstrated favor for the AOT-32523 at low concentrations (2-3 μM) over the other oligomers that then disappears at higher concentration. Oddly, this favor also disappears at lower concentration as well (~2 μM). At these low concentrations, this error could be explained by a low response in the original curve at these concentrations or by the subsequence decrease in OL* that has made fitting Loss(OL*) difficult before. Nonetheless, this weak concentration dependence is similar the antibacterial action of these oligomers where only the AOT-32523 is active at low concentrations (MIC ~1.7 uM) and the other oligomers become antibacterial at higher concentrations. Thus, the Loss(OL*) could appear to correlate with biological activity. Practically speaking, this indicates that the ability of this oligomer to remove the aggregate, separates it from the other oligomers.

Discussion

We have shown in this study that the backbone sequence of constitutionally isomeric oligoTEAs affects their interaction with the bacterial membrane and thus their antibacterial activity. Four isomeric oligoTEAs were synthesized with varying alkyl

backbone composition and sequence. Rearrangement of their backbone sequence didn't appear to affect their global hydrophobicity as measured via their retention time on a HPLC. However, their sequence was shown to play a significant role in their interactions with the cell membrane, indicating that local effects (i.e. local hydrophobicity and spacing between charged groups) are important. In the published article, no definitive conclusions were made about the reasons behind the higher potency demonstrated by AOT-32523.

However, additional analysis with modeling with surface plasmon resonance is able to provide a rationalization of the unique ability of AOT-32523, with its increased in aggregates evolved from the surface (Loss(OL*)). However, within the model findings, the concentration dependence of Loss(OL*) as it is favored over another oligomers is not dramatic and should be investigated further, perhaps with a lipid extraction experiment. If the difference is large enough, fluorescence microscopy could potentially corroborate this finding as well. On its own, the model finding is a good suggestion to create a hypothesis. Comparatively, all other parameters demonstrate highly similar absolute values and concentration dependence (Appendix D, Figures 5-{5-6}), which indicates along with other measures (MIC, PI Assay, MTT toxicity) the fine difference that the oligomers are demonstrating. Thus, it is likely that these oligomers represent the "lower limit" of what biophysical characterization can delineate.

Conclusions

Both pieces of work in this Chapter continue to highlight the importance of biophysical characterization to rationalize biological activity. With both cases, the lipid aggregate was implicated with activity as one of the only parameters that correlated with antibacterial activity (MIC). Specifically, with the library of constitutional isomers, the amount of lipid removed from the aggregate itself, Loss(OL*) correlated with activity. With the library comparing guanidine and amine containing oligoTEAs, the amount of lipid aggregation, OL* was correlated with antibacterial activity. These results highlight the fact that different systems that could be undergoing distinctly different mechanisms. At the very least, they do implicate the nature of the aggregate and its pathological effects on the bacteria as potential drivers of antibacterial action. Both studies uniquely demonstrate the utility of oligoTEAs to create, decouple, and precisely control molecular properties and positioning via sequence control of these molecules. Moreover, the methods of utilizing biophysical characterization of fluorescence microscopy and surface plasmon resonance in tandem appear able to answer complex questions, such as in the case of the constitutional isomers where there was no clear distinction between the oligomers via PI assay. This Chapter adds breadth to the ability of the biophysical methods developed through this work as a whole, with two special and specific test libraries of known biological characterization.

Materials and Methods

General chemicals were purchased from Sigma Aldrich. Precursors for the monomer synthesis were purchased from Aldrich and Alfa Aesar. Fluorous BOC-ON (C_8F_{17} BOC-ON) and fluorous silica were purchased from Boron Specialties. 1-palmitoyl-2-oleoyl-sn-glycero-3-phosphoglycerol (16:0-18:1, POPG), 1',3'-bis[1,2-dipalmitoyl-sn-glycero-3-phospho]-sn-glycerol (16:0 cardiolipin, TPCL) and 1,2-dioleoyl-sn-glycerol (18:1 DG) were purchased from Avanti Polar Lipids and cholesterol (≥99%) was purchased from Sigma-Aldrich. CellTiter 96® AQ_{ueous} Non-Radioactive Cell-Proliferation Assay (MTS) solution was purchased from Promega.

LCMS experiments were carried out on a Poroshell 120 EC-C18 column, 3x100 mm, 2.7 µm from Agilent Technology monitoring at 210 and 254 nm with positive mode for mass detection. Solvents for LCMS were water with 0.1% acetic acid (solvent A) and acetonitrile with 0.1% acetic acid (solvent B). Compounds were eluted at a flow rate of 0.6 mL/min with a linear gradient of 5% to 100% solvent B over 12 min, constant at 100% solvent B for 2 min before equilibrating the column back to 5% solvent B over 1 min. HPLC purification was performed on a 1100 Series Agilent HPLC system equipped with a UV diode array detector and a 1100 Infinity analytical scale fraction collector using a reverse phase C18 column (9.4 x 250mm, 5 µm). Surface plasmon resonance (SPR) was completed using a Biacore 3000 with an L1 Chip at 25°C.

General procedure for oligoTEA synthesis

OligoTEAs were synthesized using alternating thiol-ene and thiol-Michael addition reactions, followed by cleavage of the fluorous tag. Completed oligoTEAs were purified using reverse-phase HPLC and verified using LCMS and ^{1}H NMR. Fluorous solid-phase extraction (FSPE) as previously described[18] was used after each thiol-ene and thiol-Michael addition reaction to remove excess non-fluorous reagents.

Thiol-ene reaction

Five equivalents of dithiol and 5 mol% (of the dithiol) of 2,2-dimethoxy-2-phenylacetophenone (DMPA) were added to a solution of corresponding fluorous-olefin (100 mM in MeOH). The solution was irradiated for 270 s with UV light at 20 mW/cm^2. The product (fluorous-thiol) was purified using FSPE.

Thiol-Michael addition reaction

Two equivalents of corresponding *N*-allyl-acrylamide monomer and dimethylphenylphosphine (5 mol% of monomer) were added to the eluted fluorous-thiol in methanol eluted from the FSPE purification of the previous thiol-ene reaction. The mixture was dried under reduced pressure, during which time the reaction went to completion. Excess non-fluorous reagent was removed using FSPE.

Fluorous tag cleavage reaction

Completed oligoTEAs were dissolved at 5 mM in trifluoroacetic acid (TFA) and stirred for 1 hour at room temperature. TFA was removed under nitrogen, and the oligoTEAs were purified using reverse-phase HPLC.

Guanidine monomer synthesis

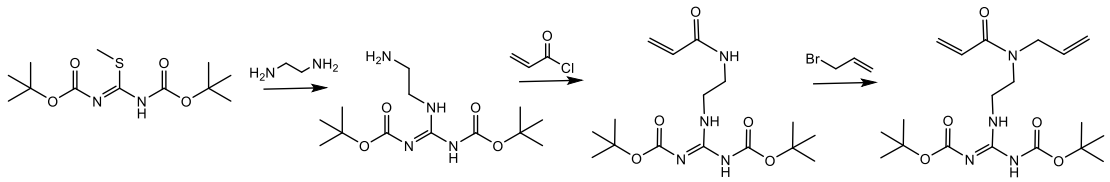

Figure 5-13: *Scheme for N-(ethylene-(bis-Boc-guanidine))-N-allyl-N-acrylamide*

Reaction 1: *2-(2-aminoethyl)-1,3-di-Boc-guanidine synthesis:* 1 equivalent 1,3-Di-boc-2-methylisothiourea at a concentration of 250 mM in dichloromethane (DCM) was reacted with 2.5 eq ethylenediamine for 70 min at room temperature. The reaction mixture was washed 3x with water and 1x with brine. It was used immediately in the acylation reaction.

Reaction 2: *Acylation reaction:* Additional DCM was added to the resulting solution of Reaction 1 for a final concentration of 150 mM. 3 eq triethylamine were added and the mixture was stirred on ice for 10-15 min. 1.5 eq acryloyl chloride was dissolved in 25% the total volume of DCM to be used and added dropwise to the reaction mixture over 20 min. The reaction was stirred 1 hr on ice and 1 hr at room temperature, then quenched with water and extracted three times with DCM. All organic layers were combined, washed with brine, and dried with anhydrous sodium sulfate before solvent removal under reduced pressure.

Reaction 3: *Alkylation reaction:* 1 eq acylation product was dissolved in dry dimethylformamide (DMF) for a final reaction concentration of 200 mM. 4 eq. sodium hydride was added and the mixture was stirred at room temperature for 10 minutes. 2.5 eq allyl bromide was dissolved in 25% the final volume DMF and added dropwise over

15 minutes. The mixture was stirred 1 hour at room temperature before the reaction was quenched with water. The product was extracted three times with diethyl ether and washed with brine. Solvent was removed under reduced pressure to yield a yellow oil which was purified using silica-column flash chromatography on a gradient of 0-100% ethyl acetate in hexanes. The desired guanidine monomer product eluted at 24% hexanes in ethyl acetate. Product was verified by ^{1}H NMR and LCMS.

Boc-protected amine monomer synthesis

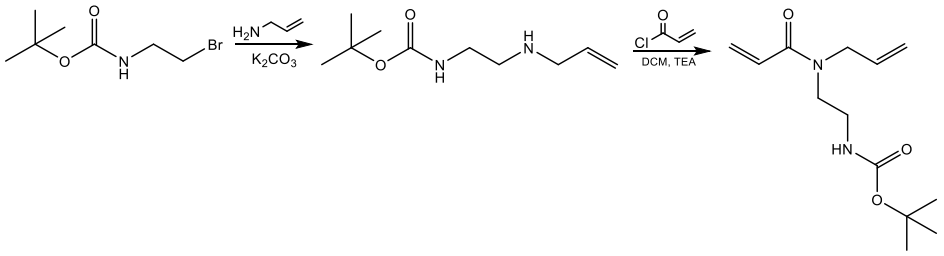

Figure 5-14: *Scheme to synthesize N-(ethylene-N-Boc)-N-allyl-N-acrylamide*

Reaction 1: 1 equivalent Boc-bromoethylamine was dissolved in twice its volume of dichloromethane and added dropwise to a mixture of 6 eq potassium carbonate dissolved in 50 eq allylamine. After 3 hours, the mixture was filtered through Celite to remove the potassium carbonate, and allylamine was removed under reduced pressure.

Reaction 2: The product of reaction 1 was dissolved in dichloromethane for a final reaction concentration of 200 µM, and stirred for 15 min at 0 °C. Acryloyl chloride, diluted in five times its volume of dichloromethane, was added dropwise over 30 min. The mixture was stirred for one hour at 0 °C and one hour at room temperature before being quenched with water. Product was extracted with dichloromethane and dried with

anhydrous sodium sulfate. Solvent was removed under reduced pressure to yield a yellow oil. This was further purified using silica column flash chromatography on a gradient of 15-75% ethyl acetate in hexanes. The desired product, the amine monomer, eluted at 55% ethyl acetate in hexanes and was verified using ^{1}H NMR and LCMS.

Minimum inhibitory concentration (MIC) assay

5-6 colonies of methicillin-resistant *Staphylococcus aureus* (MRSA), ATCC33591 or CA-MRSA (ATCC BAA-1556) was selected and incubated in tryptic soy broth at 37°C overnight. Bacteria were sub-cultured and grown to mid-exponential phase (2.5-3-hour incubation). The subculture was diluted to an OD_{600} of 0.001 in cation-adjusted tryptic soy broth (12.5 mg/L Mg^{2+} and 25 mg/L Ca^{2+}).[22] 1.5-2 mM AOT stocks in water were serially diluted into the bacterial suspensions in a clear 96-well plate. The well plate was incubated overnight at 37^{o}C and the absorbance was measured at 600 nM using a TECAN Infinite® M1000 PRO Microplate Reader (Männdorf, Switzerland). The MIC was calculated as the first point at which the absorbance was below 10% of the maximum.

MTS cell proliferation assay

15,000 of human embryonic kidney (HEK293) cells were plated in a clear, 96-well plate and incubated at 37 °C overnight. Cells were then washed with 1xPBS (pH 7.4) and incubated with 100 µL regular culture media containing 1 to 50 µM of samples at 37°C for 1 hour. Each well was again washed with 1xPBS. 90 µL of clear media (i.e., without

phenol red) and 10 μL of MTS solution were added, and the plate was incubated for 1 hour. Absorbance measurements were taken at 490 nm on a TECAN Infinite M1000 PRO Microplate reader and normalized to untreated cells (100%) or clear media (0%). All experiments were performed in duplicates.

Propidium iodide assay

5-6 colonies of MRSA was selected and incubated at 37 ºC in tryptic soy overnight, then sub-cultured and incubated until mid-exponential phase. Bacteria were harvested, washed, and resuspended in a solution of 5 mM HEPES, 5 mM glucose, and 10 μM propidium iodide (pH 7.4). 150 μL bacteria solution was added to each well of a black 96-well plate. Fluorescence measurements were taken at 535 nm excitation, 617 nm emission on a TECAN Infinite M1000 PRO Microplate reader (Männdorf) (TECAN) for 2 minutes with shaking. AOT stock solutions (1.5-2 mM in water) were added to make a final concentration of 15 μM, and fluorescence measurements were taken for an additional 20 minutes with shaking.

Surface plasmon resonance

Small unilamellar vesicles (SUVs) were prepared similarly to Avanti Polar Lipids protocols. Lipids were combined at the desired ratios from chloroform stock solutions and dried using dry nitrogen at room temperature, then placed in a lyophilizer for at least 6 hours. The dried lipids were suspended in 1xPBS (pH 6.8) by vigorous vortexing for 5 minutes and then gently mixed overnight to age. The suspension was then

sonicated in an ice bath using a probe-tip Branson Sonifier 450 equipped with a micro-tip at 35% power and 35% duty for 30-60 minutes. The nearly-translucent solution was centrifuged at 17k RCF for 10 minutes to remove undispersed lipid and titanium from the probe-tip. The solution was then filtered through a sterile 0.2 μm PES filter and the hydrodynamic size was verified to be 20-50 nm by dynamic light scattering. SUVs were stored at 4°C and verified to be stable before use.

SPR was completed using a Biacore 3000 with an L1 Chip at 25°C as described.[23] Before use, the system was prepared by desorption, sanitizing, and an overnight wash with ultrapure water. Conditioning of the L1 chip was completed at the beginning and end of each run with 7 μL of 40 mM octyl α-D-glucopyranoside (10 μL/min). 1xPBS (pH 6.8) was used throughout the run and in all solutions. SUV capture was performed at 5 μL/min for 10 minutes to ensure surface saturation. Control runs of 60-second pulses of 10 mM NaOH and 0.1 mg/mL BSA showed little change in the baseline. Approximate resonance unit (RU) increases for POPG, 7:3 POPG:TPCL, 4:5:11 DAG:TPCL:POPG, and 9:1 POPC:Cholesterol SUV capture were 3-5k. At an equilibrated flow of 30 μL/min, samples were injected (kinject) for 5 minutes and dissociated for 6 minutes with buffer.

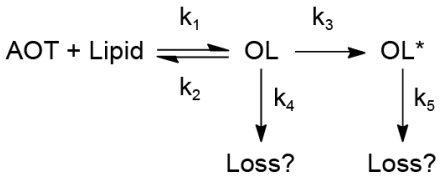

$$\frac{dOL}{dt} = k_1[AOT][C_{Lipid,Total} - OL - OL^* - Loss(OL) - Loss(OL^*)] - k_2OL - k_3OL - k_4OL \quad (1)$$

$$\frac{dOL^*}{dt} = k_3OL - k_5OL^* \quad (2)$$

$$\frac{dLoss(OL)}{dt} = k_4OL \quad (3)$$

$$\frac{dLoss(OL^*)}{dt} = k_5OL^* \quad (4)$$

$$\frac{dSignal_{SPR}}{dt} = \frac{dOL}{dt} + \frac{dOL^*}{dt} \quad (5)$$

Equation 5-1: *Ordinary differential equations from kinetic framework*
Excerpt of two-state model with loss on each step translated to mass action kinetics rates (Equations 5-1). SPR observes effective refractive index changes near the gold sensor surface, encoding both mass and structural changes. Thus, the SPR cannot observe material lost from the surface seen in Equation 3 and 4 and Equation 5 sums up the combined observations.

Use of MATLAB to model and fit SPR data

Fitting of the kinetic rates to the SPR sensorgram data was completed using lsqcurvefit. The function incorporated two separate nested ODEs for the association and dissociation phases, where $C_{oligoTEA}$ was the designated concentration and 0uM, respectively. The ODEs were numerically solved by ode15s with RelTol and AbsTol as 1e-8. Convergence of lsqcurvefit was seen typically in less than 1k function iterations to a resnorm less than 5e5 to capture the behavior of the curve. Kinetic rate parameters k_1,k_2,k_3,k_4, and k_5 were not bounded, while $C_{Lipid,total}$ was kept constant (3000 ±

<0.01%). $C_{Lipid,total}$ should be dependent on the physical number of binding spots of the lipid surface, only changing based on SUV lipid composition, not the oligomer concentration (only the MRSA lipid composition was fit). $C_{Lipid,total}$ must be greater than the highest RU value in the experimental data. For example, $C_{Lipid,total}$ must be at least ~2100 RU worth of lipid in order to fit the BDT-4G from Figure S19. $C_{Lipid,total}$ scales the curve response, with little change to the curve shape. Since the kinetic rates significantly affect curve shape, $C_{Lipid,total}$ was held constant to allow comparison.

Fluorescence Microscopy

To form planar supported lipid bilayers, polydimethylsiloxane (PDMS) wells of ~1 cm diameter were attached to piranha-washed glass slides (70% sulfuric acid, 30% hydrogen peroxide). PDMS consisted of 10:1 elastomer:cross-linker mixture of Sylgard 184 (Robert McKeown Company). Wells were coated with 100 µL of poly-L-lysine (0.1%wt/vol in water, Sigma P8920) for 30 minutes at room temperature, then washed with 1X PBS pH 6.8. SUVs were labeled with 0.05-0.1 mol% Octadecyl Rhodamine B or Texas Red™ DHPE (Molecular Probes). The labeling amount was kept low to prevent surface quenching. G25 spin column (GE Healthcare) removed excess fluorophore. Labeled vesicles were added to the well and incubated for 10 minutes to rupture and form a bilayer. The well was gently rinsed with PBS to wash away excess vesicles. Scratches were made on the bilayer to aid in determining the focus. Imaging was performed with a Zeiss Axio Observer.Z1 microscope with α Plan-Apochromat 20X objective. Time-lapse imaging was completed before and after oligomer exposure (10min).

Chapter 6 : Future Directions and Outlook

Introduction

The field of sequence-defined materials has always been strong, because of the demonstrations by nature and sequence-structure-function relationships we continue to uncover through scientific study. Thus, the applications of sequence-defined materials are hard to summarize as it depends on the size produced. The larger and longer the material, the more structural interactions it would be able to participate in. For example, peptides with tertiary structures are larger than those that only have secondary structure; yet, tertiary structure allows the formation of catalytic sites and molecular recognition. Specific to this work, oligothioetheramides has significant potential over other sequence-defined scaffolds due to their ability to control the oligomer backbone. Thus, oligoTEAs can create specific, regioselective structures and interactions.

Beyond the scope of this work, there are several future directions that could be explored and they will be discussed in this last chapter. First and foremost, work should be done to harness the oligoTEA backbone for the development of an oligomer with a "structured" or ordered conformation. Much work was performed toward this effort and recommendations for future directions can be given. Second, there were several new developments in this work that detail the importance of biophysical characterization to understand the potential of membrane-targeting antibiotics. There are a large number of recommendations and possible future directions that will be discussed.

The development of a structured oligoTEA

While it is not a requirement of function, structure within macromolecular scaffolds does the ability for some functions to be designed, including those of molecular recognition, drug discovery, and catalysis. Moreover, oligoTEAs have an excellent opportunity to develop a variety of structure-forming backbones through the development and inclusion of custom dithiols. Researchers working with peptoids were able to develop an alpha-helix mimetic within a few years, demonstrating their utility to form specific structured molecules. While one may never know, this demonstration established their ability and inspired the formation of other structured materials (e.g., zinc clamp,[102] helicies,[178] nanosheets[180]).

De novo development of structured oligoTEA requires an understanding of the contributions of monomer hydrogen bonding, hydrophobicity, and electrostatic interaction within the scaffold. Previous sequence-structure relationships can best be seen in the fields of foldamers[94–96] and single-chain folding[480–483], which have pioneered relationships between chemical functionality, thermodynamics, self-assembly, and molecular ordering. Larger hydrophobic groups to restrict conformational freedom; however, this strategy can limit water solubility.[101,175,181] Hydrogen bonding is well-known to induce modes of structural formation as an attractive force (e.g. alpha helices and beta sheets within peptides).[2,483] Lastly, macrocyclization restricts molecular conformational and lowers the entropic cost of interaction or binding.[36,416] Overall, these examples demonstrate how a balance of intramolecular forces can control entropic chain collapse.

To achieve this goal, various molecular forces could be utilized including hydrogen bonding, electrostatics, and sterically restrictive groups. As one of the strongest forces, electrostatic interactions are long range interactions, but can be screened by ions and water and highly ionic structures can have unpredictable bioavailability.[484] Moreover, in Chapter 3, we a highly sulfonated oligoTEA in mild buffer conditions was unable to demonstrated single-chain collapse and showed no preference of any ordered conformation. Thus, other strong molecular forces could build structured oligoTEAs.

N-allyl-N-acrylamides with structure-forming motifs

Through the course of this work, there were several *N*-allyl-*N*-acrylamides that were synthesized that could be useful in the future. And generally speaking, incorporation of structure forming moieties into *N*-allyl-*N*-acrylamides is straightforward. Their structures and synthetic schemes are shown in Appendix E (Figure E-1). Of note, the methyl-propanoic acid *N*-allyl-*N*-acrylamide demonstrated conformational preferences of the rotamer that centers around the tertiary amide of the *N*-allyl-*N*-acrylamide scaffold as seen in both the singlet and non-rotamer splitting in both the ^{1}H and ^{13}C NMR (Appendix E, Figure E-2) that would routinely be seen otherwise (see Figure A-2 “HSQC” for example). This has also been seen in literature for peptoids, which also features a tertiary amide that can be conformationally restrained sterically.[485] However, these efforts utilizing *N*-allyl-*N*-acrylamide pendant group of the oligoTEA scaffold is not as preferred as using the backbone.

Developments toward hydrogen bonding dithiol monomers

Our specific goal was to create synthetic schemes toward the development of a structured oligoTEA that do not sacrifice the diversity of sequence and chemistries available to use. We are also keeping in mind that the reduction of macromolecular conformation is not an explicit requirement of biological function. Thus, the ability to define sequence is more important, as demonstrated by several examples of precisely defined flexible macromolecules in Nature.[12,17,486,487]

Hydrogen bonding is the molecular force of choice for many evolutionarily optimized structures including peptides and nucleic acids.[1] Hydrogen bonding is a relatively short-range interaction and is specific, limited by the participating atoms. Peptides make use of the hydrogen bonding of their secondary amides in an elegant way, where the amino acid backbone is a main mode of structural development described in Chapter 1 (see Figure 1-1). Pendant groups affect the formation of structures including α-helices and β-sheets, but remain relatively independent and available for specific functionality.[2]

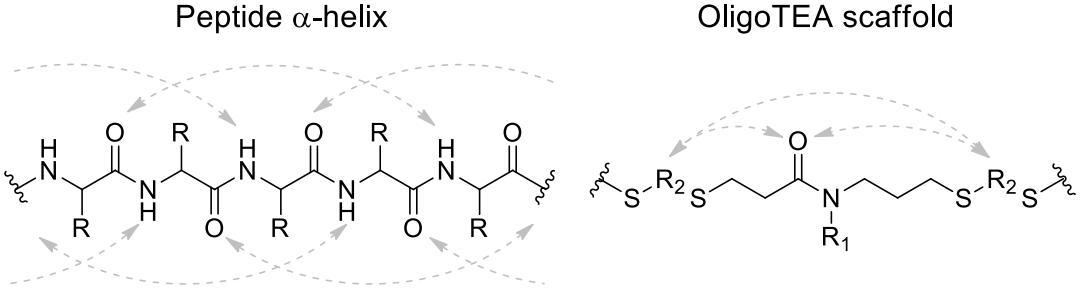

Figure 6-1: *Comparison of a peptide α-helix to the oligoTEA scaffold. The arrows represent hydrogen bonding that can take place between hydrogen bond donors and acceptors. In the oligoTEA scaffold the carbonyl can act as an acceptor, while the dithiol backbone could act as a donor and/or acceptor.*

Thus, much work was performed to attempt to develop hydrogen bonding along the backbone to attempt to direct the oligoTEA conformation and structure to cause intramolecular association (Figure 6-1). The goal of this design was to allow independent pendant group functionality, similar to peptides. Thus, the synthesis of several dithiol comonomers were attempted with varying amounts of hydrogen bond donor and acceptors. Several attempts were made across a variety of chemistries that will be briefly discussed with recommendations for future directions.

The first target compound was 2,3-dimercaptosuccinamide, which could be prepared from the amidation of 2,3-dimercaptosuccinic acid, which has been successfully incorporated into oligoTEAs before, or the thiolation of acetylenedicarboxamide. Both schemes were challenging and unsuccessful as described in Figure 6-2. Acetylenedicarboxamide presented challenging solubility, and was only soluble in solvents with high hydrogen bonding character as well as high polarity, likely because of the primary amide itself (e.g., DMF). It was not soluble in any typical organic solvents (ethyl acetate, DCM, etc), making normal phase silica purification likely not possible. TLC also confirmed that high-polarity solvent conditions (20% MeOH in DCM + 1% NH_4OH) would not elute any of the the primary amide containing reaction mixture. If this avenue was pursued, reverse phase purification would need to be explored.

Thus, methylamide versions were pursued, and were soluble with TLC confirming their potential for normal phase purification. However, upon the attempted coupling of methylamine to the 2,3-dimercaptosuccinic acid, polymerization occurred upon addition of the coupling reagent before the methylamine was introduced, possibly

from cross-reaction with the thiol. Therefore, it is recommended to pursue thiol protection of the 2,3-dimercaptosuccinic acid before coupling to enable the synthesis of this dithiol monomer. There is also the consideration that this dithiol monomer would contain chiral centers that were not specified, resulting a racemic mixture unless purified as well.

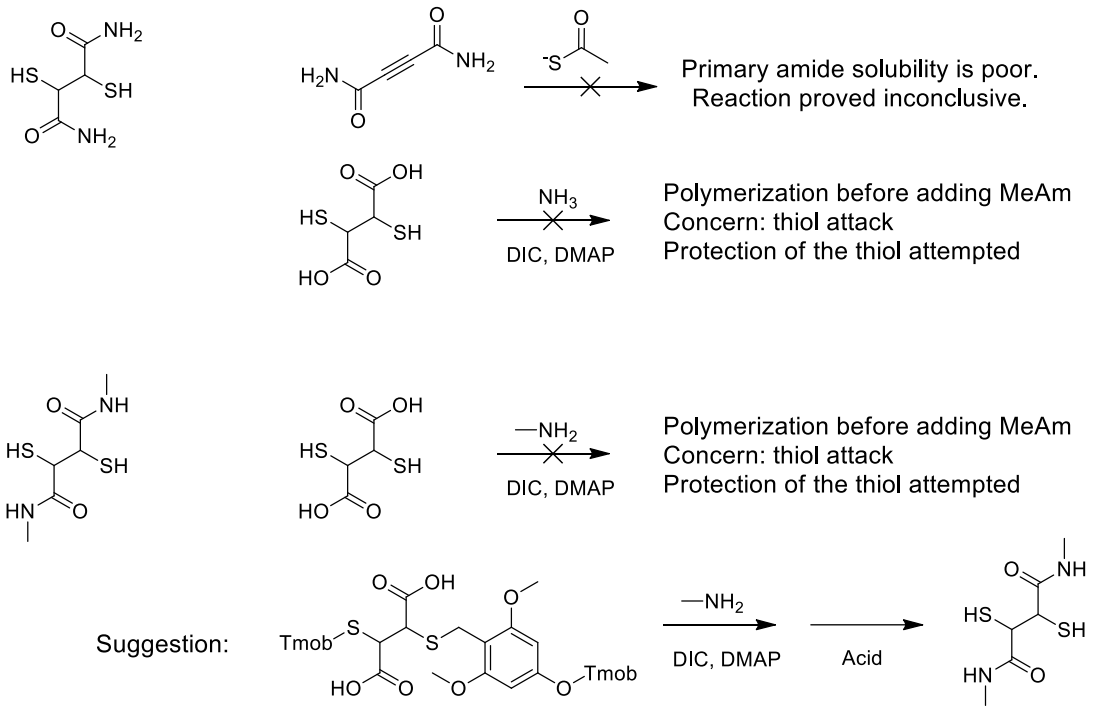

Figure 6-2: *Synthetic attempts toward an amide containing dithiol*

Another approach was to synthesize urea containing dithiol monomers. One of the first attempts was for the creation of a dimercaptocyclohexyl urea (DMCU). The DMCU monomer seemed promising because the use of a chiral monomer and that urea containing monomers have tamed flexible scaffolds before.[168,170] However, the scheme to produce it was challenging. At first, the scheme to product the DMCU was proposed with selective Boc-protection of the amine, activation of the alcohol to form a protected

thiol, acidic Boc-deprotection, and then coupling of the amines to form the urea (Figure 6-3a). However, selective Boc-protection was not possible. Moreover, selective Boc-protection was unadvised upon further literature search, revealing the facile formation of the oxazolidinone upon treatment with Boc-anhydride.[488] Another protocol from literature was located performing similar chemistry with saccharide substrates, resulting in the second scheme (Figure 6-3b).[488] However, yield for the first full step of the reaction was poor (5-10%) as it was not possible to purify by column chromatography and HPLC was necessary. Crystallization or titration was also attempted. Nevertheless, enough urea dioxazolidinone product was isolated to determine feasibility of step 2 in the thiolation, revealing that the reaction did not proceed by LCMS. The starting material remained regardless of duration and heat (ranging from RT to 120C).

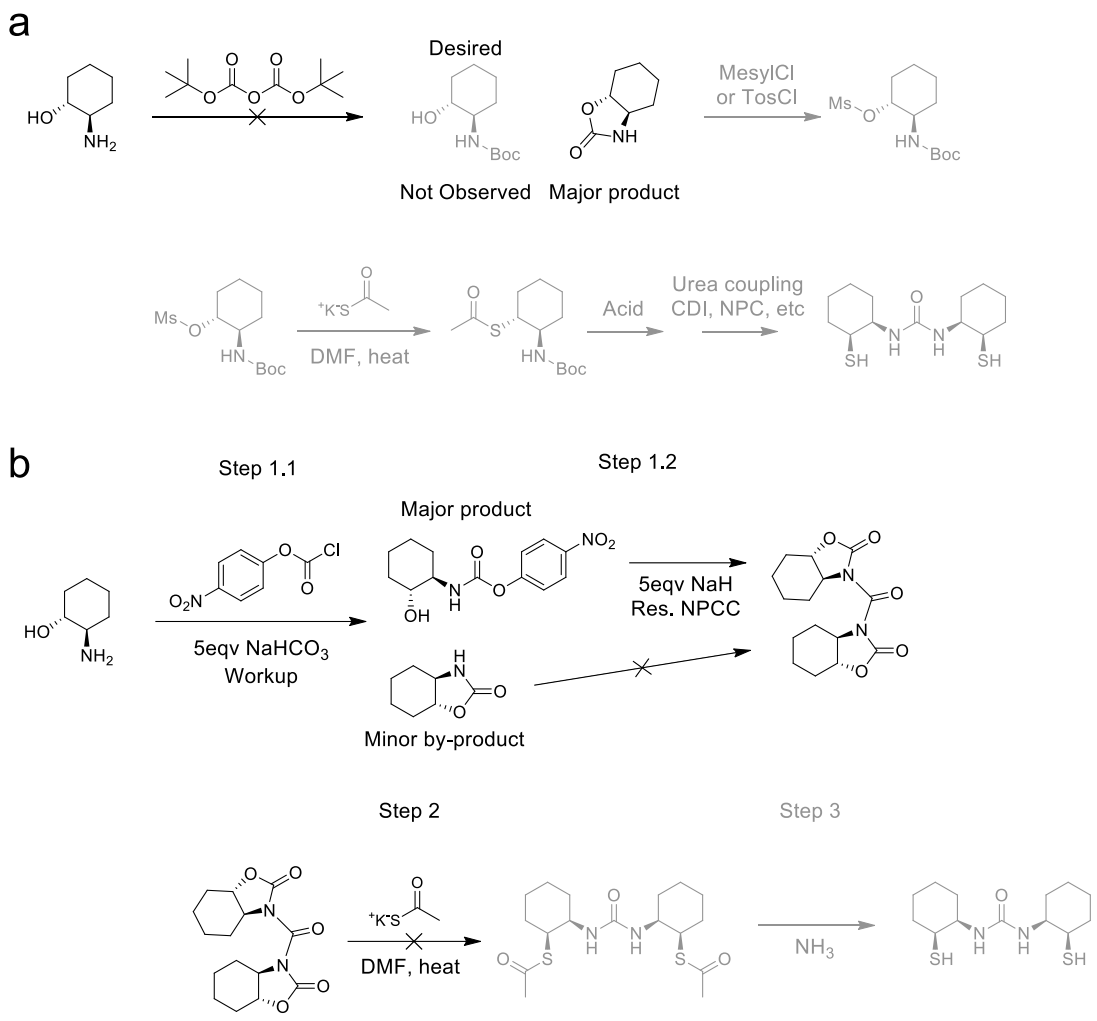

Figure 6-3: *Schemes toward the production of dimercaptocyclohexyl urea*

Thus, the scheme was abandoned and another comparable scheme was created and investigated, where aminothiols were thiol protected and then the amines were coupled into a urea (Figure 6-4). A model urea dithiol was produced to demonstrate the synthesis all the way to the synthesis and verification with oligoTEA synthesis (see Appendix E Figure E-3). The oligomer was not explored for its conformational preferences; nor were longer oligoTEAs prepared.

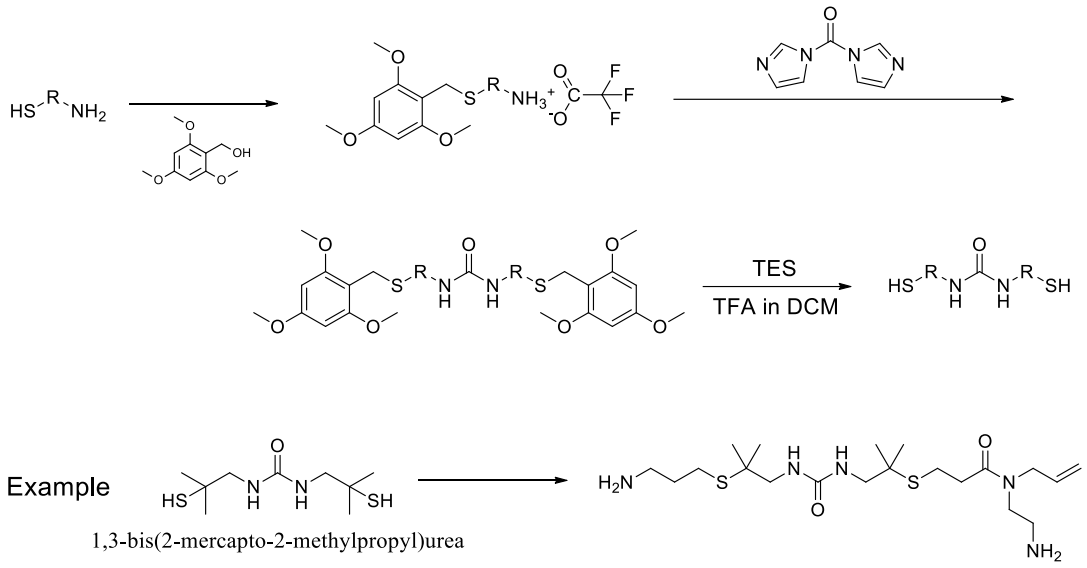

Figure 6-4: *General scheme to create urea dithiols from amino thiols with example*

From here, chiral precursors were sought out with limited findings; however, cysteine derivatives were available and the following scheme was constructed to provide a simple starting cysteine-derived urea dithiol (Figure 6-5a). L-Cysteine was selectively protected by the 2,4,6-trimethoxy benzyl alcohol (Tmob) group and then urea formation was attempted. However, for the case of the H-Cys(Tmob)-OH, urea formation was not readily observed and the major side product was the amide coupling product (Figure 6-5b) verified by LCMS and ^{13}C NMR (the ^{1}H is ambiguous). Intramolecular coupling could be interesting to pursue in order to create cyclic 2,5-piperazinedione dithiol derivatives shown; however, none of this product was observed. 2,5-piperazinedione would only provide 2 secondary amides per dithiol (2 H-bond donors and acceptors), whereas the intended product will have much more hydrogen bonding nature.

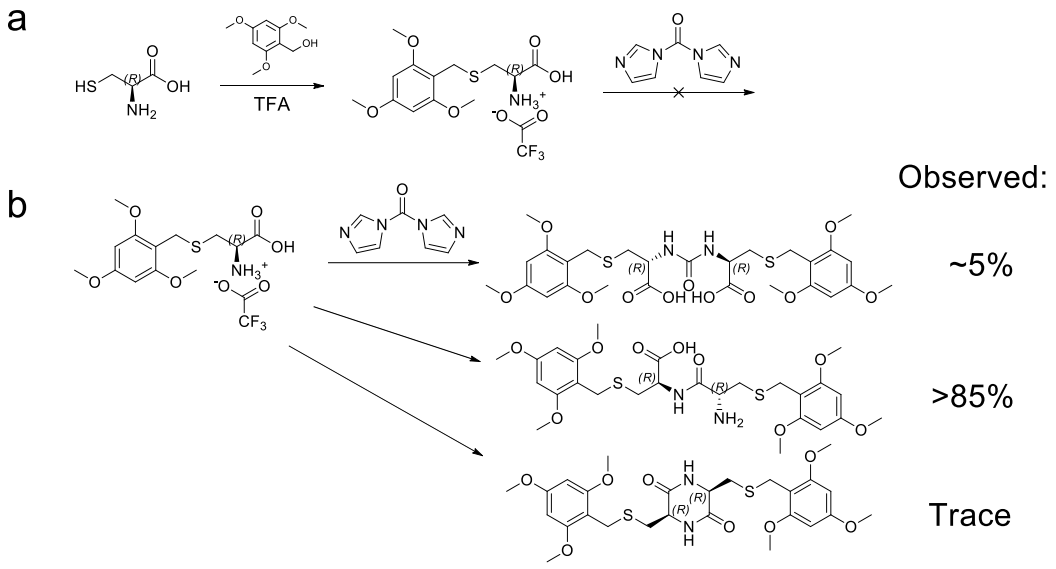

Figure 6-5: *Unsuccessful attempt to produce the Tmob-protected bis-cysteine urea*

Thus, another scheme to produce cysteine-derived urea dithiol monomers was developed by incorporating a tBu protecting group on the carboxylic acid (Figure 6-6). The best way to incorporate this was by perform the tBu protection of Boc-Cys(Trt)-OH via tert-butyl-2,2,2-trichloroacetamide. The Tmob group unfortunately cannot be used because after tBu protection, selective Boc deprotection is carried out with 1M HCl in dioxane/ethyl acetate, which the Tmob could not survive. Thus, the trityl group had to be utilized.

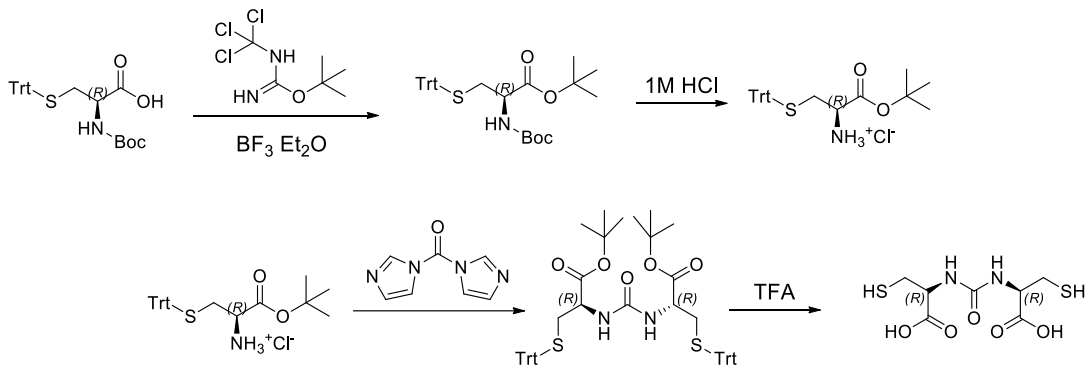

Figure 6-6: *Successful scheme to produce bis-cysteine urea (BCU)*

The synthesis was completed, but ultimately purification was challenging. The final compound developed after TFA cleavage gave inconsistent results between the TLC and the actual silica column purification. After attempted column chromatography, there were some impurities remaining from the mono- and di-protected carboxylic acid product and the isolated fractions showed low yield (~25%). Removal of the t-butyl protecting groups is necessary at this stage before oligoTEA assembly because these conditions will be more stringent conditions than those for oligoTEA cleavage (100% for 1hr or 50% TFA for 3 hours). However, even after increasing the stringency of the reaction (overnight, addition of heat), the TFA treatment of the t-butyl and trityl protected product still contained a distribution of di-, mono-, and un-protected carboxylic acid.

Unfortunately, at the time of this writing, these issues were not resolved, but future work is recommended. Complete deprotection of the bis-cysteine urea (BCU) could likely be achieved by breaking the deprotection into two stages. First, a reductive deprotection (e.g. NH_3, possibly $NaBH_4$) can release of the t-butyl protecting group on the carboxylic acid under specific conditions. Then, acidic treatment of the product can

remove the trityl groups. If this strategy is not successful, another protecting group for the carboxylic acid could be considered, though the t-butyl ester is one of the most acid-liable protecting groups.

In addition to those recommendations for the synthesis of a bis-cysteine urea, there is also interest in still forming cyclic urea dithiols. Another precursor was located that would similarly follow the synthesis of the previously discussed DMCU to produce a hydroxylated dimercaptocyclopentyl urea dithiol. The scheme starts with a deoxyribose mimetic that is commercially available (~$6.5/g) because it has been used to prepare adenosine mimetics and Ticagrelor, an antithrombotic agent from AstraZeneca. The aminoalcohol structure contains multiple chiral centers and an acetonide (protected 1,2 diol). The Boc protection and mesylation are reported in literature.[489] The deprotection of the acetonide into the chiral alcohols by dilute acid is observed as well in multiple sources. With the amino alcohol being an additional carbon apart (e.g. 1,3-aminoalcohol), it is likely that an N-S acyl shift is not as possible as before with the 1,2-aminoalcohol. Thus, there are no obvious potential issues with the synthesis and it could be attempted (Figure 6-7).

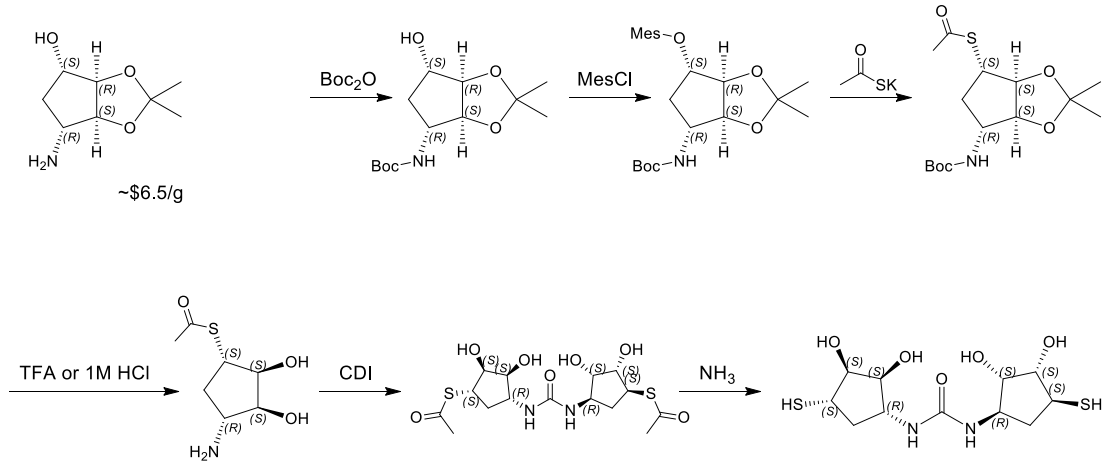

Figure 6-7: *Proposed scheme to produce dimercaptocyclopentyl urea*

Developments toward sterically restrictive dithiol monomers

Aforementioned, larger molecular groups are often used to restrict conformational freedom. However, frequently this involves the use of hydrophobic groups, which can limit water solubility.[101,175,181] Indeed, the first peptoid helices utilized naphthyl and ethylene phenyl groups to effectively block out conformational freedom.[178] Therefore, coupled with other hydrophilic groups, it could be possible to develop a structured, water-soluble oligoTEA. As such, some monomers were attempted; specifically a dibenzyl dithiol (Figure 6-8). Overall, this monomer was approached from 1,2-diphenylethyne and also 1,2-dibromo-1,2-diphenylethane precursors, both of which were not successful (see Figure 6-8 for details).

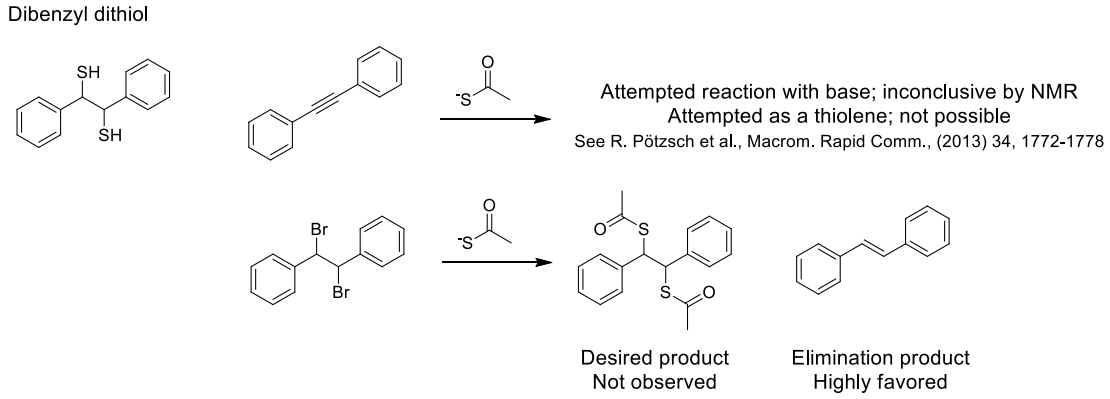

Figure 6-8: *Schemes of attempts to produce dibenzyl dithiol*

However, it seems likely that hydrogen bonding has a higher chance of success, as an attractive force that brings energetic stabilization to a preferred conformation, rather than sterically restrictive groups. Blocking conformations would be very challenging in the oligoTEA scaffold due the extensive number of methylenes in the

backbone repeat unit already (5 with the *N*-allyl-*N*-acrylamide + any dithiol). Moreover, the *N*-allyl-*N*-acrylamide itself generally exists as a rotamer due around its tertiary amide. These elements must be tamed by any prospective dithiol. If using a sterically restrictive group on a dithiol, excluding available conformations of the *N*-allyl-*N*-acrylamide would require very large groups (e.g., anthracene or larger) to physically extend into the space the *N*-allyl-*N*-acrylamide occupies.

Future directions for biophysical characterization

There are several future directions for the biophysical characterization that was performed in this work. Specifically, work can be done to i) perform as systematic study to observe the effect of molecular properties such as hydrophobicity and size of the lipid aggregate phenomena observed, ii) expand this characterization to bacterial derived membranes, iii) understand more about the multimeric lipid aggregate, specifically if it is bactericidal or the result of bactericidal action, iv) connect the current observation to smaller length scales (i.e. molecular and nanoscale) of biophysical observation, v) quantify the error on parameters of the model fit of the surface plasmon resonance (SPR) data, and vi) examine single oligoTEA association to membranes. Overall, a better understanding of the phenomena observed in this work can be pursued to improve our ability to recommend design parameters for the next generation of membrane-targeting antimicrobials.

Seek molecular properties that affect lipid aggregate

Upon exposure of a membrane-targeting oligoTEA to a bacterial mimetic membrane, we observed the formation of lipid aggregates that contain both the oligoTEA and lipids (Chapter 4 and 5). This aggregate formation was also understood through surface plasmon resonance (SPR) and modeling of the results. Moreover, the aggregate was correlated to the biological activity alone over other parameters in three separate studies. Both the biological activity of the Meta and Para oligoTEAs (Chapter 4) and guanidine-containing compounds including PDT-4G (Chapter 5) correlated with the aggregate population (OL*), which represents the amount of aggregates formed likely by mass. For the antibacterial constitutional isomers (e.g. AOT 32523) in Chapter 5, their biological activity was loosely correlated with the amount loss from the aggregate, Loss(OL*), also likely by mass.

Throughout this study, only twelve oligoTEAs were analyzed by SPR, with only four analyzed by fluorescence microscopy. Thus, a systematic study can be completed with several oligomers of different sizes and hydrophobicities. The effect of both properties are understood biologically,[278] but their effect on the lipid aggregate is not understood and could be studied. As understood, it is likely that increased molecular hydrophobicity will increase the ability of the oligomer to embed into the membrane, which could drive aggregate formation. However, it is unclear what changes in the morphology would be observed and what changes in the amount of lipid extracted from the surface would be. Changes in oligomer size are curious to contemplate as well. Oligomer size could easily affect lipid aggregate morphology and alter kinetic rates. For example, multivalent binding would likely increase irreversibility in binding.

Utilize real bacterial membranes

In this work, bacterial mimetic membranes were utilized as stand-ins for real bacterial membranes. Therefore, characterization of membrane disruption and potential aggregate formation could be done utilizing either cryogenic scanning or transmission electron microscopy. Or, methods could be developed to be able to extract bacterial membranes and create acceptable supported lipid bilayers, to enable fluorescence microscopy. For these future experiments, it is likely that the differences observed in aggregate formation would become more nuanced and difficult to observed, especially between the Meta and the Para (Chapter 4). Therefore, oligoTEAs with greater differences in activity and design could be used including the PDT-4G and PDT-4Am (Chapter 5)

Furthering our understanding about the lipid aggregate

Overall though, these data demonstrate a correlation and do not directly inform us about the bactericidal action that results in inhibition of bacterial growth and/or bacterial death. Therefore, steps can be taken to understand if the aggregate is a result of bactericidal action or if the aggregate itself is directly bactericidal. It seems likely that the membrane disruption and rearrangement to cause the aggregate to form would be bactericidal. We know that 1-2% of the bacterial membrane evolved into solution after treatment with the Meta and the Para (Figure 4-5c). It is unclear the critical amount of membrane that would be required to disrupt to cause bactericidal action, but it could

be possible for this to be insufficient. After all, bacteria can become resistant to treatment the membrane-disruption of these antimicrobials.[454]

Therefore, one could answer these questions by examining the antimicrobial activity of the oligoTEA-lipid aggregate itself. It does not seem likely that the aggregate is antibacterial, but it must be examined. To do this, the oligoTEA-lipid aggregate must be prepared. Thus, the required ratio of the oligoTEA to the lipid must be characterized, analogous to the peptide-to-lipid ratio for other antimicrobial peptides (AMPs).[400] It might be possible to calculate this by an experiment similar to a cloud point test, which assesses the solubility of a compound. However, in this case, varying concentration of oligoTEA would be added to SUVs to determine at which concentration the SUVs are completely solubilized. This would then give a molar oligoTEA to lipid ratio. Otherwise, literature methods could be utilized.[400] Second, with the known ratio of the oligoTEA-lipid complex, one could prepare the mixture and preform an minimum inhibitory concentration (MIC) assay with it.

The bacterial activity of the lipid-oligoTEA complex will indicate if the oligoTEA-lipid aggregate itself is antibacterial or not. It is likely that it will not be antibacterial. But, if it is, one must then characterize the actual aggregate from the membrane surface to understand its chemical composition and bacterial action further.

Connecting our observations of the aggregate to smaller length scales

If the aggregate itself is not directly antibacterial, then the aggregate must be a result of bactericidal action that is occurring at smaller length scales than observed in these studies. One can seek to expand our characterization ability toward these scales,

approaching and connecting to other established models. Specifically, fluorescence microscopy is unable to observe nanoscale phenomena that occurs to result in the aggregate. Others have utilized cryogenic electron microscopy to start to observe this scale, indicating the importance of lipid aggregate formation as well.[490] Additionally, surface plasmon resonance encodes all mass and structural changes that occur to the membrane during oligomer exposure. Similar to other models, our two-state model with loss is unable to further deconvolute the nano- and molecular-scale phenomena occurring, likely within the "OL" state.

Overall, there is a long history of understanding membrane disruption from the molecular level that could be connected to the current work.[404,491] There are several known molecular mechanism of action including "barrel-stave" model, "toroidal" model, and the "carpet" model. The barrel-stave model involves oligomer monomers binding individually to the membrane and then aggregating at the membrane surface. During this surface aggregation, the hydrophobic regions of the oligomers clump together and penetrate the membrane, often to form pores of the oligomer itself.[492,493] The "toroidal" model creates a pore by rearrangement of the lipid membrane to create a pore as well, but the pore channel contains both lipids and oligomers, rather than a simple expansion of the membrane. Several AMPs are known to follow this mechanism including magainin 2,[494,495] protegrin-1,[496,497] melittin,[498,499] and MSI-78.[500] Last, in the "carpet" model, oligomers bind and solubilize parts of the membrane into solution. Known examples of this mechanism include dermaseptin,[501] cecropin,[502] caerin 1.1,[503] and ovispirin.[504]

Across all of these mechanisms, there are a variety of methods to characterize and distinguish between which molecular actions are occurring. Excluding circular dichroism as oligoTEAs have no secondary structure,[498] simple characterizations from literature include dynamic scanning calorimetry,[500] characterization of partition coefficient with a fluorescently labeled oligomer,[490,501] and the calcein leakage assay.[494,499] Other more complex characterizations are valuable for the amount of information they reveal and include solid-state NMR,[496,500,504] computational modeling[497,502,503] neutron or x-ray scattering,[495,498] and voltage sensing across black lipid membranes (similar to other collaborative work with the Alabi lab[505]).[492,493] With any of these additional characterization, one could begin to discern the molecular sequence of events, capturing time evolution if possible.

These characterizations would enable an unprecedented multi-scale, comprehensive understanding of membrane disruption and bridge gaps across multiple characterizations. Distinctions in the molecular phenomena should inform nanoscale phenomena, which in turn will connect to the macroscale changes observed here in this work with the lipid aggregate via fluorescence microscopy and SPR.

Quantification of error on model fit parameters

Future work could be dedicated toward improving and understanding the fit of the two-state model with loss developed in Chapter 4. Specifically, there is not an obvious way to report an error tolerance on the parameters that are calculated. It is clear that this error tolerance should reflect the "goodness of fit." However, the goodness of fit as reported represents the entirety of the fit, which is also problematic. This is due in

part because the data resolution (data points per second) is set and captures quick occurring events at the same resolution as slower events. Therefore, when MATLAB fits the data, it has a tendency to improve the fit around the slow "plateau-like" regions of the SPR data curve, giving less importance to quick events (e.g., initial binding).

To improve on this mathematical issue, there might be ways to independently fit parts of the SPR data curve for specific parameters. For example, K_1 could be determined by the first 20-50 data points. The rate of loss from OL* (k_5) could be fit from the slope of the last 100 data points. Other parameters are much more challenging, including the rate of desorption of the oligomer (k_2), which changes the curvature during the initial period of each the association and dissociation phases. This complex behavior in the resulting curve can be hard to manage in an independent fitting procedure, but could possibly be deconvoluted if other aforementioned independent fits are applied.

Overall, it is important to find a way to better fit these data, such that an error tolerance can be establish and significance and be discerned in the data. An excellent example of this appears in the data in Chapter 5 of the constitutional antibacterial oligoTEA isomers that were explored (e.g., AOT 32523). The loss from the aggregate population, Loss(OL*), correlated with the biological activity, but it is hard to tell if the result is statistically significant.

Examine single oligoTEA association to the membrane surface

One curious suggestion can be made through a potential collaboration with the Abbott lab, which recently joined the department. The Abbott group has expertise in examining single molecule interactions with specific surfaces utilizing a custom atomic

force microscopy (AFM) method.[161] While they have previously used β-peptides for their studies (from Prof Sam Gellman), oligoTEAs could also be analyzed. In these experiments, a molecule is typically attached to a surface at such a low density that an AFM tip would only interact with a single molecule at a time. Then, the AFM tip probes the pull-off force from the surface, allowing the analysis of the attraction of the AFM tip to the molecule. When combined examined across a variety of conditions (solvent, pH, ionic strength, etc.), the interaction with the molecule can be broken into the its specific forces of interaction (e.g., hydrophobicity, charge, etc.). This method could extend several oligoTEAs in this study to examine and complement the interface of the oligomers with lipid membrane surfaces.

Similar to the above recommendation, oligoTEAs with greater differences in activity and design could be used including the PDT-4G and PDT-4Am (Chapter 5) to start and assess if there are significant differences in their actions at membrane interfaces. This is specifically recommended because SPR clearly shows that the initial binding of many oligoTEAs studied in this work is nearly identical. This is due in part because they all function by electrostatically associating with the lipid membrane. If this AFM characterization is sufficiently sensitive, it should be able to visualize the increases in hydrogen bonding with the PDT-4G over the PDT-4Am. It is unclear if this method will allow the evolution of membrane disruption. As understood, the process by which membrane disruption occurs is somewhat stochastic,[400,405] meaning any specific pathways and mechanisms observed in these single- or potentially multi-molecule studies would be very significant to the field.

Appendix A : Additional Supplementary Material for Chapter 2

Part of this appendix are taken from a manuscript in preparation by J.S. Brown, A.W. Ruttinger, A.J. Vaidya, P Clancy, and C.A. Alabi, "Mechanistic Insight into the Thiol-Michael Addition Utilized in Oligothioetheramide Assembly," where J.S. Brown and A.W. Ruttinger contributed equally the work.

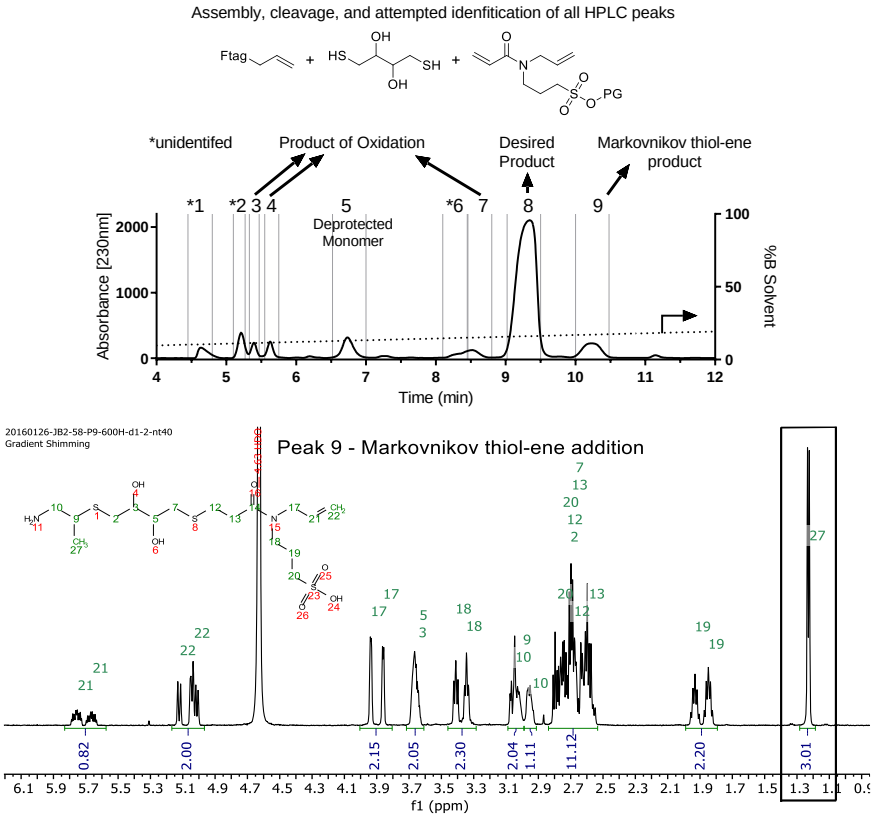

Figure A-1: *Characterization of HPLC fractions from oligoTEA assembly* ***(top)*** *Assembly of an example oligoTEA was performed, specifically of dithiothreitol (DTT) and protected sulfonate N-allyl-N-acrylamide.* ***(middle)*** *After cleavage, HPLC fractionated the desired product and impurities. LCMS and NMR analysis was mostly inconclusive, because of their limited quantity. However, the Markovnikov product of the thiol-ene was identified.* ***(bottom)*** *^1H NMR in D_2O confirmation of the Markovnikov product, with its characteristic -CH3 methyl peak at 1.25 ppm.*

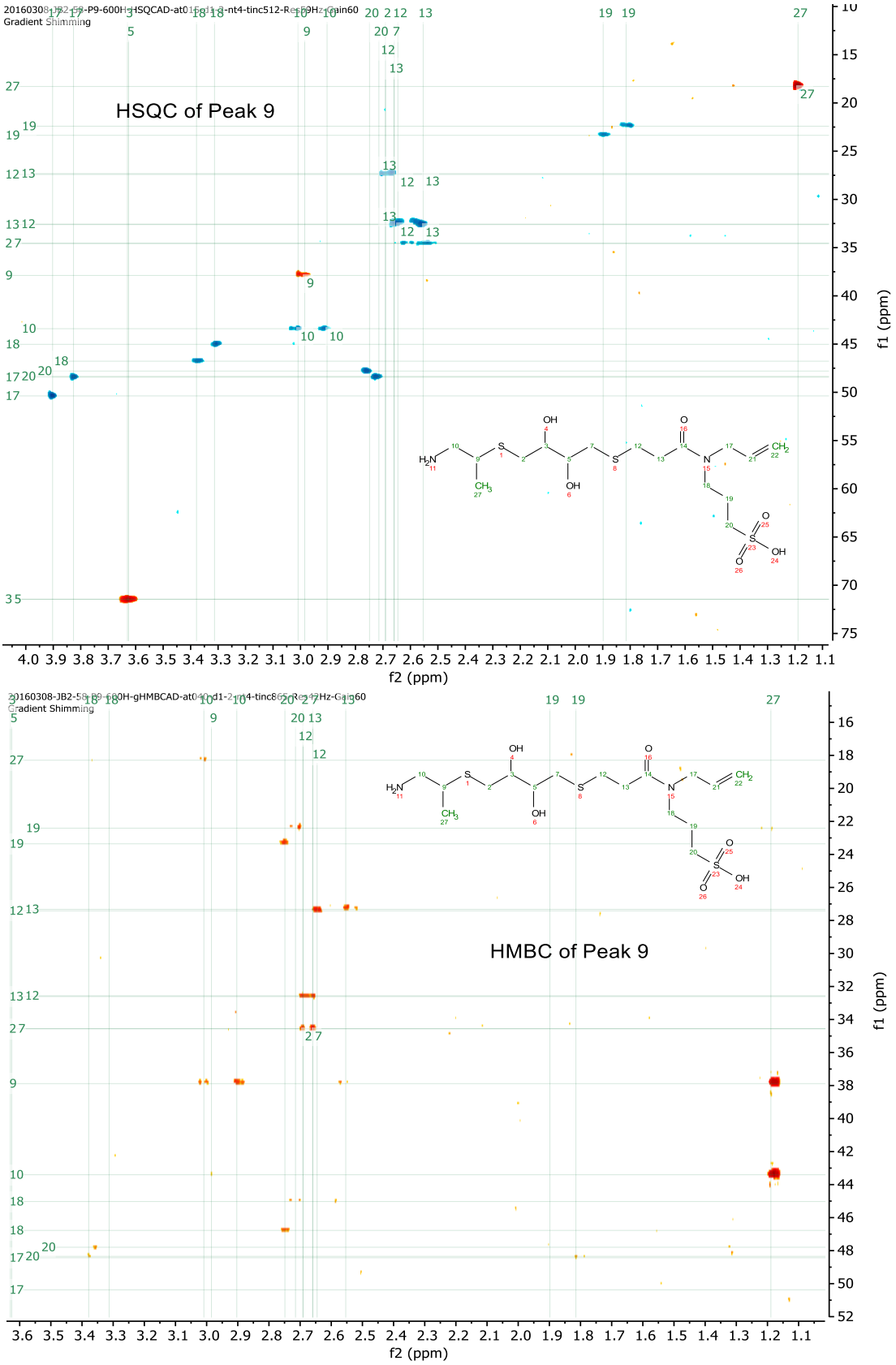

Figure A-2: *HSQC and HMBC confirmation of the Markovnikov product.*

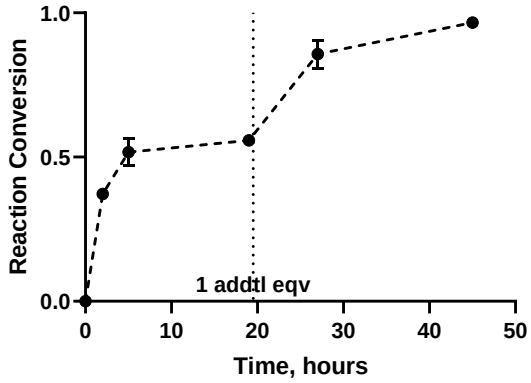

Figure A-3: *Reaction conversion of the N-phthalimide monomer with fluorous thiol Reaction conditions: 2 equivalents of N-phthalimide protected N-allyl-N-acrylamide monomer with fluorous propane thiol and 5 mol% of dimethylphenylphosphine (DMPP), 100mM in MeOH at 40°C. One additional equivalent of N-phthalimide protected N-allyl-N-acrylamide monomer with 5 mol% DMPP was added at the 19 hour mark when the reaction was observed to be ~50% complete.*

Table A-1: *Statistical analysis of kinetic reaction rate data from Figure 2-7*

Species		Temp, C	Significance	P-value	Type	df
Methyl	Ethyl	25	*	0.0238	Two-tailed, Welch's	2.247
		40	**	0.0012	Two-tailed, Welch's	3.139
	Butyl	25	***	0.0002	Two-tailed, Welch's	2.795
		40	****	<0.0001	Two-tailed, Welch's	3.975
	Hexyl	25	****	<0.0001	Two-tailed, Welch's	3.998
		40	***	0.0006	Two-tailed, Welch's	3.221
Ethyl	Butyl	25	ns	0.2369	Two-tailed, Welch's	2.051
		40	*	0.0107	Two-tailed, Welch's	2.996
	Hexyl	25	ns	0.6461	Two-tailed, Welch's	2.237
		40	ns	0.1351	Two-tailed, Welch's	3.992
Methyl	EtPhenyl	25	ns	0.0994	Two-tailed, Welch's	2.578
		40	ns	0.0631	Two-tailed, Welch's	3.125
Benzyl	EtPhenyl	25	**	0.0034	Two-tailed, Welch's	2.09
		40	*	.0277	Two-tailed, Welch's	2.427

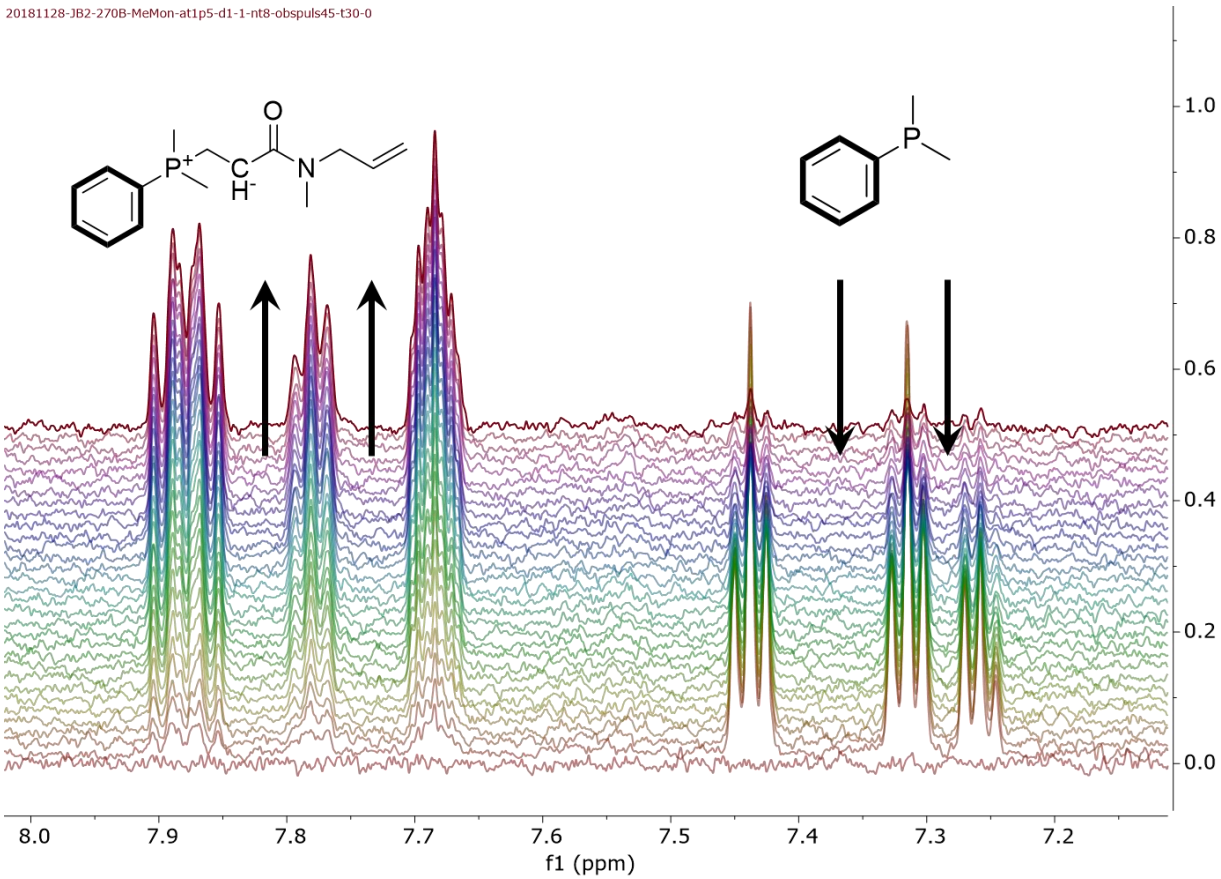

Figure A-4: *Reaction of methyl N-allyl-N-acrylamide and DMPP tracked by NMR Reaction conditions: 20mM methyl monomer, 0.05 eqv of dimethylphenylphosphine (DMPP) in 10% MeOH in dMeOD. Spectra are stacked starting from the bottom spectra at t=0 and the top spectra at approximately 30 minutes. Arrows show the behavior of the specific peaks observed. The DMPP is consumed from solution and reacts onto the acrylamide, forming a stable zwitterion catalyst complex that is prepared for the start of the thiol-Michael addition.*

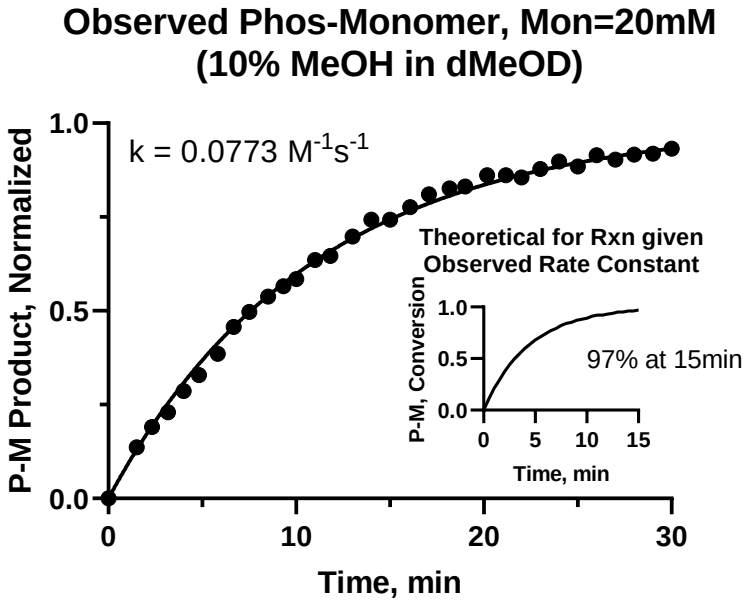

Figure A-5: *Kinetic analysis of NMR experiment from Figure A-4*
NMR spectra were integrated to provide the normalized product formation in the reaction of DMPP with methyl N-allyl-N-acrylamide. Kinetic analysis was performed in GraphPad Prism assuming a bimolecular mechanism. At full reaction concentration (50mM prior to thiol addition), the reaction is complete and the initiator (phosphine + N-allyl-N-acrylamide) is prepared for the start of the thiol-Michael addition

Appendix B : Additional Supplementary Material for Chapter 3

Materials in this appendix have been adapted from the Supplementary Information provided adapted with permission from Brown, J. S.; Acevedo, Y. M.; He, G. D.; Freed, J. H.; Clancy, P.; Alabi, C. A. *Macromolecules* **2017**, *50* (21), 8731–8738. Copyright 2017 American Chemical Society.

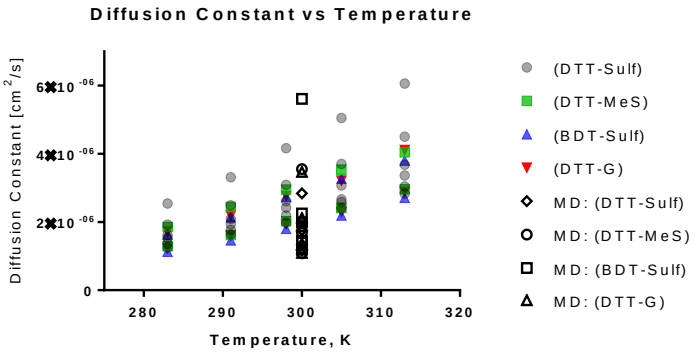

Figure B-1. *All diffusion data (PFG-NMR and MD)*
All diffusion data from both PFG NMR and single-chain MD simulations in water. Similar range of diffusion and trends were observed, providing validation for the MD simulations with respect to the oligomer dynamics. At most a factor of 3 difference was observed between the PFG NMR and MD, which is reasonable for a macroscopic property.

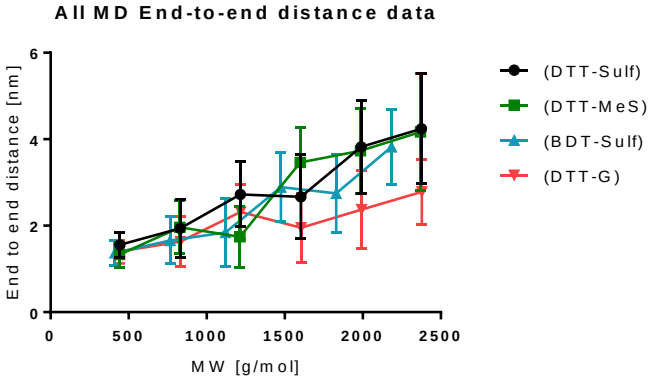

Figure B-2: *All end-to-end distance measurements by MD*

All end-to-end distance measurements produced by single-chain molecular dynamics (MD) simulations at 300K in explicit water solvent versus the oligoTEA molecular weight. Error bars represent standard deviation of the end-to-end distance over the MD time evolution.

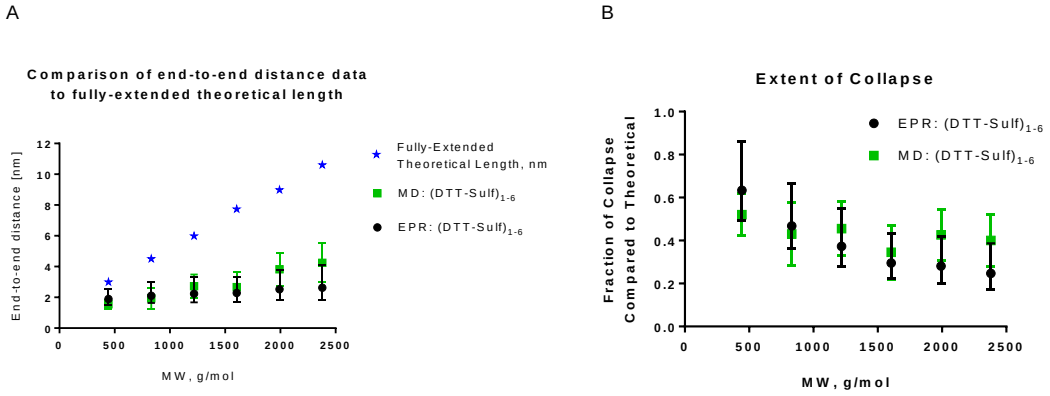

Figure B-3: *End-to-end distance vs theoretical length and extent of collapse* ***A.*** *Comparison of the fully-extended theoretical length of 100uM (DTT-Sulf)1-6 oligoTEAs in 20% ethylene glycol in water vitrified to 70K from room temperature revealing the extent of molecular collapse experienced in solution. All oligomers appear to experience some level of collapse likely due to entropy, hydrophobic collapse, and/or screening of intramolecular electrostatic repulsion.* ***B.*** *Calculation of the fraction of (DTT-Sulf)1-6 oligoTEA collapse.*

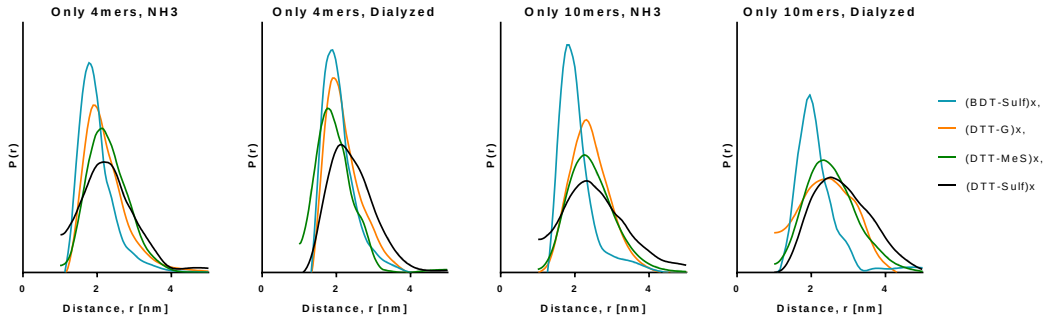

Figure B-4: *All end-to-end distance reconstructions of 4 and 10mers.*
All end-to-end distance reconstructions of DEER distributions of (BDT-Sulf)2,5 in blue, (DTT-G)2,5 in red, (DTT-MeS)2,5 in green, and (DTT-Sulf)2,5 in black measured by DEER and DQC EPR. Samples were measured at 100 uM in 20% ethylene glycol in water and vitrified to 70K from room temperature. Detail is described in Supplementary Methods.

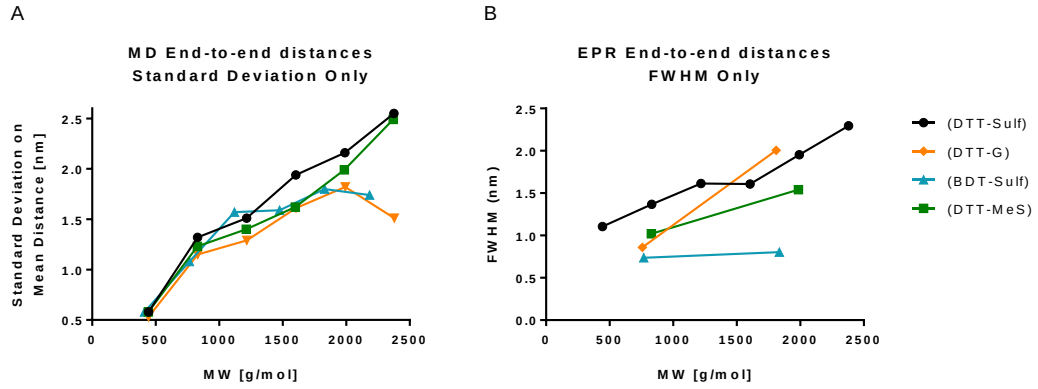

Figure B-5: *Standard deviation on end-to-end distances (MD)*
The standard deviation on the mean end-to-end distance calculated by single-chain MD simulations (300K, explicit water solvent), which qualitatively assesses the size of the conformational space. ***B.*** *The full-width at half maximum (FWHM) of the EPR distance distributions. In almost all cases, the DTT-MeS has a smaller distribution width (SD or FWHM) than other hydroxylated oligomers, with the exception of (DTT-G)₂.*

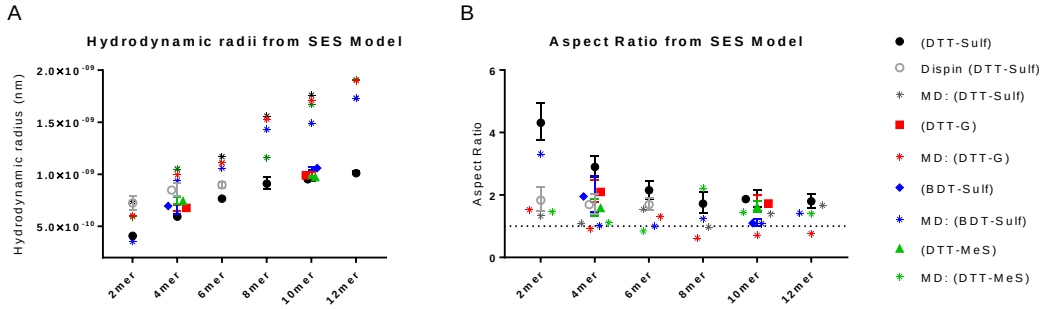

Figure B-6: *Hydrodynamic radii and aspect ratio results from SES model*
This SES model utilizes the rod model assuming the end-to-end distance data describes the long dimension (length) of the rod. ***A.*** *Hydrodynamic radii results derived from the DEER data (solid lines) and MD (dashed lines).* ***B.*** *The aspect ratio calculated simultaneously in the SES solution. The PEG3 is also reported from an additional control experiment. In both graphs, the error bars represent the distribution propagated through the SES model (SD from MD, FWHM from DEER).*

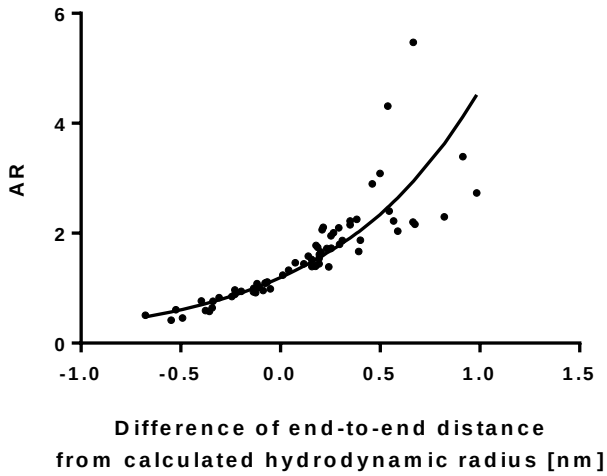

Figure B-7: *Aspect ratio versus difference in experiment size measurements*
The correlation between the difference of the end-to-end distance from DEER or MD input into the SES model (solved in MATLAB) and the calculated hydrodynamic radius versus the aspect ratio. An exponential fit is shown for illustration. This correlation demystifies the SES method by showing that the end-to-end distance as it differs from the hydrodynamic radius produces the aspect ratio. Thus, the accuracy of the end-to-end distance measurement is very important to measure an accurate aspect ratio.

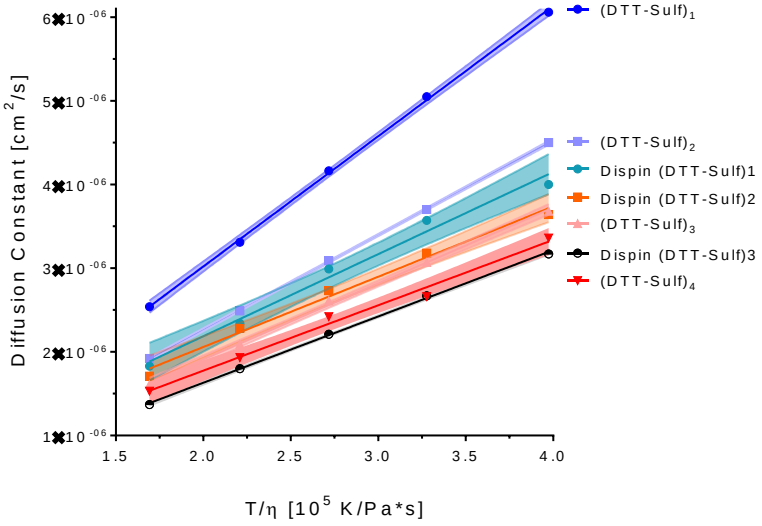

Figure B-8: *PFG-NMR of dispin-labeled (DTT-Sulf)1-3 vs regular scaffold*
Variable temperature diffusion measurement of 1-3 mM regular and dispin labeled (DTT-Sulf) oligomers in D_2O.

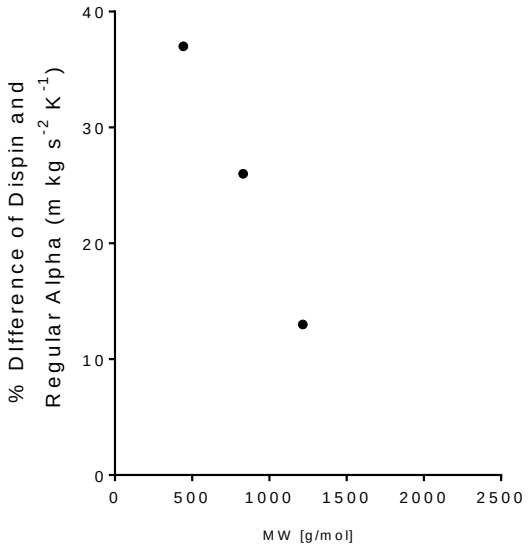

Figure B-9: *PFG-NMR difference between dispin and regular oligomers. This data demonstrates a significant increase at low oligomer lengths, where the spin label contributes significantly to the oligomer diffusion.*

Supplementary Spectra (EPR, CD, NMR, LCMS)

Note: All figure caption and descriptions are below the figure itself.

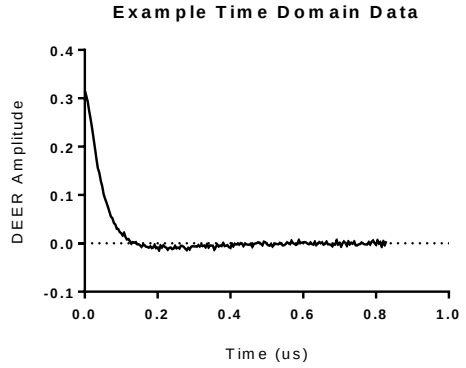

Example time domain data collected from DEER of 100 uM dispin labeled oligoTEAs in 20% ethylene glycol vitrified to 70K from room temperature.

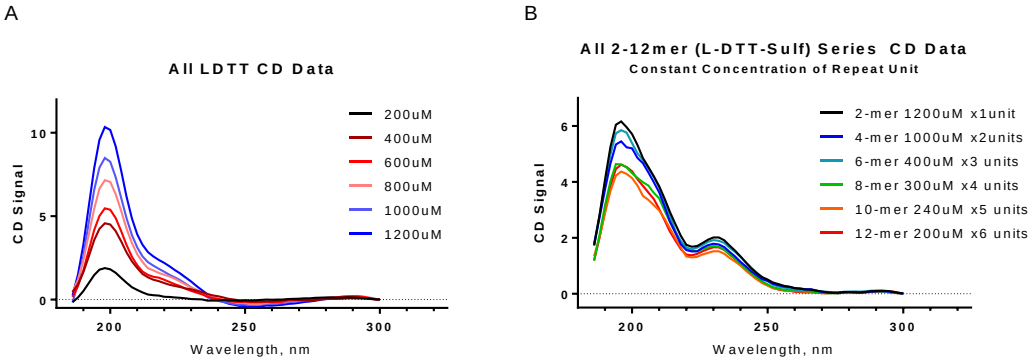

Oligomers were synthesized with L(-)-DTT as described, purified by HPLC, and measured with circular dichroism (CD), showing chirality of monomer units is maintained during synthesis. ***A.*** *Circular dichroism data of L(-)-DTT as a control and* ***B.*** *2-12mer sulfonated hydroxylated oligoTEAs at room temperature in water. The oligoTEA CD can be normalized by the concentration of the repeat unit of thiolene and Michael addition cycle. The L(-)-DTT has clear signals on its own at 200 and 220 nm, which are slightly modified when incorporated in to the oligomer, which shows signals at 200 and 232 nm. There is not any evolution of the CD signal as a function of synthetic length, indicating no clear secondary structure is developed.*

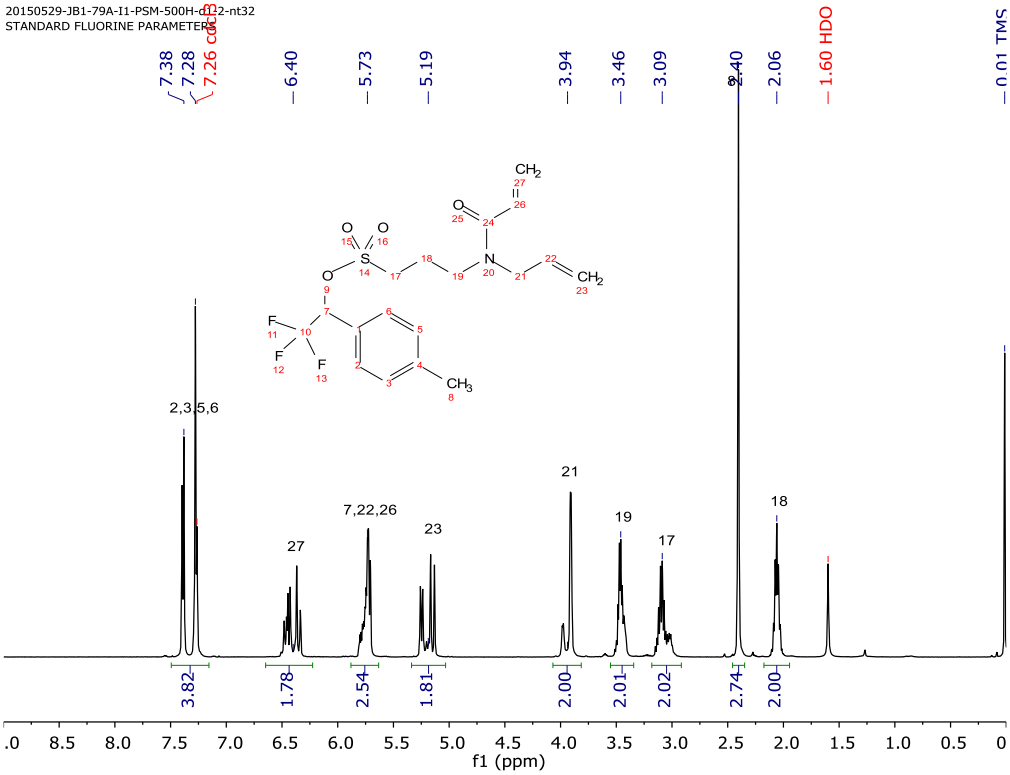

^{1}H NMR of the protected sulfonate N-allyl acrylamide monomer (PSM) in d-chloroform.

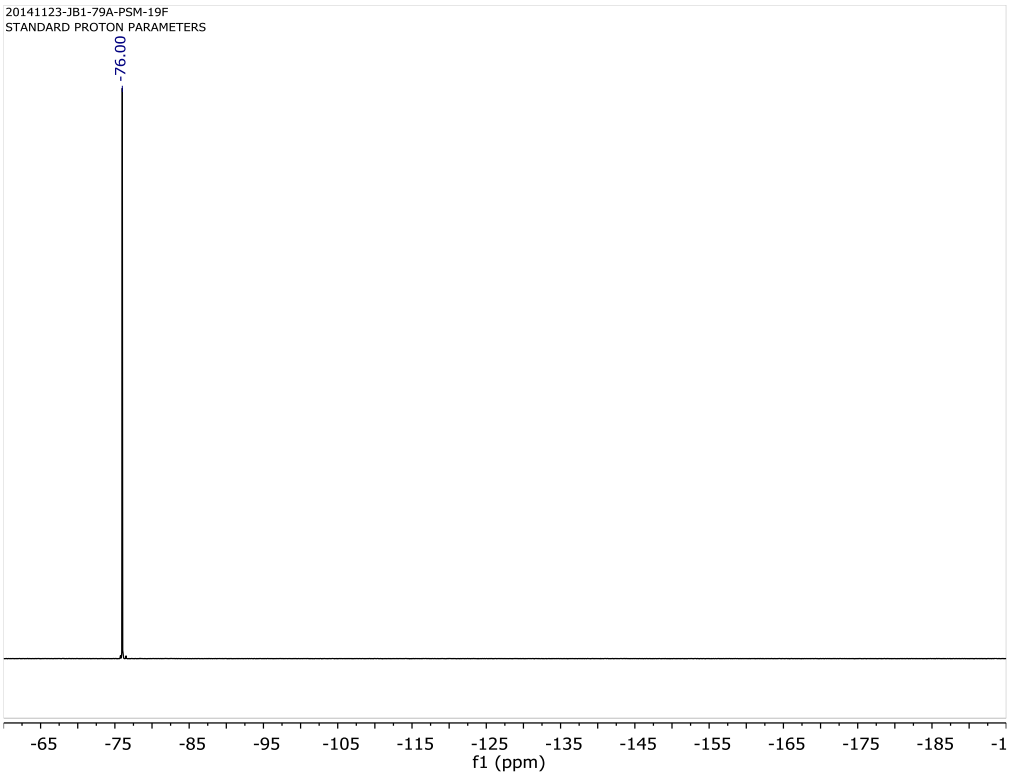

^{19}F NMR of the PSM in d-chloroform.

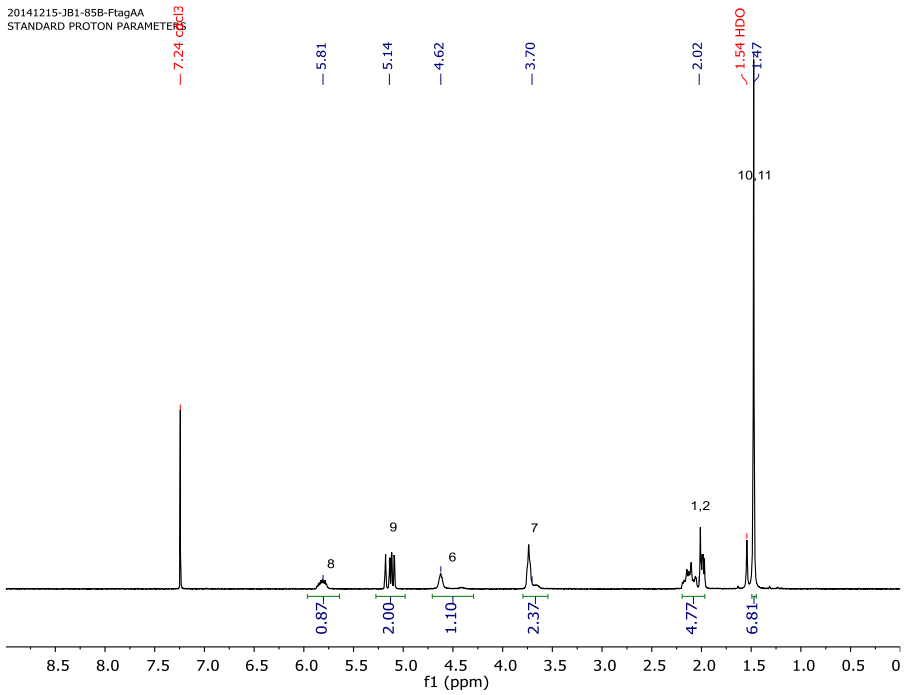

^{1}H NMR of "fluorous allyl amine" or 5,6,6,7,7,8,8,9,9,9-decafluoro-2-methyl-5-(perfluorobutyl)nonan-2-yl allylcarbamate in d-chloroform.

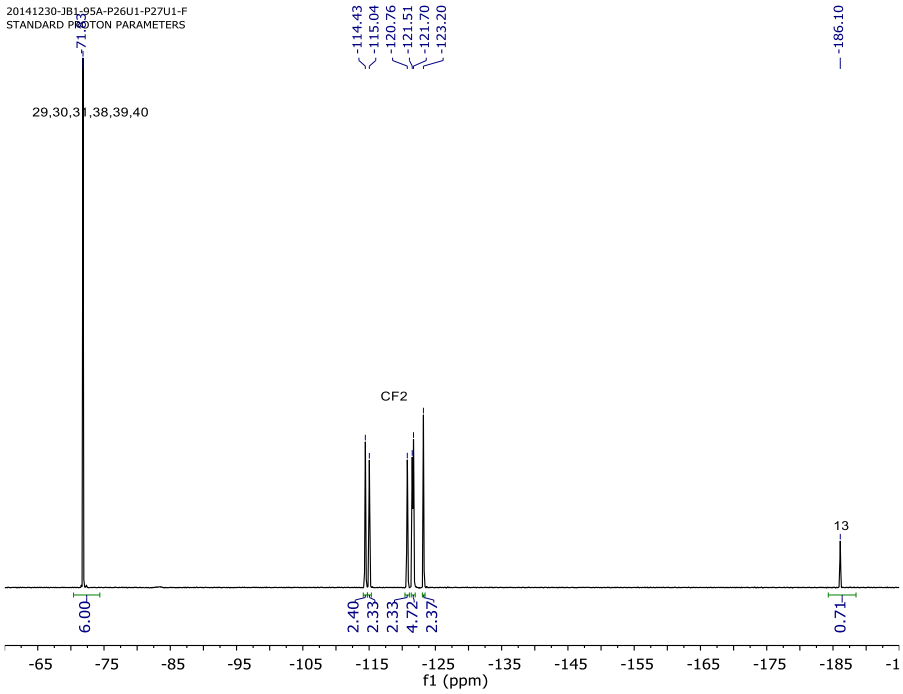

[19]F NMR of "fluorous allyl amine" or 5,6,6,7,7,8,8,9,9,9-decafluoro-2-methyl-5-(perfluorobutyl)nonan-2-yl allylcarbamate in d-chloroform.

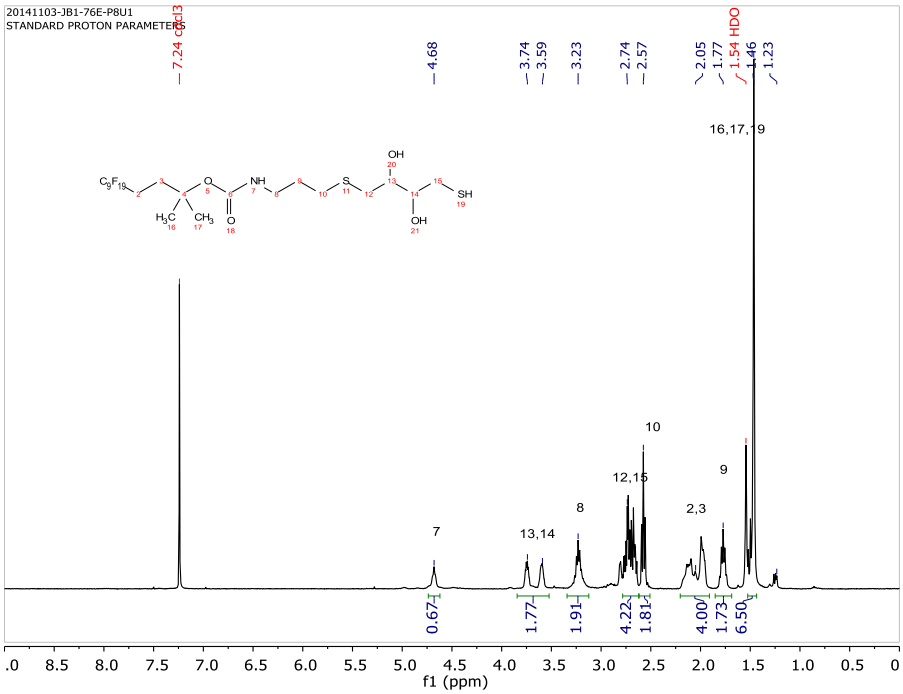

[1]H NMR of "fluorous DTT" the fluorous purified product of the thiolene reaction of fluorous allyl amine and DTT in d-chloroform. Note the disappearance of the allyl peaks.

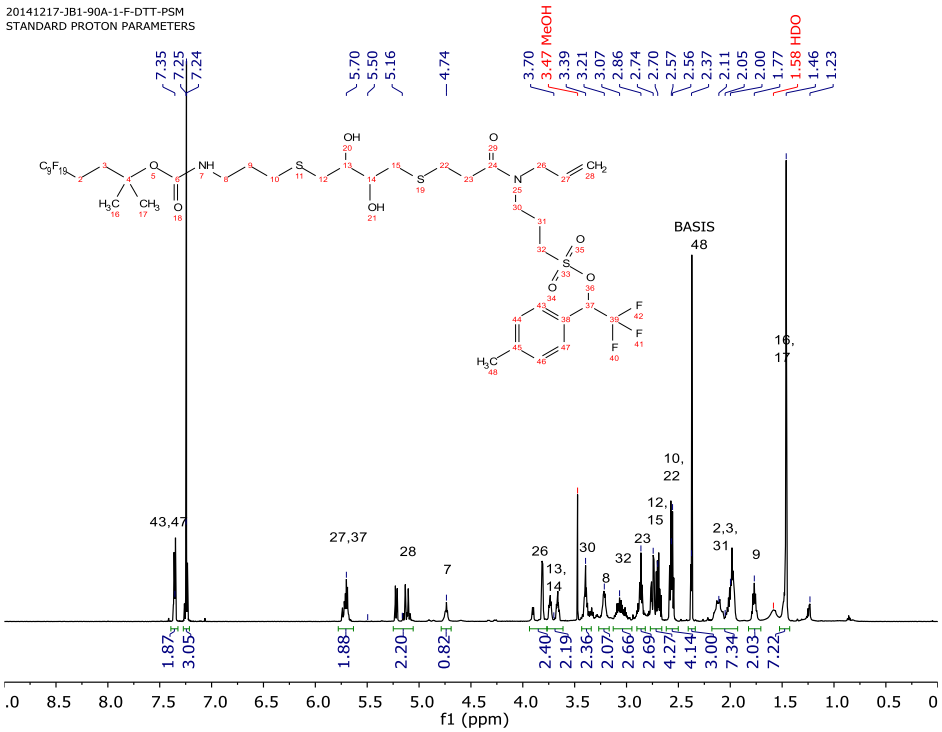

[1]H NMR of "fluorous DTT-PSM" the FSPE purified product of fluorous DTT and the protected sulfonate allyl acrylamide monomer thiol-Michael in d-chloroform. Note the allyl peaks.

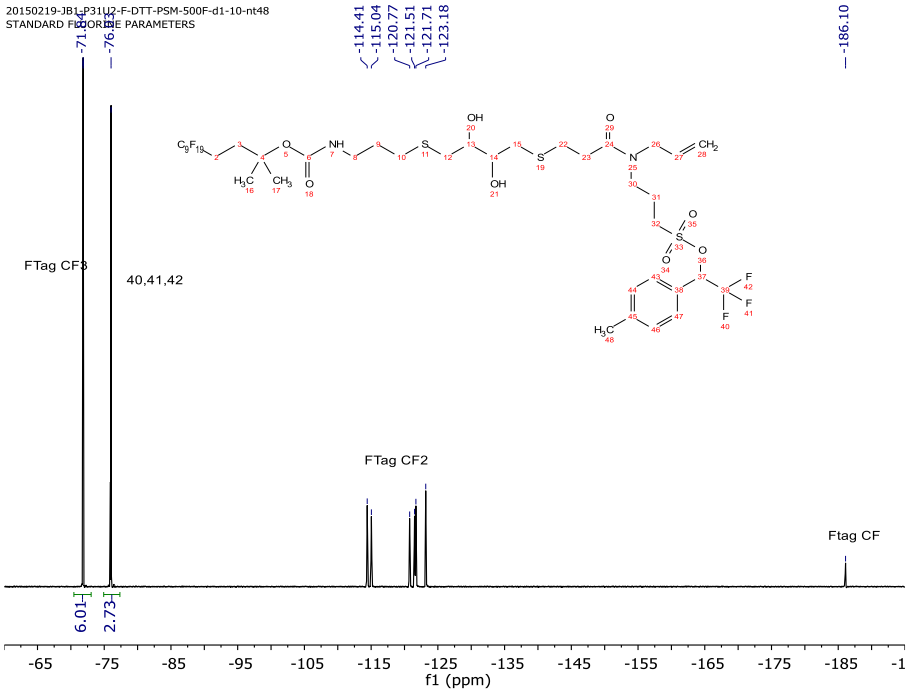

[19]F NMR of "fluorous DTT-PSM" in d-chloroform. Note the PSM trifluoro peaks.

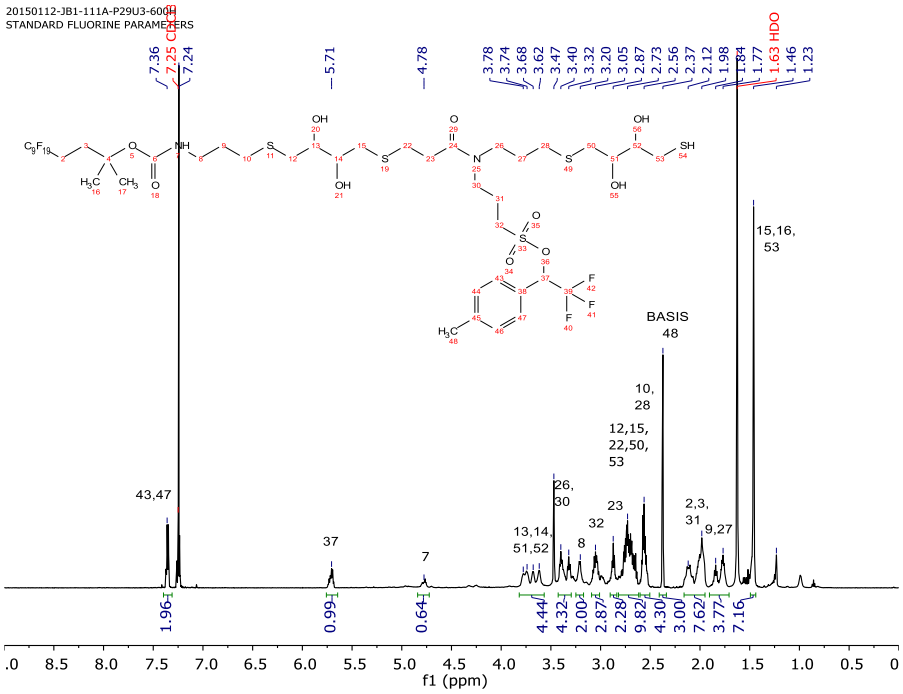

^{1}H NMR of "fluorous DTT-PSM-DTT" the fluorous purified product of the thiolene of the fluorous DTT-PSM and DTT in d-chloroform. Note the disappearance of the allyl peaks.

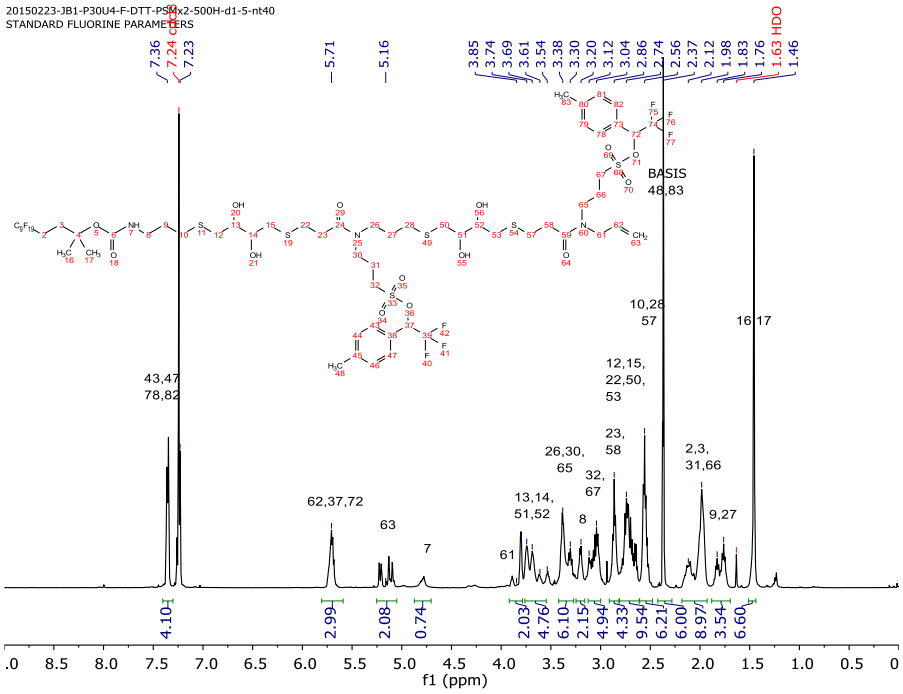

^{1}H NMR of "fluorous (DTT-PSM)$_2$" the fluorous purified product of the thiol-Michael of the fluorous DTT-PSM-DTT and the PSM in d-chloroform. Note the allyl peaks.

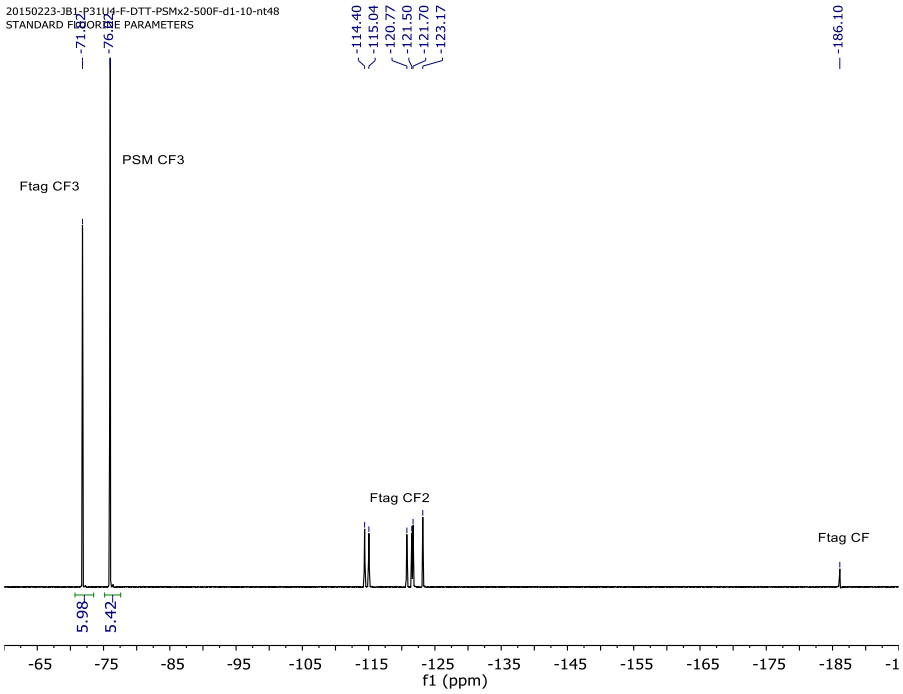

^{19}F NMR of "fluorous (DTT-PSM)$_2$" the fluorous purified product of the thiol-Michael of the fluorous DTT-PSM-DTT and the PSM in d-chloroform.

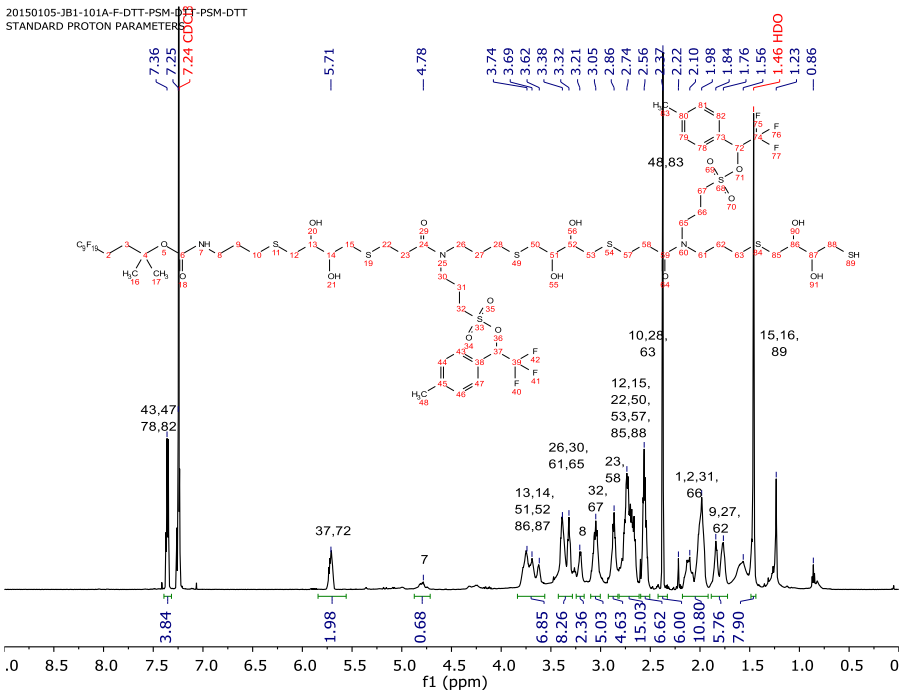

^{1}H NMR of "fluorous (DTT-PSM)$_2$-DTT" the fluorous purified product of the thiolene of the fluorous (DTT-PSM)$_2$ and DTT in d-chloroform. Note the disappearance of the allyl peaks.

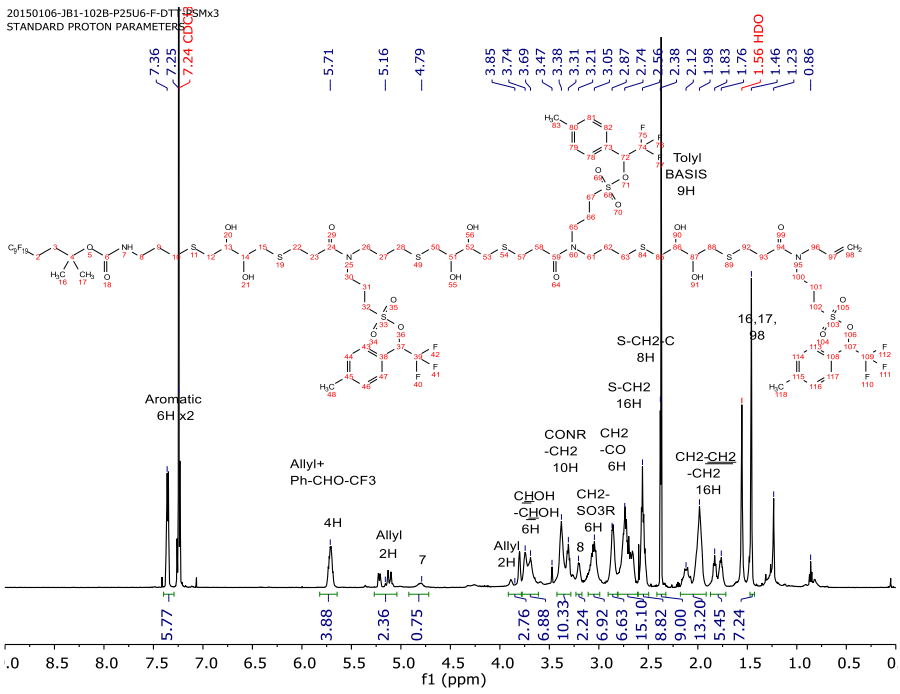

^{1}H NMR of "fluorous (DTT-PSM)$_3$" the fluorous purified product of the thiol-Michael of the fluorous (DTT-PSM)$_2$-DTT and the PSM in d-chloroform. Note the allyl peaks.

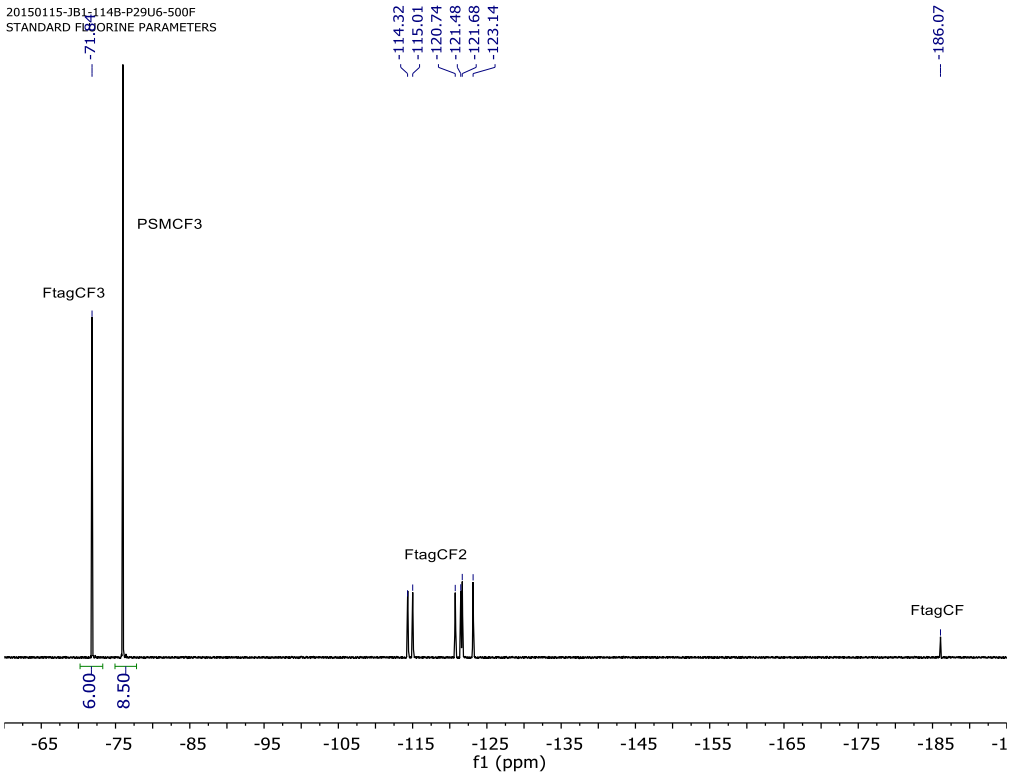

^{19}F NMR of "fluorous (DTT-PSM)$_3$" the fluorous purified product of the thiol-Michael of the fluorous (DTT-PSM)$_2$-DTT and the PSM in d-chloroform.

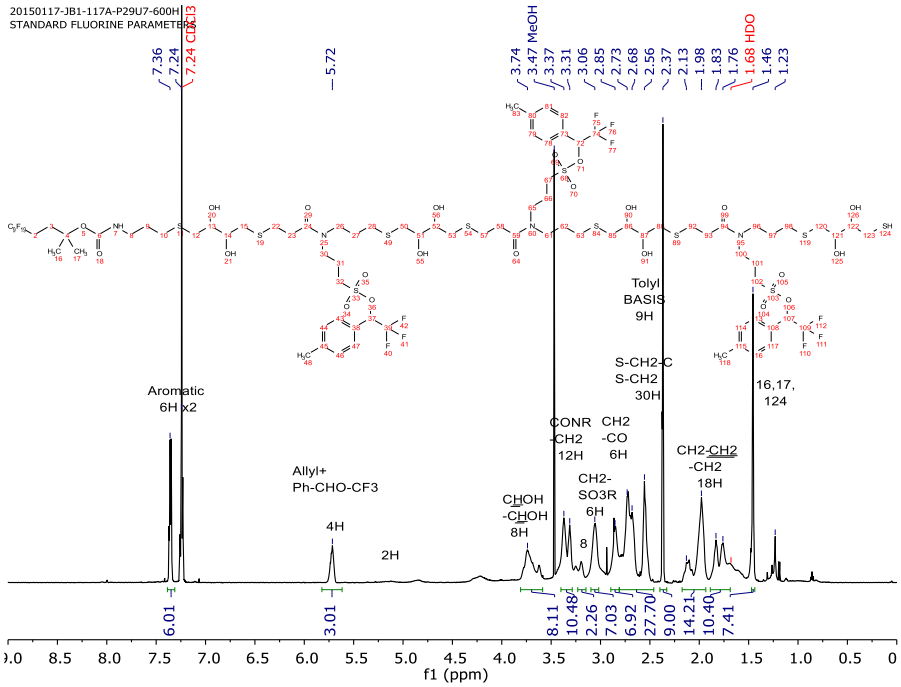

^{1}H NMR of "fluorous (DTT-PSM)$_3$-DTT" the fluorous purified product of the thiolene of the fluorous (DTT-PSM)$_3$ and DTT in d-chloroform. Note the disappearance of the allyl peaks.

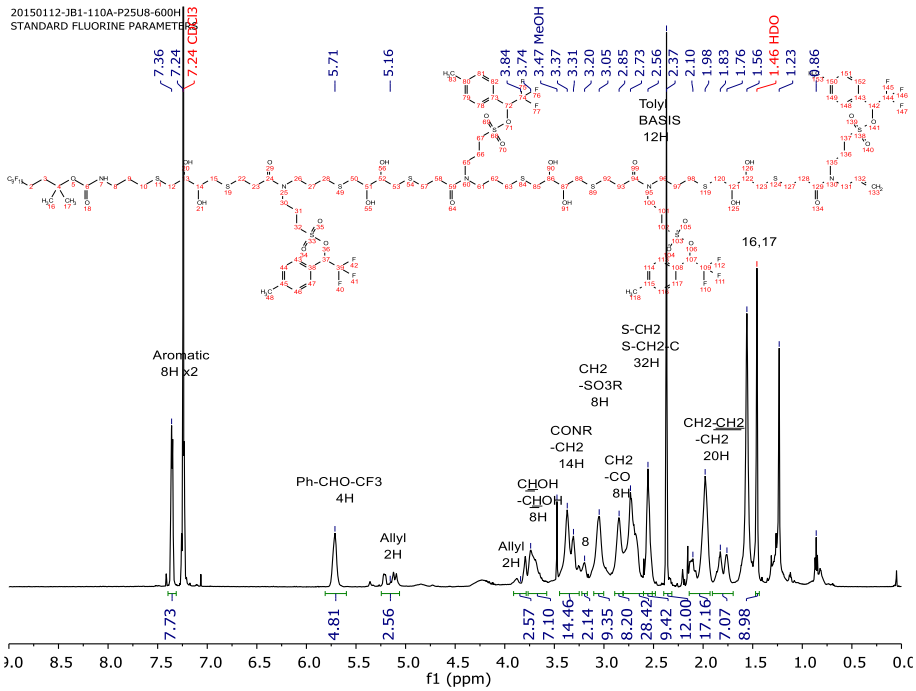

^{1}H NMR of "fluorous (DTT-PSM)$_4$" the fluorous purified product of the thiol-Michael of the fluorous (DTT-PSM)$_3$-DTT and the PSM in d-chloroform. Note the allyl peaks.

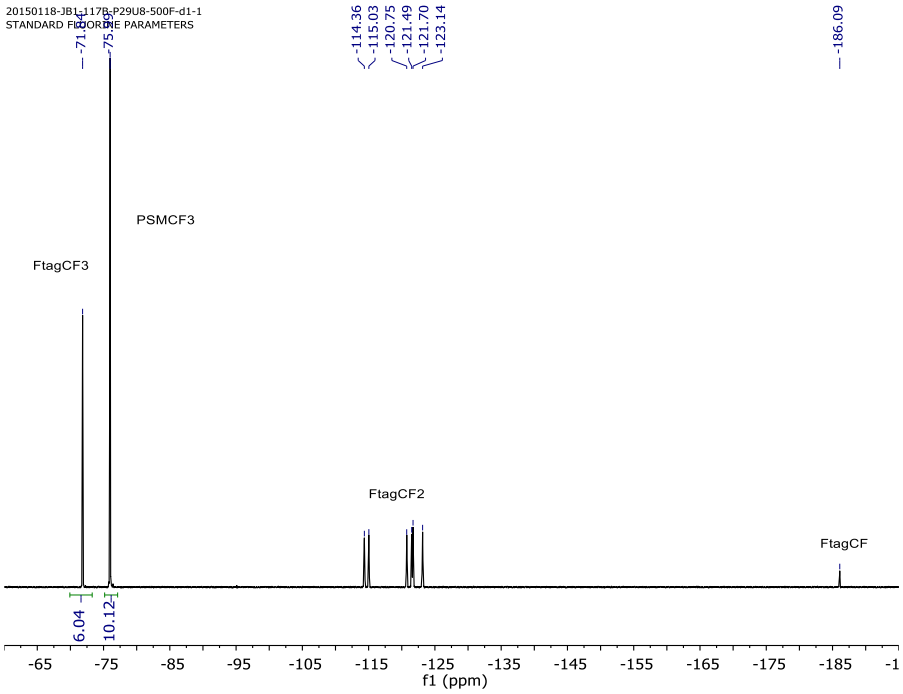

^{19}F NMR of "fluorous (DTT-PSM)$_4$" the fluorous purified product of the thiol-Michael of the fluorous (DTT-PSM)$_3$-DTT and the PSM in d-chloroform.

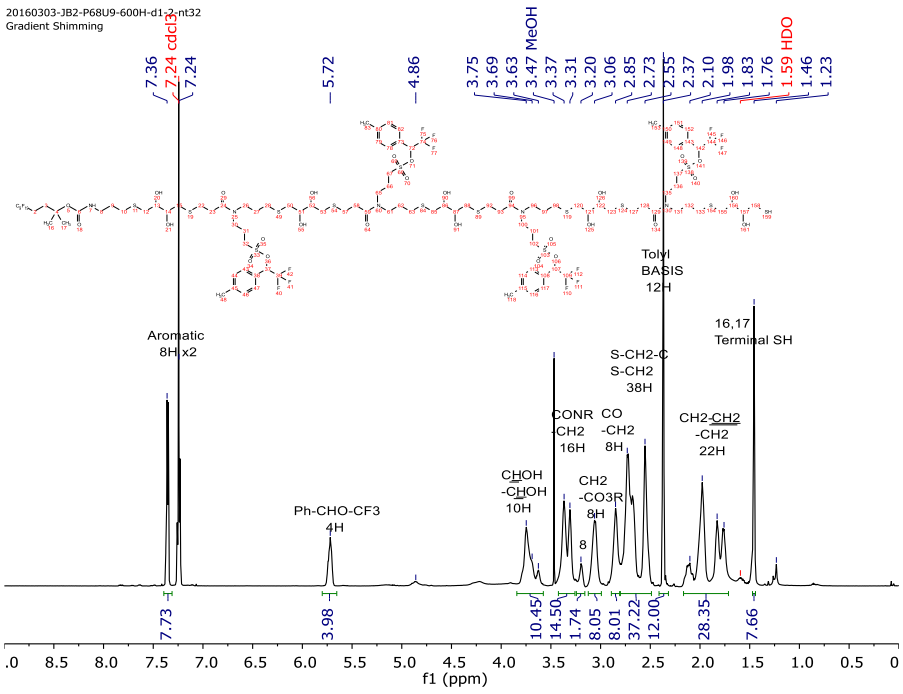

^{1}H NMR of "fluorous (DTT-PSM)$_4$-DTT" the fluorous purified product of the thiolene of the fluorous (DTT-PSM)$_4$ and DTT in d-chloroform. Note the disappearance of the allyl peaks.

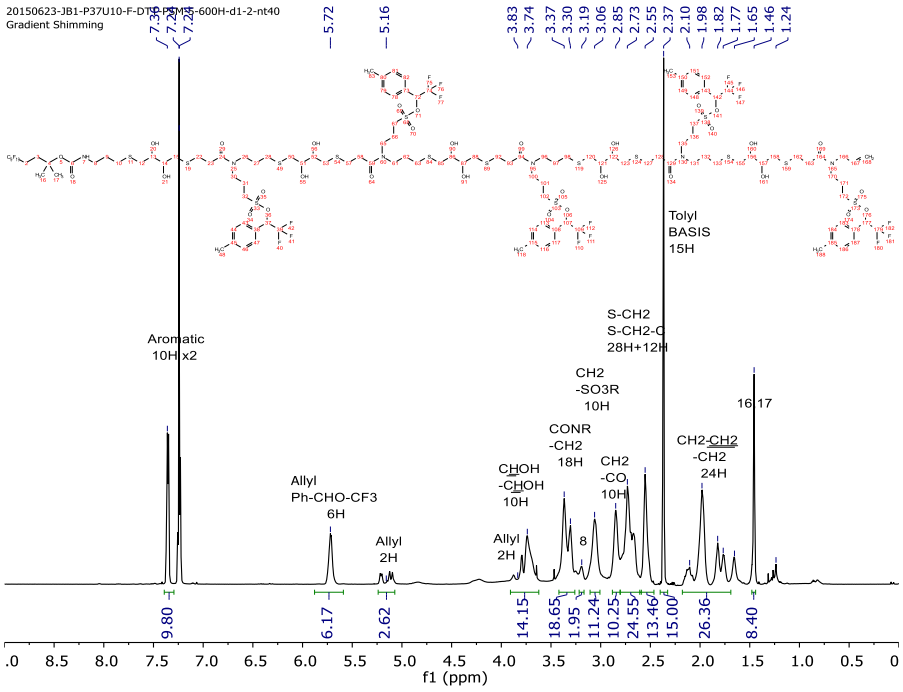

^{1}H NMR of "fluorous (DTT-PSM)$_5$" the fluorous purified product of the thiol-Michael of the fluorous (DTT-PSM)$_4$-DTT and the PSM in d-chloroform. Note the allyl peaks.

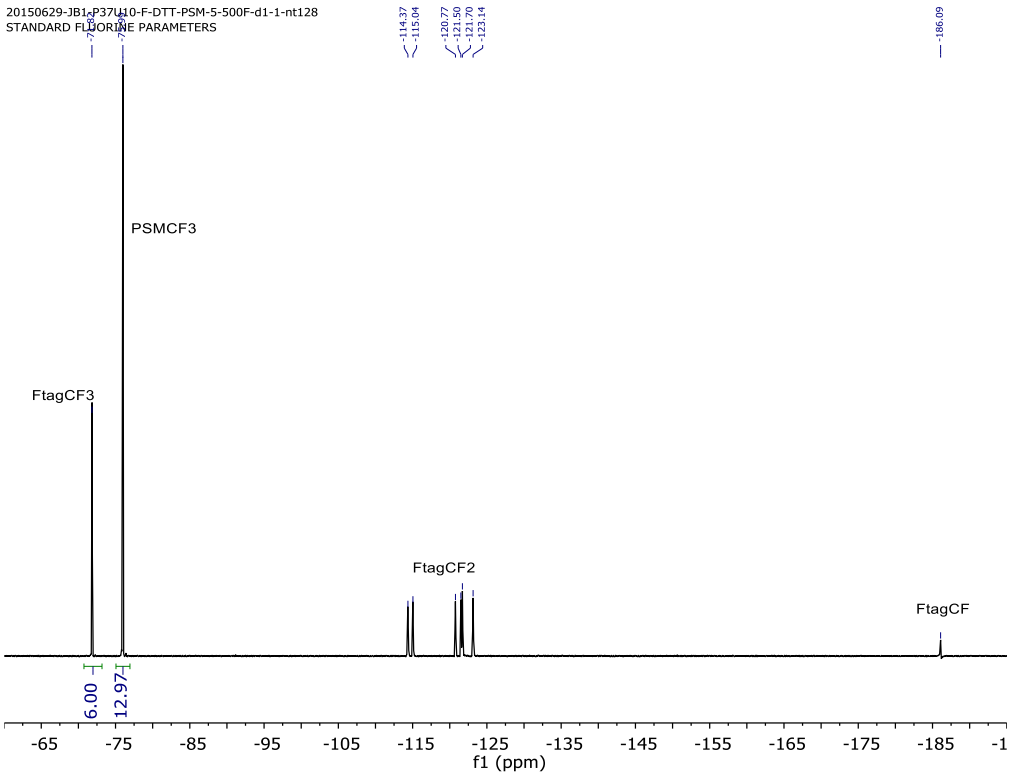

^{19}F NMR of "fluorous (DTT-PSM)$_5$" the fluorous purified product of the thiol-Michael of the fluorous (DTT-PSM)$_4$-DTT and the PSM in d-chloroform.

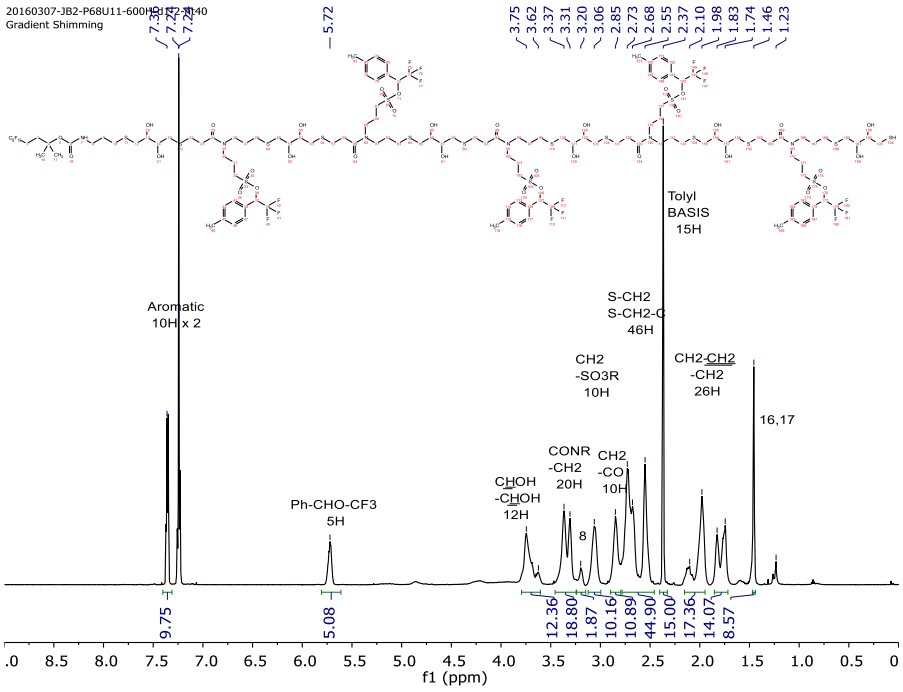

^{1}H NMR of "fluorous (DTT-PSM)$_5$-DTT" the fluorous purified product of the thiolene of the fluorous (DTT-PSM)$_5$ and DTT in d-chloroform. Note the disappearance of the allyl peaks.

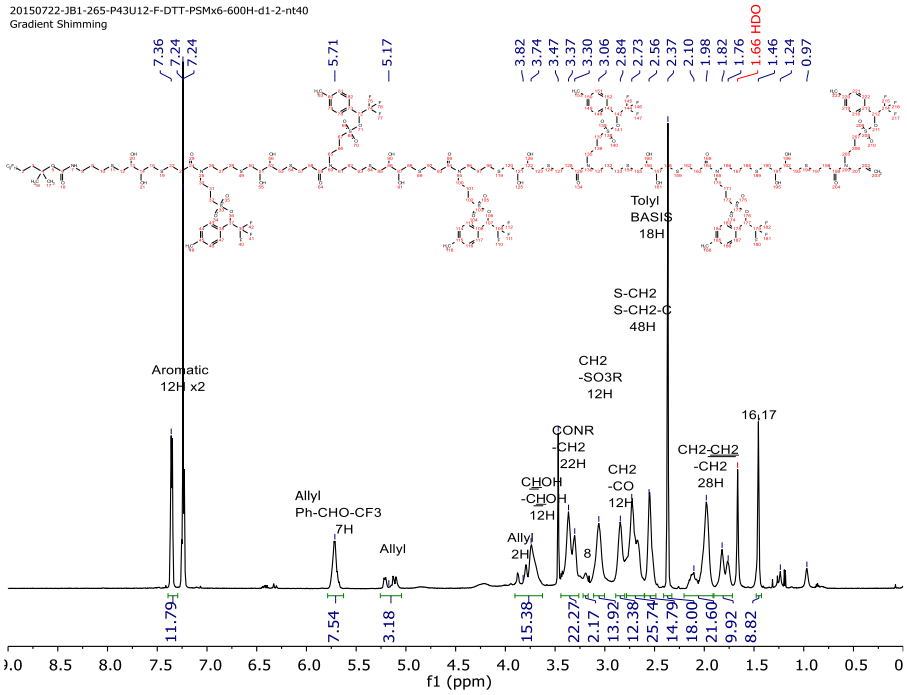

^{1}H NMR of "fluorous (DTT-PSM)$_6$" the fluorous purified product of the thiol-Michael of the fluorous (DTT-PSM)$_5$-DTT and PSM in d-chloroform. The appearance of small allyl peaks and acrylamide peaks indicates a small amount of PSM remains.

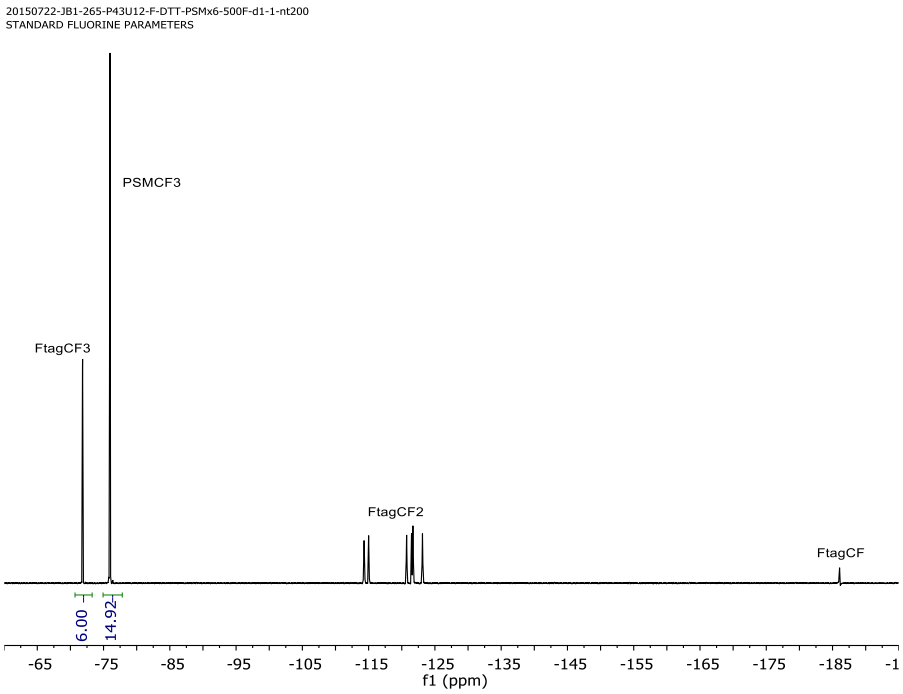

^{19}F NMR of "fluorous (DTT-PSM)$_6$" the fluorous purified product of the thiol-Michael of the fluorous (DTT-PSM)$_6$-DTT and the PSM in d-chloroform.

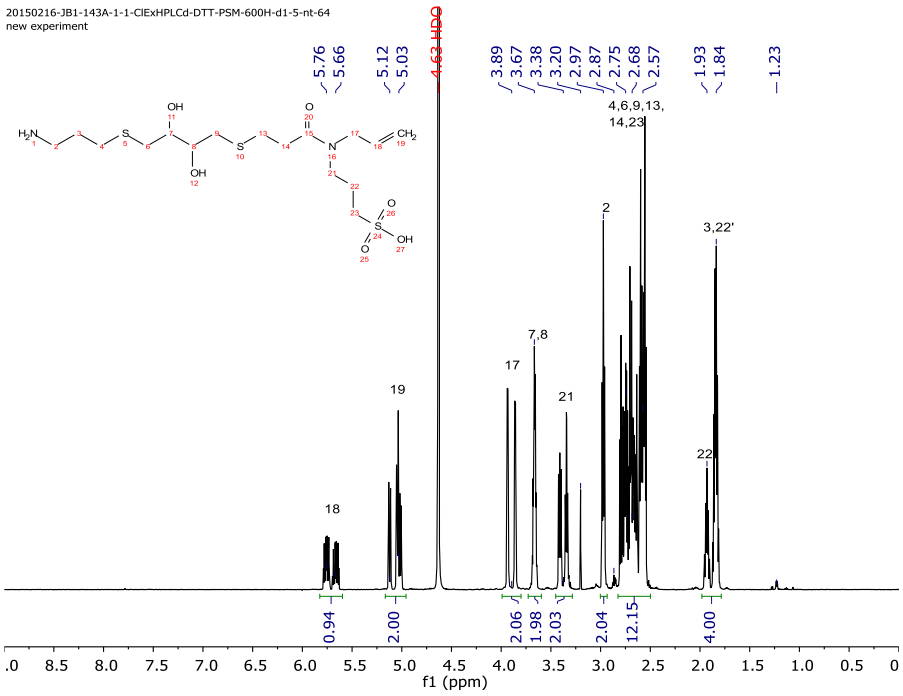

^{1}H NMR of the "2mer," the NH$_2$-(DTT-PSM)$_1$ product in deuterated water obtained from the TFA-cleavage of the fluorous-DTT-PSM after HPLC purification.

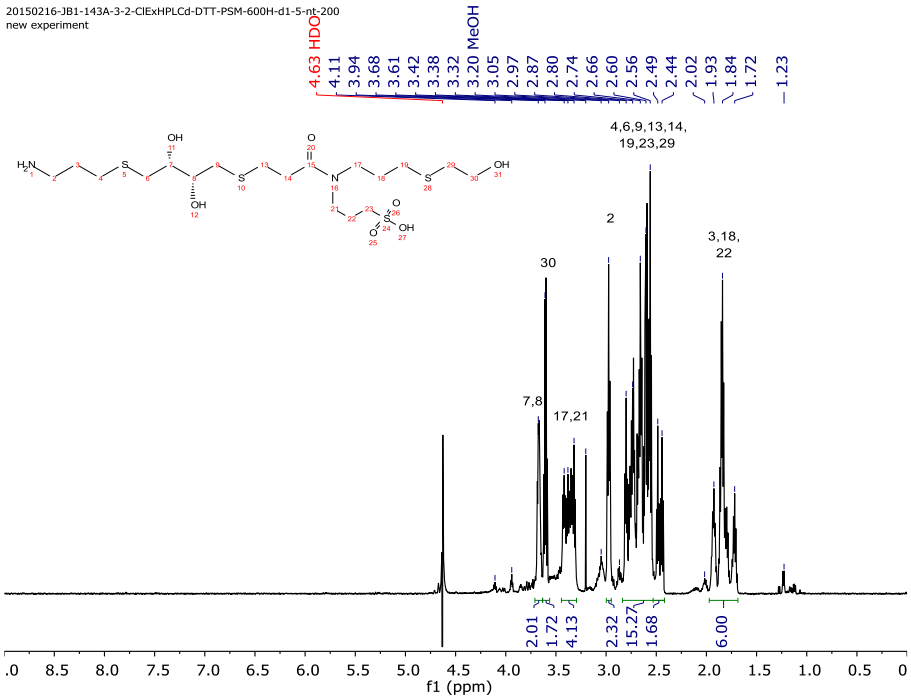

^{1}H NMR of a "3mer" in deuterated water with solvent suppression on the HDO peak, where the fluorous-DTT-PSM was reacted with 2-mercaptoethanol (BME), fluorous and HPLC purified. This was prepared to understand other oligomer assignments.

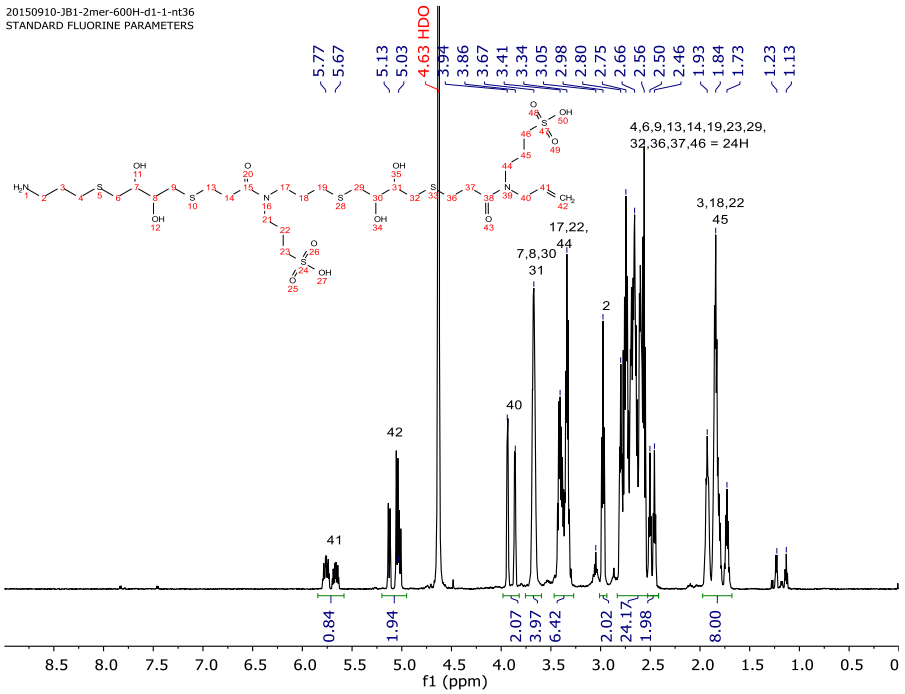

^{1}H NMR of the "4mer," the NH$_2$-(DTT-PSM)$_2$ product in deuterated water obtained from the TFA-cleavage of the fluorous-(DTT-PSM)$_2$ after HPLC purification.

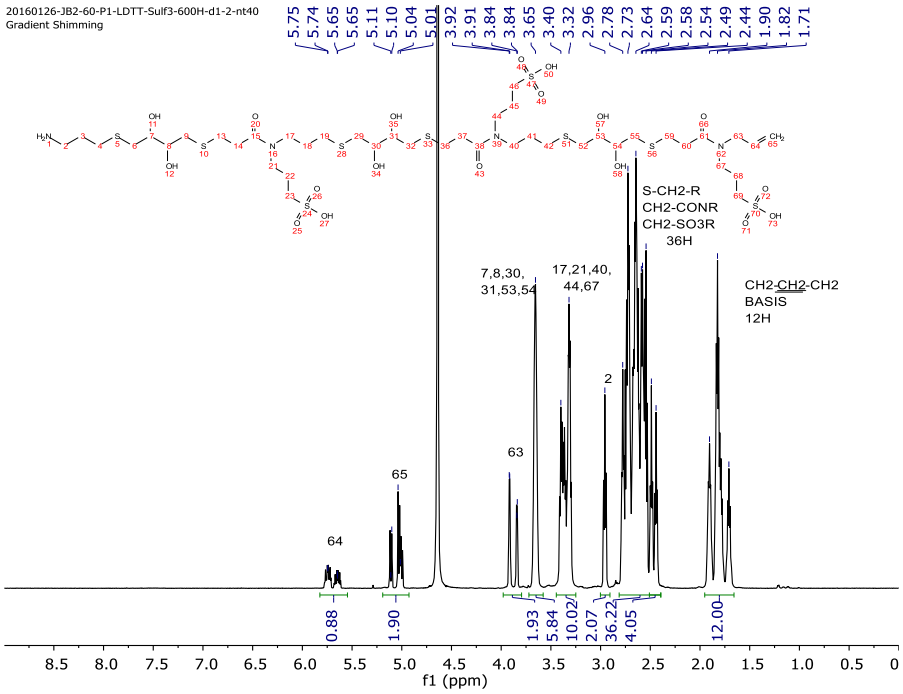

^{1}H NMR of the "6mer," the NH_2-(DTT-PSM)$_3$ product in deuterated water obtained from the TFA-cleavage of the fluorous-(DTT-PSM)$_3$ after HPLC purification.

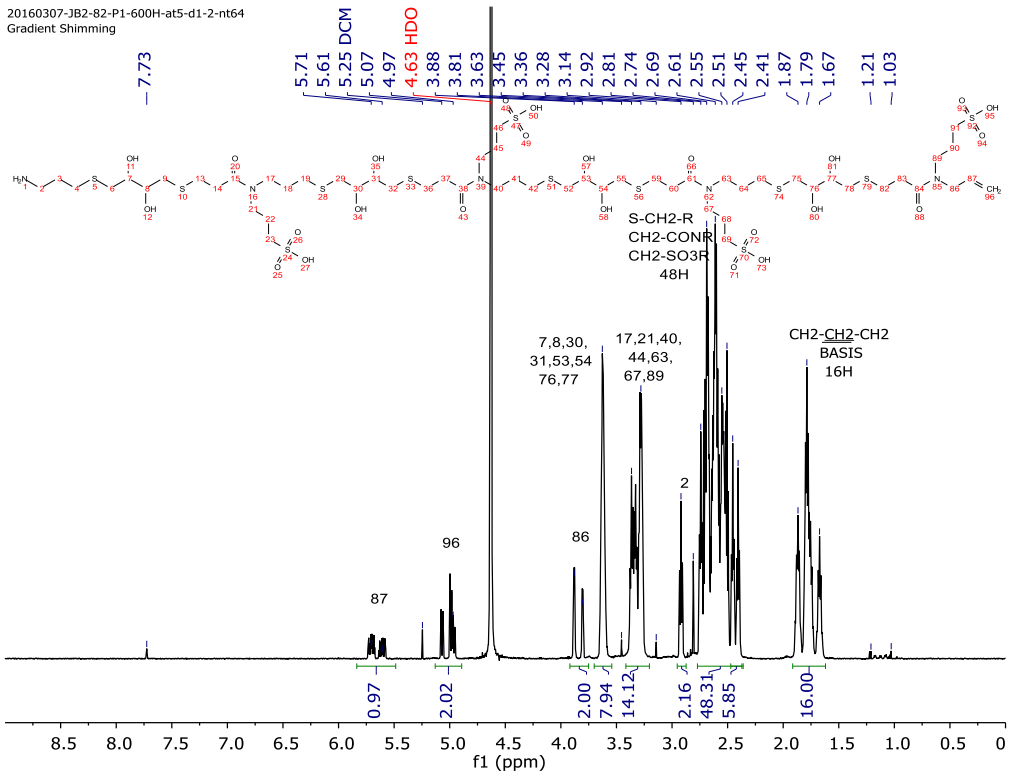

^{1}H NMR of the "8mer," the NH_2-(DTT-PSM)$_4$ product in deuterated water obtained from the TFA-cleavage of the fluorous-(DTT-PSM)$_4$ after HPLC purification.

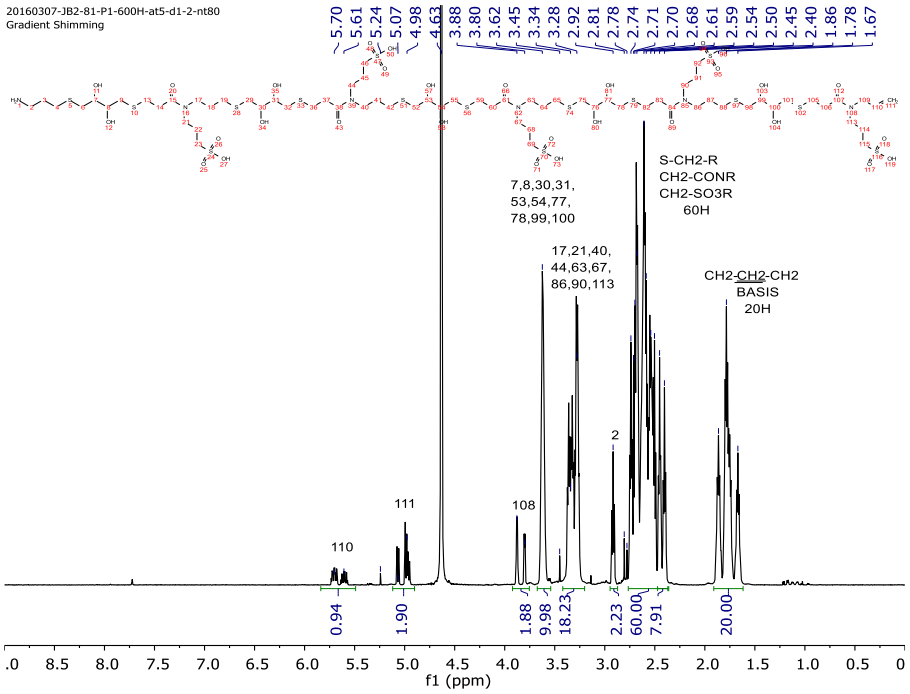

^{1}H NMR of the "10mer," the NH$_2$-(DTT-PSM)$_5$ product in deuterated water obtained from the TFA-cleavage of the fluorous-(DTT-PSM)$_5$ after HPLC purification.

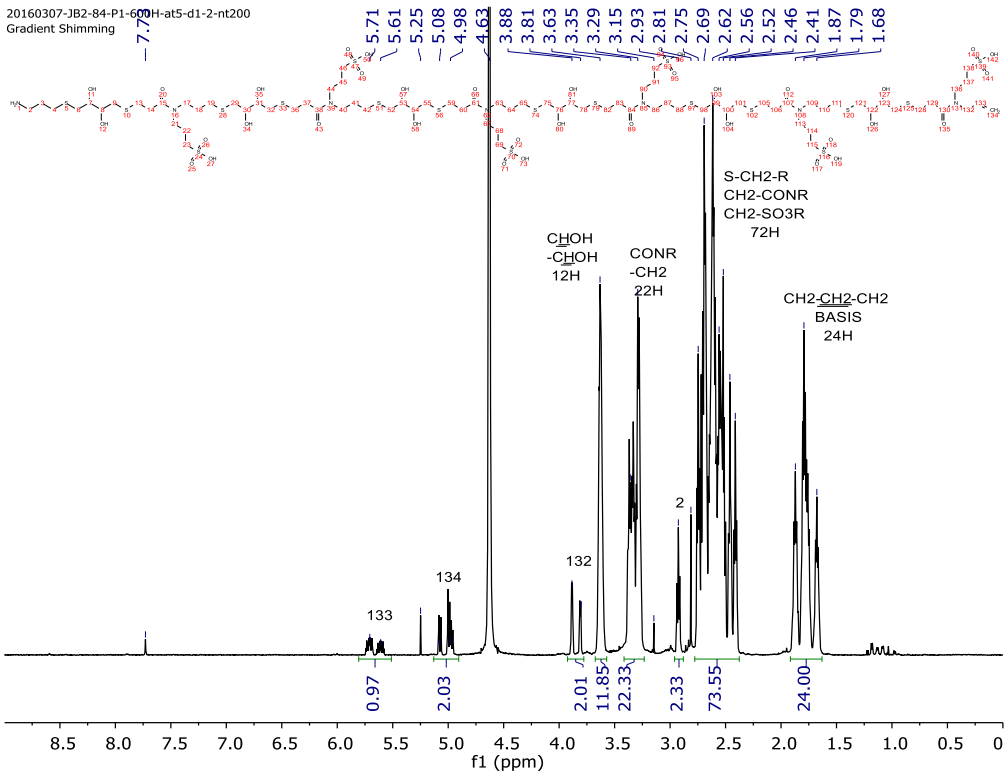

^{1}H NMR of the "12mer," the NH$_2$-(DTT-PSM)$_6$ product in deuterated water obtained from the TFA-cleavage of the fluorous-(DTT-PSM)$_6$ after HPLC purification.

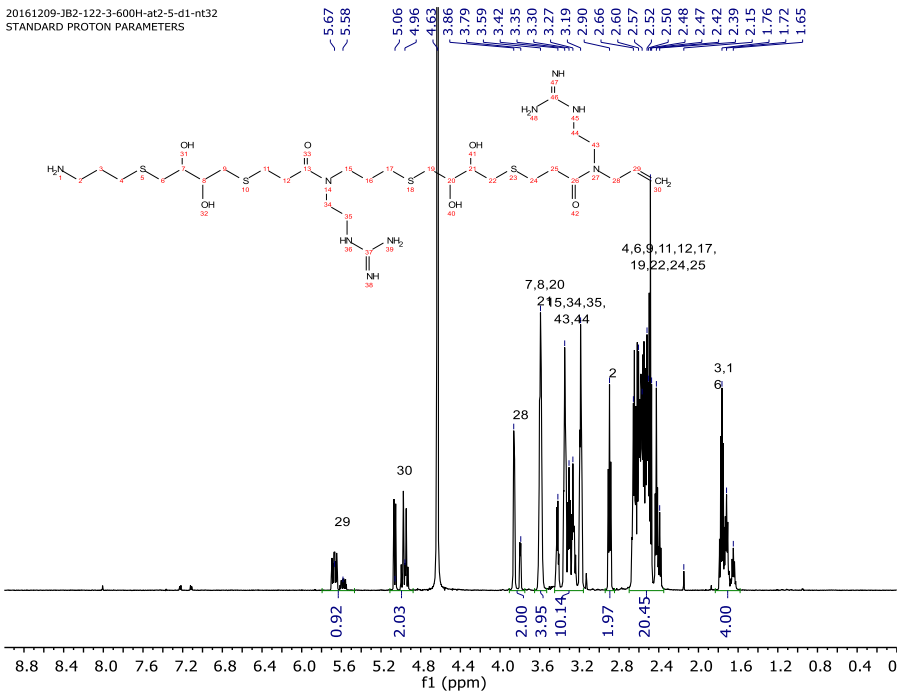

^{1}H NMR of the "4mer" of the NH_2-(DTT-G)$_2$ product in deuterated water obtained from the TFA-cleavage of the fluorous-(DTT-G)$_2$ after HPLC purification.

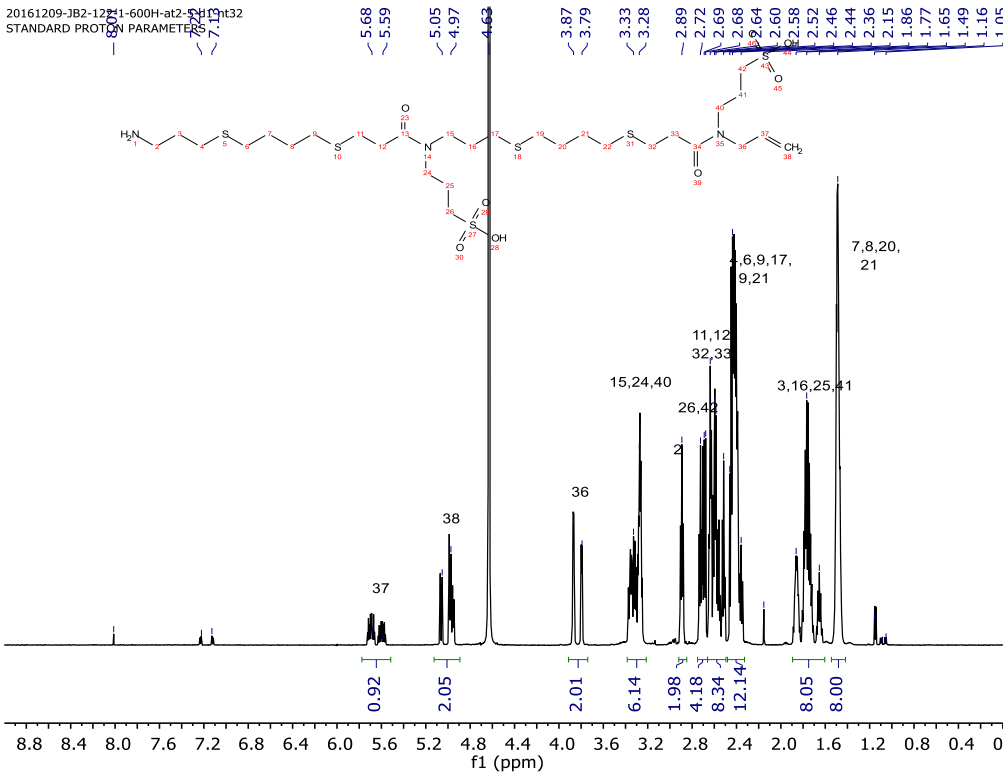

^{1}H NMR of the "4mer" of the NH_2-(BDT-Sulf)$_2$ product in deuterated water obtained from the TFA-cleavage of the fluorous-(BDT-Sulf)$_2$ after HPLC purification.

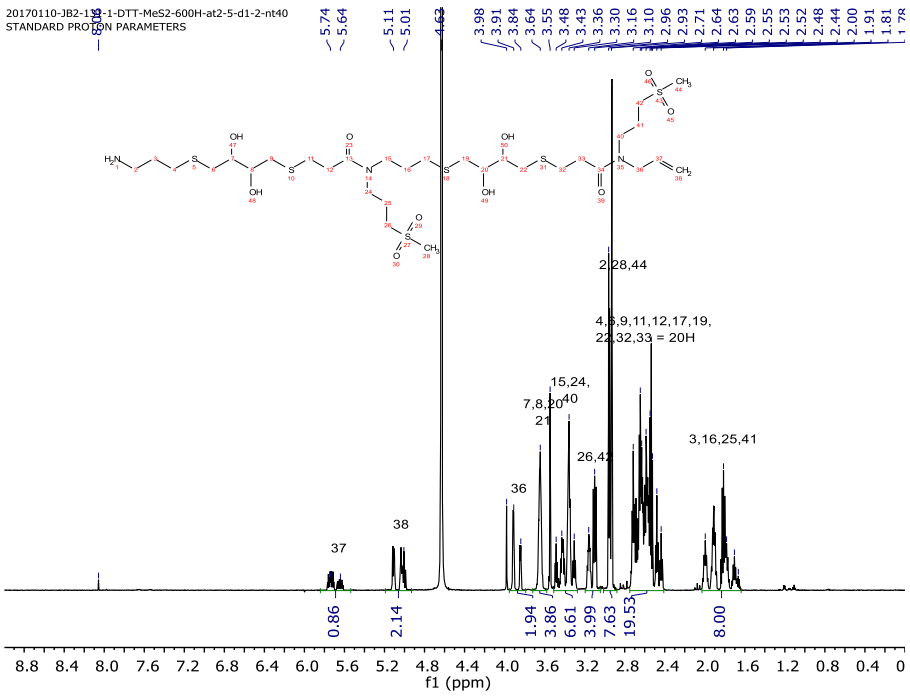

^{1}H NMR of the "4mer" of the NH_2-(DTT-MeS)$_2$ product in deuterated water obtained from the TFA-cleavage of the fluorous-(DTT-MeS)$_2$ after HPLC purification.

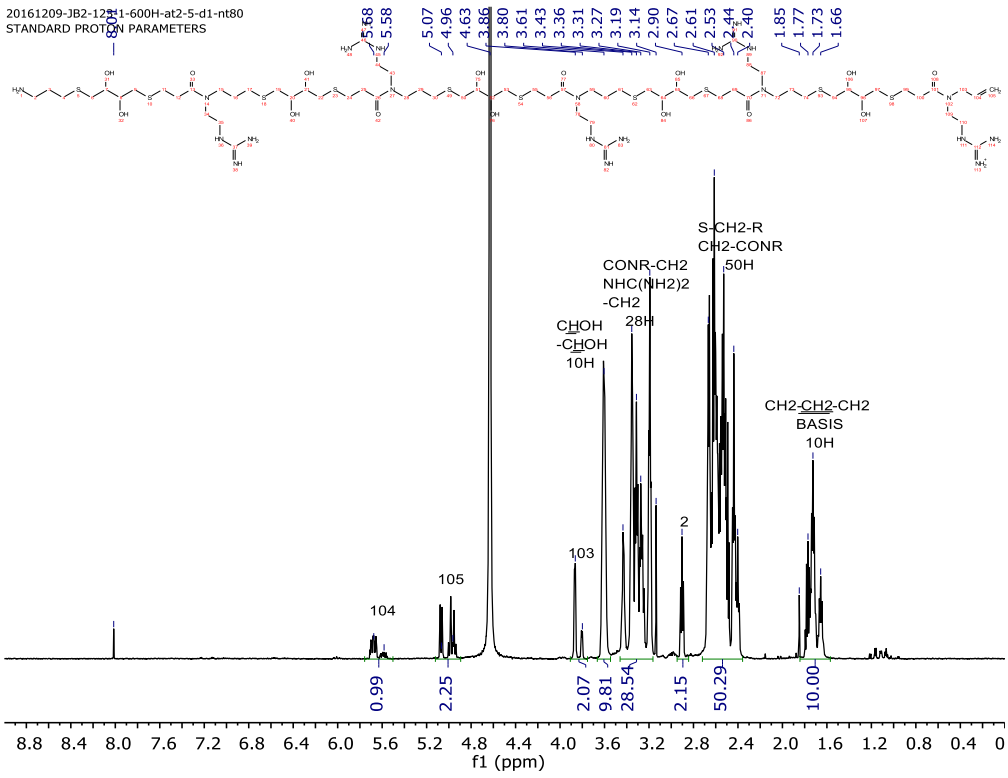

^{1}H NMR of the "10mer" of the NH_2-(DTT-G)$_5$ product in deuterated water obtained from the TFA-cleavage of the fluorous-(DTT-G)$_5$ after HPLC purification.

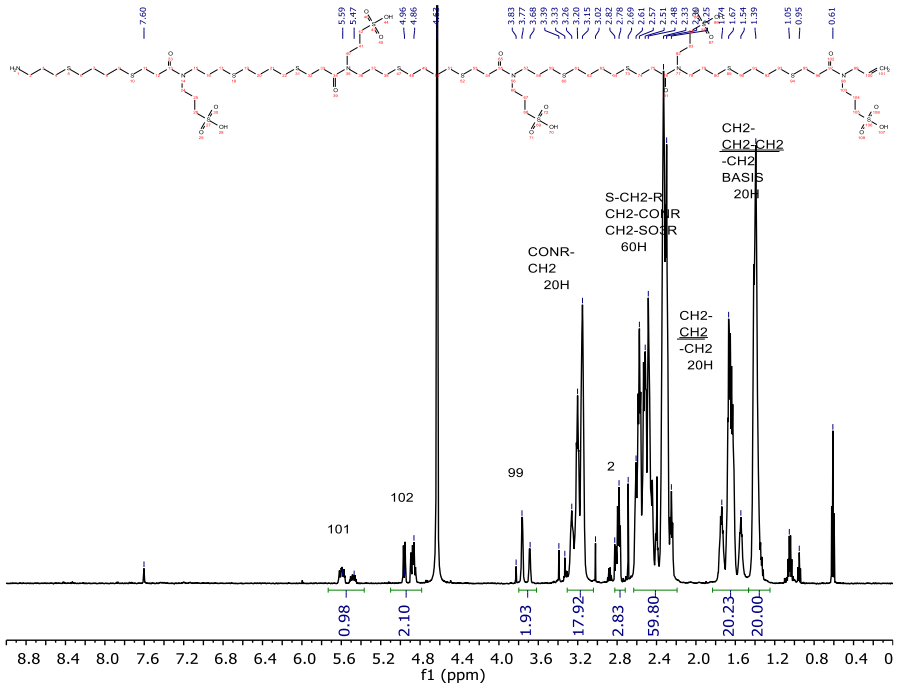

^{1}H NMR of the "10mer" of the NH_2-(BDT-Sulf)$_5$ product in deuterated water obtained from the TFA-cleavage of the fluorous-(BDT-Sulf)$_5$ after HPLC purification.

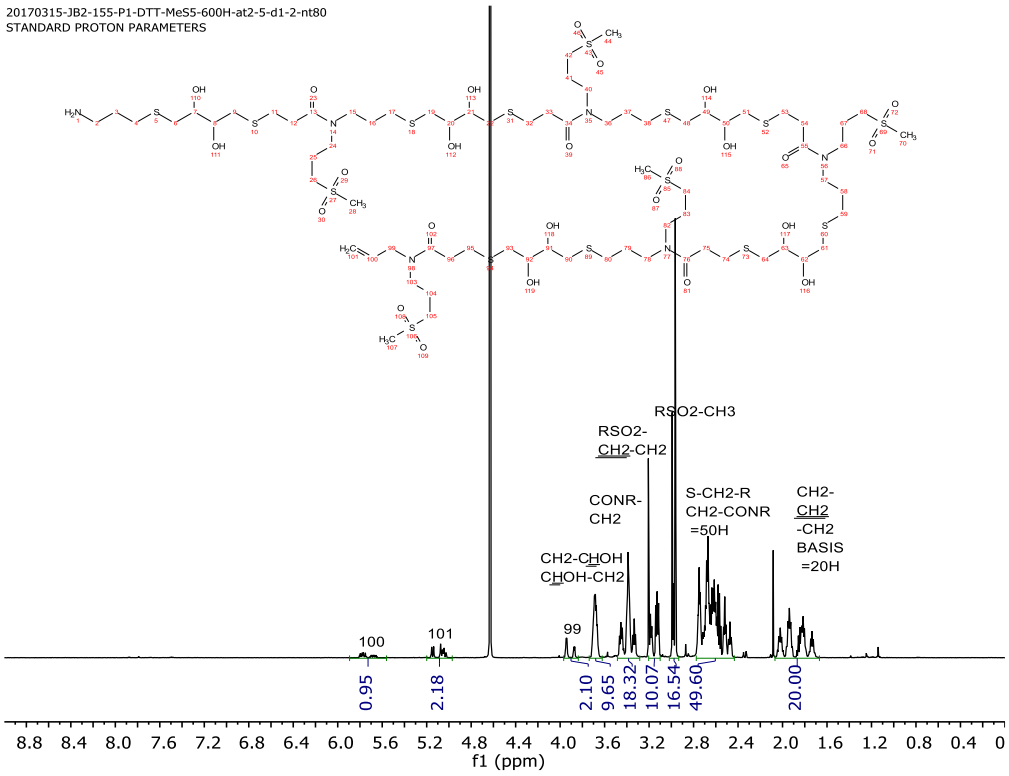

^{1}H NMR of the "10mer" of the NH_2-(DTT-MeS)$_5$ product in deuterated water obtained from the TFA-cleavage of the fluorous-(DTT-MeS)$_5$ after HPLC purification.

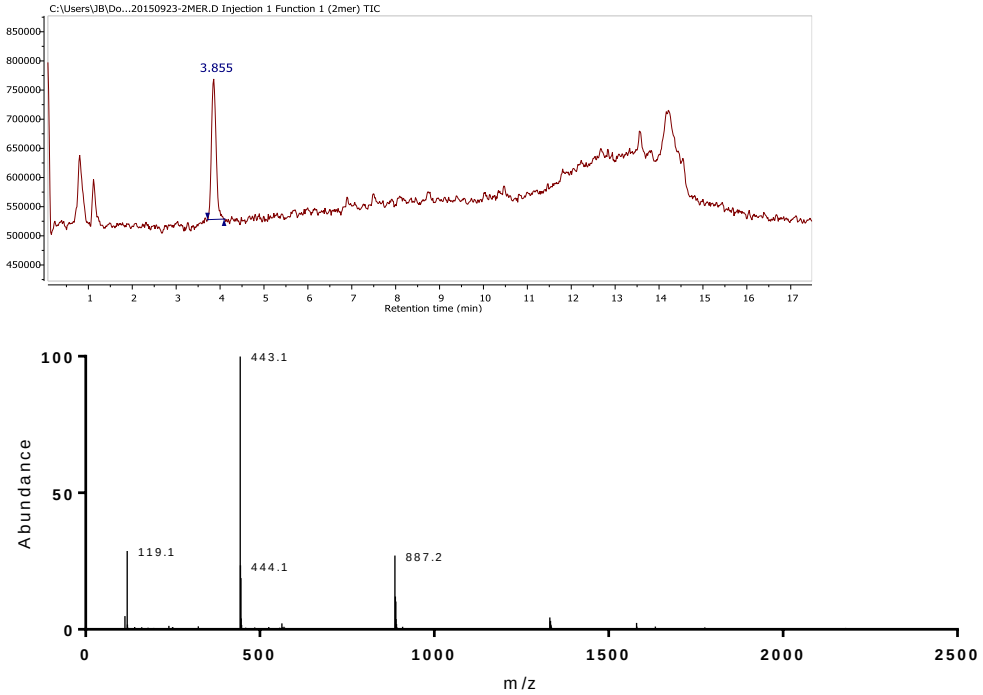

Negative mode LCMS of the (DTT-Sulf)$_1$ with the TIC (top) and the corresponding mass spectra (bottom). Parent mass: 444.14; [M-H]$^{-1}$ Expected: 443.13 Obs. 443.1; [2M-H]$^{-1}$ Expected: 887.27 Obs. 887.2.

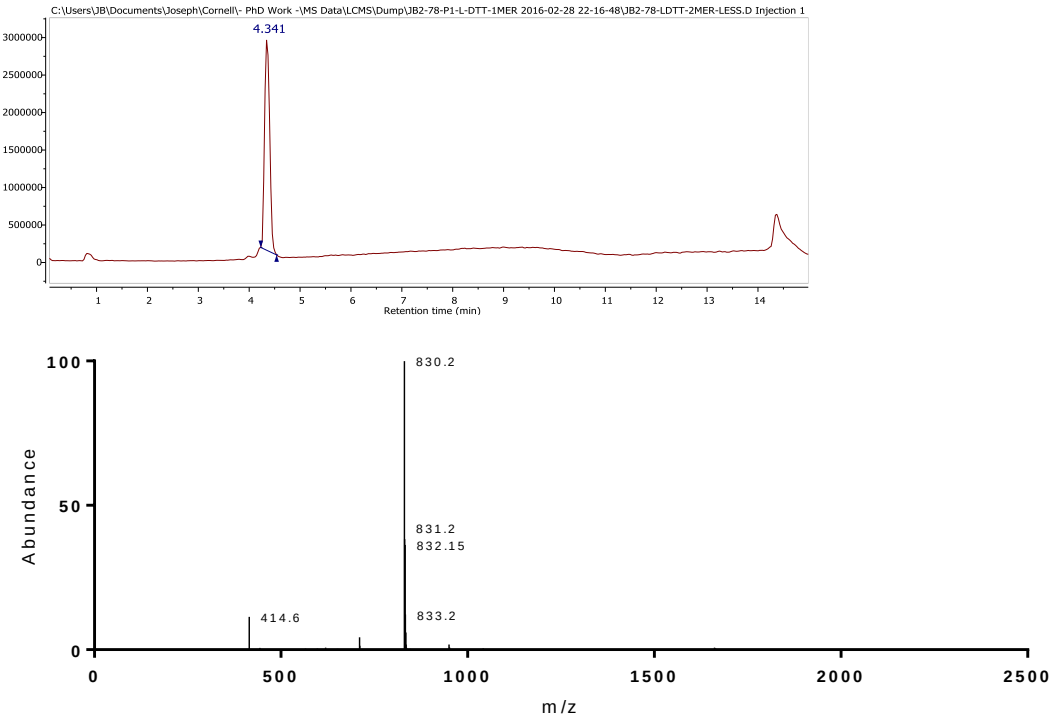

Negative mode LCMS of the (DTT-Sulf)$_2$ with the TIC (top) and the corresponding mass spectra (bottom). Parent mass: 831.23; [M-H]$^{-1}$ Expected: 830.22 Obs. 830.2; [M-2H]$^{-2}$ Expected: 414.61 Obs. 414.6.

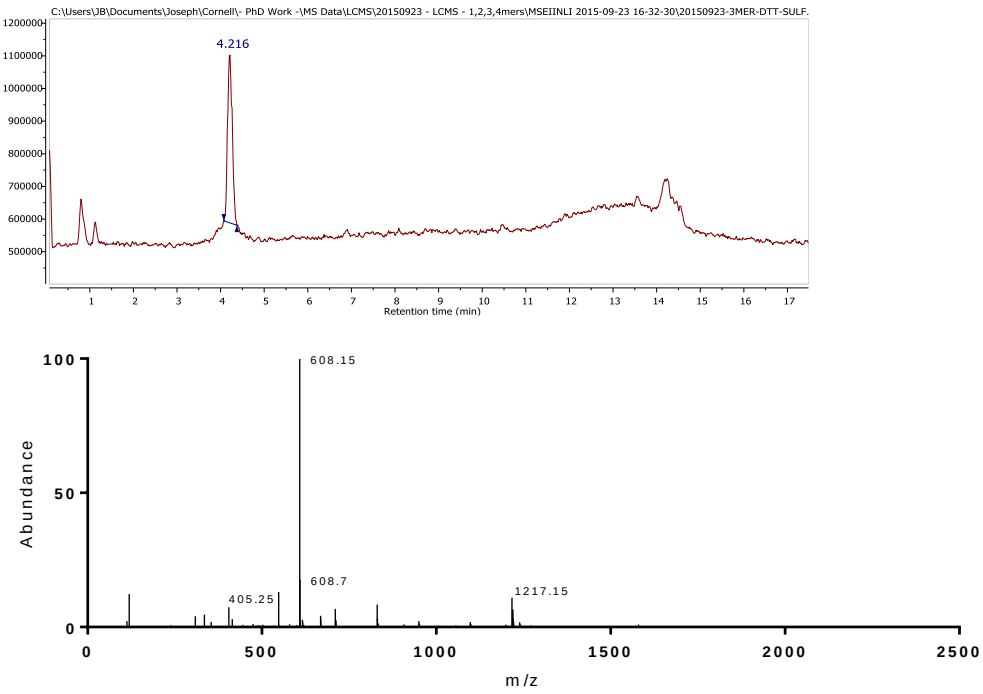

Negative mode LCMS of the (DTT-Sulf)$_3$ with the TIC (top) and the corresponding mass spectra (bottom). Parent mass: 1218.31; [M-H]$^{-1}$ Expected: 1217.30 Obs. 1217.15; [M-2H]$^{-2}$ Expected: 608.15 Obs. 608.15; [M-3H]$^{-3}$ Expected: 405.10 Obs. 405.25.

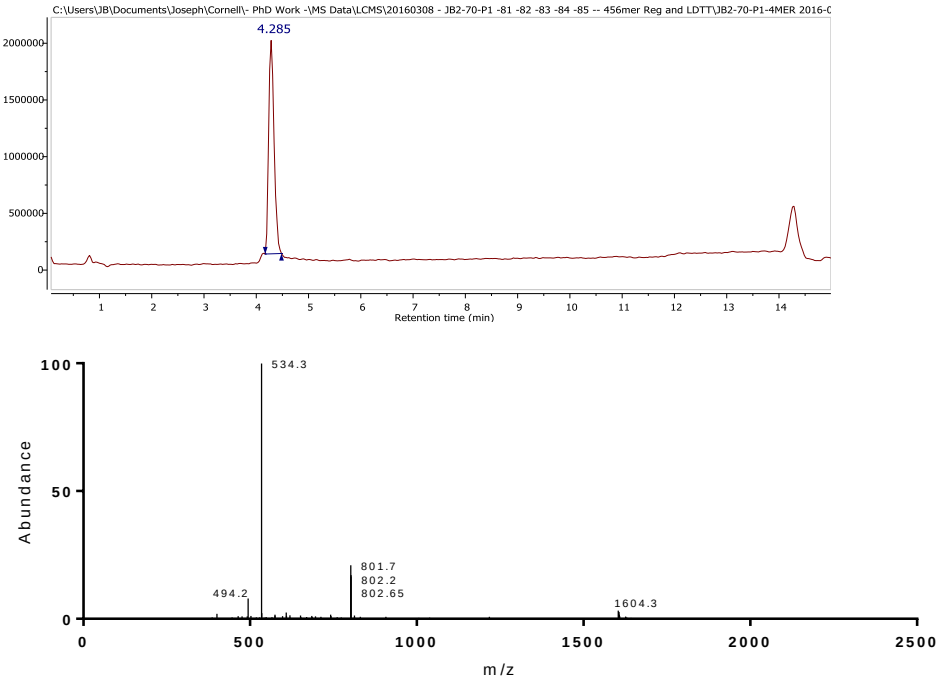

Negative mode LCMS of the (DTT-Sulf)$_4$ with the TIC (top) and the corresponding mass spectra (bottom). Parent mass: 1605.40; [M-H]$^{-1}$ Expected: 1604.39 Obs. 1604.3; [M-2H]$^{-2}$ Expected: 801.69 Obs. 801.7; [M-3H]$^{-3}$ Expected: 534.13 Obs. 534.3.

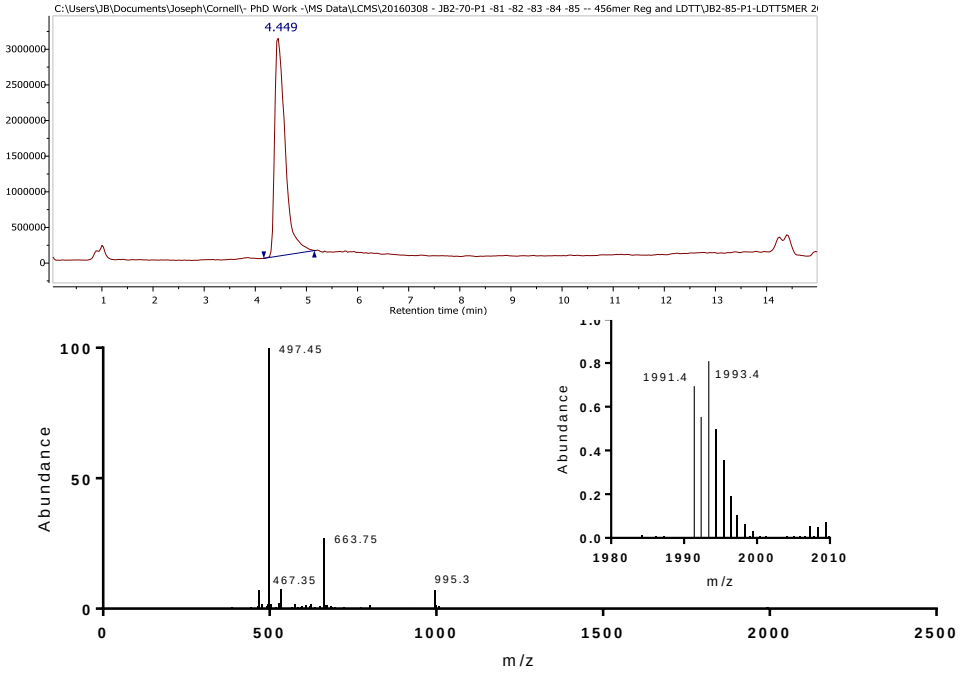

Negative mode LCMS of the (DTT-Sulf)$_5$ with the TIC (top) and the corresponding mass spectra (bottom). Parent mass: 1992.48; [M-H]$^{-1}$ Expected: 1991.47 Obs. 1991.4 (inset); [M-2H]$^{-2}$ Expected: 995.23 Obs. 995.3; [M-3H]$^{-3}$ Expected: 663.15 Obs. 663.75; [M-4H]$^{-4}$ Expected: 497.11 Obs. 497.45.

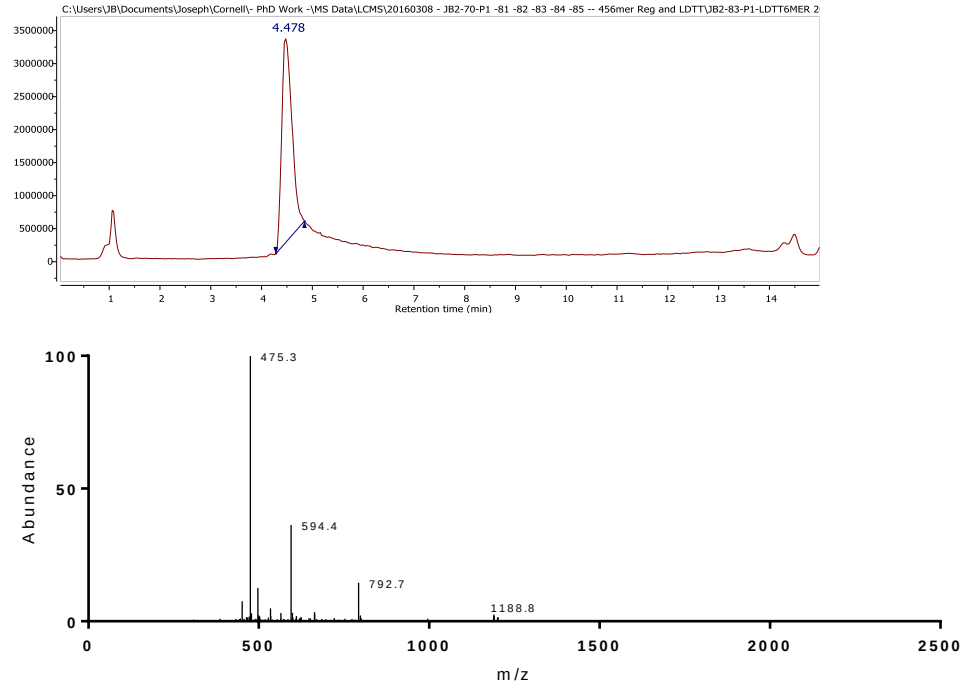

Negative mode LCMS of the (DTT-Sulf)$_6$ with the TIC (top) and the corresponding mass spectra (bottom). Parent mass: 2379.56; [M-2H]$^{-2}$ Expected: 1188.77 Obs. 1188.8; [M-3H]$^{-3}$ Expected: 792.18 Obs. 792.7; [M-4H]$^{-4}$ Expected: 474.90 Obs. 475.3.

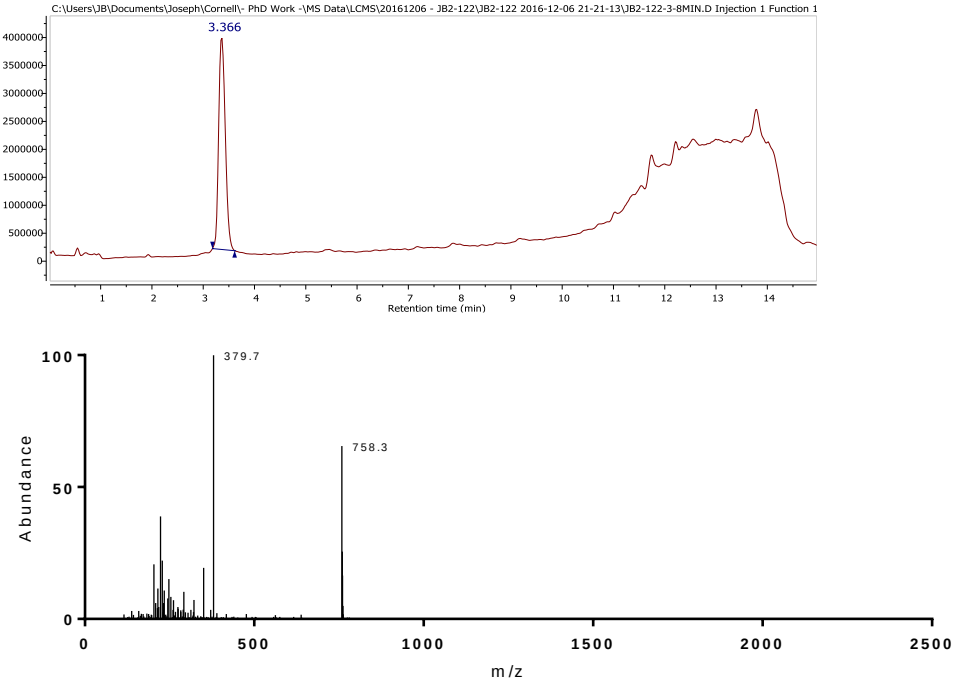

Positive mode LCMS of the NH_2-(DTT-G)$_2$ with the TIC (top) and the corresponding mass spectra (bottom). Parent mass: 757.35; $[M+H]^{+1}$ Expected: 758.35 Obs. 758.3; $[M+2H]^{+2}$ Expected: 379.68 Obs. 379.7.

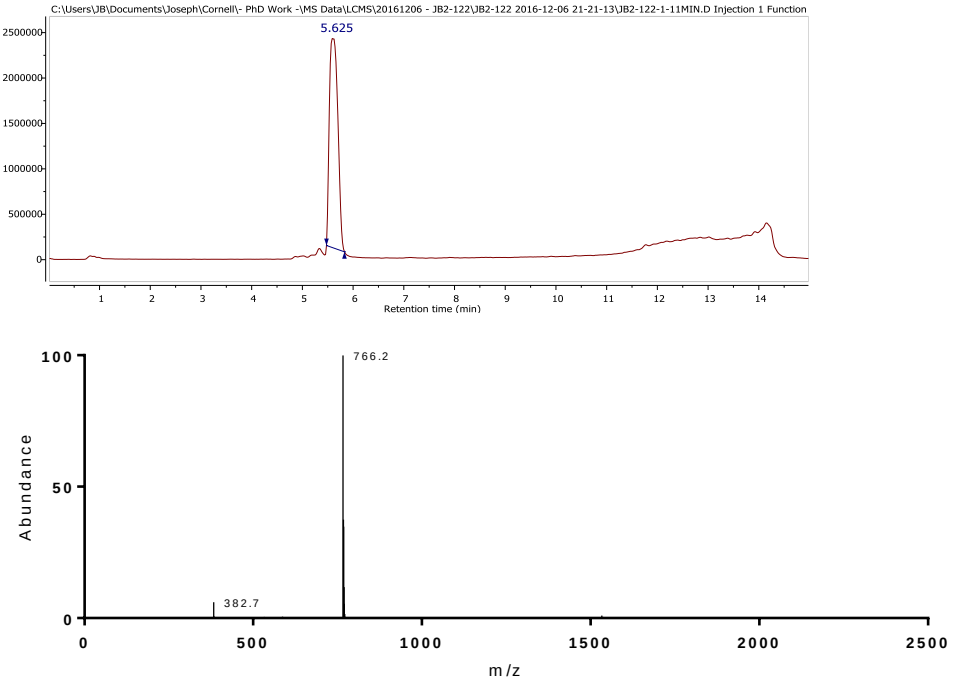

Negative mode LCMS of the NH_2-(BDT-Sulf)$_2$ with the TIC (top) and the corresponding mass spectra (bottom). Parent mass: 767.25; $[M-H]^{-1}$ Expected: 766.24 Obs. 762.2; $[M-2H]^{-2}$ Expected: 382.62 Obs. 382.7.

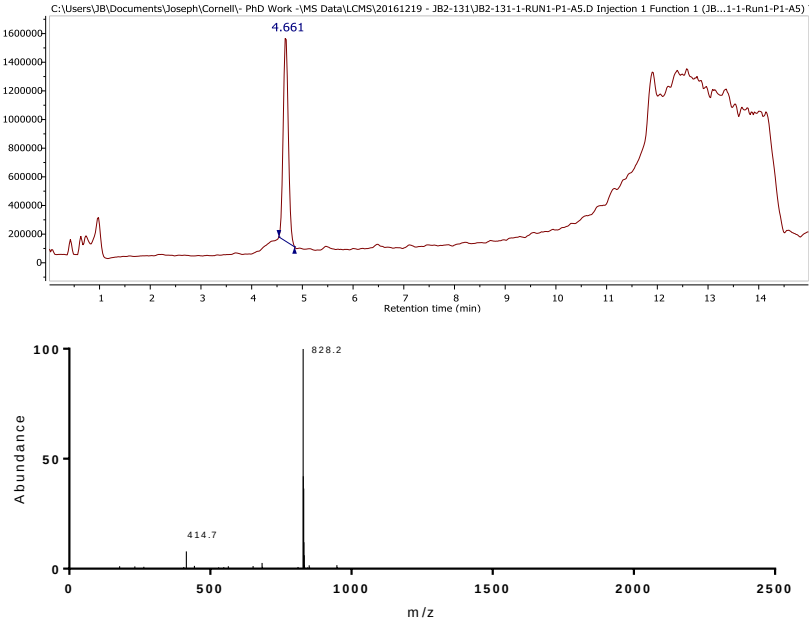

Positive mode LCMS of the NH_2-(DTT-MeS)$_2$ with the TIC (top) and the corresponding mass spectra (bottom). Parent mass: 827.27; $[M+H]^{+1}$ Expected: 828.28 Obs. 828.2; $[M+2H]^{+2}$ Expected: 414.64 Obs. 414.7.

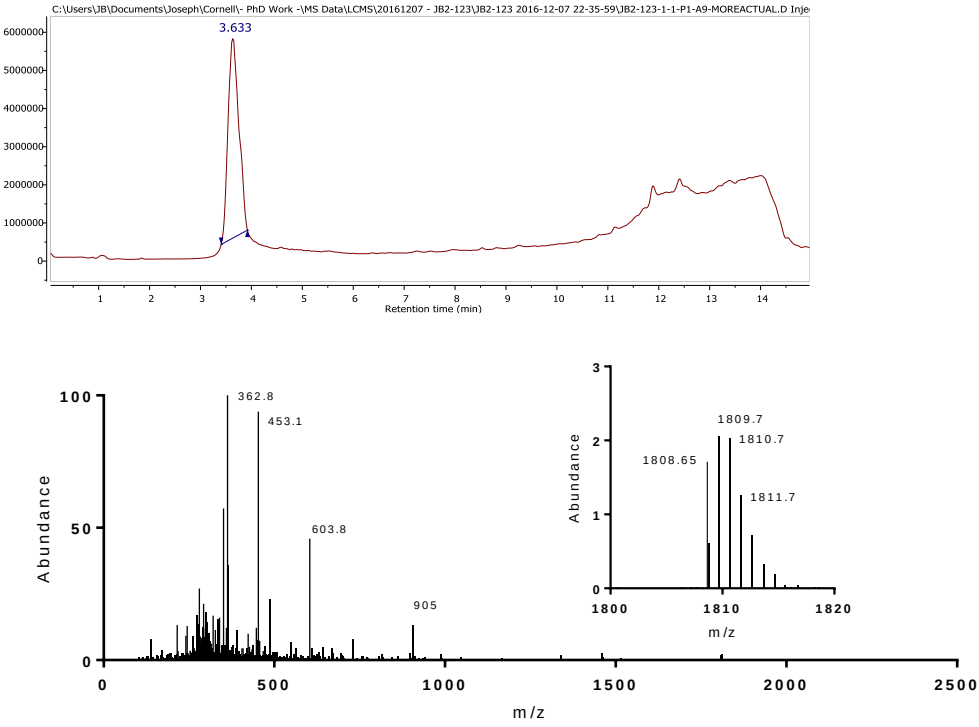

Positive mode LCMS of NH_2-(DTT-G)$_5$ with the TIC (top) and the corresponding mass spectra (bottom). Parent mass: 1807.78; $[M+H]^{+1}$ Expected: 1808.79 Obs. 1808.65; $[M+2H]^{+2}$ Expected: 904.90 Obs. 905.0; $[M+3H]^{+3}$ Expected: 603.60 Obs. 603.8; $[M+4H]^{+4}$ Expected: 452.95 Obs. 453.1; $[M+5H]^{+5}$ Expected: 362.56 Obs. 362.8.

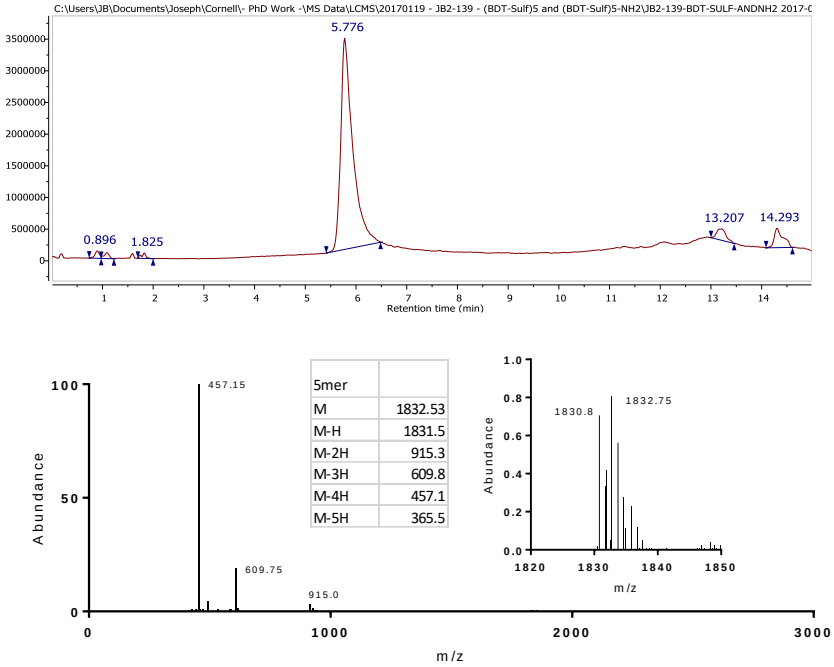

Negative mode mass spectra from the LCMS of the (BDT-Sulf)$_5$. The parent mass (M+H)$^{+1}$ is observed as well as the 2nd, 3rd, and 4th expected masses in table shown.

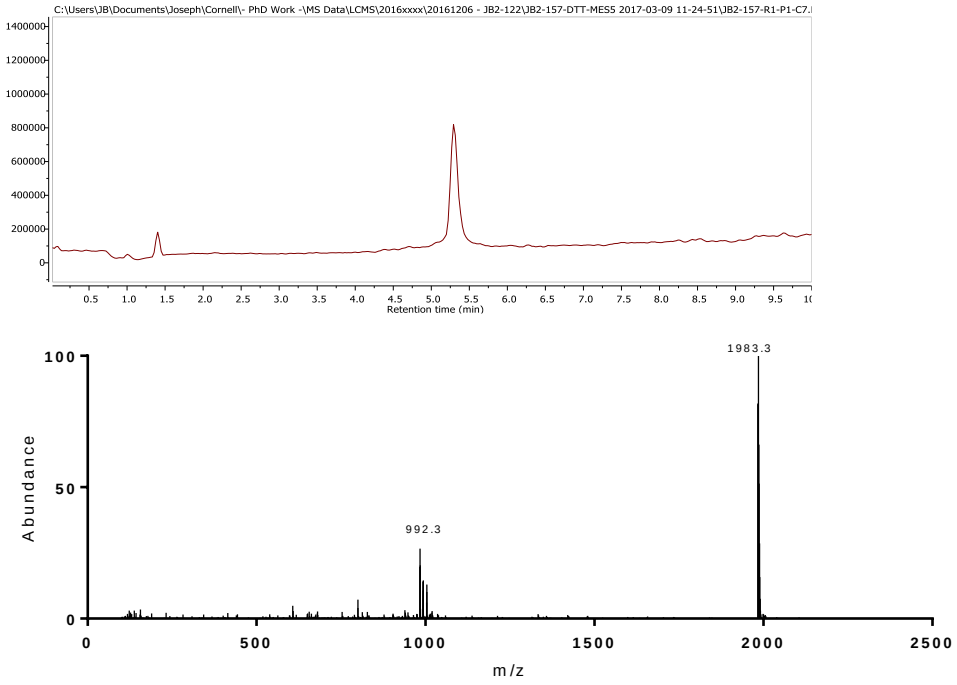

Positive mode LCMS TIC (top) and mass spectra (bottom) of the purified (DTT-MeS)$_5$. Parent mass: 1982.6; [M+1]$^{+1}$ Expected: 1983.6 Obs. 1983.3; [M+2H]$^{+2}$ Expected 992.3 Obs. 992.3.

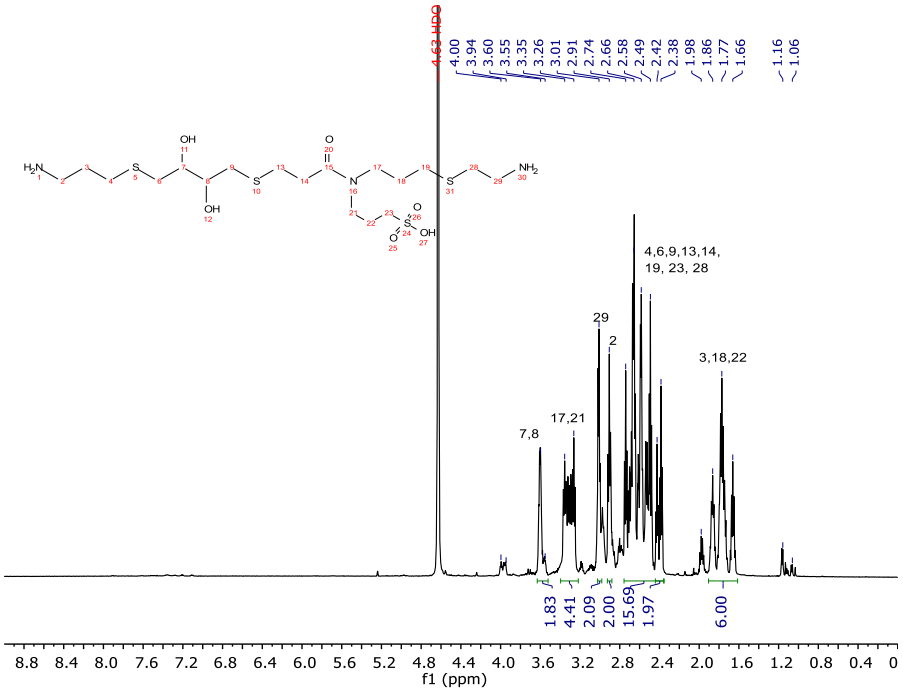

^{1}H NMR of the crude mixture of the amine-capped 2mer NH_2-(DTT-PSM)$_1$-NH_2 after TFA cleavage in deuterated water prepared for ESR di-spin labeling with a TEMPO NHS.

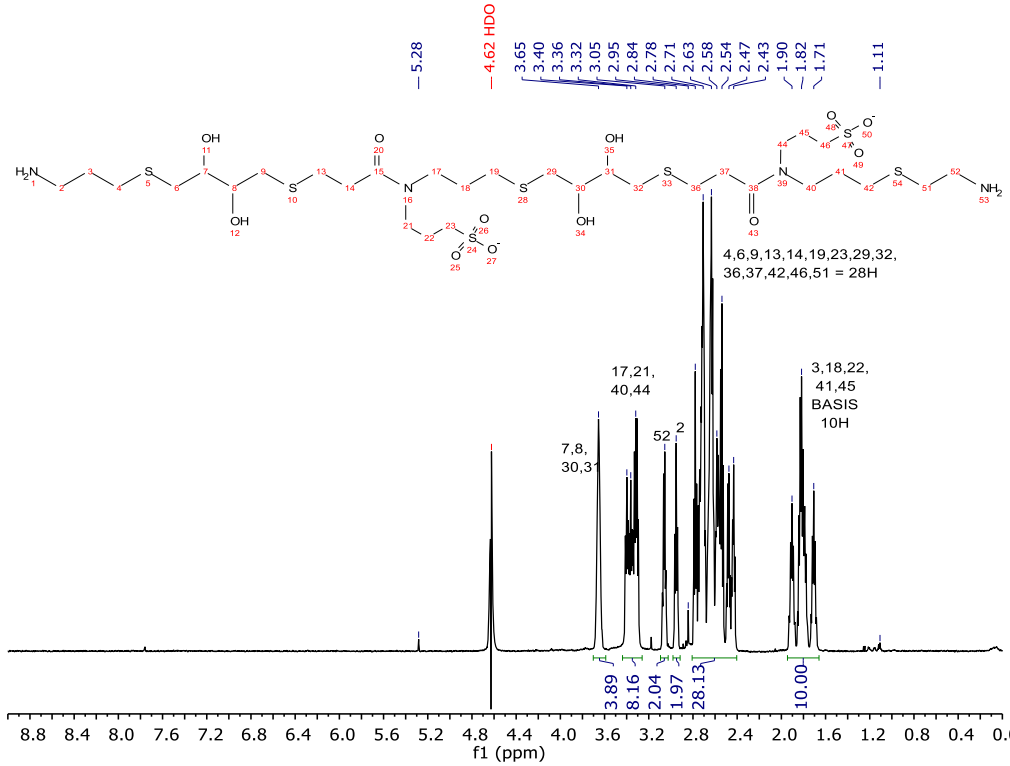

^{1}H NMR of the amine-capped 4mer NH_2-(DTT-PSM)$_2$-NH_2 after TFA cleavage and HPLC in deuterated water prepared for ESR di-spin labeling. Solvent suppression was used on the HDO peak.

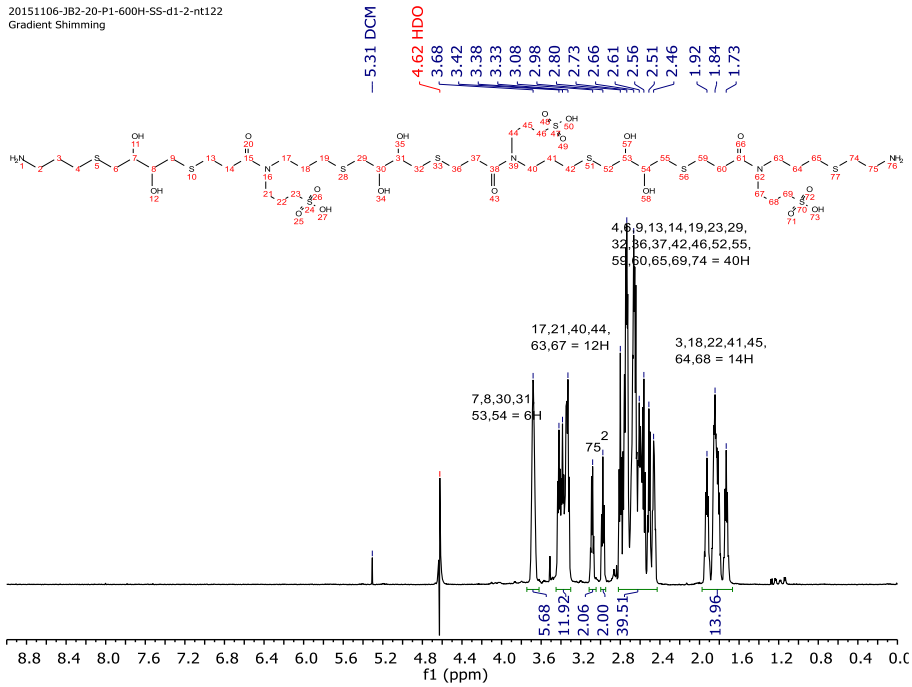

^{1}H NMR of the amine-capped 6mer NH_2-(DTT-PSM)$_3$-NH_2 after HPLC in deuterated water for ESR di-spin labeling. Solvent suppression was used on the HDO peak.

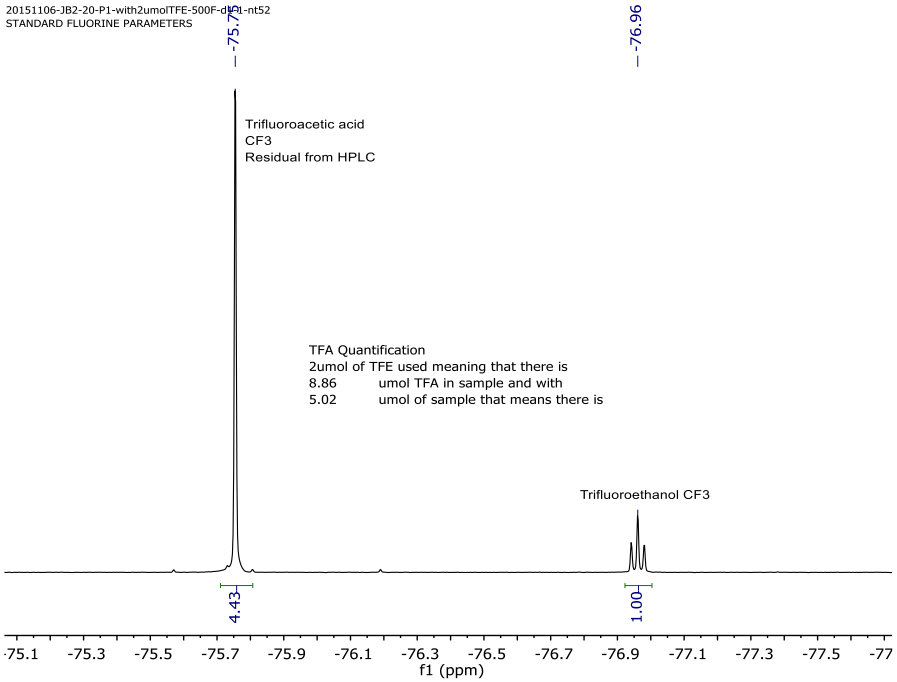

^{19}F NMR of the amine-capped 6mer to quantify residual TFA after HPLC where the trifluoro groups for TFA and a trifluoroethanol standard appear at -75.75 and -76.96ppm, respectively. This spectra is shown as an example of the other oligomers where the TFA quantification ensured the correction to the amount of base used in the NHS spin labeling.

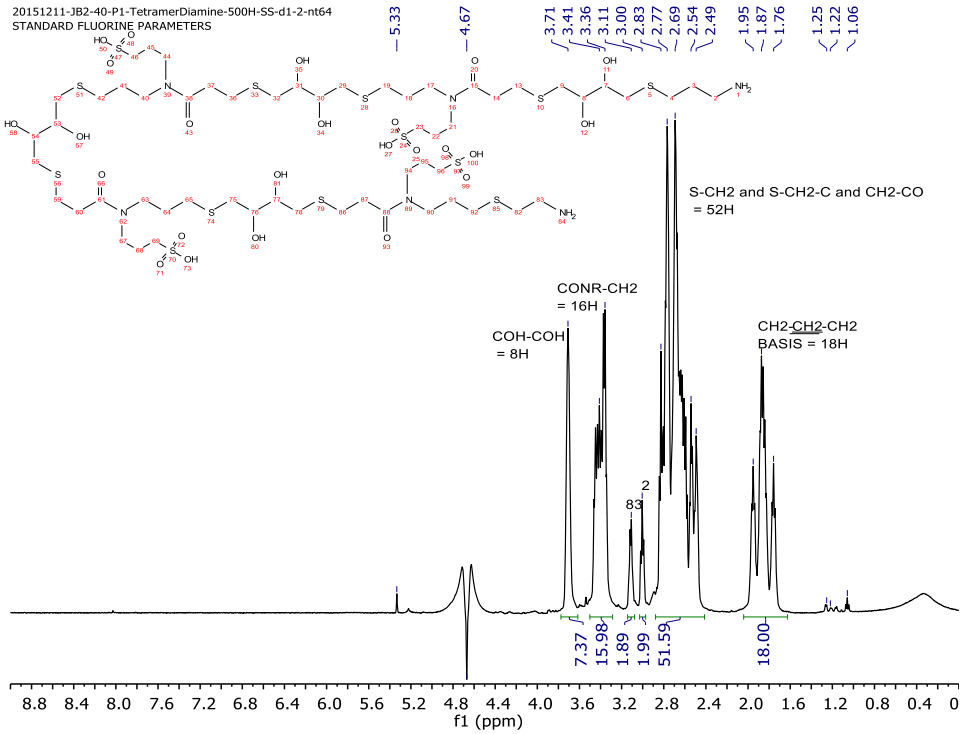

^{1}H NMR of the amine-capped 8mer NH_2-(DTT-PSM)$_4$-NH_2 after HPLC in deuterated water for ESR di-spin labeling. Solvent suppression was used on the HDO peak.

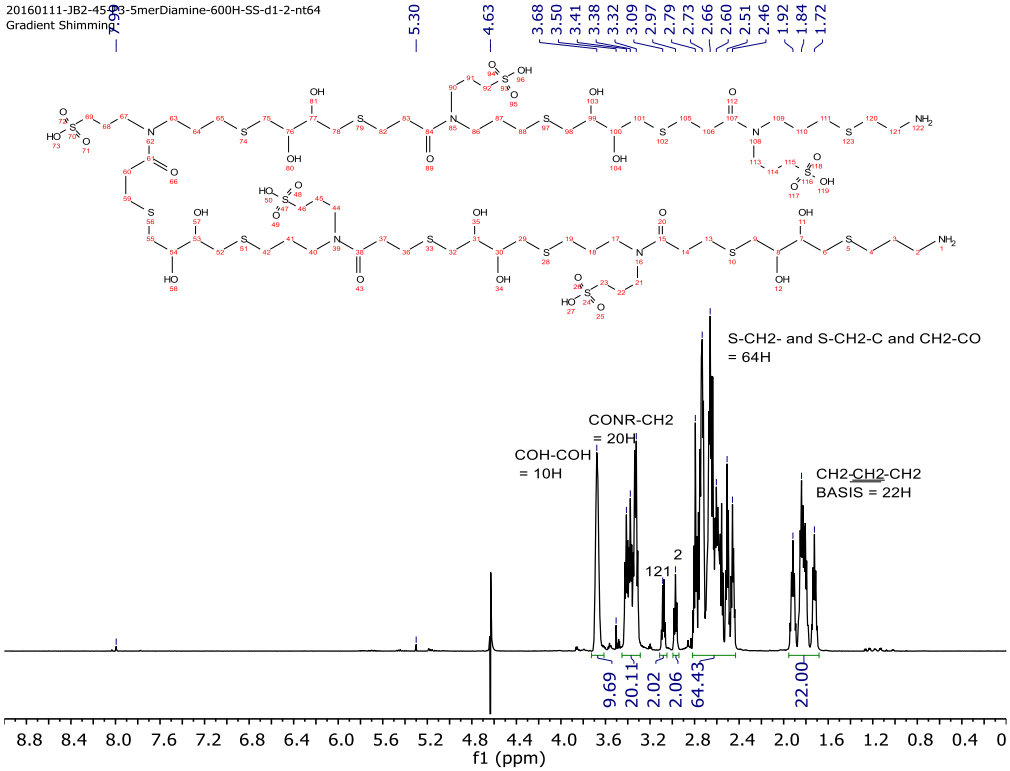

^{1}H NMR of the amine-capped 10mer NH_2-(DTT-PSM)$_5$-NH_2 after HPLC in deuterated water for ESR di-spin labeling. Solvent suppression was used on the HDO peak.

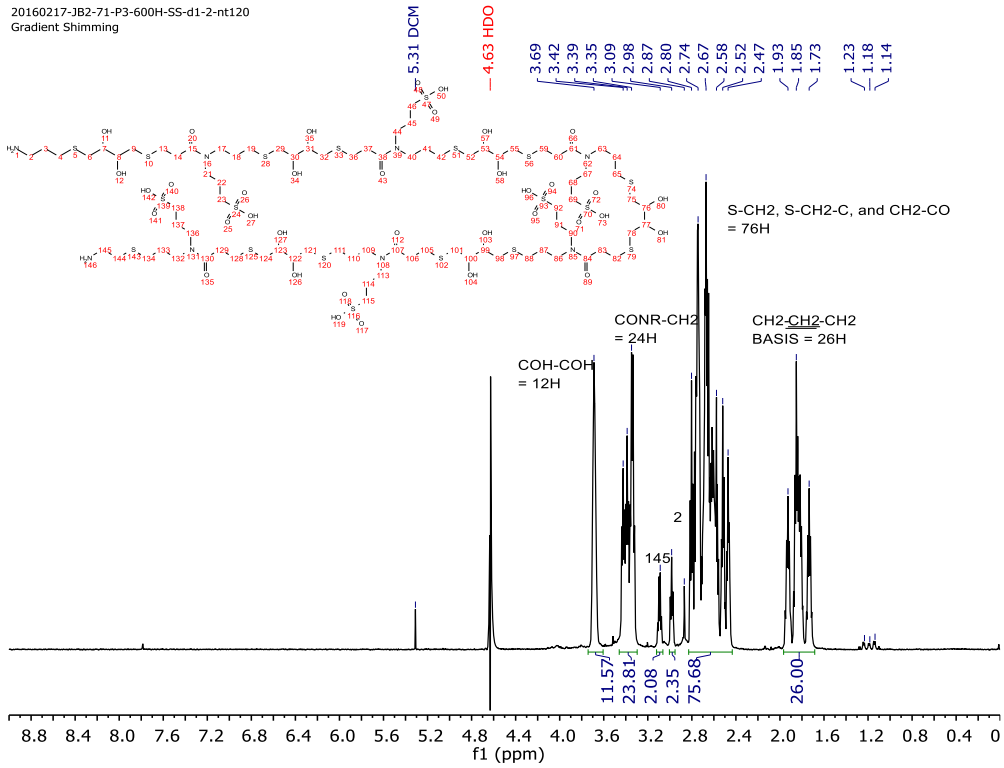

^{1}H NMR of the amine-capped 12mer NH_2-(DTT-PSM)$_6$-NH_2 after HPLC in deuterated water for ESR di-spin labeling. Solvent suppression was used on the HDO peak.

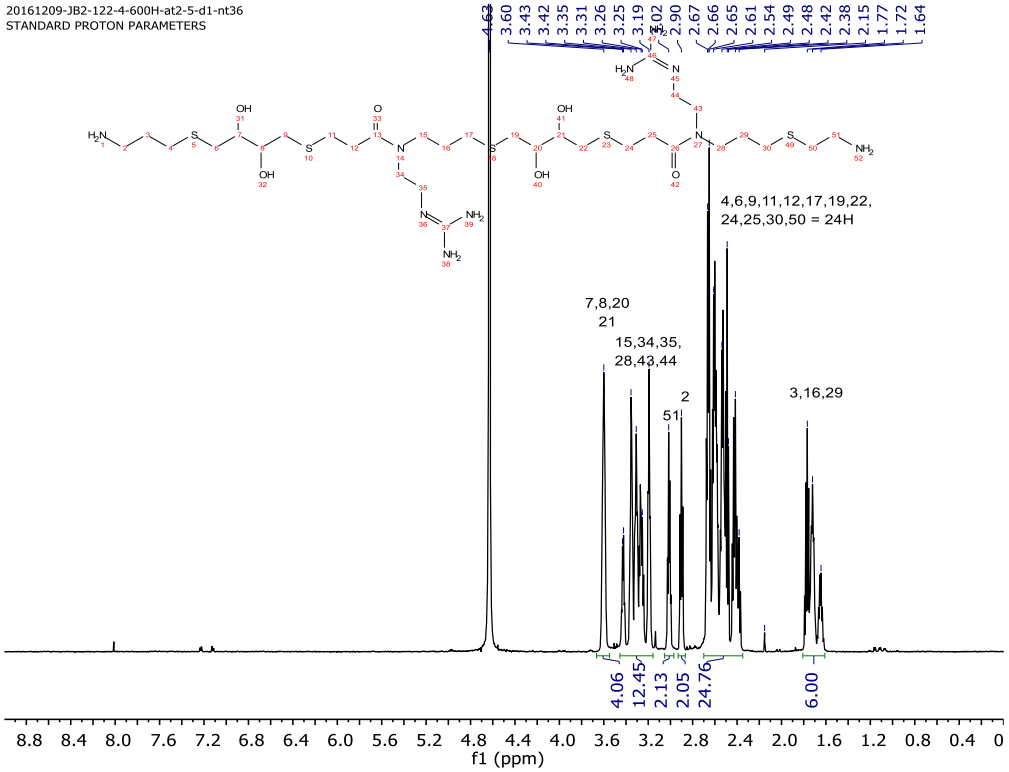

^{1}H NMR of the amine-capped 4mer NH_2-(DTT-G)$_2$-NH_2 after HPLC in deuterated water for ESR di-spin labeling.

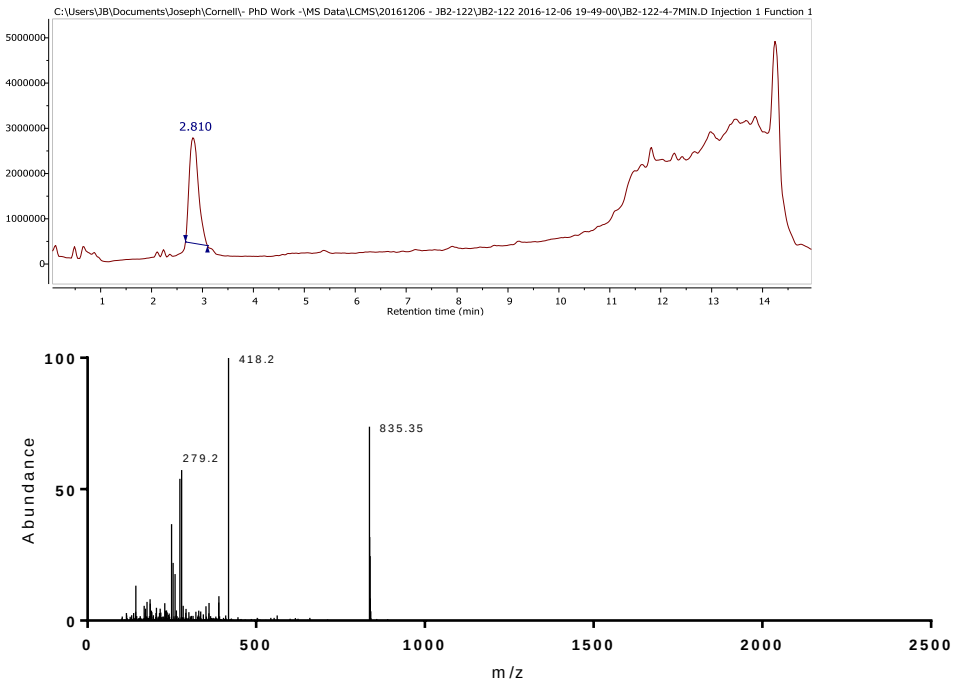

Positive mode LCMS of the amine capped NH_2-(DTT-G)$_2$-NH_2 with the TIC (top) and the mass spectra (bottom). Parent mass: 834.38 as [M]; $[M+H]^{+1}$ Expected: 835.38 Obs. 835.35; $[M+2H]^{+2}$ Expected: 418.20 Obs. 418.2; $[M+3H]^{+3}$ Expected: 279.13 Obs. 279.2.

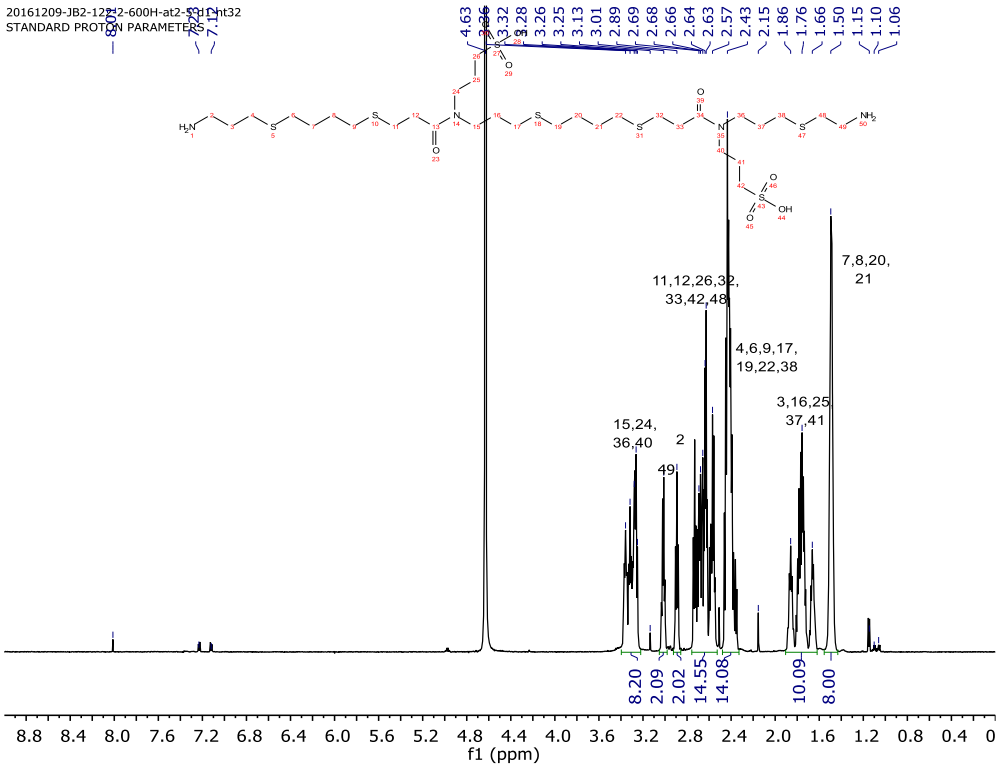

^{1}H NMR of the amine-capped 4mer NH_2-(BDT-Sulf)$_2$-NH_2 after HPLC in deuterated water for ESR di-spin labeling.

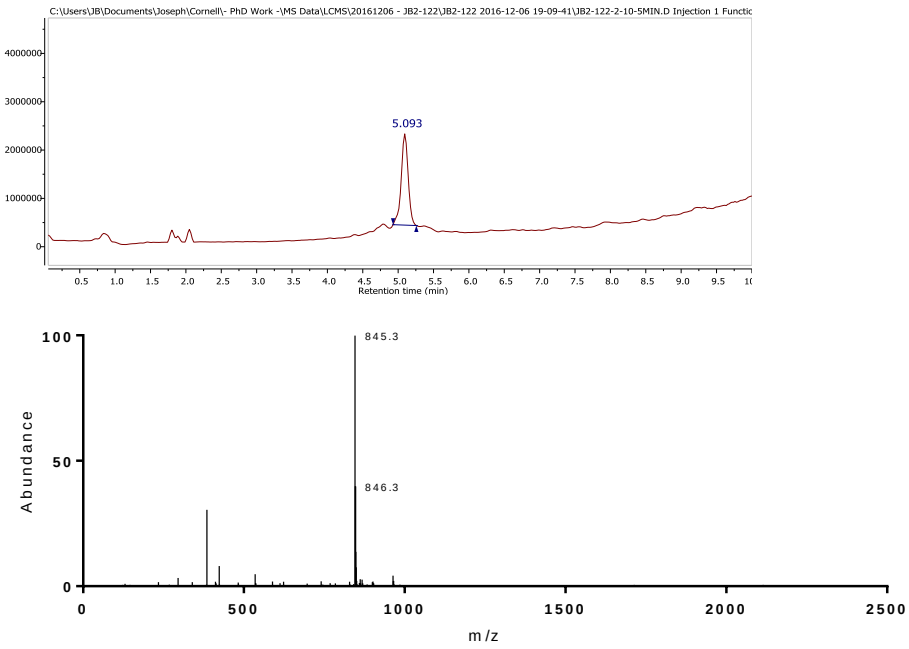

Positive mode LCMS of the amine capped NH_2-(BDT-Sulf)$_2$-NH_2 with the TIC (top) and the mass spectra (bottom). Parent mass: 844.28 as [M]; $[M+H]^{+1}$ Expected: 843.29 Obs. 845.3

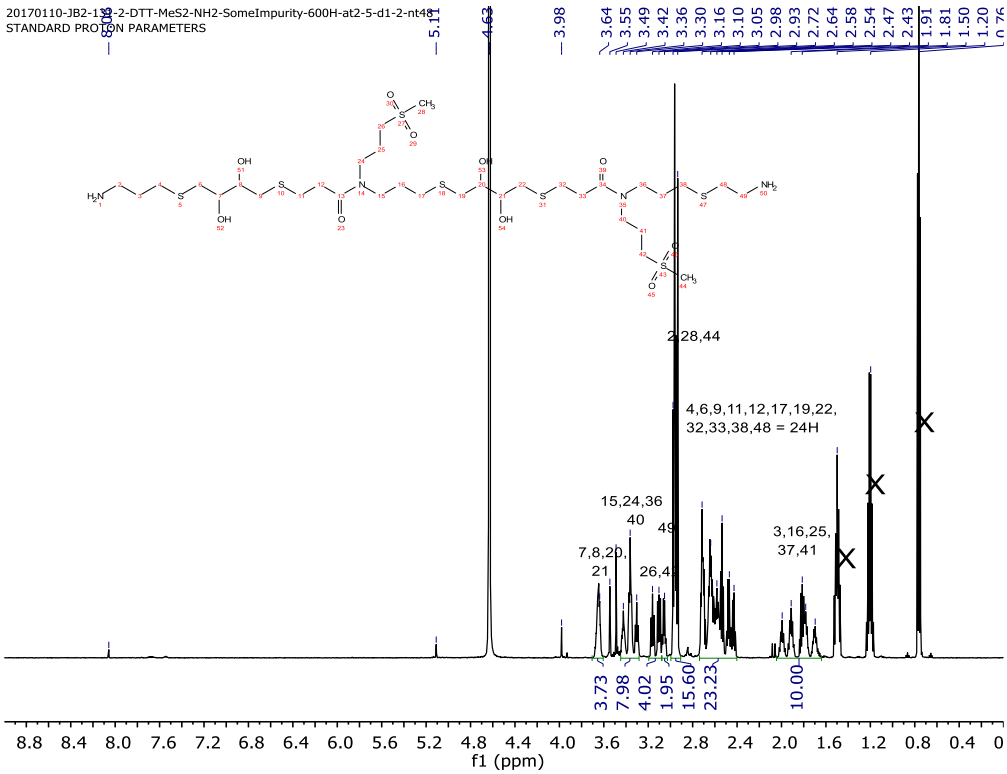

^{1}H NMR of the amine-capped 4mer NH_2-(DTT-MeS)$_2$-NH_2 after HPLC in deuterated water for ESR di-spin labeling. The X's mark propylamine contaminant from co-solvent evaporation.

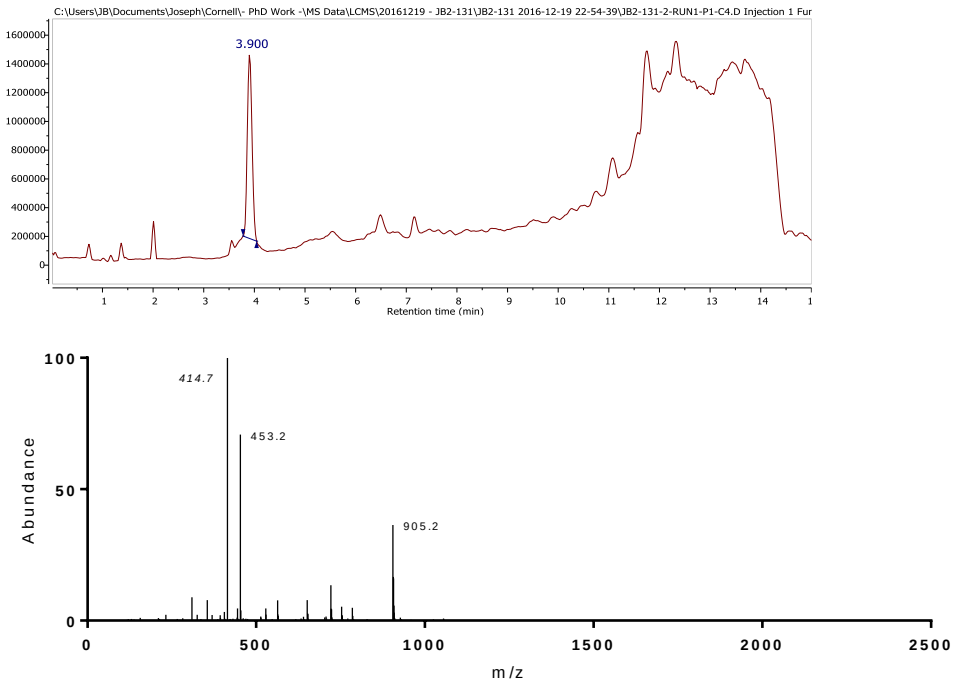

Positive mode LCMS of the amine capped NH_2-(DTT-MeS)$_2$-NH_2 with the TIC (top) and the mass spectra (bottom). Parent mass: 904.30 as [M]; $[M+H]^{+1}$ Expected: 905.31 Obs. 905.2; $[M+2H]^{+2}$ Expected: 453.16 Obs. 453.2. The 414.7m/z is unknown.

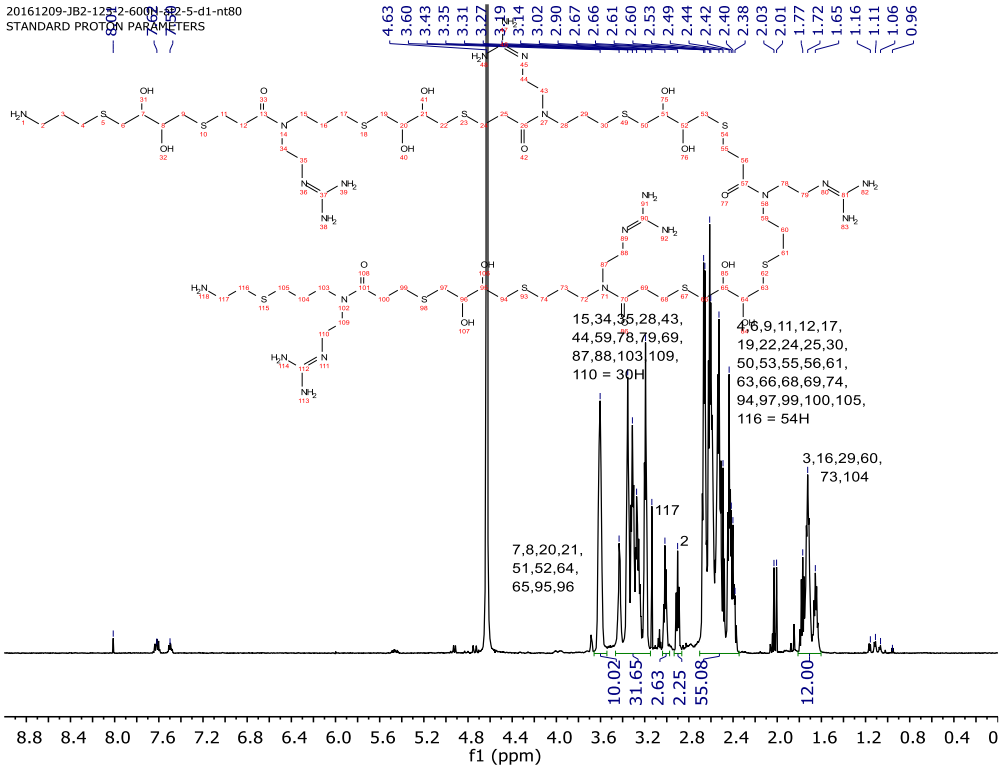

^{1}H NMR of the amine-capped 10mer NH_2-(DTT-G)$_5$-NH_2 after HPLC in deuterated water for ESR di-spin labeling.

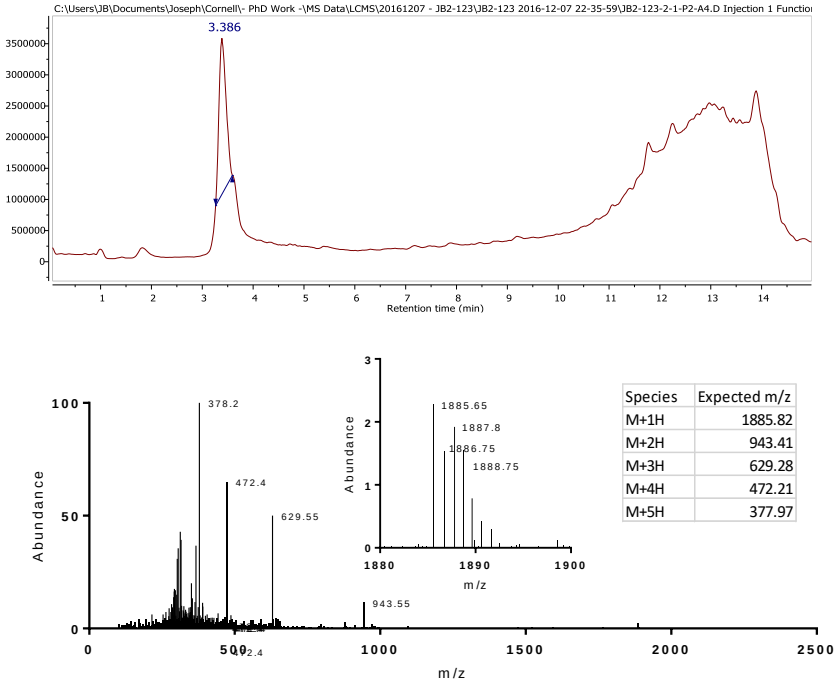

Positive mode LCMS of the amine capped NH_2-(DTT-G)$_5$-NH_2 with the TIC (top) and the mass spectra (bottom). Masses were expected as indicated in the inset table and observed as seen.

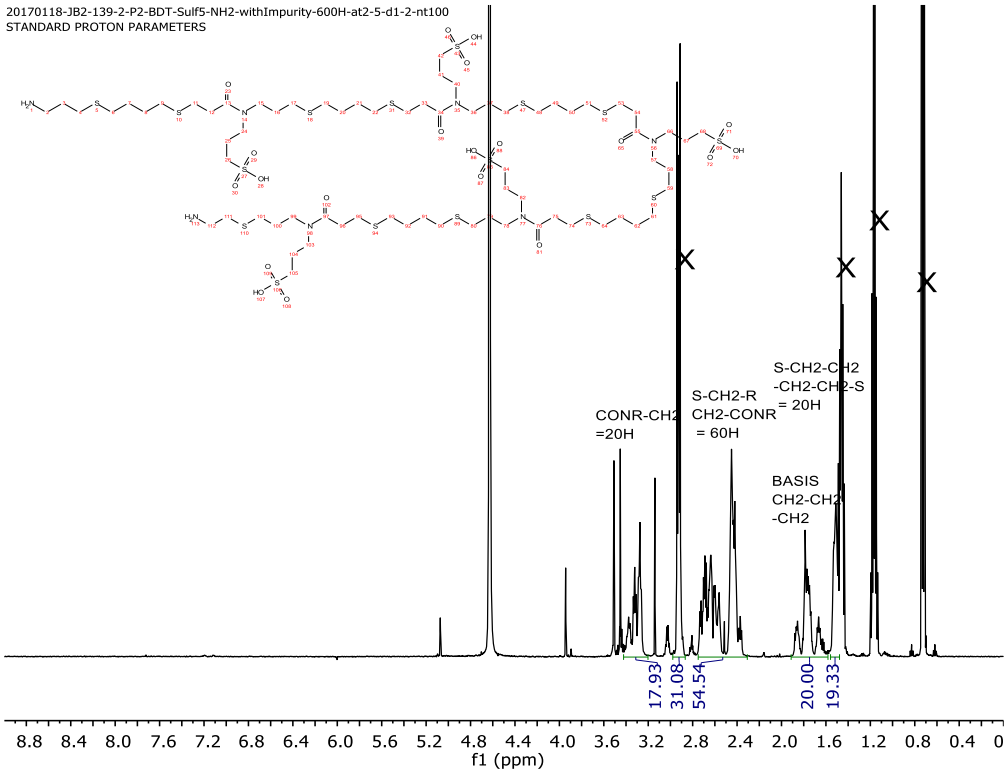

^{1}H NMR of the amine-capped 10mer NH_2-(BDT-Sulf)$_5$-NH_2 after HPLC in deuterated water for ESR di-spin labeling.

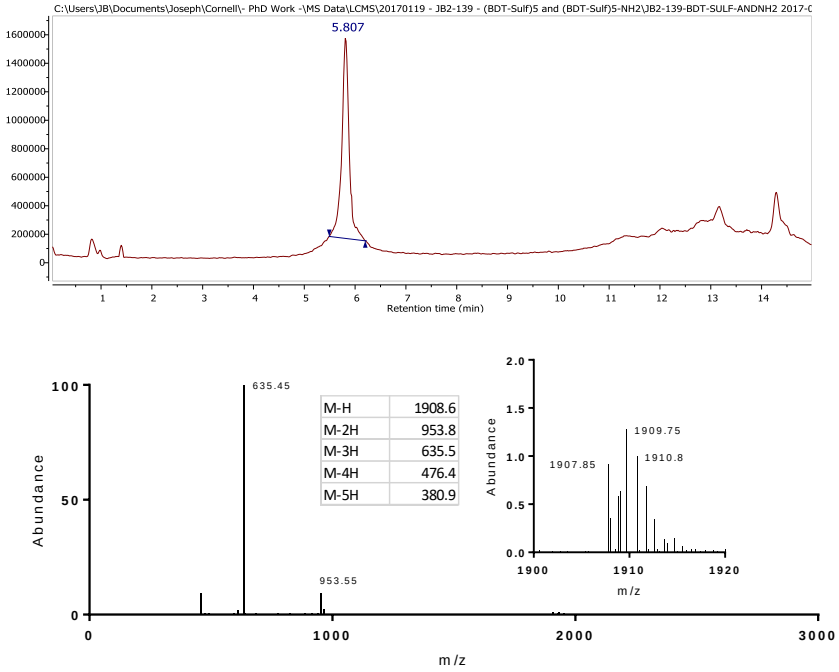

Negative mode LCMS of the amine capped NH_2-(BDT-Sulf)$_5$-NH_2 with the TIC (top) and the mass spectra (bottom). Masses were expected as indicated in the inset table and observed as seen.

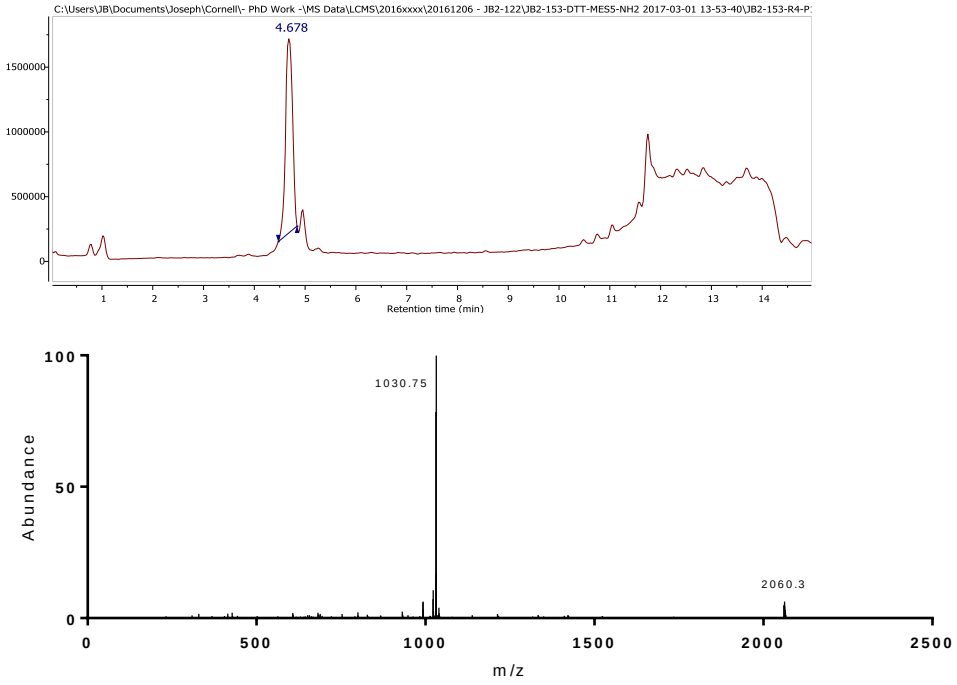

Positive mode LCMS of the amine capped NH_2-(DTT-MeS)$_5$-NH_2 with the TIC (top) and the mass spectra (bottom). Parent mass: 2059.61; $[M+H]^{+1}$ Expected 2060.62 Obs. 2060.3; $[M+2H]^{+2}$ Expected 1030.81 Obs. 1030.75.

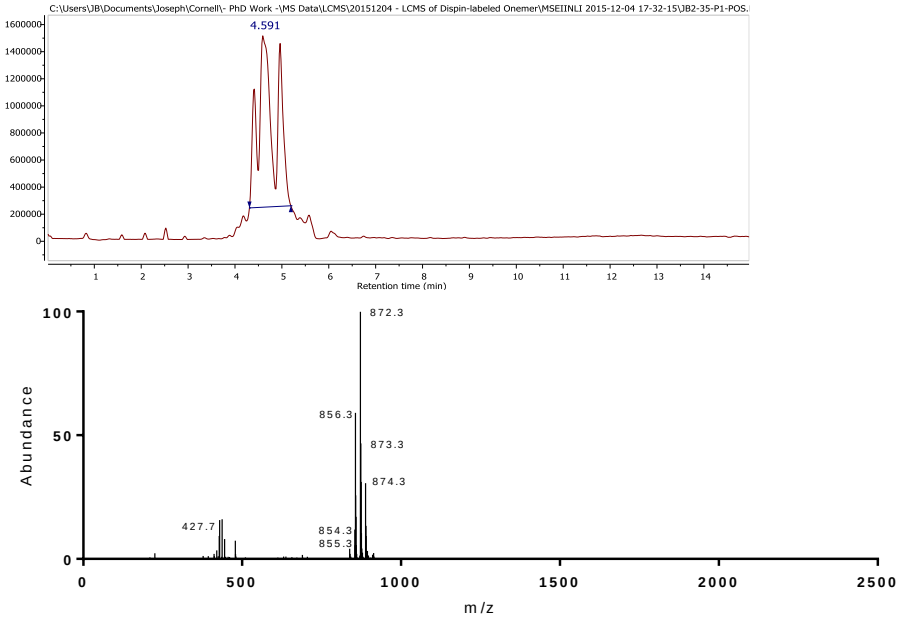

Positive mode LCMS of the dispin labeled (Proxyl) 2mer with the TIC (top) and the mass spectra (bottom) showing a distribution of the nitroxide oxidation states. Parent mass: 853.35 as [M]••; $[M+H]^{+1}$•• Expected: 854.36 Obs. 854.3; $[M+H]^{+1}$• Expected: 855.37 Obs. 855.3; $[M+H]^{+1}$ Expected: 856.37 Obs. 856.3; $[M+NH_4]^{+1}$• Expected: 872.40 Obs. 872.3; $[M+NH_4]^{+1}$ Expected: 873.40 Obs. 873.3.

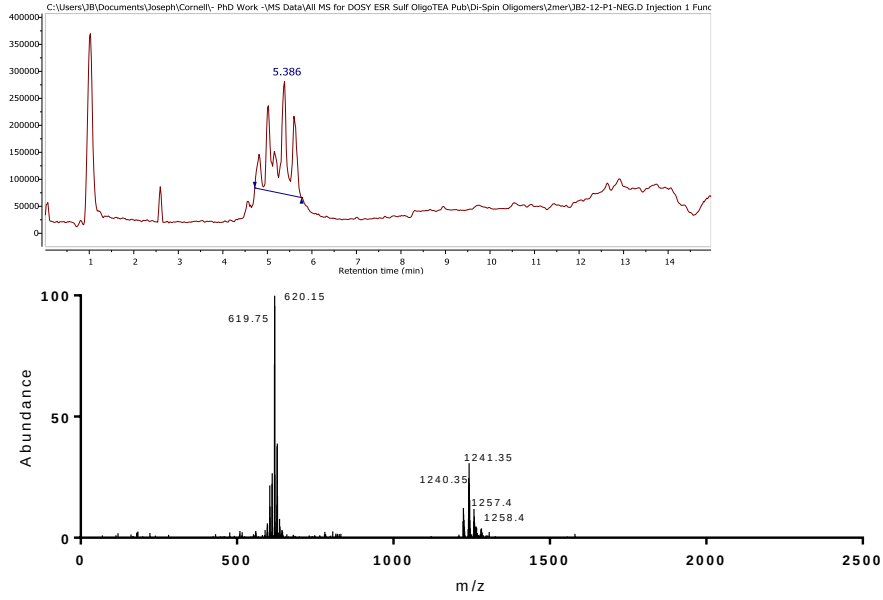

Negative mode LCMS of the dispin labeled (Proxyl) 4mer with the TIC (top) and the mass spectra (bottom) showing a distribution of the nitroxide oxidation states. Parent mass: 1240.43 as [M]••; $[M-H]^{-1}$• Expected: 1240.43 Obs. 1240.35; $[M-H]^{-1}$ Expected: 1241.44 Obs. 1241.35; $[M-2H+NH_4]^{-1}$• Expected: 1257.46 Obs. 1257.4; $[M-2H+NH_4]^{-1}$ Expected: 1258.47 Obs. 1258.4; $[M-2H]^{-2}$• Expected: 619.71 Obs. 619.75; $[M-2H]^{-2}$ Expected: 620.22 Obs. 620.15.

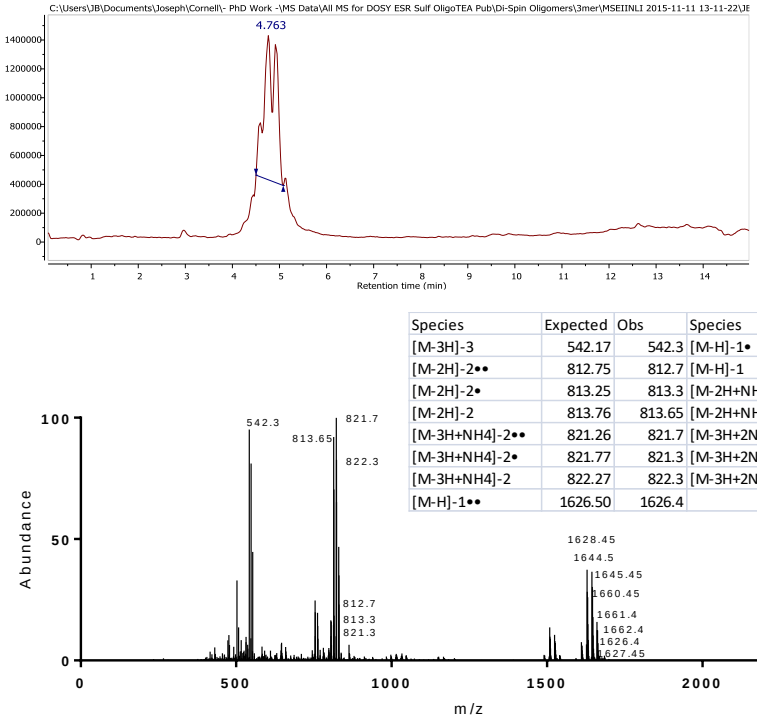

Species	Expected	Obs	Species	Expected	Obs
[M-3H]-3	542.17	542.3	[M-H]-1•	1627.51	1627.45
[M-2H]-2••	812.75	812.7	[M-H]-1	1628.52	1628.45
[M-2H]-2•	813.25	813.3	[M-2H+NH4]-1•	1644.54	1644.5
[M-2H]-2	813.76	813.65	[M-2H+NH4]-1	1645.55	1645.45
[M-3H+NH4]-2••	821.26	821.7	[M-3H+2NH4]-1••	1660.56	1660.45
[M-3H+NH4]-2•	821.77	821.3	[M-3H+2NH4]-1•	1661.57	1661.4
[M-3H+NH4]-2	822.27	822.3	[M-3H+2NH4]-1	1662.58	1662.4
[M-H]-1••	1626.50	1626.4			

Negative mode LCMS of the dispin labeled (TEMPO) 6mer with the TIC (top) and the mass spectra (bottom) showing a distribution of the nitroxide oxidation states. Parent mass: 1627.51 as [M]•• where observed species are indicated in the inset table.

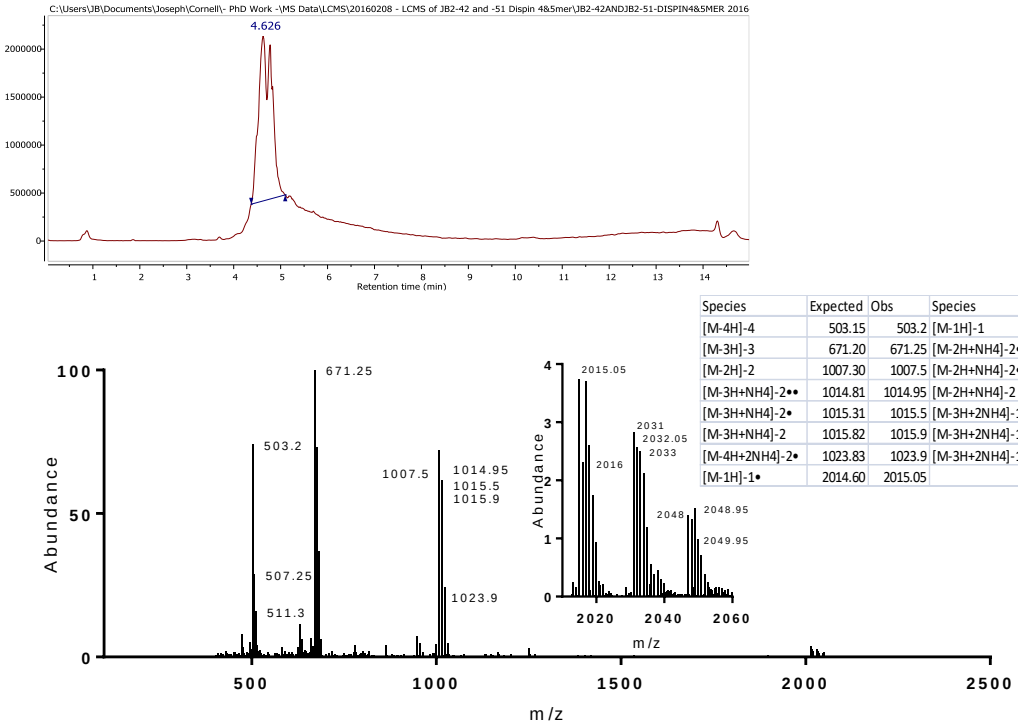

Species	Expected	Obs	Species	Expected	Obs
[M-4H]-4	503.15	503.2	[M-1H]-1	2015.61	2016.0
[M-3H]-3	671.20	671.25	[M-2H+NH4]-2••	2030.62	2031.0
[M-2H]-2	1007.30	1007.5	[M-2H+NH4]-2•	2031.63	2032.05
[M-3H+NH4]-2••	1014.81	1014.95	[M-2H+NH4]-2	2032.64	2033.0
[M-3H+NH4]-2•	1015.31	1015.5	[M-3H+2NH4]-1••	2047.65	2048.0
[M-3H+NH4]-2	1015.82	1015.9	[M-3H+2NH4]-1•	2048.66	2048.95
[M-4H+2NH4]-2•	1023.83	1023.9	[M-3H+2NH4]-1	2049.67	2049.95
[M-1H]-1•	2014.60	2015.05			

Negative mode LCMS of the dispin labeled (Proxyl) 8mer with the TIC (top) and the mass spectra (bottom) showing a distribution of the nitroxide oxidation states. Parent mass: 2014.60 as [M]•• where observed species are indicated in the inset table.

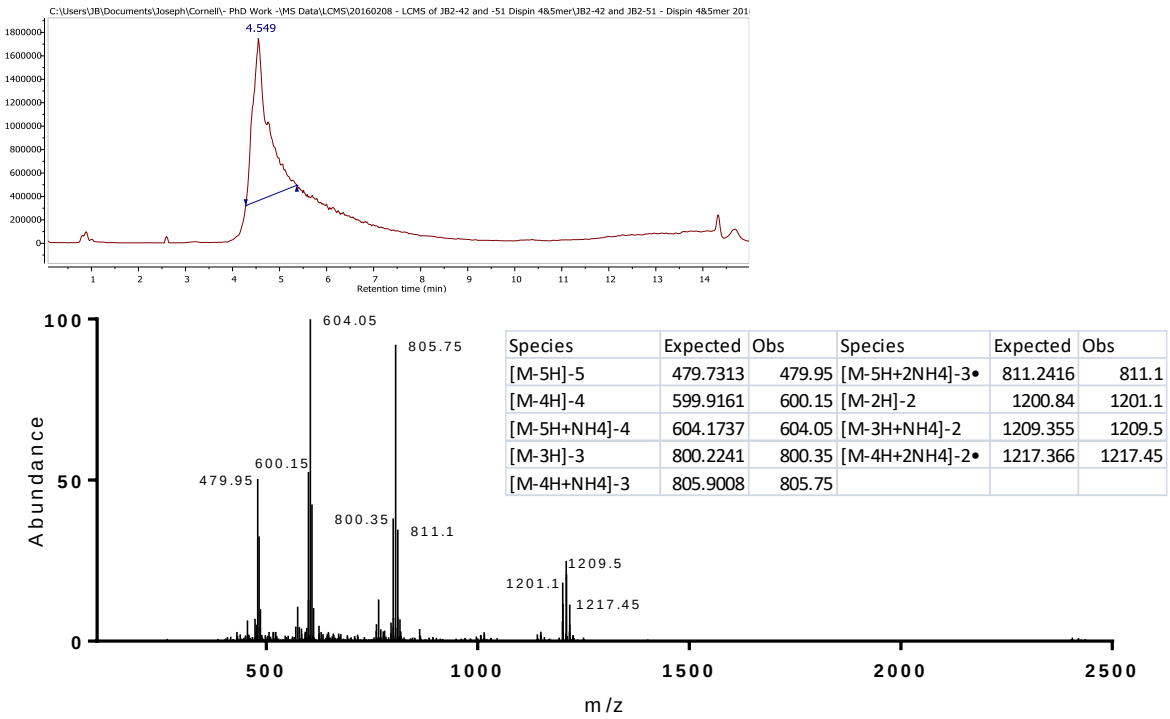

Species	Expected	Obs	Species	Expected	Obs
[M-5H]-5	479.7313	479.95	[M-5H+2NH4]-3•	811.2416	811.1
[M-4H]-4	599.9161	600.15	[M-2H]-2	1200.84	1201.1
[M-5H+NH4]-4	604.1737	604.05	[M-3H+NH4]-2	1209.355	1209.5
[M-3H]-3	800.2241	800.35	[M-4H+2NH4]-2•	1217.366	1217.45
[M-4H+NH4]-3	805.9008	805.75			

Negative mode LCMS of the dispin labeled (Proxyl) 10mer with the TIC (top) and the mass spectra (bottom) showing a distribution of the nitroxide oxidation states. Parent mass: 2401.68 as [M]•• where observed species are indicated in the inset table.

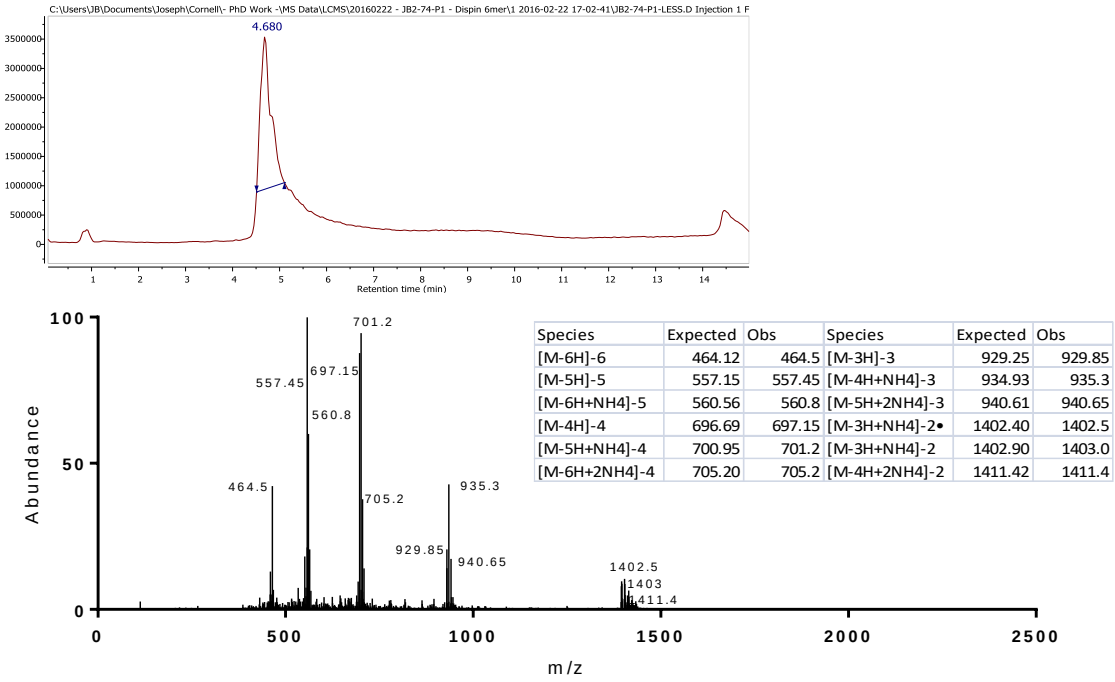

Species	Expected	Obs	Species	Expected	Obs
[M-6H]-6	464.12	464.5	[M-3H]-3	929.25	929.85
[M-5H]-5	557.15	557.45	[M-4H+NH4]-3	934.93	935.3
[M-6H+NH4]-5	560.56	560.8	[M-5H+2NH4]-3	940.61	940.65
[M-4H]-4	696.69	697.15	[M-3H+NH4]-2•	1402.40	1402.5
[M-5H+NH4]-4	700.95	701.2	[M-3H+NH4]-2	1402.90	1403.0
[M-6H+2NH4]-4	705.20	705.2	[M-4H+2NH4]-2	1411.42	1411.4

Negative mode LCMS of the dispin labeled (Proxyl) 12mer with the TIC (top) and the mass spectra (bottom) showing a distribution of the nitroxide oxidation states. Parent mass: 2788.77 as [M]•• where observed species are indicated in the inset table.

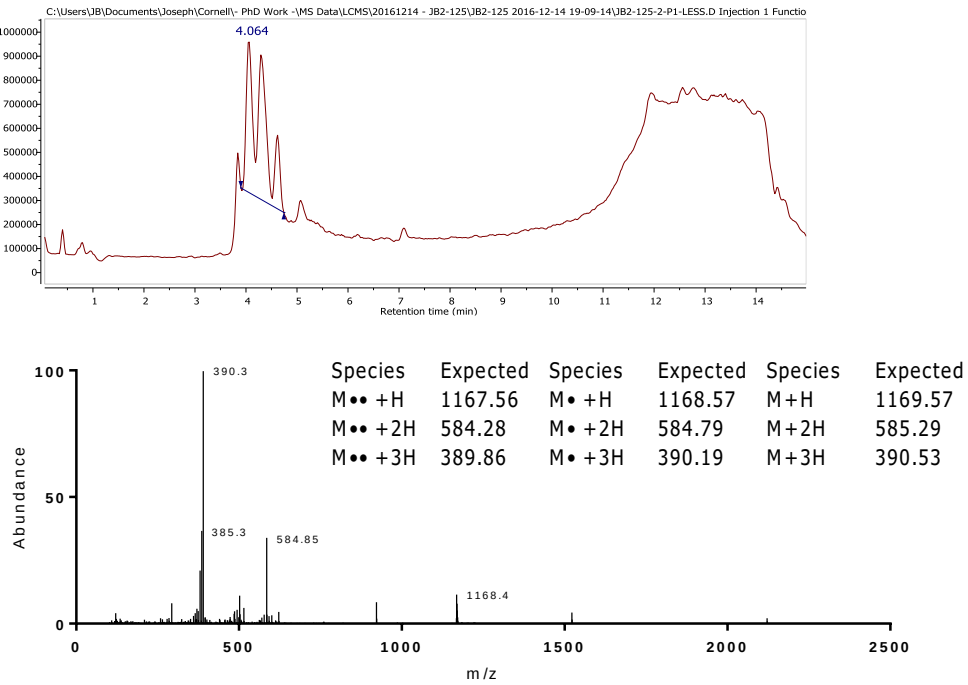

Positive mode LCMS of the dispin labeled (Proxyl) (DTT-G)$_2$ where the parent and half-mass are observed as indicated in the table showing a distribution of the nitroxide oxidation states.

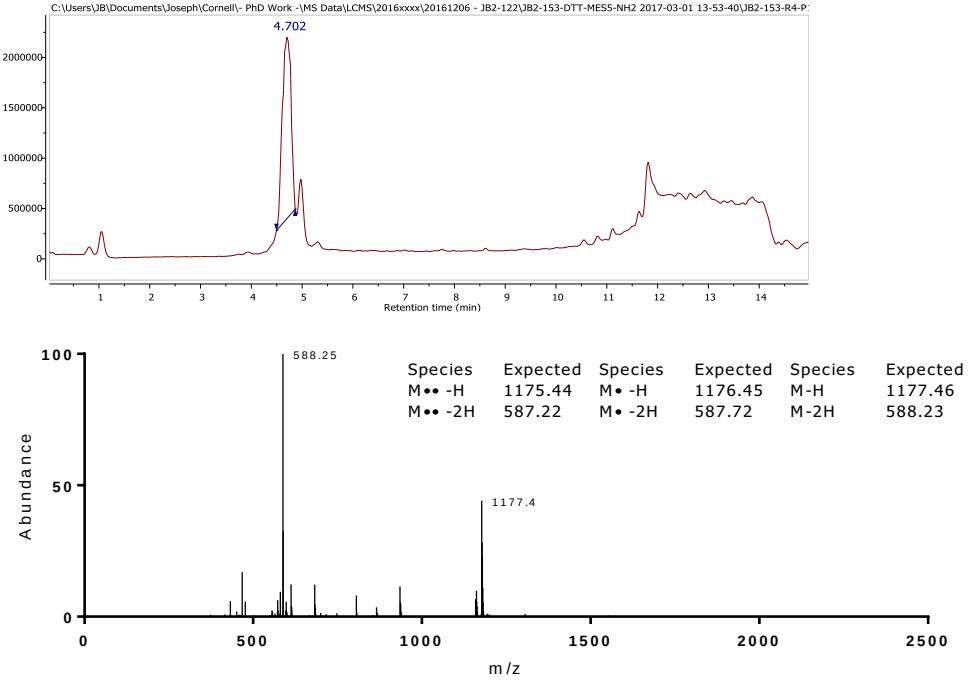

Negative mode LCMS of the dispin labeled (Proxyl) (BDT-Sulf)$_2$ where the parent and half-mass are observed as indicated in the table showing a distribution of the nitroxide oxidation states.

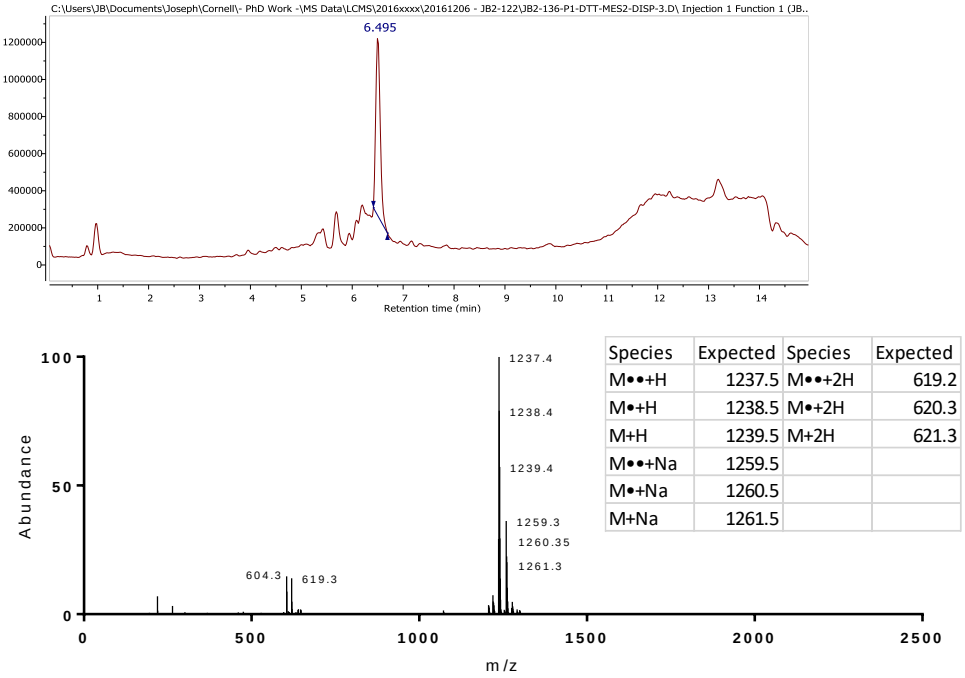

Species	Expected	Species	Expected
M••+H	1237.5	M••+2H	619.2
M•+H	1238.5	M•+2H	620.3
M+H	1239.5	M+2H	621.3
M••+Na	1259.5		
M•+Na	1260.5		
M+Na	1261.5		

Positive mode mass spectra from the LCMS of the collected peak from HPLC of the dispin labeled (DTT-MeS)$_2$-NH$_2$. The parent and half masses are observed showing a distribution of the nitroxide oxidation states.

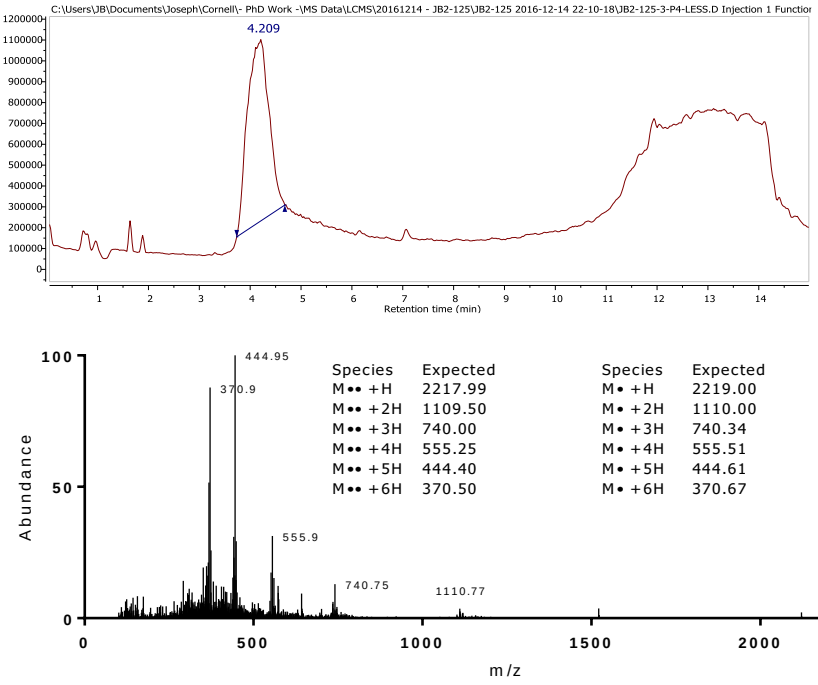

Species	Expected
M•• +H	2217.99
M•• +2H	1109.50
M•• +3H	740.00
M•• +4H	555.25
M•• +5H	444.40
M•• +6H	370.50

Species	Expected
M• +H	2219.00
M• +2H	1110.00
M• +3H	740.34
M• +4H	555.51
M• +5H	444.61
M• +6H	370.67

Species	Expected
M +H	2220.01
M +2H	1110.51
M +3H	740.67
M +4H	555.76
M +5H	444.81
M +6H	370.84

Positive mode mass spectra from the LCMS of the collected peak from HPLC of the dispin labeled (DTT-G)$_5$-NH$_2$. The parent mass is not observed, but the half, third, fourth, and fifth masses are observed showing a distribution of the nitroxide oxidation states.

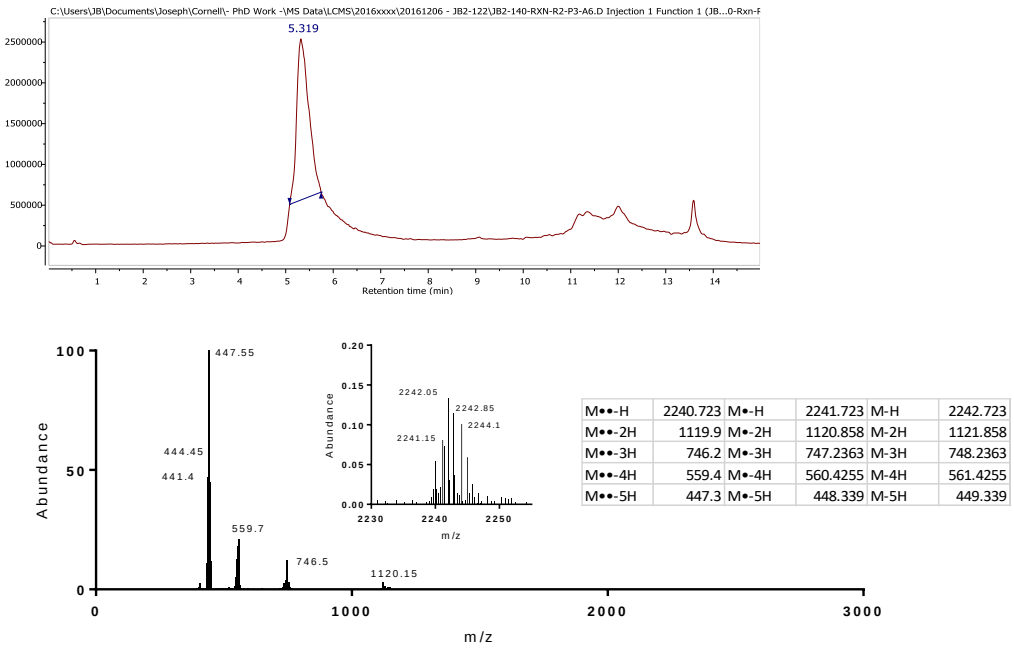

Negative mode mass spectra from the LCMS of the dispin labeled (BDT-Sulf)$_5$-NH$_2$. The parent mass (M+H)$^{+1}$ is observed as well as the 2nd and 3rd masses showing a distribution of the nitroxide oxidation states.

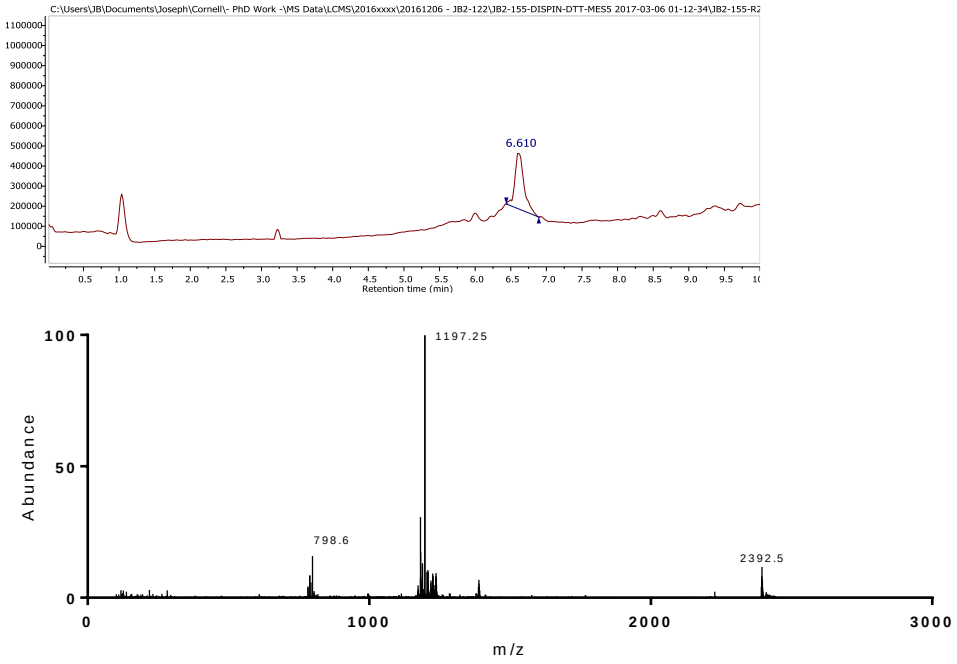

Positive mode LCMS TIC (top) and mass spectra (bottom) of the purified dispin labeled (DTT-MeS)$_5$-NH$_2$. The full (expected 2392.8 m/z), half mass (expected 1196.9 m/z), and third mass (expected 798.3 m/z) are observed. The Proxyl-(DTT-MeS)$_5$-Proxyl does not ionize that well, which makes sense with no simple means of ionization (amine, etc).

Appendix C : Additional Supplementary Material for Chapter 4

Materials in this appendix have been adapted from the Supplementary Information provided adapted with permission from Brown, J. S.; Mohamed, Z. J.; Artim, C. M.; Thornlow D. N.; Hassler J. F.; Rigoglioso V. P.; Daniel S. D.; and Alabi C. A. Communications Biology 2018, 1 (220) under a Creative Commons Attribution 4.0 International License (http://creativecommons.org/licenses/by/4.0/) with modifications.

Hemolysis Assay

200 μL of red blood cells (Innovative Research Novi, MI) were washed twice with 500 μL PBS by centrifugation (5 min at 500g) and resuspended in PBS at 4 v/v%. OligoTEA solutions or controls were mixed 1:1 with the RBC solution in a v-bottom 96-well plate (100 μL total). The resulting mixture was incubated at 37°C for 1 h and then centrifuged (Beckman Coulter, 5 min at 1000g) at 4 °C. A total of 75 μL of supernatant was transferred to a new plate. Hemolysis was measured via absorbance of released hemoglobin at 540 nm on a TECAN Infinite M1000 PRO Microplate reader (Männdorf, Switzerland) and normalized to 0.1% Triton-X (100%) or PBS buffer (0%). All experiments were performed in duplicate.

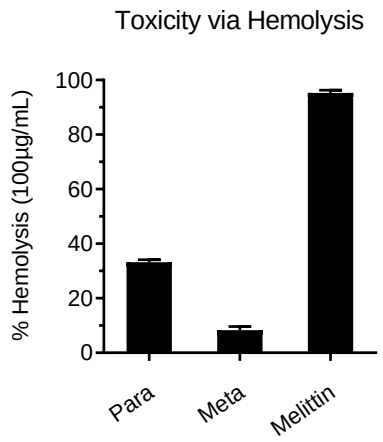

Figure C-1: *Hemolysis (Red blood cell) assay of Meta and Para*
Hemolysis was done at 75 µM with the method above. Melittin included as a positive control of a pore-forming membrane-disrupting agent. Error bar represents the standard deviation (n=2 biological replicates).

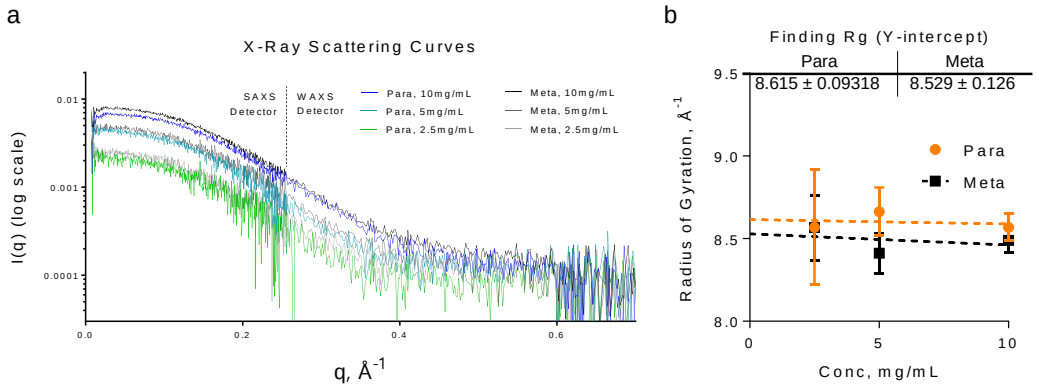

Figure C-2: *X-ray scattering and radius of gyration (Rg) determination*
(a) *PBS subtracted x-ray scattering curves were reduced as described above. Signal from the oligomers decays broadly into the wide-angle regime reflecting their small size.* ***(b)*** *The radius of gyration was determined by extrapolating to infinite dilution (y-intercept) from the radii at individual concentrations determined by fitting within the Guinier regime (Table C-1).*

Table C-1: *Outputs from Guinier Fits from BioXTAS RAW (v1.4.0)*

	Concentration, mg/mL	Rg (Å)	Error (Å)	r^2	qRg (low q)	qRg (hi q)	qmin	qmax
Para	10	8.568	0.082	0.951	0.454	1.183	0.053	0.138
	5	8.663	0.146	0.843	0.273	1.096	0.032	0.126
	2.5	8.588	0.341	0.523	0.280	1.001	0.033	0.117
	1.25			< 0.3	Not used for Rg analysis due to noise			
Meta	10	8.489	0.077	0.952	0.352	1.078	0.041	0.127
	5	8.413	0.121	0.851	0.139	1.087	0.017	0.129
	2.5	8.567	0.196	0.708	0.170	1.102	0.020	0.129
	1.25			< 0.3	Not used for Rg analysis due to noise			

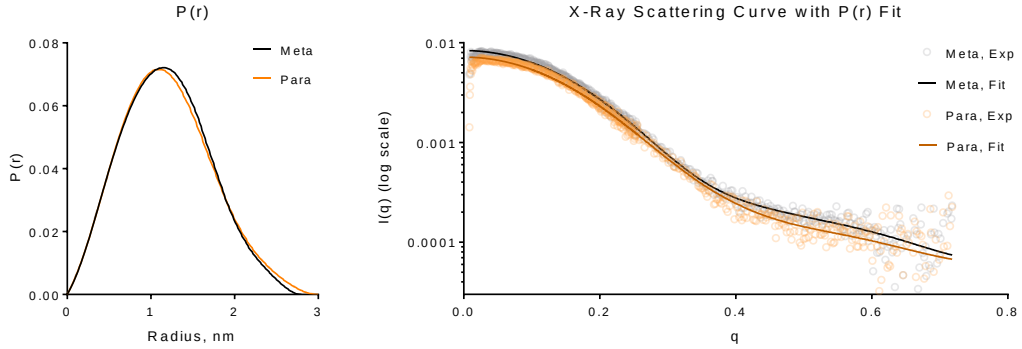

Figure C-3: *Pair-wise distributions reconstructed from SAXS/WAXS profiles* ***(left)*** *Pair-wise distribution generated by GNOM*[506] *within BioXTAS RAW.*[435] *Dmax was calculated to be 2.8nm and 3.0nm for the Meta and Para, respectively, based on DATGNOM.* ***(right)*** *Raw scattering data and the fit solution used in the reconstructed pair-wise distribution.*

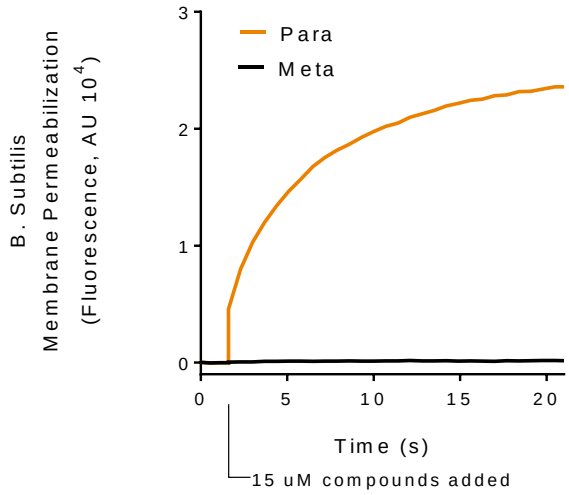

Figure C-4: *Hemolysis of Meta and Para with B. subtilis*

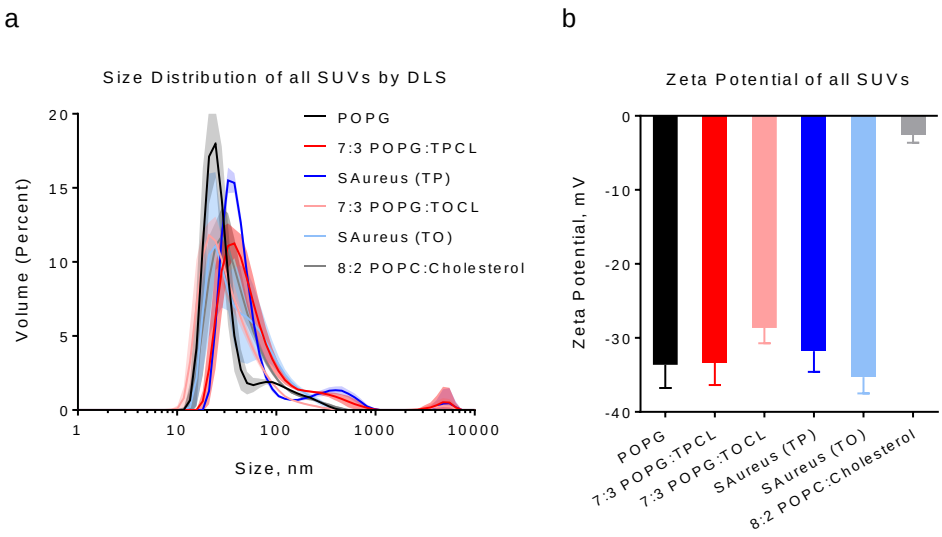

Figure C-5: *Dynamic light scattering and zeta potential of all SUVs*
(a) *Volume distribution of all SUVs revealing compositions are comprised of mostly 20-80 nm particles.* ***(b)*** *Zeta potential measurements of all SUVs revealing their strong anionic surface charge, with the exception of the mammalian mimetic composition 8:2 POPC:Cholesterol. Even with the addition of neutral lipids, the S. aureus mimetic SUVs maintained a strong negative charge. TP and TO refer to the cardiolipin tail lengths explored. TPCL was used because it provided a better quality membrane after inspection by fluorescence microscopy.*

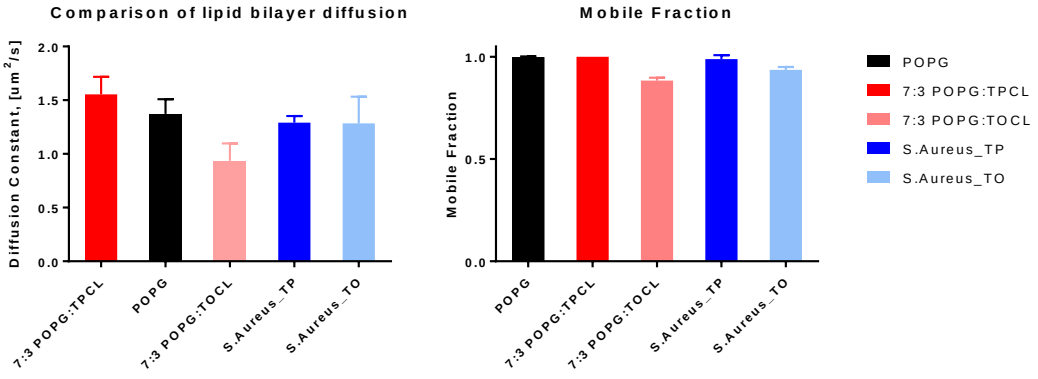

Figure C-6: *Fluorescence recovery after photobleaching of all mimetic membranes FRAP of all membrane mimetics show similar membrane fluidity and diffusion between 1-1.5 $\mu m^2/s$ and mobile fractions at room temperature (22°C). The diffusivity of these membranes is modestly faster than bacterially isolated membranes from outer membrane vesicles (OMVs), which demonstrate a diffusivity of approximately ~0.5 $\mu m^2/s$.*[429]

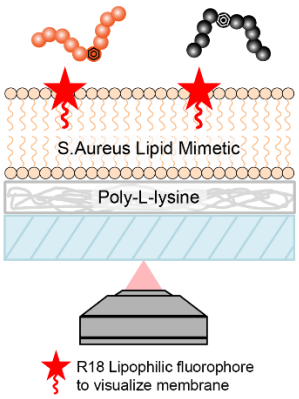

Figure C-7: *Diagram of fluorescence microscopy set-up*
The lipid bilayer is visualized by a lipophilic dye R18 at 0.05-0.1 mol% (rhoadmine with C18 alkyl tail). A poly-L-lysine (Sigma P8920, 150-300k MW) was necessary to enable the formation of lipid bilayers on glass microscope slides due to the SUVs' net negative charge.

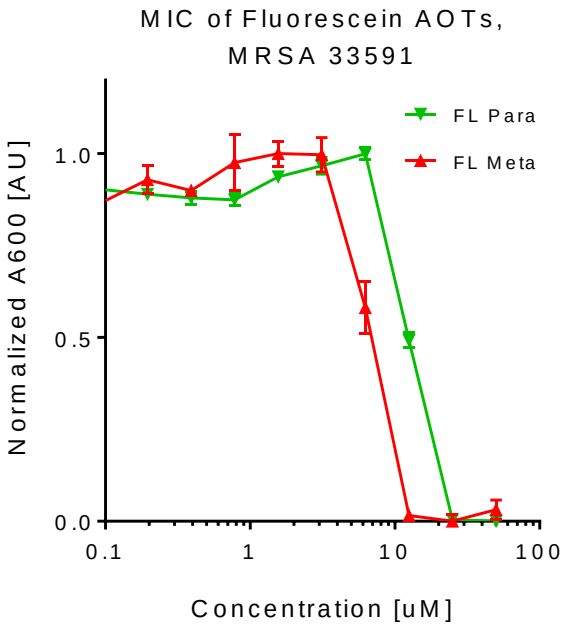

Figure C-8: *MIC of fluorescein oligomers.*
The fluorescein labeling of the Meta and Para decreases their potency against MRSA 33591 by about 10-fold, but should hopefully serve to similarly localize and/or function with the unlabeled oligomers.

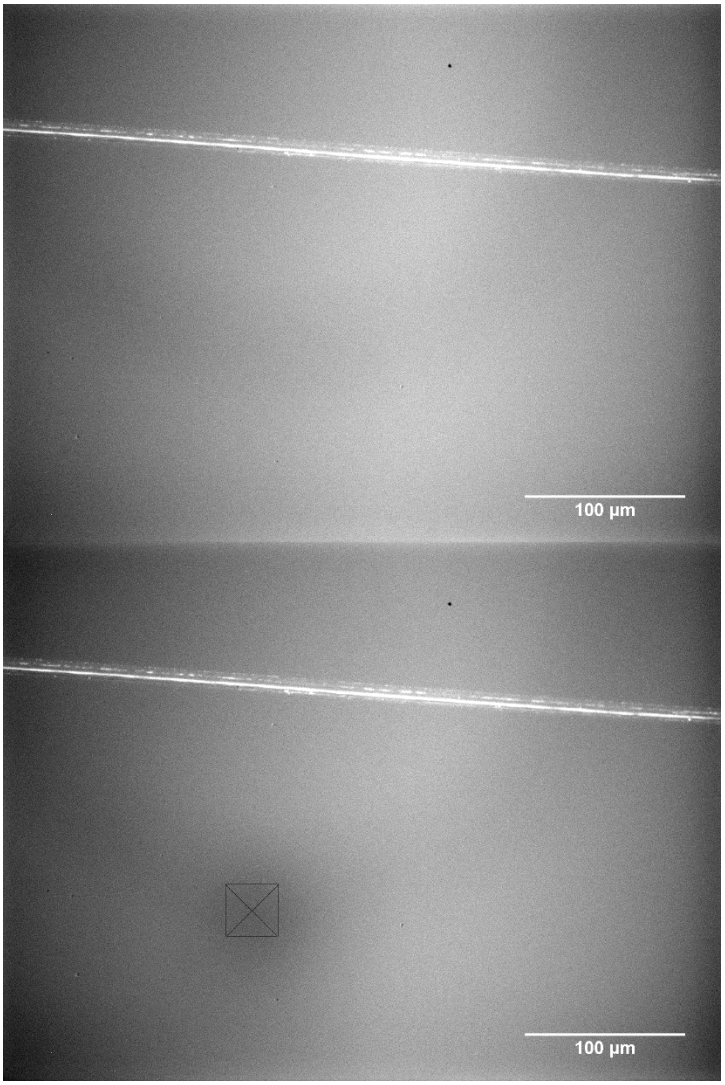

Figure C-9: *Confirmation of lipid extraction by Triton-X detergent*
There was little remaining signal, but these images were captured by maximizing the fluorescence excitation and using a long exposure time. The scratch was created while the bilayer was present (before removal) to find the focal plane. Microscopy slide was then treated with 5mM Triton-X to remove the R18-labeled lipid bilayer. ***(top)*** *The bilayer removal was verified visually* ***(bottom)*** *and also by the lack of a photo-bleached spot by the FRAP laser (100ms exposure, which was located in the black crosshairs).*

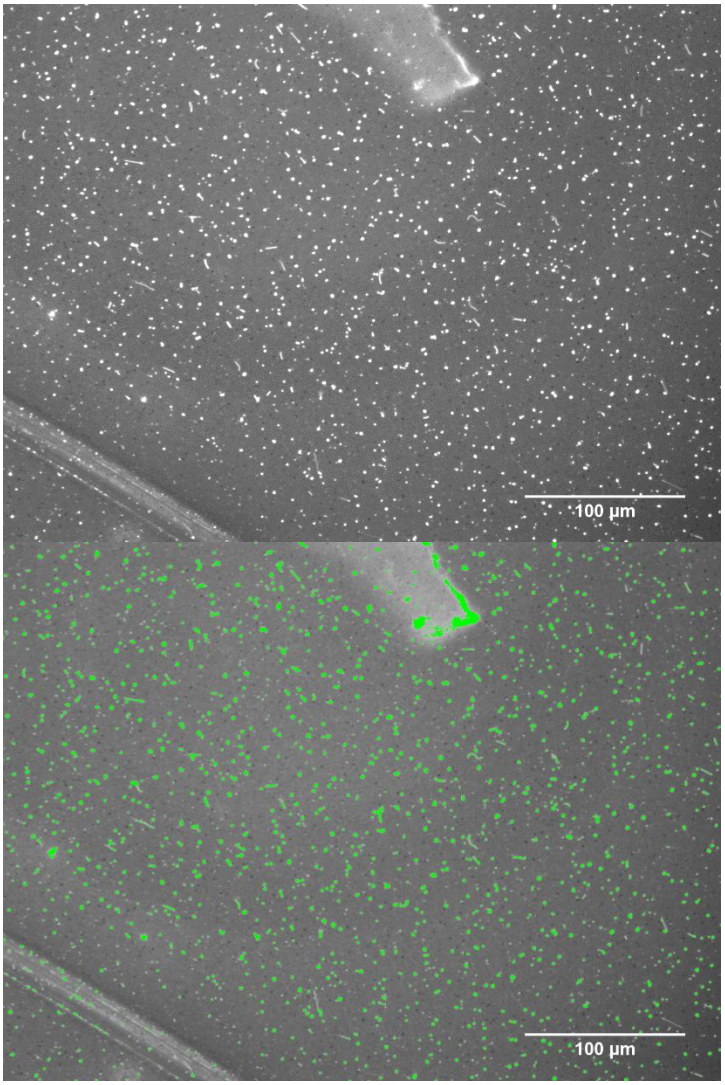

Figure C-10: *ImageJ thresholding of aggregates after 5uM Meta exposure* ***(top)*** *The original microscopy image with aggregates (white dots) that form after treatment of the S. aureus mimetic membrane with 5µM Meta for 10 minutes. The scratch in the lower left corner was created to aid focus on the lipid bilayer.* ***(bottom)*** *ImageJ composite image of thresholding, highlighting green where aggregates are located. Some minor undercounting of small particles is observed. Particle thresholds were then processed with ImageJ using Particle Analysis to report the number and size of the aggregates.*

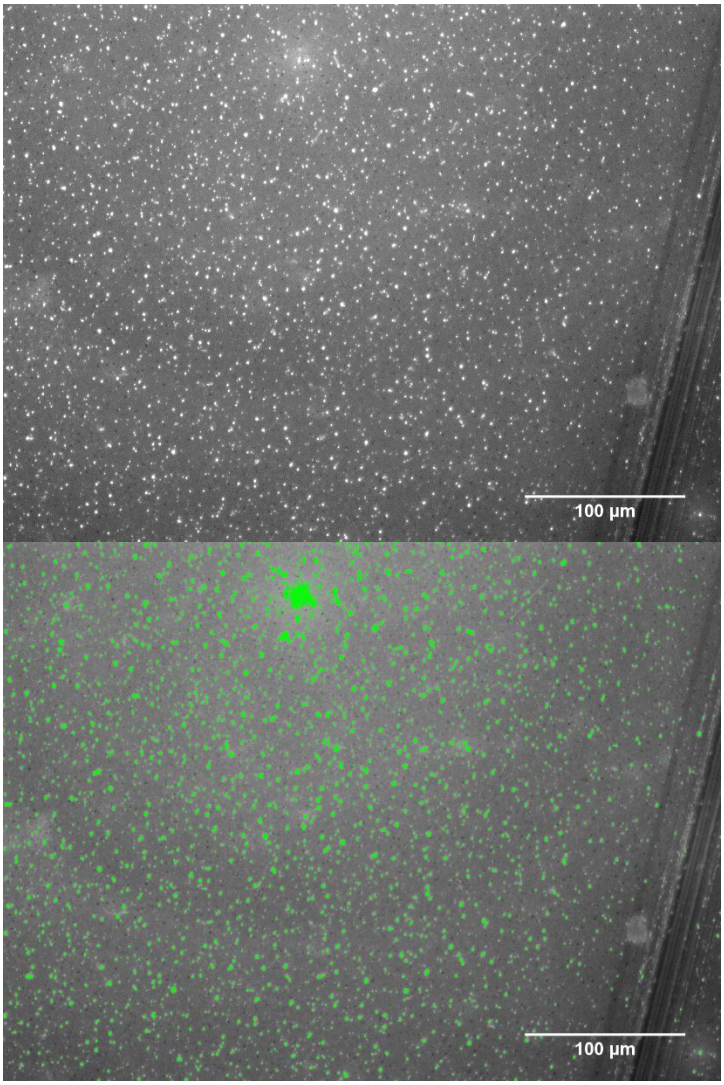

Figure C-11: *ImageJ thresholding of aggregates after 5uM Para exposure* ***(top)*** *The original microscopy image with aggregates (white dots) that form after treatment of the S. aureus mimetic membrane with 5µM Para for 10 minutes. The scratch in the lower left corner was created to aid focus on the lipid bilayer.* ***(bottom)*** *ImageJ composite image of thresholding, highlighting green where aggregates are located. Some minor undercounting of small particles is observed. Particle thresholds were then processed with ImageJ using Particle Analysis to report the number and size of the aggregates.*

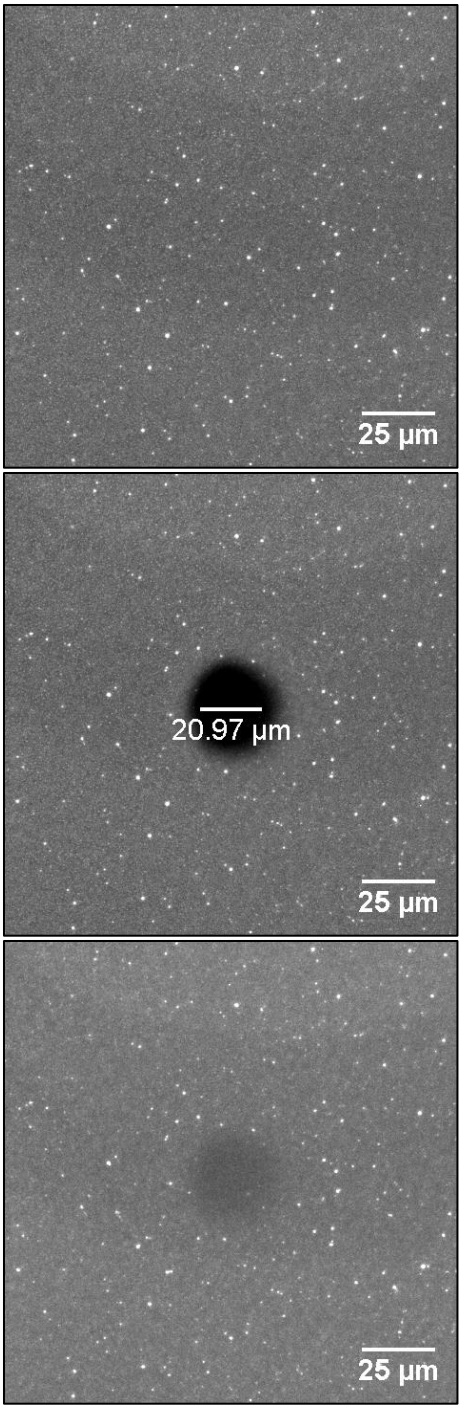

Figure C-12: *Size of FRAP photobleached spot*

(top) *An S. aureus mimetic membrane on a PLL substrate was treated with 5µM Para for 1 hour and washed with PBS. (t=0)* ***(middle)*** *A ~20 µm diameter spot in bilayer was photo-bleached by 150 mW 561 nm optically pumped semiconductor laser (Coherent, Inc.) for 100 ms* ***(bottom)*** *The recovered FRAP spot 30 minutes later showing that the aggregates are immobilized and they do not recover their spot fluorescence with a small immobile fraction.*

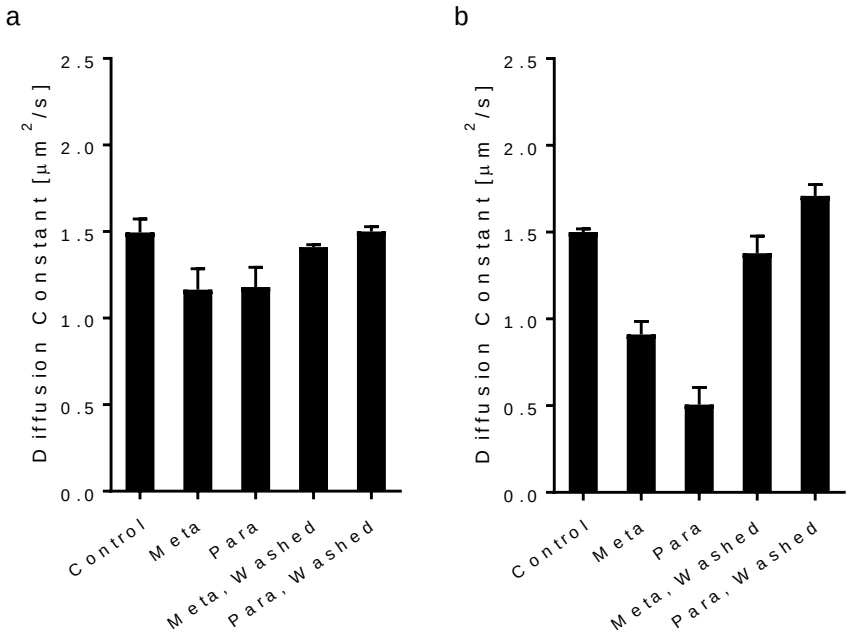

Figure C-13: *FRAP revealing reversible binding*
SLBs were treated and equilibrated with ***(a)*** *2.5 and* ***(b)*** *5 μM oligomer to show reversible binding of a molecular, non-aggregate state.*

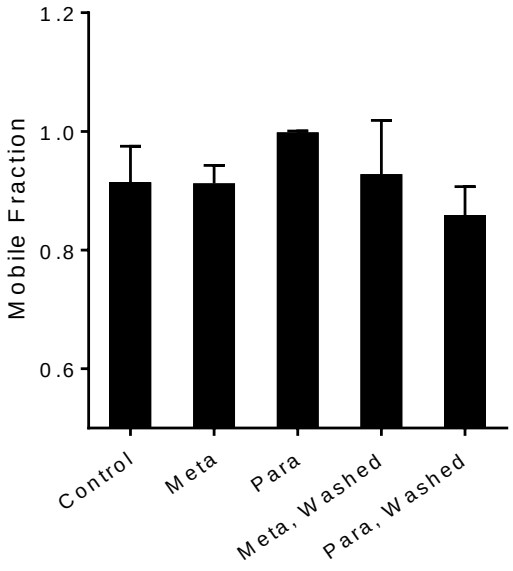

Figure C-14: *Mobile fraction of FRAP measurements in main text.*
A small immobile fraction is present as shown by the FRAP as described in Figure 4g.

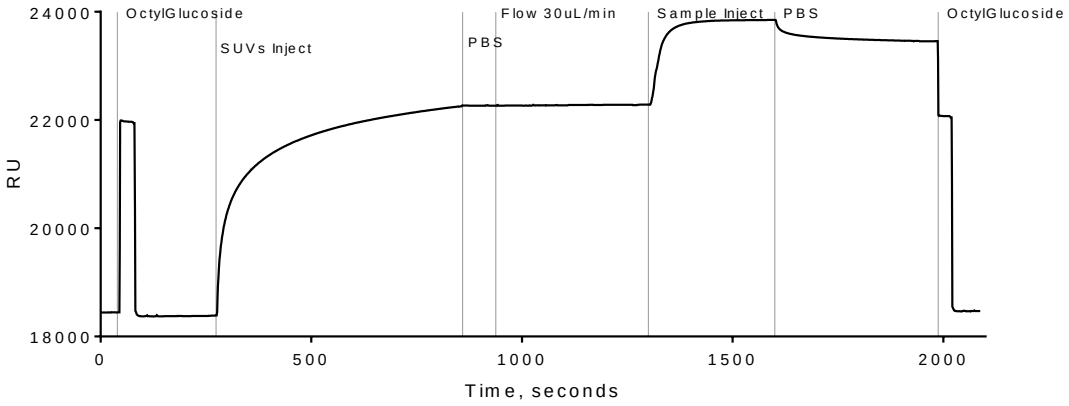

Figure C-15: *Full sensorgram example of SPR run 5uM Meta on a S. aureus captured mimetic membrane.*

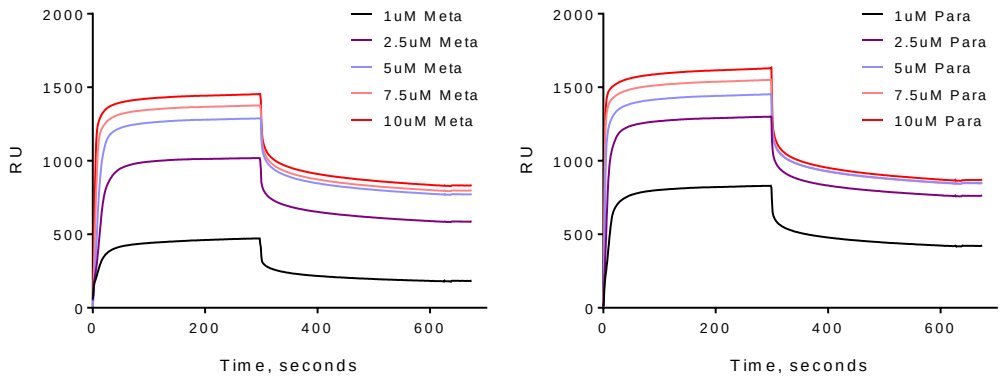

Figure C-16: *SPR sensorgram of Meta and Para on S. aureus lipid mimetic*
Per literature search and discussion above, the S. aureus lipid mimetic composition was 4:5:11 neutral lipids (18:1 DG): TPCL: POPG.

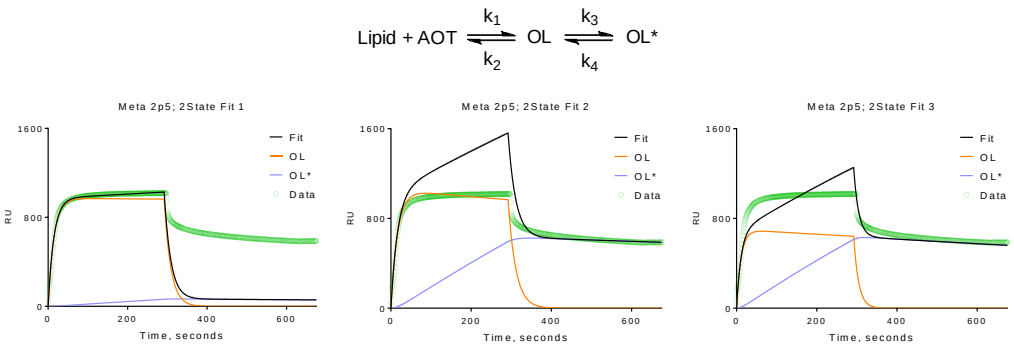

Figure C-17: *Failure of the two-state model without loss to fit SPR data*

The attempts to fit the data of the 2.5μM Meta with the 2-State model shown were unsuccessful. Fits shown demonstrate that the model could fit the association or the dissociation phase, but not both simultaneously.

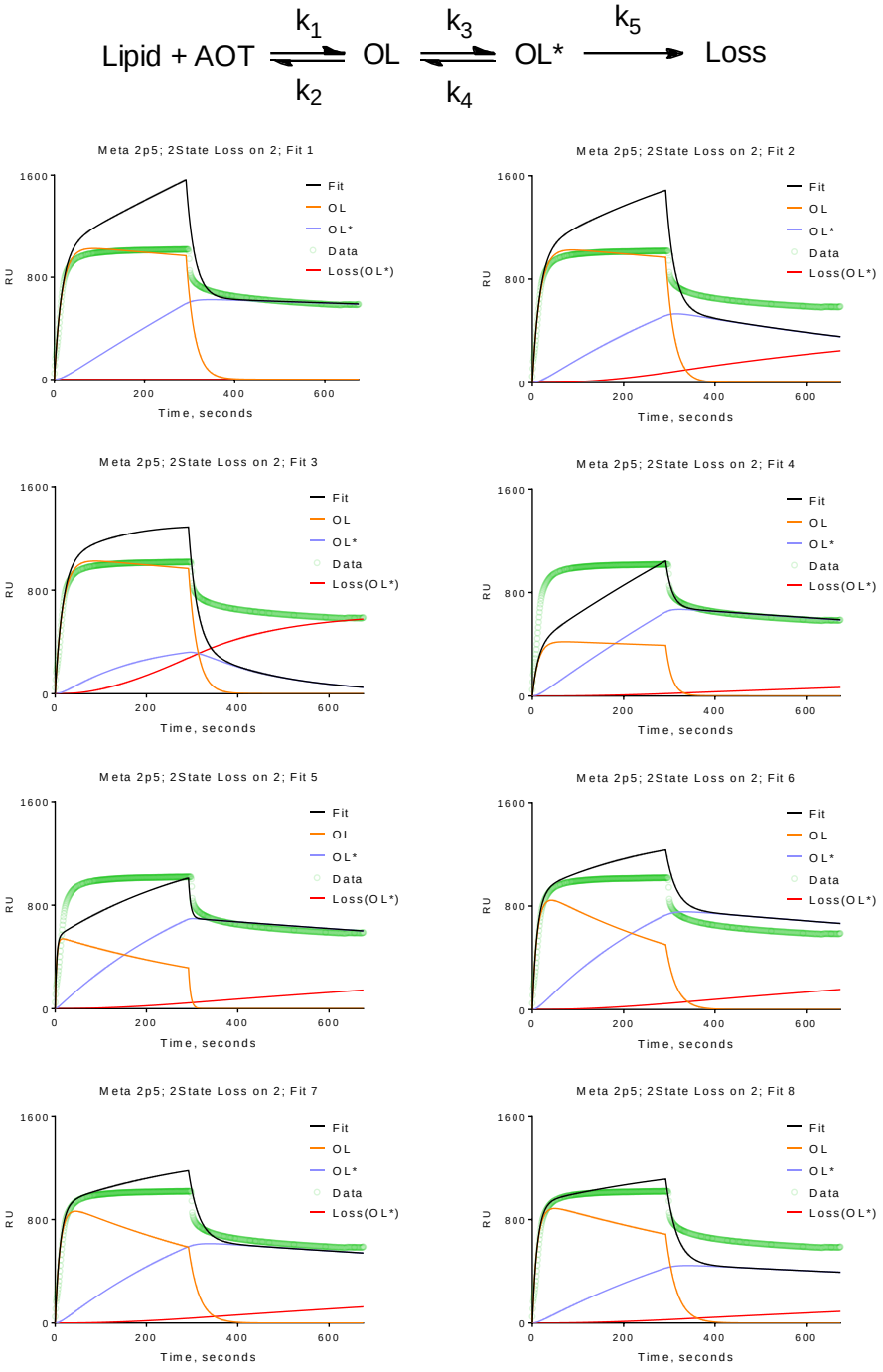

Figure C-18: *Failure of the two-state model with loss to fit SPR data. Several attempts to make the 2 State Model with Loss on 2 fit, as it is the prevailing model within literature. However, one can observe how this model can fit multiple sensorgrams seen in other literature. For this observed data, the model could not converge, likely because of either a) the lack of an upward slope in the association phase or b) the substantially elevated baseline in the dissociation phase.*

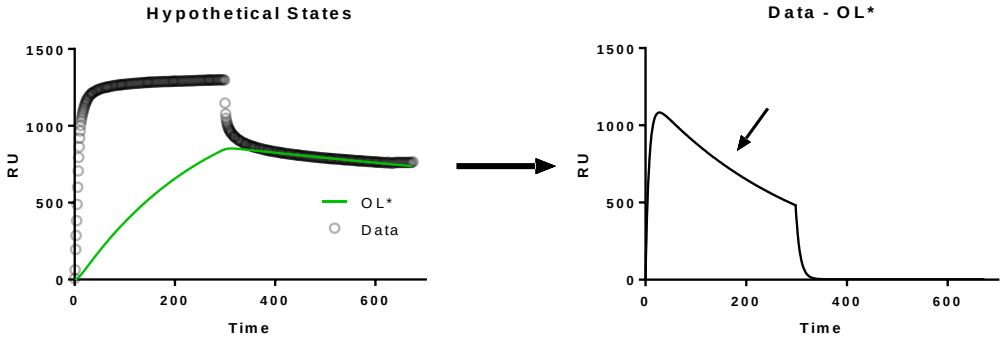

Figure C-19: *Data shows evidence for loss on intermediate step*
In assuming irreversible aggregation (OL) to be responsible for the elevated baseline during dissociation, the data remaining from that assumption shows a curve that would be challenging for fitting with the two state model with loss on the second step. In particulate, the curvature of downward slope (see arrow), would be difficult to fit.*

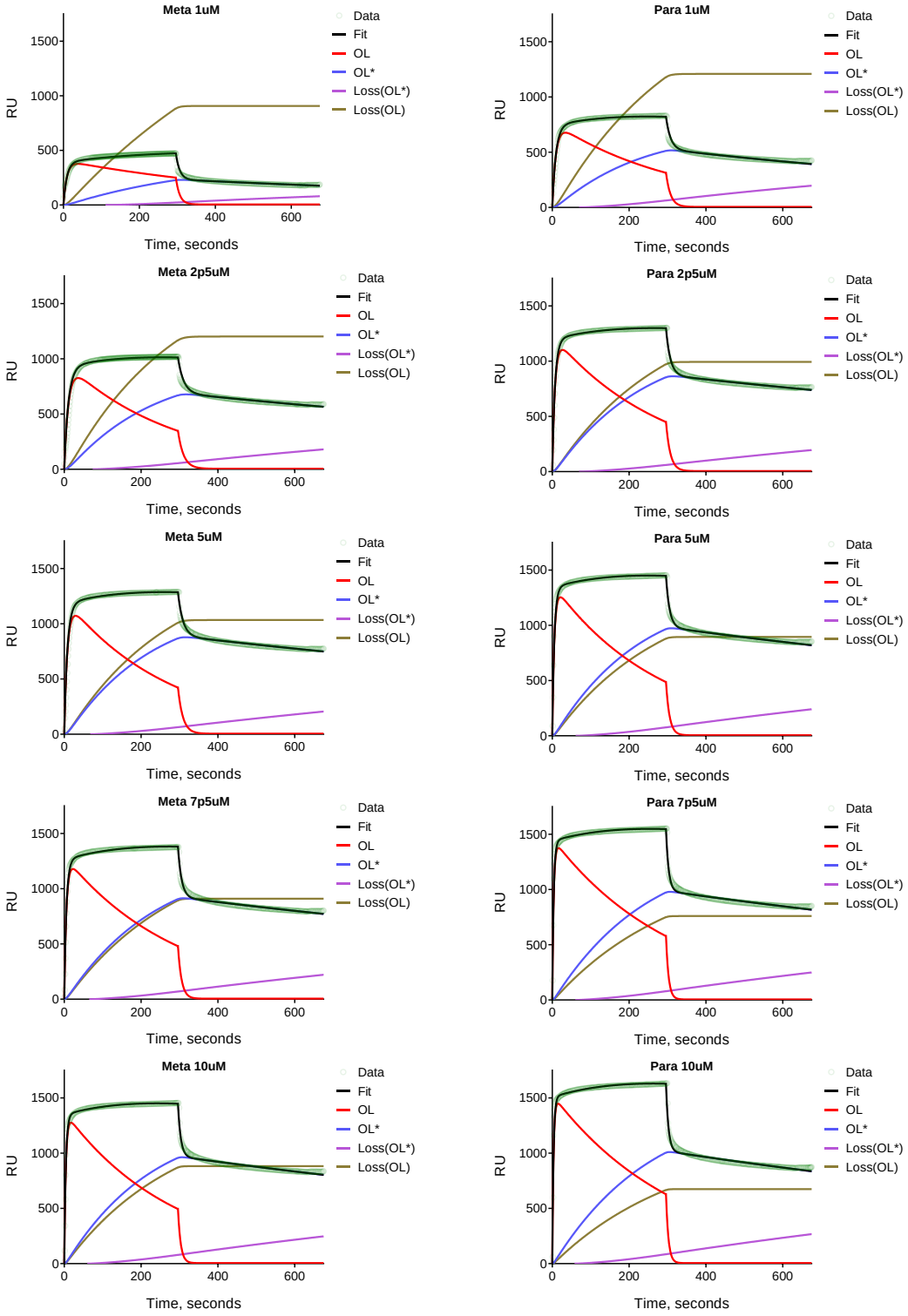

Figure C-20: *All model fits of SPR data on S. aureus mimetic membranes*

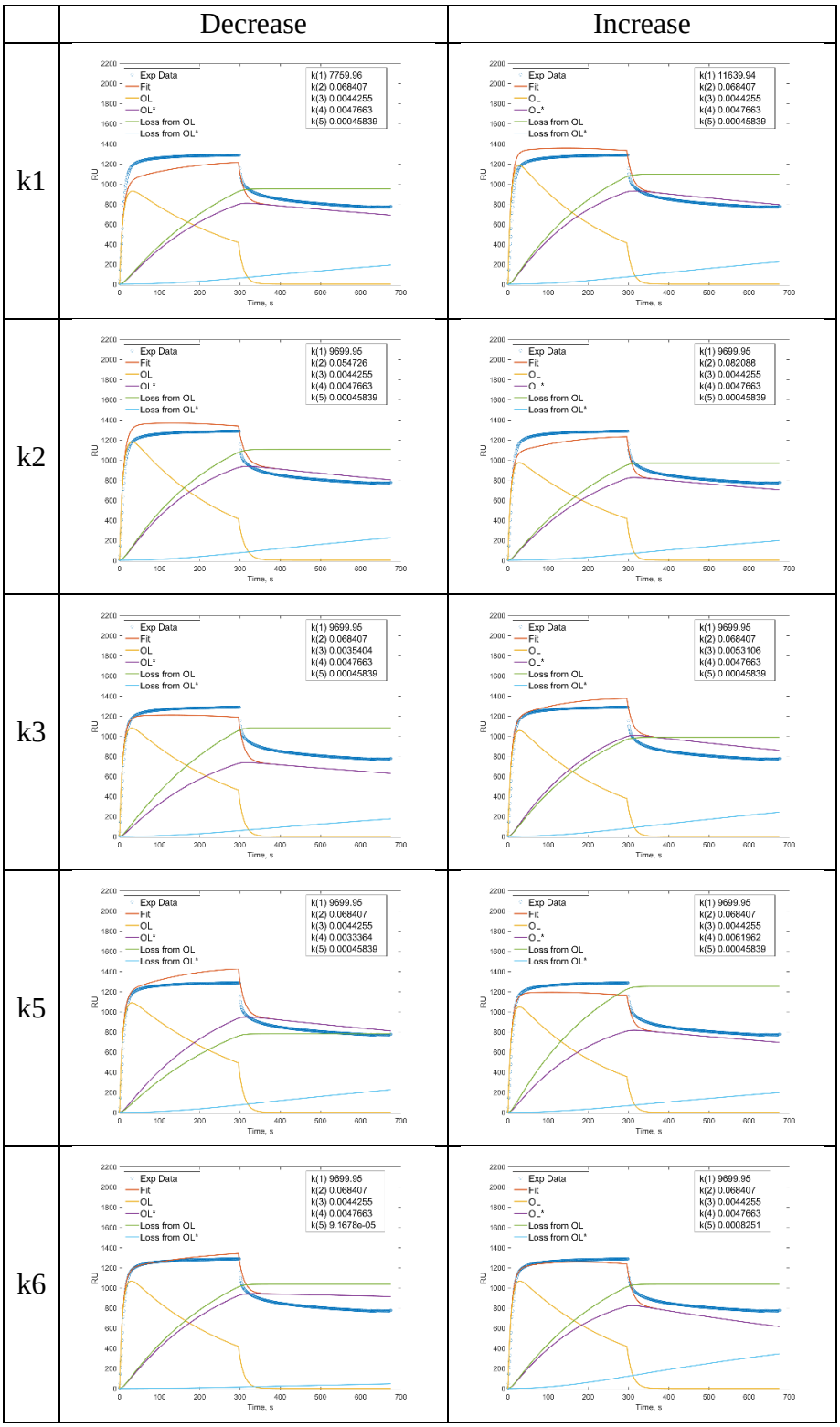

Figure C-21: *Model behavior demonstrated by varying all parameters Provided to aid the reader is how the model behaves based on its parameter set. (5uM Meta SPR Data, S. aureus mimetic memrbane)*

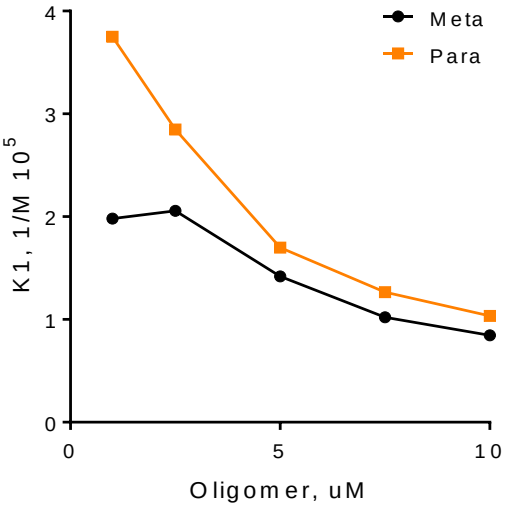

Figure C-22: *K1 versus oligomer concentration showing a concentration threshold*
The equilibrium constant K1 does show the desired concentration trend for a parameter that trends close to the biological threshold (i.e. MIC). Specifically, the Meta K1 does not continue increasing as the oligomer concentration decreases. Physically, it is hard to interpret K1 because it is not simply "binding," as it does encompass several physical states as understood in literature (e.g. binding, tighter binding, insertion, molecular aggregation)[401]*. Therefore, this data shows there is perhaps a limit to the cooperativity of this process (i.e. the equilibrium decreases as the concentration increases).*

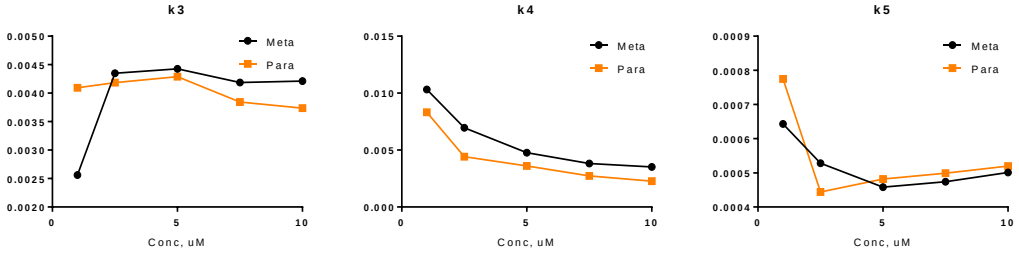

Figure C-23: *Rate constants not showing a strong concentration threshold*
These rate constants show behavior where the parameter mostly trends with concentration and do not show the expected behavior of a differential at low concentration and similarities at high concentration. Parameters k5 and k6 are interesting because they indicate that the losses incurred by the membrane are functions of concentration. These losses may be representations of complex states that are not properly described by a single parameter, which could be cooperative or competing (aggregates, micelle formation, etc).

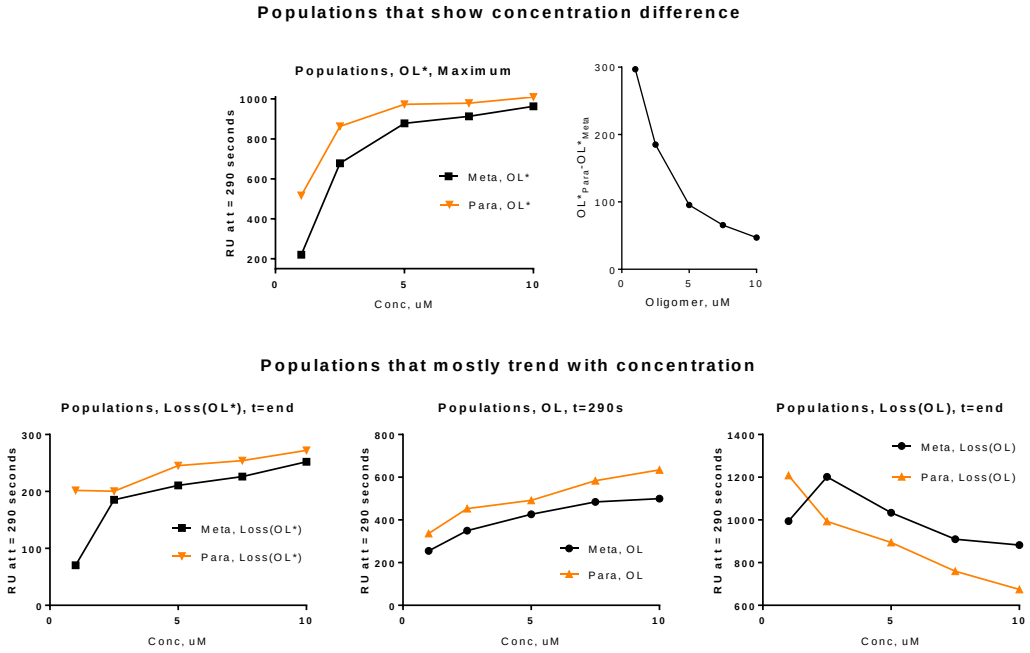

Figure C-24: *Populations from the Meta and Para model fits versus concentration* ***(Top)*** *The population of OL* represents the aggregate, and it shows a differential in behavior between the Meta and Para as a function of concentration made more clear when looking at the difference between the two oligomers.* ***(Bottom)*** *These populations show behavior where the parameter mostly trends with concentration and do not show the expected behavior of a differential at low concentration and similarities at high concentration. Loss(OL*) does show some indication of trending with OL*, but only around 1μM.*

Table C-2: *All parameters from model fits from all data with RMSD error*

	Concentration, μM	k1 (10^4)	k2 (10^{-2})	k3 (10^{-3})	k4 (10^{-3})	k5 (10^{-4})	$C_{Lipid,Total}$	RMSD of Fit
Meta	1	1.00	5.06	2.56	10.3	6.43	3000	9.10
	2.5	1.10	5.28	4.32	6.97	5.25	3000	22.7
	5	0.97	6.84	4.43	4.77	4.58	3000	24.9
	7.5	1.00	9.80	4.19	3.82	4.74	3000	17.3
	10	1.10	13.0	4.21	3.52	5.01	3000	18.2
Para	1	2.65	7.07	4.09	8.31	7.75	3000	11.4
	2.5	2.28	8.00	4.18	4.42	4.44	3000	15.9
	5	1.70	10.0	4.29	3.60	4.82	3000	22.4
	7.5	1.77	14.0	3.84	2.73	4.99	3000	25.2
	10	1.55	15.0	3.74	2.27	5.20	3000	28.6

More details, discussion, methodology, and source code is available in Chapter 4, Materials and Methods, Use of MATLAB to model and fit SPR data. Parameters from MATLAB fitting shown in table format where RMSD of Fit is defined as $RMSD = \sqrt{\frac{\sum_i^n (Exp_i - Fit_i)^2}{n}}$*, where i is the index point in time, n is the total number of time points, Exp is the experimental data point, and Fit is the fitted model data point at that time index.*

Supplementary Spectra (NMR, LCMS)

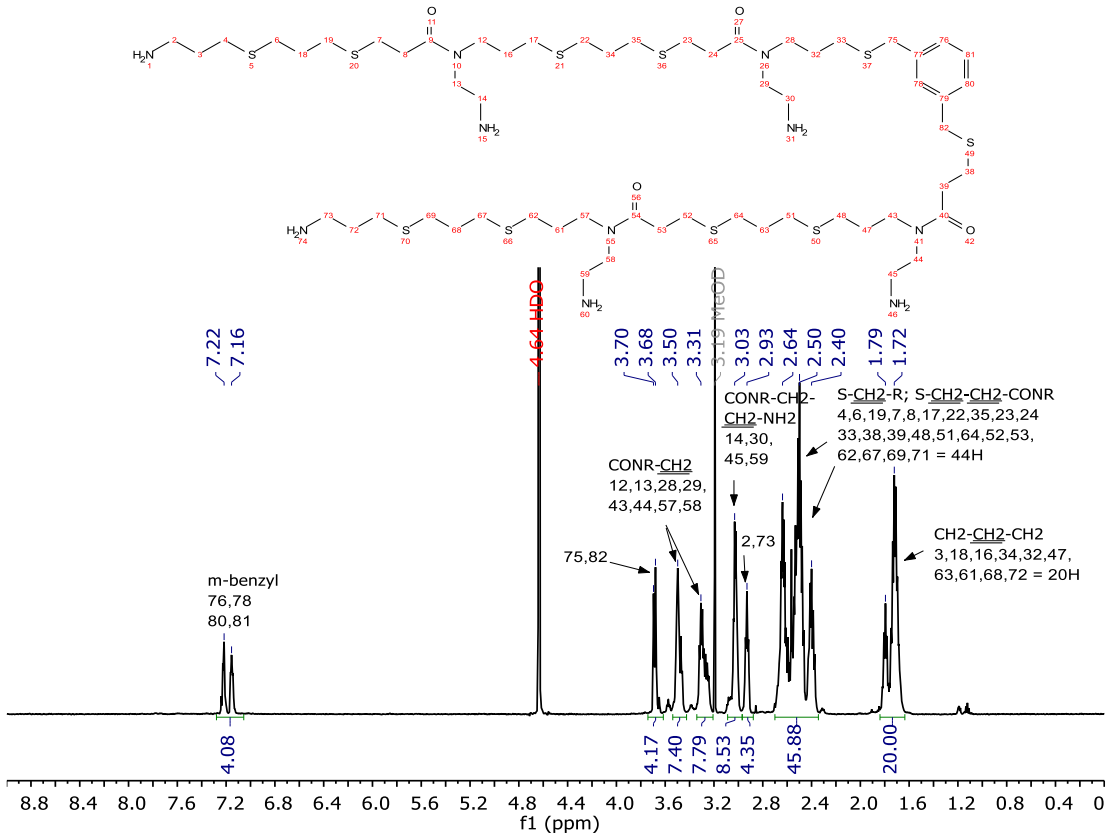

^{1}H NMR of the Meta in (D_2O, 600 MHz)

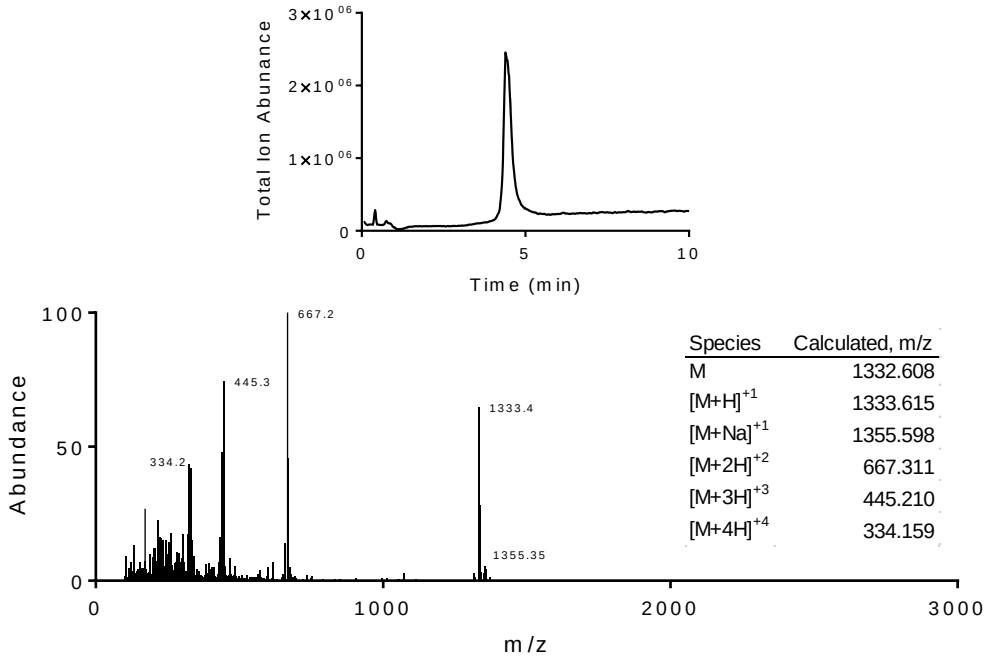

LCMS of the Meta. (Top) *Total ion count abundance versus time over a 10 minute gradient.* ***(Bottom)*** *Mass spectra confirming the presence of the Meta in the TIC peak.*

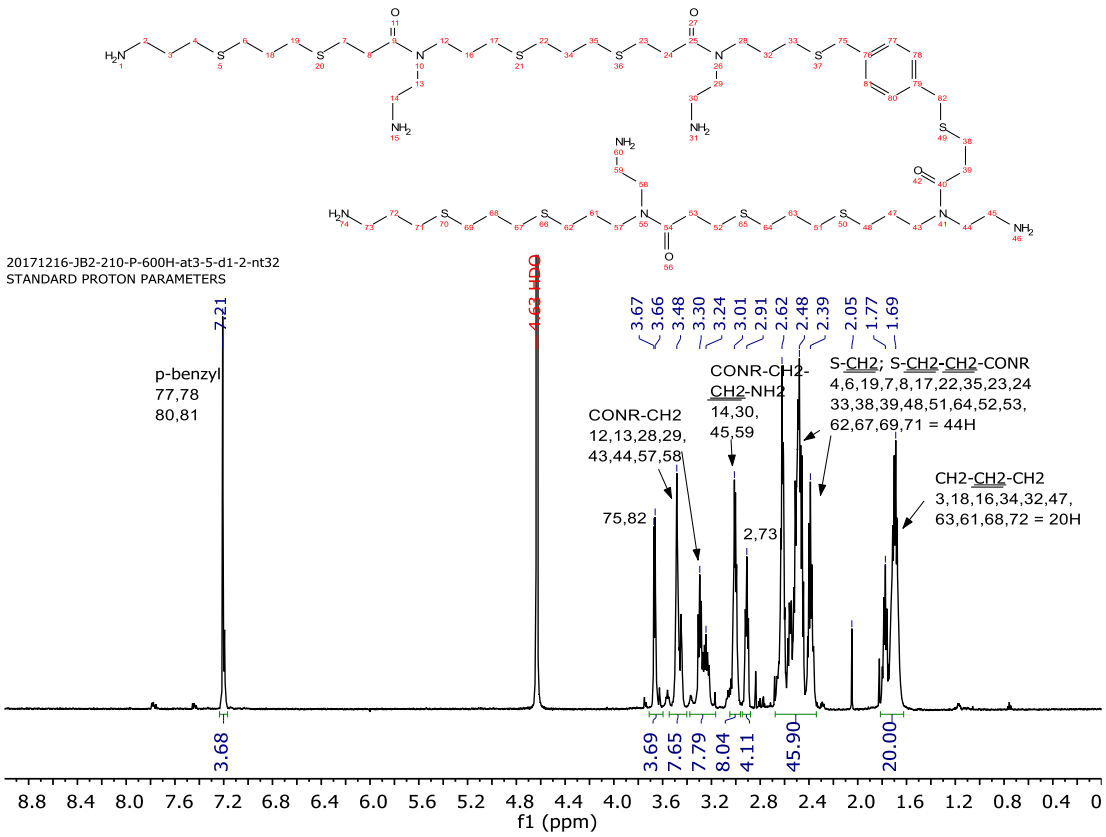

^{1}H NMR of the Para (D_2O, 600 MHz).

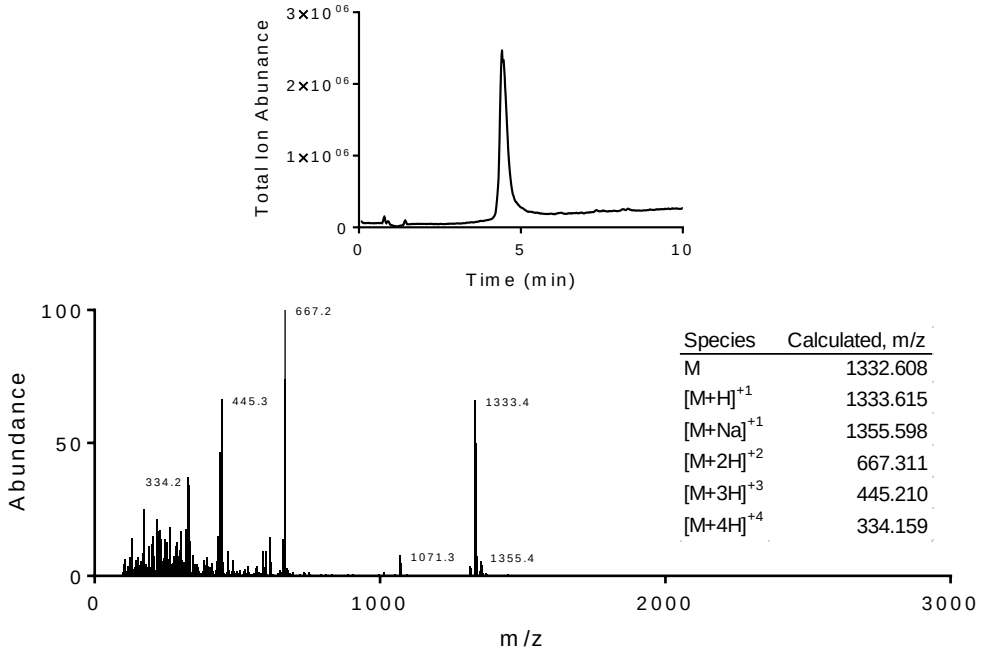

LCMS of the Para. (Top) *Total ion count abundance versus time over a 10 minute gradient.* ***(Bottom)*** *Mass spectra confirming the presence of the Meta in the TIC peak.*

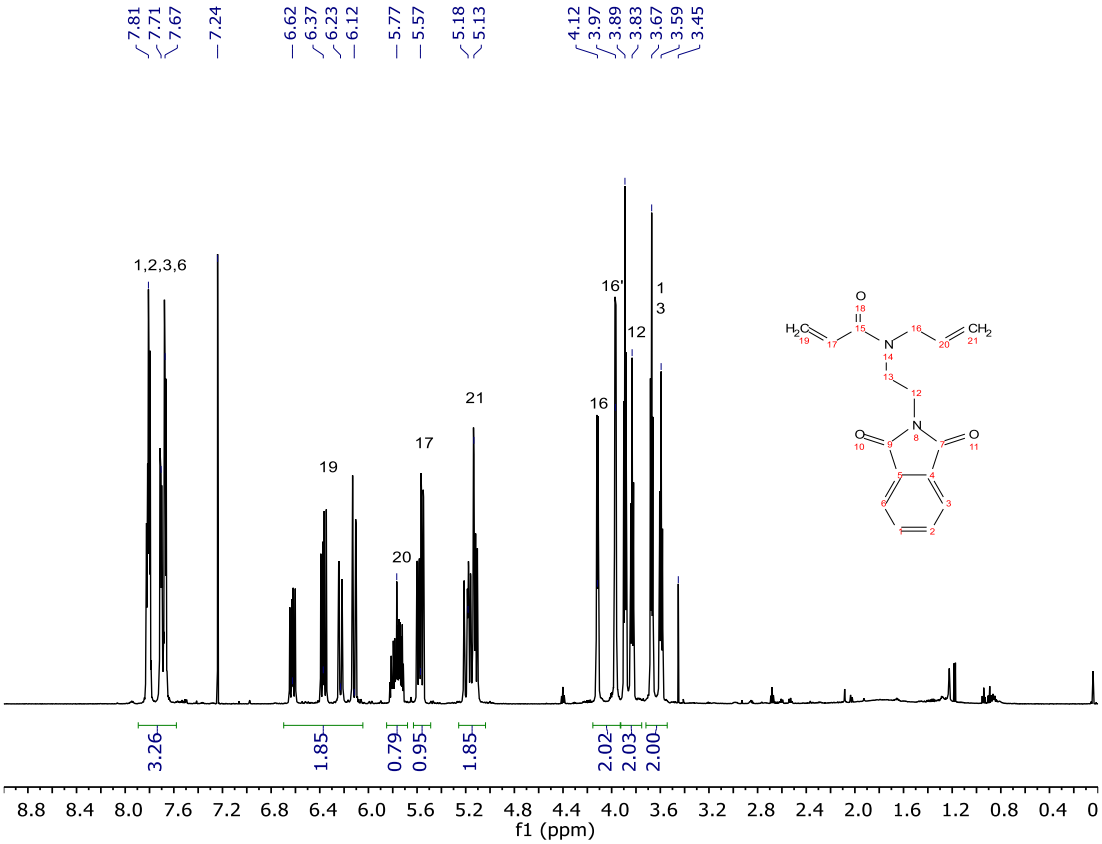

^{1}H NMR of the (N-phthalimide)ethylene N-allyl-N-acrylamide ($CDCl_3$, 600 MHz)

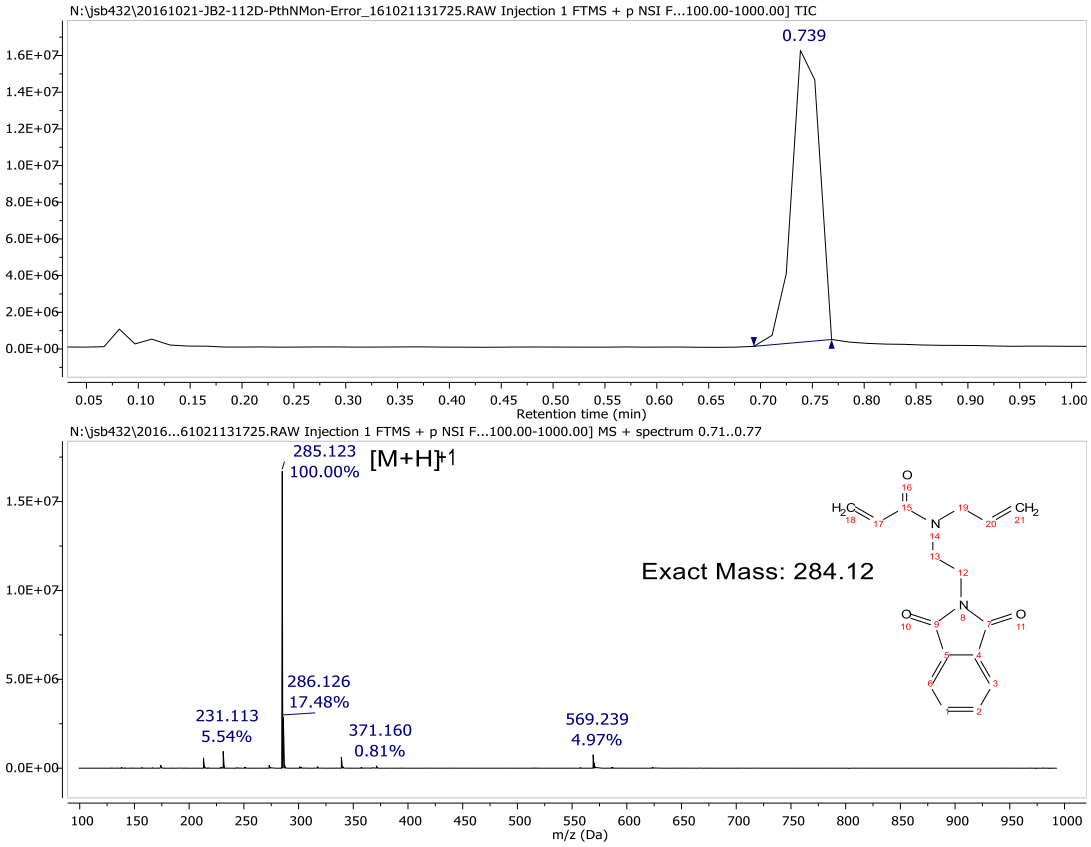

DART HR-MS of the (N-phthalimide)ethylene N-allyl-N-acrylamide

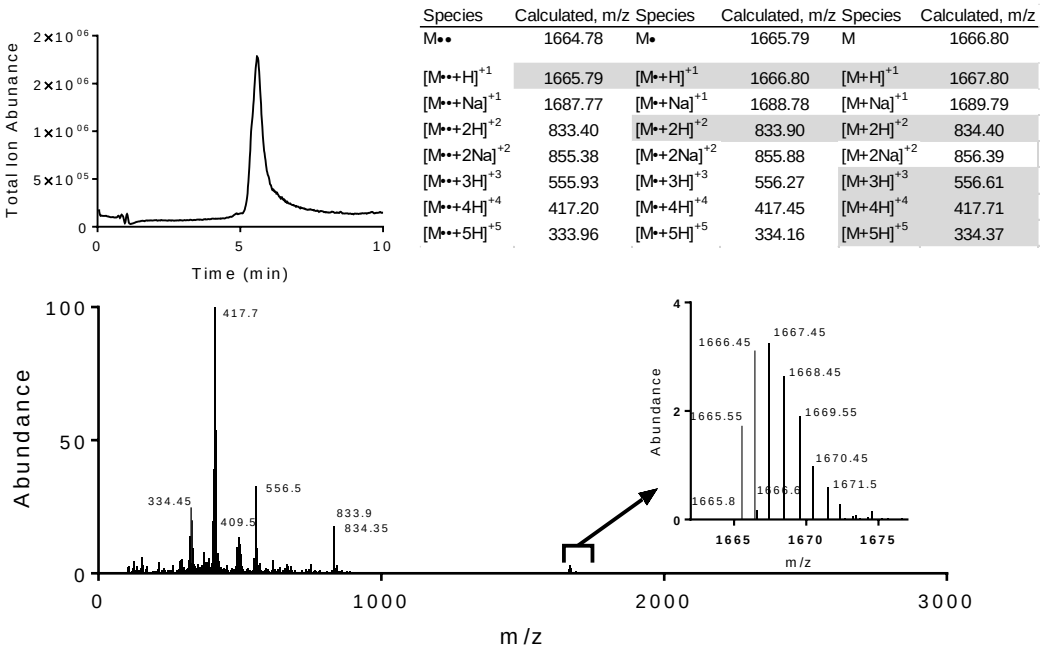

Species	Calculated, m/z	Species	Calculated, m/z	Species	Calculated, m/z
M••	1664.78	M•	1665.79	M	1666.80
$[M••+H]^{+1}$	1665.79	$[M•+H]^{+1}$	1666.80	$[M+H]^{+1}$	1667.80
$[M••+Na]^{+1}$	1687.77	$[M•+Na]^{+1}$	1688.78	$[M+Na]^{+1}$	1689.79
$[M••+2H]^{+2}$	833.40	$[M•+2H]^{+2}$	833.90	$[M+2H]^{+2}$	834.40
$[M••+2Na]^{+2}$	855.38	$[M•+2Na]^{+2}$	855.88	$[M+2Na]^{+2}$	856.39
$[M••+3H]^{+3}$	555.93	$[M•+3H]^{+3}$	556.27	$[M+3H]^{+3}$	556.61
$[M••+4H]^{+4}$	417.20	$[M•+4H]^{+4}$	417.45	$[M+4H]^{+4}$	417.71
$[M••+5H]^{+5}$	333.96	$[M•+5H]^{+5}$	334.16	$[M+5H]^{+5}$	334.37

LCMS of the dispin-labeled Meta. (Top, Left) *Total ion count abundance versus time over a 10 minute gradient.* ***(Top, Right)*** *Expected masses to be observed demonstrating that the spin-label is mostly oxidized (will be reduced before measurement). Masses that were observed experimentally in the mass spectra are highlighted in gray.* ***(Bottom)*** *Mass spectra confirming the presence of the Meta in the TIC peak.* ***(Insert)*** *Closer examination of the mass spectra shows the parent masses.*

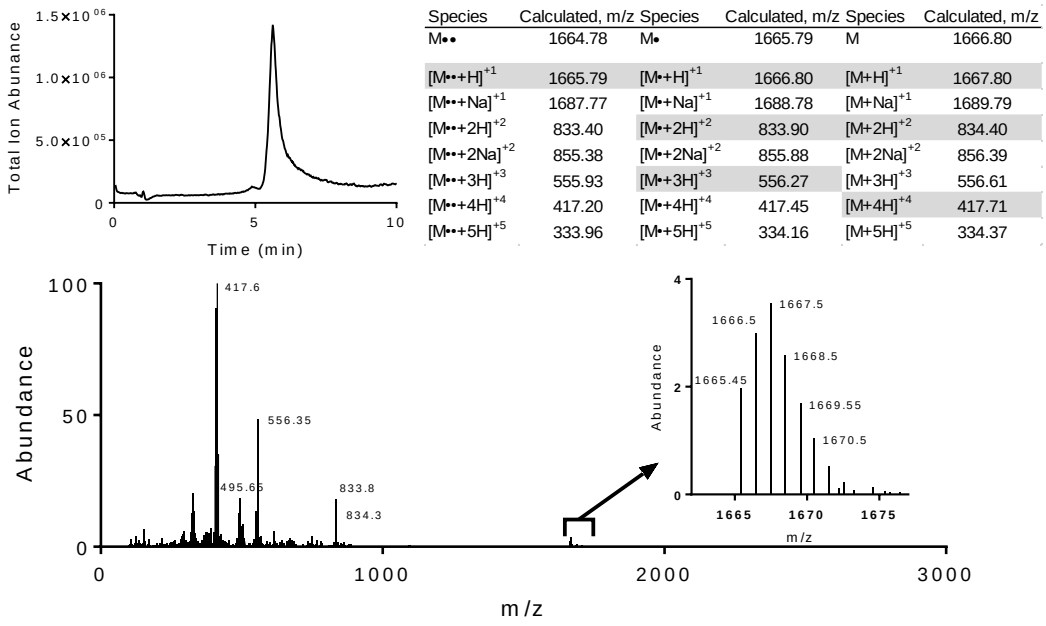

Species	Calculated, m/z	Species	Calculated, m/z	Species	Calculated, m/z
M••	1664.78	M•	1665.79	M	1666.80
$[M••+H]^{+1}$	1665.79	$[M•+H]^{+1}$	1666.80	$[M+H]^{+1}$	1667.80
$[M••+Na]^{+1}$	1687.77	$[M•+Na]^{+1}$	1688.78	$[M+Na]^{+1}$	1689.79
$[M••+2H]^{+2}$	833.40	$[M•+2H]^{+2}$	833.90	$[M+2H]^{+2}$	834.40
$[M••+2Na]^{+2}$	855.38	$[M•+2Na]^{+2}$	855.88	$[M+2Na]^{+2}$	856.39
$[M••+3H]^{+3}$	555.93	$[M•+3H]^{+3}$	556.27	$[M+3H]^{+3}$	556.61
$[M••+4H]^{+4}$	417.20	$[M•+4H]^{+4}$	417.45	$[M+4H]^{+4}$	417.71
$[M••+5H]^{+5}$	333.96	$[M•+5H]^{+5}$	334.16	$[M+5H]^{+5}$	334.37

LCMS of the dispin-labeled Para. (Top, Left) *Total ion count abundance versus time (10 min gradient).* ***(Top, Right)*** *Expected masses; experimentally observed are highlighted in gray.* ***(Bottom)*** *Mass spectra confirming the presence of the Meta in the TIC peak, demonstrating that the spin-label is partially oxidized (will be reduced before measurement).* ***(Insert)*** *Closer examination of the mass spectra shows the parent masses.*

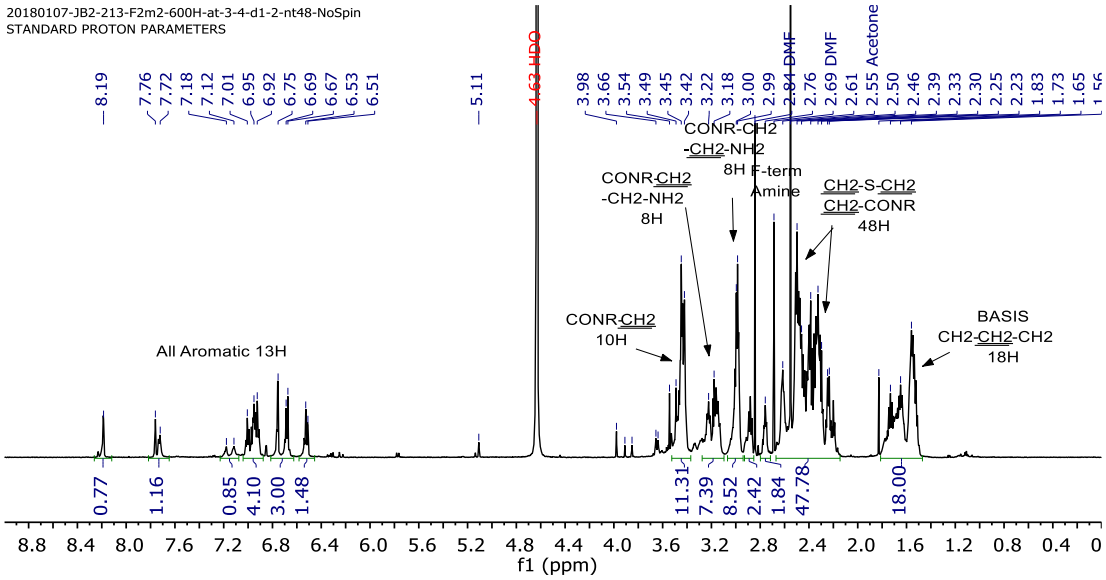

^{1}H NMR of the fluorescein-labeled Meta (D_2O at 600 MHz).

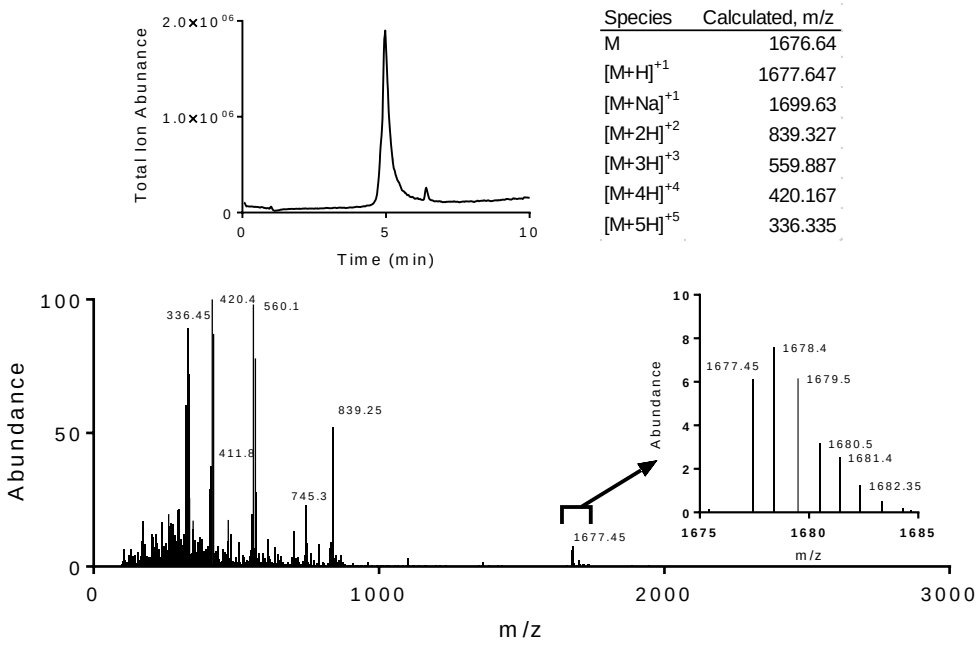

LCMS of the fluorescein-labeled Meta. (Top, Left) *Total ion count abundance versus time over a 10 minute gradient.* ***(Top, Right)*** *Expected masses to be observed* ***(Bottom)*** *Mass spectra confirming the presence of the Meta in the TIC peak.* ***(Insert)*** *Closer examination of the mass spectra shows the parent masses.*

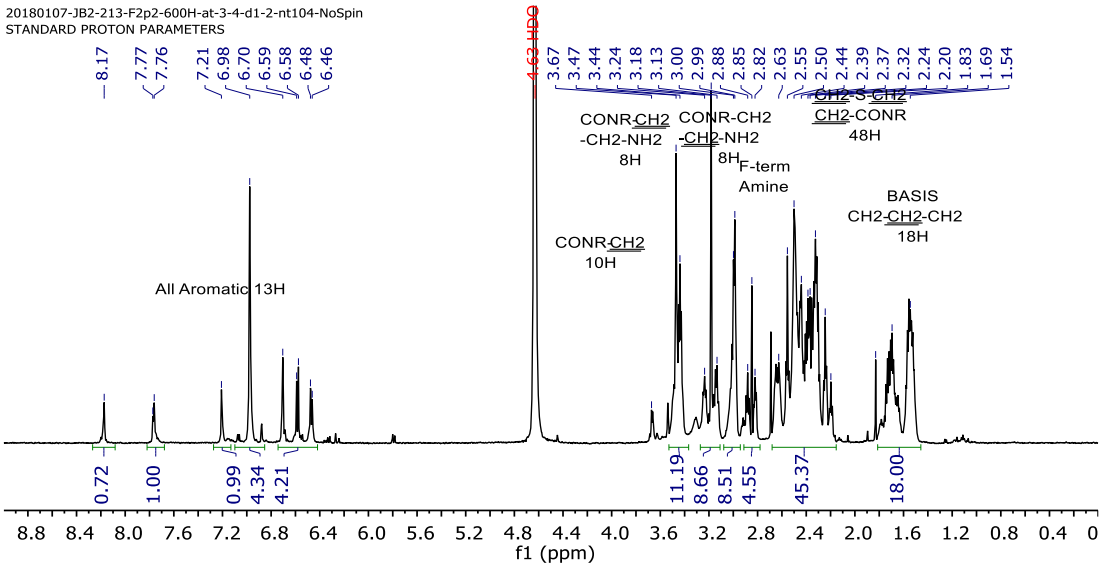

^{1}H NMR of the fluorescein-labeled Para (D_2O at 600 MHz).

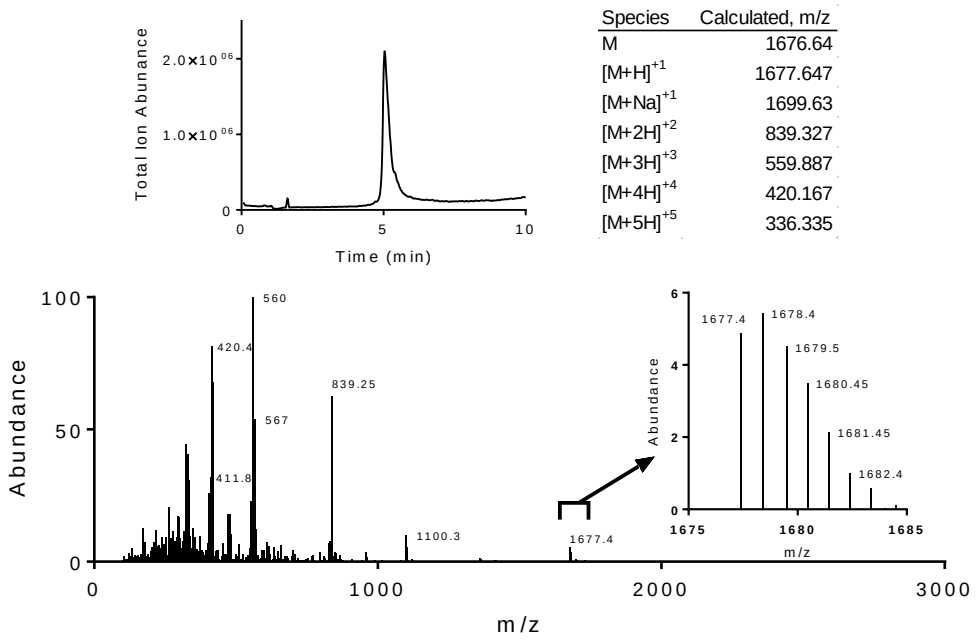

LCMS of the fluorescein-labeled Para. (Top, Left) *Total ion count abundance versus time over a 10 minute gradient.* ***(Top, Right)*** *Expected masses to be observed* ***(Bottom)*** *Mass spectra confirming the presence of the Meta in the TIC peak.* ***(Insert)*** *Closer examination of the mass spectra shows the parent masses.*

Appendix D : Additional Supplementary Material for Chapter 5

Materials in this appendix were work adapted with permission from C. M. Artim, J. S. Brown, and C. A. Alabi, Analytical Chemistry **2019**, 91, 3118-3124 Copyright © 2018 American Chemical Society and also with permission from E. A. Hoff, C. M. Artim, J. S. Brown, C. A. Alabi, *Macromolecular Bioscience* **2018**, 1800241 Copyright © 2018 John Wiley and Sons (License #4507220586910). Outside of those two works, additional analysis has been performed and added to enrich the biophysical understanding of the first article from E.A. Hoff et al (2018), specifically with modeling of the biophysical characterization.

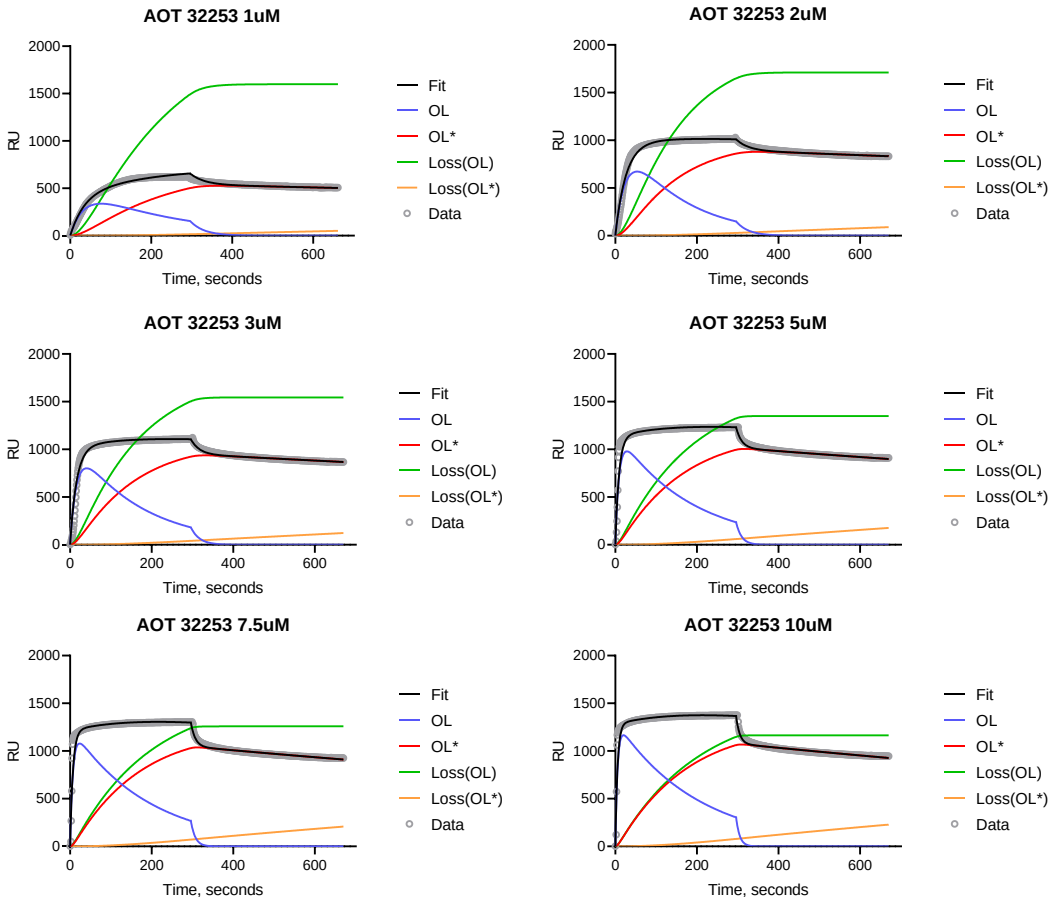

Figure D-1: *Model fits to AOT 32253 SPR Data*

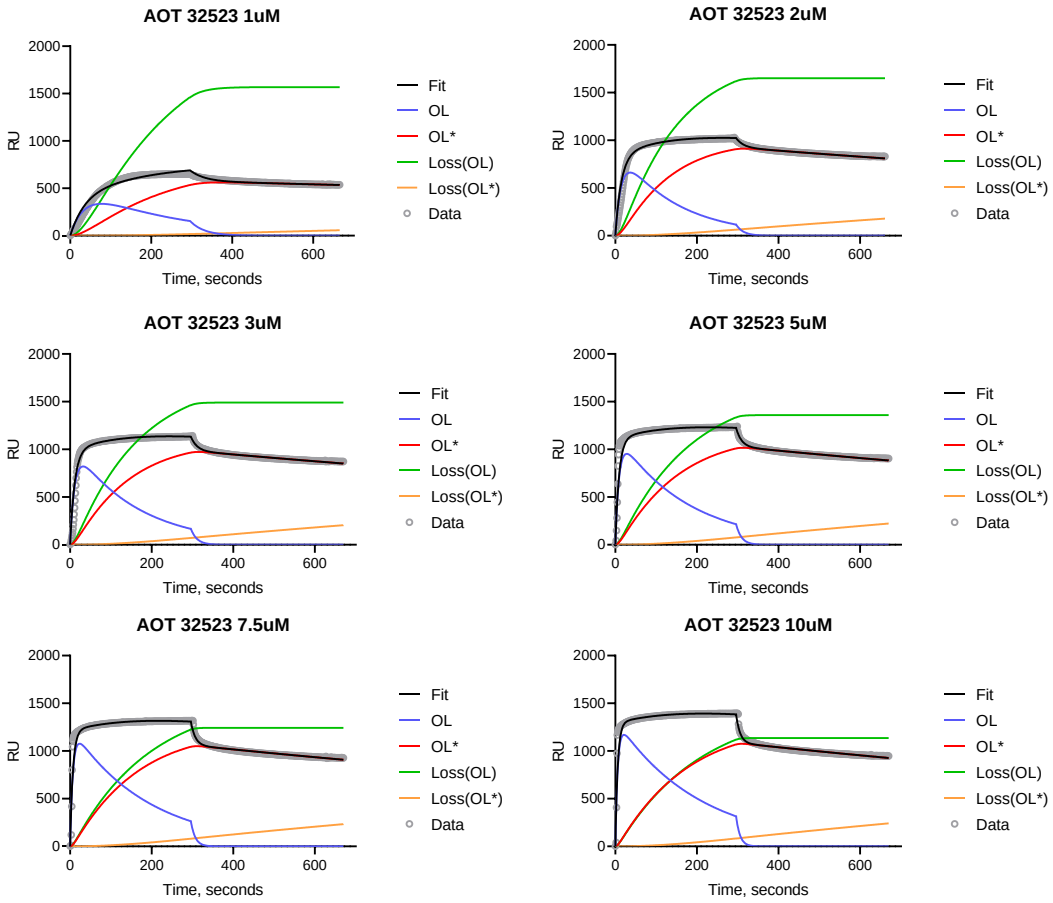

Figure D-2: *Model fits to AOT 32523 SPR data*

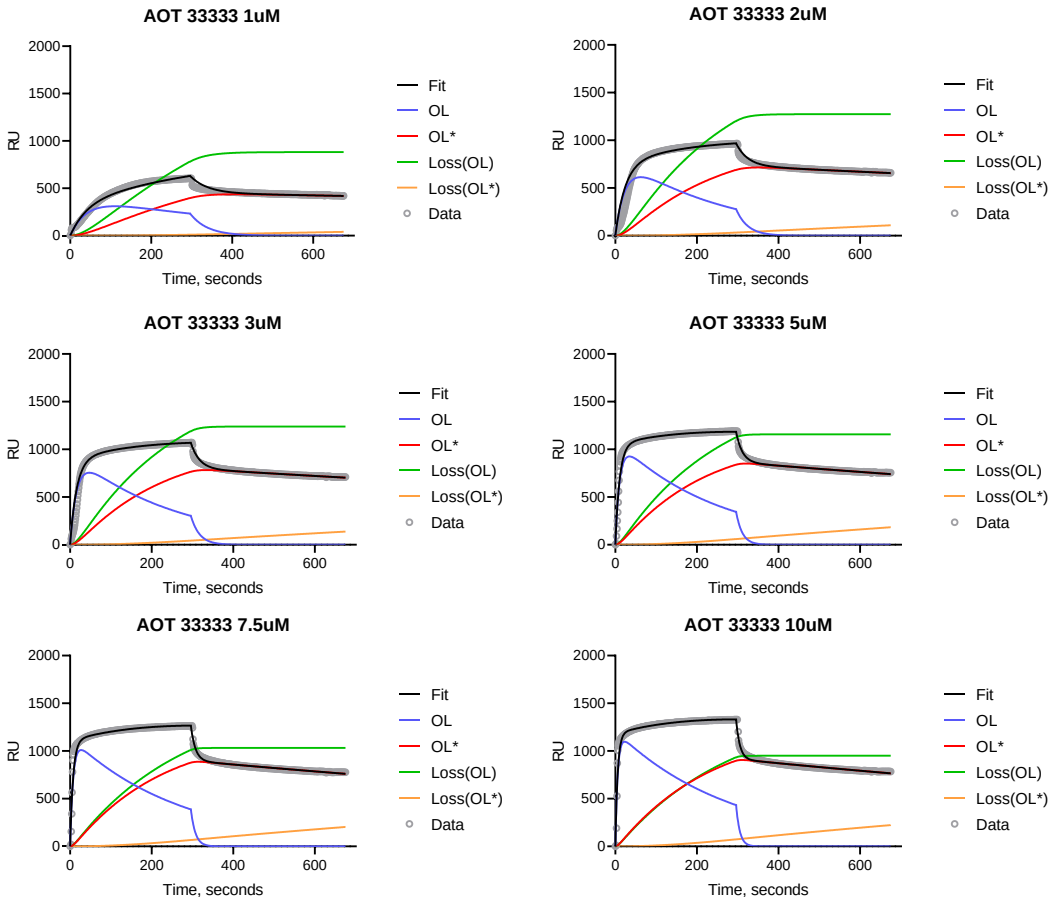

Figure D-3: *Model fits to AOT 33333 SPR Data*

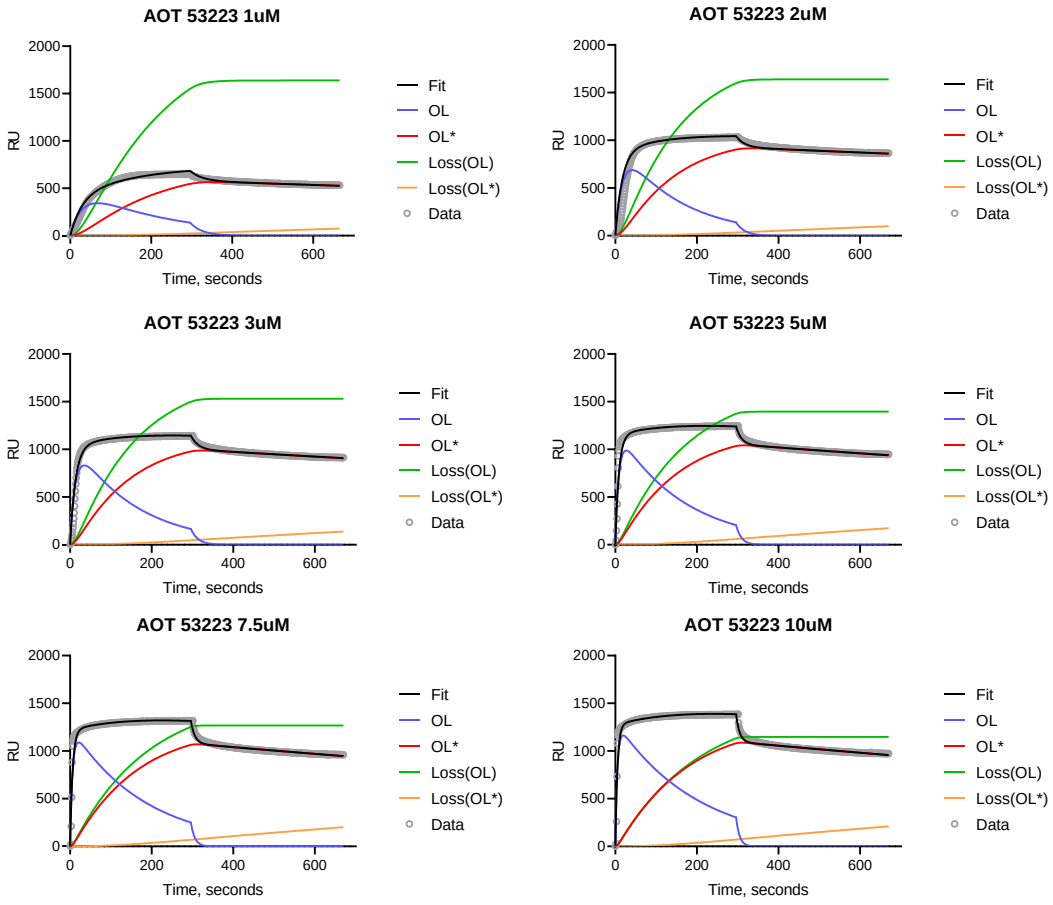

Figure D-4: *Model fits to AOT 53223 SPR Data*

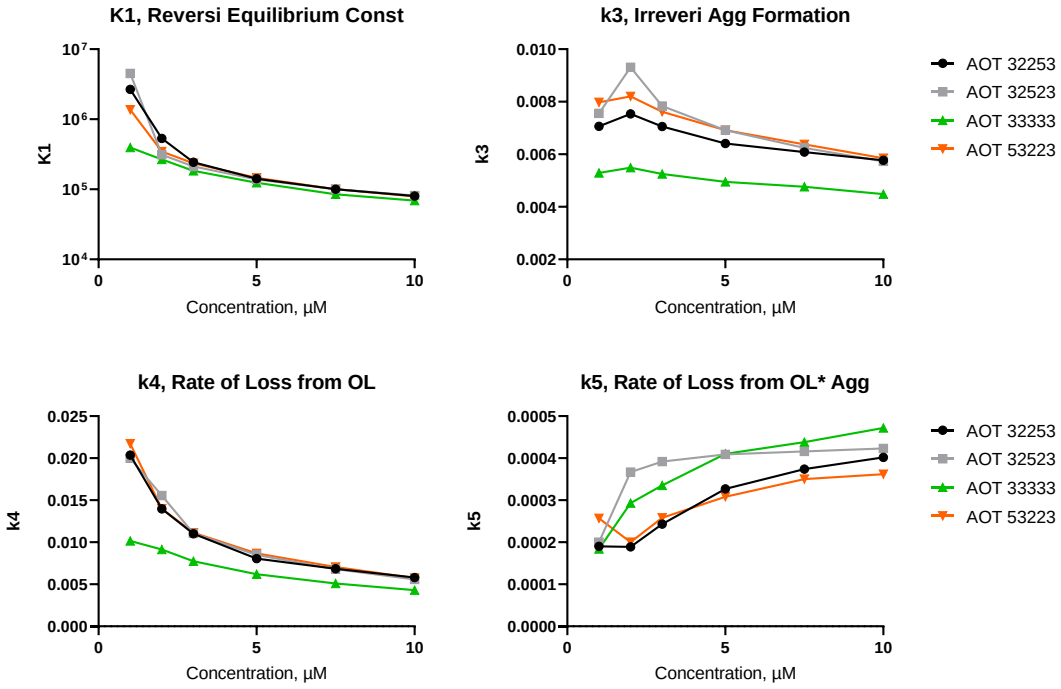

Figure D-5: *All parameters of the two-state with two loss model fit to SPR data to antibacterial constitutional oligoTEA isomers.*

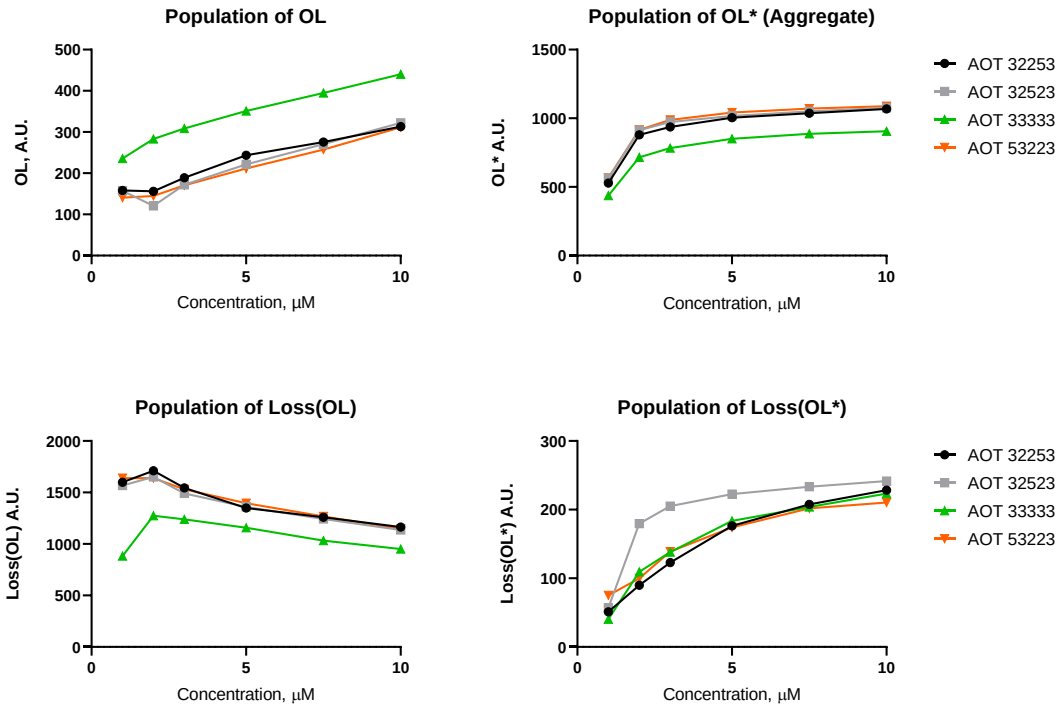

Figure D-6: *All populations of the two-state with two loss model fit to SPR data to antibacterial constitutional oligoTEA isomers.*

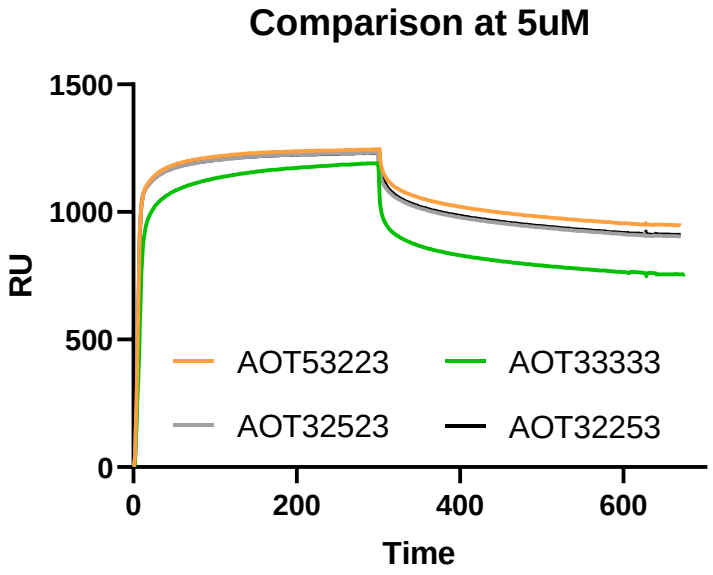

Figure D-7: *SPR Comparison of antibacterial oligoTEA constitutional isomers*

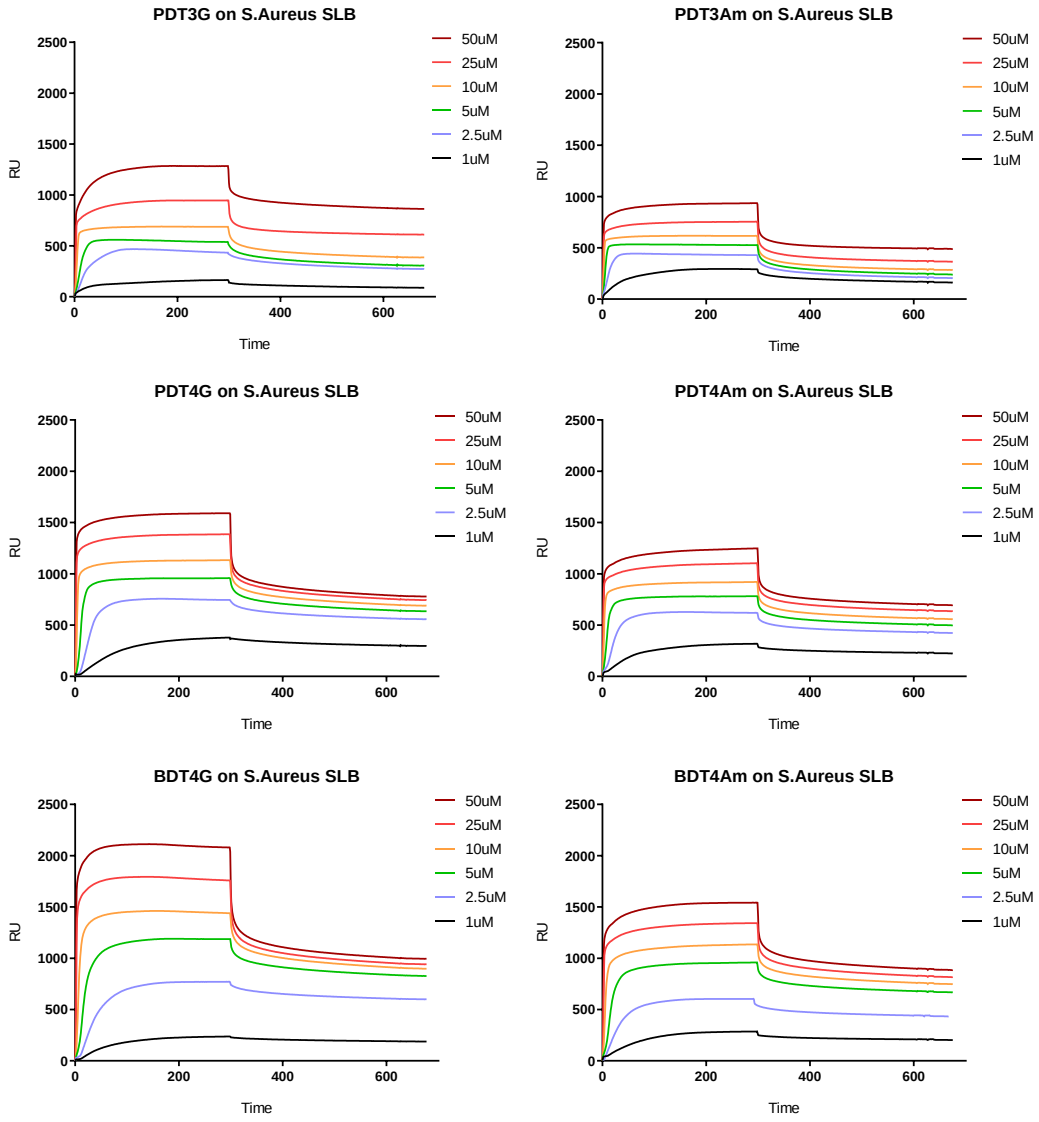

Figure D-8: *All SPR data for cationic oligoTEAs at all concentrations*

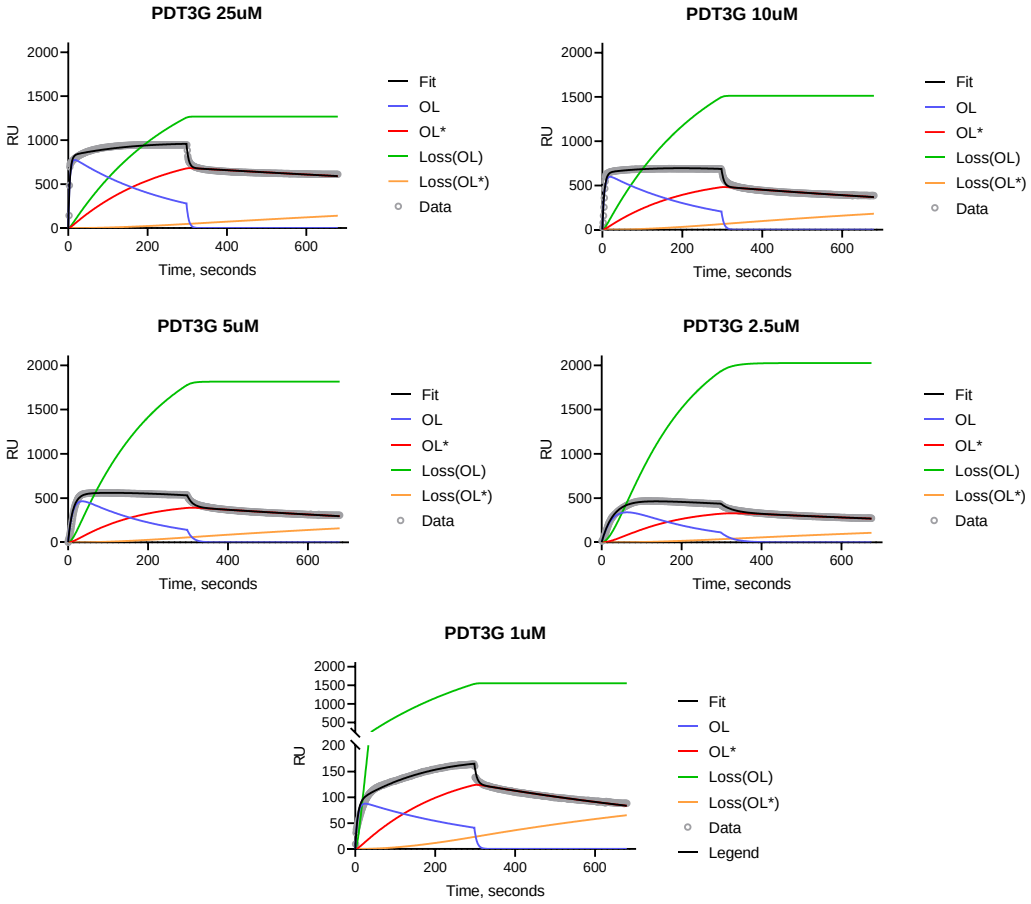

Figure D-9: *Model fits of SPR of PDT-3G*

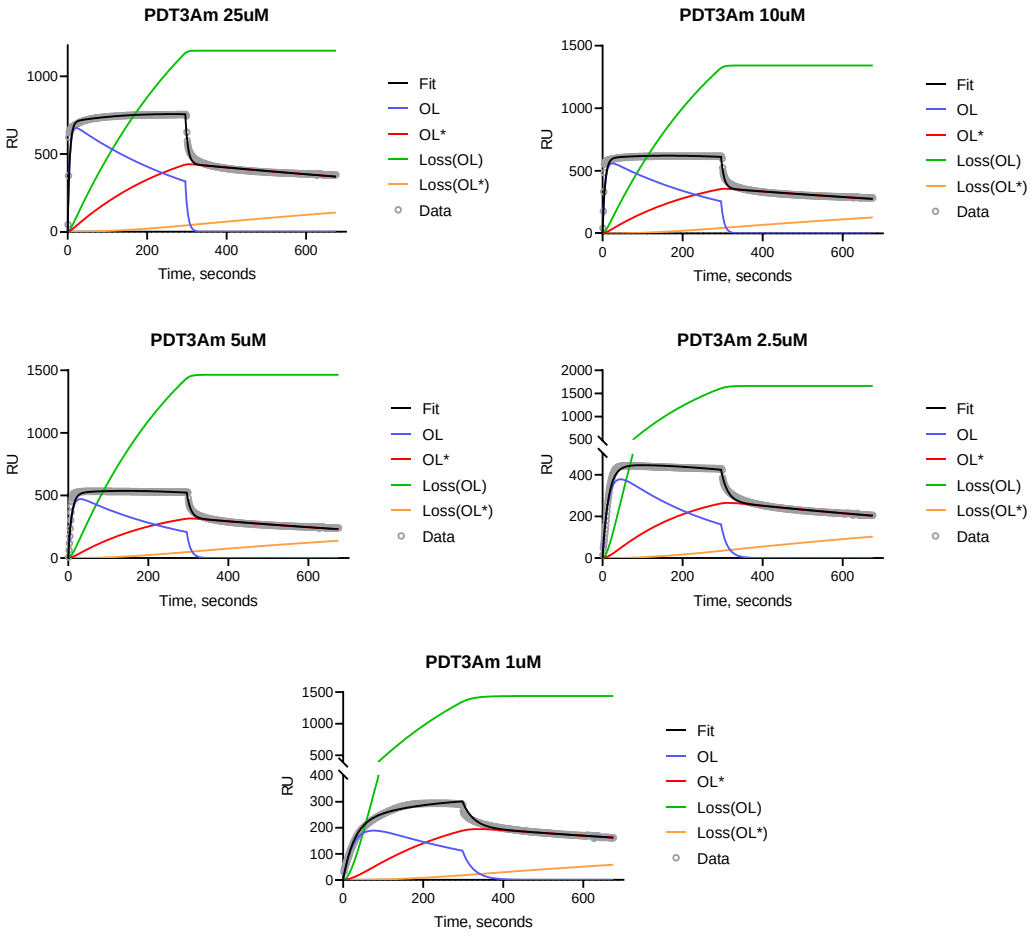

Figure D-10: *Model fits of SPR of PDT-3Am*

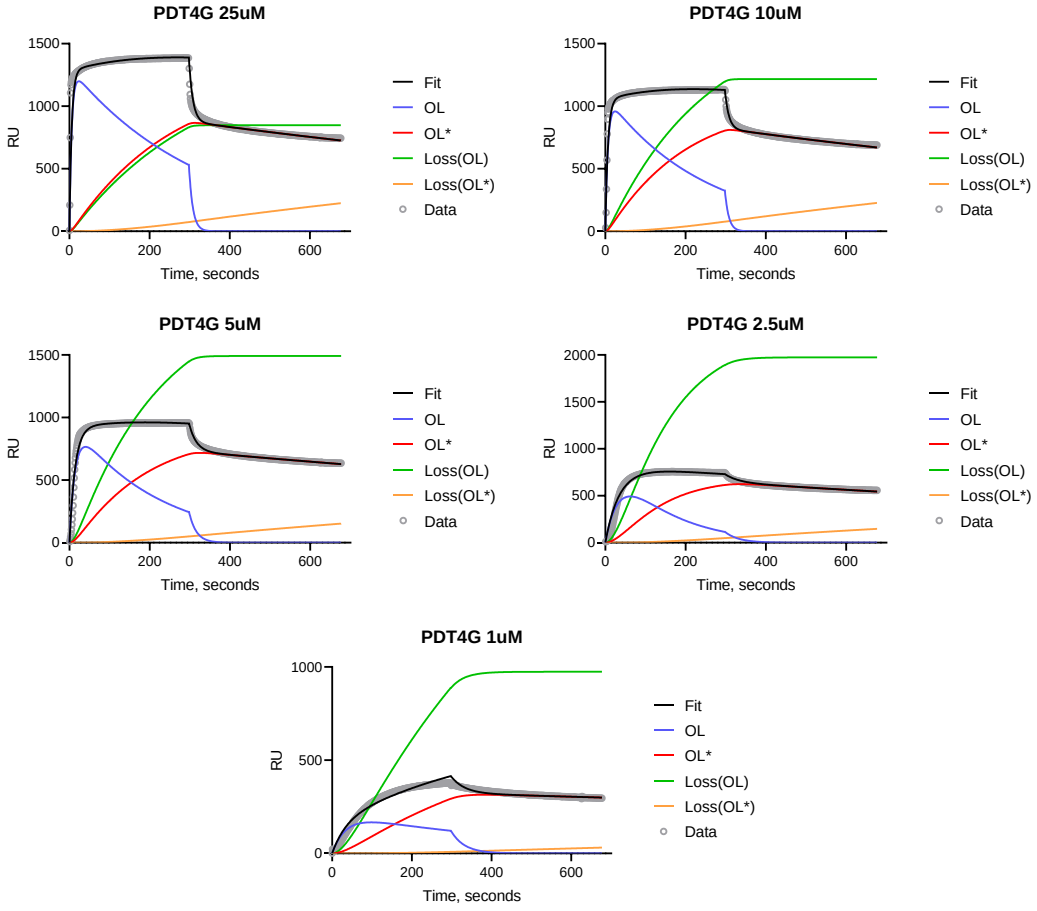

Figure D-11: *Model fits of SPR of PDT-4G*

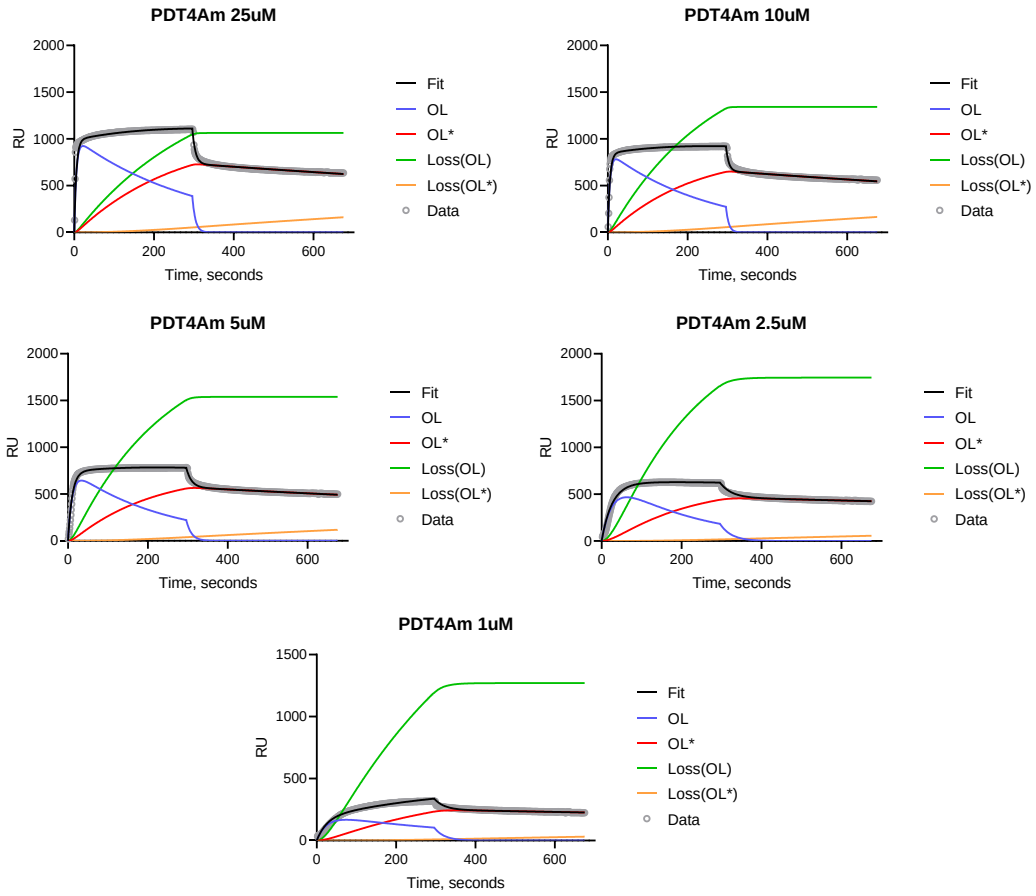

Figure D-12: *Model fits of SPR of PDT-4Am*

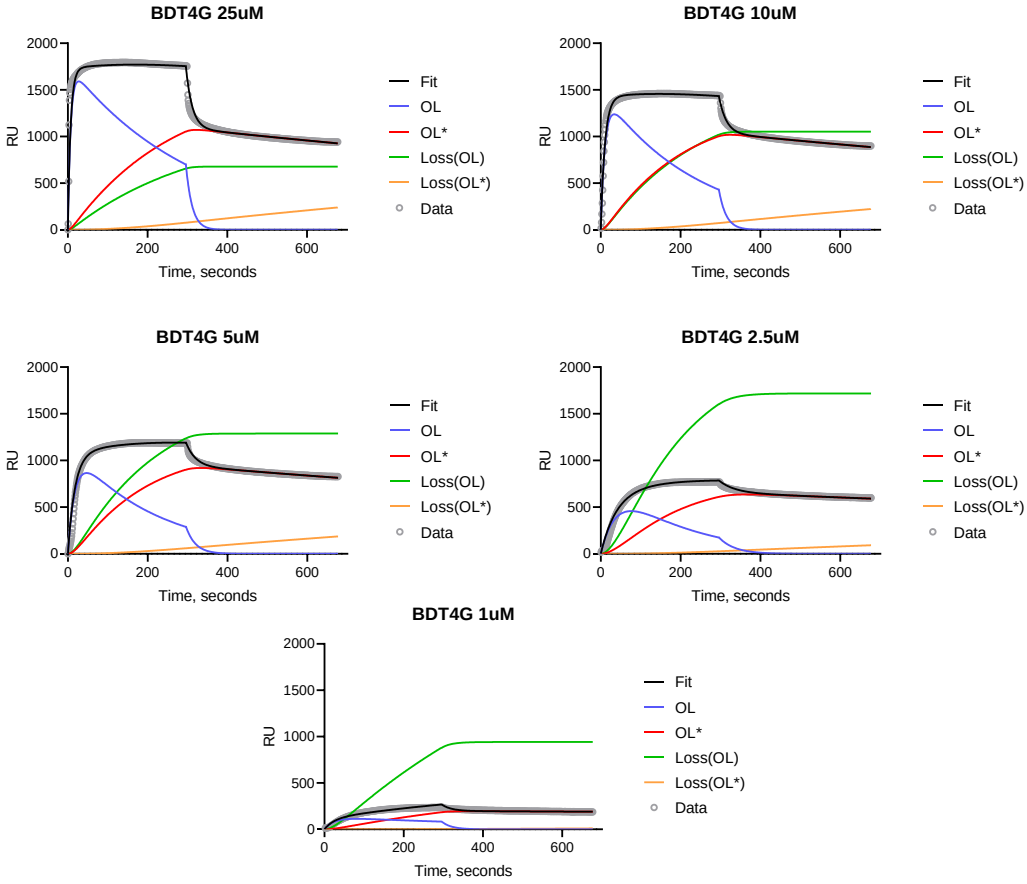

Figure D-13: *Model fits of SPR of BDT-4G*

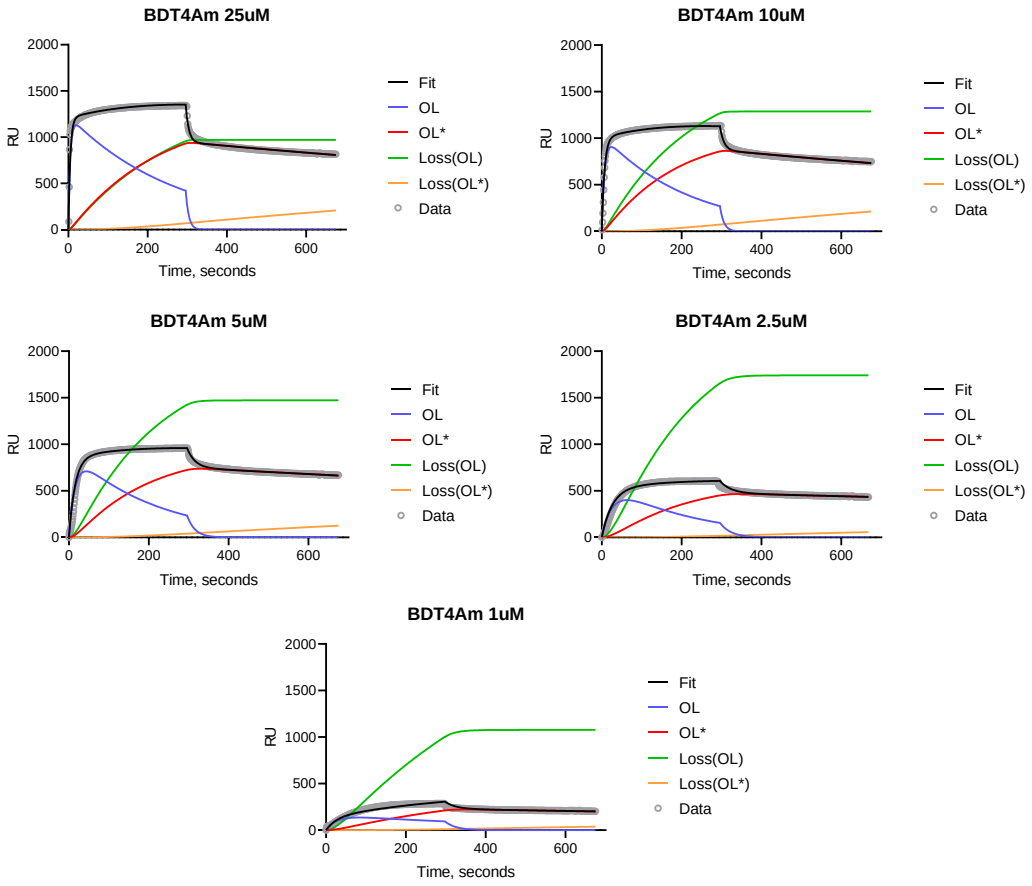

Figure D-14: *Model fits of SPR of BDT-4Am*

Table D-1: *All parameters from model fits of SPR data of cationic oligoTEAs*
Note: K1 (equilibrium constant) = k_1/k_2

	Conc, uM	PDT3G	PDT3Am	PDT4G	PDT4Am	BDT4G	BDT4Am
K1	**1**	71550	1737699	1844168	671792	460794	2000540
	2.5	261146	107363	2983064	242892	1296666	261159
	5	63942	49461	112503	79981	146159	108327
	10	30004	27562	58920	42318	100048	55907
	25	16001	13076	31376	20837	56918	28333
k3	**1**	0.00789	0.00464	0.00726	0.00609	0.00662	0.00665
	2.5	0.00607	0.00378	0.00737	0.00475	0.00671	0.00570
	5	0.00518	0.00371	0.00523	0.00486	0.00577	0.00564
	10	0.00483	0.00339	0.00489	0.00477	0.00454	0.00574
	25	0.00490	0.00331	0.00374	0.00415	0.00344	0.00460
k4	**1**	0.0823	0.0303	0.0214	0.0300	0.0311	0.0299
	2.5	0.0285	0.0205	0.0210	0.0172	0.0169	0.0201
	5	0.0207	0.0147	0.0100	0.0122	0.0074	0.0105
	10	0.0133	0.0113	0.0066	0.0090	0.0043	0.0078
	25	0.0085	0.0081	0.0033	0.0056	0.0020	0.0044
k5	**1**	0.001069	0.000596	0.000196	0.000250	0.000101	0.000336
	2.5	0.000770	0.000767	0.000443	0.000235	0.000275	0.000235
	5	0.000784	0.000875	0.000400	0.000396	0.000381	0.000321
	10	0.000726	0.000706	0.000533	0.000484	0.000413	0.000465
	25	0.000388	0.000557	0.000499	0.000426	0.000427	0.000420

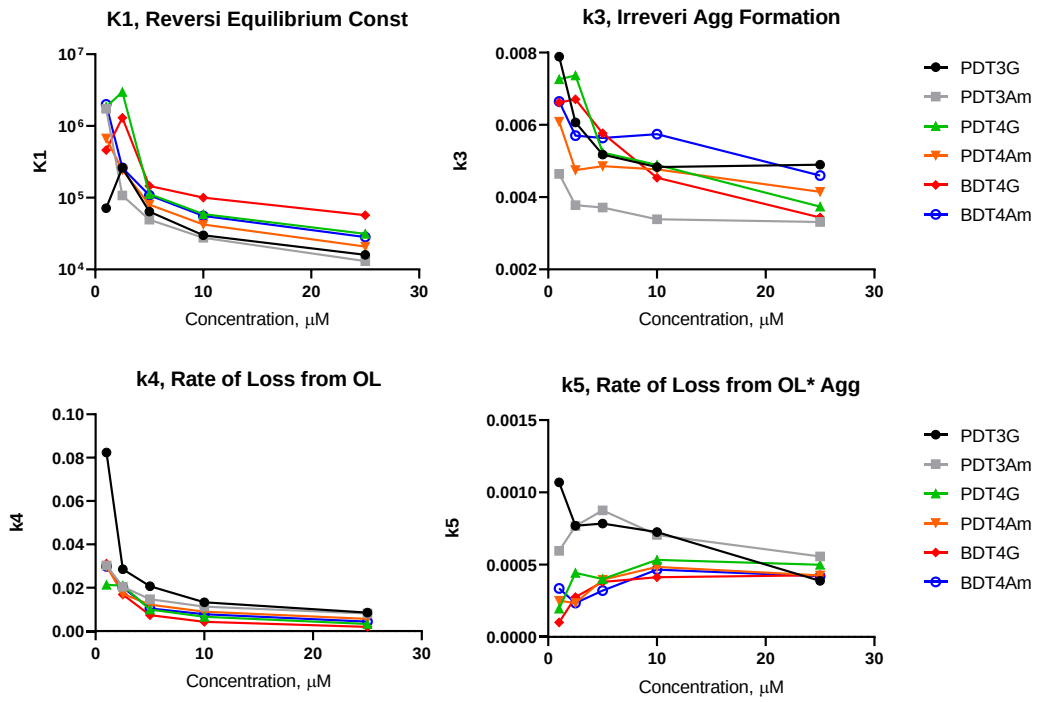

Figure D-15: *All kinetic parameters from model fit of SPR data of cationic oligoTEAs*
Note: K1 is the equilibrium constant (k1/k2)

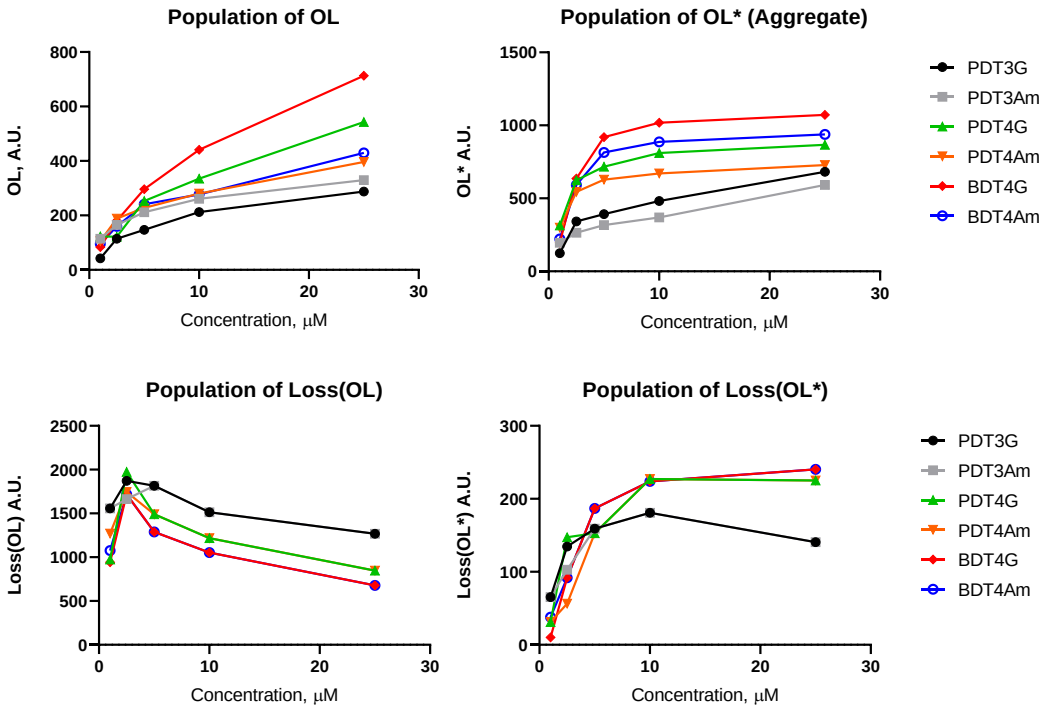

Figure D-16: *All populations from model fits of SPR data of cationic oligoTEAs*

Supplementary Spectra (NMR, LCMS)

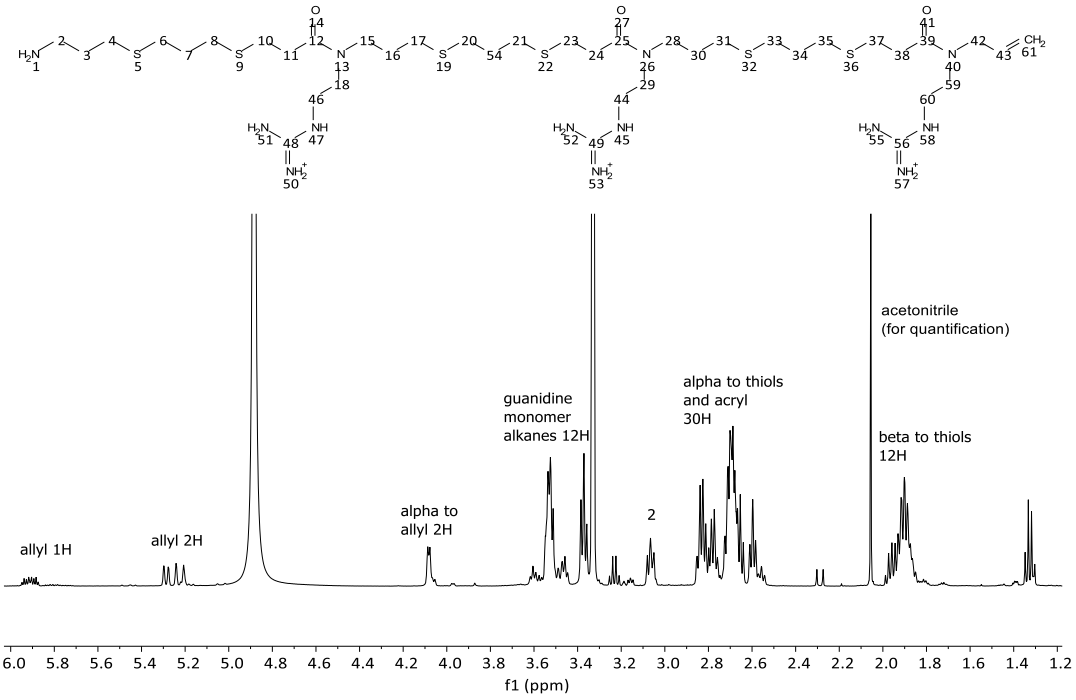

^{1}H NMR of PDT-3G, taken in methanol D4. Acetonitrile used for quantification

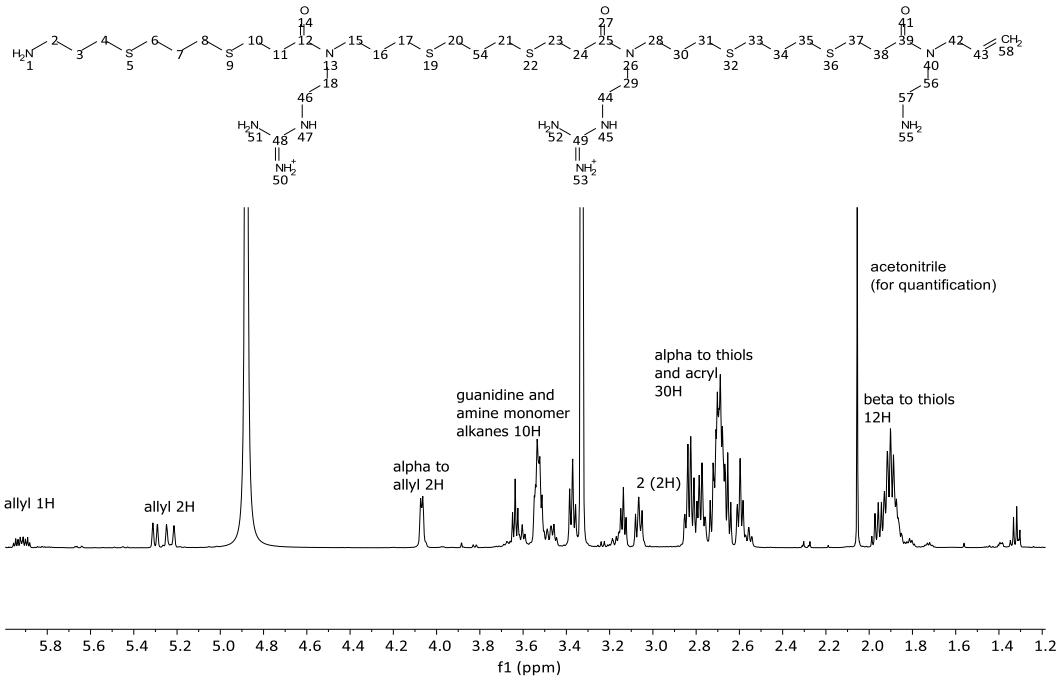

^{1}H NMR of PDT-2GAm, taken in methanol D4. Acetonitrile used for quantification

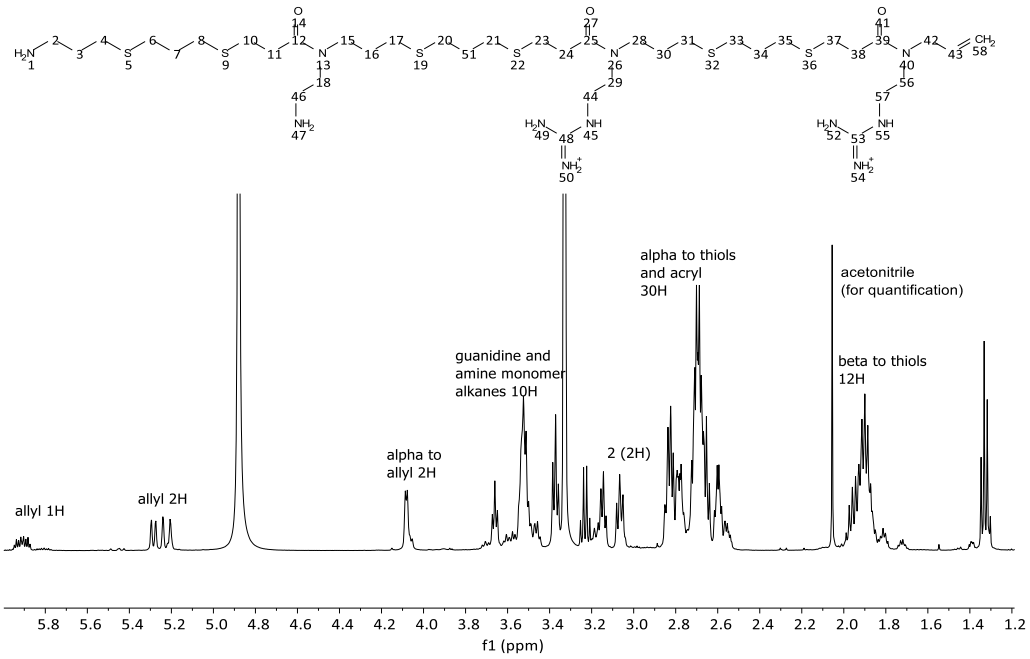

^{1}H NMR of PDT-Am2G, taken in methanol D4. Acetonitrile used for quantification

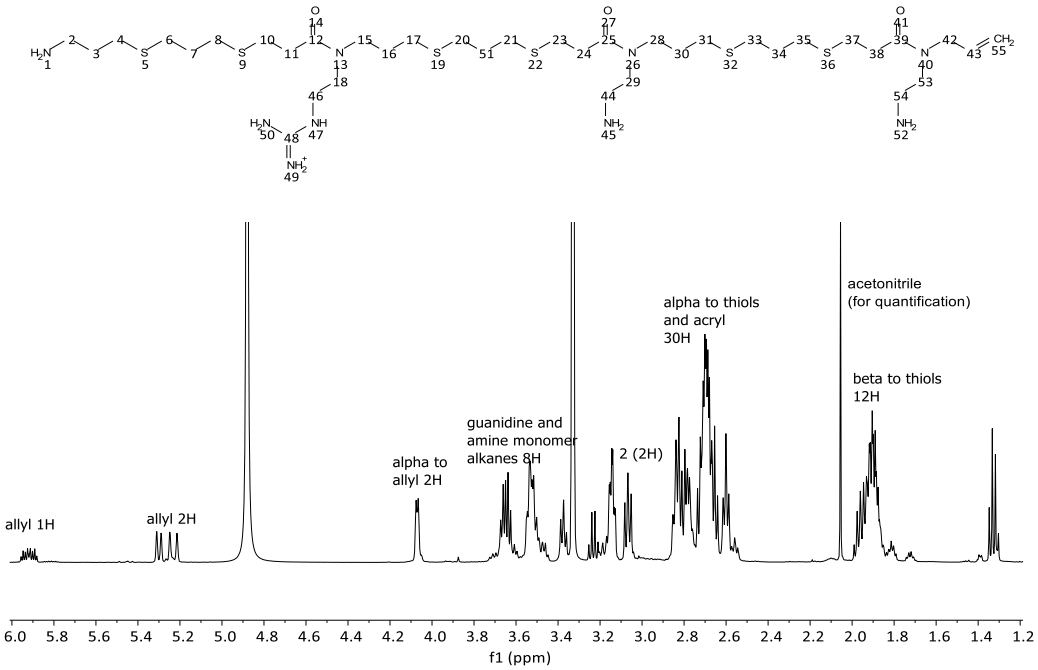

[1]H NMR of PDT-G2Am, taken in methanol D4. Acetonitrile used for quantification

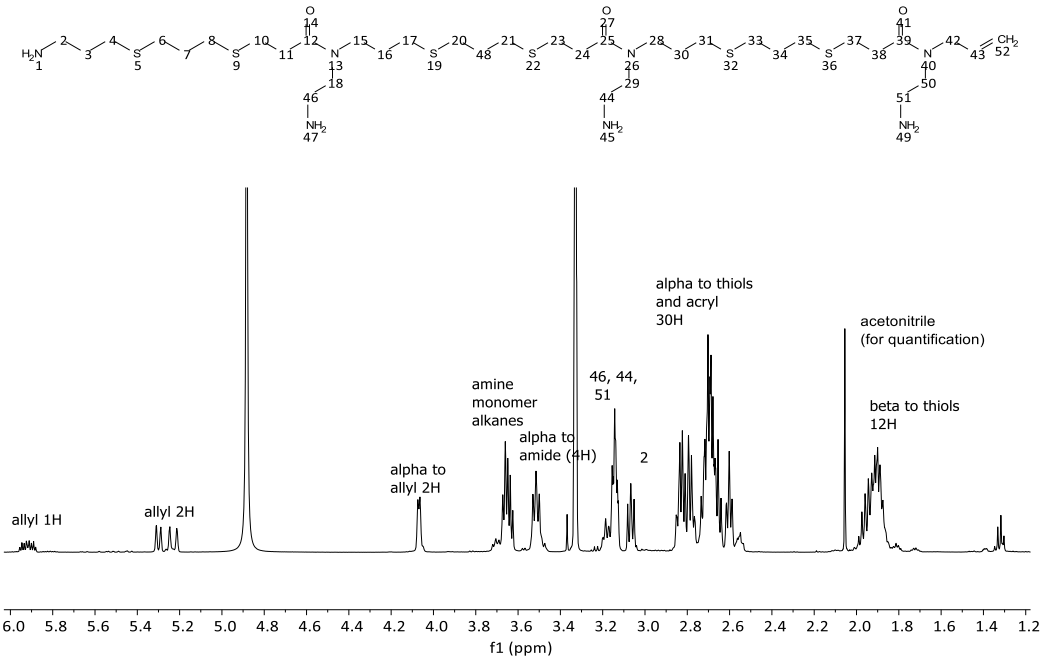

[1]H NMR of PDT-3Am, taken in methanol D4. Acetonitrile used for quantification

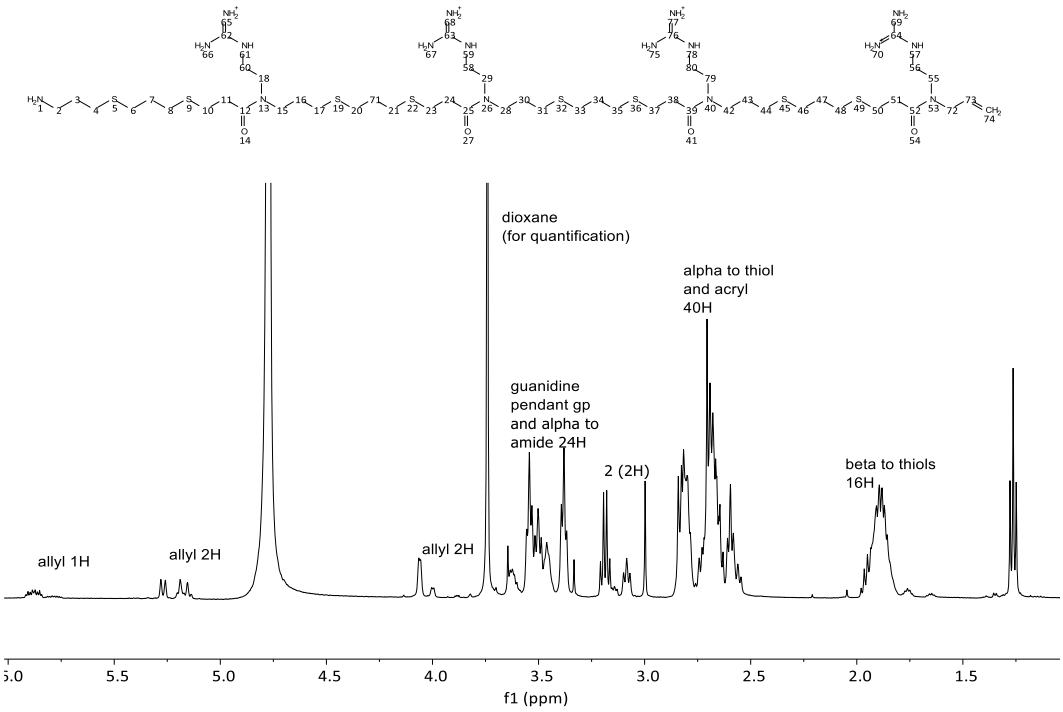

^{1}H NMR of PDT-4G, taken in D_2O. 1,4-dioxane used for quantification

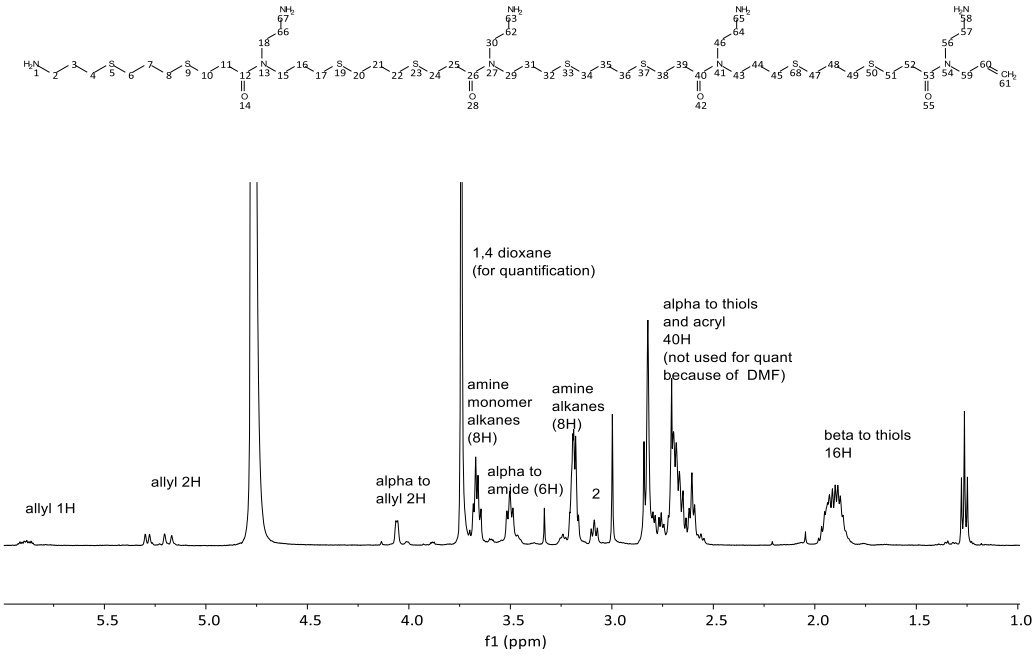

^{1}H NMR of PDT-4Am, taken in D_2O. 1,4-dioxane used for quantification

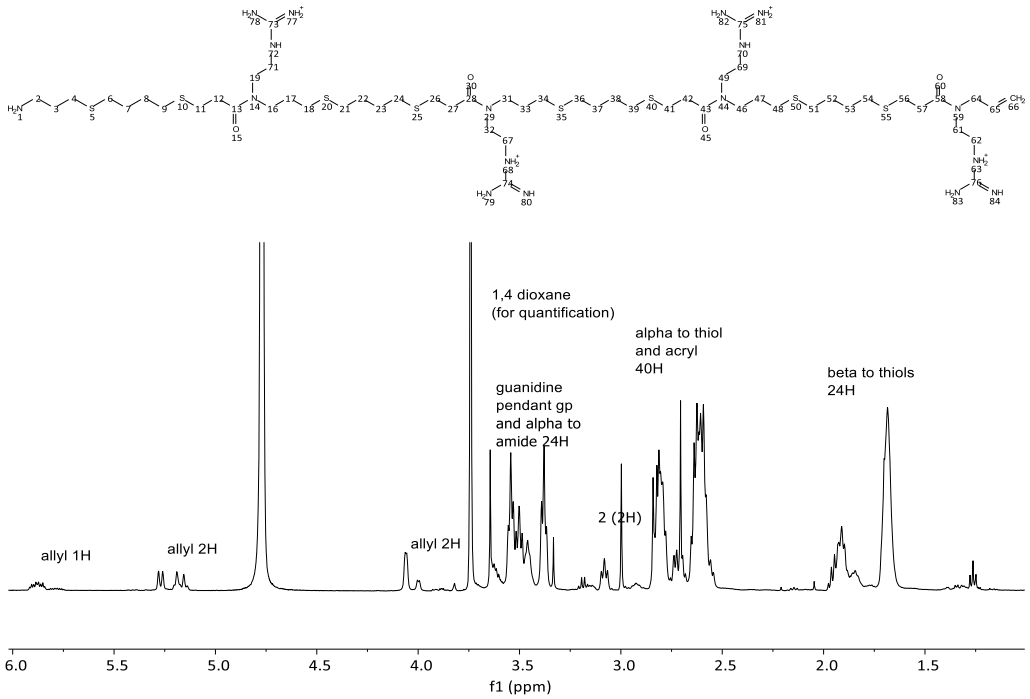

^{1}H NMR of BDT-4G, taken in D_2O. 1,4-dioxane used for quantification

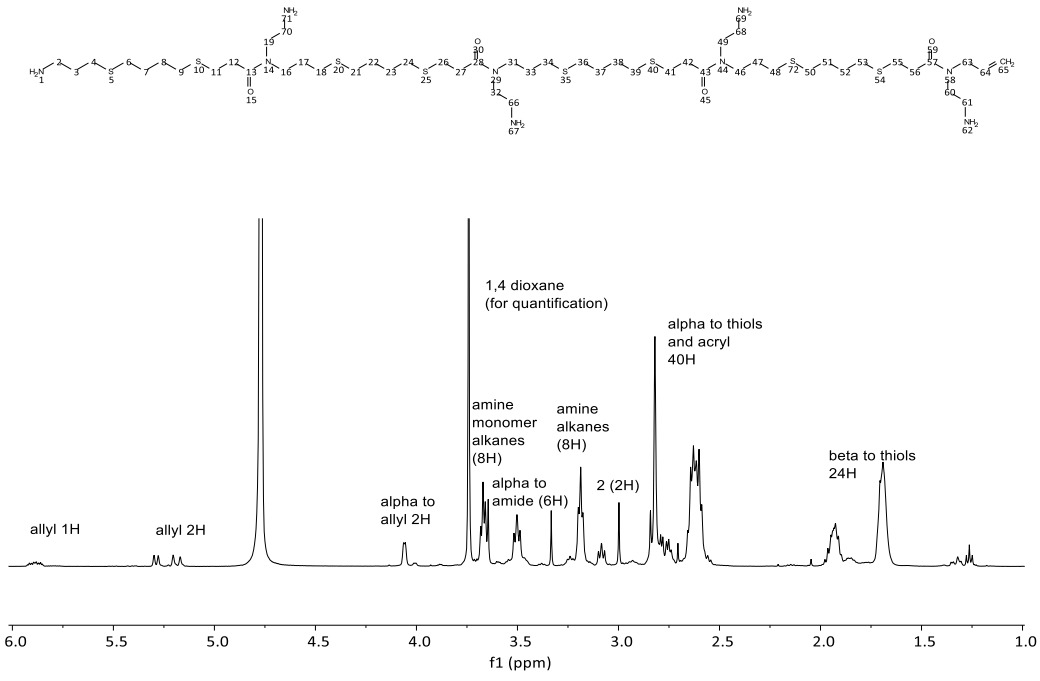

^{1}H NMR of BDT-4Am, taken in D_2O. 1,4-dioxane used for quantification

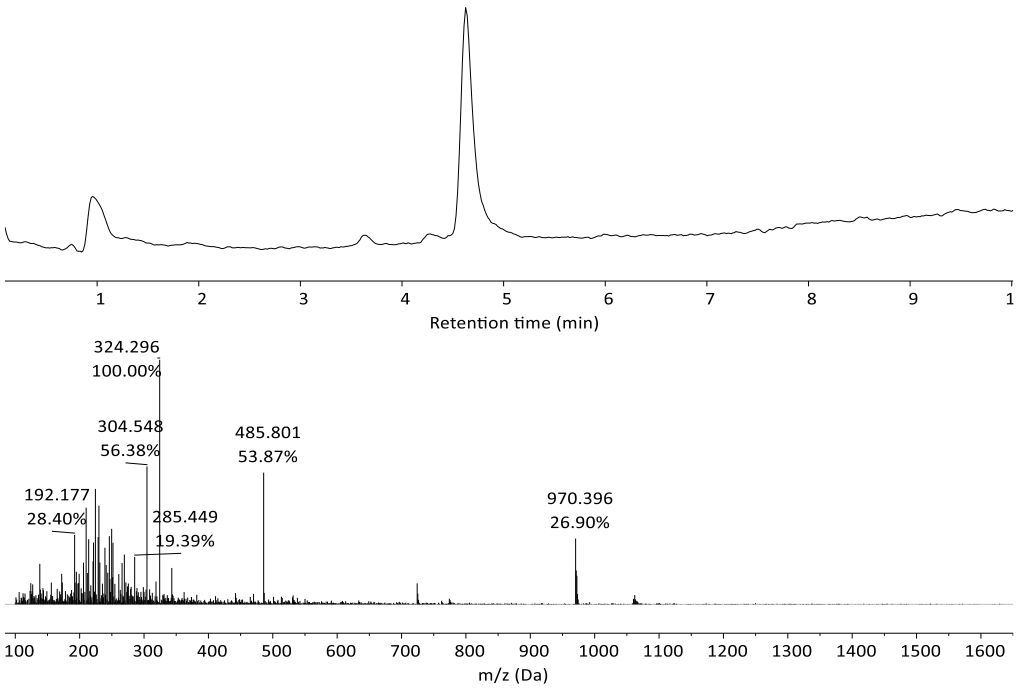

LCMS of PDT-3G

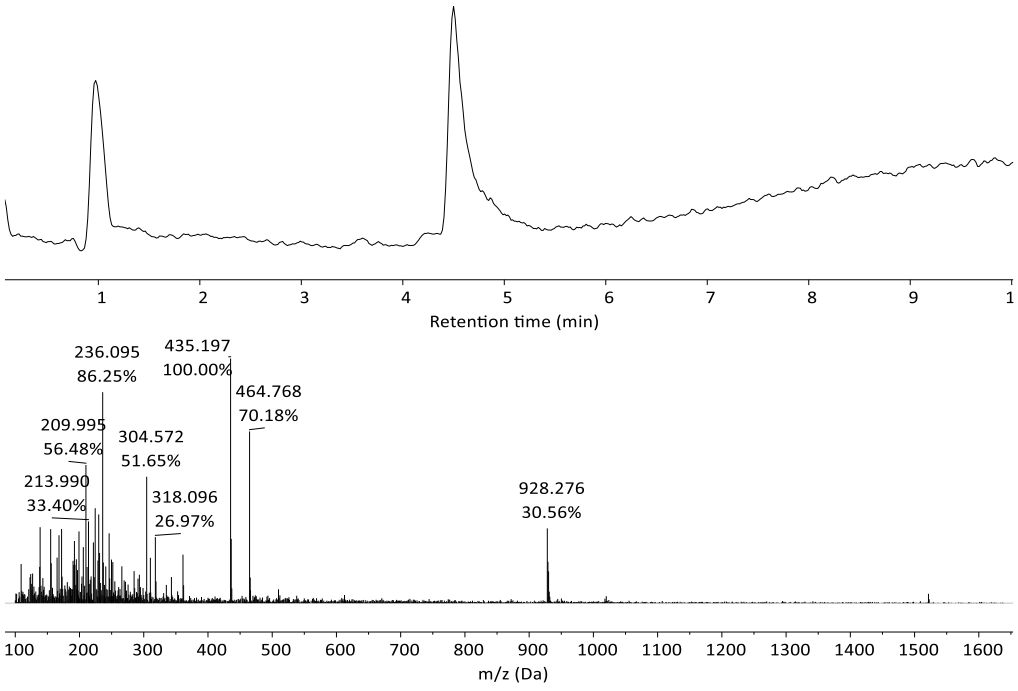

LCMS of PDT-2GAm

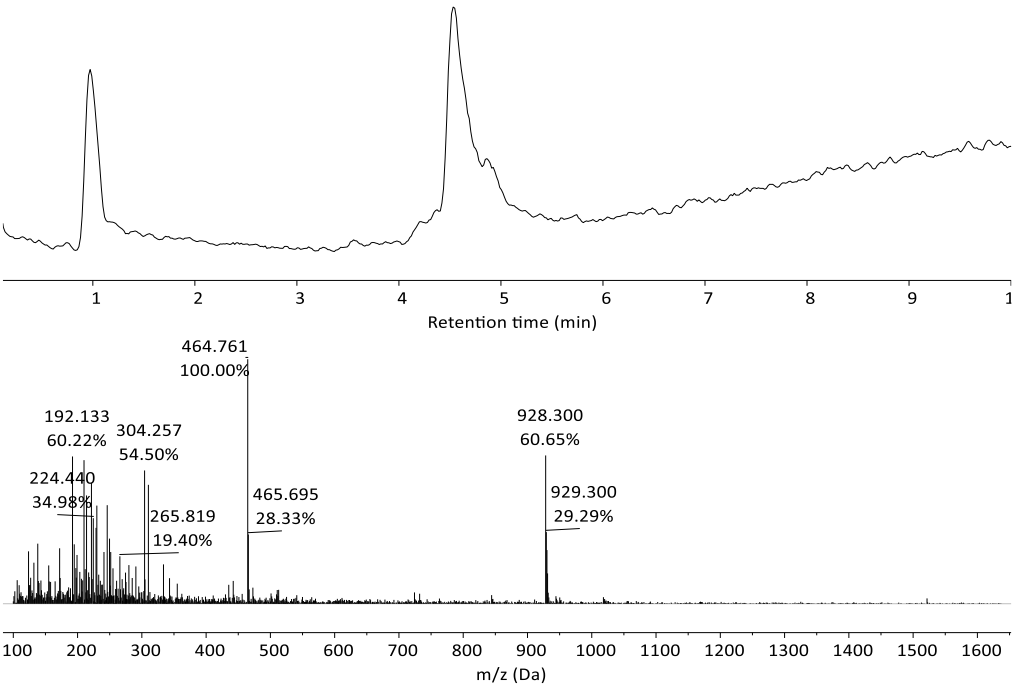

LCMS of PDT-Am2G

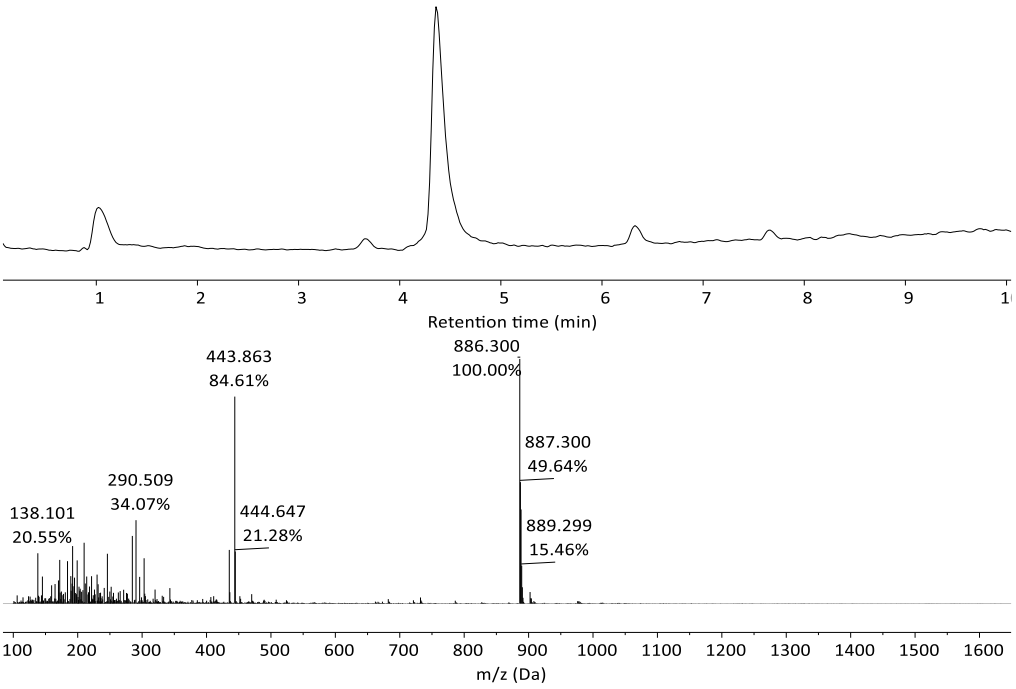

LCMS of PDT-G2Am

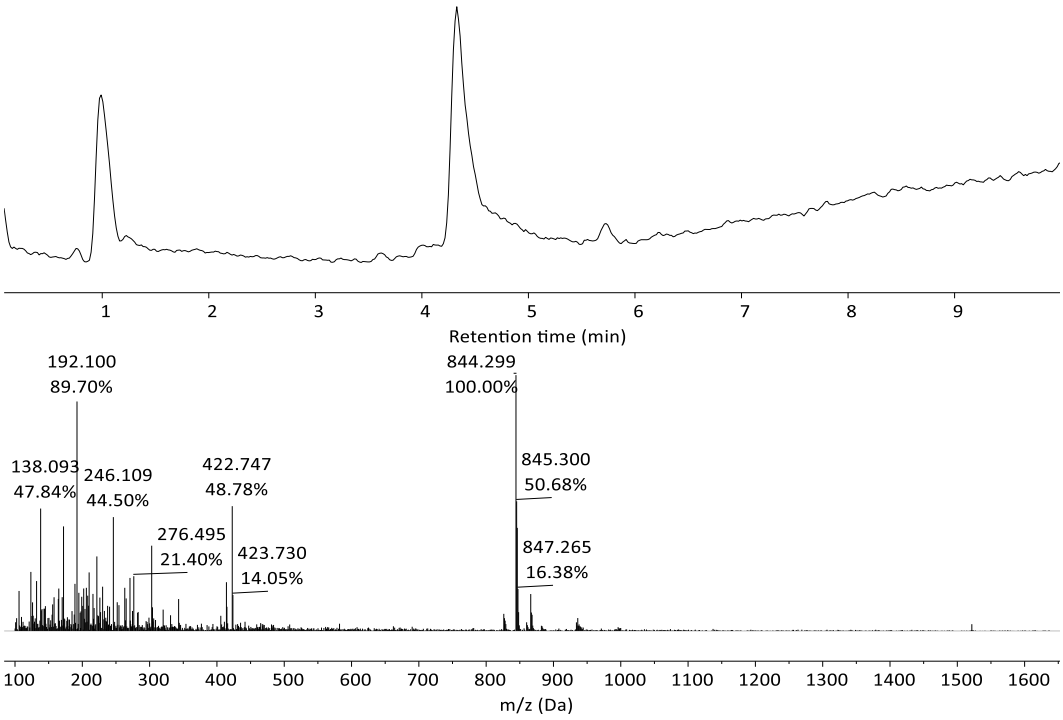

LCMS of PDT-3Am

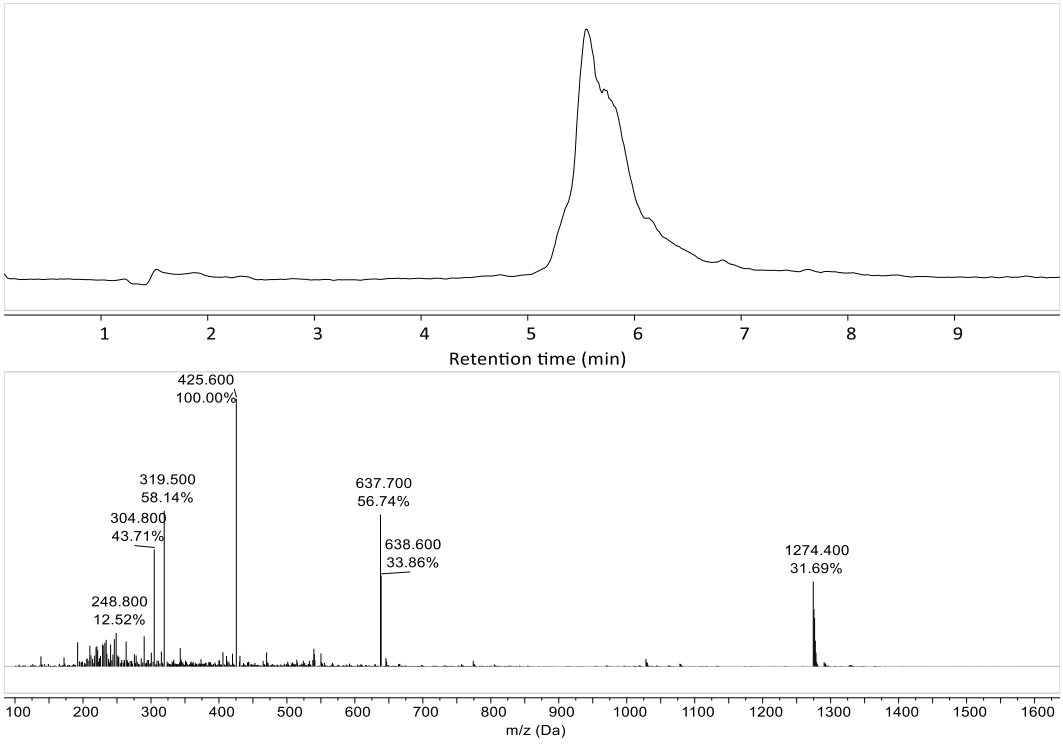

LCMS of PDT-4G

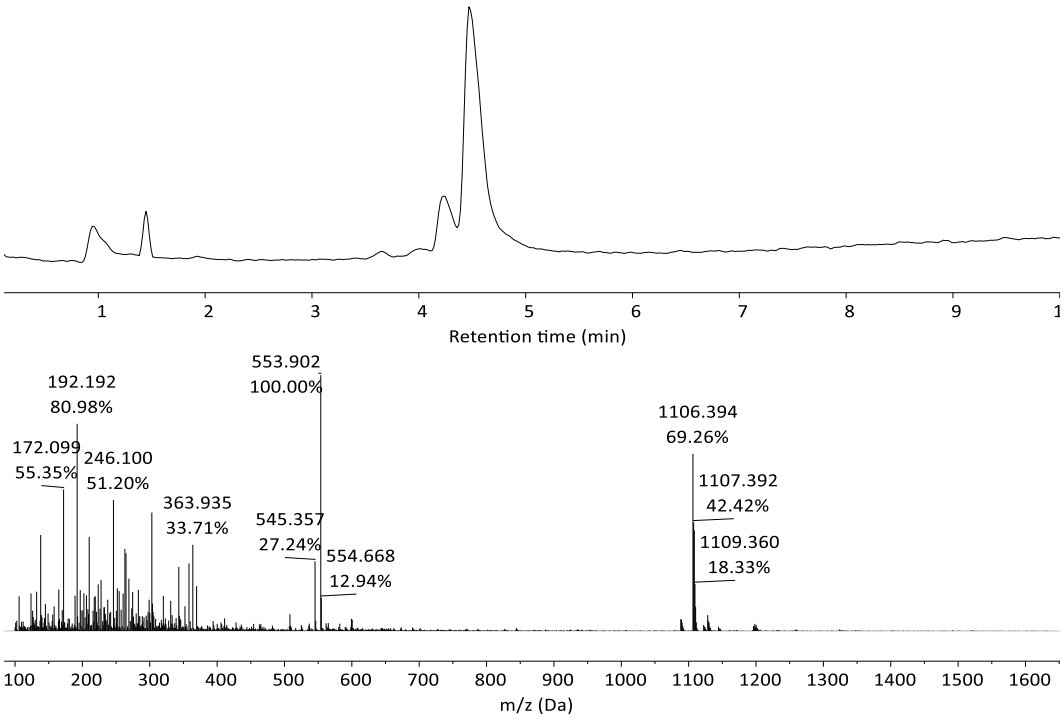

LCMS of PDT-4Am

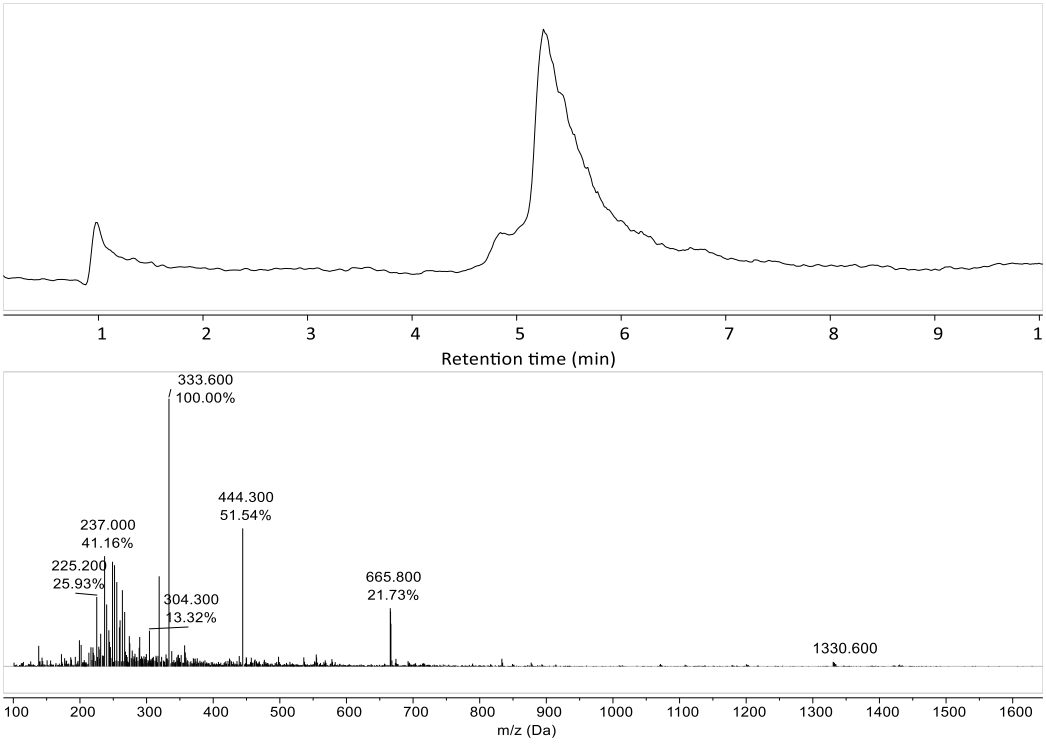

LCMS of BDT-4G

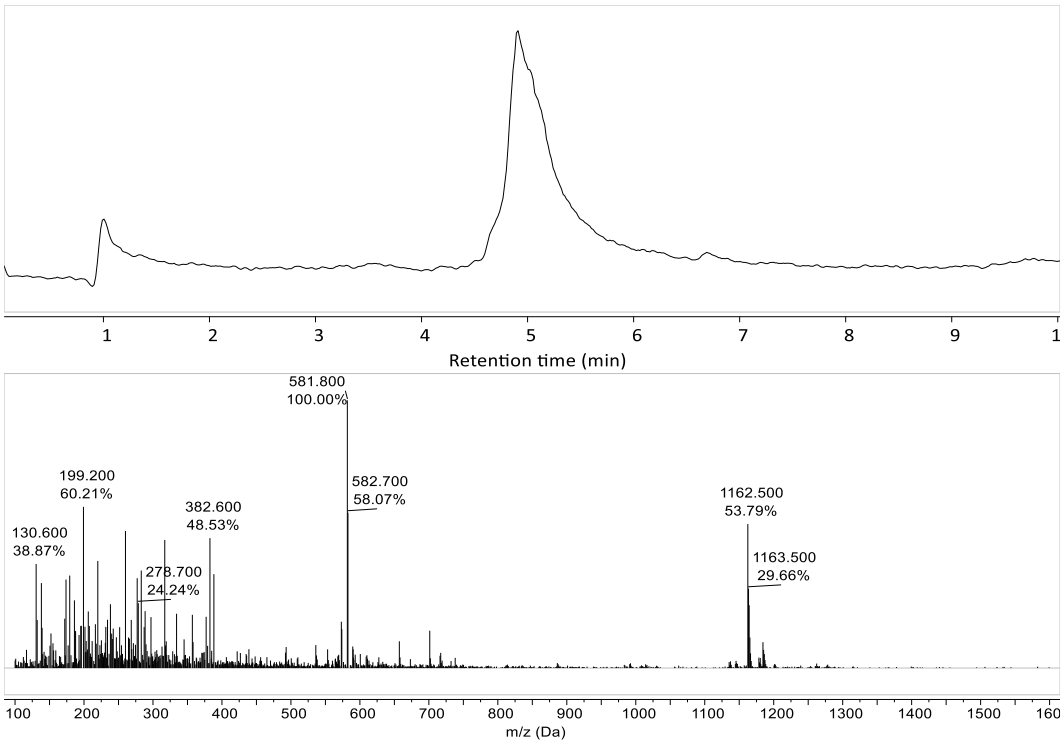

LCMS of BDT-4Am

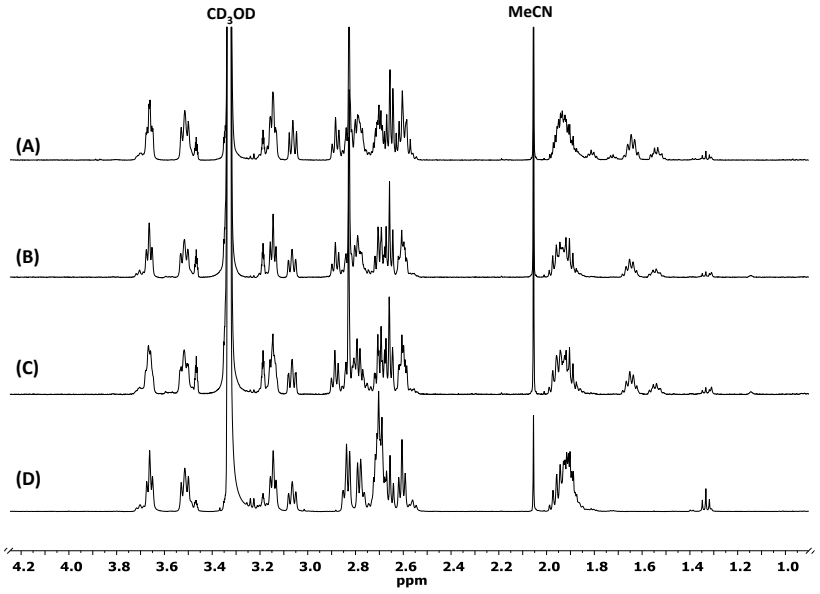

^{1}H NMR of (A) AOT 53223 (B) AOT 32523 (C) AOT 32253 (D) AOT 33333

Appendix E : Additional Supplementary Material for Chapter 6

Text

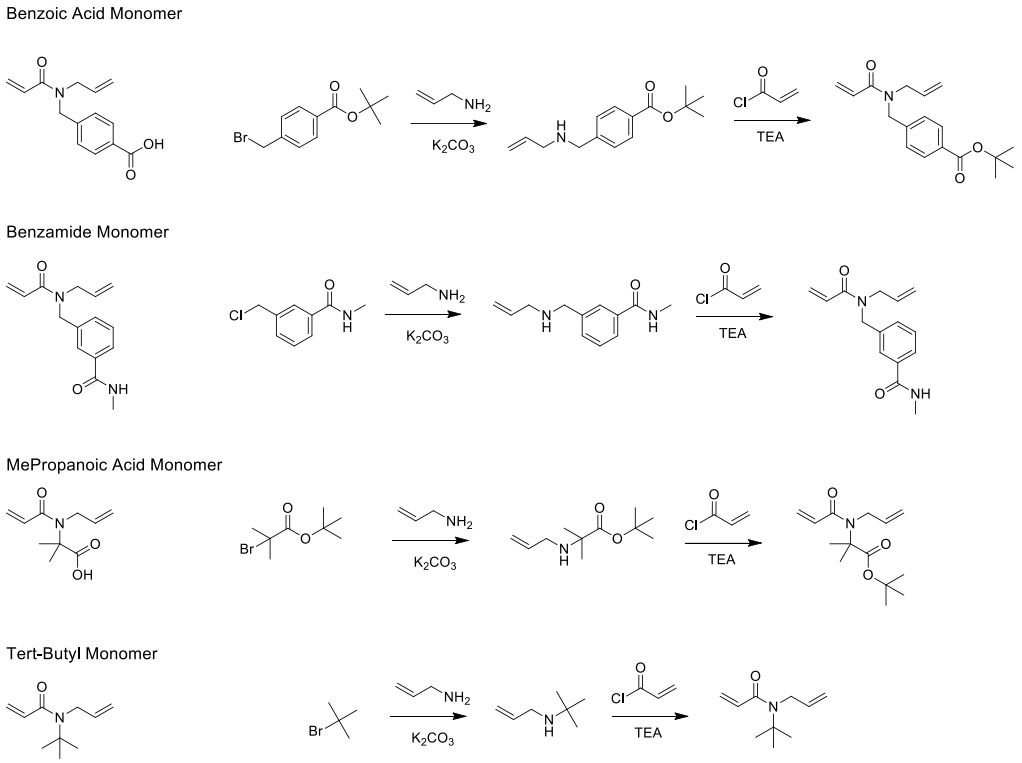

Figure E-1: *Potential structure forming N-allyl-N-acrylamides that were synthetized*

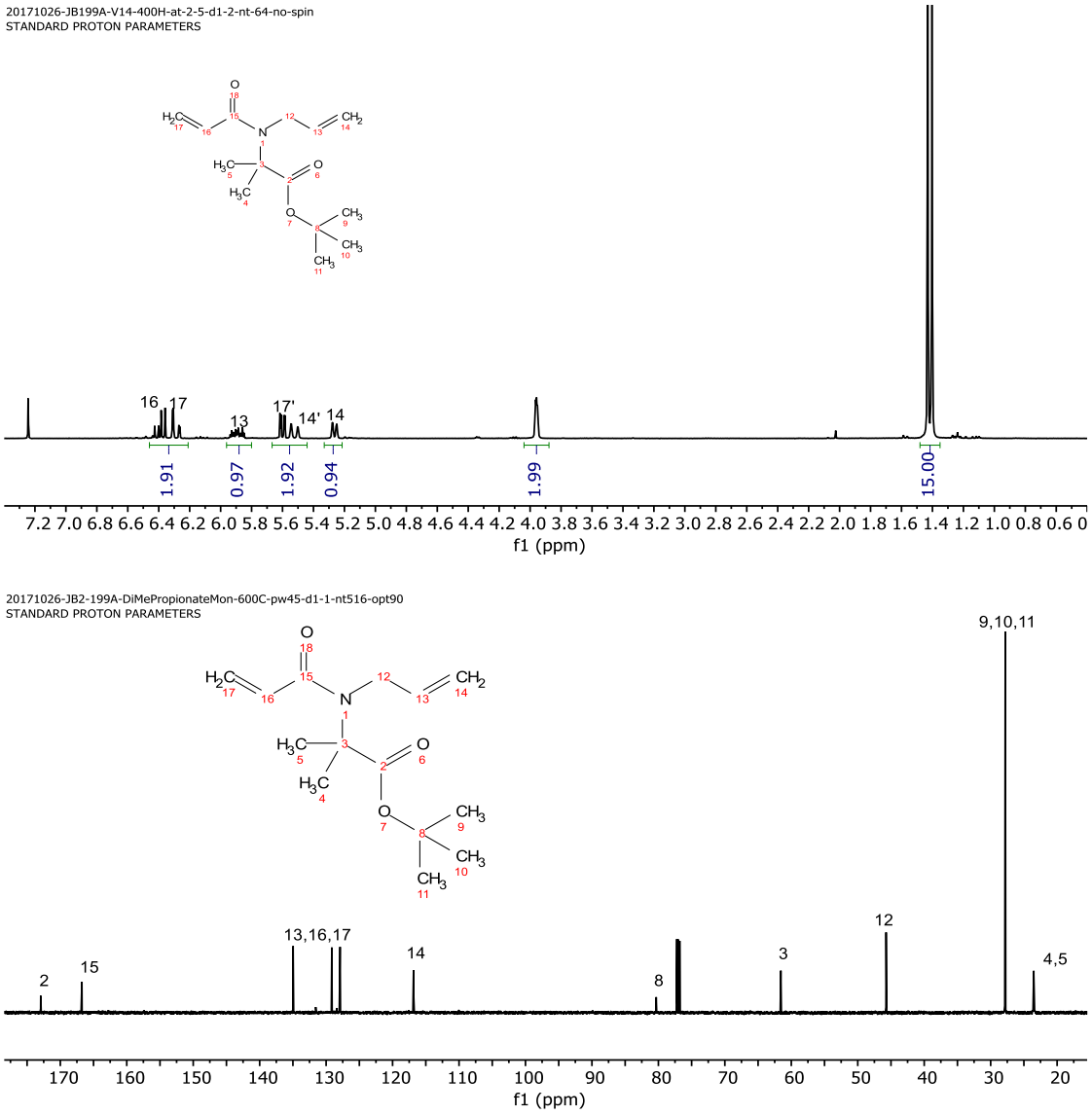

Figure E-2: *^{1}H and ^{13}C NMR of MePropanoic acid N-allyl-N-acrylamide*

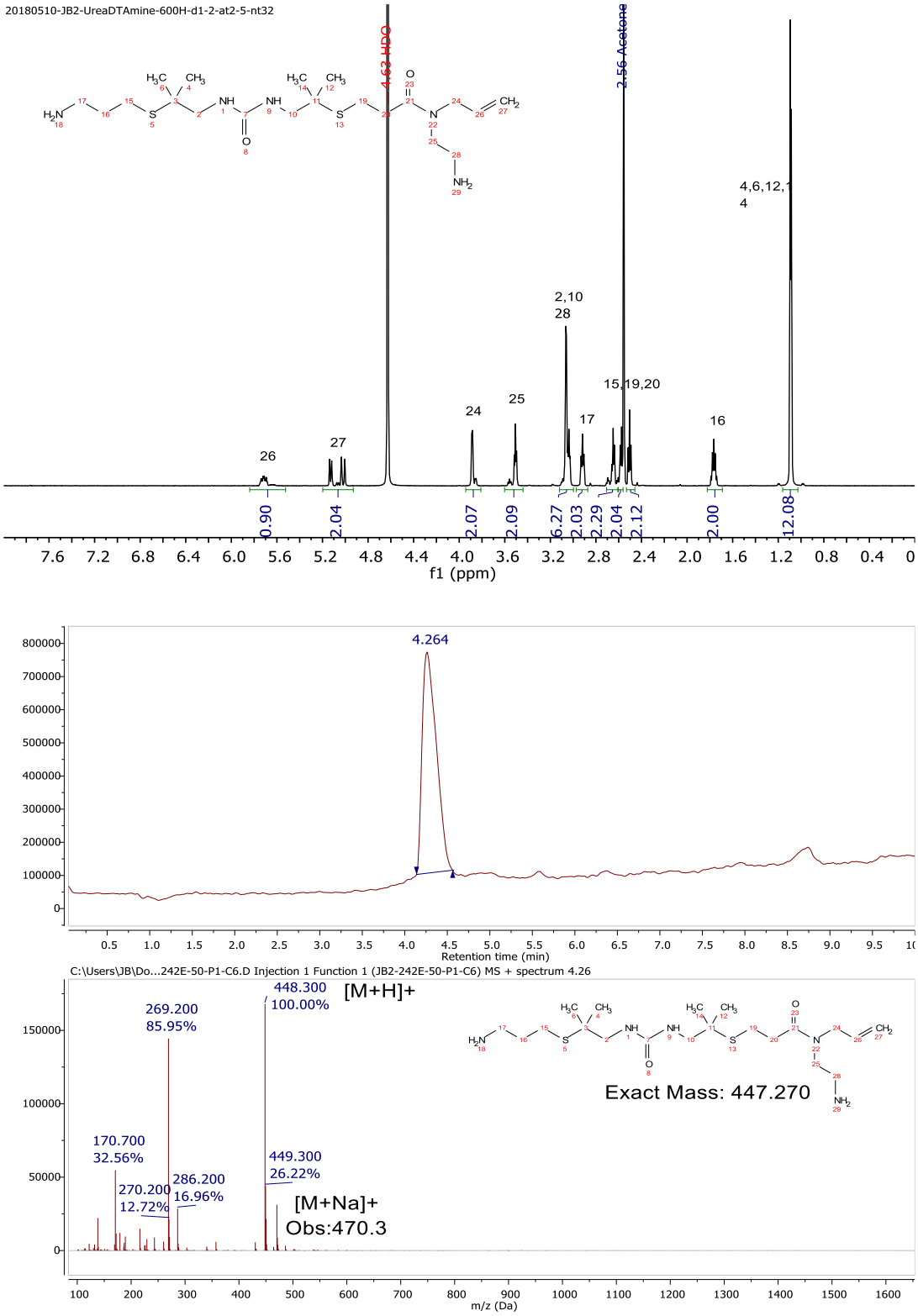

Figure E-3: *1H NMR (top) and LCMS (bottom) of model urea dithiol in an oligoTEA*

Appendix F : References

1. Martin, T. W. & Derewenda, Z. S. The name is bond - H bond. *Nat. Struct. Biol.* **6,** 403–406 (1999).
2. Pace, C. N. & Scholtz, J. M. A helix propensity scale based on experimental studies of peptides and proteins. *Biophys. J.* **75,** 422–427 (1998).
3. Pauling, L., Corey, R. B. & Branson, H. R. The structure of proteins: Two hydrogen-bonded helical configurations of the polypeptide chain. *Proc. Natl. Acad. Sci.* **37,** 205–211 (1951).
4. Pauling, L. & Corey, R. B. Atomic Coordinates and Structure Factors for Two Helical Configurations of Polypeptide Chains. *Proc. Natl. Acad. Sci.* **37,** 235–240 (1951).
5. Walters, R. F. S. & DeGrado, W. F. Helix-packing motifs in membrane proteins. *Proc. Natl. Acad. Sci.* **103,** 13658–13663 (2006).
6. Branden, C. I. & Tooze, J. *Introduction to Protein Structure*. (Garland Science, Taylor & Francis Group, 1999).
7. Jaakola, V.-P. *et al.* The 2.6 Angstrom Crystal Structure of a Human A2A Adenosine Receptor Bound to an Antagonist. *Science (80-.).* **322,** 1211–1217 (2008).
8. Gribskov, M., Wesson, L. & Eisenberg, D. PDB 2MLT: Melittin. *The RCSB Protein Data Bank* (1990). doi:10.2210/pdb2MLT/pdb
9. Brownlie, P. *et al.* The crystal structure of an intact human Max-DNA complex: new insights into mechanisms of transcriptional control. *Structure* **5,** 509–520 (1997).

10. Schreiter, E. R., Rodríguez, M. M., Weichsel, A., Montfort, W. R. & Bonaventura, J. S-Nitrosylation-induced conformational change in blackfin tuna myoglobin. *J. Biol. Chem.* **282,** 19773–19780 (2007).

11. Koshland, D. E. The Key–Lock Theory and the Induced Fit Theory. *Angew. Chemie Int. Ed. English* **33,** 2375–2378 (1995).

12. van der Lee, R. *et al.* Classification of Intrinsically Disordered Regions and Proteins. *Chem. Rev.* **114,** 6589–6631 (2014).

13. Papaleo, E. *et al.* The Role of Protein Loops and Linkers in Conformational Dynamics and Allostery. *Chem. Rev.* **116,** 6391–6423 (2016).

14. Dyson, H. J. & Wright, P. E. Intrinsically unstructured proteins and their functions. *Nat. Rev. Mol. Cell Biol.* **6,** 197–208 (2005).

15. Keul, N. D. *et al.* The entropic force generated by intrinsically disordered segments tunes protein function. *Nature* **563,** 584–588 (2018).

16. Eliezer, D. Biophysical characterization of intrinsically disordered proteins. *Curr. Opin. Struct. Biol.* **19,** 23–30 (2009).

17. Wright, P. E. & Dyson, H. J. Intrinsically disordered proteins in cellular signalling and regulation. *Nat. Rev. Mol. Cell Biol.* **16,** 18–29 (2014).

18. Poongavanam, V., Doak, B. C. & Kihlberg, J. Opportunities and guidelines for discovery of orally absorbed drugs in beyond rule of 5 space. *Curr. Opin. Chem. Biol.* **44,** 23–29 (2018).

19. Bickerton, G. R., Paolini, G. V., Besnard, J., Muresan, S. & Hopkins, A. L. Quantifying the chemical beauty of drugs. *Nat. Chem.* **4,** 90–98 (2012).

20. Austin, M. J. & Rosales, A. M. Tunable biomaterials from synthetic, sequence-

controlled polymers. *Biomater. Sci.* (2019). doi:10.1039/C8BM01215F

21. Sorkin, M. R., Walker, J. A., Brown, J. S. & Alabi, C. A. Versatile Platform for the Synthesis of Orthogonally Cleavable Heteromultifunctional Cross-Linkers. *Bioconjug. Chem.* **28,** 907–912 (2017).

22. Liang, Y., Li, L., Scott, R. A. & Kiick, K. L. 50th Anniversary Perspective : Polymeric Biomaterials: Diverse Functions Enabled by Advances in Macromolecular Chemistry. *Macromolecules* **50,** 483–502 (2017).

23. Buvailo, A. Will Biologics Surpass Small Molecules In The Pharma Race? *BiopharmaTrend.com* (2018). Available at: https://www.biopharmatrend.com/post/67-will-small-molecules-sustain-pharmaceutical-race-with-biologics/. (Accessed: 24th January 2019)

24. Lu, Y. & Freeland, S. On the evolution of the standard amino-acid alphabet. *Genome Biol.* **7,** 102 (2006).

25. Hohsaka, T. & Sisido, M. Incorporation of non-natural amino acids into proteins. *Curr. Opin. Chem. Biol.* **6,** 809–815 (2002).

26. Wagner, I. & Musso, H. New Naturally Occurring Amino Acids. *Angew. Chemie Int. Ed. English* **22,** 816–828 (1983).

27. Mijalis, A. J. *et al.* A fully automated flow-based approach for accelerated peptide synthesis. *Nat. Chem. Biol.* **13,** 464–466 (2017).

28. Carter, P. J. & Lazar, G. A. Next generation antibody drugs: Pursuit of the 'high-hanging fruit'. *Nat. Rev. Drug Discov.* **17,** 197–223 (2018).

29. Altman, L. K. A New Insulin Given Approval for Use in U.S. *The New York Times* 1001001 (1982).

30. Lowe, D. The Smallest Drugs. *In The Pipeline* (2014). Available at: https://blogs.sciencemag.org/pipeline/archives/2014/08/27/the_smallest_drugs. (Accessed: 23rd January 2019)

31. Gulland, J. M. & Robinson, R. CXII.—The morphine group. Part I. A discussion of the constitutional problem. *J. Chem. Soc., Trans.* **123,** 980–998 (1923).

32. Gates, M. & Tschudi, G. The Synthesis of Morphine. *J. Am. Chem. Soc.* **78,** 1380–1393 (1956).

33. Erlanson, D. A., Fesik, S. W., Hubbard, R. E., Jahnke, W. & Jhoti, H. Twenty years on: the impact of fragments on drug discovery. *Nat. Rev. Drug Discov.* **15,** 605–619 (2016).

34. Heinis, C. Drug discovery: Tools and rules for macrocycles. *Nat. Chem. Biol.* **10,** 696–698 (2014).

35. Villar, E. a *et al.* How proteins bind macrocycles. *Nat. Chem. Biol.* **10,** 723–31 (2014).

36. Driggers, E. M., Hale, S. P., Lee, J. & Terrett, N. K. The exploration of macrocycles for drug discovery--an underexploited structural class. *Nat. Rev. Drug Discov.* **7,** 608–624 (2008).

37. Porel, M., Thornlow, D. N., Phan, N. N. & Alabi, C. A. Sequence-defined bioactive macrocycles via an acid-catalysed cascade reaction. *Nat. Chem.* **8,** 590–596 (2016).

38. Schneider, G. Automating drug discovery. *Nat. Rev. Drug Discov.* **17,** 97–113 (2018).

39. Fleming, N. How artificial intelligence is changing drug discovery. *Nature* **557,**

S55–S57 (2018).

40. Warner, K. D. *et al.* Principles for targeting RNA with drug-like small molecules. *Nat. Rev. Drug Discov.* **17,** 547–558 (2018).

41. Yang, W. Y., Gao, R., Southern, M., Sarkar, P. S. & Disney, M. D. Design of a bioactive small molecule that targets r(AUUCU) repeats in spinocerebellar ataxia 10. *Nat. Commun.* **7,** 1–11 (2016).

42. Disney, M. D., Yildirim, I. & Childs-Disney, J. L. Methods to enable the design of bioactive small molecules targeting RNA. *Org. Biomol. Chem.* **12,** 1029–1039 (2014).

43. Scott, D. E., Bayly, A. R., Abell, C. & Skidmore, J. Small molecules, big targets: drug discovery faces the protein-protein interaction challenge. *Nat. Rev. Drug Discov.* **15,** 533–550 (2016).

44. Brannigan, J. A. & Wilkinson, A. J. Protein engineering 20 years on. *Nat. Rev. Mol. Cell Biol.* **3,** 964–970 (2002).

45. Robinson, M.-P. *et al.* Efficient expression of full-length antibodies in the cytoplasm of engineered bacteria. *Nat. Commun.* **6,** 8072 (2015).

46. Staunton, J. & Weissman, K. J. Polyketide biosynthesis: a millennium review. *Nat. Prod. Rep.* **18,** 380–416 (2001).

47. Johnson, J. A., Lu, Y. Y., Van Deventer, J. A. & Tirrell, D. A. Residue-specific incorporation of non-canonical amino acids into proteins: recent developments and applications. *Curr. Opin. Chem. Biol.* **14,** 774–780 (2010).

48. d'Aquino, A. E., Kim, D. S. & Jewett, M. C. Engineered Ribosomes for Basic Science and Synthetic Biology. *Annu. Rev. Chem. Biomol. Eng.* **9,** 311–340

(2018).

49. Brown, A. S., Calcott, M. J., Owen, J. G. & Ackerley, D. F. Structural, functional and evolutionary perspectives on effective re-engineering of non-ribosomal peptide synthetase assembly lines. *Nat. Prod. Rep.* **35,** 1210–1228 (2018).

50. Czaplewski, L. *et al.* Alternatives to antibiotics-a pipeline portfolio review. *Lancet Infect. Dis.* **16,** 239–251 (2016).

51. Watson, J. D. & Crick, F. H. C. Molecular Structure of Nucleic Acids: A Structure for Deoxyribose Nucleic Acid. *Nature* **171,** 737–738 (1953).

52. Michelson, A. M. & Todd, A. R. Nucleotides part XXXII. Synthesis of a dithymidine dinucleotide containing a 3′: 5′-internucleotidic linkage. *J. Chem. Soc.* 2632–2638 (1955). doi:10.1039/JR9550002632

53. Beaucage, S. L. & Iyer, R. P. Advances in the Synthesis of Oligonucleotides by the Phosphoramidite Approach. *Tetrahedron* **48,** 2223–2311 (1992).

54. Sanger, F., Nicklen, S. & Coulson, A. R. DNA sequencing with chain-terminating inhibitors. *Proc. Natl. Acad. Sci.* **74,** 5463–5467 (1977).

55. Saiki, R. *et al.* Primer-directed enzymatic amplification of DNA with a thermostable DNA polymerase. *Science (80-.).* **239,** 487–491 (1988).

56. Venter, J. C. *et al.* The Sequence of the Human Genome. *Science (80-.).* **291,** 1304–1351 (2001).

57. Kosuri, S. & Church, G. M. Large-scale de novo DNA synthesis: Technologies and applications. *Nat. Methods* **11,** 499–507 (2014).

58. Coin, I., Beyermann, M. & Bienert, M. Solid-phase peptide synthesis: from standard procedures to the synthesis of difficult sequences. *Nat. Protoc.* **2,** 3247–

3256 (2007).

59. Bray, B. L. Innovation: Large-scale manufacture of peptide therapeutics by chemical synthesis. *Nat. Rev. Drug Discov.* **2,** 587–593 (2003).

60. Zhou, J. & Rossi, J. Aptamers as targeted therapeutics: current potential and challenges. *Nat Rev Drug Discov* **advance on,** (2016).

61. Tuerk, C. & Gold, L. Systematic evolution of ligands by exponential enrichment: RNA ligands to bacteriophage T4 DNA polymerase. *Science (80-.).* **249,** 505–510 (1990).

62. Ellington, A. D. & Szostak, J. W. In vitro selection of RNA molecules that bind specific ligands. *Nature* **346,** 818–822 (1990).

63. Bock, L. C., Griffin, L. C., Latham, J. A., Vermaas, E. H. & Toole, J. J. Selection of single-stranded DNA molecules that bind and inhibit human thrombin. *Nature* **355,** 564–6 (1992).

64. Rusconi, C. P. *et al.* RNA aptamers as reversible antagonists of coagulation factor IXa. *Nature* **419,** 90–94 (2002).

65. Merrifield, R. B. Solid Phase Peptide Synthesis. I. The Synthesis of a Tetrapeptide. *J. Am. Chem. Soc.* **85,** 2149–2154 (1963).

66. Merrifield, R. B. Solid-Phase Peptide Synthesis. III. An Improved Synthesis of Bradykinin *. *Biochemistry* **3,** 1385–1390 (1964).

67. Anderson, G. W. & McGregor, A. C. t-Butyloxycarbonylamino Acids and Their Use in Peptide Synthesis. *J. Am. Chem. Soc.* **79,** 6180–6183 (1957).

68. Fields, G. B. & Noble, R. L. Solid phase peptide synthesis utilizing 9-fluorenylmethoxycarbonyl amino acids. *Int. J. Pept. Protein Res.* **35,** 161–214

(1990).

69. Carpino, L. A. & Han, G. Y. 9-Fluorenylmethoxycarbonyl function, a new base-sensitive amino-protecting group. *J. Am. Chem. Soc.* **92,** 5748–5749 (1970).

70. Lau, J. L. & Dunn, M. K. Therapeutic peptides: Historical perspectives, current development trends, and future directions. *Bioorg. Med. Chem.* **26,** 2700–2707 (2018).

71. Fosgerau, K. & Hoffmann, T. Peptide therapeutics: current status and future directions. *Drug Discov. Today* **20,** 122–128 (2015).

72. Otvos, L. & Wade, J. D. Current challenges in peptide-based drug discovery. *Front. Chem.* **2,** 8–11 (2014).

73. Furman, J. L., Chiu, M. & Hunter, M. J. Early Engineering Approaches to Improve Peptide Developability and Manufacturability. *AAPS J.* **17,** 111–120 (2015).

74. Klein, T., Eckhard, U., Dufour, A., Solis, N. & Overall, C. M. Proteolytic Cleavage—Mechanisms, Function, and "Omic" Approaches for a Near-Ubiquitous Posttranslational Modification. *Chem. Rev.* **118,** 1137–1168 (2018).

75. Janeway, C. A. & Medzhitov, R. Innate Immune Recognition. *Annu. Rev. Immunol.* **20,** 197–216 (2002).

76. Hu, Q., Katti, P. S. & Gu, Z. Enzyme-responsive nanomaterials for controlled drug delivery. *Nanoscale* **6,** 12273–12286 (2014).

77. Choi, K. Y., Swierczewska, M., Lee, S. & Chen, X. Protease-Activated Drug Development. *Theranostics* **2,** 156–179 (2012).

78. Tsuchikama, K. & An, Z. Antibody-drug conjugates: recent advances in

conjugation and linker chemistries. *Protein Cell* **9,** 33–46 (2018).

79. Purcell, A. W. *et al.* Dissecting the role of peptides in the immune response: Theory, practice and the application to vaccine design. *J. Pept. Sci.* **9,** 255–281 (2003).

80. Neefjes, J. & Ovaa, H. A peptide's perspective on antigen presentation to the immune system. *Nat. Chem. Biol.* **9,** 769–775 (2013).

81. Grohmann, U. *et al.* Immunogenicity of tumor peptides: importance of peptide length and stability of peptide/MHC class II complex. *Cancer Immunol. Immunother.* **48,** 195–203 (1999).

82. Knappe, D., Henklein, P., Hoffmann, R. & Hilpert, K. Easy Strategy To Protect Antimicrobial Peptides from Fast Degradation in Serum. *Antimicrob. Agents Chemother.* **54,** 4003–4005 (2010).

83. Lau, Y. H., Wu, Y., de Andrade, P., Galloway, W. R. J. D. & Spring, D. R. A two-component 'double-click' approach to peptide stapling. *Nat. Protoc.* **10,** 585–594 (2015).

84. Walensky, L. D. & Bird, G. H. Hydrocarbon-Stapled Peptides: Principles, Practice, and Progress. *J. Med. Chem.* **57,** 6275–6288 (2014).

85. Lautrette, G., Touti, F., Lee, H. G., Dai, P. & Pentelute, B. L. Nitrogen Arylation for Macrocyclization of Unprotected Peptides. *J. Am. Chem. Soc.* **138,** 8340–8343 (2016).

86. Gentilucci, L., De Marco, R. & Cerisoli, L. Chemical Modifications Designed to Improve Peptide Stability: Incorporation of Non-Natural Amino Acids, Pseudo-Peptide Bonds, and Cyclization. *Curr. Pharm. Des.* **16,** 3185–3203 (2010).

87. Mathur, D. *et al.* PEPlife: A Repository of the Half-life of Peptides. *Sci. Rep.* **6,** 1–7 (2016).

88. Pollaro, L. & Heinis, C. Strategies to prolong the plasma residence time of peptide drugs. *Medchemcomm* **1,** 319 (2010).

89. Simon, M. D. *et al.* D -Amino Acid Scan of Two Small Proteins. *J. Am. Chem. Soc.* **138,** 12099–12111 (2016).

90. Reinscheid, R. K., Ardati, A., Monsma, F. J. & Civelli, O. Structure-Activity Relationship Studies on the Novel Neuropeptide Orphanin FQ. *J. Biol. Chem.* **271,** 14163–14168 (1996).

91. Verdine, G. L. & Hilinski, G. J. Stapled Peptides for Intracellular Drug Targets. in *Methods in Enzymology* **503,** 3–33 (Elsevier Inc., 2012).

92. Chang, Y. S. *et al.* Stapled α−helical peptide drug development: A potent dual inhibitor of MDM2 and MDMX for p53-dependent cancer therapy. *Proc. Natl. Acad. Sci.* **110,** E3445–E3454 (2013).

93. Ripka, A. S. & Rich, D. H. Peptidomimetic design. *Curr. Opin. Chem. Biol.* **2,** 441–452 (1998).

94. *Foldamers*. (Wiley-VCH Verlag GmbH & Co. KGaA, 2007). doi:10.1002/9783527611478

95. Hill, D. J., Mio, M. J., Prince, R. B., Hughes, T. S. & Moore, J. S. A field guide to foldamers. *Chem. Rev.* **101,** 3893–4011 (2001).

96. Goodman, C. M., Choi, S., Shandler, S. & DeGrado, W. F. Foldamers as versatile frameworks for the design and evolution of function. *Nat. Chem. Biol.* **3,** 252–262 (2007).

97. Lutz, J.-F., Lehn, J.-M., Meijer, E. W. & Matyjaszewski, K. From precision polymers to complex materials and systems. *Nat. Rev. Mater.* 16024 (2016). doi:10.1038/natrevmats.2016.24

98. Lutz, J.-F. An Introduction to Sequence-Controlled Polymers. *Seq. Polym. Synth. Self-Assembly, Prop.* **1170,** 1 (2014).

99. Lutz, J.-F., Ouchi, M., Liu, D. R. & Sawamoto, M. Sequence-Controlled Polymers. *Science (80-.).* **341,** 1238149–1238149 (2013).

100. Kline, M. A., Guo, L. & Zuckermann, R. N. Sequence-Controlled Peptoid Polymers: Bridging the Gap between Biology and Synthetic Polymers. in *Sequence-Controlled Polymers* 183–227 (Wiley-VCH Verlag GmbH & Co. KGaA, 2017). doi:10.1002/9783527806096.ch7

101. Sun, J. & Zuckermann, R. N. Peptoid Polymers: A Highly Designable Bioinspired Material. *ACS Nano* **7,** 4715–4732 (2013).

102. Lee, B.-C., Chu, T. K., Dill, K. A. & Zuckermann, R. N. Biomimetic Nanostructures: Creating a High-Affinity Zinc-Binding Site in a Folded Nonbiological Polymer. *J. Am. Chem. Soc.* **130,** 8847–8855 (2008).

103. Roy, R. K. *et al.* Design and synthesis of digitally encoded polymers that can be decoded and erased. *Nat. Commun.* **6,** 7237–7239 (2015).

104. Minoda, M., Sawamoto, M. & Higashimura, T. Sequence-regulated oligomers and polymers by living cationic polymerization. 2. Principle of sequence regulation and synthesis of sequence-regulated oligomers of functional vinyl ethers and styrene derivatives. *Macromolecules* **23,** 4889–4895 (1990).

105. Nakatani, K., Ogura, Y., Koda, Y., Terashima, T. & Sawamoto, M. Sequence-

Regulated Copolymers via Tandem Catalysis of Living Radical Polymerization and In Situ Transesterification. *J. Am. Chem. Soc.* **134,** 4373–4383 (2012).

106. Satoh, K., Ozawa, S., Mizutani, M., Nagai, K. & Kamigaito, M. Sequence-regulated vinyl copolymers by metal-catalysed step-growth radical polymerization. *Nat. Commun.* **1,** 1–6 (2010).

107. Zhang, J., Matta, M. E. & Hillmyer, M. A. Synthesis of Sequence-Specific Vinyl Copolymers by Regioselective ROMP of Multiply Substituted Cyclooctenes. *ACS Macro Lett.* **1,** 1383–1387 (2012).

108. Ida, S., Ouchi, M. & Sawamoto, M. Template-Assisted Selective Radical Addition toward Sequence-Regulated Polymerization: Lariat Capture of Target Monomer by Template Initiator. *J. Am. Chem. Soc.* **132,** 14748–14750 (2010).

109. Zamfir, M. & Lutz, J.-F. Ultra-precise insertion of functional monomers in chain-growth polymerizations. *Nat. Commun.* **3,** 1138 (2012).

110. Tong, X., Guo, B. & Huang, Y. Toward the synthesis of sequence-controlled vinyl copolymers. *Chem. Commun.* **47,** 1455–1457 (2011).

111. Pfeifer, S. & Lutz, J.-F. A Facile Procedure for Controlling Monomer Sequence Distribution in Radical Chain Polymerizations. *J. Am. Chem. Soc.* **129,** 9542–9543 (2007).

112. Gody, G., Maschmeyer, T., Zetterlund, P. B. & Perrier, S. Rapid and quantitative one-pot synthesis of sequence-controlled polymers by radical polymerization. *Nat. Commun.* **4,** 2505 (2013).

113. Dijk, M. van *et al.* Synthesis and Characterization of Biodegradable Peptide-Based Polymers Prepared by Microwave-Assisted Click Chemistry.

Biomacromolecules **9,** 2834–2843 (2008).

114. Gutekunst, W. R. & Hawker, C. J. A General Approach to Sequence-Controlled Polymers Using Macrocyclic Ring Opening Metathesis Polymerization. *J. Am. Chem. Soc.* **137,** 8038–8041 (2015).

115. Niu, J., Hili, R. & Liu, D. R. Enzyme-free translation of DNA into sequence-defined synthetic polymers structurally unrelated to nucleic acids. *Nat. Chem.* **5,** 282–292 (2013).

116. Chen, Z., Lichtor, P. A., Berliner, A. P., Chen, J. C. & Liu, D. R. Evolution of sequence-defined highly functionalized nucleic acid polymers. *Nat. Chem.* **10,** 420–427 (2018).

117. Lewandowski, B. *et al.* Sequence-Specific Peptide Synthesis by an Artificial Small-Molecule Machine. *Science (80-.).* **339,** 189–193 (2013).

118. Gartner, Z. J., Kanan, M. W. & Liu, D. R. Multistep Small-Molecule Synthesis Programmed by DNA Templates. *J. Am. Chem. Soc.* **124,** 10304–10306 (2002).

119. Chen, Z., Lichtor, P. A., Berliner, A. P., Chen, J. C. & Liu, D. R. Evolution of sequence-defined highly functionalized nucleic acid polymers. *Nat. Chem.* **10,** 420–427 (2018).

120. ten Brummelhuis, N. Controlling monomer-sequence using supramolecular templates. *Polym. Chem.* **6,** 654–667 (2015).

121. Barnes, J. C. *et al.* Iterative exponential growth of stereo- and sequence-controlled polymers. *Nat. Chem.* **7,** 810–815 (2015).

122. Beaucage, S. L. & Caruthers, M. H. Deoxynucleoside phosphoramidites—A new class of key intermediates for deoxypolynucleotide synthesis. *Tetrahedron Lett.*

22, 1859–1862 (1981).

123. Hartmann, L., Krause, E., Antonietti, M. & Börner, H. G. Solid-Phase Supported Polymer Synthesis of Sequence-Defined, Multifunctional Poly(amidoamines). *Biomacromolecules* **7,** 1239–1244 (2006).

124. Ponader, D., Wojcik, F., Beceren-Braun, F., Dernedde, J. & Hartmann, L. Sequence-Defined Glycopolymer Segments Presenting Mannose: Synthesis and Lectin Binding Affinity. *Biomacromolecules* **13,** 1845–1852 (2012).

125. Schaffert, D., Badgujar, N. & Wagner, E. Novel Fmoc-Polyamino Acids for Solid-Phase Synthesis of Defined Polyamidoamines. *Org. Lett.* **13,** 1586–1589 (2011).

126. Hahn, F. & Schepers, U. Versatile Procedure for Asymmetric and Orthogonal Protection of Symmetric Polyamines and Its Advantages for Solid Phase Synthesis. *J. Comb. Chem.* **10,** 267–273 (2008).

127. Zuckermann, R. N. Peptoid origins. *Biopolymers* **96,** 545–555 (2011).

128. Martens, S. *et al.* Multifunctional sequence-defined macromolecules for chemical data storage. *Nat. Commun.* **9,** 4451 (2018).

129. Solleder, S. C., Schneider, R. V., Wetzel, K. S., Boukis, A. C. & Meier, M. A. R. Recent Progress in the Design of Monodisperse, Sequence-Defined Macromolecules. *Macromol. Rapid Commun.* **38,** 1600711 (2017).

130. Bayer, E. & Mutter, M. Liquid Phase Synthesis of Peptides. *Nature* **237,** 512–513 (1972).

131. Han, H., Wolfe, M. M., Brenner, S. & Janda, K. D. Liquid-phase combinatorial synthesis. *Proc. Natl. Acad. Sci.* **92,** 6419–6423 (1995).

132. Bonora, G. M., Scremin, C. L., Colonna, F. P. & Garbesi, A. HELP (High Efficiency Liquid Phase) new oligonucleotide synthesis on soluble polymeric support. *Nucleic Acids Res.* **18,** 3155–3159 (1990).

133. Douglas, S. P., Whitfield, D. M. & Krepinsky, J. J. Polymer-supported solution synthesis of oligosaccharides. *J. Am. Chem. Soc.* **113,** 5095–5097 (1991).

134. Gladysz, J. A., Dennis, P. & Horva, T. *Handbook of Fluorous Chemistry*. (Wiley-VCH Verlag GmbH & Co. KGaA, 2004). doi:10.1002/3527603905

135. Dickerson, T. J., Reed, N. N. & Janda, K. D. Soluble Polymers as Scaffolds for Recoverable Catalysts and Reagents. *Chem. Rev.* **102,** 3325–3344 (2002).

136. Solleder, S. C. & Meier, M. A. R. Sequence Control in Polymer Chemistry through the Passerini Three-Component Reaction. *Angew. Chemie Int. Ed.* **53,** 711–714 (2014).

137. Loiseau, F. A., Hii, K. K. (Mimi) & Hill, A. M. Multigram Synthesis of Well-Defined Extended Bifunctional Polyethylene Glycol (PEG) Chains. *J. Org. Chem.* **69,** 639–647 (2004).

138. Studer, A. Fluorous Synthesis: A Fluorous-Phase Strategy for Improving Separation Efficiency in Organic Synthesis. *Science (80-.).* **275,** 823–826 (1997).

139. Zhang, W. & Curran, D. P. Synthetic applications of fluorous solid-phase extraction (F-SPE). *Tetrahedron* **62,** 11837–11865 (2006).

140. Chu, Q., Yu, M. S. & Curran, D. P. New fluorous/organic biphasic systems achieved by solvent tuning. *Tetrahedron* **63,** 9890–9895 (2007).

141. Matsugi, M. & Curran, D. P. Reverse Fluorous Solid-Phase Extraction: A New Technique for Rapid Separation of Fluorous Compounds. *Org. Lett.* **6,** 2717–

2720 (2004).

142. Horváth, I. T. Fluorous Biphase Chemistry. *Acc. Chem. Res.* **31,** 641–650 (1998).

143. Zhang, W. & Lu, Y. 96-Well Plate-to-Plate Gravity Fluorous Solid-Phase Extraction (F-SPE) for Solution-Phase Library Purification. *J. Comb. Chem.* **9,** 836–843 (2007).

144. Vegas, A. J. *et al.* Fluorous-based small-molecule microarrays for the discovery of histone deacetylase inhibitors. *Angew. Chemie - Int. Ed.* **46,** 7960–7964 (2007).

145. Jian, H. & Tour, J. M. Preparative Fluorous Mixture Synthesis of Diazonium-Functionalized Oligo(phenylene vinylene)s. *J. Org. Chem.* **70,** 3396–3424 (2005).

146. Porel, M. & Alabi, C. A. Sequence-defined polymers via orthogonal allyl acrylamide building blocks. *J. Am. Chem. Soc.* **136,** 13162–13165 (2014).

147. Porel, M., Brown, J. S. & Alabi, C. a. Sequence-defined oligothioetheramides. *Synlett* **26,** 565–571 (2015).

148. Kanasty, R. L. *et al.* Sequence-Defined Oligomers from Hydroxyproline Building Blocks for Parallel Synthesis Applications. *Angew. Chemie Int. Ed.* **55,** 9529–9533 (2016).

149. Li, Y. *et al.* Fluorous synthesis of mono-dispersed poly(ethylene glycols). *Tetrahedron Lett.* **55,** 2110–2113 (2014).

150. Paynter, O. I., Simmonds, D. J. & Whiting, M. C. The synthesis of long-chain unbranched aliphatic compounds by molecular doubling. *J. Chem. Soc. Chem. Commun.* 1165 (1982). doi:10.1039/c39820001165

151. Takizawa, K., Tang, C. & Hawker, C. J. Molecularly Defined Caprolactone Oligomers and Polymers: Synthesis and Characterization. *J. Am. Chem. Soc.* **130,** 1718–1726 (2008).

152. Leibfarth, F. A., Johnson, J. A. & Jamison, T. F. Scalable synthesis of sequence-defined, unimolecular macromolecules by Flow-IEG. *Proc. Natl. Acad. Sci.* **112,** 10617–10622 (2015).

153. Pelay-Gimeno, M., Glas, A., Koch, O. & Grossmann, T. N. Structure-Based Design of Inhibitors of Protein-Protein Interactions: Mimicking Peptide Binding Epitopes. *Angew. Chemie - Int. Ed.* **54,** 8896–8927 (2015).

154. Jayatunga, M. K. P., Thompson, S. & Hamilton, A. D. α-Helix mimetics: Outwards and upwards. *Bioorg. Med. Chem. Lett.* **24,** 717–724 (2014).

155. Welch, B. D., VanDemark, A. P., Heroux, A., Hill, C. P. & Kay, M. S. Potent D-peptide inhibitors of HIV-1 entry. *Proc. Natl. Acad. Sci.* **104,** 16828–16833 (2007).

156. Milton, R., Milton, S. & Kent, S. Total chemical synthesis of a D-enzyme: the enantiomers of HIV-1 protease show reciprocal chiral substrate specificity [corrected]. *Science (80-.).* **256,** 1445–1448 (1992).

157. Seebach, D., Beck, A. K. & Bierbaum, D. J. The World ofβ- andγ-Peptides Comprised of Homologated Proteinogenic Amino Acids and Other Components. *Chem. Biodivers.* **1,** 1111–1239 (2004).

158. DeGrado, W. F., Schneider, J. P. & Hamuro, Y. The twists and turns of β-peptides. *J. Pept. Res.* **54,** 206–217 (2008).

159. Misra, R. *et al.* Structural Dimorphism of Achiral α,γ-Hybrid Peptide Foldamers:

Coexistence of 12- and 15/17-Helices. *Chem. - A Eur. J.* **23,** 3764–3772 (2017).

160. Baldauf, C., Günther, R. & Hofmann, H.-J. δ-Peptides and δ-Amino Acids as Tools for Peptide Structure DesignA Theoretical Study. *J. Org. Chem.* **69,** 6214–6220 (2004).

161. Ma, C. D., Wang, C., Acevedo-Vélez, C., Gellman, S. H. & Abbott, N. L. Modulation of hydrophobic interactions by proximally immobilized ions. *Nature* **517,** 347–350 (2015).

162. Raguse, T. L., Lai, J. R. & Gellman, S. H. Environment-independent 14-helix formation in short β-peptides: Striking a balance between shape control and functional diversity. *J. Am. Chem. Soc.* **125,** 5592–5593 (2003).

163. Radzishevsky, I. S. *et al.* Improved antimicrobial peptides based on acyl-lysine oligomers. *Nat. Biotechnol.* **25,** 657–9 (2007).

164. Hamada, Y. & Shioiri, T. Recent Progress of the Synthetic Studies of Biologically Active Marine Cyclic Peptides and Depsipeptides. *Chem. Rev.* **105,** 4441–4482 (2005).

165. Yang, D., Li, W., Qu, J., Luo, S.-W. & Wu, Y.-D. A New Strategy to Induce γ-Turns: Peptides Composed of Alternating α-Aminoxy Acids and α-Amino Acids. *J. Am. Chem. Soc.* **125,** 13018–13019 (2003).

166. Yang, D. *et al.* Novel Turns and Helices in Peptides of Chiral α-Aminoxy Acids. *J. Am. Chem. Soc.* **121,** 589–590 (1999).

167. Soth, M. J. & Nowick, J. S. Unnatural oligomers and unnatural oligomer libraries. *Curr. Opin. Chem. Biol.* **1,** 120–129 (1997).

168. Chingle, R., Proulx, C. & Lubell, W. D. Azapeptide Synthesis Methods for

Expanding Side-Chain Diversity for Biomedical Applications. *Acc. Chem. Res.* **50,** 1541–1556 (2017).

169. Violette, A. *et al.* Mimicking Helical Antibacterial Peptides with Nonpeptidic Folding Oligomers. *Chem. Biol.* **13,** 531–538 (2006).

170. Pendem, N. *et al.* Helix-forming propensity of aliphatic urea oligomers incorporating noncanonical residue substitution patterns. *J. Am. Chem. Soc.* **135,** 4884–4892 (2013).

171. Han, H. & Janda, K. D. Azatides: Solution and Liquid Phase Syntheses of a New Peptidomimetic. *J. Am. Chem. Soc.* **118,** 2539–2544 (1996).

172. Menchise, V. *et al.* Insights into peptide nucleic acid (PNA) structural features: The crystal structure of a D-lysine-based chiral PNA-DNA duplex. *Proc. Natl. Acad. Sci.* **100,** 12021–12026 (2003).

173. Pellestor, F. & Paulasova, P. The peptide nucleic acids (PNAs), powerful tools for molecular genetics and cytogenetics. *Eur. J. Hum. Genet.* **12,** 694–700 (2004).

174. Simon, R. J. *et al.* Peptoids: a modular approach to drug discovery. *Proc. Natl. Acad. Sci. U. S. A.* **89,** 9367–71 (1992).

175. Mannige, R. V. *et al.* Peptoid nanosheets exhibit a new secondary-structure motif. *Nature* **526,** 415–420 (2015).

176. Zuckermann, R. N., Kerr, J. M., Kent, S. B. H. & Moos, W. H. Efficient method for the preparation of peptoids [oligo(N-substituted glycines)] by submonomer solid-phase synthesis. *J. Am. Chem. Soc.* **114,** 10646–10647 (1992).

177. Armand, P. *et al.* Chiral N-substituted glycines can form stable helical

conformations. *Fold. Des.* **2,** 369–375 (1997).

178. Kirshenbaum, K. *et al.* Sequence-specific polypeptoids: a diverse family of heteropolymers with stable secondary structure. *Proc. Natl. Acad. Sci. U. S. A.* **95,** 4303–4308 (1998).

179. Sun, J. *et al.* Self-assembly of crystalline nanotubes from monodisperse amphiphilic diblock copolypeptoid tiles. *Proc. Natl. Acad. Sci.* 201517169 (2016). doi:10.1073/pnas.1517169113

180. Nam, K. T. *et al.* Free-floating ultrathin two-dimensional crystals from sequence-specific peptoid polymers. *Nat. Mater.* **9,** 454–460 (2010).

181. Laursen, J. S., Harris, P., Fristrup, P. & Olsen, C. a. Triangular prism-shaped β-peptoid helices as unique biomimetic scaffolds. *Nat. Commun.* **6,** 7013 (2015).

182. Smith, A. B. *et al.* De Novo Design, Synthesis, and X-ray Crystal Structures of Pyrrolinone-Based beta-Strand Peptidomimetics. *J. Am. Chem. Soc.* **116,** 9947–9962 (1994).

183. Choi, S. *et al.* De novo design and in vivo activity of conformationally restrained antimicrobial arylamide foldamers. *Proc. Natl. Acad. Sci. U. S. A.* **106,** 6968–6973 (2009).

184. Li, Z.-T., Hou, J. & Li, C. Peptide Mimics by Linear Arylamides: A Structural and Functional Diversity Test. *Acc. Chem. Res.* **41,** 1343–1353 (2008).

185. Hou, J.-L. *et al.* Hydrogen Bonded Oligohydrazide Foldamers and Their Recognition for Saccharides. *J. Am. Chem. Soc.* **126,** 12386–12394 (2004).

186. Berl, V., Krische, M. J., Huc, I., Lehn, J.-M. & Schmutz, M. Template-Induced and Molecular Recognition Directed Hierarchical Generation of Supramolecular

Assemblies from Molecular Strands. *Chem. - A Eur. J.* **6,** 1938–1946 (2000).

187. Grate, J. W., Mo, K. F. & Daily, M. D. Triazine-Based Sequence-Defined Polymers with Side-Chain Diversity and Backbone-Backbone Interaction Motifs. *Angew. Chemie - Int. Ed.* **55,** 3925–3930 (2016).

188. Ziener, U. & Godt, A. Synthesis and Characterization of Monodisperse Oligo(phenyleneethynylene)s. *J. Org. Chem.* **62,** 6137–6143 (1997).

189. Zhang, J., Pesak, D. J., Ludwick, J. L. & Moore, J. S. Geometrically-Controlled and Site-Specifically-Functionalized Phenylacetylene Macrocycles. *J. Am. Chem. Soc.* **116,** 4227–4239 (1994).

190. Huang, S. & Tour, J. M. Rapid Solid-Phase Synthesis of Oligo(1,4-phenylene ethynylene)s by a Divergent/Convergent Tripling Strategy. *J. Am. Chem. Soc.* **121,** 4908–4909 (1999).

191. Jones, L., Schumm, J. S. & Tour, J. M. Rapid Solution and Solid Phase Syntheses of Oligo(1,4-phenylene ethynylene)s with Thioester Termini: Molecular Scale Wires with Alligator Clips. Derivation of Iterative Reaction Efficiencies on a Polymer Support. *J. Org. Chem.* **62,** 1388–1410 (1997).

192. Malenfant, P. R. L. & Fréchet, J. M. J. The first solid-phase synthesis of oligothiophenes. *Chem. Commun.* 2657–2658 (1998). doi:10.1039/a807091a

193. Zhang, L., Colella, N. S., Cherniawski, B. P., Mannsfeld, S. C. B. & Briseno, A. L. Oligothiophene semiconductors: Synthesis, characterization, and applications for organic devices. *ACS Appl. Mater. Interfaces* **6,** 5327–5343 (2014).

194. Church, G. M., Gao, Y. & Kosuri, S. Next-generation digital information storage in DNA. *Science (80-.).* **337,** 1628 (2012).

195. Rutten, M. G. T. A., Vaandrager, F. W., Elemans, J. A. A. W. & Nolte, R. J. M. Encoding information into polymers. *Nat. Rev. Chem.* **2,** 365–381 (2018).

196. Goldman, N. *et al.* Towards practical, high-capacity, low-maintenance information storage in synthesized DNA. *Nature* **494,** 77–80 (2013).

197. Lutz, J.-F. Coding Macromolecules: Inputting Information in Polymers Using Monomer-Based Alphabets. *Macromolecules* **48,** 4759–4767 (2015).

198. Washington, M. A. *et al.* The impact of monomer sequence and stereochemistry on the swelling and erosion of biodegradable poly(lactic- co -glycolic acid) matrices. *Biomaterials* **117,** 66–76 (2017).

199. Golder, M. R. *et al.* Stereochemical Sequence Dictates Unimolecular Diblock Copolymer Assembly. *J. Am. Chem. Soc.* **140,** 1596–1599 (2018).

200. Ruoslahti, E. & Pierschbacher, M. D. Arg-Gly-Asp: a versatile cell recognition signal. *Cell* **44,** 517–8 (1986).

201. Frederix, P. W. J. M. *et al.* Exploring the sequence space for (tri-)peptide self-assembly to design and discover new hydrogels. *Nat. Chem.* **7,** 30–37 (2014).

202. Krstenansky, J. L., Owen, T. J., Hagaman, K. A. & McLean, L. R. Short model peptides having a high α-helical tendency: Design and solution properties. *FEBS Lett.* **242,** 409–413 (1989).

203. Lee, D., Redfern, O. & Orengo, C. Predicting protein function from sequence and structure. *Nat Rev Mol Cell Biol* **8,** 995–1005 (2007).

204. Hudson, W. H. & Ortlund, E. A. The structure, function and evolution of proteins that bind DNA and RNA. *Nat Rev Mol Cell Biol* **15,** 749–760 (2014).

205. Vagner, J., Qu, H. & Hruby, V. J. Peptidomimetics, a synthetic tool of drug

discovery. *Curr. Opin. Chem. Biol.* **12,** 292–296 (2008).

206. Burkoth, T. S., Fafarman, A. T., Charych, D. H., Connolly, M. D. & Zuckermann, R. N. Incorporation of unprotected heterocyclic side chains into peptoid oligomers via solid-phase submonomer synthesis. *J. Am. Chem. Soc.* **125,** 8841–8845 (2003).

207. Isidro-Llobet, A., Álvarez, M. & Albericio, F. Amino Acid-Protecting Groups. *Chem. Rev.* **109,** 2455–2504 (2009).

208. Thirumurugan, P., Matosiuk, D. & Jozwiak, K. Click Chemistry for Drug Development and Diverse Chemical–Biology Applications. *Chem. Rev.* **113,** 4905–4979 (2013).

209. Pfeifer, S., Zarafshani, Z., Badi, N. & Lutz, J.-F. Liquid-Phase Synthesis of Block Copolymers Containing Sequence-Ordered Segments. *J. Am. Chem. Soc.* **131,** 9195–9197 (2009).

210. Chan, J. W., Hoyle, C. E. & Lowe, A. B. Sequential Phosphine-Catalyzed, Nucleophilic Thiol−Ene/Radical-Mediated Thiol−Yne Reactions and the Facile Orthogonal Synthesis of Polyfunctional Materials. *J. Am. Chem. Soc.* **131,** 5751–5753 (2009).

211. Chan, J. W., Hoyle, C. E., Lowe, A. B. & Bowman, M. Nucleophile-Initiated Thiol-Michael Reactions: Effect of Organocatalyst, Thiol, and Ene. *Macromolecules* **43,** 6381–6388 (2010).

212. Alabi, C. A. *et al.* Multiparametric approach for the evaluation of lipid nanoparticles for siRNA delivery. *Proc. Natl. Acad. Sci.* **110,** 12881–12886 (2013).

213. Nair, D. P. *et al.* The Thiol-Michael Addition Click Reaction: A Powerful and Widely Used Tool in Materials Chemistry. *Chem. Mater.* **26,** 724–744 (2014).

214. Heggli, M., Tirelli, N., Zisch, A. & Hubbell, J. A. Michael-Type Addition as a Tool for Surface Functionalization. *Bioconjug. Chem.* **14,** 967–973 (2003).

215. Resetco, C., Hendriks, B., Badi, N. & Du Prez, F. Thiol–ene chemistry for polymer coatings and surface modification – building in sustainability and performance. *Mater. Horizons* **4,** 1041–1053 (2017).

216. Koo, S. P. S. *et al.* Limitations of radical thiol-ene reactions for polymer-polymer conjugation. *J. Polym. Sci. Part A Polym. Chem.* **48,** 1699–1713 (2010).

217. Brown, J. S. *et al.* Synthesis and Solution-Phase Characterization of Sulfonated Oligothioetheramides. *Macromolecules* **50,** 8731–8738 (2017).

218. Hoyle, C. E. & Bowman, C. N. Thiol-ene click chemistry. *Angew. Chemie - Int. Ed.* **49,** 1540–1573 (2010).

219. Kade, M. J., Burke, D. J. & Hawker, C. J. The power of thiol-ene chemistry. *J. Polym. Sci. Part A Polym. Chem.* **48,** 743–750 (2010).

220. Hoyle, C. E., Lee, T. Y. & Roper, T. Thiol-enes: Chemistry of the past with promise for the future. *J. Polym. Sci. Part A Polym. Chem.* **42,** 5301–5338 (2004).

221. Lowe, A. B. Thiol-ene "click" reactions and recent applications in polymer and materials synthesis. *Polym. Chem.* **1,** 17–36 (2010).

222. Akiba, M. Vulcanization and crosslinking in elastomers. *Prog. Polym. Sci.* **22,** 475–521 (1997).

223. Li, G. Z. *et al.* Investigation into thiol-(meth)acrylate Michael addition reactions using amine and phosphine catalysts. *Polym. Chem.* **1,** 1196–1204 (2010).

224. Klemm, E. & Beil, U. Unusual addition by the thiol-ene photopolymerization. *Polym. Bull.* **28,** 653–656 (1992).

225. Mirjafari, A., O'Brien, R. A., West, K. N. & Davis, J. H. Synthesis of New Lipid-Inspired Ionic Liquids by Thiol-ene Chemistry: Profound Solvent Effect on Reaction Pathway. *Chem. - A Eur. J.* **20,** 7576–7580 (2014).

226. Cramer, N. B., Reddy, S. K., O'Brien, A. K. & Bowman, C. N. Thiol - Ene Photopolymerization Mechanism and Rate Limiting Step Changes for Various Vinyl Functional Group Chemistries. *Macromolecules* **36,** 7964–7969 (2003).

227. Northrop, B. H. & Coffey, R. N. Thiol-ene click chemistry: Computational and kinetic analysis of the influence of alkene functionality. *J. Am. Chem. Soc.* **134,** 13804–13817 (2012).

228. Fındık, V., Degirmenci, I., Çatak, Ş. & Aviyente, V. Theoretical investigation of thiol-ene click reactions: A DFT perspective. *Eur. Polym. J.* **110,** 211–220 (2019).

229. Delaittre, G., Pauloehrl, T., Bastmeyer, M. & Barner-Kowollik, C. Acrylamide-Based Copolymers Bearing Photoreleasable Thiols for Subsequent Thiol–Ene Functionalization. *Macromolecules* **45,** 1792–1802 (2012).

230. Hawker, C. J., Killops, K. L. & Campos, L. M. Robust, Efficient, and Orthogonal Synthesis of Dendrimers via Thiol-ene "Click" Chemistry. *J. Am. Chem. Soc.* **130,** 5062–5064 (2008).

231. McKay, C. S. & Finn, M. G. Click Chemistry in Complex Mixtures: Bioorthogonal Bioconjugation. *Chem. Biol.* **21,** 1075–1101 (2014).

232. Dondoni, A., Massi, A., Nanni, P. & Roda, A. A New Ligation Strategy for

Peptide and Protein Glycosylation: Photoinduced Thiol-Ene Coupling. *Chem. - A Eur. J.* **15,** 11444–11449 (2009).

233. Li, Y. *et al.* Genetically encoded alkenyl–pyrrolysine analogues for thiol–ene reaction mediated site-specific protein labeling. *Chem. Sci.* **3,** 2766 (2012).

234. Yee, D. W., Schulz, M. D., Grubbs, R. H. & Greer, J. R. Functionalized 3D Architected Materials via Thiol-Michael Addition and Two-Photon Lithography. *Adv. Mater.* **29,** (2017).

235. Hoyle, C. E., Lowe, A. B. & Bowman, C. N. Thiol-click chemistry: a multifaceted toolbox for small molecule and polymer synthesis. *Chem. Soc. Rev.* **39,** 1355 (2010).

236. Michael, A. Ueber die Addition von Natriumacetessig- und Natriummalonsäureäthern zu den Aethern ungesättigter Säuren. *J. für Prakt. Chemie* **35,** 349–356 (1887).

237. Tokoroyama, T. Discovery of the Michael Reaction. *European J. Org. Chem.* **2010,** 2009–2016 (2010).

238. Desmet, G. B. *et al.* Quantitative First-Principles Kinetic Modeling of the Aza-Michael Addition to Acrylates in Polar Aprotic Solvents. *J. Org. Chem.* **81,** 12291–12302 (2016).

239. Nising, C. F. & Bräse, S. The oxa-Michael reaction: From recent developments to applications in natural product synthesis. *Chem. Soc. Rev.* **37,** 1218–1228 (2008).

240. Wang, X., Li, S. & Jiang, Y. A theoretical study of the mechanism of phosphine-catalyzed hydroalkoxylation of methyl vinyl ketone. *J. Phys. Chem. A* **109,**

10770–10775 (2005).

241. Allen, C. F. H., Fournier, J. O. & Humphlett, W. J. THE THERMAL REVERSIBILITY OF THE MICHAEL REACTION: IV. THIOL ADDUCTS. *Can. J. Chem.* **42,** 2616–2620 (1964).

242. Frayne, S. H. & Northrop, B. H. Evaluating Nucleophile Byproduct Formation during Phosphine- and Amine-Promoted Thiol-Methyl Acrylate Reactions. *J. Org. Chem.* **83,** 10370–10382 (2018).

243. Chen, J., Jiang, X., Carroll, S. L., Huang, J. & Wang, J. Theoretical and Experimental Investigation of Thermodynamics and Kinetics of Thiol-Michael Addition Reactions: A Case Study of Reversible Fluorescent Probes for Glutathione Imaging in Single Cells. *Org. Lett.* **17,** 5978–5981 (2015).

244. Firouzabadi, H., Iranpoor, N. & Jafari, A. A. Micellar solution of sodium dodecyl sulfate (SDS) catalyzes facile Michael addition of amines and thiols to α,β-unsaturated ketones in water under neutral conditions. *Adv. Synth. Catal.* **347,** 655–661 (2005).

245. Sun, Y. *et al.* Thiol Michael addition reaction: a facile tool for introducing peptides into polymer-based gene delivery systems. *Polym. Int.* **67,** 25–31 (2018).

246. Desmet, G. B. *et al.* Thiol-Michael addition in polar aprotic solvents: nucleophilic initiation or base catalysis? *Polym. Chem.* **8,** 1341–1352 (2017).

247. Wang, C. & Qi, C. Mechanistic insights into N- or P-centered nucleophile promoted thiol–vinylsulfone Michael addition. *Tetrahedron* **69,** 5348–5354 (2013).

248. Jones, M. W. *et al.* Phosphine-mediated one-pot thiol–ene “click” approach to

polymer–protein conjugates. *Chem. Commun.* 5272 (2009). doi:10.1039/b906865a

249. Khire, V. S., Lee, T. Y. & Bowman, C. N. Surface Modification Using Thiol−Acrylate Conjugate Addition Reactions. *Macromolecules* **40,** 5669–5677 (2007).

250. Xi, W., Wang, C., Kloxin, C. J. & Bowman, C. N. Nitrogen-Centered Nucleophile Catalyzed Thiol-Vinylsulfone Addition, Another Thiol-ene 'Click' Reaction. *ACS Macro Lett.* **1,** 811–814 (2012).

251. Chatani, S., Nair, D. P. & Bowman, C. N. Relative reactivity and selectivity of vinyl sulfones and acrylates towards the thiol–Michael addition reaction and polymerization. *Polym. Chem.* **4,** 1048–1055 (2013).

252. Mather, B. D., Viswanathan, K., Miller, K. M. & Long, T. E. Michael addition reactions in macromolecular design for emerging technologies. *Prog. Polym. Sci.* **31,** 487–531 (2006).

253. Seto, H. *et al.* Surface modification of siliceous materials using maleimidation and various functional polymers synthesized by reversible addition-fragmentation chain transfer polymerization. *ACS Appl. Mater. Interfaces* **4,** 5125–5133 (2012).

254. Tedja, R. *et al.* Effect of TiO2 nanoparticle surface functionalization on protein adsorption, cellular uptake and cytotoxicity: the attachment of PEG comb polymers using catalytic chain transfer and thiol–ene chemistry. *Polym. Chem.* **3,** 2743 (2012).

255. Renault, K., Fredy, J. W., Renard, P. Y. & Sabot, C. Covalent Modification of

Biomolecules through Maleimide-Based Labeling Strategies. *Bioconjug. Chem.* **29,** 2497–2513 (2018).

256. Hong, V., Kislukhin, A. A. & Finn, M. G. Thiol-Selective Fluorogenic Probes for Labeling and Release. *J. Am. Chem. Soc.* **131,** 9986–9994 (2009).

257. Northrop, B. H., Frayne, S. H. & Choudhary, U. Thiol-maleimide 'click' chemistry: Evaluating the influence of solvent, initiator, and thiol on the reaction mechanism, kinetics, and selectivity. *Polym. Chem.* **6,** 3415–3430 (2015).

258. Xi, W. *et al.* Spatial and temporal control of thiol-michael addition via photocaged superbase in photopatterning and two-stage polymer networks formation. *Macromolecules* **47,** 6159–6165 (2014).

259. Kilambi, H., Stansbury, J. W. & Bowman, C. N. Enhanced reactivity of monovinyl acrylates characterized by secondary functionalities toward photopolymerization and Michael addition: Contribution of intramolecular effects. *J. Polym. Sci. Part A Polym. Chem.* **46,** 3452–3458 (2008).

260. Stewart, I. C., Bergman, R. G. & Toste, F. D. Phosphine-catalyzed hydration and hydroalkoxylation of activated olefins: Use of a strong nucleophile to generate a strong base. *J. Am. Chem. Soc.* **125,** 8696–8697 (2003).

261. Zhang, D.-H., Knelles, J. & Plietker, B. Iron-Catalyzed Michael Addition of Ketones to Polar Olefins. *Adv. Synth. Catal.* **358,** 2469–2479 (2016).

262. Arrhenius, S. On the reaction rate of the inversion of non-refined sugar upon souring. *Zeitschrift für Phys. Chemie* **4,** 226–248 (1889).

263. Krenske, E. H., Petter, R. C., Zhu, Z. & Houk, K. N. Transition states and energetics of nucleophilic additions of thiols to substituted α,β-unsaturated

ketones: Substituent effects involve enone stabilization, product branching, and solvation. *J. Org. Chem.* **76,** 5074–5081 (2011).

264. Galkin, V. I. Inductive substituent effects. *J. Phys. Org. Chem.* **12,** 283–288 (1999).

265. Sun, S. & Bernstein, E. R. Aromatic van der Waals Clusters: Structure and Nonrigidity. *J. Phys. Chem.* **100,** 13348–13366 (1996).

266. Chelli, R., Gervasio, F. L., Procacci, P. & Schettino, V. Stacking and T-shape Competition in Aromatic−Aromatic Amino Acid Interactions. *J. Am. Chem. Soc.* **124,** 6133–6143 (2002).

267. Egwim, I. O. & Gruber, H. J. Spectrophotometric measurement of mercaptans with 4,4'-dithiodipyridine. *Anal. Biochem.* **288,** 188–194 (2001).

268. Grassetti, D. R. & Murray, J. F. Determination of sulfhydryl groups with 2,2'- or 4,4'-dithiodipyridine. *Arch. Biochem. Biophys.* **119,** 41–49 (1967).

269. Huang, S. *et al.* Mechanistic Modeling of the Thiol–Michael Addition Polymerization Kinetics: Structural Effects of the Thiol and Vinyl Monomers. *Macromolecules* **51,** 5979–5988 (2018).

270. Li, G.-Z. *et al.* Investigation into thiol-(meth)acrylate Michael addition reactions using amine and phosphine catalysts. *Polym. Chem.* **1,** 1196–1204 (2010).

271. Smith, J. M., Jami Alahmadi, Y. & Rowley, C. N. Range-separated DFT functionals are necessary to model thio-Michael additions. *J. Chem. Theory Comput.* **9,** 4860–4865 (2013).

272. Jónsson, H., Mills, G. & Jacobsen, K. W. Nudged elastic band method for finding minimum energy paths of transitions. in *Classical and Quantum Dynamics in*

Condensed Phase Simulations 385–404 (World Scientific, 1998). doi:10.1142/9789812839664_0016

273. Henkelman, G., Uberuaga, B. P. & Jónsson, H. A climbing image nudged elastic band method for finding saddle points and minimum energy paths. *J. Chem. Phys.* **113,** 9901–9904 (2000).

274. Henkelman, G. & Jónsson, H. Improved tangent estimate in the nudged elastic band method for finding minimum energy paths and saddle points. *J. Chem. Phys.* **113,** 9978–9985 (2000).

275. Stevenson, J. M., Ruttinger, A. W. & Clancy, P. Uncovering the reaction mechanism initiating the nucleation of lead sulfide quantum dots in a hines synthesis. *J. Mater. Chem. A* **6,** 9402–9410 (2018).

276. Cohen, A. J., Mori-Sánchez, P. & Yang, W. Challenges for Density Functional Theory. *Chem. Rev.* **112,** 289–320 (2012).

277. Phan, N. N., Li, C. & Alabi, C. A. Intracellular Delivery via Noncharged Sequence-Defined Cell-Penetrating Oligomers. *Bioconjug. Chem.* **29,** 2628–2635 (2018).

278. Porel, M., Thornlow, D. N., Artim, C. M. & Alabi, C. A. Sequence-Defined Backbone Modifications Regulate Antibacterial Activity of OligoTEAs. *ACS Chem. Biol.* **12,** 715–723 (2017).

279. Hoff, E. A., Artim, C. M., Brown, J. S. & Alabi, C. A. Sensitivity of Antibacterial Activity to Backbone Sequence in Constitutionally Isomeric OligoTEAs. *Macromol. Biosci.* **18,** 1800241 (2018).

280. Artim, C. M., Phan, N. N. & Alabi, C. A. Effect of Composition on Antibacterial

Activity of Sequence-Defined Cationic Oligothioetheramides. *ACS Infect. Dis.* **4,** 1257–1263 (2018).

281. Brown, J. S. *et al.* Antibacterial isoamphipathic oligomers highlight the importance of multimeric lipid aggregation for antibacterial potency. *Commun. Biol.* **1,** 220 (2018).

282. Artim, C. M., Brown, J. S. & Alabi, C. A. Biophysical Characterization of Cationic Antibacterial Oligothioetheramides. *Anal. Chem.* **91,** 3118–3124 (2019).

283. Schrödinger, E. An Undulatory Theory of the Mechanics of Atoms and Molecules. *Phys. Rev.* **28,** 1049–1070 (1926).

284. Thomas, L. H. The calculation of atomic fields. *Math. Proc. Cambridge Philos. Soc.* **23,** 542 (1927).

285. Fermi, E. Eine statistische Methode zur Bestimmung einiger Eigenschaften des Atoms und ihre Anwendung auf die Theorie des periodischen Systems der Elemente. *Zeitschrift für Phys.* **48,** 73–79 (1928).

286. Hohenberg, P. & Kohn, W. Inhomogeneous Electron Gas. *Phys. Rev.* **136,** B864–B871 (1964).

287. Kohn, W. & Sham, L. J. Self-Consistent Equations Including Exchange and Correlation Effects. *Phys. Rev.* **140,** A1133–A1138 (1965).

288. Goerigk, L. & Grimme, S. A thorough benchmark of density functional methods for general main group thermochemistry, kinetics, and noncovalent interactions. *Phys. Chem. Chem. Phys.* **13,** 6670–6688 (2011).

289. Goerigk, L. *et al.* A look at the density functional theory zoo with the advanced

GMTKN55 database for general main group thermochemistry, kinetics and noncovalent interactions. *Phys. Chem. Chem. Phys.* **19,** 32184–32215 (2017).

290. Trautz, M. Das Gesetz der Reaktionsgeschwindigkeit und der Gleichgewichte in Gasen. Bestätigung der Additivität von C v -3/2R. Neue Bestimmung der Integrationskonstanten und der Moleküldurchmesser. *Zeitschrift für Anorg. und Allg. Chemie* **96,** 1–28 (1916).

291. Zhang, Q., Bell, R. & Truong, T. N. Ab Initio and Density Functional Theory Studies of Proton Transfer Reactions in Multiple Hydrogen Bond Systems. *J. Phys. Chem.* **99,** 592–599 (1995).

292. Clary, D. C. & Connor, J. N. L. Existence of a bound state for the three-dimensional IHI molecule on a purely repulsive potential energy surface. *Chem. Phys. Lett.* **94,** 81–84 (1983).

293. Eggert, D. W., Lorusso, A. & Fisher, R. B. Estimating 3-D rigid body transformations: a comparison of four major algorithms. *Mach. Vis. Appl.* **9,** 272–290 (1997).

294. Eyring, H. The Activated Complex in Chemical Reactions. *J. Chem. Phys.* **3,** 107–115 (1935).

295. Henkelman, G. Atomistic Simulations of Activated Processes in Materials. *Annu. Rev. Mater. Res.* **47,** 199–216 (2017).

296. Neese, F. The ORCA program system. *Wiley Interdiscip. Rev. Comput. Mol. Sci.* **2,** 73–78 (2012).

297. Grimme, S. Semiempirical GGA-type density functional constructed with a long-range dispersion correction. *J. Comput. Chem.* **27,** 1787–1799 (2006).

298. Schäfer, A., Horn, H. & Ahlrichs, R. Fully optimized contracted Gaussian basis sets for atoms Li to Kr. *J. Chem. Phys.* **97,** 2571–2577 (1992).

299. Weigend, F. & Ahlrichs, R. Balanced basis sets of split valence, triple zeta valence and quadruple zeta valence quality for H to Rn: Design and assessment of accuracy. *Phys. Chem. Chem. Phys.* **7,** 3297 (2005).

300. Weigend, F., Häser, M., Patzelt, H. & Ahlrichs, R. RI-MP2: optimized auxiliary basis sets and demonstration of efficiency. *Chem. Phys. Lett.* **294,** 143–152 (1998).

301. Nocedal, J. Updating quasi-Newton matrices with limited storage. *Math. Comput.* **35,** 773–773 (1980).

302. Herbol, H. C., Stevenson, J. & Clancy, P. Computational Implementation of Nudged Elastic Band, Rigid Rotation, and Corresponding Force Optimization. *J. Chem. Theory Comput.* **13,** 3250–3259 (2017).

303. Mangiatordi, G. F., Brémond, E. & Adamo, C. DFT and proton transfer reactions: A benchmark study on structure and kinetics. *J. Chem. Theory Comput.* **8,** 3082–3088 (2012).

304. Lane, D. A., Philippou, H. & Huntington, J. A. Directing thrombin. *Blood* **106,** 2605–12 (2005).

305. Siegert, R., Leroux, M. R., Scheufler, C., Hartl, F. U. & Moarefi, I. Structure of the Molecular Chaperone Prefoldin. *Cell* **103,** 621–632 (2000).

306. Harris, L. J., Larson, S. B., Hasel, K. W. & McPherson, A. Refined structure of an intact IgG2a monoclonal antibody. *Biochemistry* **36,** 1581–1597 (1997).

307. Hingerty, B., Brown, R. S. & Jack, A. Further refinement of the structure of yeast

tRNAPhe. *J. Mol. Biol.* **124,** 523–534 (1978).

308. Luger, K., Mäder, A. W., Richmond, R. K., Sargent, D. F. & Richmond, T. J. Crystal structure of the nucleosome core particle at 2.8 A resolution. *Nature* **389,** 251–260 (1997).

309. Rühmann, E., Betz, M., Heine, A. & Klebe, G. Fragment Binding Can Be Either More Enthalpy-Driven or Entropy-Driven: Crystal Structures and Residual Hydration Patterns Suggest Why. *J. Med. Chem.* **58,** 6960–6971 (2015).

310. Gilbert, E. E. & Jones, E. P. Sulfonation and Sulfation. *Ind. Eng. Chem.* **46,** 1895–1912 (1954).

311. Fasl, H. *et al.* Improvement of the hemocompatibility of PET surfaces using different sulphated polysaccharides as coating materials. *Biomacromolecules* **11,** 377–381 (2010).

312. Jones, C. J. & Larive, C. K. Carbohydrates: Cracking the glycan sequence code. *Nat. Chem. Biol.* **7,** 758–759 (2011).

313. Habuchi, H., Habuchi, O. & Kimata, K. Sulfation pattern in glycosaminoglycan: Does it have a code? *Glycoconj. J.* **21,** 47–52 (2004).

314. Ashikari-Hada, S. *et al.* Characterization of Growth Factor-binding Structures in Heparin/Heparan Sulfate Using an Octasaccharide Library. *J. Biol. Chem.* **279,** 12346–12354 (2004).

315. Tully, S. E. *et al.* A chondroitin sulfate small molecule that stimulates neuronal growth. *J. Am. Chem. Soc.* **126,** 7736–7737 (2004).

316. Xu, Y. *et al.* Chemoenzymatic Synthesis of Homogeneous Ultralow Molecular Weight Heparins. *Science (80-.).* **334,** 498–501 (2011).

317. Witvrouw, M. & De Clercq, E. Sulfated polysaccharides extracted from sea algae as potential antiviral drugs. *Gen. Pharmacol.* **29,** 497–511 (1997).

318. Miller, S. C. Profiling Sulfonate Ester Stability: Identification of Complementary Protecting Groups for Sulfonates. *J. Org. Chem.* **75,** 4632–4635 (2010).

319. Turnbull, J. E. Getting the Farm Out of Pharma for Heparin Production. *Science (80-.).* **334,** 462–463 (2011).

320. Liang, A., Thakkar, J. N. & Desai, U. R. Study of physico-chemical properties of novel highly sulfated, aromatic, mimetics of heparin and heparan sulfate. *J. Pharm. Sci.* **99,** 1207–1216 (2010).

321. Jemth, P. *et al.* Biosynthetic oligosaccharide libraries for identification of protein-binding heparan sulfate motifs: Exploring the structural diversity by screening for fibroblast growth factor (FGF) 1 and FGF2 binding. *J. Biol. Chem.* **277,** 30567–30573 (2002).

322. Parish, C. R., Freeman, C., Brown, K. J., Francis, D. J. & Cowden, W. B. Identification of sulfated oligosaccharide-based inhibitors of tumor growth and metastasis using novel in vitro assays for angiogenesis and heparanase activity. *Cancer Res.* **59,** 3433–3441 (1999).

323. Huang, Y., Shaw, M. A., Warmin, M. R., Mullins, E. S. & Ayres, N. Blood compatibility of heparin-inspired, lactose containing, polyureas depends on the chemistry of the polymer backbone. *Polym. Chem.* **7,** 3897–3905 (2016).

324. Huang, Y., Shaw, M. A., Mullins, E. S., Kirley, T. L. & Ayres, N. Synthesis and anticoagulant activity of polyureas containing sulfated carbohydrates. *Biomacromolecules* **15,** 4455–4466 (2014).

325. Oh, Y. I., Sheng, G. J., Chang, S. K. & Hsieh-Wilson, L. C. Tailored glycopolymers as anticoagulant heparin mimetics. *Angew. Chemie - Int. Ed.* **52,** 11796–11799 (2013).

326. Rawat, M., Gama, C. I., Matson, J. B. & Hsieh-Wilson, L. C. Neuroactive chondroitin sulfate glycomimetics. *J. Am. Chem. Soc.* **130,** 2959–2961 (2008).

327. Holmes, B. B. *et al.* Heparan sulfate proteoglycans mediate internalization and propagation of specific proteopathic seeds. *Proc. Natl. Acad. Sci. U. S. A.* **110,** E3138-47 (2013).

328. Mende, M. *et al.* Chemical Synthesis of Glycosaminoglycans. *Chem. Rev.* acs.chemrev.6b00010 (2016). doi:10.1021/acs.chemrev.6b00010

329. Petitou, M. & Van Boeckel, C. A. A. A synthetic antithrombin III binding pentasaccharide is now a drug! What comes next? *Angew. Chemie - Int. Ed.* **43,** 3118–3133 (2004).

330. Avci, F. Y., Karst, N. A. & Linhardt, R. J. Synthetic oligosaccharides as heparin-mimetics displaying anticoagulant properties. *Curr. Pharm. Des.* **9,** 2323–2335 (2003).

331. Jin, L. *et al.* The anticoagulant activation of antithrombin by heparin. *Proc. Natl. Acad. Sci. U. S. A.* **94,** 14683–8 (1997).

332. Xu, Y. *et al.* Homogeneous low-molecular-weight heparins with reversible anticoagulant activity. *Nat. Chem. Biol.* **10,** 248–250 (2014).

333. Noti, C., De Paz, J. L., Polito, L. & Seeberger, P. H. Preparation and use of microarrays containing synthetic heparin oligosaccharides for the rapid analysis of heparin-protein interactions. *Chem. - A Eur. J.* **12,** 8664–8686 (2006).

334. Kitagawa, K. *et al.* Facile solid-phase synthesis of sulfated tyrosine-containing peptides: Total synthesis of human big gastrin-II and cholecystokinin (CCK)-39. *J. Org. Chem.* **66,** 1–10 (2001).

335. Vale, N., Carvalho Veloso, R. & Gomes, P. Exploring the Solid-Phase Synthesis of Sulfotyrosine Peptides. *European J. Org. Chem.* **2015,** 7413–7425 (2015).

336. Al-Horani, R. A. & Desai, U. R. Chemical sulfation of small molecules-advances and challenges. *Tetrahedron* **66,** 2907–2918 (2010).

337. Ingram, L. J. & Taylor, S. D. Introduction of 2,2,2-trichloroethyl-protected sulfates into monosaccharides with a sulfuryl imidazolium salt and application to the synthesis of sulfated carbohydrates. *Angew. Chemie - Int. Ed.* **45,** 3503–3506 (2006).

338. Rusha, L. & Miller, S. C. Design and application of esterase-labile sulfonate protecting groups. *Chem. Commun. (Camb).* **47,** 2038–2040 (2011).

339. Pauff, S. M. & Miller, S. C. A trifluoroacetic acid-labile sulfonate protecting group and its use in the synthesis of a near-IR fluorophore. *J. Org. Chem.* **78,** 711–716 (2013).

340. Matthews, B. W. Protein Structure Initiative: getting into gear. *Nat. Struct. Mol. Biol.* **14,** 459–460 (2007).

341. Hura, G. L. *et al.* Robust, high-throughput solution structural analyses by small angle X-ray scattering (SAXS). *Nat. Methods* **6,** 606–12 (2009).

342. Blundell, T. L., Jhoti, H. & Abell, C. High-Throughput Crystallography for Lead Discovery in Drug Design. *Nat. Rev. Drug Discov.* **1,** 45–54 (2002).

343. Wlodawer, A., Minor, W., Dauter, Z. & Jaskolski, M. Protein crystallography for

aspiring crystallographers or how to avoid pitfalls and traps in macromolecular structure determination. *FEBS J.* **280,** 5705–5736 (2013).

344. Liu, G. *et al.* NMR data collection and analysis protocol for high-throughput protein structure determination. *Proc. Natl. Acad. Sci. U. S. A.* **102,** 10487–92 (2005).

345. Laskowski, R. a. *Structural quality assurance*. *Structural Bioinformatics* **44,** (2005).

346. Pellecchia, M. *et al.* Perspectives on NMR in drug discovery: a technique comes of age. *Nat. Rev. Drug Discov.* **7,** 738–745 (2008).

347. Mertens, H. D. T. & Svergun, D. I. Structural characterization of proteins and complexes using small-angle X-ray solution scattering. *J. Struct. Biol.* **172,** 128–141 (2010).

348. Volkov, V. V. & Svergun, D. I. Uniqueness of ab initio shape determination in small-angle scattering. *J. Appl. Crystallogr.* **36,** 860–864 (2003).

349. Svergun, D. I. & Koch, M. H. J. Small-angle scattering studies of biological macromolecules in solution. *Reports Prog. Phys.* **66,** 1735–1782 (2003).

350. Tsutakawa, S. E., Hura, G. L., Frankel, K. A., Cooper, P. K. & Tainer, J. A. Structural analysis of flexible proteins in solution by small angle X-ray scattering combined with crystallography. *J. Struct. Biol.* **158,** 214–223 (2007).

351. Snyder, D. A. *et al.* Comparisons of NMR spectral quality and success in crystallization demonstrate that NMR and X-ray crystallography are complementary methods for small protein structure determination. *J. Am. Chem. Soc.* **127,** 16505–16511 (2005).

352. Kojima, M. *et al.* Structural refinement by restrained molecular-dynamics algorithm with small-angle X-ray scattering constraints for a biomolecule. *J. Appl. Crystallogr.* **37,** 103–109 (2004).

353. Putnam, C. D., Hammel, M., Hura, G. L. & Tainer, J. A. X-ray solution scattering (SAXS) combined with crystallography and computation: defining accurate macromolecular structures, conformations and assemblies in solution. *Q. Rev. Biophys.* **40,** 191–285 (2007).

354. Lever, R. & Page, C. P. Novel Drug Development Opportunities for Heparin. *Nat. Rev. Drug Discov.* **1,** 140–148 (2002).

355. Antalek, B. Using pulsed gradient spin echo NMR for chemical mixture analysis: How to obtain optimum results. *Concepts Magn. Reson. Part A Bridg. Educ. Res.* **14,** 225–258 (2002).

356. Borbat, P. P. & Freed, J. H. Pulse Dipolar Electron Spin Resonance: Distance Measurements. in *Structural Information from Spin-Labels and Intrinsic Paramagnetic Centres in the Biosciences* 1–82 (2013). doi:10.1007/430_2012_82

357. Sahu, I. D., McCarrick, R. M. & Lorigan, G. A. Use of electron paramagnetic resonance to solve biochemical problems. *Biochemistry* **52,** 5967–5984 (2013).

358. Fafarman, A. T., Borbat, P. P., Freed, J. H. & Kirshenbaum, K. Characterizing the structure and dynamics of folded oligomers: Pulsed ESR studies of peptoid helices. *Chem. Commun.* 377–379 (2007). doi:10.1039/B612198E

359. Godt, A., Schulte, M., Zimmermann, H. & Jeschke, G. How Flexible Are Poly(para-phenyleneethynylene)s? *Angew. Chemie* **118,** 7722–7726 (2006).

360. Pfannebecker, V. *et al.* Determination of End-to-End Distances in Oligomers by Pulsed EPR. *J. Phys. Chem.* **100,** 13428–13432 (1996).

361. Banham, J. E. *et al.* Distance measurements in the borderline region of applicability of CW EPR and DEER: A model study on a homologous series of spin-labelled peptides. *J. Magn. Reson.* **191,** 202–218 (2008).

362. Macchioni, A., Ciancaleoni, G., Zuccaccia, C. & Zuccaccia, D. Determining accurate molecular sizes in solution through NMR diffusion spectroscopy. *Chem. Soc. Rev.* **37,** 479–489 (2008).

363. Murnen, H. K., Rosales, A. M., Dobrynin, A. V., Zuckermann, R. N. & Segalman, R. A. Persistence length of polyelectrolytes with precisely located charges. *Soft Matter* **9,** 90–98 (2013).

364. Schulze, B. M., Watkins, D. L., Zhang, J., Ghiviriga, I. & Castellano, R. K. Estimating the shape and size of supramolecular assemblies by variable temperature diffusion ordered spectroscopy. *Org Biomol Chem* **12,** 7932–7936 (2014).

365. Perrin, F. Mouvement brownien d'un ellipsoide - I. Dispersion diélectrique pour des molécules ellipsoidales. *J. Phys. le Radium* **5,** 497–511 (1934).

366. Perrin, F. Mouvement Brownien d'un ellipsoide (II). Rotation libre et dépolarisation des fluorescences. Translation et diffusion de molécules ellipsoidales. *J. Phys. le Radium* **7,** 1–11 (1936).

367. Koenig, S. H. Brownian Motion of an Ellipsoid: A correction to Perrin's Results. *Biopolymers* **14,** 2421–2423 (1975).

368. Ortega, A. & García de la Torre, J. Hydrodynamic properties of rodlike and

disklike particles in dilute solution. *J. Chem. Phys.* **119,** 9914 (2003).

369. Barrowcliffe, T. W. History of Heparin. in *Handbook of Experimental Pharmacology: Heparin - A Century of Progress* (eds. Lever, R., Mulloy, B. & Page, C.) 3–22 (Springer, Berlin, Heidelberg, 2012). doi:10.1007/978-3-642-23056-1_1

370. Nimjee, S. M., Povsic, T. J., Sullenger, B. A. & Becker, R. C. Translation and Clinical Development of Antithrombotic Aptamers. *Nucleic Acid Ther.* **00,** nat.2015.0581 (2016).

371. Di Nisio, M., Middeldorp, S. & Büller, H. R. Direct Thrombin Inhibitors. *N. Engl. J. Med.* **353,** 1028–1040 (2005).

372. Lee, C. J. & Ansell, J. E. Direct thrombin inhibitors. *Br. J. Clin. Pharmacol.* **72,** 581–592 (2011).

373. Mehta, A. Y., Jin, Y. & Desai, U. R. An update on recent patents on thrombin inhibitors (2010 - 2013). *Expert Opin. Ther. Pat.* **24,** 47–67 (2014).

374. Glauser, B. F., Mourão, P. A. S. & Pomin, V. H. *Marine Sulfated Glycans with Serpin-Unrelated Anticoagulant Properties*. *Advances in Clinical Chemistry* **62,** (Elsevier Inc., 2013).

375. Adams, R. L. C. & Bird, R. J. Review article: Coagulation cascade and therapeutics update: Relevance to nephrology. Part 1: Overview of coagulation, thrombophilias and history of anticoagulants. *Nephrology* **14,** 462–470 (2009).

376. Olson, S. T., Björk, I. & Shore, J. D. Kinetic Characterization of Heparin-Catalyzed and Uncatalyzed Inhibition of Blood Coagulation Proteinases by Antithrombin. *Methods Enzymol.* **222,** 525–559 (1993).

377. Desai, U. R., Petitou, M., Björk, I. & Olson, S. T. Mechanism of heparin activation of antithrombin. Role of individual residues of the pentasaccharide activating sequence in the recognition of native and activated states of antithrombin. *J. Biol. Chem.* **273,** 7478–7487 (1998).

378. Boothello, R. S. *et al.* Chemoenzymatically Prepared Heparan Sulfate Containing Rare 2-O-Sulfonated Glucuronic Acid Residues. *ACS Chem. Biol.* **10,** 1485–1494 (2015).

379. Henry, B. L., Monien, B. H., Bock, P. E. & Desai, U. R. A novel allosteric pathway of thrombin inhibition: Exosite II mediated potent inhibition of thrombin by chemo-enzymatic, sulfated dehydropolymers of 4-hydroxycinnamic acids. *J. Biol. Chem.* **282,** 31891–31899 (2007).

380. Gunnarsson, G. T. & Desai, U. R. Exploring new non-sugar sulfated molecules as activators of antithrombin. *Bioorganic Med. Chem. Lett.* **13,** 679–683 (2003).

381. Alexej, J. & Norbert, M. Suppression of Convection Artifacts in Stimulated-Echo Diffusion Experiemnts. Double-Stimulated-Echo Experiments. *J. Magn. Reson.* **375,** 372–375 (1997).

382. Holz, M., Heil, S. R. & Sacco, A. Temperature-dependent self-diffusion coefficients of water and six selected molecular liquids for calibration in accurate 1H NMR PFG measurements. *Phys. Chem. Chem. Phys.* **2,** 4740–4742 (2000).

383. Longsworth, L. G. The mutual diffusion of light and heavy water. *J. Phys. Chem.* **64,** 1914–1917 (1960).

384. Lapham, J., Rife, J. P., Moore, P. B. & Crothers, D. M. Measurement of diffusion constants for nucleic acids by NMR. *J. Biomol. NMR* **10,** 255–62 (1997).

385. Plimpton, S. Fast Parallel Algorithms for Short-Range Molecular Dynamics. *Journal of Computational Physics* **117,** 1–19 (1995).

386. Jorgensen, W. L., Maxwell, D. S. & Tirado-Rives, J. Development and Testing of the OLPS All-Atom Force Field on Conformational Energetics and Properties of Organic Liquids. *J. Am. Chem. Soc.* **118,** 11225–11236 (1996).

387. Canongia Lopes, J. N., Pádua, A. A. H. & Shimizu, K. Molecular Force Field for Ionic Liquids IV: Trialkylimidazolium and Alkoxycarbonyl-Imidazolium Cations; Alkylsulfonate and Alkylsulfate Anions. *J. Phys. Chem. B* **112,** 5039–5046 (2008).

388. Canongia Lopes, J. N. & Pádua, A. A. H. CL&P: A generic and systematic force field for ionic liquids modeling. *Theor. Chem. Acc.* **131,** 1–11 (2012).

389. Jorgensen, W. L., Chandrasekhar, J., Madura, J. D., Impey, R. W. & Klein, M. L. Comparison of simple potential functions for simulating liquid water. *J. Chem. Phys.* **79,** 926–935 (1983).

390. Chen, H. C. & Chen, S. H. Diffusion of crown ethers in alcohols. *J. Phys. Chem.* **88,** 5118–5121 (1984).

391. Grant, A. C., Linhardt, R. J., Fitzgerald, G. L., Park, J. J. & Langer, R. Metachromatic activity of heparin and heparin fragments. *Anal. Biochem.* **137,** 25–32 (1984).

392. Shriver, Z. *et al.* Cleavage of the antithrombin III binding site in heparin by heparinases and its implication in the generation of low molecular weight heparin. *Proc. Natl. Acad. Sci.* **97,** 10365–10370 (2000).

393. Centers for Disease Control and Prevention. Outpatient antibiotic prescriptions

— United States, 2015. https://www.cdc.gov/antibiotic-use/community/pdfs/Annual-Report-2015.pdf.

394. Payne, D. J., Gwynn, M. N., Holmes, D. J. & Pompliano, D. L. Drugs for bad bugs: confronting the challenges of antibacterial discovery. *Nat. Rev. Drug Discov.* **6,** 29–40 (2007).

395. Klein, E. Y. *et al.* Global increase and geographic convergence in antibiotic consumption between 2000 and 2015. *Proc. Natl. Acad. Sci.* **115,** E3463–E3470 (2018).

396. Review on Antimicrobial Resistance. Antimicrobial Resistance: Tackling a Crisis for the Health and Wealth of Nations. 2014.

397. Arias, C. A. & Murray, B. E. Antibiotic-Resistant Bugs in the 21st Century — A Clinical Super-Challenge. *N. Engl. J. Med.* **360,** 439–443 (2009).

398. Hancock, R. E. W. & Sahl, H. G. Antimicrobial and host-defense peptides as new anti-infective therapeutic strategies. *Nat. Biotechnol.* **24,** 1551–1557 (2006).

399. Zasloff, M. Antimicrobial peptides of multicellular organisms. *Nature* **415,** 389–395 (2002).

400. Melo, M. N., Ferre, R. & Castanho, M. A. R. B. Antimicrobial peptides: Linking partition, activity and high membrane-bound concentrations. *Nat. Rev. Microbiol.* **7,** 245–250 (2009).

401. Hall, K., Lee, T.-H., Mechler, A. I., Swann, M. J. & Aguilar, M.-I. Real-time Measurement of Membrane Conformational States Induced by Antimicrobial Peptides: Balance Between Recovery and Lysis. *Sci. Rep.* **4,** 1–9 (2014).

402. Andersson, D. I., Hughes, D. & Kubicek-Sutherland, J. Z. Mechanisms and

consequences of bacterial resistance to antimicrobial peptides. *Drug Resist. Updat.* **26,** 43–57 (2016).

403. Pachón-Ibáñez, M. E., Smani, Y., Pachón, J. & Sánchez-Céspedes, J. Perspectives for clinical use of engineered human host defense antimicrobial peptides. *FEMS Microbiol. Rev.* **41,** 323–342 (2017).

404. Brogden, K. A. Antimicrobial peptides: pore formers or metabolic inhibitors in bacteria? *Nat. Rev. Microbiol.* **3,** 238–50 (2005).

405. Almeida, P. F. & Pokorny, A. Mechanisms of antimicrobial, cytolytic, and cell-penetrating peptides: From kinetics to thermodynamics. *Biochemistry* **48,** 8083–8093 (2009).

406. Palumbi, S. R. Humans as the World's Greatest Evolutionary Force. *Science (80-.).* **293,** 1786–1790 (2001).

407. Fjell, C. D., Hiss, J. A., Hancock, R. E. W. & Schneider, G. Designing antimicrobial peptides: Form follows function. *Nat. Rev. Drug Discov.* **11,** 37–51 (2012).

408. Lee, M. T. *et al.* Molecular State of the Membrane-Active Antibiotic Daptomycin. *Biophys. J.* **113,** 82–90 (2017).

409. Baltz, R. H. Daptomycin: mechanisms of action and resistance, and biosynthetic engineering. *Curr. Opin. Chem. Biol.* **13,** 144–151 (2009).

410. Van Epps, H. L. René Dubos: unearthing antibiotics. *J. Exp. Med.* **203,** 259–259 (2006).

411. Lim, L. M. *et al.* Resurgence of colistin: A review of resistance, toxicity, pharmacodynamics, and dosing. *Pharmacotherapy* **30,** 1279–1291 (2010).

412. Prenner, E. J., Lewis, R. N. A. H., Jelokhani-Niaraki, M., Hodges, R. S. & McElhaney, R. N. Cholesterol attenuates the interaction of the antimicrobial peptide gramicidin S with phospholipid bilayer membranes. *Biochim. Biophys. Acta - Biomembr.* **1510,** 83–92 (2001).

413. Bolt, H. L. *et al.* Exploring the links between peptoid antibacterial activity and toxicity. *Med. Chem. Commun.* **8,** 886–896 (2017).

414. Epand, R. F., Raguse, T. L., Gellman, S. H. & Epand, R. M. Antimicrobial 14-helical β-peptides: Potent bilayer disrupting agents. *Biochemistry* **43,** 9527–9535 (2004).

415. Hamuro, Y., Schneider, J. P. & DeGrado, W. F. De Novo Design of Antibacterial β-Peptides. *J. Am. Chem. Soc.* **121,** 12200–12201 (1999).

416. Porel, M., Thornlow, D. N., Phan, N. N. & Alabi, C. A. Sequence-defined bioactive macrocycles via an acid-catalysed cascade reaction. *Nat. Chem.* **8,** 590–596 (2016).

417. Ma, Z. *et al.* Insights into the Antimicrobial Activity and Cytotoxicity of Engineered α-Helical Peptide Amphiphiles. *J. Med. Chem.* **59,** 10946–10962 (2016).

418. Zelezetsky, I. *et al.* Controlled alteration of the shape and conformational stability of α-helical cell-lytic peptides: effect on mode of action and cell specificity. *Biochem. J.* **390,** 177–188 (2005).

419. Chen, Y. *et al.* Role of peptide hydrophobicity in the mechanism of action of α-helical antimicrobial peptides. *Antimicrob. Agents Chemother.* **51,** 1398–1406 (2007).

420. Fernandes, P. & Martens, E. Antibiotics in late clinical development. *Biochem. Pharmacol.* **133,** 152–163 (2017).

421. Yin, L. M., Edwards, M. A., Li, J., Yip, C. M. & Deber, C. M. Roles of hydrophobicity and charge distribution of cationic antimicrobial peptides in peptide-membrane interactions. *J. Biol. Chem.* **287,** 7738–7745 (2012).

422. Matsuzaki, K. Control of cell selectivity of antimicrobial peptides. *Biochim. Biophys. Acta - Biomembr.* **1788,** 1687–1692 (2009).

423. Artim, C. M., Phan, N. N. & Alabi, C. A. Effect of Composition on Antibacterial Activity of Sequence-Defined Cationic Oligothioetheramides. *ACS Infect. Dis.* **4,** 1257–1263 (2018).

424. Brogden, N. K. & Brogden, K. A. Will new generations of modified antimicrobial peptides improve their potential as pharmaceuticals? *Int. J. Antimicrob. Agents* **38,** 217–225 (2011).

425. Mariathasan, S. & Tan, M. W. Antibody–Antibiotic Conjugates: A Novel Therapeutic Platform against Bacterial Infections. *Trends Mol. Med.* **23,** 135–149 (2017).

426. Hirst, D. J., Lee, T. H., Swann, M. J. & Aguilar, M. I. Combined mass and structural kinetic analysis of multistate antimicrobial peptide-membrane interactions. *Anal. Chem.* **85,** 9296–9304 (2013).

427. Olaru, A., Gheorghiu, M., David, S., Wohland, T. & Gheorghiu, E. Assessment of the multiphase interaction Between a membrane disrupting peptide and a lipid membrane. *J. Phys. Chem. B* **113,** 14369–14380 (2009).

428. Cho, N.-J., Frank, C. W., Kasemo, B. & Höök, F. Quartz crystal microbalance

with dissipation monitoring of supported lipid bilayers on various substrates. *Nat. Protoc.* **5,** 1096–1106 (2010).

429. Hsia, C.-Y., Chen, L., Singh, R. R., DeLisa, M. P. & Daniel, S. A Molecularly Complete Planar Bacterial Outer Membrane Platform. *Sci. Rep.* **6,** 32715 (2016).

430. Lee, T. H., Hirst, D. J. & Aguilar, M. I. New insights into the molecular mechanisms of biomembrane structural changes and interactions by optical biosensor technology. *Biochim. Biophys. Acta - Biomembr.* **1848,** 1868–1885 (2015).

431. Mottamal, M., Shen, S., Guembe, C. & Krilov, G. Solvation of transmembrane proteins by isotropic membrane mimetics: A molecular dynamics study. *J. Phys. Chem. B* **111,** 11285–11296 (2007).

432. Girvin, M. E., Rastogi, V. K., Abildgaard, F., Markley, J. L. & Fillingame, R. H. Solution Structure of the Transmembrane H + -Transporting Subunit c of the F 1 F o ATP Synthase †. *Biochemistry* **37,** 8817–8824 (1998).

433. Osby, J. O., Martin, M. G. & Ganem, B. An exceptionally mild deprotection of phthalimides. *Tetrahedron Lett.* **25,** 2093–2096 (1984).

434. Skou, S., Gillilan, R. E. & Ando, N. Synchrotron-based small-angle X-ray scattering of proteins in solution. *Nat. Protoc.* **9,** 1727–39 (2014).

435. Hopkins, J. B., Gillilan, R. E. & Skou, S. BioXTAS RAW: Improvements to a free open-source program for small-angle X-ray scattering data reduction and analysis. *J. Appl. Crystallogr.* **50,** 1545–1553 (2017).

436. Ramamoorthy, A., Thennarasu, S., Lee, D. K., Tan, A. & Maloy, L. Solid-state NMR investigation of the membrane-disrupting mechanism of antimicrobial

peptides MSI-78 and MSI-594 derived from magainin 2 and melittin. *Biophys. J.* **91,** 206–216 (2006).

437. Hladky, S. B. & Rink, T. J. Potential difference and the distribution of ions across the human red blood cell membrane; a study of the mechanism by which the fluorescent cation, diS-C3-(5) reports membrane potential. *J. Physiol.* **263,** 287–319 (1976).

438. Fukunaga, B. T., Sumida, W. K., Taira, D. A., Davis, J. W. & Seto, T. B. Hospital-Acquired Methicillin-resistant Staphylococcus aureus Bacteremia Related to Medicare Antibiotic Prescriptions: A State-Level Analysis. *Hawaii. J. Med. Public Health* **75,** 303–309 (2016).

439. Heath, G. R. *et al.* Layer-by-layer assembly of supported lipid bilayer poly-l-lysine multilayers. *Biomacromolecules* **17,** 324–335 (2016).

440. Patra, S. K., Alonso, A. & Goñi, F. M. Detergent solubilisation of phospholipid bilayers in the gel state: the role of polar and hydrophobic forces. *Biochim. Biophys. Acta - Biomembr.* **1373,** 112–118 (1998).

441. Papo, N. & Shai, Y. Exploring peptide membrane interaction using surface plasmon resonance: Differentiation between pore formation versus membrane disruption by lytic peptides. *Biochemistry* **42,** 458–466 (2003).

442. Mozsolits, H. & Aguilar, M. I. Surface plasmon resonance spectroscopy: An emerging tool for the study of peptide-membrane interactions. *Biopolym. - Pept. Sci. Sect.* **66,** 3–18 (2002).

443. Rakowska, P. D. *et al.* Nanoscale imaging reveals laterally expanding antimicrobial pores in lipid bilayers. *Proc. Natl. Acad. Sci.* **110,** 8918–8923

(2013).

444. Hayouka, Z. *et al.* Binary Encoding of Random Peptide Sequences for Selective and Differential Antimicrobial Mechanisms. *Angew. Chemie Int. Ed.* **56,** 8099–8103 (2017).

445. Järvå, M. *et al.* X-ray structure of a carpet-like antimicrobial defensin–phospholipid membrane disruption complex. *Nat. Commun.* **9,** 1962 (2018).

446. Datta, A. *et al.* Antimicrobial Peptides: Insights into Membrane Permeabilization, Lipopolysaccharide Fragmentation and Application in Plant Disease Control. *Sci. Rep.* **5,** 11951 (2015).

447. Nederberg, F. *et al.* Biodegradable nanostructures with selective lysis of microbial membranes. *Nat. Chem.* **3,** 409–414 (2011).

448. Gee, M. L. *et al.* Imaging the action of antimicrobial peptides on living bacterial cells. *Sci. Rep.* **3,** 1–6 (2013).

449. Mozsolits, H., Wirth, H. J., Werkmeister, J. & Aguilar, M. I. Analysis of antimicrobial peptide interactions with hybrid bilayer membrane systems using surface plasmon resonance. *Biochim. Biophys. Acta* **1512,** 64–76 (2001).

450. Wang, C. Z. *et al.* Synthesis and characterization of cationic polymeric nanoparticles as simvastatin carriers for enhancing the osteogenesis of bone marrow mesenchymal stem cells. *J. Colloid Interface Sci.* **432,** 190–199 (2014).

451. Arbuse, A. *et al.* DNA-cleavage induced by new macrocyclic schiff base dinuclear Cu(I) complexes containing pyridyl pendant arms. *Inorg. Chem.* **48,** 11098–11107 (2009).

452. Salzberg, L. I. & Helmann, J. D. Phenotypic and transcriptomic characterization

of Bacillus subtilis mutants with grossly altered membrane composition. *J. Bacteriol.* **190,** 7797–7807 (2008).

453. Beining, P. R., Huff, E., Prescott, B. & Theodore, T. S. Characterization of the lipids of mesosomal vesicles and plasma membranes from Staphylococcus aureus. *J. Bacteriol.* **121,** 137–143 (1975).

454. Cheng, J. T. J., Hale, J. D., Elliott, M., Hancock, R. E. W. & Straus, S. K. The importance of bacterial membrane composition in the structure and function of aurein 2.2 and selected variants. *Biochim. Biophys. Acta - Biomembr.* **1808,** 622–633 (2011).

455. Mishra, N. N. & Bayer, A. S. Correlation of cell membrane lipid profiles with daptomycin resistance in methicillin-resistant staphylococcus aureus. *Antimicrob. Agents Chemother.* **57,** 1082–1085 (2013).

456. Haest, C. W. M., De Gier, J., Op Den Kamp,]J.A.F., Bartels, P. & Van Deenen, L. L. M. Changes in permeability of Staphylococcus aureus and derived liposomes with varying lipid composition. *Biochim. Biophys. Acta - Biomembr.* **255,** 720–733 (1972).

457. Yasuhiro, K., Tieko, Y. & Hideo, H. Alteration of the phospholipid composition of Staphylo-coccus aureus cultured in medium containing NaCl. *Biochim. Biophys. Acta - Lipids Lipid Metab.* **280,** 444–450 (1972).

458. García-Fernández, E. *et al.* Membrane Microdomain Disassembly Inhibits MRSA Antibiotic Resistance. *Cell* **171,** 1354–1367.e20 (2017).

459. Tsai, M. *et al.* Staphylococcus aureus requires cardiolipin for survival under conditions of high salinity. *BMC Microbiol.* **11,** (2011).

460. Mishra, N. N. *et al.* Carotenoid-related alteration of cell membrane fluidity impacts Staphylococcus aureus susceptibility to host defense peptides. *Antimicrob. Agents Chemother.* **55,** 526–531 (2011).

461. Hayami, M., Okabe, A., Kariyama, R. & Kanemasa, Y. Lipid Composition of Staphylococcus and Its Derived L-forms. *Microbiol. Immunol.* **23,** 435–442 (1979).

462. White, D. C. & Frerman, F. E. Extraction, Characterization, and Cellular Localization of the Lipids of Staphylococcus aureus. *J. Bacteriol.* **94,** 1854–1867 (1967).

463. White, D. C. & Frerman, F. E. Fatty acid composition of the complex lipids of Staphylococcus aureus during the formation of the membrane-bound electron transport system. *J. Bacteriol.* **95,** 2198–2209 (1968).

464. Short, S. A. & White, D. C. Metabolism of the glycosyl diglycerides and phosphatidylglucose of Staphylococcus aureus. *J. Bacteriol.* **104,** 126–32 (1970).

465. Liu, H. Y. *et al.* Supported Planar Mammalian Membranes as Models of in Vivo Cell Surface Architectures. *ACS Appl. Mater. Interfaces* **9,** 35526–35538 (2017).

466. Soumpasis, D. M. Theoretical analysis of fluorescence photobleaching recovery experiments. *Biophys. J.* **41,** 95–97 (1983).

467. Zack, G. W., Rogers, W. E. & Latt, S. A. Automatic measurement of sister chromatid exchange frequency. *J. Histochem. Cytochem.* **25,** 741–53 (1977).

468. Locock, K. E. S. *et al.* Guanylated Polymethacrylates: A Class of Potent Antimicrobial Polymers with Low Hemolytic Activity. *Biomacromolecules* **14,** 4021–4031 (2013).

469. Andreev, K. *et al.* Guanidino groups greatly enhance the action of antimicrobial peptidomimetics against bacterial cytoplasmic membranes. *Biochim. Biophys. Acta - Biomembr.* **1838,** 2492–2502 (2014).

470. Grace, J. L. *et al.* Cationic acrylate oligomers comprising amino acid mimic moieties demonstrate improved antibacterial killing efficiency. *J. Mater. Chem. B* **5,** 531–536 (2017).

471. Neue, U. D., Tran, K., Méndez, A. & Carr, P. W. The combined effect of silanols and the reversed-phase ligand on the retention of positively charged analytes. *J. Chromatogr. A* **1063,** 35–45 (2005).

472. Sokolowski, A. & Wahlund, K.-G. Peak tailing and retention behaviour of tricyclic antidepressant amines and related hydrophobic ammonium compounds in reversed-phase ion-pair liquid chromatography on alkyl-bonded phases. *J. Chromatogr. A* **189,** 299–316 (1980).

473. Hof, W. van t, Veerman, E. C. I., Helmerhorst, E. J. & Amerongen, A. V. N. Antimicrobial Peptides: Properties and Applicability. *Biol. Chem.* **382,** 597–619 (2005).

474. Mahlapuu, M., Håkansson, J., Ringstad, L. & Björn, C. Antimicrobial Peptides: An Emerging Category of Therapeutic Agents. *Front. Cell. Infect. Microbiol.* **6,** 1–12 (2016).

475. Guilhelmelli, F. *et al.* Antibiotic development challenges: the various mechanisms of action of antimicrobial peptides and of bacterial resistance. *Antimicrob. Resist. Chemother.* **4,** 353 (2013).

476. Yarlagadda, V. *et al.* Glycopeptide Antibiotic To Overcome the Intrinsic

Resistance of Gram-Negative Bacteria. *ACS Infect. Dis.* **2,** 132–139 (2016).

477. M.L., L. *et al.* Epidemiology of Staphylococcus aureus blood and skin and soft tissue infections in the US Military Health System, 2005-2010. *JAMA - J. Am. Med. Assoc.* **308,** 50–59 (2012).

478. Ellis, M. W. *et al.* Presence and molecular epidemiology of virulence factors in Methicillin-resistant Staphylococcus aureus strains colonizing and infecting soldiers. *J. Clin. Microbiol.* **47,** 940–945 (2009).

479. Wiegand, I., Hilpert, K. & Hancock, R. E. W. Agar and broth dilution methods to determine the minimal inhibitory concentration (MIC) of antimicrobial substances. *Nat. Protoc.* **3,** 163–175 (2008).

480. Ouchi, M., Badi, N., Lutz, J.-F. & Sawamoto, M. Single-chain technology using discrete synthetic macromolecules. *Nat. Chem.* **3,** 917–924 (2011).

481. Terashima, T., Sugita, T., Fukae, K. & Sawamoto, M. Synthesis and single-chain folding of amphiphilic random copolymers in water. *Macromolecules* **47,** 589–600 (2014).

482. Perez-Baena, I. *et al.* Endowing single-chain polymer nanoparticles with enzyme-mimetic activity. *ACS Macro Lett.* **2,** 775–779 (2013).

483. Kulkarni, C., Meijer, E. W. & Palmans, A. R. A. Cooperativity Scale: A Structure-Mechanism Correlation in the Self-Assembly of Benzene-1,3,5-tricarboxamides. *Acc. Chem. Res.* **50,** 1928–1936 (2017).

484. Leeson, P. Drug discovery: Chemical beauty contest. *Nature* **481,** 455–456 (2012).

485. Roy, O. *et al.* The tert-butyl side chain: A powerful means to lock peptoid amide

bonds in the cis conformation. *Org. Lett.* **15,** 2246–2249 (2013).

486. You, W., Huang, Y. ming M., Kizhake, S., Natarajan, A. & Chang, C. en A. Characterization of Promiscuous Binding of Phosphor Ligands to Breast-Cancer-Gene 1 (BRCA1) C-Terminal (BRCT): Molecular Dynamics, Free Energy, Entropy and Inhibitor Design. *PLoS Comput. Biol.* **12,** 1–25 (2016).

487. Cozzini, P. *et al.* Target Flexibility: An Emerging Considertaion in Drug Discovery. *J. Med. Chem.* **51,** 6237–6255 (2008).

488. Bedini, E., Cirillo, L. & Parrilli, M. Versatile and self-assembling urea-linked neosaccharides from sugar aminoalcohols. *Tetrahedron* **69,** 1285–1296 (2013).

489. Kim, K.-H. & Miller, M. J. An enantioselective synthesis of the cyclopentene fragment of nucleoside Q. *Tetrahedron Lett.* **44,** 4571–4573 (2003).

490. Lee, M.-R., Raman, N., Ortiz-Bermúdez, P., Lynn, D. M. & Palecek, S. P. 14-Helical β-Peptides Elicit Toxicity against C. albicans by Forming Pores in the Cell Membrane and Subsequently Disrupting Intracellular Organelles. *Cell Chem. Biol.* **0,** 1–11 (2018).

491. Huang, H. W. Action of Antimicrobial Peptides: Two-State Model. *Biochemistry* **39,** 8347–8352 (2000).

492. Eisenberg, M., Hall, J. E. & Mead, C. A. The nature of the voltage-dependent conductance induced by alamethicin in black lipid membranes. *J. Membr. Biol.* **14,** 143–176 (1973).

493. Gordon, L. G. M. & Haydon, D. A. The unit conductance channel of alamethicin. *Biochim. Biophys. Acta - Biomembr.* **255,** 1014–1018 (1972).

494. Matsuzaki, K., Murase, O. & Miyajima, K. Kinetics of Pore Formation by an

Antimicrobial Peptide, Magainin 2, in Phospholipid Bilayers. *Biochemistry* **34,** 12553–12559 (1995).

495. Ludtke, S. J. *et al.* Membrane pores induced by magainin. *Biochemistry* **35,** 13723–13728 (1996).

496. Yamaguchi, S., Hong, T., Waring, A., Lehrer, R. I. & Hong, M. Solid-State NMR Investigations of Peptide−Lipid Interaction and Orientation of a β-Sheet Antimicrobial Peptide, Protegrin †. *Biochemistry* **41,** 9852–9862 (2002).

497. Lazaridis, T., He, Y. & Prieto, L. Membrane Interactions and Pore Formation by the Antimicrobial Peptide Protegrin. *Biophys. J.* **104,** 633–642 (2013).

498. Yang, L., Harroun, T. A., Weiss, T. M., Ding, L. & Huang, H. W. Barrel-stave model or toroidal model? A case study on melittin pores. *Biophys. J.* **81,** 1475–1485 (2001).

499. Zhou, L., Narsimhan, G., Wu, X. & Du, F. Pore formation in 1,2-dimyristoyl-sn-glycero-3-phosphocholine/cholesterol mixed bilayers by low concentrations of antimicrobial peptide melittin. *Colloids Surfaces B Biointerfaces* **123,** 419–428 (2014).

500. Hallock, K. J., Lee, D.-K. & Ramamoorthy, A. MSI-78, an Analogue of the Magainin Antimicrobial Peptides, Disrupts Lipid Bilayer Structure via Positive Curvature Strain. *Biophys. J.* **84,** 3052–3060 (2003).

501. Pouny, Y., Rapaport, D., Shai, Y., Mor, A. & Nicolas, P. Interaction of Antimicrobial Dermaseptin and its Fluorescently Labeled Analogs with Phospholipid Membranes. *Biochemistry* **31,** 12416–12423 (1992).

502. Gazit, E., Miller, I. R., Biggin, P. C., Sansom, M. S. P. & Shai, Y. Structure and

Orientation of the Mammalian Antibacterial Peptide Cecropin P1 within Phospholipid Membranes. *J. Mol. Biol.* **258,** 860–870 (1996).

503. Pukala, T. L., Brinkworth, C. S., Carver, J. A. & Bowie, J. H. Investigating the Importance of the Flexible Hinge in Caerin 1.1: Solution Structures and Activity of Two Synthetically Modified Caerin Peptides †. *Biochemistry* **43,** 937–944 (2004).

504. Yamaguchi, S. *et al.* Orientation and Dynamics of an Antimicrobial Peptide in the Lipid Bilayer by Solid-State NMR Spectroscopy. *Biophys. J.* **81,** 2203–2214 (2001).

505. Pitsalidis, C. *et al.* Biomimetic Electronic Devices for Measuring Bacterial Membrane Disruption. *Adv. Mater.* **30,** 1803130 (2018).

506. Svergun, D. I. Determination of the regularization parameter in indirect-transform methods using perceptual criteria. *J. Appl. Crystallogr.* **25,** 495–503 (1992).